



HAL
open science

Synthesis of hybrid core-shell nanoparticles for theranostic applications

Mathilde Ménard

► **To cite this version:**

Mathilde Ménard. Synthesis of hybrid core-shell nanoparticles for theranostic applications. Chemical Physics [physics.chem-ph]. Université de Strasbourg, 2017. English. NNT : 2017STRAE050 . tel-01820658

HAL Id: tel-01820658

<https://theses.hal.science/tel-01820658>

Submitted on 22 Jun 2018

HAL is a multi-disciplinary open access archive for the deposit and dissemination of scientific research documents, whether they are published or not. The documents may come from teaching and research institutions in France or abroad, or from public or private research centers.

L'archive ouverte pluridisciplinaire **HAL**, est destinée au dépôt et à la diffusion de documents scientifiques de niveau recherche, publiés ou non, émanant des établissements d'enseignement et de recherche français ou étrangers, des laboratoires publics ou privés.

École doctorale de Physique et Chimie-Physique (ED182)
INSERM U1121 Biomatériaux et Bioingénierie
Institut de Physique et Chimie des Matériaux de Strasbourg

THÈSE

présentée par :

Mathilde MENARD

Soutenue le : 06 juin 2017

pour obtenir le grade de :

Docteur de l'université de Strasbourg

Discipline/ Spécialité : Chimie-Physique des Matériaux

Synthèse de nanoparticules hybrides de type cœur-coquille à visées théranostiques

THÈSE dirigée par :

Pr. MEYER Florent

PU-PH, Faculté de chirurgie dentaire,
INSERM U1121, Strasbourg

Pr. BEGIN-COLIN Sylvie

Professeur, IPCMS Université de Strasbourg

RAPPORTEURS :

Dr. DURAND Jean-Olivier

Directeur de recherche, ICGM, Montpellier

Dr. BEGU Sylvie

Maître de conférences, ICGM, Montpellier

AUTRES MEMBRES DU JURY :

Dr. HEURTAULT Béatrice

Maître de conférences, UMR 7199, Strasbourg

Dr. SANDRE Olivier

Directeur de recherche, LCPO, Bordeaux

Remerciements

J'aimerais commencer par remercier les membres de mon jury, Dr. Jean-Olivier Durand, Dr. Sylvie Bégu, Dr. Béatrice Heurtault et Dr. Olivier Sandre pour avoir accepté de juger mes travaux de thèse. Merci tout particulièrement au Dr. Jean-Olivier Durand que j'ai eu le plaisir de rencontrer lors de conférences pour ses discussions passionnantes, sa grande gentillesse et son enthousiasme.

Je tiens à remercier Dr. Stefan Haacke et Dr. Carlo Massobrio pour m'avoir accueillie au sein de l'IPCMS et pour m'avoir amenée avec eux en conférence en Corée. Merci aux directeurs successifs du DCMI, Dr. Geneviève Pourroy, Dr. Pierre Rabu, et Pr. Natalie Viart pour leur accueil, leur sympathie et leur aide. Merci au Pr. Pierre Schaaf pour m'avoir permis d'effectuer une partie de ma thèse dans l'unité U1121 de l'INSERM.

Je tiens à exprimer ma plus profonde gratitude à mon directeur de thèse Pr. Florent Meyer. Merci pour ton écoute, ton soutien. Tu as été le phare qui m'a guidée jusqu'à la soutenance de cette thèse. J'espère avoir le plaisir de continuer à travailler avec toi dans le futur.

Je remercie également ma co-directrice de thèse Pr. Sylvie Bégin pour m'avoir fait découvrir le monde des nanoparticules superparamagnétiques et m'avoir permis de participer à plusieurs conférences.

Je remercie l'ensemble des membres de l'unité U1121 pour tous les bons moments passés avec eux, que ce soit au laboratoire ou à l'extérieur. Je remercie tout particulièrement Cynthia, Christine et Jean-Baptiste pour m'avoir formée à la culture cellulaire et Morgane pour m'avoir formée au confocal.

Un grand merci à mes anciens professeurs de l'ECPM : Pr. Aziz Dinia, Pr. Sylvie Bégin, Pr. Pierre Schaaf, Pr. Corinne Petit, Pr. Silviu Colis, Dr. Loïc Jerry, Dr. Benoît Pichon, Dr. François Roulland, Dr. Anne Carton... Beaucoup d'entre vous sont devenus des collègues par la suite et certains même des amis. Vous m'avez connue toute jeune, il y a 8 ans, et à vos côtés, grâce vos conseils, votre enseignement, votre bienveillance et votre soutien j'ai pu m'épanouir et construire mon projet professionnel.

Je tiens à exprimer une grande affection à mes 3 camarades de bureau actuels : Mathias, Elodie et Florian. Merci pour votre soutien quotidien, votre bonne humeur qui a fait du bureau un espace où nous nous sentions tous bien. Vous allez me manquer... Un merci tout particulier à Mathias avec qui j'ai partagé le bureau pendant 3 ans et demi. Je ne sais comment exprimer ma reconnaissance pour ton amitié, ta complicité et ton soutien au cours de cette thèse. Le mot merci semble faible... J'ai les larmes aux yeux à l'idée de partir et de ne plus voir ton sourire au quotidien (et de ne plus chanter avec toi sur les tubes de Nostalgie!).

Merci également à mes collègues du « bureau d'à côté » Cédric et Didier et leur acolyte Xavier pour les pauses cafés qui se terminent en fou rire. Merci pour les séances piscines très matinales et pour tous les petits pains au chocolat qui ont suivis! Enfin merci pour votre affection, votre amitié et votre soutien.

Merci aux Dr. Catalina Bordeianu, Dr. Jean-Louis Gallani, Dr. Audrey Parat, Dr. Bertrand Donnio, Dr. Stéphane Bellemin et Nicolas Beyer du DMO, mon lieu de refuge! Merci pour votre immense bienveillance, votre gentillesse et votre soutien. Un merci tout particulier à toi Catalina, mon amie, ma confidente. Je garde en mémoire tous les bons moments passés ensemble ces dernières années, nos voyages à Barcelone, en Corse, et j'espère que l'on se reverra bientôt même si les années de postdoc à venir risquent de nous éloigner pendant un moment...

Merci à l'ensemble des thésards et postdocs avec qui j'ai eu la chance de lier de belles amitiés: Dr. Filip Schleicher, Dr. Michal Studniarek, Dr. Jérôme Hurst, Dr. Manuel Gruber, Dr. Stanislav Makarchuk, Etienne Urbain, Ziyad Chaker, Dr. Zo Raolison, Dr. Wojciech Szewe, Dr. Yu Liu, Dr. Cristina Blanco-Andujar, Dr. Pierre Farger, Dr. Andra Craciun, Dr. Yanhui Wang, Dr. Ufuk Halisdemir, Beata Taudul, Quentin Evrard, Mathilde Boucher et Damien Bissessar.

Merci à mes amis du Club Alpin Français et de l'escalade qui m'ont permis d'appliquer à la lettre l'adage « Mens sana in corpore sano »: Médine, Ozan, Cécile, Jérôme, Julie, Fred B., Marco, Guido, Manon, Yvon, Michel, Fred, Myriam, Renaud, Sophie et Philippe. Et tout particulièrement un immense merci à Médine et Ozan pour m'avoir appris les bases de l'escalade et de l'alpinisme et pour m'avoir emmenée avec eux dans de nombreuses sorties. Merci pour ces bouffées d'oxygène et pour votre belle amitié.

Je tiens à remercier et à exprimer ma profonde affection à mes colocataires avec qui j'ai partagé l'appartement pendant plus de 4 ans : Saba, Aleksandra et Filip. C'est un déchirement de devoir vous quitter après avoir habité si longtemps avec vous... Merci pour les rires, les pleurs, les confidences, les sorties, les soirées dans la montagne, les voyages (Roumanie, Turquie, Pologne...) bref merci pour ces innombrables moments passés avec vous ces dernières années... Merci également à mes autres amis de Strasbourg avec qui j'ai passé des moments inoubliables: Elsa, Andres, Dzana, Maud, Michaël, Marilia et Martin. Je remercie enfin mes amis intimes loin géographiquement mais pourtant si proche dans mon cœur: Anne-Béatrice, Laetitia, Caroline, Chloé, Matthieu, Adam.

Pour finir je tiens à remercier les personnes les plus importantes dans ma vie: ma famille, pour leur amour inconditionnel. Merci à mes parents pour m'avoir toujours soutenue et m'avoir permis de faire de belles et grandes études. Merci à mon frère et ma sœur pour avoir été mes plus proches complices depuis toujours. Enfin je dédie cette thèse à mon grand-père et mon grand-oncle, décédés récemment et qui auraient été immensément fiers de ma réussite comme tout le reste de ma famille.

Ainsi comme ces quelques lignes de remerciements le montrent j'ai eu l'immense chance de rencontrer au cours de ces années des personnes formidables qui m'ont beaucoup appris autant humainement que professionnellement. Je terminerai donc sur une pointe d'humour (sûrement nécessaire avant de se plonger dans la lecture des 250 pages sérieuses qui suivent...) en citant une réplique culte ayant marquée l'adolescence de ma génération ¹:

"_ C'est une bonne situation ça ~~scribe~~ doctorant ?

_ Vous savez, moi je ne crois pas qu'il y ait de bonne ou de mauvaise situation. Moi, si je devais résumer ma vie aujourd'hui avec vous, je dirais que c'est d'abord des rencontres. Des gens qui m'ont tendu la main, peut-être à un moment où je ne pouvais pas, où j'étais seul chez moi. Et c'est assez

¹ Astérix et Obélix mission Cléopâtre

curieux de se dire que les hasards, les rencontres forgent une destinée... Parce que quand on a le goût de la chose, quand on a le goût de la chose bien faite, le beau geste, parfois on ne trouve pas l'interlocuteur en face je dirais, le miroir qui vous aide à avancer. Alors ça n'est pas mon cas, comme je disais là, puisque moi au contraire, j'ai pu : et je dis merci à la vie, je lui dis merci, je chante la vie, je danse la vie... je ne suis qu'amour ! Et finalement, quand beaucoup de gens aujourd'hui me disent « Mais comment fais-tu pour avoir cette humanité ? », et bien je leur réponds très simplement, je leur dis que c'est ce goût de l'amour ce goût donc qui m'a poussé aujourd'hui à entreprendre une ~~construction mécanique~~ thèse, mais demain qui sait ?" ... à suivre...

Table of content

Table of Abbreviations	viii
<u>Chapter 1: Literature review</u>	<u>5</u>
1 Mesoporous silica nanoparticles in nanomedicine (MS NPs).....	7
1.1 Synthesis of MS NPs.....	7
1.2 MS NPs for biological applications.....	11
2 Iron oxide nanoparticles (IO NPs)	13
2.1 IO NPs synthesis	13
2.1.1 Synthesis methods.....	13
2.1.2 Coprecipitation.....	14
2.1.3 Hydrothermal synthesis.....	14
2.1.4 Microemulsion.....	14
2.1.5 Thermal decomposition	15
2.1.6 Conclusion.....	15
2.2 Surface modification of IO NPs for stabilization in aqueous media.....	15
2.3 Biomedical applications of IO NPs.....	16
2.3.1 Diagnosis by magnetic resonance imaging (MRI)	16
2.3.1.1 Principle of MRI.....	16
2.3.1.2 MRI contrast agents.....	18
2.3.1.3 IO NPs as T ₂ contrast agents	19
2.3.2 Therapy by magnetic hyperthermia.....	24
3 Iron Oxide/Mesoporous silica core-shell nanostructures (IO@MS NPs) for theranostic applications	25
3.1 IO@MS synthesis.....	25
3.2 IO@MS NPs as theranostic agents	28
3.2.1 Diagnosis.....	28
3.2.2 Therapy	30
3.2.2.1 IO@MS NPs as therapeutics using magnetic hyperthermia	30
3.2.2.2 IO@MS NPs as cargo for drug delivery.....	30
4 HSA NPs for biomedical applications.....	35
<u>Chapter 2: Materials and Methods.....</u>	<u>37</u>
1 Characterization techniques.....	39
1.1 Physico-chemical analyses.....	39

1.1.1	Transmission electron microscopy (TEM)	39
1.1.2	Scanning electron microscopy (SEM)	39
1.1.3	Adsorption/Desorption nitrogen isotherms	40
1.1.4	Dynamic light scattering (DLS).....	42
1.1.5	Zeta potential	45
1.2	Composition analyses	46
1.2.1	Inductively coupled plasma-absorption emission spectroscopy (ICP-AES).....	46
1.2.2	Energy Dispersive X-ray spectroscopy (EDX)	46
1.2.3	Infra-red spectroscopy.....	47
1.2.4	Fluorescence and UV-vis spectroscopies	47
1.3	Magnetic resonance studies	47
1.3.1	Nuclear magnetic resonance (NMR) ¹ H relaxivity measurements	47
1.3.2	Magnetic resonance imaging (MRI).....	48
1.3.3	Magnetic hyperthermia (MH)	50
1.4	Biological studies	51
1.4.1	2D cell culture.....	51
1.4.1.1	Evaluation of NPs internalization by flow cytometry	51
1.4.1.2	Cytotoxicity studies by MTT assays.....	52
1.4.2	3D cell culture.....	52
1.4.2.1	Preparation of Huh7 MCTS.....	53
1.4.3	Evaluation of particle diffusion by imaging.....	54
1.4.3.1	Preparation of MCTS for confocal imaging.....	54
1.4.3.2	Principle of confocal laser scan microscopy (CLSM)	54
1.4.4	Evaluation of antitumoral effect on MCTS	54
1.5	Conclusion on characterization techniques.....	55
2	Experimental synthesis protocols	56
2.1	Synthesis of IO NPs.....	56
2.1.1	Protocol for 10 nm IO NPs.....	56
2.1.2	Protocols for 20 nm IO NPs.....	56
2.2	Synthesis of silica NPs.....	56
2.2.1	Protocol for Bimodal Mesoporous Silica NPs synthesis (BMS NPs).....	56
2.2.2	Protocol for small porosities silica synthesis (raspberry morphology: RB).....	57
2.2.3	Protocol for large porosities silica synthesis (stellar morphology: ST)	57
2.3	Protocol for core-shell particle synthesis	57
2.3.1	IO@RB.....	57

2.3.2	IO@ST	57
2.4	Standard protocol for IBAM-HSA coating on silica	58
2.5	Fluorescent labeling of HSA.....	58
2.6	Protocol for the synthesis of HSA _{Dox} NPs	59
2.6.1	Synthesis of maleimide-modified Doxorubicin (Dox-EMCH)	59
2.6.2	Synthesis of HSA-SPDP	59
2.6.3	Synthesis of Protein-Drug Conjugates HSA-Dox	59
2.6.4	Preparation of HSA _{Dox} NPs	59
<u>Chapter 3: Silanization of IO NPs for MRI applications</u>		61
1	Optimizing the silanization of thermally-decomposed iron oxide nanoparticles for efficient aqueous phase transfer and MRI applications	63
1.1	Abstract.....	63
1.2	Introduction	63
1.3	Silanization of oleic acid-coated IONPs.....	66
1.3.1	Starting conditions	66
1.3.2	Reference silanization method in hexane (De Palma et al. ²⁸).....	66
1.4	Results and discussion.....	67
1.4.1	Synthesis of iron oxide NPs by thermal decomposition.....	67
1.4.2	Grafting of APTS aminosilanes	67
1.4.2.1	Starting conditions.....	67
1.4.2.2	Influence of the reaction time	68
1.4.2.3	Influence of the stoichiometry	69
1.4.3	Grafting of TPED, TPDT aminosilanes	69
1.4.4	Grafting of TPEDTA carboxylate silanes.....	70
1.4.5	Evaluation of MRI contrast enhancement properties	71
1.4.6	Cell viability study.....	73
1.5	Conclusions.....	74
1.6	Supporting information.....	75
1.6.1	S1: FTIR follow-up of the purification of oleic acid-coated IONPs.....	75
1.6.2	S2: Dosage of Fe in IONPs by relaxometry.....	76
1.6.3	S3: FTIR study of IO-APTS NPs	76
1.6.4	S4: Energy dispersive X rays (EDX) analysis of IO-APTS NPs.....	77
1.6.5	S5: DLS size distribution of IO-TPED and IO-TPDT NPs in acidified water (pH=3.5)	77
1.6.6	S6: FTIR spectra of TPED and TPDT grafted IO-NPs	78
1.6.7	S7: Energy dispersive X rays (EDX) analysis of IO -TPEDTA NPs	78

1.6.8	S8: Tables.....	78
<u>Chapter 4: MS NPs as sacrificial templates for the formation of Dox-loaded HSA NPs 81</u>		
1	Introduction.....	83
2	Large pores mesoporous silica: Bimodal Mesoporous Silica Nanoparticles (BMS NPs).....	85
2.1	Introduction	85
2.2	Synthesis.....	85
2.2.1	Synthesis strategy	85
2.2.2	Control of size and porosity.....	86
2.2.2.1	Influence of the PAA dissolution.....	86
2.2.2.2	Influence of the temperature.....	88
2.2.2.3	PAA quantities variation.....	91
2.3	Self-supported vesicles for drug delivery.....	93
2.3.1	Dox covalent grafting to HSA.....	93
2.3.1.1	Grafting strategy	93
2.3.1.2	Results and discussions	94
2.3.2	HSA coating on BMS NPs.....	95
2.3.3	HSA _{DOX} nanoparticles.....	96
2.4	Conclusion and outlooks.....	97
3	Mesoporous silica with small porosity: Raspberry morphology (RB)	98
3.1	Introduction	98
3.2	Synthesis and characterization of RB and RB-NH ₂ NPs.....	99
3.2.1	Synthesis protocol	99
3.2.2	Characterization of the RB and RB-NH ₂ NPs.....	99
3.3	Dox loading studies on RB-NH ₂ in water.....	102
3.3.1	Protocol.....	102
3.3.2	Results and discussion.....	103
3.3.2.1	Dox loading study.....	103
3.3.2.2	Estimation of Dox release from Dox loaded RB-NH ₂ NPs after solvent exchange from water to DMF (necessary for IBAM coupling).....	104
3.3.2.3	Influence of RB-NH ₂ aging on Dox loading.....	106
3.4	Protein coating studies on RB-IBAM.....	107
3.4.1	Protocol.....	107
3.4.2	Results and discussion.....	107
3.5	HSA capsules formation by silica dissolution	109
3.5.1	Silica dissolution trials with NaOH	109

3.5.2	Silica dissolution trials with HF.....	111
3.6	Dox-HSA nanocapsules: cargo for drug delivery	112
3.6.1	Synthesis	112
3.6.2	Characterization of RB-Dox-HSA NPs	112
3.6.3	Estimation of Dox loading.....	114
3.6.4	Dox-HSA nanocapsules formation.....	116
3.6.5	Drug release from capsules degradation by proteases	119
3.6.6	Multicellular spheroids growth inhibition study	119
3.7	Conclusion and outlooks.....	121
Chapter 5: IO@RB core-shell NPs as theranostic agents		123
1	Introduction.....	125
2	Synthesis	125
2.1	Parameter influences	125
2.1.1	Establishment of the best protocol inspired from literature	125
2.1.1.1	Highlighting of the phase transfer importance.....	126
2.1.1.2	Base type for base-catalyzed sol-gel process.....	128
2.1.1.3	Reactant molar ratio for controlling IO@RB sizes.....	128
2.1.1.4	In-situ silanization trials.....	129
2.1.1.5	Conclusion	129
2.1.2	Scale-up.....	131
2.1.3	Influence of [CTAB]/[Fe] ratio on shell thickness	134
2.2	Washing steps versus calcination	136
2.3	Characterization of IO@RB NPs.....	139
3	Evaluation of MRI contrast properties of IO@RB and IO@RB-HSA	142
4	Dox impregnation and release studies	144
4.1	Introduction	144
4.2	Dox impregnation in the porosities.....	144
4.2.1	Influence of the surface modification	144
4.2.2	Influence of the solvent	145
4.2.2.1	Experimental procedure.....	145
4.2.2.2	Results and discussions	146
4.2.3	Conclusions on Dox impregnation studies	148
4.3	Dox release studies	149
4.3.1	Concept validation: degradation of the protein shell.....	149
4.3.2	Dox release trials.....	150

5	Dox encapsulation in IO@RB NPs by IBAM-HSA versus HSA-IBAM-HSA coatings..	152
5.1	Introduction	152
5.2	Protocols and observations	152
5.2.1	Synthesis of IO@RB NPs of 30 nm	152
5.2.2	Silanization of the batches.....	152
5.2.3	Synthesis of IO@RB-Dox-HSA-IBAM-HSA and IO@RB-Dox-IBAM-HSA NPs.....	153
5.2.3.1	Dox loading	153
5.2.3.2	Protocol of HSA-IBAM-HSA and IBAM-HSA coatings	153
5.2.4	Synthesis of the IO@RB-HSA-IBAM-HSA and IO@RB-IBAM-HSA NPs	155
5.3	Results and discussion.....	157
5.3.1	Characterization of raw IO@RB, IO@RB-NH ₂ , IO@RB-Dox-IBAM-HSA and IO@RB-Dox-HSA-IBAM-HSA NPs	157
5.3.2	Dox loading analyses	161
5.3.3	Dox release trials from IO@RB-Dox-HSA-IBAM-HSA NPs	164
5.3.4	Conclusion.....	167
6	Influence of the mesoporous silica shell thickness on biological activities	167
6.1	Introduction	167
6.2	Comparative biological studies on IO@RB-HSA NPs of 30 and 85 nm.....	168
6.2.1	Cytotoxicity studies	168
6.2.1.1	Impact of the silica shell thickness on cytotoxicity	168
6.2.1.2	Effect of the Dox loaded into IO@RB NPs on cytotoxicity	168
6.2.2	Cellular uptake studies	174
6.2.2.1	NPs internalization study in 2D culture system	174
6.2.2.2	Confocal study on 3D IO@RB internalization into spheroids.....	177
7	Conclusion	182
<u>Chapter 6: Core-shell morphology tuning for enhancement of theranostic properties ..183</u>		
1	Introduction.....	185
2	Syntheses	185
2.1	IO@RB with 20 nm core size.....	185
2.2	IO@ST with various core size	186
2.2.1	Synthesis strategies.....	186
2.2.2	Synthesis of ST NPs	186
2.2.3	Synthesis of IO@ST NPs	188
3	Improvement of Dox soaking into IO@ST compared to IO@RB	194
4	IO@ST versus IO@RB with IO core of 20 nm as theranostic agents	198

4.1	Introduction	198
4.2	IO@ST and IO@RB as MRI contrast agents.....	199
4.2.1	Relaxivity measurements and MRI images of raw IO@ST and IO@RB NPs	199
4.2.2	Effect of HSA coating on MRI contrast.....	204
4.3	IO@ST and IO@RB for cancer therapy	206
4.3.1	Magnetic Hyperthermia.....	206
4.3.2	Dox loading and release.....	208
4.3.2.1	Dox loading and release from IO@ST and IO@RB samples.....	208
4.3.2.2	Dox release study from IO@RB-Dox-HSA sample	210
4.3.2.3	Conclusion	211
4.4	Conclusion.....	212
<u>Chapter 7: General Conclusion and Outlooks</u>		213
<u>Chapter 8: Résumé en français.....</u>		219
1	Formation de nanocapsules d’HSA chargée en Dox pour la délivrance de médicament en utilisant la silice mésoporeuse comme modèle sacrificiel	224
1.1	Introduction	224
1.2	Synthèse du modèle sacrificiel RB NPs	225
1.3	Encapsulation de Doxorubicine	226
1.4	Etude in-vitro des nanocapsules Dox-HSA sur des modèles cellulaires en 3D	229
2	Création de nanoparticules cœur-coquille pour le diagnostic par IRM et la délivrance de médicament.....	231
2.1	IO@RB NPs synthèse et caractérisation.....	231
2.2	IO@RB NPs pour l’imprégnation de Doxorubicine.....	233
2.3	Revêtement d’HSA, son rôle en tant que gatekeeper: dégradation par les enzymes et libération de Dox	235
2.4	IO@RB NPs comme agents de contrastes pour l’imagerie IRM.....	237
2.5	Etudes <i>in-vitro</i>	238
3	Optimisation de la morphologie des nanoparticules afin d’obtenir les meilleures propriétés théranostiques	239
3.1	IO@ST et IO@RB NPs comme agents de contrastes pour l’imagerie IRM	239
3.2	IO@ST et IO@RB pour la thérapie cancéreuse.....	241
3.2.1	Par hyperthermie magnétique.....	241
3.2.2	Par chimio-thérapie	242
<u>References.....</u>		245

Table of Abbreviations

AHMPD	2-amino-2-(hydroxymethyl)propane-1,3-diol
APTES	(3-aminopropyl)triethoxysilane
BET	Brunauer, Emmett and Teller measurements for specific surface area
BMS NPs	Bimodal mesoporous silica nanoparticles
BJH	Barrett-Joyner-Halenda calculation of pore size distribution
CTAB	Cetylmethylammonium bromide
DLC	Drug loading content
DLE	Drug loading efficiency
DMF	N,N-Dimethylformamide
DMSO	Dimethyl sulfoxide
Dox	Doxorubicin
EtOAc	Ethyl acetate
EtOH	Ethanol
Et₃N	Triethylamine
FITC	Fluorescein <i>isothiocyanate</i>
FITR	Fourier transform infrared spectroscopy
fwr	Feed weight ratio
HF	Hydrofluoric acid
HSA	Human serum albumin
IBC	<i>Isobutrylchloride</i>
IC₅₀	50% inhibitory concentration
IO@RB NPs	Core-shell nanoparticles with iron oxide core and silica shell with small porosities around 3 nm
IO@ST NPs	Core-shell nanoparticles with iron oxide core and silica shell with large porosities with stellar morphology
ICP-AES	Inductively coupled plasma-absorption emission spectroscopy
IEP	Isoelectric point
LCT	Liquid crystal templating
MCTS	Multicellular tumor spheroid
MRI	Magnetic resonance imaging
MTT	3-[4,5-dimethylthiazol-2-yl]-2,5-diphenyltetrazolium bromide
NaOH	Sodium hydroxide
OA	Oleic acid
PAA	Poly(acrylic acid)
PFA	Paraformaldehyde
PSD	Pore size distribution
RB NPs	Mesoporous silica nanoparticles with raspberry pore morphology
SEM	Scanning electron microscopy
ST NPs	Mesoporous silica nanoparticles with stellar pore morphology
TEA	Triethylamine
TEAH₃	Triethanolamine
TEM	Transmission electron microscopy
TEOS	Tetraethyl orthosilicate
TGA	Thermogravimetry analysis
THF	Tetrahydrofuran
US	Ultrasound

Introduction

Since the last decades, syntheses of nano-objects combining therapy and diagnosis, the so called theranostic agents, are widely investigated for nanomedicine. The main advantage of this combination is the possibility to follow the effect of therapy by imaging such as drug delivery, drug release and drug efficiency (1). Imaging can be achieved by several techniques such as optical, positron emission tomography (PET), magnetic resonance (MR), single photon emission computed tomography (SPECT), computed tomography (CT), and/or ultrasound (US) imaging (2) and therapy by magnetic or photo-hyperthermia, drug delivery (chemotherapeutics), gene delivery and/or radiotreatment.

Among current developed theranostic agents, a lot of works are devoted to iron oxide nanoparticles (IO NPs) as they are FDA approved, biocompatible, biodegradable and show both diagnosis and therapeutic abilities. Indeed, IO NPs are already commercially used as negative contrast agents for MRI and are also recently developed as therapeutics for thermotherapy by magnetic hyperthermia. Furthermore, it is nowadays admitted that the combination of therapies considerably increase the efficiency of anti-cancer treatment. Thereby, designing nano-objects combining hyperthermia with the delivery of drugs, appear to be a very promising approach for cancer treatment. The main challenges of this strategy are thus to load large amount of drugs on iron oxide based nano-objects and, in the same time to keep their size smaller than 200 nm to be suitable for cancer treatment by enhanced permeability retention effect (EPR) after *in vivo* injection. Besides the widely studied liposomes or polymersomes, mesoporous silica nanoparticles (MS NPs) were shown to allow large drug loading and the coating of iron oxide nanoparticles by a silica shell has already been demonstrated.

In that context, the research project, illustrated in Figure 1-1, deals with the design of a theranostic agent consisting in core-shell nanoparticles with an iron oxide core, which ensures, through its magnetic properties, diagnosis by magnetic resonance imaging (MRI) and therapy by magnetic hyperthermia, surrounded by a mesoporous silica shell in which the porosities can be loaded with fluorescent agents for optical imaging diagnosis and anticancer drugs for chemotherapy.

For the mesoporous silica shell the main challenges remain the loading efficiency and the control of drug release. Indeed, if the drug release is not controlled, the drug loaded in the silica pore could slowly leak outside of the nanoparticles with time (3). One possibility to keep the drug inside the porosity is to covalently bind it to the silica by a chemical bond which can break with external stimuli. Another way to control the drug delivery is to use gatekeepers to block the pore, in which the drugs are capped and, at the right moment, to release them by external stimuli. In this PhD project, we envision encapsulating drug by coating the silica shell with proteins and testing the release by using either enzymatic degradation or by heating through magnetic hyperthermia.

Indeed, IO core can be designed to control the magnetic properties in order to have a relevant T_2 contrast agent for MRI as well as a significant hyperthermia effect. The saturation magnetization (M_s) of IO NPs, their aggregation state, and the ability of the coating to diffuse water molecules are important parameters to provide a good and efficient MRI contrast. Furthermore, the amount of heat generated by IO NPs is highly dependent of the NPs structural and magnetic properties (high M_s and high magnetocrystalline anisotropy). Moreover, first

studies demonstrated that spherical IO NPs with mean size around 20 nm are suitable for clinical magnetic hyperthermia (4–6).

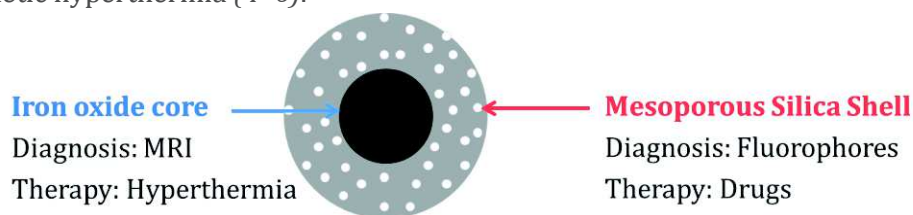


Figure 1-1: Schematic explanation of theranostic abilities of the nano-carriers developed in this thesis

The main project goal is, as described in Figure 1-4, to load silica pores with an anticancer drug the doxorubicin (Dox) and to use a thick shell of protein, human serum albumin (HSA), as gatekeeper. One originality is to coat the silica shell with HSA by introducing an intermediate layer consisting in *isobutyramide* (IBAM) grafts. This IBAM approach will allow obtaining a thick HSA shell and to induce a stronger anchoring of the HSA shell onto the silica surface through non-covalent bonds. The HSA shell has the high advantages to be biocompatible and biodegradable, and it should also help the system to be stable in physiological media. Furthermore, as gatekeeper it should ensure a controlled drug delivery by degradation of HSA with proteases. The pore sizes of the silica shell were modulated to enhance the loading content of Dox but also to load larger molecules such as SiRNA, widely used in gene therapy, which cannot be load into smaller porosities of 3 nm. Finally, magnetic hyperthermia and MRI properties of the IO core, with mean sizes of either 10 or 20 nm, on the final hybrid core-shell system were also investigated in this project.

Thus this manuscript is divided in six chapters:

- **Chapter 1** introduces the state of art in the field of nanomedicine with focus on MS, IO, IO@MS and protein coated NPs.
- **Chapter 2** details the different used characterization techniques and the experimental protocols.
- **Chapter 3** is devoted to the surface functionalization of iron oxide nanoparticles (IO NPs) to allow their colloid stability in water. Indeed, IO NPs were obtained by thermal decomposition of iron stearate in a high boiling point solvent in presence of a ligand, oleic acid. After the synthesis and purification steps, the spherical NPs stabilized with oleic acid are dispersible in organic solvent as chloroform and show a high monodispersity in size and shape as shown in Figure 1-2. These NPs need to be coated with molecules or by inorganic shells to form stable colloidal suspensions in physiological media. To attend this purpose, silanisation of the surface of IO NPs was optimized. Another widely used strategy for IO NPs stabilization in aqueous media is to coat it with a mesoporous silica shell. This strategy is deeply detailed in the other chapters.

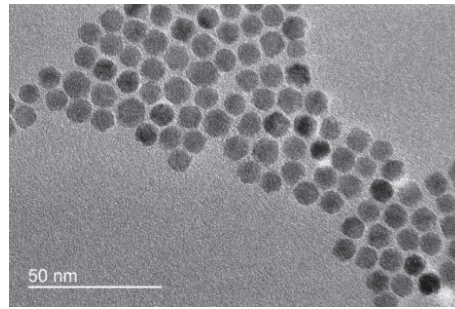


Figure 1-2: Iron oxide nanoparticles of 10 nm synthesized by thermal decomposition

- Chapter 4** is dedicated to the study of mesoporous silica nanoparticles with two various porosity types. Mesoporous silica with small porosities of 3 nm exhibiting a raspberry (RB) morphology and bimodal particles (BMS) of 500 nm with porosities of 3 and 20 nm were synthesized, Figure 1-3. In a first part, the use of BMS NPs as sacrificial template for the formation of self-supported HSA_{Dox} NPs, after having covalently bind Dox to HSA by a pH-cleavable bond, was investigated. In a second part, the formation of Dox-HSA nanocapsules after Dox impregnation into RB porosities and dissolution of the silica template as well as their cytotoxic effect on spheroids were evaluated.

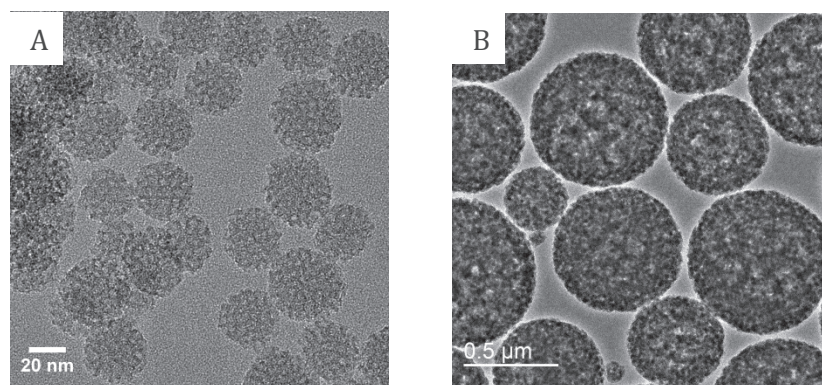


Figure 1-3: Mesoporous silica nanoparticles with three different porosity morphologies: (A) raspberry RB and (B) bimodal BMS

- Chapter 5** focuses on core-shell nanoparticles with an iron oxide core of 10 nm and a silica shell with small porosities called IO10@RB, Figure 1-5 A. The synthesis process to obtain well shaped and monodispersed in size NPs was discussed. After checking by relaxometry their potential as MRI diagnosis probes, their ability to be as well efficient drug delivery system was investigated. The drug delivery strategy describes in Figure 1-4 consists in loading the silica porosities with Dox, deposits a HSA shell solidifying by IBAM as gatekeeper that can be degraded by proteases action to deliver the Dox. First, the influence of the surface modification and the nature of solvent on Dox impregnation into the porosities were investigated. After determining the best way to soak Dox, the protein capping was achieved. HSA degradation by proteases and the resulting Dox release were then studied and the synthesis strategy was modified in order to find the optimal protocol for Dox loading and release. Finally, the impacts of the shell size and Dox loading on cytotoxicity, cellular uptake and diffusion in spheroids (3 D cellular models) were tested *in vitro* on cancer cell lines.

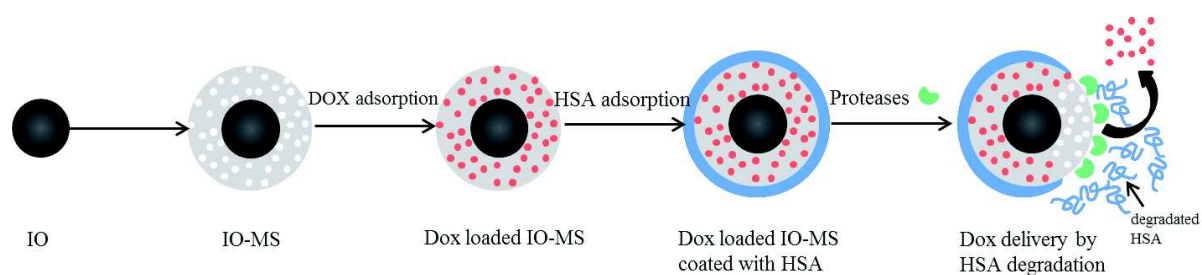


Figure 1-4: Scheme of the protease-mediated drug delivery strategy for IO@RB NPs

- Chapter 6** is devoted to the tuning of core-shell NPs morphology to enhance their theranostic abilities. Thus, four types of core-shell nanoparticles were synthesized with various IO core sizes (10 or 20 nm) and various silica shell porosity morphologies (raspberry and stellar), Figure 1-5. Dox impregnation in IO10@ST was investigated and the loading contents compared with them obtained with IO10@RB. Finally the interest of having an iron oxide core of 20 nm compared to smaller one in term of enhanced magnetic properties was determined by relaxometry, MRI and magnetic hyperthermia. The ability of these systems to be used for combined therapy was also discussed through Dox loading and release studies.

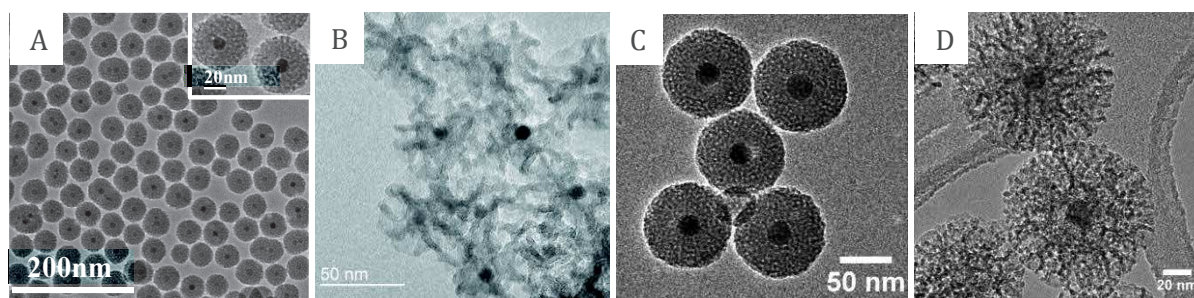


Figure 1-5: Core-shell nanoparticles with (A) small core small pores IO10@RB, (B) small core big pores IO10@ST, (c) big core small pores IO20@RB, (d) big core big pores IO20@ST

- Chapter 7** ends this manuscript with general conclusions and outlooks.

Chapter 1: Literature review

1 Mesoporous silica nanoparticles in nanomedicine (MS NPs)

Mesoporous silica nanoparticles have emerged as versatile cargos for specific drug delivery to organs and tissues. Indeed, they possess features that are prior for drug delivery systems such as ordered pore network, high surface area, high pore volume as well as a silanol surface that can be easily functionalized.

1.1 Synthesis of MS NPs

MS materials studies started in 1992, when Mobil Oil Corporation developed a new family of ordered mesoporous silicate based molecular sieves named the M41S-family (7–10). This family was obtained by self-organization surfactants procedure in which the surfactants act as mesoporous templates.

This discovery truly initiated the field of mesoporous materials. Indeed, as depicted in the graph in Figure 1-1, the rapid and continual increase of publications number related to mesoporous materials over years showed the large worldwide attraction for this field. Furthermore, Kresge *et al.* Nature paper (7) signed the true start of this research area as shown by the simultaneously increase of its citation number.

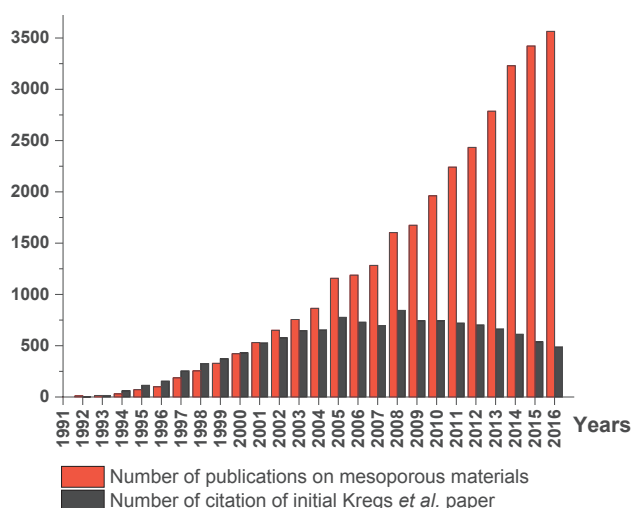


Figure 1-1: Number of publications with the key word “mesoporous materials” under Web of Science versus the number of citations of initial Kresge *et al.* Nature paper published in 1992 (7) till now

M41S-family, as represented in Figure 1-2, possesses three members which distinguish from each other through their porosity network: MCM-41, MCM-48 and MCM-50.

The first discovered MCM-41 material became the most popular member of the M41S-family. MCM-41 exhibits unidimensional hexagonally structured pores with narrow pore size distribution. The pore size can be adjusted from 2 to 8 nm depending on the surfactant chain length or by adding organic auxiliaries such as 1,3,5-trimethylbenzene during the synthesis process. The two other structures discovered a bit later resulted from a detailed study about the effect of the surfactant/silica molar ratios on the formation of the mesoporous molecular sieves. MCM-48 has the particularity to display a cubic structure with 3 D pore system whereas MCM-50 shows a lamellar morphology. All of these phases are crystallized and exhibit well-defined X-ray diffraction patterns.

The formation mechanism of these mesoporous molecular sieves was called liquid crystal templating (LCT) by analogy to surfactant-water liquid-crystal phases (11) that these materials

mimicking with the alkyltrimethylammonium salts in water. Figure 1-3 shows the schematic representation of the synthesis pathways (12).

Based on this mechanism many different mesoporous materials were synthesized by varying synthesis parameters such as alcohol-water ratio, pH, catalyst, silica precursor, surfactant type... In 2001, in a review presenting the recent advances in processing and characterization of MCM-41 materials (13), Selvam *et al.* summarized the several mesoporous silica materials obtained inspired from the MCM-41 synthesis strategy (Table 1-1).

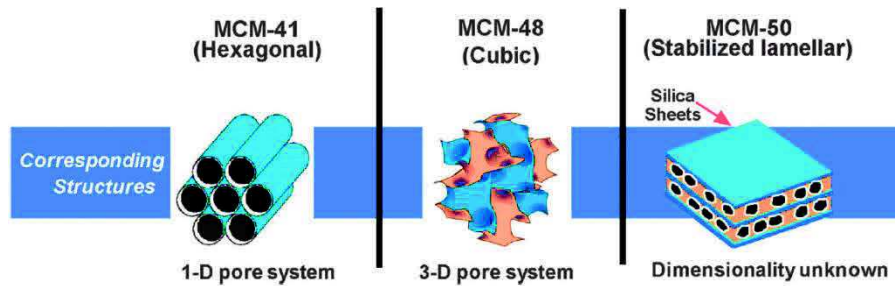


Figure 1-2: M41S family of mesoporous molecular sieves from Kresge and Roth (12)

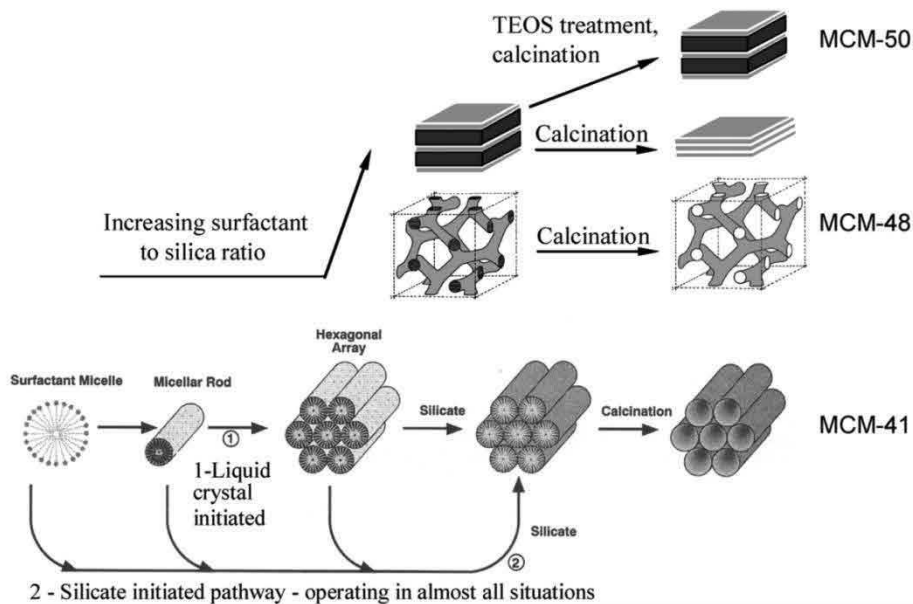
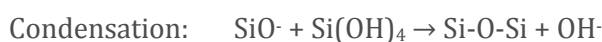


Figure 1-3: Initial proposed LCT formation pathway mechanism (lower half) and its further addition, from Kresge and Roth (12)

Table 1-1: Various mesoporous silica materials synthesized by adapting MCM-41 process (from Selvam et al. (13))

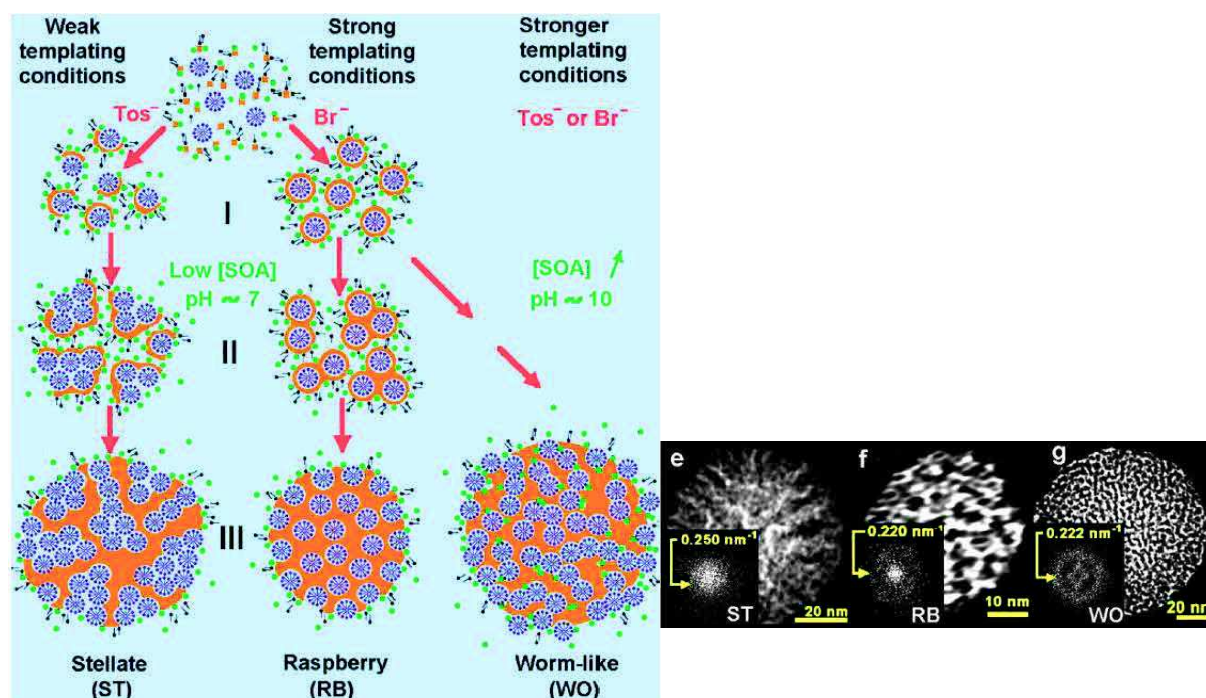
	Dimension	Crystal system	Space group	Pore size (nm)	Reference
MCM-41	2D	Hexagonal	P6mm	3.70	(8)
MCM-48	-	Cubic	Ia3d	3.49	(8)
FSM-16	2D	Hexagonal	P6mm	2.80	(14)
SBA-1	-	Cubic	Pm3n	2.00	(15)
SBA-2	3D	Hexagonal	P6 ₃ /mmc	2.22	(16)
SBA-3	2D	Hexagonal	P6mm	2.77	(15)
SBA-8	2D	Rectangular	Cmm	1.87	(17)
SBA-11	-	Cubic	Pm3m	2.50	(18)
SBA-12	3D	Hexagonal	P6 ₃ /mmc	3.10	(18)
SBA-14	-	Cubic	Pm3n	2.40	(18)
SBA-15	2D	Hexagonal	P6mm	7.80	(19)
SBA-16	-	Hexagonal	Im3m	5.40	(18)
HMM	2D	Hexagonal	P6mm	3.10	(20)
MSU-1	-	Hexagonal	disordered	3.10	(21)
MSU-2	-	Hexagonal	disordered	3.50	(21)
MSU-3	-	Hexagonal	disordered	5.80	(21)
MSU-4	-	Hexagonal	disordered	-	(22)
MSU-V	-	Lamellar	-	-	(23)
MSU-G	-	Lamellar	-	3.20	(24)
HMS	-	Hexagonal	disordered	2.80	(25)
KIT-1	-	Hexagonal	disordered	3.52	(26)
CMK-1	-	Cubic	I4 ₁ 32	3.00	(27)
APO	2D	Hexagonal	P6mm	2.80	(28)

The synthesis of monodisperse silica particles was first reported by Stöber et al. in 1968 (29). This process was based on a base-catalyzed sol-gel process, in which organosilane precursors, such as tetraorthosilicate (TEOS), formed a sol phase that then condense into a gel phase through hydrolysis and condensation reactions:



In 1997, Grün *et al.* were the first to synthesize spherical silica micrometer-sized particles with MCM-41 structure by coupling the Stöber method to the LCT strategy (30). Few years later, the development of nanometric MCM-41 particles was reported (31–33). The large majority of mesoporous silica nanoparticles (MS NPs) are synthesized by cetyltrimethylammonium bromide (CTAB)-templated silica condensation in basic conditions which yields to pore diameters of about 3 nm. In a similar way than mesoporous molecular sieves, the porosity of their nanoparticulate analogues could be tuned by the modification of some synthesis parameters (34). For example, the use of a co-solvent and/or co-temple can change the porosity morphology. Thus, the use of ethyl ether as co-solvent was reported to led to “chrysanthemum-like”/stellar pore channels (35, 36). In addition, with ethanol used as co-solvent to water and with also ethyl acetate as co-temple to CTAB, a significant evolution of pore structure from parallel to radial and to worm-like was achieved by increasing the ethanol/ethyl acetate volume ratio (37). Addition of polymers to the synthesis process can also tune the porosity. For example, styrene was added as co-temple to CTAB in a water/octane phase. The simultaneous

hydrolytic condensation of TEOS to form silica and polymerization of styrene into polystyrene led to HMM (Hiroshima Mesoporous Material) type NPs with controllable pore size (4–15 nm) and outer diameter (20–80 nm) (38). Anionic poly(acrylic acid) (PAA) is also known to form complex colloids with the cationic surfactant CTAB in basic solution. The further condensation of silica on these systems led to hollow silica spheres with mesoporous shells templated by CTAB and the core by PAA domains or under hydrothermal treatment to NPs with bimodal porosities (39, 40). Furthermore it was found that the addition of growth inhibitors such as triethanol amines could also tune the porosity and enhance the particle size control. Thus, based on this strategy, Zhang *et al.* reported recently a process for large scale synthesis of MS with various porosity morphologies and outer diameters below 130 nm (41). The tuning of the porosity was achieved by modifying the cetyltrimethyl ammonium (CTA⁺) counterions (tosylate (Tos⁻) or bromide (Br⁻)) and by the variation of small organic amine (SOA) concentration (such as triethyleneamine (TEA), triethanolamine (TEAH₃) and 2-amino-2-(hydroxymethyl)propane-1,3-diol (AHMPD)) that were used as growth inhibitors but also as base catalysts for the Stöber sol-gel process. Thus, as pictured in Figure 1-4, at high pH (~10), *i.e.* at high SOA concentration, the worm-like (WO) pore channel morphology was obtained with both CTA⁺ counterions, whereas at lower SOA concentration, *i.e.* pH~7, Tos⁻ counterion favored the stellate (ST) and Br⁻ favored the raspberry (RB) morphology. Indeed, at low pH, Br⁻ counterion has less affinity than Tos⁻ with CTA⁺ and thus allows the silicate to diffuse and condense around each micelle, which lead to raspberry morphology. This phenomenon is called by its authors “strong templating”. On the contrary, Tos⁻ has good affinity with CTA⁺ and so the silicate is too small to displace Tos⁻ efficiently leading to the formation of large porosities made from “micelle aggregates”. Based on these synthesis, the size-control of RB and ST NPs were investigated in further publications (42–44).



^a(I) partly silicated micelles, (II) block formation, and (III) block aggregation into stellate or raspberry nanoparticles.

Figure 1-4: Schematic representation of the synthesis strategy for the formation of stellate (ST), raspberry (RB) and worm-like (WO) NPs (left) and their corresponding HRTEM images with diffraction pattern in inset (right)

1.2 MS NPs for biological applications

In 2001, Vallet-Regi *et al.* were the first to use MCM-41 as drug delivery systems (45). Since then, a lot of work has been done in this field as proved by the large amount of literature reviews about the use of MS as cargo for drug delivery (46–51).

MS NPs are promising materials for drug delivery applications because of their ability to encapsulate different types of drug molecules within their pore channels. This incorporation is commonly carried out by simple soaking of MS NPs in a concentrated drug solution. Therefore, textural properties of MS, such as pore size, pore morphology, surface area and pore volume, have a huge influence of the drug loading capacity (46, 47, 52–54).

After being loaded into MS porosity, the drug should be release in tumor cells. However, some leakage of the drug from MS before reaching the target may occur as, in some cases, the drug slowly diffuses out the porosity with time.

To overcome the potential problems of drug leakage, controlled drug delivery systems were developed. Thus these systems are design in order to release the drug only when they are exposed to specific stimuli. The stimuli frequently used to trigger the drug delivery can be classified in two categories (Figure 1-5): internal (pH, redox potential, enzymes...) and external stimuli (temperature, photoirradiation...). The internal triggers are directly related to the endocytosis of NPs (55, 56). Indeed, as pictured in Figure 1-6, these parameters vary a lot after endocytosis: pH decreases slowly to 5, proteases concentration increases and the ionic environment is also modified. Finally, two types of strategies can be used for controlled-drug delivery: the addition of a sensitive linker between the drug and the silica surface or the use of such called “gatekeepers” to close the pore entrance.

MS NPs can also be used in cancer diagnosis by loading into the porosity or directly in the silica matrix imaging agents such as quantum dots, near infra-red contrast agents, fluorophores... (57–59)

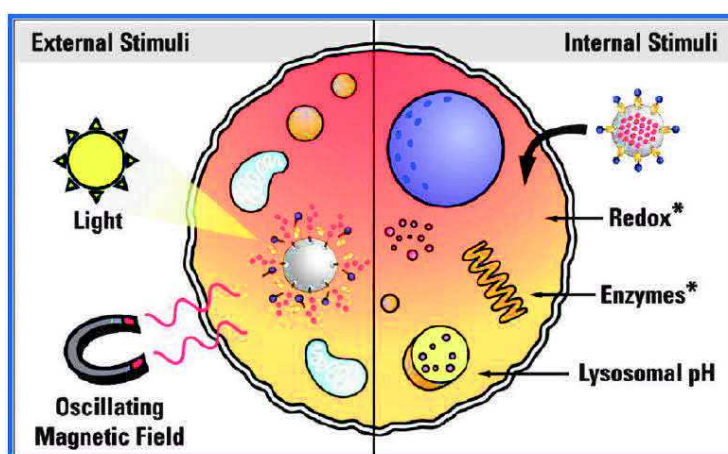


Figure 1-5: Schematic representation of stimuli used to trigger drug delivery, from (60)

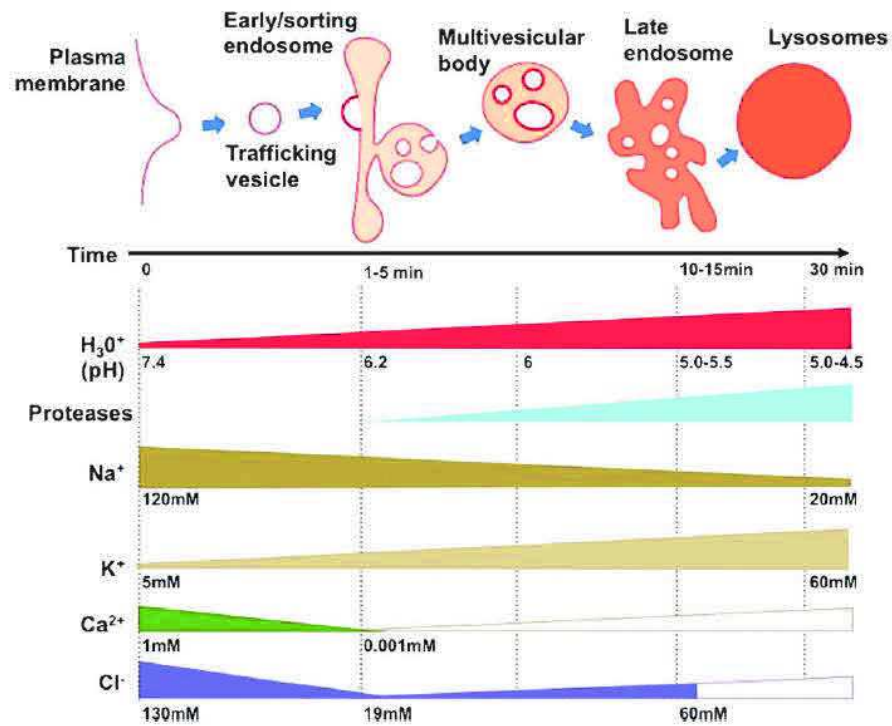


Figure 1-6: Schematics of the different endocytic compartments from trafficking vesicle to early endosome, to multivesicular bodies, to late endosome to lysosome. The time that the endocytosed material takes from its entry to each organelle is plotted alongside the organelle internal pH, protease and several ions concentration, from Canton and Battaglia (56)

2 Iron oxide nanoparticles (IO NPs)

Among the eight iron oxides structures referenced (61), hematite ($\alpha\text{-Fe}_2\text{O}_3$), magnetite (Fe_3O_4) and maghemite ($\gamma\text{-Fe}_2\text{O}_3$) are the most developed. As shown in Figure 1-7, hematite, which is the most stable iron oxide, has a rhombohedral structure. Magnetite has a face centered cubic spinel structure based on 32 oxygen anions and contains both divalent and trivalent iron as cations. For one unit cell containing 32 O^{2-} 64 tetrahedral and 32 octahedral sites are generated. For each unit 8 divalent and 8 trivalent iron cations fill the octahedral sites whereas the tetrahedral sites are filled with 8 trivalent iron ions. Finally maghemite (corresponding to the oxidized form of magnetite) also exhibits a cubic crystalline spinel structure which contains only trivalent iron cations. The presence of only Fe^{3+} (due to Fe^{2+} oxidation) is compensated by the presence of vacancies in the octahedral sites. Thus each unit of maghemite contains 32 O^{2-} , $21\frac{1}{3}\text{Fe}^{3+}$ and $2\frac{1}{3}$ vacancies.

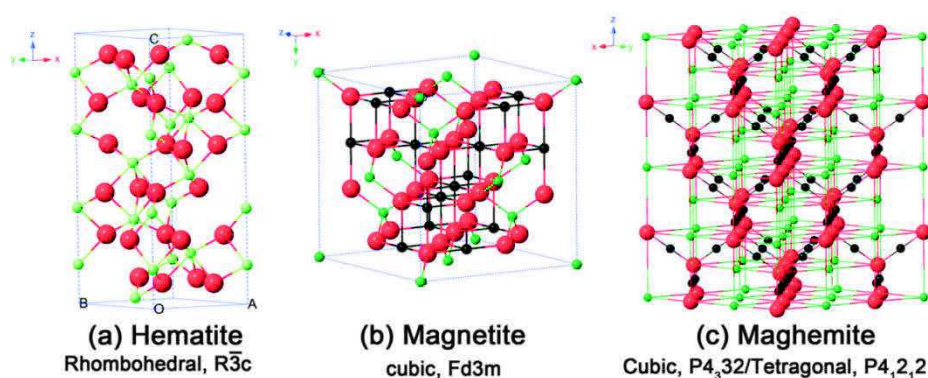


Figure 1-7: Crystal structure of hematite, magnetite and maghemite (black balls: Fe^{2+} ; green balls: Fe^{3+} and red balls O^{2-}) (62)

2.1 IO NPs synthesis

2.1.1 Synthesis methods

IO NPs can be synthesized by either top-down (physical synthesis) or bottom-up (chemical or biological synthesis) methods. Figure 1-8 showed that chemical methods are the most published route to produce IO NPs. In the following the most popular chemical synthesis methods to produce IO NPs will be introduced.

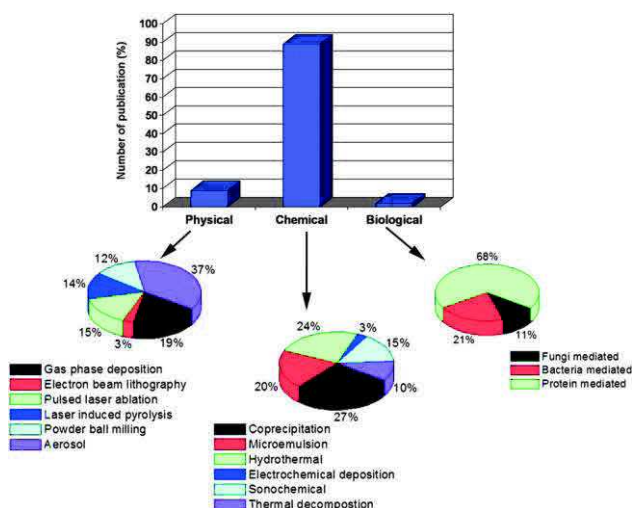


Figure 1-8: A comparison of the three most published routes to synthesize IO NPs (63)

2.1.2 Coprecipitation

Coprecipitation is the most widely used method to produce commercial IO NPs because of its cheap, efficient and simple procedure. This method consists of adding a highly basic solution (like NaOH or NH₄OH) to a mixture of ferrous (Fe²⁺) and ferric (Fe³⁺) ions under inert atmosphere which creates a black precipitate of spherical IO NPs. The most common synthesis procedures reported by Massart (64) and Sugimoto (65) in the early 80's involved the use of ferric and ferrous chlorides and ferrous sulfates respectively. A comparison of these two methods showed that the Massart's method leads to spherical particles smaller than 10 nm whereas Sugimoto's method produced larger rhombic particles (30-150 nm) under stirring and excess of base or spherical particles of 40 nm without stirring and without base excess (66). This comparison showed that the nature of salts and the stirring conditions can change the size and the shape of the IO NPs. The characteristics of IO NPs (size, shape and composition) can be also tailored by adjusting a wide range of synthesis parameters like pH, ionic strength of medium, the iron(III)/iron(II) concentration ratio, salt type, base type, reaction temperature, stirring rate (67-72)... Despite all the advantages of this method the resulting IO NPs generally present a large polydispersity and a not well-controlled shape, which result of the reaction temperature limited by the boiling point of water. To overcome these disadvantages other synthetic processes were developed.

2.1.3 Hydrothermal synthesis

According to Figure 1-8 the hydrothermal method is the second most used process for IO NPs synthesis. This method is similar to coprecipitation but the synthesis occurs in reactors or autoclaves in order to obtain higher temperature and higher pressure. The high temperature and pressure strongly improve the quality and better control the size of the nanocrystals compared to the coprecipitation. There are two hydrothermal methods: without (73-75) and with surfactants (76-82). Unfortunately the reaction times are relatively long, so to decrease them, the synthesis can be achieved under microwave (83). Hydrothermal treatment can be also performed on IO NPs synthesized beforehand by coprecipitation in order to obtain IO NPs with high crystallinity, larger size and good monodispersity. The IO NPs before the hydrothermal step display an average size of 12 nm and grown to 39 nm after hydrothermal treatment (84).

2.1.4 Microemulsion

Microemulsion is a thermodynamically stable isotropic dispersion of two immiscible phases, water and oil under presence of surfactant molecules. The microemulsion can be direct (oil dispersed in water o/w) or reversed (water in oil w/o) (85). The surfactants stabilize the microemulsion by forming monolayer micelles at the interface between oil and water with their hydrophilic heads dissolved in the aqueous phase and their hydrophobic tails in the oil phase (86-88). Two methods can be used to form IO NPs. The most common process called the two-microemulsion method consists in mixing two different microemulsions: one containing the iron precursor and another containing a base (89-92). The second process is composed of a single microemulsion containing the iron precursors in which the base is added (92). Tuning the size of the final IO NPs is achieved by adjusting the synthesis parameters such as the surfactant type, the molar ratio of water to surfactant, the nature of the counterion, the temperature... Although microemulsion is a simple and fast process, the size and shape are not well controlled, the yield is poor and, as the process requires the use of large amounts of solvents and surfactants, the

scale-up of the process is difficult and the purification to eliminate the surfactants after synthesis is fastidious.

2.1.5 Thermal decomposition

The synthesis of magnetic particles with control over size and shape can be obtained by thermal decomposition method inspired by synthesis of high-quality semiconductor nanocrystals in non-aqueous media (93–97). The process consists in decomposing metallic precursors in high-boiling organic solvents containing stabilizing surfactants. The first thermal decomposition method to synthesize crystalline monodisperse IO NPs was reported by Rockenberger et al. (98). In this process (Fe(cup)₃) was quickly injected into a trioctylamine solution at 300°C under argon atmosphere and vigorous stirring. At the end of a thermal decomposition synthesis, the IO NPs produced are dispersed in organic solvent stabilized by surfactant molecules. This thermal decomposition method presents the main advantages to produce well crystalline IO NPs with a narrow control on size and shape.

2.1.6 Conclusion

The advantages and drawbacks of the previous described methods for the synthesis of IO NPs are summarized in Table 1-2. Thus, the IO NPs synthesis by thermal decomposition appears as the most promising synthesis to produce monodisperse NPs. Consequently, thermal decomposition is the selected pathway for the present work.

Table 1-2: Summary comparison of the synthetic methods for producing magnetic IO NPs (99)

Synthetic method	Synthesis	Reaction temp. [°C]	Reaction period	Solvent	Surface-capping agents	Size distribution	Shape control	Yield
co-precipitation	very simple, ambient conditions	20–90	minutes	water	needed, added during or after reaction	relatively narrow	not good	high/ scalable
thermal decomposition	complicated, inert atmosphere	100–320	hours–days	organic compound	needed, added during reaction	very narrow	very good	high/ scalable
microemulsion	complicated, ambient conditions	20–50	hours	organic compound	needed, added during reaction	relatively narrow	good	low
hydrothermal synthesis	simple, high pressure	220	hours ca. days	water-ethanol	needed, added during reaction	very narrow	very good	medium

2.2 Surface modification of IO NPs for stabilization in aqueous media

After their synthesis by thermal decomposition, IO NPs are covered by a hydrophobic coating through oleic acid ligands, adsorbed on IO surface by chemisorption (100), and thus are dispersible only in organic solvents. However, to be used for biomedical applications, the biocompatibility and the colloidal stability of IO NPs in water are primordial characteristics. Thus, it is essential to modify the surface coating of IO NPs in order to make it hydrophilic. For this purpose two main strategies are used: ligand addition or ligand exchange.

The ligand addition strategy consists in adding amphiphilic molecules, called usually surfactants, that will interact with oleic acid present onto IO NPs surface. Thus, the hydrophobic parts of those molecules will interact with hydrophobic segment of oleic acid and their hydrophilic parts pointing towards the outside allow the phase transfer of IO NPs from organic phase to aqueous media. This results in the formation of a bilayer at the IO NP surface. Among most reported ligand used for these strategy we found polymers, such as pluronic acid (101),

alkylammonium salts, such as cetyltrimethylammonium bromide CTAB (this interaction will be described in detail later in page 25) and lipids, such as phospholipids or fatty acids (102).

Ligand exchange strategy consists in the replacement of initial capping agent with another one. According to the nature of ligand, the link between the IO NP surface and the coating molecules could be either quite covalent or ionic. Most molecules bear thus an anchoring group to interact with the surface of IO NPs such as phosphonate, carboxylate, catechol, silane.... Among the ligand commonly used in this strategy we focus on IO surface modification by silanes.

Indeed, silanization is a reaction widely used for stabilization of colloidal suspensions in water. The direct silanization process is based on the formation of a covalent network of silane molecules at the surface of the NPs. It occurs in non-polar solvents or in a mixture of polar and non-polar solvents. De Palma *et al.* described a versatile method for IO surface functionalization with various silane coupling agents (Figure 1-9 (103)). Briefly, the reaction occurred by mixing IO NPs dispersed in n-hexane with the trialkoxysilane in presence of oleic acid. However, this synthesis method is highly time consuming as the reaction occurred for three days.

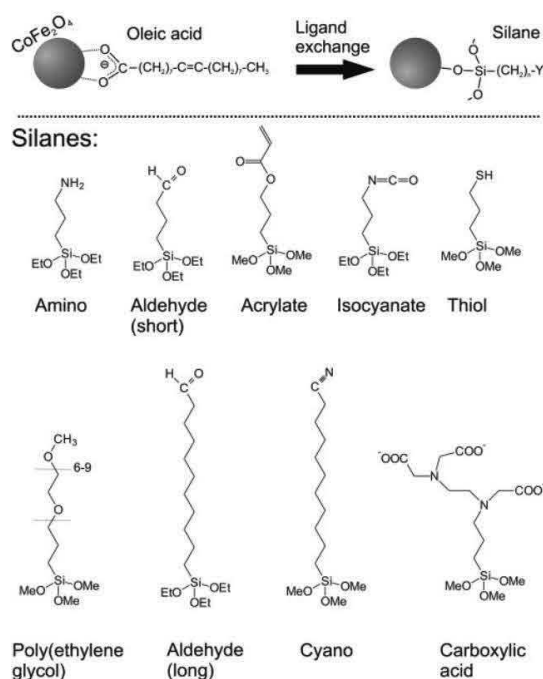


Figure 1-9: Exchange of the chemisorbed oleic acid ligands on IO NPs surface by silanes. Different silanes bearing a wide variety of endgroups were deposited on the nanoparticle surface in order to evaluate which groups can render these nanoparticles water-dispersible (103)

2.3 Biomedical applications of IO NPs

2.3.1 Diagnosis by magnetic resonance imaging (MRI)

2.3.1.1 Principle of MRI

MRI is a non-invasive widely used clinical diagnosis imaging technique to detect potential tumors in soft tissues. The principle of MRI is based on the measurement of NMR signal of water protons contained in tissues induced by a strong static magnetic field B_0 up to 2 T and a transverse radiofrequency-field (5-100 MHz). Briefly when the protons are exposed to B_0 their spins precess under the Larmor frequency ω_0 to align parallel to the direction of the magnetic field along the z axis called longitudinal direction (Figure 1-10 a). Then when a radiofrequency (RF) pulse with a resonance frequency equal to the Larmor frequency is applied on the

transversal plan xy perpendicularly to B_0 , the protons are excited and got a magnetic moment M with two contributions: a longitudinal magnetization called M_z and a transversal magnetization M_{xy} (Figure 1-10 b). When the RF pulse disappears the excited protons relax to their initial state. There are two relaxation pathways:

- The longitudinal relaxation, called T_1 relaxation, involves the recovering of the longitudinal magnetization M_z to initial state due to spin-lattice interaction (the absorbed energy is released to the surrounding tissue (lattice)). The relaxation time T_1 given by the following equation is defined as the time required after the RF pulse for the longitudinal magnetization M_z to reach 63% of the initial magnetization $M_{z,0}$ (Figure 1-10 Figure 1-4 c).

$$M_z(t) = M_{z,0} \left(1 - e^{-\frac{t}{T_1}} \right)$$

- The transversal relaxation, called T_2 relaxation or spin-spin relaxation, involves the disappearance of the transversal magnetization M_{xy} resulting of the exchange of energy between spinning protons. The relaxation time T_2 given by the following equation is defined as the time duration until 63% of M_{xy} is lost (Figure 1-10 c).

$$M_{xy}(t) = M_{xy,0} \left(e^{-\frac{t}{T_2}} \right)$$

Finally the electromagnetic signals during the relaxation are transmitted and recorded by the spectrometer. The changes induced in these electromagnetic signals in the presence of linear field gradients are then used to reconstruct 3-D images of soft tissues.

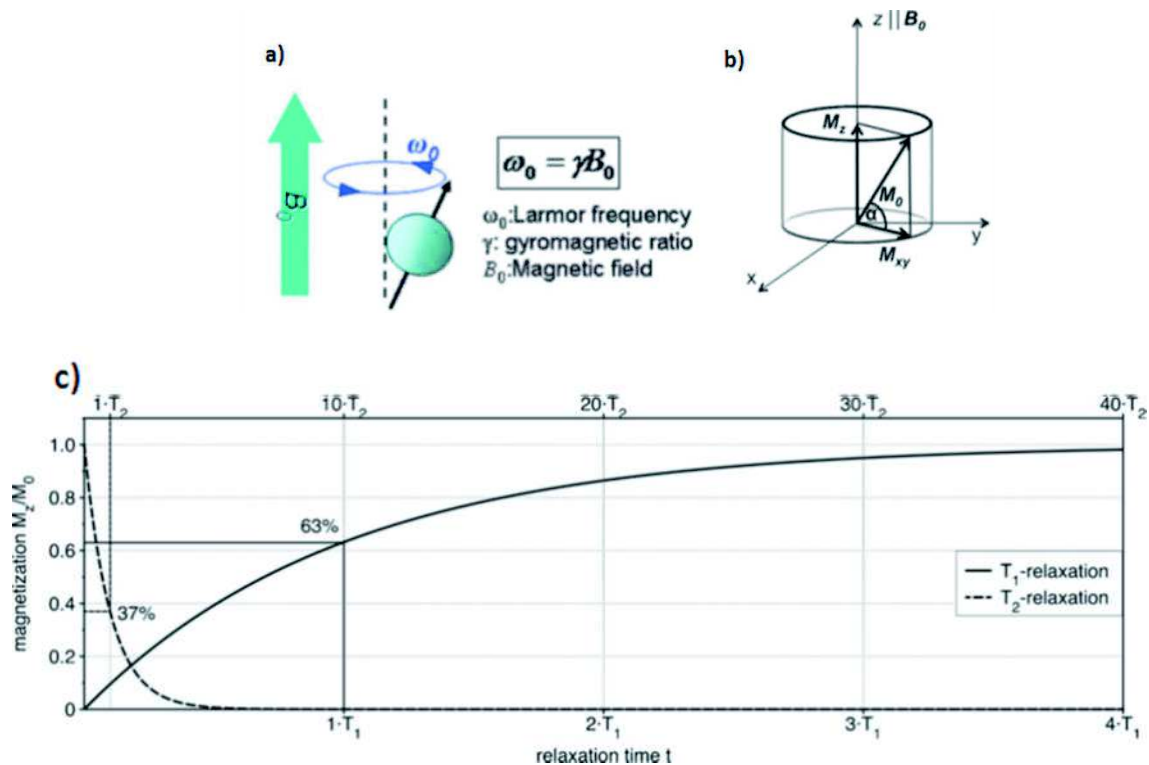


Figure 1-10: Principle of MRI: a) Spins align parallel or antiparallel to the magnetic field and precess under Larmor frequency (ω_0) (104) b) after induction of R_f pulse, magnetization M_0 of spins changes c) T1 and T2 relaxation after the flipping of the net magnetization M_0 with an angle of 90° (105)

2.3.1.2 MRI contrast agents

The predominant parameters that influence the contrast of a sample are listed in Table 1-3. To facilitate the distinction between tumors and normal tissues and clarify MRI images for better interpretation, contrast agents are often being injected to patient before the analysis to help to selectively highlight the abnormal cells. These contrast agents are usually divided into two classes:

- positive contrast agents called T_1 contrast agents will reduce the longitudinal relaxation time T_1 resulting in hypersignal giving a bright contrast in T_1 -weighted images. T_1 contrast agents are usually paramagnetic such as Gadolinium (Gd^{3+}) and Manganese (Mn^{2+}) complexes.
- negative contrast agents called T_2 contrast agents will shorten the transversal relaxation times T_2 and T_2^* resulting in hyposignal giving a dark contrast in T_2 -weighted images. The most common used T_2 contrast agents are superparamagnetic iron oxides (magnetite or maghemite) which under an applied magnetic field generate induced local magnetic fields which perturb the relaxation process of the protons in the surrounding water molecules (Figure 1-11 a).

Figure 1-11 b and c gives a comparison of the contrast induced by the presence or the absence of IO contrast agents. After the injection of IO NPs the liver becomes darker so the contrast between the lesion and the normal liver increases and the lesion appears on the picture (arrow).

Table 1-3: MRI parameters: factors influencing the signal from each location (106)

Parameter	Description
T_1	Spin-lattice/longitudinal relaxation time. The T_1 relaxation time constant is a material property describing the characteristics of how this energy is given back to the surroundings
T_2	Transverse relaxation time. T_2 relaxation time constant describes the energy transfer between adjacent protons
T_2^*	Same as T_2 , but also contains heterogeneities in the environment
ρ	Spin density: the concentration of H nuclei in tissue

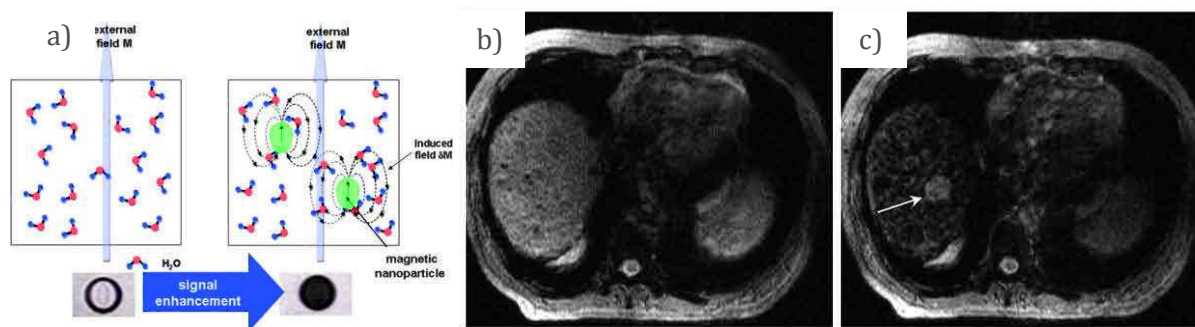


Figure 1-11: a) Magnetic contrast effect of magnetic nanoparticles in water. Induced magnetic field by magnetic nanoparticles perturbs the magnetic relaxation processes of the protons in water molecules, which results in the shortening of T_2 of the proton with a dark MR contrast. (107) IO NPs as contrast media for MRI. MR images of the hepatic dome before (b) and after injection of iron oxide nanoparticles (Ferumoxide: 1.4 ml) (c). (108)

2.3.1.3 IO NPs as T_2 contrast agents

Many commercial superparamagnetic IO NPs were developed and used clinically, with predominance for Dextran-coated IO NPs. Unfortunately, during the last years many of these commercial contrast agents were withdrawn mainly because of their lower contrast efficiencies compared to Gd^{3+} based T_1 contrast agents. For example, Heesakkers *et al.* showed that using ferumoxtran-10 as contrast agent for MRI gave 24 % false positive analysis leading to unnecessary surgical intervention (109). After the Committee for Medicinal Products for Human Use (CHMP) questioned Guerbet about the efficiency of their ferumoxtran product the company decided to stop its commercialization (110). Thus, the withdrawal of commercial SPION was in some cases due to the recent development of nanoparticle-based T_1 contrast agents created to overcome the drawbacks of SPION T_2 contrast agents (104). Table 1-4 summarizes some of the different commercially IO NPs, their dates of approval and withdrawal. However, Gd^{3+} based T_1 contrast agents are known to be toxic when dissociating from their chelating ligands. Indeed, they may be responsible of nephrogenic systemic fibrosis in patients with renal insufficiency and recent literature showed that gadolinium might also deposit in the brain (111–113). Thus, thanks to their biocompatibility and low toxicity, IO NPs are nowadays widely studied in order to improve their efficiencies as T_2 contrast agents.

The reported longitudinal and transversal relaxivities of commercial IO NPs are summarized in Table 1-5. These values are commonly used as references to compare the efficiencies of new IO based contrast agents.

Table 1-4: Summary of some commercial IO NPs, their approvals and withdrawals

General name	Name in USA	Name Europe	Description	Administration	Company	FDA		EMA	
						Approved	Withdrawn	Approved	Withdrawn
Ferucarbotran SHU 555A	-	Resovist Cliavist (France)	Carboxydextran coated SPIO	Intravenous	Bayer Schering Pharma AG	-	-	2001	2009
Ferumoxides AMI-25	Feridex	Endorem	Dextran coated SPIO	Intravenous	-	1996	2012	1994	2012
Ferumoxtran-10 AMI-227	Combindex	Sinerem	USPIO coated by dextran and sodium citrate	-	AMAG	Refused (not enough clinical tests) ⁱ	-	2006	2007
Ferumoxsil AMI-121	Gastromark	Lumirem	Siloxane coated SPIO	Oral, rectally (Europe)	AMAG Distributors : Guerbet (EU, Brasil) Covidien (USA)	1996	february 2013	1993	-
Ferumoxtyol (not for MIR use)	Feraheme	Rienso	SPIO coated by polyglucose sorbitol carboxymethyl ether	Intravenous	AMAG Pharmaceutical/ Takeda	2009	-	2012	-

Table 1-5: Relaxometric properties of commercial IO NPs contrast agents

Name	Coating agent	Core size (nm)	Hydrodynamic size (nm)	B ₀ (T)	r ₁ (mM ⁻¹ s ⁻¹)	r ₂ (mM ⁻¹ s ⁻¹)	r ₂ /r ₁	Ref.
AMI-25	Dextran T10	5	60	0,47	24	107	4	(114)
			72		40	160	4	(115)
		-	120-180	0,47	24	98	4	(116)
				1,5	10	120	12	(117)
		-	-	3	5	130	26	(118)
				7,1	1,8	132	73	(118)
AMI-227 BMS 180549	Dextran T10	5	30	0,47	23	53	2	(114)
			15-30	1,5	10	65	7	(117)
		-	-	3	5	66	13	(118)
				7,1	1,4	71	51	(118)
				-	10	60	6	(116)
SHU 555 A	Carboxy-dextran	38	65	0,47	25	164	7	(115)
		multiple 4 nm single cristals	62	0,94	12	188	16	(119)
		-	60	1,5	10	189	19	(117)
		4.2	62	n.a.	25	151	6	(120)
SHU 555 C	Carboxy-dextran	-	21	1,5	11	38	3	(117)
AMI-121	siloxane	8	300	0,47	3	72	24	(114)
VSOP-C184			7	1,5	14	33	2	(117)

Many parameters can influence the contrast efficiency of IO NPs such as their saturation magnetization M_s , their aggregation and their functionalization (121, 122).

First, it is important to notice that the size of IO NPs strongly influences their T_2 contrast properties. Indeed, as shown in Figure 1-12, Jun *et al.* reported that if the size of IO NPs coated

with 2,3-Dimercaptosuccinic Acid (DMSA) increases, the T_2 -weighted MR signal intensity continuously decreases, which means that the dark contrast increases (123).

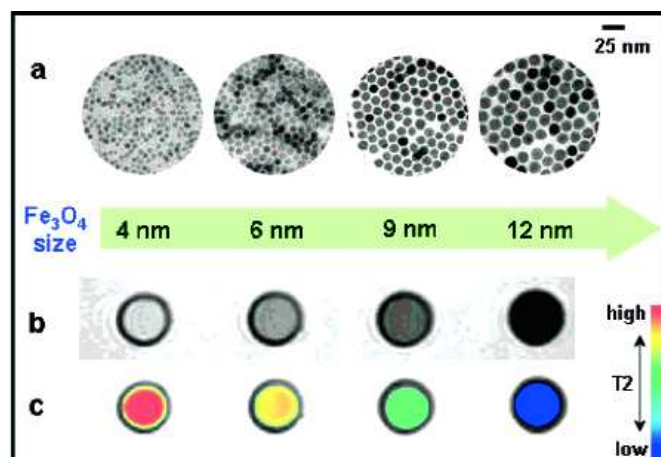


Figure 1-12: Influence of the size of IO NPs on T_2 contrast a) TEM images of IO NPs of 4, 6, 9 and 12 nm ; B) Size-dependent T_2 -weighted MRI of IO NPs in aqueous solution at 1.5 T; c) Size-dependent changes from red to blue in color-coded MR images based on T_2 values (123)

Surface functionalization of IO NPs has also a great influence on their T_2 contrast properties in MRI: the coating should favour the diffusion of water around the magnetic core and allow affecting the highest amount of water molecules. Indeed, many studies showed that modifying the IO NPs with biocompatible polymers, like PEG, modified the magnetic relaxivities. Table 1-6 summarized the transversal and longitudinal relaxivities obtained with various IO's polymer coatings. LaConte *et al.* (124) tuned the coating layer thickness of IO by varying the PEG molecular weights (PEG 550, PEG 750, PEG 1000, PEG 2000 and PEG 5000) to observe the impact of PEG coating on the relaxivity characteristics of IO NPs independently of the IO size. They showed that increasing the IO NPs size by coating it with PEG 750 instead of PEG 550 slightly increased r_2 from 317 to 360 $\text{mM}^{-1}\text{s}^{-1}$ and the r_1 value stay similar (around 13 $\text{mM}^{-1}\text{s}^{-1}$). But, when they increased the Mw of PEG chain over 1000 (1000, 2000 and 5000), r_2 decreased drastically under 200 $\text{mM}^{-1}\text{s}^{-1}$ and r_1 increased to values between 20 and 25 $\text{mM}^{-1}\text{s}^{-1}$. They concluded that for Mw of PEG chains over PEG 1000 the value of r_2 decreased and r_1 increased significantly. Recently Hajesmaelzadeh *et al.* (125) also studied the effect of PEG coating on IO NPs relaxivity properties. They showed that the r_1 and r_2 values both decreased when increasing hydrodynamic size via coating thickness and so for two different Mw of PEG (PEG 300 and PEG 600). Duan *et al.* (126) compared proton relaxivity data for two IO NPs sizes (10 and 30 nm) and three different organic surface coatings to vary hydrophilicity: polyethylenimine (PEI), polyethylene glycol grafted polyethylenimine (PEG-g-PEI) and copolymer of poly(maleic acid) and octadecene (PMO). They demonstrated that for the three different polymer coatings, an increase in IO NPs core size induce higher relaxation rates which is consistent with Jun *et al.* study described above (123). Furthermore, they reported that the hydrophilicity of the coating layer enhanced the proton relaxivities r_1 and r_2 for IO NPs. Finally, Hu *et al.* showed that the coating exchange from diethylene glycol (DEG) to PEG increase the transverse relaxivity (127). They explained that this r_2 increase may be due to the increased volume of slowly diffusing water surrounding each nanoparticle.

Table 1-6: Proton relaxivity data for IO NPs coated with various polymers

Coating agent	Core size (nm)	Hydrodynamic size (nm)	B ₀ (T)	r ₁ (mM ⁻¹ s ⁻¹)	r ₂ (mM ⁻¹ s ⁻¹)	r ₂ /r ₁	Ref.
PEG-550		12,5 ± 1,3		12,7 ± 3,7	317 ± 59	25	(124)
PEG-750		10,5 ± 2,6		12,6 ± 2,4	360 ± 40	29	
PEG-1000	6,6 ± 0,7	12,0 ± 0,8	0,47	25,2 ± 4,9	194 ± 57	8	
PEG-2000		16,4 ± 3,1		24,4 ± 5,9	147 ± 34	6	
PEG-5000		21,6 ± 3,6		21,5 ± 3,2	173 ± 30	8	
Cross-linked dextran and PEG-300	8,86 ± 1,6	74	3	0,22	13,12	60	(125)
	8,69 ± 1,7	93		0,19	11,33	60	
	10,4 ± 2	100		0,16	10,69	67	
Dextran and PEG-600	8,86 ± 1,6	70		0,91	31,44	35	
	8,69 ± 1,7	82		0,67	27,76	41	
	10,4 ± 2	116		0,58	18,33	32	
PMO	10	15	1,5	7,8	27,2	3,5	(126)
	30	45		10,9	70,5	6,5	
PEG-g-PEI	10	25		11,2	39,8	3,5	
	30	56,6		14,1	93,3	6,6	
PEI	10	15		21,5	75,2	3,5	
	30	45		29	107,3	3,7	
DEG	3	8 ± 2,4	1,41	12	29	2,4	(127)
	4	9 ± 2,1		15	42	2,8	
	5	9 ± 2,6		16	48	3	
	6	10 ± 1,3		20	61	3,1	
PEG	3	16 ± 2,8		11	47	4,3	
	4	17 ± 4,0		12	69	5,7	
	5	19 ± 4,1		13	86	6,6	
	6	20 ± 3,3		16	119	7,4	

2.3.2 Therapy by magnetic hyperthermia

Hyperthermia therapy is defined in medicine by the increase in temperature of the region to treat above the physiological temperature of 37 °C. Regarding tumor tissues, as their intrinsic rapid growth lead to defective vascular architecture, these cells are more sensitive than healthy tissues. Thus, heating values over 43 °C are not sufficient but necessary for inducing cell death (128). Hyperthermia can be achieved by magnetic particles that have the feature to produce heat by application of an alternating current magnetic field. The capacity of a material to generate heat under such magnetic field is characterized by a value called specific adsorption rate (SAR) or specific loss power (SLP). A variation of heating effectiveness of IO NPs can be observed by the modification of NP size, anisotropy, concentration or by collective behavior (122).

Recently, the magnetic hyperthermia potential of IO NPs was demonstrated clinically with the favorable results of the “nanothermotherapy” study in clinical phase II led by a German company MagForce Nanotechnology (hospital Charité in Berlin) (129–131). It was very interesting to notice that it has been shown to enhance the sensitivity of tumor cells towards chemo- or radio-therapy and to be able to trigger a thermally-induced release of drugs. Moreover, clinical study also demonstrated that, compared to radio-therapy alone, its combination with thermos-therapy can double the survival rate after 2 years (132). Thus, combining magnetic hyperthermia treatment to other therapies seemed to be an attractive approach, especially in order to solve the chemo-resistance problems observed in some cases (133).

3 Iron Oxide/Mesoporous silica core-shell nanostructures (IO@MS NPs) for theranostic applications

3.1 IO@MS synthesis

The synthesis strategy of the formation of IO@MS NPs is to reproduce the MS synthesis strategy based on Stöber method but at the surface of IO NPs. Thus, IO NPs should act as seeds for silica condensation yielding to core-shell morphology. As the IO NPs were synthesized by thermal decomposition, they are stabilized by oleic acid chains in oil phase, usually chloroform. Thus, the first step for core-shell synthesis is the phase transfer of IO NPs from chloroform into water before the mesoporous silica coating formation, Figure 1-13.

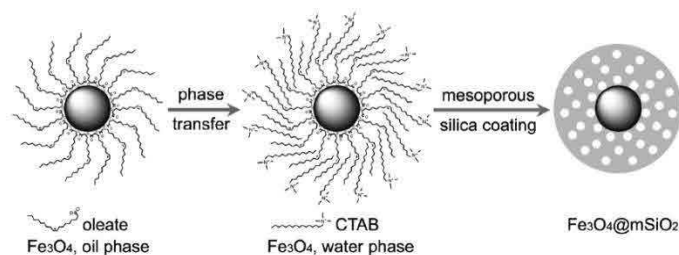


Figure 1-13: General schematic representation of IO@MS synthesis process (115)

This phase transfer strategy, widely described by Fan *et al.* (134–138), is based on the formation of water-soluble nanosized micelles. As pictured in Figure 1-14, the oleic acid stabilized NPs suspension in chloroform is added to a surfactant aqueous solution under vigorous stirring resulting in the formation of an oil-in-water microemulsion. Then the chloroform is evaporated during heating (usually at temperatures of 40–80 °C for about 10 min) to transfer the NPs into the aqueous phase. As shown on the schematic representation of oil evaporation in Figure 1-14, it is important to completely remove chloroform during the phase transfer process in order to obtain water-dispersible micelles without clustering. This phase transfer is driven by the hydrophobic van der Waals interactions between the alkyl chains of surfactant and of oil-stabilizing ligand resulting in the formation of thermodynamically defined interdigitated bilayer structures Figure 1-14.

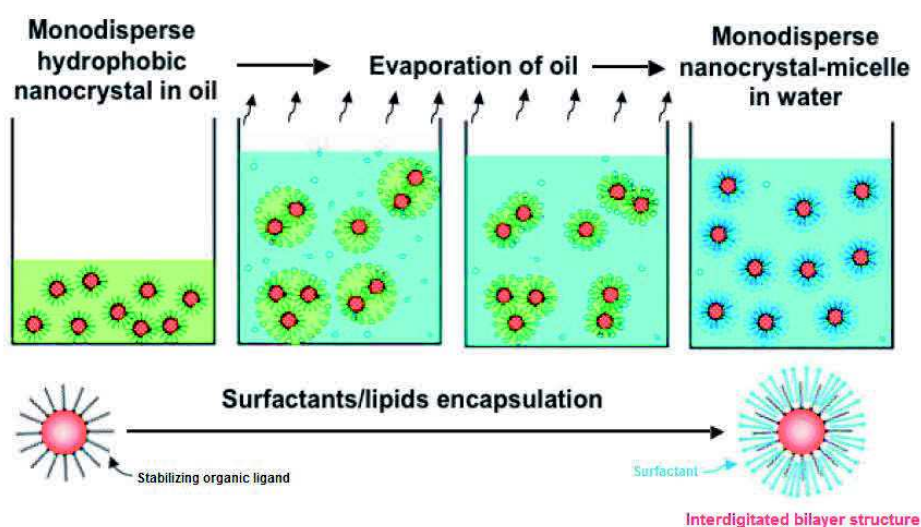


Figure 1-14: Schematic representation of formation of water-soluble nanocrystal micelles through surfactant/lipid encapsulation (136)

The surfactant molecules used for phase transfer of NPs in aqueous phase also act as organic template for the formation of mesoporous silica coating via base-catalyzed hydrolysis of TEOS precursors and subsequent silica condensation onto surfactant micelles surface. Thus, as it was the case for MS NPs synthesis, the porosity is templated by the surfactant micelles size and their 3D self-assembly. The syntheses of IO@MS NPs were mostly carried out using CTAB as surfactant, leading to porosities of about 3 nm. Zhang *et al.* (139) reported that using different alkyltrimethylammonium bromide surfactant chain lengths they were able to template precisely the pore sizes of MS shell. Indeed, the porosity was tuned from 2.4, 2.8 to 3.4 nm by varying the carbon chain length of surfactant from C₁₄, C₁₆ to C₁₈ respectively.

To get a better control of IO@MS formation, Suteewong *et al.* (140) investigated the structural evolution of IO@MS synthesis at room temperature to elucidate key steps of the process. From their observations and analyses they proposed, as depicted on Figure 1-15, a formation mechanism of IO@MS NPs divided into three parts. The first part described the stepwise addition of reactants, the second part, taking place for 5 min after TEOS addition, described the mixing step and finally, the third part described the aging step. They explained that during the second part the classical sol-gel process described by Stöber occurred. Indeed, as TEOS is immiscible in water, it forms small TEOS droplets and the TEOS molecules hydrolyzed at the water interface. This hydrolysis generates ethanol which gradually changes the polarity of the media and thus increases TEOS solubility. Thanks to electrostatic interactions with free surfactant, surfactant micelles and above all, in this case, with surfactant-stabilized IO NPs the hydrolyzed TEOS molecules will condense along them leading to the formation of IO@MS NPs. At this step, as the surfactant-stabilized IO NPs act as seeds, they are located in the center of the core-shell NPs. But with the addition of water, initiating the third part, the TEOS solubility changes suddenly. This induces a second nucleation yielding to the formation of secondary silica nanoparticles which were consumed by the growing primary IO@MS through an Ostwald ripening-type process. During this growing step, the silica matrix ordered into a hexagonal structure. They also observed that this ordering stage repels the IO NPs to the grain boundaries leading to IO@MS NPs with the IO core located at the edges of NPs.

However, many reported syntheses based on the same principle lead to uniform IO@MS NPs with the IO core at the middle (115, 141). These syntheses differed from the one described above by the fact that they were performed at 80 °C for 2h and that no additional water was added after TEOS addition. Thus the pH did not decrease drastically by water addition that should silica condensation acceleration and subsequent silica hydrolysis slow-down. The pH decrease was only due to gradually ethyl acetate hydrolyzation, thereby the silica condensation will occur slower. However the reaction rate was increased by increasing the reaction temperature.

In this method, the amount of TEOS added as well as the ratio between IO NPs and CTAB surfactant are key factors for the tuning of silica shell thickness. This silica shell thickness is important to master as it has a huge impact on the core MRI abilities as well as on the drug loading.

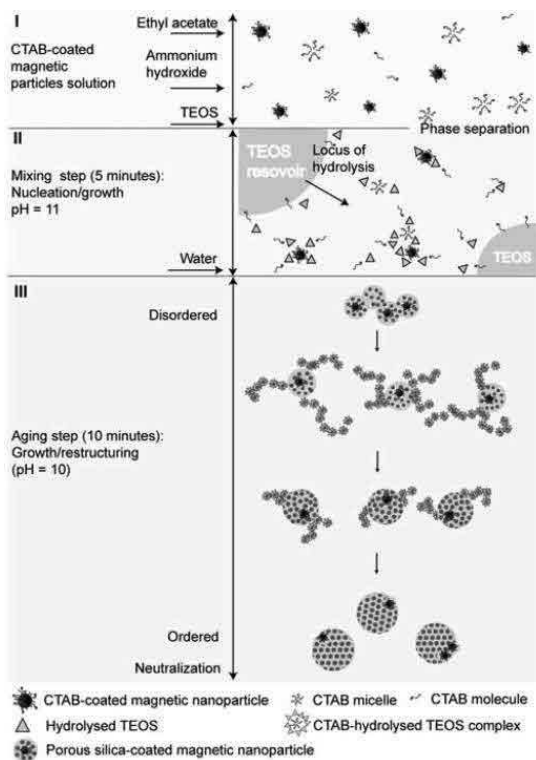


Figure 1-15: Formation mechanism of IO-RB NPs proposal (140)

3.2 IO@MS NPs as theranostic agents

The major interest in the design of core-shell materials such as IO@MS NPs for biomedical application is the combination of the diagnosis and therapy abilities of each entity. Thus, as illustrated in Figure 1-16, IO@MS NPs could be used for diagnosis by MRI thanks to the IO core and by the use of fluorophores thanks to the MS shell. Moreover, cancer therapy can be achieved by the release of drugs loaded into the MS shell and also by magnetic hyperthermia thanks to IO core.

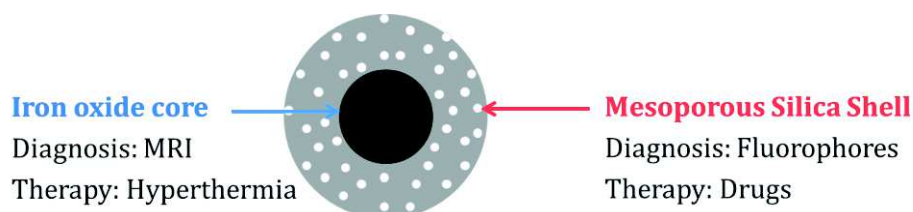


Figure 1-16: Schematic representation of potential theranostic properties of IO@MS NPs

3.2.1 Diagnosis

Forming silica shell around IO NPs strongly modified the contrast efficiency of IO NPs. Indeed, as summarized by some examples in Table 1-7, the addition of silica shell onto IO NPs, whether amorphous or mesoporous, drastically decreases r_1 values. Furthermore, the increase in silica shell thickness decreases both r_1 and r_2 values.

Ye *et al.* (115) studied in details the impact of the thickness of the mesoporous silica shell on magnetic relaxivities. They showed that adding a MS shell around IO NPs did not significantly modify r_2 values but on the contrary drastically decreased the r_1 values, which increased by approximately 10 the r_2/r_1 ratio. This is for them due to the difference between CTAB and MS coating layers on the mobility of water molecules. Furthermore, by increasing the MS shell thickness, r_1 continued to decrease as well as r_2 . From the smallest to the thickest coating the r_1 values decreased by ca. 70% whilst r_2 decreased by only ca. 40%, resulting in a great increase in r_2/r_1 ratio up to 179 for 95 nm NPs at 60 MHz. They explained that the decreased value of r_1 with increased MS shell thickness may reflect the ability of MS coatings to separate the water from the IO NPs. They also demonstrated by NMR-relaxometry studies that the MS shell is partially permeable to water molecules that explained the decrease of longitudinal relaxivity r_1 . In addition, the decreasing r_2 values with MS shell thickness increase may suggest that the locally generated magnetic field by IO cores has been slightly weakened. These results are in accordance to the study made by Pinho *et al.* on amorphous silica coating on IO NPs (142, 143).

Furthermore, the incorporation of a fluorescent probe in magnetic silica nanocomposites may be useful for complementary bimodal MRI and fluorescence bio imaging. The combination of these two imaging mode is particularly attractive as the fluorescence property brings a high sensitivity of detection associated tough to a weak depth penetration (\leq several mm) while MRI brings a good spatial resolution without issue regarding the magnetic wave penetration.

Table 1-7: Some examples of proton relaxivities of IO@MS NPs at 60 MHz

Coating agent	Core size (nm)	Diameter (nm) (TEM)	B ₀ (T)	r ₁	r ₂	r ₂ /r ₁	Ref
Amorphous silica	-	10	1,5	1,67	81,8	49	(144)
		11,5		1,88	112,8	59	
		14		2,27	128,2	57	
Amorphous silica	9,6 ± 1,2	9,9 ± 1,6	1,5	0,55	339,8	618	(145)
APTMS		10,5 ± 2,4		1,17	134,4	115	
AEAPTMS		10,9 ± 2,8		1,05	84,8	81	
No coating	9,6 ± 1,3	9,6 ± 1,3	1,5	15,96	130,28	8	(143)
		11,2 ± 1,7		7,66	117,03	15	
		24,7 ± 3,2		2,05	102,08	50	
		46,4 ± 8		0,72	92,91	129	
Amorphous silica		73,8 ± 8,1		0,4	55,02	138	
		94,9 ± 7		0,32	43,63	136	
		114,2 ± 12,7		0,34	43,06	127	
		152,9 ± 13,1		0,34	43,06	127	
No coating	11	11	1,41	13,69	82,18	6,01	(115)
Mesoporous silica		50		1,31	92,13	70,3	
		75		0,97	87,54	90,3	
		95		0,31	55,44	179	

3.2.2 Therapy

3.2.2.1 IO@MS NPs as therapeutics using magnetic hyperthermia

To the best of our knowledge, the impact of mesoporous silica shell on IO NPs magnetic hyperthermia abilities is scarcely described in the literature. Some publications indicate that IO@MS NPs are able to generate heat upon exposure to an alternating magnetic field thanks to their IO core (146–151). But only few of them compared the heating capacities of their final IO@MS systems to those of the initial IO NPs. Zhu and Tao reported that the addition of a stellar MS shell on their IO NPs decreased their heating capacities (152) whereas Majeed et al reported that, on the contrary, the coating of IO NPs with non-porous silica shell increased their heating capacities (148). They explained that, since the silica coating helps to prevent IO NPs aggregation it preserves their Brownian motion and thus helps to preserve the heat generation. However they also showed that their SAR value decreased with increasing the silica shell thickness.

Thus, according to these contradictory observations, a lot of work has still to be done to highlight clearly the impact of the MS shell addition on IO magnetic hyperthermia capacities.

3.2.2.2 IO@MS NPs as cargo for drug delivery

3.2.2.2.1 Drug loading

A large variety of drugs such as taxol, ibuprofen, cisplatin, doxorubicin can be encapsulated into many kind of materials as nanotubes, polymers, liposomes, mesoporous silica... To this end, as porosity is known to allow high loading and release of drug, porous drug carriers got a huge development and some formulations such as porous silica, polypropylene foams and porous magnesium aluminosilicate were commercialized under the trade names of Sylysia, Accurel and Neusilin respectively. Thus in the following we will focus only on nanosystems that are the closest to those we developed in this thesis, *i.e.* NPs containing a mesoporous silica shell, for the encapsulation of a specific antitumoral agent, the Doxorubicin (Dox).

Two essential entities are widely used in literature to evaluate the drug loading abilities of NPs: Drug Loading Content (DLC) and the Drug Loading Efficiency (DLE). DLC is defined by the weight percentage of the ratio between Dox loaded amount and the weight of NPs, Equation 1-1, whereas DLE corresponds to the percentage of Dox loaded into NPs for a specific amount of Dox initially introduced in solution during the reaction, Equation 1-2.

$$DLC\% = \frac{\text{weight of Dox loaded}}{\text{weight of NPs}} \times 100$$

Equation 1-1: Formula of Drug Loading Content (DLC)

$$DLE\% = \frac{\text{weight of Dox loaded}}{\text{weight of Dox fed}} \times 100$$

Equation 1-2: Formula of Drug Loading Efficiency (DLE)

Dox loading into mesoporous silica is usually performed by simple soaking of Dox with NPs in a solution. The soaking is achieved at a feed weight ratio (fwr) corresponding to the percentage of the ratio between the weight of Dox fed initially in the soaking media and the weight of NPs, Equation 1-4.

$$fwr\% = \frac{\text{weight of Dox fed}}{\text{weight of NPs}} \times 100$$

Equation 1-3: Formula of feed weight ratio (fwr)

Table 1-8 presents some examples of reported procedures for Dox loading into mesoporous silica shell. This table highlights that, besides physical and morphological properties of MS (see section 1.2 page 11), soaking parameters also influence the drug loading. Indeed, the impact of the following soaking parameters on drug loading was reported:

- Surface functionalization of MS
- Nature of soaking media
- pH of soaking media
- Presence of coupling agent or gatekeeper

Thus, as shown in Table 1-8, the silica shell surface modification and the choice of solvent could influence the Dox loading. Indeed, Yang *et al.* described two methods for Dox loading into the same NPs achieved with the same fwr. In one case the loading was carried out in EtOH on non-modified silica (153) whereas in the second study the loading occurred in PBS on amino-functionalized silica surface (154). They obtained low DLC values between 1.23 and 2.16 % for the first experiment and a little higher DLC value of 4.7 % in the second trial. So for the same fwr the DLC was more than twice higher for the Dox loading on amino-functionalized silica surface in PBS than in EtOH on raw silica surface. To conclude, either the surface modification or the solvent choice or both influenced the drug loading in these studies. These observations support previous reports that showed that functionalization of MS is a major factor boosting drug uptake. Indeed, Vallet-Regi team showed that amine functionalization of MS surface enhanced considerably the drug uptake (ibuprofen and bisphosphonate) compared to non-modified silanol surface of MS (155, 156).

Furthermore, Chang *et al.* reported that Dox loading behavior into MS was pH-dependent (157). Indeed, both DLC and DLE increased from 0.9 % to 21.5 % and from 2.9 % to 91.3 % respectively by increasing the pH from 5 to 10. This effect was probably due to Dox precipitation into mesoporous channels as Dox started to be insoluble under alkaline conditions (158).

Finally, the presence of coupling agent or gatekeeper also modifies the DLC and DLE. For example, Li *et al.* reported that the Dox loading into MS exhibited higher loading content, 39 % against 13 %, and loading efficiency, 61 % against 7 %, by introducing an urea bond to conjugate Dox to silica than without any coupling agent (159).

3.2.2.2.2 Drug release

Allowing high DLC values is not a sufficient ability for NPs to be considered as a good cargo for drug delivery. Indeed, the NPs should be able to release a maximal amount of the drug they encapsulated. Thus, that is defined by the weight percentage of Dox released versus Dox loaded, Equation 1-4: Formula of % of Dox released.

$$\text{Dox released \%} = \frac{\text{weight of Dox released}}{\text{weight of Dox loaded}} \times 100$$

Equation 1-4: Formula of % of Dox released

As described in Table 1-8, the drug release can be modulated by some parameters such as pH or temperature that are directly related to the stimuli selected to trigger drug delivery. For

example, Lee *et al.* introduced hydrazone bonds to covalently bind Dox into MS channels. As this bond is pH cleavable at pH values below 5, they observed controlled drug release by pH decrease. Thus, after 56 h, at pH 7.4 only 4 % of Dox was released whereas at pH 5 and 4 high values of 50 and 78 % of Dox released were respectively achieved (160). Liu *et al.* developed thermoresponsive drug delivery systems by using 1-tetradecanol as gatekeeper that has the ability to melt at temperatures above 39 °C. Thus at 37 °C they observed only a Dox release lower than 4 % whereas by increasing the temperature to 40 °C the Dox release also increased to 37 %. Moreover, they proved the efficiency of their gatekeeper by controlling the Dox release by “ON and OFF” sequences of 12 h each (ON: 40 °C and OFF: 37°C), and by showing that without 1-tetradecanol to gate the porosities, Dox release was not temperature dependent as, in the absence of gatekeepers, 25 % of Dox released was measured at both 37 °C and 40 °C (161).

However, % Dox release and DLC do not fully evaluate the ability of NPs to be good cargos if they are not taking into account together. Indeed, it can be seen that in some cases even if a high DLC value was reached, the maximal Dox released was poor and vice versa. So we wonder what is the most efficient: having high DLC and low release or low DLC and high release? Moreover, how nanosystems can be compared to each other if they all exhibit different DLC and maximal Dox release values?

Thus, to evaluate simultaneously the drug loading and the drug release, we introduced a simple value called Drug Release Content (DRC) that, for the best of our knowledge, was not discussed in the literature. Thus, we defined DRC by the percentage of Drug released for a specific amount of NPs, Equation 1-5. Thereby, the higher the DRC, the lower the NPs amount to inject to patients.

$$DRC\% = \frac{\text{weight of Dox released}}{\text{weight of NPs}} \times 100$$

Equation 1-5: Formula of Drug Release Content (DRC)

This DRC value can also be expressed by the following Equation 1-6:

$$DRC\% = \frac{DLC \times \text{Maximal Dox released}}{100}$$

Equation 1-6: Second definition of Drug Release Content (DRC)

The advantage of introducing this DRC value is illustrated in the following example. Yang *et al.* designed IO@MS core-shell NPs for enzyme controlled drug delivery by introducing disulfide bonds that could break by GSH and allow drug release (153). Thus, they showed that, as expected, the higher the amount of initial disulfide bonds to gate the porosities, the higher the DLC. However, they found higher maximal drug release % for the sample synthesized with low amount of disulfide bonds. Indeed, maximal drug releases were about 95 %, 69 % and 43 % whereas the DLC values were about 1.23 %, 1.6 % and 2.16 % for the samples obtained with low, medium and high amount of disulfide bonds. Thus, without introducing the concept of DRC, we were not able to conclude which sample is the most suitable for drug delivery. Finally, according to DRC calculations, the sample synthesized with low disulfide bond amount was the most efficient for drug loading and release.

Table 1-8: Overview of some Dox loading experiments into MS (PS: Particle Size; PD: Pore Diameter)

Nanoparticles Characteristics				Dox Loading conditions								Dox release				Ref.			
Core	Shell	Gatekeeper	External stimuli	Dox type	MS surface	Buffer	Time, T°C	pH	DLC (%)	DLE (%)	pH	Buffer	T°C	Maximal Dox release (%)	DRC (%)	Time (h)	Ref.		
IO@RB NPs type	IO PS: 7.5	MS PS: 59 PD: 3	1-tetradecanol (TD)	Thermo-responsive (>39°C)	Dox	NH ₂ and PEG	EtOH	5h at 80°C then 1h with 10mg TD	-	9.3	37.3	7.4	PBS	37°C	< 4	0.38	96	(161)	
			40°C	37										3.4					
	ON: 40°C (12h) OFF: 37°C (12h)	18	1.7																
	IO PS: 13	MS PS: 60	urea bound Dox-ICPTES	pH	Dox.HCl	One-pot synthesis of MS in presence of Dox	Water ICPTES Water TEOS	24h at RT	-	39.4 ± 2.4	60.5 ± 3.7	7.4	PBS	RT	13.3 ± 3.4		5.2	261	(159)
			none	-											90 ± 3.6	11.4	22,5		
	IO PS: 15	MS PS: 45-105 PD: 2-3	none	-	-	PEG stabilized	PBS	overnight at RT	-	-	-	-	-	-	-	-	-	(141)	
	IO PS: 15	MS PS: 160 ± 20 PD: 2,8	P(NIPAM-co-MAA)		Dox.HCl	Si-OH	water and NaOH (0,1M) to adjust pH	24 h at 25°C	5.1	0.9	2.9	7.4	PBS	37°C	7.2	0.06	24	(157)	
									8	16.2	72	6.5	PBS	37°C	37.1	6			
									10	21.5	91.3	5.0	acetate	37°C	80.2	17.2			
	IO PS: 20	MS PS: 60 PD: 2.4	Disulfide bond low amount medium amount high amount	enzyme responsive: glutathione reductase (GSH)	Dox.HCl	Si-OH	EtOH	12h at 25°C	-	1.23	-	6.5	PBS	-	94.89 (without GSH ~20)		1.17	24	(153)
1.6										-	69.06 (without GSH ~10)				1.1				
2.16										-	42.76 (without GSH ~5)				0.92				
IO PS: 20	MS PS: 59 PD: 2.4	Sodium hyaluronic acid (HA)	Enzyme: HAase None	Dox.HCl	NH ₂	PBS	12h at 25°C	7.4	4.7		5	PBS	37°C	43	2	48	(154)		
											7.4			10	0.47				
IO@ST NPs type	IO PS: -	MS stellar PS: 100-200 PD: 3 and 10	DNA	Dox.HCl	NH ₂ and DNA	HEPES	24h at RT	-	4	-	7.4	PBS	37°C	7	0.28	9	(162)		
											50°C		27	1.08					
	5	-	37°C	17	0.68														
	50°C	50	2																
IO PS: 15-20	MS stellar PS: 150 PD: 3 and 10			Dox.HCl	Si-OH	PBS	24 h at RT	-	4.5	90	7.4	-	37°C	7-8	0.35	23	(152)		
											5		-	37°C	55-65			2.7	

MS NPs without core	IO PS: -	MS stellar PS: 100- 200 PD: 3	DNA		Dox.HCl	NH ₂	-	24h at RT	-	5-6	-	5	PBS	37°C	<10	0.6	6	(150)
														43°C	~50	3		
														47°C	~60	3.6		
														ON: 43°C (1h) OFF: 37°C (12h)	~50	3	72	
	MS; PS: 70 PD 2,3	IO	none		Dox.HCl	PEG stabilized	Water	overnight at RT	-	8	-	7.4	PBS	37°C	55	4.4	300	(3)
	MS PS: 80 PD: 3	IO PS: -	Hydrazone bond	pH	Dox	Diamine -NH-NH ₂ and PEG	Methanol	overnight at 30°C	-	1.1	-	7.4	PBS (10mM)	37°C	4	0.04	56	(160)
												5	acetate (10mM)		~50	0.55		
												4	acetate (10mM)		78	0.86		

4 HSA NPs for biomedical applications

Intrinsic properties of proteins such as biocompatibility, biodegradability, biofunctionality render them attractive as materials for biomedical application. Nowadays, human serum albumin (HSA) is emerging as a promising protein drug carrier. Indeed, since these last 10 years three albumin drug carriers derivatives have been clinically evaluated: a methotrexate-albumin conjugate, an albumin-binding prodrug of doxorubicin and an albumin paclitaxel NP (Abraxane) (163, 164).

Recently, Mertz *et al.* described a new route for the formation of self-supported HSA NPs or nanocapsules using silica NPs as sacrificial templates. As shown in Figure 1-17, this procedure consists in HSA adsorption on the surface of silica templates, modified beforehand with IBAM groups, followed by template removal (165). Depending on the porosity of the silica template HSA NPs (large mesoporous silica NPs) or HSA nanocapsules (full silica NPs) were obtained. It was assumed that the driving force of the assemblies between IBAM and HSA is attributed to significantly strong H-bonds. However the exact mechanism of interaction of the IBAM grafts with many macromolecules remains still unelucidated at this stage.

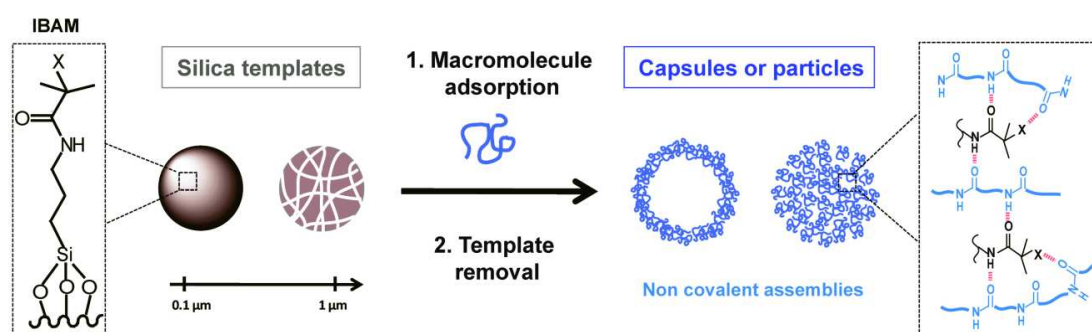


Figure 1-17: Scheme of the IBAM-mediated process to form non-covalent macromolecular micro- and nanoparticles. A hypothetical mechanism is given (right). X stands for bromine or hydrogen atoms (165)

This approach is generalizable to various biomacromolecules and yielded to the formation of particles made of a range of proteins, nucleic acids and polysaccharides (Figure 1-18). The process allows the formation, after template removal, of protein hollow capsules with finely controlled wall thickness at nano-scale. The functionalization of these capsules with other biological macromolecules yielded hybrid biopolymeric capsules (e.g., HSA-alkaline phosphatase, HSA-dextran, HSA-DNA) which can find applications as biosensors or nanovehicles for drug delivery and cell-targeting (166, 167).

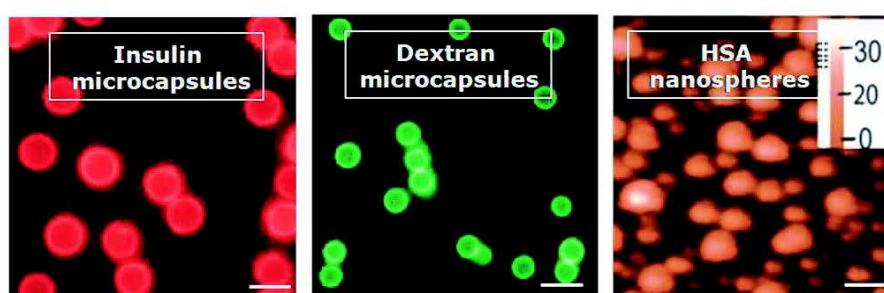


Figure 1-18: Fluorescence and AFM microscopy images of microcapsules and nanoparticles made of various biomacromolecules, scale bars are 5 μm for fluorescence and 200 nm for AFM.

Chapter 2:

Materials and Methods

1 Characterization techniques

1.1 Physico-chemical analyses

1.1.1 Transmission electron microscopy (TEM)

Detailed morphological information was obtained by transmission electron microscopy, TEM. Basically, as pictured on Figure 2-1, an electron beam, issued from an electron gun composed of a filament and a voltage accelerator (voltage accelerations between 100 and 400 kV), is diffracted by passing through the sample and thanks to magnetic lenses is recombining to impact a fluorescent screen or numerical camera positioned in the image plan. Thus a contrast image of the sample is obtained.

The TEM images were performed on microscope TOPCON 002B operating at an accelerating voltage of 200 kV.

To be analyzed by TEM, a sample should be thin for allowing a maximum of electron to pass through, should not contain any solvent or volatile substance which could foul the microscope, and should be stable under electron beam. Thus, for each experiment, a drop of diluted solution of NPs suspension was deposited on a Formvar-coated copper grid. The liquid was evaporated at room temperature, or the evaporation could be accelerated in some cases by placing the sample under a lamp.

The statistical treatment of TEM images was performed with the ImageJ software. At least 200 particles were measured on the pictures to obtain relevant size distributions.

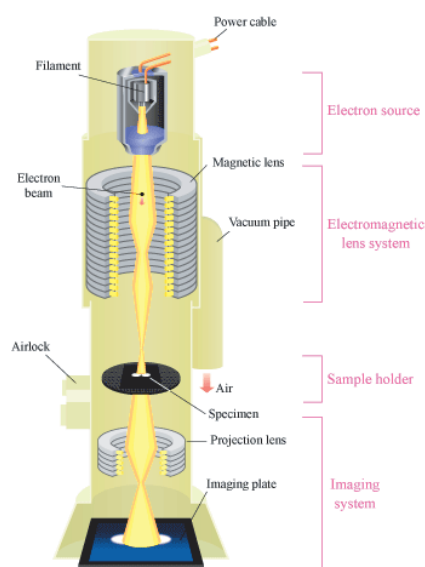


Figure 2-1: Schematic representation of TEM principle

1.1.2 Scanning electron microscopy (SEM)

To investigate their surface morphologies, the samples were analyzed by scanning electron microscopy (SEM). Typically, as pictured on Figure 2-2, an electron beam is generated by an electron gun with energies from 0.2 to 40 KeV, and is focused by condenser lenses to a spot about 0.4 to 5 nm in diameter. The beam passes through pairs of scanning coils in the electron column, typically in the final lens, which deflect the beam in the x and y axes so that it scans a rectangular area of the sample surface. When the beam is interacting with various atoms of the sample it loses energy. These energy variations produce signals that contain information about

the sample's surface topography and composition such as secondary electrons (SE), reflected or back-scattered electrons (BSE), photons of characteristic X-rays, light cathodoluminescence (CL), absorbed current (specimen current) and transmitted electrons.

SEM is most commonly used on the detection of secondary electron mode. These secondary electrons possess low energies and are produced within few nanometers of the sample surface. The brightness of resulting images depends in the number of secondary electrons reaching the detector. On a flat surface, the beam enters the sample perpendicular to its surface creating a uniform activated region about the beam axis from which a certain number of electrons escape from the sample. If the angle of incidence increases resulting in a larger activated region and a lower electron escape distance on one side of the beam. So more secondary electrons are emitted from the sample and the signal becomes brighter. Thus edges tend to be brighter than flat surfaces, which results in images with a well-defined, three-dimensional appearance.

The SEM can also be used in transmission mode by simply incorporating an appropriate detector below a thin specimen section. Both bright and dark field imaging has been reported in the generally low accelerating beam voltage range used in SEM, which increases the contrast of samples at high magnifications with a field emission electron gun. This mode of operation was called STEM.

The instruments used for our SEM images were JEOL 6700F and Zeiss Gemini microscopes.

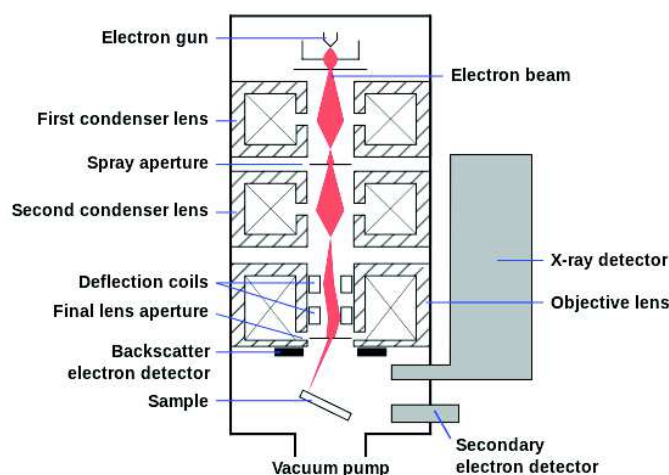


Figure 2-2: Schematic representation of SEM principle

1.1.3 Adsorption/Desorption nitrogen isotherms

The pore volume, pore size distribution and surface area of mesoporous silica materials were determined by nitrogen adsorption and desorption isotherms. An adsorption isotherm is obtained by measuring the volume of gas adsorbed across a wide range of relative pressures at constant temperature. On the contrary, desorption isotherms are achieved by measuring gas removed as pressure is reduced.

According to IUPAC (168, 169), the adsorption-desorption isotherms can be classified into six main groups related to the type of porous materials and the hysteresis loops can be classified into five main groups depending on the porous morphology Figure 2-3. The three first types of adsorption-desorption isotherms does not exhibit any hysteresis, so are reversible. Type I isotherms are specific for microporous (pore size below 2 nm) materials whereas Type II

isotherms, exhibiting a point B which indicates the relative pressure at which monolayer is complete, are given by non-porous or macroporous (pore size above 50 nm) materials. Type III isotherms do not exhibit any point B, so have no identifiable monolayer formation, and are specific for non-porous solids. Type IV isotherms are given by mesoporous (pore sizes between 2 and 50 nm) materials. In this case, the initial monolayer-multilayer adsorption on the mesopore walls, which is similar to Type II isotherm, is followed by pore condensation. A typical feature of Type IV isotherms is a final saturation plateau. In the case of a Type IVa isotherm, capillary condensation is accompanied by hysteresis. This occurs when the pore width exceeds a certain critical width, which is dependent on the adsorption gas and temperature. With adsorbents having mesopores of smaller width, completely reversible Type IVb isotherms are observed. Type IVb isotherms are also given by conical and cylindrical mesopores that are closed at the tapered end. Type V isotherms exhibit similar shape than Type III at low p/p^0 , which is specific to weak adsorbent-adsorbate interactions. At higher p/p^0 , pore filling occurs. Type V isotherms are observed for water adsorption on hydrophobic microporous and mesoporous adsorbents. Finally, Type VI isotherms exhibit a reversible stepwise shape which is representative of layer-by-layer adsorption on a highly uniform nonporous surface.

The Type H1, steep and narrow hysteresis loop, is observed for uniform mesopores. More complex pore structures, with important network effects, lead to Type H2 hysteresis loop. Type H2a exhibits a very steep desorption branch, which can be attributed to pore-blocking/percolation in a narrow range of pore necks or to cavitation-induced evaporation. Type H2b is also significant for pore-blocking effect but for larger size distribution of neck widths. Type H3 loop, with adsorption branch behavior similar to Type II isotherm, does not exhibit any limiting adsorption at high p/p^0 and is usually observed with aggregates of plate-like particles. Type H4 has a similar behavior but the higher uptake at very low p/p^0 is associated with the filling of micropores. Type H4 loops are observed with narrow slit-like pores. Finally Type H5 loop is very unusual and is observed for pore structures containing both open and partially blocked mesopores.

On well-defined Type II and Type IVa isotherms the surface area can be calculated applying the Brunauer-Emmett-Teller (BET) gas adsorption method. The pore volume and size could be investigated through Barrett-Joyner-Halenda (BJH) computations from nitrogen isotherms (170). For microporosity estimation the Horvath-Kawazoe (HK) method was applied.

Prior to the adsorption-desorption isotherm measurements, the sample should be outgassed, i.e. exposed to high vacuum at elevated temperatures. During this process all of the physisorbed species should be removed from the surface of the material. In our experiments the samples were outgassed at 250 °C for at least 6 hours and the adsorption-desorption isotherms were obtained from an ASAP 2420 V instrument at 77 K under nitrogen.

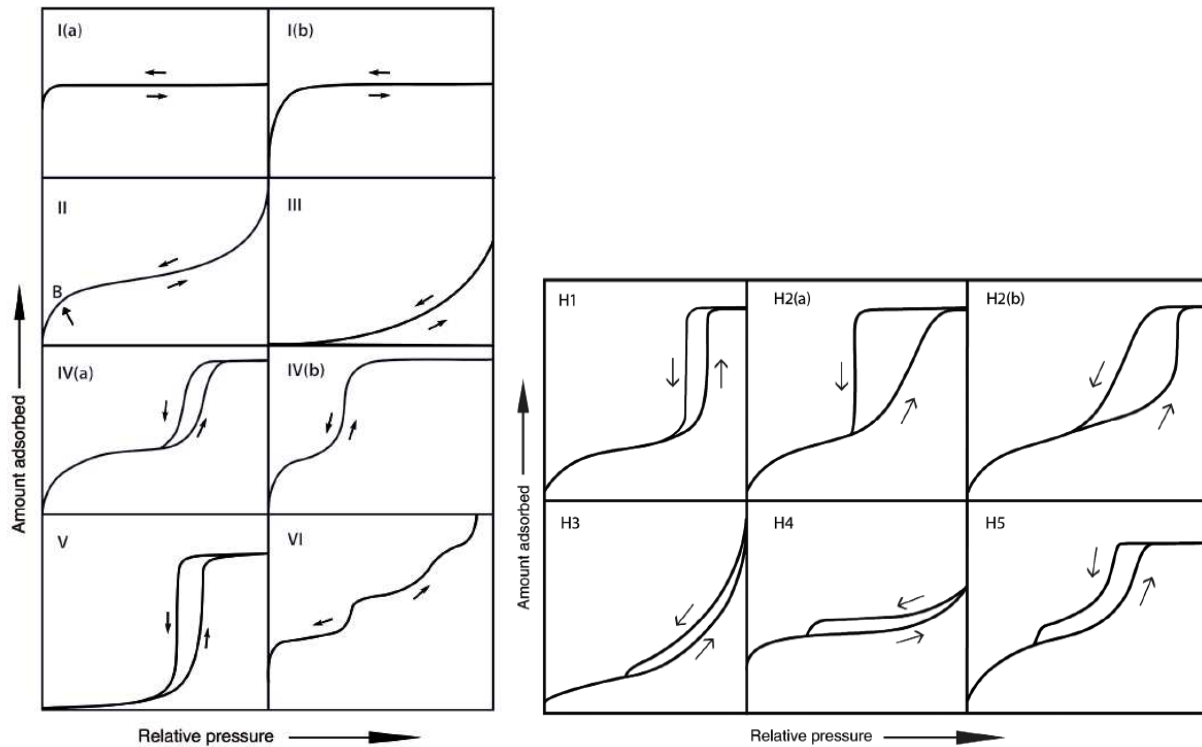


Figure 2-3: A) types of physisorption isotherms B) types of hysteresis loops

1.1.4 Dynamic light scattering (DLS)

DLS, also called photon correlation spectroscopy (PCS), is a non-invasive granulometric method which measures the hydrodynamic size, between 1 nm and few μm , of NPs in suspension in a media. The hydrodynamic diameter of a NP includes the solid inorganic particle but also the polymers or molecules graft onto the surface as well as the ionic double layer.

The DLS principle is based on the Brownian motion theory, defined by the random motion of particles suspended in a fluid, Equation 2-1. DLS measures the diffusion coefficient (D) of the particles and calculates the hydrodynamic size of NPs applying the Stokes-Einstein law, Equation 2-2.

$$\overline{X^2} = 2Dt$$

Equation 2-1: Brownian motion; $\overline{X^2}$: position variance of the particle, Brownian motion; D translational diffusion coefficient (cm^2/s); t : time (s)

$$d(H) = \frac{kT}{3\pi\eta D}$$

Equation 2-2: Stokes-Einstein law; $d(H)$: hydrodynamic diameter (nm); T : absolute temperature; D translational diffusion coefficient (cm^2/s), η : dynamic viscosity (cP), k : Boltzmann's constant

The calculation of the diffusion coefficient D in the instrument followed this principle. When a laser penetrates a solution of particles in suspension, it deflected by the particles: small particles with a high Brownian motion will diffused faster than bigger particles with a slower Brownian motion. Thus, the DLS sends a laser to the particles solution and measures, with a detector placed at a specific angle, the scattered light density fluctuations over time. These variations were then analyzed by numerical auto-correlator to calculate the delay time, τ . Thus, smaller the particles, faster scattered light density fluctuation and smaller the subsequent delay

time. From the τ value the instrument calculates then the autocorrelation function $G(t)$, an exponential decreasing function, which describes the immobility probability of a particle in function of time, Equation 2-3. This autocorrelation function is related to the diffusion coefficient by the Equation 2-4 in which $\gamma_i = D_i q^2$. The constant q which is a wave vector is calculated from the parameters introduced in the instrument before measurement by the Equation 2-5.

$$G(t) = \sum i(t) \cdot i(t + \tau)$$

Equation 2-3: Autocorrelation function $G(t)$

$$G(t) = \sum c_i \exp(-\gamma_i t)$$

Equation 2-4: Autocorrelation function $G(t)$ in function of: c_i intensity of the light scattered by particles with i size; $\gamma_i = D_i q^2$ with D_i is the diffusion coefficient for i sized particles and q a wave function

$$q = \frac{4n\pi (\sin \alpha/2)}{\lambda}$$

Equation 2-5: q calculation with n is the refraction index of the media, λ the wavelength of the laser, α the angle between the laser and the detector scheduled from the recording

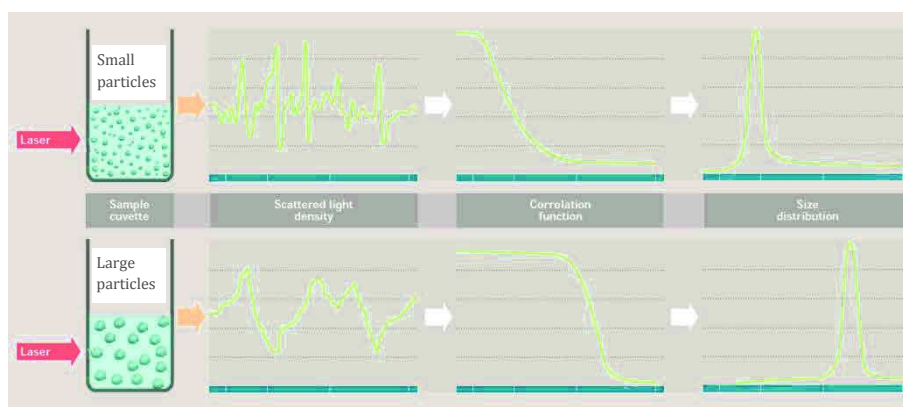


Figure 2-4: (from Malvern)

Through all these calculations a DLS curve in intensity is obtained. Thus, the size results obtained in DLS intensity are always trustable and more precise, because they are directly issued from the scattering light measurement. However, applying some algorithms, the software also indicates size results in volume and number. These results could be less trustable because the algorithms could introduce some approximations.

It is also important to visualize the difference between the results obtained in number and in volume. Indeed, as pictured in Figure 2-5, if the solution contains 3 particles of $1\mu\text{m}$, 3 of $2\mu\text{m}$ and 3 of $3\mu\text{m}$, the DLS in number, Figure 2-6 A, will indicate that one third of the particles got a diameter of $1\mu\text{m}$, on third a diameter of $2\mu\text{m}$ and the last third a diameter of $3\mu\text{m}$. On the other hand if we calculate the volume occupied by each particle size we obtained a volume of $1.6\mu\text{m}^3$ for the $1\mu\text{m}$, $12.6\mu\text{m}^3$ for the $2\mu\text{m}$ and $42.3\mu\text{m}^3$ for the $3\mu\text{m}$ particles, so a total volume of $56.6\mu\text{m}^3$. Thus, as pictured on Figure 2-6 B, the DLS in volume for this solution will indicate that 4.3 % of the particles have a size of $1\mu\text{m}$, which means that 4.3 % of the total volume is occupied by $1\mu\text{m}$ particles, 22 % have a size of $2\mu\text{m}$ and 75 % have a size of $3\mu\text{m}$. To conclude it can be interesting to compare the size distributions in volume and in number to investigate if, for example, the intensity obtained at high size range corresponds to a small number of aggregates,

which can be removed by centrifugation, sedimentation, filtration, or of the majority of the particles have indeed a strong aggregation.

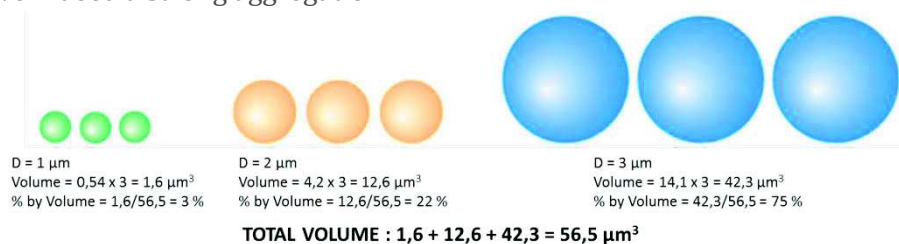


Figure 2-5: Size repartition of a solution of 9 particles with three different sizes: 1, 2, 3 μm (Horiba)

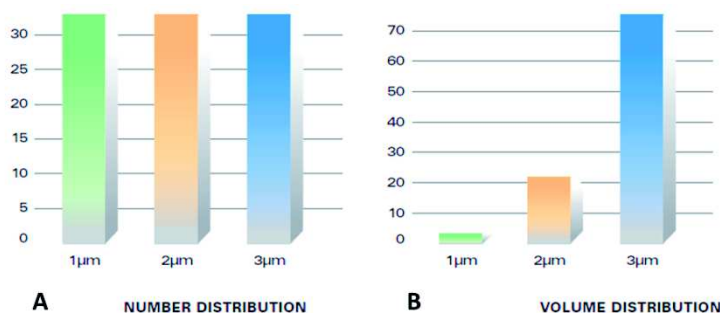


Figure 2-6: Size distributions in A) number and B) volume of the solution presented in Figure 2-5 (Horiba)

Measurements of hydrodynamic diameter were performed on an instrument from Malvern, the Zetaziser NanoZS, possessing a laser emitting at 623.8 nm. The measurement temperature was fixed at 25 °C and the angle for the detector position was fixed at 173°, which is favorable for the analysis of small particles. Depending on the media and the particle type, the specific solvent viscosities and refractive index should be entered in the software before each experiment. Table 2-1 summarized the viscosities at 25 °C of the solvents used in our experiments and Table 2-2 summarized the refractive index of the particles frequently analyzed. For core-shell particles, which are made from different materials, we decided to choose the last coating as material for the refractive index. In a typical procedure, the instrument sets up the temperature of the sample at 25 °C before starting the analysis, then three measurements were process. For each measurement, three runs were set up with a delay of 30 s between each run and the instrument measured an average from these three runs. A delay of 30 s was also applied between the three measurements.

Table 2-1: viscosities at 25 °C of solvents commonly used

	Solvent viscosity at 25 °C (cP)	Refractive index
Water	0.8872	1.330
EtOH	1.2000	1.361
Chloroform	0.5370	1.445
THF	0.4549	1.409

Table 2-2: Refractive indexes of materials frequently studied

	Refractive index	Absorption
Iron oxide	2.420	0.100
Silica	1.460	0.010
Protein	1.450	0.001

1.1.5 Zeta potential

The measure of zeta potential determines the dispersion state and colloidal stability of NPs in suspension. A suspension is considered as colloidal stable when the particles do not aggregate and when no precipitate forms in time. Due to their high surface/volume ratio, NPs tend usually to aggregate to minimize the interfacial energy.

The colloidal stability of suspensions results from two opposite forces between NPs, attractive (mostly Van der Waals attraction) and repulsive (mostly electrostatic repulsion) forces, Figure 2-7, defined in the DLVO theory developed by Derjaguin, Landau, Verwey and Overbeek. The DLVO theory assumes that the colloidal stability strongly depends on the total potential distribution defined as the sum of attractive and repulsive potentials. Figure 2-7 B describes the evolution of total interaction energy (U_T) as a function of the distance between two particles and the contribution of both potential: attractive (U_A) and repulsive (U_R). At short distance between two particles, the attractive forces are predominant and the total potential exhibits a primary minimum which corresponds to an irreversible agglomeration of the particles. At higher distance U_T exhibits a potential barrier. The height of this barrier indicates how stable the system is. Indeed, in order to aggregate the particles need to get enough energy to pass this barrier. Finally U_T shows a secondary minimum where reversible flocculation is observed and at high distance between particles the solution is stable.

Around each particle is a double electrical layer composed of a compact layer (called Stern layer) and a diffuse layer. Three potentials are delimiting these two layers: the surface, Stern and Zeta potentials. The Zeta potential delimits the area between the ions bound to the particle and the free ions. The pH influences a lot the Zeta potential of a particle: higher the pH, higher the number of negative charges. On the contrary at low pH the number of positive charges will be high. So by progressively varying the pH of a nanoparticle suspension, the measure of the Zeta potential will give a curve similar to Figure 2-8 B. The point where the solution has no charge is called the isoelectric point (IEP). Close to this point, as the charges are low, the electrostatic repulsion is not high enough and the particles tend to flocculate, the suspension is unstable. We consider a nanoparticle suspension stable at pH values where the Zeta potential is higher than 30 mV or lower than -30 mV.

In typical experiments the Zeta potential measurements were performed at 25 °C on aqueous nanoparticles suspension on the same instrument than for the DLS measurements: the Zetasizer Nano ZS from Malvern. To determine the isoelectric point (IEP) zeta potential was measured at various pH of the suspension. For each experiment the pH was adjusted with the help of HCl or NaOH solutions (0.1, 0.01 or 0.001 M) and was controlled with pH-meter before zeta potential measurement.

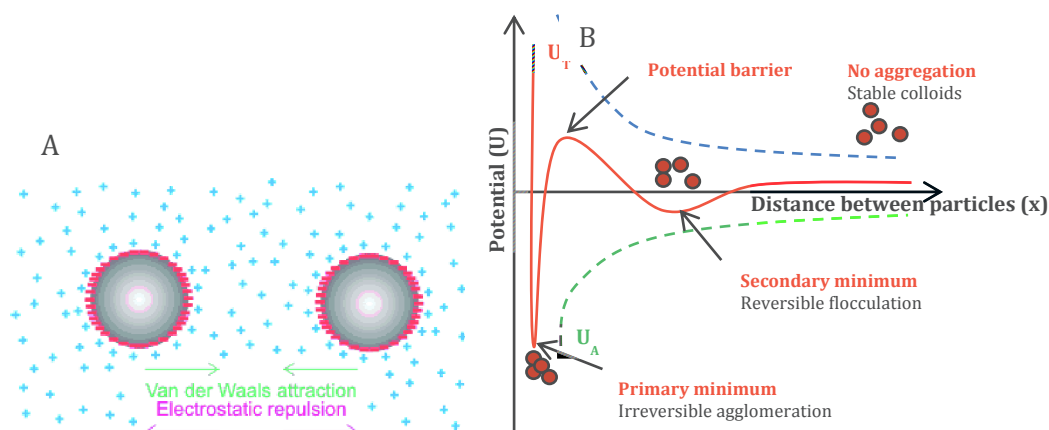


Figure 2-7: Schematic representations of A) the forces between particles B) the evolution of potential energy with the distance between particles

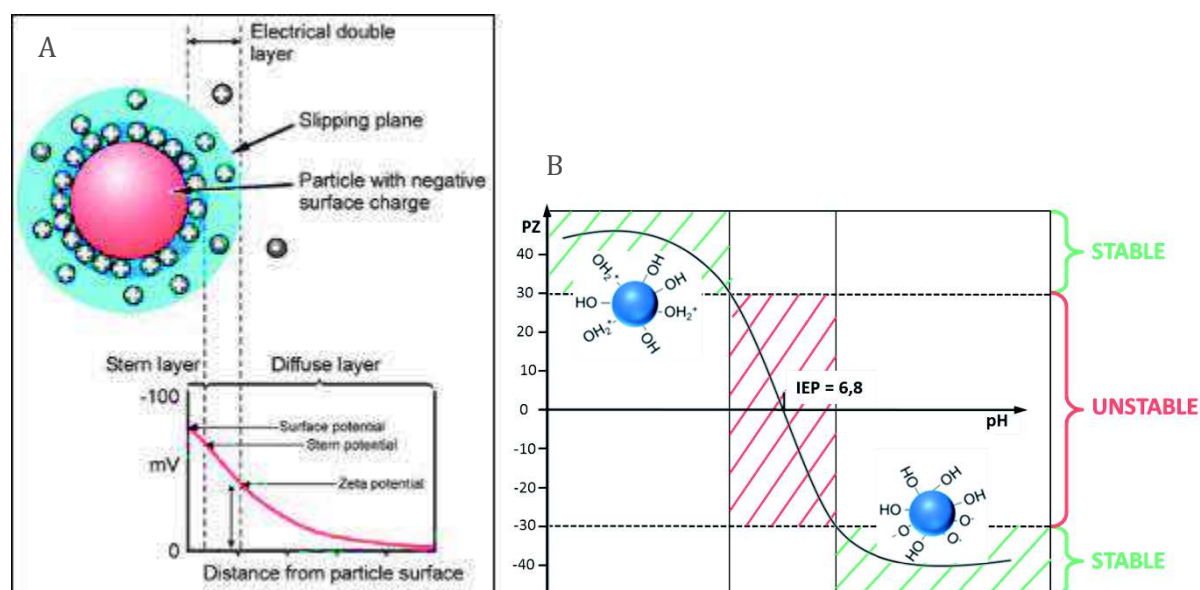


Figure 2-8: Schematic representations of A) the double electrical layer and the subsequent potential; B) Zeta-potential curve in function of pH

1.2 Composition analyses

1.2.1 Inductively coupled plasma-absorption emission spectroscopy (ICP-AES)

Dosage of selective atoms like Fe, Si and S was performed, after acidic digestion, by ICP-AES (Varian 720ES) at RePSeM, inorganic analyses platform, UMR 7178, directed by Anne Boos.

1.2.2 Energy Dispersive X-ray spectroscopy (EDX)

Energy-dispersive X-ray spectroscopy (EDX) is an analytical technique used for the elemental analysis or chemical characterization of a sample. It characterizes the interaction of some source of X-ray excitation and a sample by the fundamental principle that each element has a unique atomic structure allowing a unique set of peaks on its electromagnetic emission spectrum. As an electron beam can be used as X-ray excitation, EDX detector can be placed on SEM or TEM. In our studies EDX analysis were obtained from TEM.

1.2.3 Infra-red spectroscopy

Infrared spectroscopy is based on the fact that molecules absorb frequencies that are characteristic of their structure. These absorptions depend of the shape of the molecular potential energy surfaces, the masses of the atoms, and the associated vibronic coupling. Thus, a particular bond type is associated with a particular frequency of vibrations.

In a typical analysis, the IR spectrum of a sample is recorded thanks an infra-red beam passing through the sample at various wavelengths (from 400 to 4000 cm^{-1}). Collecting information about transmitted light reveals how much energy was absorbed by the sample for each wavelength.

IR spectra were recorded thanks to Perkin Elmer Spectrum instrument. ATR analyses were performed by pressing powder of the sample on the instrument. FTIR analyses were performed by preparation of KBr disks mixed with the sample.

1.2.4 Fluorescence and UV-vis spectroscopies

Fluorescence and UV-vis spectroscopies analyze fluorescence and absorbance respectively of a sample. For fluorescence analyses, a beam of UV light, setting up at a specific wavelength, excites the electrons in molecules of certain compounds called fluorophores and causes them to emit at a specific wavelength. Thus the excitation and emission wavelength set up in the instrument should correspond to the type of fluorophores we want to measure. Two fluorescent probes were used in our studies, FITC with $\lambda_{\text{exc}}=488$ nm and $\lambda_{\text{em}}=520$ nm and Dox with $\lambda_{\text{exc}}=488$ nm and $\lambda_{\text{em}}=595$ nm. For absorbance measurement the instrument should be set up at the wavelength of maximal absorption of the colored sample. For Dox $\lambda_{\text{abs}}=480$ or 495 nm and for MTT $\lambda_{\text{abs}}=595$ nm. To estimate a sample concentration from the fluorescence or absorbance measurements a calibration curve from various known concentrations should be previously obtained.

Both, fluorescence and absorbance, measurements were performed on a SAFAS (Monaco) spectrophotometer.

1.3 Magnetic resonance studies

1.3.1 Nuclear magnetic resonance (NMR) ^1H relaxivity measurements

T_1 and T_2 relaxation times were measured at 37 °C on a Bruker Minispec 60 (Karlsruhe, Germany) working at a Larmor frequency of 60 MHz (1.41 T). Henoumont *et al.* wrote a fully paper on how to perform accurate and reliable T_1 and T_2 measurements of MRI contrast media in aqueous solutions on a Bruker Minispec 20 (20 MHz) (171). We inspired from their explanations to set up our experimental procedure. According to them several parameters, summarized in Table 2-3, need to be adjusted for T_1 and T_2 measurements.

The T_1 measurements were performed using the inversion-recovery sequence which consists in a pulse inversion of 180 ° followed by a 90 ° reading pulse after a delay τ . The T_2 was measured by the Carl-Purcell-Meiboom-Gill (CPMG) pulse sequence.

Because the recovery delay of T_2 depends on T_1 values, T_1 measurements were performed before the T_2 . The first T_1 and T_2 values injected in the software were of 100 ms and were adjusted with the values obtained after the measurements until reaching adequate amplitude between 75-90 % and reproducible values. When the right T_1 and T_2 values were found, at least four measurements were done for T_1 and at least seven for the T_2 in order to get relevant averages.

Relaxivity measurements could also be used for the titration of IO NPs as described by Boutry *et al.* (172). For this purpose 100 μL of IO NPs in water were dissolved at 80 $^{\circ}\text{C}$ for 2 h by adding 600 μL of HNO_3 (65 %) and 300 μL of H_2O_2 (30 %). Then 18.5 mL of Milli-Q water was added to reach a HNO_3 concentration of 2 % corresponding to condition of the standard relaxometry curve for iron concentration. Finally thanks to relaxivity measurement of the solution of dissolved iron and its comparison to the standard curve, the concentration of iron was quantified.

Table 2-3: Summary of parameters set up for T_1 and T_2 measurements by relaxometry

Parameters for relaxometry	T_1	T_2
Detection mode	real	magnitude
Resonance frequency	on-resonance	on-resonance
Number of scans	1	4, "phase cycling" on
Receiver gain	59 (increase if needed, aim 75-90%)	59 (increase if needed, aim 75-90%)
Recovery delay	$5T_1$	$5T_1$
Pulse separation	First: $T_1/20$; Final: $10T_1$	$5T_2/np$
Number of data points (np)	15	150

1.3.2 Magnetic resonance imaging (MRI)

The MRI studies for the core-shell samples were performed by Professor Philippe Choquet and Pierre-Emmanuel Zorn at the Hautepierre Hospital (Strasbourg) in the Unit UF6237 of Preclinical Imaging. The MRI contrast of the solution was tested on two instruments: a mouse sized instrument running at 1.5 T the RS2D Optimouse 1.5 and a clinical instrument running at 3 T the GE Signa HDxt 3T.

Protocol on Optimouse 1.5 :

As pictured on Figure 2-9, the samples were loaded into 1 mL syringes and placed on the instrument support which can host up to 5 samples. This support leads the sample in the center of the magnet. For each measurement, endorem at 0.18 mM was used as reference and placed in the center of the support. Various concentrations of the studied sample were disposed on the four places around endorem as described in Figure 2-10 A and B. Acquisition parameters, summarized in Table 2-4, were set up in the software. Magnetic resonance images were thus obtained in T_1 and T_2 ponderation as shown in Figure 2-10 C. Regions of interest (ROIs) of same dimensions were delimited on the resulting images, green circle on Figure 2-10 C. In these ROIs the voxels average from the signal in this designed volume was calculated, resulting in T_1 and T_2 values for each concentration.

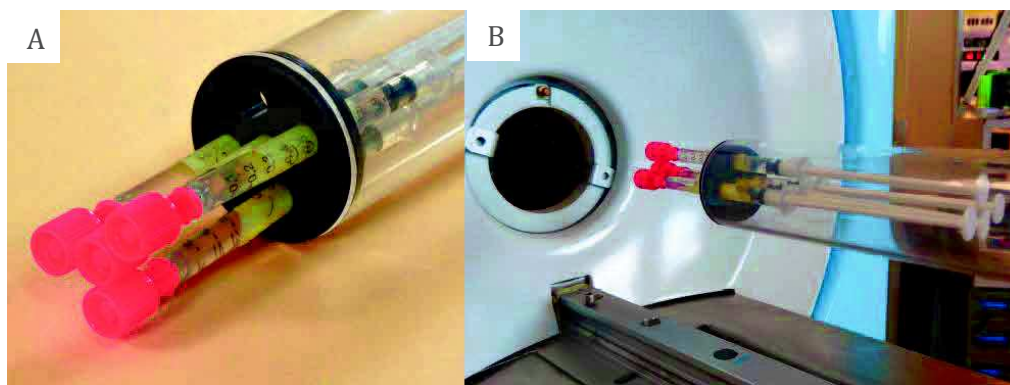


Figure 2-9: Pictures of the Optimouse 1.5 device and samples dispositions

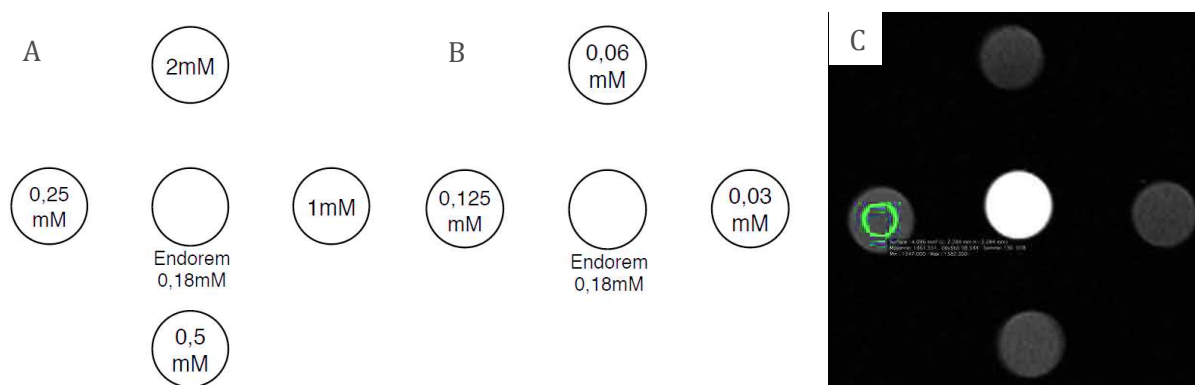


Figure 2-10: Schemes of the samples dispositions A) first measurement, B) second measurement; C) shows a typical acquisition in T_1 ponderation of samples from 2 mM to 0.25 mM (clockwise from noon), ROI on the 0.25 mM sample

Table 2-4: MRI parameters for the Optimouse 1.5 instrument

Parameters on Optimouse 1.5	T_1	T_2
	Spin echo	Fast spin echo
Repetition time (TR) (s)	400	2
FA	90°	90°
Echo time (TE) (s)	10	104
Excitation number (Nex)	10	16
Image dimension	128 x 128	128 x 128
Field of view (FOV)	30 mm x 30 mm	30 mm x 30 mm
Section number	5	5
Section thickness (mm)	6	6
Interval between section (mm)	1	1

Protocol on Signa 3T:

The MRI acquisitions for the clinical instrument Signa 3T were obtained by applying the parameters summarized in Table 2-5. MRI-phantoms were obtained on all samples in the same time.

Table 2-5: MRI parameters for the Signa 3T instrument

Parameters on Signa 3T	T ₁	T ₂
	Spin echo	Fast spin echo
Repetition time (TR) (s)	400	2
FA	90°	90°
Echo time (TE) (s)	10	49
Excitation number (N _{ex})	4	6
Image dimension	256 x 256	256 x 256
Pixel (mm)	0.7813	0.7813

1.3.3 Magnetic hyperthermia (MH)

Magnetic hyperthermia measurements were performed on DM 100 instrument from nanoscale Biomagnetics (nB) running with DM2 applicator and DCM1 controller under MaNiAc software (Figure 2-11). The device applies a user-adjustable magnetic field from 0 to 300/600 gauss, generated by means of an induction coil, on user selectable frequencies, and perform in situ temperature measurements through an advanced optical fiber sensor placed inside the sample. The sample, hold by a cylindrical probe which is introduced into a dewar flask connected to a vacuum pump, should be placed in the middle of the coil for relevant measurements, Figure 2-12. Data are registered at a rate of 200 ms with a 0.2 °C resolution and give temperature curves in function of time. Our experiments were run at various magnetic fields and frequencies at least for 2 min and up to 3 min.

From these curves the SPA index of the magnetic heated sample, Specific Power Absorption, also called SAR, Specific Absorption Rate, is calculated using the Equation 2-6. In our experiments, the differential of temperature maximum in function of time of the temperature curve of the sample, $(\Delta T/\Delta t)_{max}$, was usually calculated for t values between 40 s and 100 s. The concentration ϕ_L of the magnetic nanoparticles (Fe_3O_4), is obtained by multiplying by 1.38 the concentration of the sample in mg Fe/mL (measured by ICP-AES or relaxivity).

$$SAR = \frac{C_L \delta_L}{\phi_L} \left(\frac{\Delta T}{\Delta t} \right)_{max}$$

Equation 2-6: SAR (W/g) formula with, C_L the calorific capacity of the base liquid (J/Kg.K), δ_L the density of the base liquid (Kg/m³), ϕ_L the concentration of nanoparticles (Kg/m³), $(\Delta T/\Delta t)_{max}$ the differential of temperature maximum in function of time of the temperature curve of the sample (K/s).

As the SAR index depends on the frequency and the applied field intensity, the Intrinsic Loss Power, ILP, could be deduced by Equation 2-7. The ILP describes the intrinsic efficiency of the magnetic nanoparticles to absorb power and should be constant for a sample.

$$ILP = \frac{SAR}{fH_0^2}$$

Equation 2-7: ILP (nH.m²/kg) formula with SAR index (W/g), f the frequency of the applied magnetic field (Hz) and H_0 the intensity of the applied magnetic field (A/m)



Figure 2-11: Picture of the MH device from nB

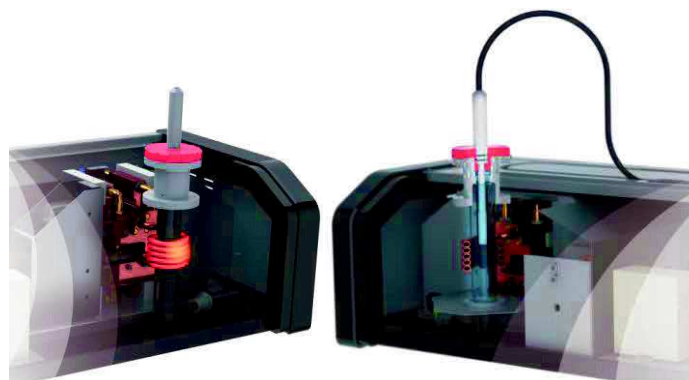


Figure 2-12: Schematic representations of the magnetic hyperthermia measurement A) whole, B) section of the instrument set-up

1.4 Biological studies

Three human cancer cell lines were studied.

The Huh7-luc is a hepatocyte derived cellular carcinoma cell line originally been taken from the tumor of 57 years old Japanese's liver in 1982. This cell line was established by Nakabayashi, H. and Sato, J.. These cells were cultured in a Dulbecco's Modified Eagle's Medium (DMEM) extended with 10 % of fetal calf serum (FCS), 5 % of PS and 1 % of non-essential amino acids.

The A549-luc cell line issued from lung carcinoma cells of a 58 years old Caucasian male, was developed in 1972 by Giard (173, 174). The culture media for these cells was made of (RPMI-1640) extended with 10 % of fetal calf serum (FCS), 5 % of PS and 1 % of non-essential amino acids.

Kelly cell line is issued from human neuroblastoma cells and was cultured in RPMI-1640 modified with 10 % of fetal calf serum (FCS), 5 % of PS and 1 % of non-essential amino acids.

1.4.1 2D cell culture

1.4.1.1 Evaluation of NPs internalization by flow cytometry

Flow cytometry was used to evaluate the internalization of nanoparticles, by eukaryotic cells, in order to compare the influence of physical and chemical modification of the particles. Huh7 (2. 10⁵ cells per well) were seeded in a 24-well plate (Greiner, Dominique Dutscher, ref 165305) and kept overnight for attachment. Cells were then incubated, with 1 mL per well of NP diluted in complete medium, for 24 or 48h at 37°C in 5% CO₂. Cells were then thoroughly rinsed with 1 mL of cold PBS. Cells were then incubated with 300 µL of trypsin/EDTA solution (GIBCO, Ref R001100, Thermofisher) for 5 minutes. Cells were then resuspended by addition of 500 µL

of PBS and harvested by centrifugation at 1000 rpm for 5 min. Cells were resuspended in 1 mL PBS + 2% paraformaldehyde (PFA) and kept at 4°C protected from light until analysis.

Cell fluorescence was analyzed by flow cytometry using a FACScan flow cytometer with Novios software at the immunology laboratory of the university hospital in Strasbourg. Basically a laser beam is focused on cells' sample flow by means of one or two lenses. The cell flow is uniformly illuminated at the analysis point where a set of lenses focused the emerging laser light onto photomultiplier tubes. Each photomultiplier tube has a specific light filter to only detect specific wavelengths. The instrument records the transmitted light (Forward scattering or FSC) and the reflected light (side scattered light or SSC) as well as the fluorescence intensity of each cell. It allows separating the cells according to their size, granulometry and fluorescence intensity. 10 000 cells were analyzed by sample and fluorescence threshold was determined using non-treated cells. Results are reported as the percentage of cells presenting fluorescence above the aforementioned fluorescence threshold. So the internalization of NPs by cells can be measured by flow cytometry with FL1 canal (Exc 488 nm Em 505 nm) by labelling the NPs with a fluorescent probe (such as FITC). Thus the cells that internalized the NPs will be fluorescent and will be detected by the flow cytometer. It is possible to assess the number of fluorescent cells above a predetermined threshold by analyzing non-fluorescent cells.

1.4.1.2 Cytotoxicity studies by MTT assays

MTT assays were carried out to investigate the cytotoxicity of NPs (175). The MTT is a yellow water-soluble tetrazolium dye that is reduced by alive cells to purple formazan crystals insoluble in aqueous media.

Briefly, the cells were plated in 96-well plate at a density of 10000 cells/well with 100 µL per well. To limit the so-called "edge effect" the border of the 96-well plate (column 1 and 12) were avoided if possible. After 24 h, the culture media of the wells was replaced with 100 µL of fresh media containing NPs at various concentrations (triplicates were done for each concentration). After 24 h and 48 h of incubation, the culture media was replaced with 100 µL of MTT diluted at 0.5 mg/mL in fresh culture media. The plate was placed in the incubator for at least 2 h and then the MTT was removed from the wells and the MTT-formazan crystals were dissolved in 100 µL of DMSO. Finally the plate was analyzed by absorbance spectroscopy at 595 nm using Xenius microplate reader (SAFAS, Monaco). The results were analyzed in terms of cell viability percentage obtained by setting the average absorbance obtained at 595 nm on non-treated (without NPs) cells at 100 % of cell viability. Each MTT experiment was reproduced three times.

1.4.2 3D cell culture

Even if two-dimensional (2D) cell monolayers have been conventionally used by the scientific community to evaluate drug efficacy, NPs cytotoxicity and their internalization, they poorly represent the complex tumor 3D microenvironment. Indeed, cells grown in 2D lack the extracellular matrix (ECM), as well as cell-cell contact and cell-matrix interactions. Thus, 3D culture models have emerged as an additional *in vitro* step study to assist drug product development and tend to reduce the requirement for unnecessary animal studies (176–183). Thus in a mini review in 2002, Jacks and Weinberg concluded their article by this well-resumed phrase: "Suddenly, the study of cancer cells in two dimensions seems quaint, if not archaic" (184).

Among various methods to engineer 3D cancer models such as spheroids, bio-printing and assemblies, our group decided to develop multicellular tumor spheroids (MCTS) cell culture

by aggregation of cells in hanging drop which is one of the easiest ways to form 3D tumor model from cancer cell lines.

The 3D cell culture was developed on Huh7-luc cells because of their particularity to grow in clusters. Preparation from this cell line of multicellular tumor spheroids was carried out by the hanging-drop method as explained below.

1.4.2.1 Preparation of Huh7 MCTS

Prior to the culture, sterile 96-well plates equipped with a lid (Corning™ Costar™ Flat Bottom Cell Culture Plates, Fisher scientific, Ref 10792552) were coated with poly(2-hydroxyethyl methacrylate) (poly-HEMA; sigma P3932-10G) in order to avoid cell adhesion at the well-bottom. The coating was done by addition of a 0.5 % (w/v) poly-HEMA solution in ethanol (50 μ L) into each well of a 96-well plate at 38°C. The plate was kept at 38°C for 24h for complete ethanol evaporation and for ensuring a total surface coating. PBS (100 μ L) was then added into each well. Adherent Huh-7 were treated with trypsin and suspended in complete medium at 5.3×10^3 cell/mL. The cell suspension (15 μ L) were deposited on the inside face of the 96-well plate lid. The lid was then replaced on the PBS-filled plate and the cells in the hanging drop were led to grow in the incubator for 3 days. As pictured in Figure 2-13, during these three days the cells present in the drop will sediment at the medium/air interface, aggregate and develop finally with subsequent proliferation and deposition of ECM into a multicellular tumor spheroid (185).

The PBS was then discarded and replaced with complete cell culture medium (100 μ L). Each drop containing one single spheroid was then transferred from the lid into the well by centrifugation at 500 RPM for 1 minute. MCTS were cultivated further at 37°C in 5 % CO₂ with medium changed every 7 days. During these 7 days the spheroid continued to grow (Figure 2-14).

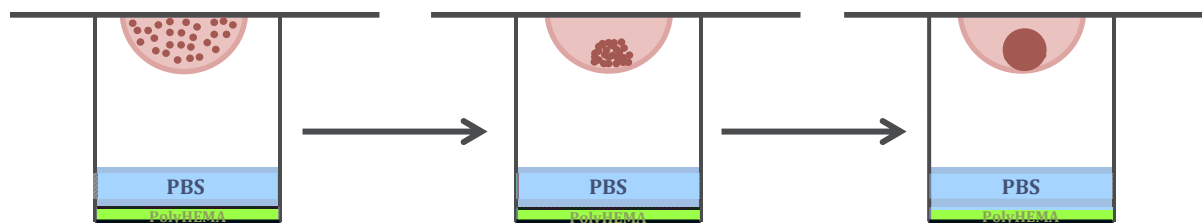


Figure 2-13: schematic representation of the drop-hanging principle

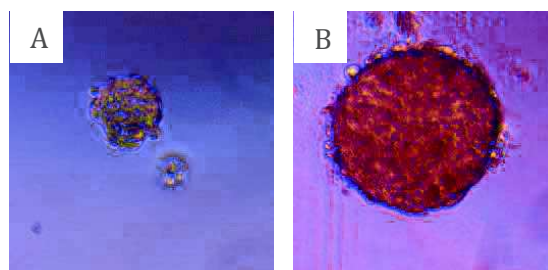


Figure 2-14: Optical microscopy images of the same spheroid A) after being collected in the well, B) 7 days later

1.4.3 Evaluation of particle diffusion by imaging

1.4.3.1 Preparation of MCTS for confocal imaging

The experiments were carried in triplicate. Huh-7 spheroid was incubated in a complete cell culture medium for 24 h with NPs. The spheroids were then fixed by addition of 8% (w/v) paraformaldehyde (EMS group, Hatfield, PA, USA) in PBS (100 μ L) to each well. After 15 min, fixed Huh7 spheroids were harvested with a 400 μ m fiber loop, were rinsed in PBS and were mounted in an Antifade Mounting Medium (Vector laboratories, H-1000, Burlingame, CA).

1.4.3.2 Principle of confocal laser scan microscopy (CLSM)

Thanks to an epifluorescence microscope, a laser beam is focused on a precise point of the sample in the focal plan. When the laser beam is passing through the sample, some side fluorescence is generated. To eliminate this fluorescence, a pinhole is placed before the detector and allows only the light from the focal plan to pass, Figure 2-15. Scanning the sample in XY, thanks to mirrors, gives an image from the focal plan. To scan the sample in Z, the objective lens is placed on a piezoelectric motor. Thus, images from different focal plans can be obtained from which a 3 D structure of the sample can be reconstructed. For imaging, excitation wavelengths were set at 488 nm and 543 nm for triggering NPs and membrane stain fluorescence, respectively. Green and red light emissions were recorded after filtration using 505-530 nm band-pass and 585 nm long pass filters. Several images were recorded along the z-axis for focal sectioning. In our experiments a ZEISS LSM 170 confocal microscope was used to image the FITC-labelled NPs internalization into cells and spheroids and the Dox diffusion into spheroids.

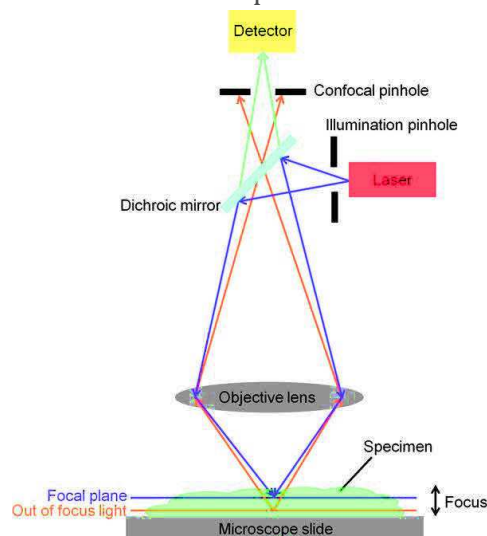


Figure 2-15: Schematic representation of the principle of confocal microscopy

1.4.4 Evaluation of antitumoral effect on MCTS

The experiments were carried out in octuplicate in 96-well plate using the spheroids as previously described. NPs were diluted at various concentrations in complete cell culture medium. NPs are immediately added to each spheroid by further dilution into the cell culture medium (100 μ L).

The spheroid growth was examined using a Nikon Eclipse TS100 microscope and a 10 X objective. Images were recorded at days 0, 4 and 7 with a Nikon Color CCD DS-Fi2 Camera and a DS-L3 camera controller. The area (A) of each spheroid was measured using the NIH Image J

software and reported in μm^2 . The MCTS growth (G) was calculated relative to the initial area (A_0 ; day 0) and express as relative growth versus control using the following equation : $G = ((P_t - P_0)/P_0) * 100$ where $P_t = A_tX/A_t0$ and $P_c = A_cX/A_c0$ with A_t = area of treated MCTS and A_0 = area of control MCTS.

1.5 Conclusion on characterization techniques

Table 2-6 summarized the different methods described previously for the analysis of NPs.

Table 2-6: Summary of methods used and the sample characteristics they measured

Studies type	Methods	Characteristics measured
Physico-chemical	TEM	<ul style="list-style-type: none"> Two dimensional images of particles, determination of structure and morphology Determination of size distribution
	SEM	<ul style="list-style-type: none"> Determination of hydrodynamic diameter of NPs in suspension in liquid media
	Nitrogen adsorption-desorption isotherm (BET, BJH)	<ul style="list-style-type: none"> Determination of specific surface area, pore volume and pore sizes
	DLS	<ul style="list-style-type: none"> Determination of hydrodynamic diameter of NPs in suspension in liquid media
	Zeta potential	<ul style="list-style-type: none"> Evaluation of the charges on NPs surface Determination of IEP
Composition	ICP-AES	<ul style="list-style-type: none"> Determination of elemental concentration in sample
	EDX	<ul style="list-style-type: none"> Elementar analysis in percentage of the sample
	IR	<ul style="list-style-type: none"> Determination of some chemical bonds
	Fluorescence, UV-vis spectroscopies	<ul style="list-style-type: none"> Dosage of fluorescent or colored sample concentration with help of calibration curves
	TGA	<ul style="list-style-type: none"> Evaluation of the weight percentage of organic moieties versus inorganics
Magnetic	Relaxometry	<ul style="list-style-type: none"> Determination of r_1 and r_2 Estimation of NPs concentration in mg Fe/mL
	MRI	<ul style="list-style-type: none"> Evaluation of the efficiency of NPs as contrast agents
	MH	<ul style="list-style-type: none"> Estimation of SAR and ILP of the NPs
Biological	Flow cytometry	<ul style="list-style-type: none"> Determination of the percentage of cells that internalized NPs
	Confocal microscopy	<ul style="list-style-type: none"> 2-D or 3-D images of NPs internalization in cells
	MTT assay	<ul style="list-style-type: none"> Estimation of the cytotoxicity of NPs on cells

2 Experimental synthesis protocols

2.1 Synthesis of IO NPs

2.1.1 Protocol for 10 nm IO NPs

In a typical procedure 1.38 g (2.22 mmol) of iron stearate were thermally decomposed in 20 mL of dioctylether in presence of 1.25 g (4.44 mmol) of oleic acid. As pictured in Figure 2-16, the mixture was first heated for 1 h at 130 °C to dissolve the reactants and evaporate the residual water. Then the reflux apparatus was placed on the round flask and, through a heating rate of 5 °C/min, the boiling temperature of the mixture was reached and was maintained for 2h30.

After the synthesis, the as-synthesized IO NPs were washed many times by centrifugation in a chloroform/acetone (1/3) mixture until removal of most of residuals/unreacted iron stearate and free oleic acid molecules. These washing steps were followed by IR spectroscopy. Finally the IO NPs stabilized by oleic acid were dispersed in chloroform.

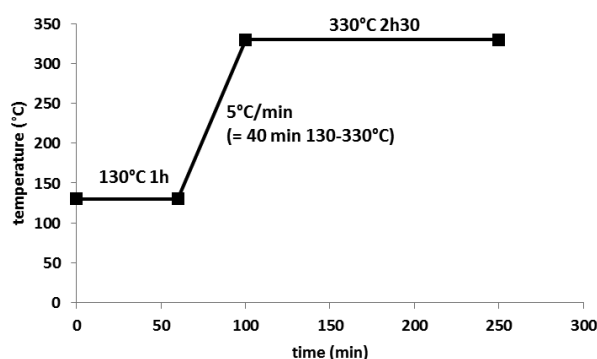


Figure 2-16: Theoretical heating profile for the synthesis of ~10 nm IO NPs

2.1.2 Protocols for 20 nm IO NPs

The synthesis of IO NPs with sizes higher than 10 nm is not so easy (186) and we know that the use of solvents with higher boiling points is a good method to increase the NPs size. However, such conditions are often reductive and led thus to core-shell NPs with a core of wustite (FeO) and a shell of magnetite. Therefore a mixture of dibenzyl ether and squalene has been used to obtain homogeneous Fe_{3-x}O₄ NPs with a mean size of 20 nm following the protocol below:

1.85 g of iron stearate (2.04 mmol) were mixed to 1.89 g of oleic acid (6.7 mmol) 0.5335 g of dibenzyl ether and 15.80 g of squalane. The mixture was first heated at 120 °C for 1 h under air, and then the temperature was increased to 370 °C with heating rate of 5 °C/min and kept at this temperature for 1 h under reflux.

After the synthesis, the as-synthesized IO NPs were washed many times by centrifugation in a chloroform/acetone (1/5) mixture with hot acetone until removal of most of residual unreacted iron stearate and free oleic acid molecules. These washing steps were followed by IR spectroscopy. Finally the IO NPs stabilized with oleic acid were dispersed in chloroform.

2.2 Synthesis of silica NPs

2.2.1 Protocol for Bimodal Mesoporous Silica NPs synthesis (BMS NPs)

The protocol was adapted from Wang *et al.* (40). In a typical process, 0.55 g of CTAB were dissolved in 25 mL of Milli-Q water. To improve and accelerate the dissolution the mixture could

be heated up to 60 °C. 3 g of PAA (25 wt% in solution) were added under vigorous stirring at room temperature. At this step the solution is clear. Then 2 g of ammonia at 25 % were added still under vigorous stirring. The pH should be between 10-11 and the solution became a milky suspension. After 20 min of stirring, 2.08 g of TEOS were added. After 15 min of stirring, the mixture was transferred in an autoclave which was then put in an oven at 50°C for 48h.

The as-synthesized BMS were washed by centrifugation twice with water and three times with ethanol. Finally the product was dried at 80 °C in an oven overnight and the organic template was removed by calcination at 550 °C for 6 h.

2.2.2 Protocol for small porosities silica synthesis (raspberry morphology: RB)

The protocol was adapted from Zhang *et al.* (41). Briefly, 960 mg of CTAB were mixed with 230 mg of TEAH₃ in 63 mL of Milli-Q water. This mixture was first placed for 1h under sonication then 1h at 80°C until the components were completely dissolved. Next, 4 mL of TEOS was quickly added to the above solution under stirring. The mixture was stirred at 80 °C for 2 h. The as-synthesized RB NPs were filtered, washed and dried in an oven at 100 °C for 24 h. The resulting powders were then calcined at 550 °C for 6 h to burn the surfactant molecules left in the porosities.

2.2.3 Protocol for large porosities silica synthesis (stellar morphology: ST)

The protocol was also adapted from Zhang *et al.* (41). In a typical procedure 960 mg of CTATos were mixed with 174 mg of TEAH₃ (or 111 mg of AHMPD) in 100 mL of Milli-Q water. This mixture was first placed for 1h under sonication then 1h at 80°C until the components were completely dissolved. Next, 7.29 mL of TEOS was quickly added to the above solution under stirring. The mixture was stirred at 80 °C for 2 h. The as-synthesized ST NPs were filtered, washed and dried in an oven at 100 °C for 24 h. The resulting powders were then calcined at 550 °C for 6 h to burn the surfactant molecules left in the porosities.

2.3 Protocol for core-shell particle synthesis

2.3.1 IO@RB

The protocol was adapted from the one of Hyeon's group (141). The procedure described below is the typical procedure to synthesize IO@RB NPs of 30 nm in size and with a core of 10 nm.

First an aqueous solution of CTAB at 28 mM was prepared (500 mg in 50 mL of Milli-Q water). After complete dissolution of CTAB, 3 mL of IO NPs dispersed at 2 mg Fe/mL were added under vigorous magnetic stirring for 30 min. At this step a brown turbid solution was obtained. Then the mixture was heated up to 65°C and maintained at this temperature for 10 min under stirring to evaporate the chloroform. The solution obtained was black and transparent. A solution of 150 mL of Milli-Q water and 60 µL of a 2M NaOH solution were added to the mixture. The so obtained solution was heated up to 70°C under vigorous stirring. 1.5 mL of TEOS and 2.55 mL of EtOAc were added and this final mixture was stirred for 3h at 70°C. The particles were then washed 3 times in ethanol by centrifugation.

2.3.2 IO@ST

The procedure described below was used to synthesize IO@ST NPs of 100 nm in size starting with an IO core of approximately 20 nm.

In a typical procedure, 192 mg of CTATos were mixed with 40 mg of AHMPD in 20 mL of Milli-Q water. This mixture was sonicated for 1h and then maintained for 1h at 80°C until the reactants were completely dissolved. Next, 5 mL of IO NPs dispersed at 1 mg Fe/mL in chloroform were added to the solution under vigorous stirring for 30 min at room temperature. Then the temperature was elevated to 65 °C for 10 min under vigorous stirring to evaporate the chloroform. After this evaporation step, 1.6 mL of TEOS were quickly added to the solution under stirring. The mixture was stirred then at 80 °C for 2 h. The as-synthesized IO@ST NPs were washed by centrifugation.

2.4 Standard protocol for IBAM-HSA coating on silica

As pictured on Figure 2-17, three synthesis steps were necessary for the HSA coating on silica: first the silica NPs are silanized to provide ammonium groups at their surface, then the surface is modified by coupling IBAM moieties and finally HSA is adsorbed on this surface by interaction with IBAM. The synthesis protocol described below was adapted from Mertz *et al.* protocols (166, 187).

In the standard silanization procedure of silica surface, 3 mL of NPs dispersed in EtOH were mixed to 320 μL of NH_3 and 1.5 mL of APTES and stirred for 2 h. The amino-modified NPs were washed by centrifugation once with EtOH and twice with DMF and finally dispersed in 2.4 mL of DMF.

Then the silanized silica surface was modified with IBAM groups. A solution containing IBC (648 μL) in DMF (4.8 mL) was added to the amino-modified NPs previously dispersed in a solution of DMF (2.4 mL) and Et_3N (480 μL). After 2 h reaction, Milli-Q water (1 mL) was added to dissolve the formed precipitate. The resulting particles modified with IBAM were collected by centrifugation and washed three times with DMF.

Finally, after re-dispersing the IBAM modified NPs in 150 μL of DMF, 1.5 mL of HSA at 2 $\text{mg}\cdot\text{mL}^{-1}$ in Milli-Q water was added and the mixture was let to react for 2 h reaction. The NPs were collected by centrifugation, washed twice with sterile water and finally dispersed in 2mL of Milli-Q water.

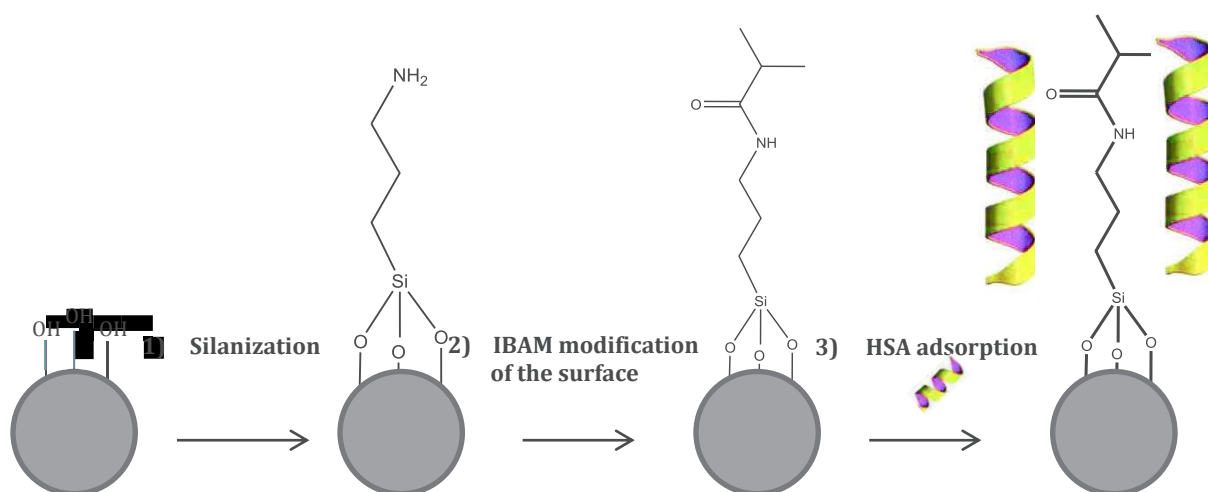


Figure 2-17: Synthesis steps for HSA coating on silica NPs via IBAM-grafting strategy

2.5 Fluorescent labeling of HSA

531 μL of a solution of FITC in DMSO at 10 $\text{mg}\cdot\text{mL}^{-1}$ were mixed to 30 mL of HSA at 10 $\text{mg}\cdot\text{mL}^{-1}$ in 0.1 M sodium bicarbonate (NaHCO_3) buffer (pH 8.5). The mixture was stirred

overnight and then dialyzed in MilliQ water to remove free FITC. The final volume was adjusted to 60 mL to reach a HSA^{FITC} concentration of 5 mg.mL⁻¹.

2.6 Protocol for the synthesis of HSA_{Dox} NPs

2.6.1 Synthesis of maleimide-modified Doxorubicin (Dox-EMCH)

To synthesize the maleimide-modified doxorubicin, 80 mg of Dox (1 equivalent) and 93.6 mg of EMCH (2 equivalents) were dissolved in 40 mL of dry methanol. Then, 0.133 mL of TFA were added to catalyze the reaction. The solution was placed in the dark and stirred overnight. Then, the product was concentrated to few milliliters by rotary evaporation and precipitated in dry ethyl acetate. The product was finally collected by centrifugation and dried at 60°C in the oven.

2.6.2 Synthesis of HSA-SPDP

The SPDP, kept at -20°C, needs before opening to be at room temperature. In order to reach 25 equivalents of SPDP per HSA, 11.73 mg of SPDP were dissolved in 1.877 mL of DMSO (20 mM SPDP in DMSO) and added to a solution of 100 mg HSA dissolved in 50 mL PBS-EDTA buffer at pH 7.5. This solution was stirred at room temperature for 2 h and then dialyzed in water with a 10000 MWCO tube for 24 h.

2.6.3 Synthesis of Protein-Drug Conjugates HSA-Dox

A solution of 150 mM DTT in a PBS-EDTA buffer (pH 7.5) is achieved by dissolving 575 mg of DTT in 25 mL of buffer which was then added to the 50 mL of the previous HSA-SPDP solution. This solution was then stirred for 30 min. Then, the solution was purified by dialysis overnight. The Dox-EMCH compound (28.2 mg) was then added to the thiolated HSA and stirred for 18 h at room temperature, protected from the light. Finally, the product was purified by dialysis.

2.6.4 Preparation of HSA_{Dox} NPs

Raw BMS NPs were modified with IBAM according to the protocol described previously in section 2.4..

14 mL of HSA_{Dox} (only the supernatant of the product synthesized in section 2.6.3 was used) were added to 700 µL of 1% IBAM-modified BMS and the mixture was incubated for 2 h. Then the NPs were washed in 5 mL Milli-Q water overnight (16 h).

Finally, to observe by microscopy replicate self-supported HSA_{Dox} NPs, 5 µL of HF buffer was added to 2.5 µL of NPs deposited on slides coated with PEI. After 3 min the slide was abundantly washed with Milli-Q water and letting dry under the fumehood.

Chapter 3:

Silanization of IO NPs for MRI applications

1 Optimizing the silanization of thermally-decomposed iron oxide nanoparticles for efficient aqueous phase transfer and MRI applications

The functionalization of IO NPs synthesized by thermal decomposition and thus, *in situ* coated with oleic acid molecules, is an important step for providing water suspension of such IO NPs but also to investigate the MRI properties of these IO NPs. The silanization was an important functionalization process in this research project and we noticed that very few works have been reported on the silanization of IO NPs synthesized by thermal decomposition. Therefore, with Master Students, the silanization of IO NPs synthesized by thermal decomposition was optimized by aiming at obtaining stable water suspensions at physiological pH and investigating their MRI properties before their silica coating. This study led to an article published in RSC advances (RSC adv., 2016, 6, 93784-93793; DOI: 10.1039/C6RA18360C (188)) which is related below.

1.1 Abstract

The design of magnetic iron oxide nanoparticles (IO NPs) as contrast agents for magnetic resonance imaging (MRI) requires good magnetic properties of the core but also an organic coating suitable for *in vivo* applications. IO NPs synthesized by thermal decomposition display optimal properties due to their excellent monodispersity, controlled morphology and high crystallinity; however, their *in situ* coating by hydrophobic ligands make them only dispersible in nonpolar solvents. A wide range of methods was developed to coat IO NPs with molecules or polymers bearing anchoring groups such as carboxylates mainly. Nonetheless, very few have dealt with silane-based molecules due to difficulties (*e.g.*, slow kinetics of reaction, NPs aggregation during reaction, non-miscibility of solvents) to graft homogeneously and efficiently silanes at the surface of hydrophobic NPs. In this work, a new and versatile method was developed to graft hydrophilic silanes on the surface of hydrophobic IO NPs based on the direct reaction of IONPs in miscible polar/apolar co-solvents: EtOH/CHCl₃. The feasibility of this efficient process was demonstrated by using various silanes bearing amino and carboxylate end-groups. We show that this novel process allows several improvements in comparison with the few existing methods to silanize hydrophobic IONPs: i) shorter reaction time, ii) increased amount of processed NPs per cycle, iii) the establishment of a silane limit stoichiometry to ensure good colloidal properties and iv) easier implementation without the need of specific or stringent treatments, which are all key issues for scale-up aspects. IONPs grafted with aminosilanes display an excellent colloidal stability in ethanol and only in acidic aqueous solutions (pH <5). By contrast, carboxylated silane-IO NPs were shown to exhibit excellent colloidal stability in the physiological pH range (pH = 6 - 8). Moreover, such new silanized NPs display MRI contrast enhancement as efficient as commercially available magnetic NPs.

1.2 Introduction

Superparamagnetic IO NPs have a great potential for several applications in biomedicine and in particular for magnetic resonance imaging (MRI), magnetic hyperthermia and drug delivery (117, 122, 189, 190). Their magnetic properties, inherent biocompatibility and low cost, make them particularly attractive for such applications. IO NPs were first used 25 years ago, as liver MRI contrast agents (190), and are currently commercially used to evidence abnormal biological

activity in liver, spleen and bone marrow (191). Moreover, they have recently been commercialized as nanoheaters in magnetic hyperthermia for treatment of cancer and they are being developed as drug carriers for targeted delivery (192–194). To achieve a high efficacy in translation of the new generations of IO NPs in nanomedicine applications, controlling the synthesis and functionalization steps of IO NPs is of paramount importance to get the desired properties such as specific size, morphology, monodispersity, magnetic structure and suitable surface properties (63, 117, 195–197). Aside from the various IO NPs synthesis routes such as coprecipitation or hydrothermal synthesis, thermal decomposition of iron precursors in high temperature-boiling organic solvents in presence of surfactants allows the synthesis of IO NPs with excellent monodispersity, controlled morphology and high crystallinity. The ratio of the reactants, the type of solvent, reaction temperature, and reaction time determine the shape and size of the NPs (186, 198, 199). However, IO NPs synthesized by this method are only dispersible in apolar solvents as they are covered and stabilized by hydrophobic surfactants. Thus, to ensure their colloidal stability in physiological media which is necessary to envision nanomedical applications, a step of ligand exchange is crucial to replace the hydrophobic surfactants with more strongly binding hydrophilic ligands, and thus stabilize IONPs in aqueous phase. Ligand exchange is a widely used strategy, which includes different chemical processes and also the use of biocompatible bifunctional molecules bearing one anchoring group and also one functional group for colloidal stability or for further grafting of dye or targeting ligands. Carboxylate anchoring groups have been proven to work well for ligand exchange processes (200). Salas et al. modified the IONPs' surface prepared by thermal decomposition through a ligand substitution process with dimercaptosuccinic acid (201). On the other hand, phosphonate groups are also widely used to couple with IO NPs to yield water-phase transfer. The phosphonate group has been proven to have a significantly higher grafting rate, stronger binding than carboxylate anchors, excellent water dispersibility and in vivo MRI properties (202–205).

Before the use of such carboxylate and phosphonate groups, several research groups have studied the process of condensation of alkoxy silanes on the surface of IONPs mainly synthesized by coprecipitation in water. Grafted silane groups are reported to have two main advantages over the former ligands: i) higher chemical stability, and ii) greater availability and versatility regarding the choice of chemical end-group functions. Indeed bifunctional molecules bearing both phosphonate and amino groups are not stable in solutions and cannot be grafted efficiently on IONPs. Aminopropyl-triethoxysilane (APTES) is the main silane molecule which has been grafted at the surface of IONPs. The silanization process by APTES is known to be sensitive to a wide range of parameters: type of solvent, temperature, reaction time and silane concentration (206, 207). The mechanism of functionalisation at the IO NPs surface was reported to be similar to that of siloxane layer formation on silica surfaces. It involves the formation of a Fe-O-Si bond between the Fe-OH bond at the IO NPs surface and the hydrolysed alkoxy silane ligand (206). However, an accurate control of the formation of a silane monolayer or oligomeric multilayers is difficult (207–211). Different routes are involved in the amino-silanization process, which makes the grafting density of silane ligands highly dependent on the reaction conditions. Therefore silanes may be attached to the IO NPs via physisorption, hydrogen bonding or electrostatic attachment, and often arise in multilayer formation. Overall, the kinetics of silanization is critical for controlling the formation process of the layer (207–209). Bruce et al. revealed that hydrophilic and protic solvents (e.g. alcohols) usually accelerate hydrolysis and condensation kinetics, thus promoting the surface modification process (206). They also observed that an increase in reaction time (from 1 to 24 h) led to an increase in the silane density at the surface of

IONPs, the effect being more significant at high temperature. Furthermore, one may notice that silanization studies were mainly performed on IO NPs prepared by co-precipitation in water suspension and thus very few silanization studies have been done on IONPs prepared by thermal decomposition (103, 212). In addition, the available ligand exchange protocols are only suitable under specific reaction conditions. The method by De Palma (103), which is considered as the reference method to perform silane ligand exchange on hydrophobic ferrite NPs, is performed under diluted conditions (0.2 mg of NPs.ml⁻¹ hexane) and takes 72 h of reaction. Other rare/scarce methods applied on thermally decomposed IO NPs require the use of continuously applied ultra-sounds (212) at 50°C for 5 h, which can be energy consuming and cost-effective.

Herein we propose a new, rapid, and easily implemented method of silane ligand exchange allowing an efficient aqueous-phase transfer of monodispersed hydrophobic IO NPs obtained by thermal decomposition. This new process is based on IO NPs silanization in miscible EtOH/CHCl₃ co-solvents (proportion ca. of 3:1). In previous works, we used an efficient procedure of silanization of silica particles in EtOH catalyzed by ammonia (Stöber-like conditions) (165, 166, 187). Noticing the miscibility of polar EtOH and apolar CHCl₃, and assuming an efficient ligand exchange using acetic acid as a catalyst, we translated these conditions for the silanization of thermally decomposed IO NPs. These optimized conditions ensure the optimal grafting of various hydrophilic alkoxy-silanes bearing functional amines or carboxylate end-groups on hydrophobic oleic-acid coated IONPs and then an efficient aqueous-phase transfer, Figure 3-1. The advantages of this process over other existing approaches of silanization are i) the reaction is more rapid than the current methods (ca. 24 and even 4 h vs 72 h), ii) the process is made in more concentrated conditions of IO NPs in low-cost solvents (ca. 1 vs 0.2 mg.ml⁻¹), iii) the process is easy to implement, as it can be done in plastic or glass vials by simply stirring the solutions in a tube rotator without stringent conditions. Hence, in this work, we demonstrate the great applicability of this new process and versatility towards various silanes. For this, an extensive characterization of the silanized thermally decomposed IONPs was performed. Colloidal stability, surface charge, nanostructural and physico-chemical properties of silanized IONPs were investigated by varying the reaction time, the stoichiometry and the type of silane ligand used. Regarding biomedical applications, to assess the potential of these new silanized IONPs as novel efficient MRI contrast agents, proton's longitudinal (r_1) and transversal (r_2) relaxivities of amino and carboxylate-ended silanized NPs dispersed in water were measured. Finally, MRI-phantom imaging and a preliminary cell viability study were performed.

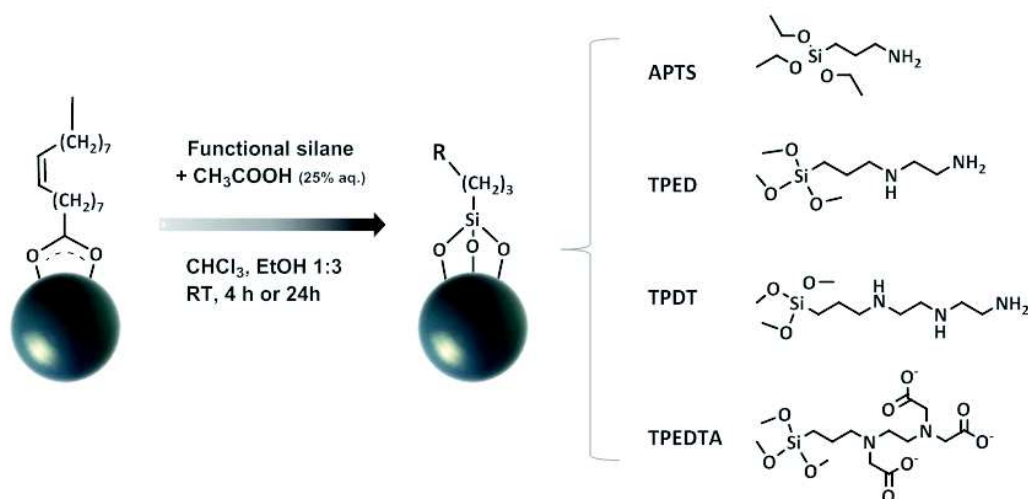


Figure 3-1: Silanization process of thermally decomposed IONPs in polar/apolar co-solvents

1.3 Silanization of oleic acid-coated IONPs

1.3.1 Starting conditions

2 mL IONPs in chloroform at 4 mg.mL⁻¹, 5.6 mL ethanol, 183 μ L APTS (stoichiometry calculated of 1101 silanes/nm² for 11 nm spherical NPs) and 240 μ L acetic acid (25% wt. in water) were added successively into a 14 mL centrifuge tube. The suspension was shaken for 24 h in a tube rotator. After this period, the suspension became limpid black-brown and well-suspended. The NPs were precipitated by addition of THF and were washed 3 times using any of the following mixed solvents: acidified water (pH=3.5)/THF (ca. 1:2) or EtOH/THF (ca. 1:2) by centrifugation (5000 g, 5 min). The IO-APTS NPs were finally dispersed in 5 ml acidified water or EtOH. Application of a magnet may help to remove small aggregates and afford highly stable colloidal suspensions. Similar silanization and washing processes were done with TPED (172 μ L), TPDT (197 μ L) and TPEDTA (628 μ L) which were incubated at a stoichiometry of 1101 silanes/nm² for 24 h. The IO-TPEDTA NPs were washed 3 times with deionized water (pH = 7)/THF (ratio 1:2 to 1:4) by centrifugation (5000 g, 5 min) and re-dispersed in 5 mL of slightly basified water (pH = 7.5). Regarding the optimization of these conditions, APTS, TPED, TPDT and TPEDTA grafting were performed at 4 h reaction time, and by varying the stoichiometry number of silanes/nm² to 6020:1; 351:1 and 100:1. For the sake of clarity, all the experimental conditions used for the silanization process are summarized in Table S 3-1 and Table S 3-2.

1.3.2 Reference silanization method in hexane (De Palma et al.²⁸)

Under ambient conditions, 0.5% (v/v) trialkoxysilane* and 0.01 % (v/v) acetic acid were added to a dispersion of IONPs in hexane (6 mg in 30 ml hexane). The mixture was shaken for 72 h, during which the NPs precipitated. The black-brown precipitate was separated using a magnet. The precipitate was washed 3 times with water/THF (ca. 1:2) by centrifugation. Finally, the NPs were re-dispersed in acidified or basified water (same conditions as the above method). *APTS, TPED and TPDT were all added in a volume of 150 μ L (corresponding to a stoichiometry of 1204, 1281 and 1115 silanes/nm² respectively).

1.4 Results and discussion

1.4.1 Synthesis of iron oxide NPs by thermal decomposition

Superparamagnetic IONPs were synthesized by thermal decomposition according to a previously published procedure (186). Iron stearate was decomposed in a high boiling solvent, dioctylether (b.p. 288 °C) in the presence of oleic acid as stabilizing agent. The purification of the as-synthesized IONPs in situ coated with oleic acid, was followed by IR spectroscopy as a function of the number of washing steps (see details in S1, Figure S 3-1). TEM images revealed the homogeneous spherical morphology of the NPs with an average diameter of 11 ± 1 nm (Figure 3-2 A). DLS measurements in chloroform indicated a mean hydrodynamic size of 12 ± 2 nm (PDI = 0.15), which is consistent with an oleic acid layer of around 1 nm at the surface of IONPs (Figure 3-2 B). The quantification of Fe element in the synthesized IONPs suspension was done by relaxometry, as described by Muller et al. (172), using a standardized calibration curve (see titration protocol in the experimental section and the calibration curve in Figure S 3-2). In a typical batch of thermally decomposed IONPs re-dispersed in chloroform, a concentration of $[\text{Fe}] = 63$ mM was determined corresponding to a IONPs concentration of $4.86 \text{ mg}\cdot\text{mL}^{-1}$. Before silanization, this batch was diluted to 52 mM of Fe ($4 \text{ mg}\cdot\text{mL}^{-1}$ IONPs). For comparison, the coating of such NPs by phosphonated dendrons is generally performed on suspensions with a concentration of $1 \text{ mg}\cdot\text{mL}^{-1}$ IONPs (199, 213, 214).

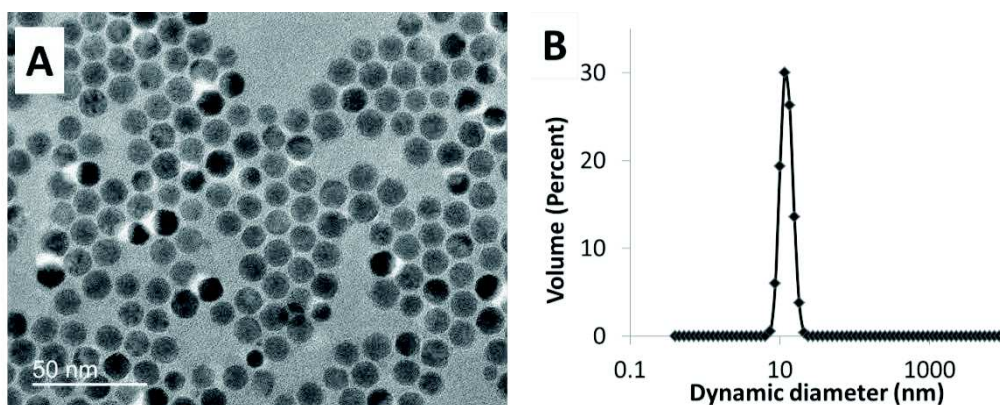


Figure 3-2: (A) TEM image and (B) DLS size distribution in CHCl_3 of oleic-acid coated IONPs

1.4.2 Grafting of APTS aminosilanes

1.4.2.1 Starting conditions

Firstly, the grafting of the often used APTS silanes was investigated under the stated starting conditions (see experimental section) in $\text{EtOH}:\text{CHCl}_3$, 3:1 co-solvents, 24 h reaction time at room temperature with a stoichiometry of 1101 silanes/ nm^2 of IONPs surface. This stoichiometry corresponds to a similar stoichiometry to that used by De Palma et al. (103) of 1204 silanes/ nm^2 of ferrite NPs (calculated value), which was shown to ensure a full coverage of the IONPs surface with a number of ca. 29 grafted APTS/ nm^2 (TGA) and a silane shell thickness of 4.7 nm (XPS). Given that a grafting degree in the range of 2-4 APTS silanes/ nm^2 on silica planar substrates was reported for a pure APTS monolayer (210, 215, 216), these results suggest that a high stoichiometry (≥ 1000 silanes/ nm^2) is a key parameter to form a siloxane multilayer of several nm thickness around the IO NPs and to ensure its colloidal stability. After the washing steps in acidified water (pH = 3.5), the hydrodynamic size distributions in volume of the IO-APTS NPs were monitored by DLS. The results show a high colloidal stability with a mean hydrodynamic

size of 26 nm (PDI=0.27) (Figure 3-3 A, black curve) in acidified water. Similar results were found after washing steps and redispersion in EtOH with a mean size of 19 nm (PDI=0.36) in EtOH (Figure 3-3 B, black curve). These results show that the silanized IO-APTS NPs are mainly dispersed as individual nanoparticles in these media and the differences found as compared with the magnetic core (11 nm) are attributed to the formation of a siloxane layer of several nm thickness and to the solvation sphere of the amino-silane layer around the IONPs. Recently, Laurent and Stanicki et al., reported the formation of highly stable carboxysilane coated IONPs (made by hydrothermal synthesis) by forming a polysiloxane shell around the magnetic NPs (217, 218).

1.4.2.2 Influence of the reaction time

With the aim to optimize the process conditions, the reaction time was decreased from 24 h to 4 h. DLS size distributions of the IO-APTS NPs dispersed in acidified water (pH = 3.5) and in EtOH with a mean hydrodynamic size of 22 nm (PDI=0.40) and 25 nm (PDI=0.39) (red curves on Figure 3-3 A and B respectively), confirmed that reducing reaction time was as efficient as the starting conditions to stabilize the NPs. ZP measurements as a function of pH were performed in water to investigate the colloidal stability at higher pH, especially under physiological pH. The results indicated that IO-APTS NPs display an isoelectric point (IEP) at around pH = 7-8 (Figure 3-3 C). This is in agreement with the loss of colloidal stability of IO-APTS NPs observed visually above this pH. Indeed, IO-APTS NPs provide a positive ammonium charge in acidified medium ensuring colloidal stability via electrostatic repulsion. However, when the ammonium groups start to be deprotonated in neutral medium, surface charge might be insufficient to stabilize IO-APTS NPs in solution. Furthermore, interactions of the amine groups with IO NPs shifting the IEP value towards lower pH ≤ 8 are not excluded in the absence of thermal treatment as shown with silica NPs (219). For both 24 and 4 h reactions, the grafting of APTS molecules on IONPs was investigated by FTIR spectroscopy and EDX analysis. FTIR study showed the effective coating of APTS on IO NPs (see details in Figure S 3-3). EDX analysis (Figure S 3-4) carried out with the TEM microscope on a zone containing thousands of IO-APTS NPs (magnitude 50000) confirmed the simultaneous presence of Si and Fe elements and thus the effective coating of the silane layers.

Furthermore, we compared our silanization method (in EtOH/ CHCl₃, 24 or 4 h reactions, IO NPs at ca. 1 mg.ml⁻¹) with the method of De Palma et al. (103) (in hexane, 72 h reaction, IO NPs at ca. 0.2 mg.ml⁻¹). This method is a seminal reference method ensuring the efficient grafting of numerous silanes on hydrophobic magnetic ferrite NPs made by thermal decomposition. Comparing both methods, very similar size, ZP distributions in acidic media, and NPs agglomeration above pH = 7 were observed. Table S2 summarizes all the silanization results obtained by the two methods with the various conditions used.

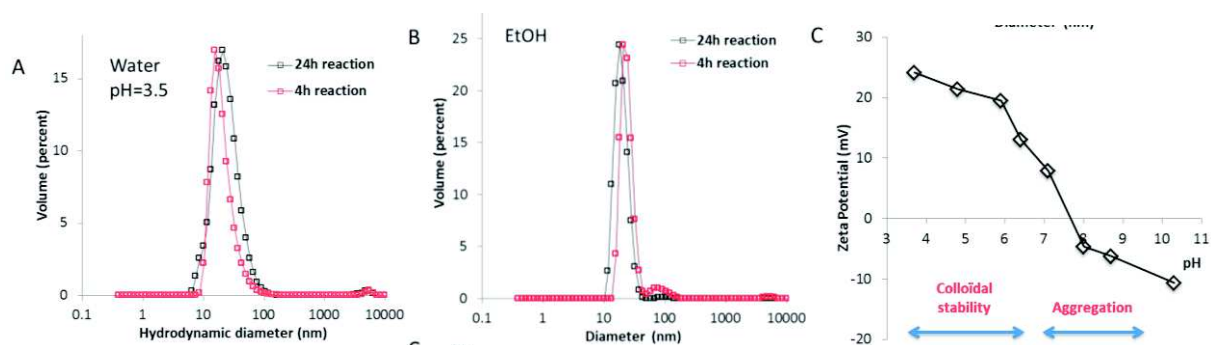


Figure 3-3: (A) DLS size distributions of IO-APTS NPs in (A) acidified water (pH = 3.5) and (B) EtOH obtained at 24 and 4 h reaction times (stoichiometry - 1101 silanes/nm² IO NPs). (C) Zeta potential evolution of IO-APTS NPs with pH in water

1.4.2.3 Influence of the stoichiometry

The influence of the stoichiometry (*i.e.*) the number of APTS reacted/nm² of IO NPs on the colloidal stability was also investigated to optimize the process conditions. The reaction time was set at 24 h and the stoichiometry number of APTS/nm² was respectively decreased to 350:1 and 100:1. The results summarized in Table S 3-3 shows that the hydrodynamic sizes measured by DLS in water at pH 3.5 at these lower ratios were higher (48 nm (PDI=0.20) at 350:1 and 78 nm (PDI=0.24) at 100:1) as compared to the 1101:1 stoichiometry which shows a loss of colloidal stability when the stoichiometry is decreased. An increased condition of stoichiometry at 6020:1 shown that the IO-APTS NPs dispersed well in water at pH=3.5 with a high colloidal stability (hydrodynamic size of 24 nm). These data indicate that below a certain amount of added silanes, the IONPs lose their colloidal stability. This suggests that with the aim to achieve a good colloidal stability of IONPs grafted with silanes, a polysiloxane shell having an enough dense, thick and cross- linked siloxane network is needed. Furthermore, in all cases, the IO-APTS NPs aggregated from pH 7.5.

1.4.3 Grafting of TPED, TPDT aminosilanes

As the IO-APTS NPs could not be stabilized in physiological pH conditions, we investigated two other aminosilanes with longer alkyl chains and more amine groups as compared to APTS: TPED and TPDT molecules (see molecular structures in Figure 3-1). TPED and TPDT silanes were grafted at 1101 silanes/nm² for 24 h. These results indicate that both IO-TPED and IO-TPDT NPs are stable in acidified water (pH = 3.5) with respective mean hydrodynamic diameters measured at 47 nm (PDI=0.20) and 42 nm (PDI=0.26) (Figure S 3-5). Better results were found with a stoichiometry of 6020:1 with respective mean hydrodynamic diameters measured at 28 nm (PDI=0.34) and 27 nm (PDI=0.40) (Figure S 3-5). These results show that a better colloidal stability was obtained by increasing the stoichiometry. This is consistent with the results obtained with APTS and the idea that the formation of a well-structured polysiloxane shell is required to ensure colloidal stability. Furthermore, as it was the case for IO-APTS NPs, IO-TPED and IO-TPDT NPs aggregated too in physiological pH (7.5) (DLS diameter \geq 1000 nm). Grafting of TPED and TPDT silanes was also assessed by FTIR spectroscopy, which confirmed the effective grafting of these two silanes with the appearance of the vibration bands at 1000 and 1100 cm⁻¹ characteristic of the Si-O bonds, and of the N-H bondings at 1633 cm⁻¹, characteristic of the presence of NH₂ groups from TPED and TPDT (Figure S 3-6). Table S 3-4 summarises all the results obtained with IONPs grafted with TPED and TPDT reporting DLS size distribution and ZP measurements. Finally, from the data obtained on the grafting of APTS,

TPED, TPDT amino-silanes, neither method was suitable to produce amino-silane-modified IONPs with a good colloidal stability at physiological pH 7.5. This emphasizes the need for other end-groups to stabilize IONPs in aqueous physiological conditions.

1.4.4 Grafting of TPEDTA carboxylate silanes

To achieve a high colloidal stability at physiological pH, the grafting of a silane bearing three carboxylate (COO^-) end groups named TPEDTA (see molecular structure in Figure 3-1) was investigated according to our silanization procedure in $\text{EtOH}/\text{CHCl}_3$. A stoichiometry of 1101 silanes/ nm^2 of IONPs was used for the two reaction times: 24 and 4 h. After washing in water/THF, IO-TPEDTA NPs were re-dispersed in deionized water and the pH was adjusted to 7.5 with NaOH. DLS analysis revealed that IO-TPEDTA NPs exhibited an excellent colloidal stability and a good monodispersity in physiological pH media (pH = 7.5) for both 24 and 4 h reactions with hydrodynamic diameters of 22 nm (PDI=0.26) and 24 nm (PDI=0.25) respectively (Figure 3-4 A). The difference in size compared to the 11 nm IO cores is attributed both to the formation of a thin siloxane shell around the IO core NPs and of the hydration layer in water. ZP measurements were performed as a function of the pH and decreasing negative values from -15 to -33 mV were observed all along the range of pH = 3-10 confirming the presence of the deprotonated carboxylate end groups (Figure 3-4 B). For IO-TPEDTA NPs, the IEP was found below pH = 3. This means that in this wide range of pH, the IO-TPEDTA NPs possess negative charge that comes from the COO^- functions. The IR spectra of IO-TPEDTA NPs and TPEDTA silane molecule (as a reference) were acquired (Figure 3-5). The appearance of vibrations bands at 1000 and 1126 cm^{-1} (Si-O) indicates the efficient coating of the TPEDTA carboxylate silane layer around the IONPs cores. The presence of carboxylate (COO^-) end groups was confirmed by the appearance of its typical vibrations asymmetric and symmetric COO^- stretching, respectively 1607 and 1407 cm^{-1} . EDX analysis (Figure S 3-7) performed with TEM apparatus on a zone at magnitude 50000 (performed on ~thousands of NPs) confirmed the presence of Si and Fe elements within the IO-TPEDTA NPs which also indicate the effective silane coating at the surface of the IONPs.

With the aim to optimize the grafting conditions, the TPEDTA grafting was investigated with a lower stoichiometry: 350:1 and 100: 1 TPEDTA reacted/ nm^2 with a reaction time set at 24h. The results obtained showed that the hydrodynamic size of TPEDTA-IO NPs dramatically increased under these conditions (≥ 1000 nm). This shows again the importance of a limit stoichiometry (number of silane/ nm^2) to ensure a high colloidal stability of the silanized IO NPs. Table 3-1 summarises all the results obtained reporting DLS size distribution and ZP measurements performed on IONPs grafted with TPEDTA carboxylate silane.

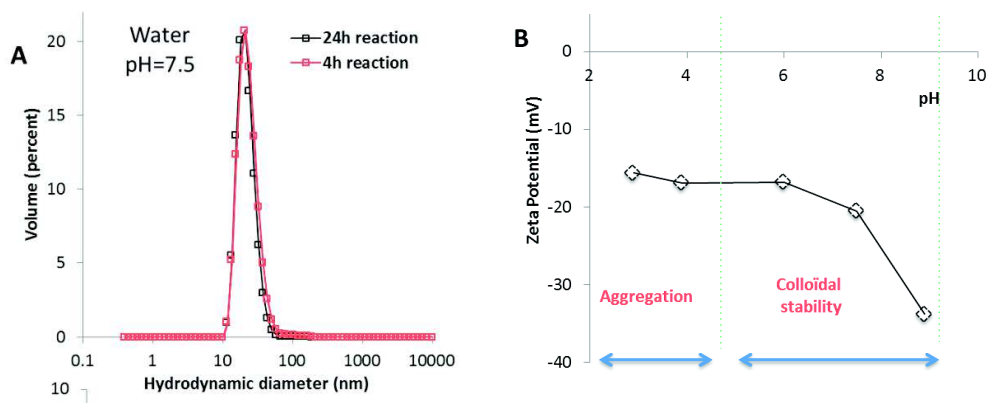


Figure 3-4: (A) DLS size distribution of IO-TPEDTA NPs in deionized water (pH = 7.5) obtained at 24 h (black curve) and at 4 h (red curve) reaction, at a stoichiometry : 1101 silanes /nm² IO NPs. (B) Zeta potential evolution of IO-TPEDTA NPs as a function of the pH in water

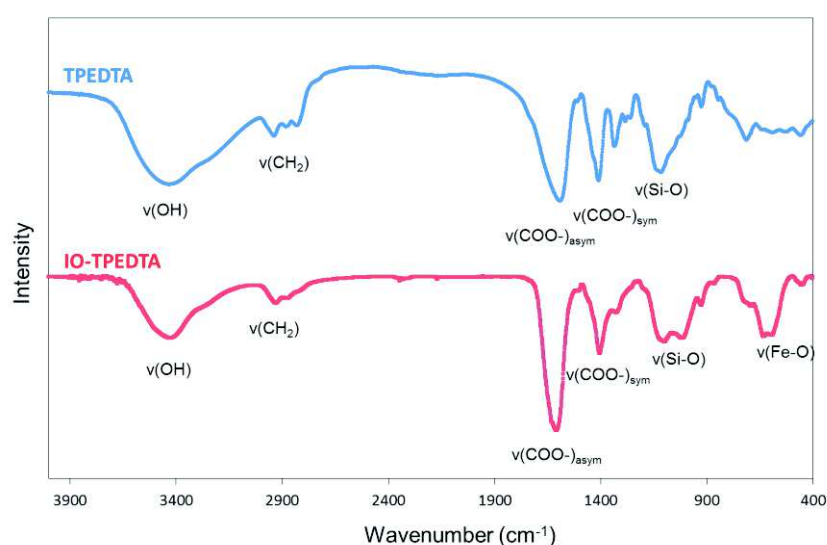


Figure 3-5: FTIR spectra of IO-TPEDTA NPs and TPEDTA molecules

Table 3-1: Summary of the conditions used for the silanization of IO NPs with TPEDTA carboxylate silane. * corresponds to results obtained following the silanization procedure with the reference method ²⁸

Silane	Reaction time (h)	Reaction solvents	Stoichiometry silane/nm ²	Dispersant medium	DLS size (nm) (PDI)	Zeta potential (mV)
TPEDTA	24	EtOH/CHCl ₃ 3:1	1101:1	Water pH=7.5	22 (0.26)	- 21
	24	EtOH/CHCl ₃ 3:1	350:1	Water pH=7.5	≥ 1000	n/a
	24	EtOH/CHCl ₃ 3:1	100:1	Water pH=7.5	≥ 1000	n/a
	4	EtOH/CHCl ₃ 3:1	1101:1	Water pH=7.5	24 (0.25)	-21

1.4.5 Evaluation of MRI contrast enhancement properties

In this section, we investigated the MRI contrast enhancement properties of APTS and TPEDTA modified-IONPs by evaluating their longitudinal (r_1) and transverse (r_2) relaxivity values in water at 37°C and 1.41 T. First, the graph representing the relaxation rates R_1 and $R_2 = f([Fe])$ of IO-APTS NPs suspensions were traced in the range 0-1 mM [Fe] in acidified water (pH = 3.5) where the NPs are colloiddally stable (Figure 3-6 A). A linear evolution for R_1 and R_2 with [Fe] was found. The slopes were fitted with linear models to afford the relaxivity values. For IO-

APTS NPs, values of $r_1 = 15.2 \text{ mM}\cdot\text{s}^{-1}$ and $r_2 = 102.7 \text{ mM}\cdot\text{s}^{-1}$ were found at $\text{pH} = 3.5$. However, when the pH of the suspensions was increased to $\text{pH} = 5.2$, the evaluation of relaxivity was not possible due to aggregation of the nanoparticles under the magnetic field of the NMR spectrometer. Figure 3-6 B illustrates the effect of the magnetic field on three successive measurements of relaxation times T_1 and T_2 of the IO-APTS suspensions. The values were found to increase considerably at $\text{pH} 5.2$ compared with those at $\text{pH} 3.5$, which were constantly reproducible. Indeed, at this $\text{pH}=5.2$ and under an applied magnetic field, IO-APTS NPs aggregate and T_1 , T_2 values increase as the water accessibility is reduced. These data evidence that the relaxometric properties of IO-APTS NPs can only be estimated in an acidic aqueous medium ($\text{pH} < 4-5$) as expected given the limited colloidal stability of IO-APTS NPs. Oppositely, IO-TPEDTA NPs are highly stable at $\text{pH} 7.5$ and remained unaffected by the applied magnetic field during the measurements. The graphs representing the relaxation rates R_1 and $R_2 = f([\text{Fe}])$ for IO-TPEDTA NPs suspensions were thus traced in water at physiological $\text{pH} (7.5)$ (Figure 3-7 A). For IO-TPEDTA NPs, values of $r_1 = 13.9 \text{ mM}\cdot\text{s}^{-1}$ and $r_2 = 88.6 \text{ mM}\cdot\text{s}^{-1}$ were found at $\text{pH} = 7.5$. To the best of our knowledge, these relaxivity values are the first measurements reported for silanized IO NPs synthesized by thermal decomposition and transferred in aqueous phase. These values of r_1 and r_2 are listed in Table 3-2 and compared with the current existing IONPs based contrast agents available in the market.

Interestingly, the TPEDTA-modified IONPs have superior relaxivity r_2 values and r_2/r_1 ratio as compared to commercially available CAs (Supravist, Sinerem) displaying similar mean hydrodynamic size. They have similar r_2 relaxivity and r_2/r_1 values with Ferumoxyl and this confirms the non-aggregation of these IONPs. Indeed the mean hydrodynamic diameter of NPs is a crucial parameter when considering in vivo applications as it has to be lower than 50 nm to ensure a good in vivo biodistribution. Therefore the TPEDTA-modified IONPs display promising MRI properties and a mean hydrodynamic size suitable for in vivo applications.

To better visualise this contrast enhancement effect, MRI of the silanized IONPs suspensions as phantoms was performed. Aqueous dispersions of IO-TPEDTA NPs were imaged in 1.5 mL plastic tubes using a 1.5 T MRI clinical research apparatus (Siemens) dedicated for research purposes. The tubes with silanized IONPs suspensions were placed into a rack, at room temperature, and inserted onto the MRI antenna. As IONPs are usually employed and investigated as T_2 -weighted hypodense MRI contrast agents, T_2 -weighted sequences were acquired to image the TPEDTA silanized IONPs (see details in experimental section). The IO-TPEDTA NPs suspensions were thus diluted in cascade in plastic tubes and imaged at the following concentrations in Fe in water: (1) control no NPs in water, (2) 0.219 mM, (3) 0.438 mM, (4) 0.875 mM, (5) 1.75 mM (6) 3.5 mM. (Figure 3-7 B). The MRI images of the tubes, taken in the sagittal plane, clearly display the T_2 -w hypocontrast effect with the concentration of the silanized IONPs. This evolution is in agreement with the r_2 values ensuring a performant hypocontrast for IO-TPEDTA at such concentrations in Fe. These data suggest the broad potential of our novel method to silanize thermally-decomposed IONPs for MRI imaging.

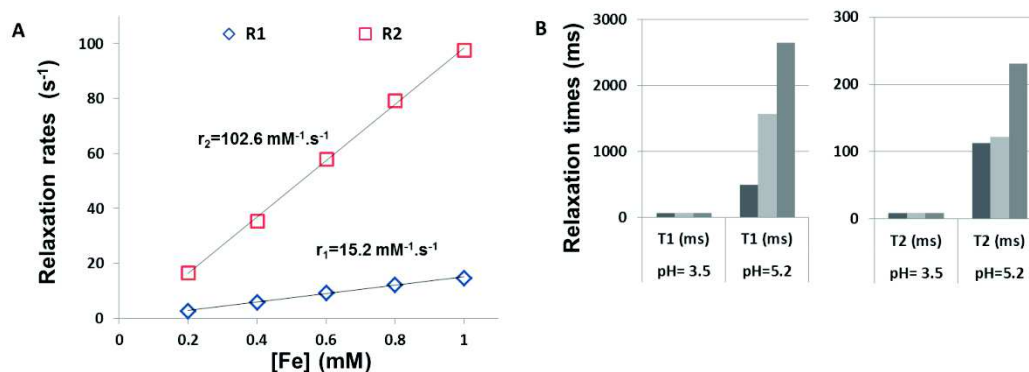


Figure 3-6: (A) Relaxation rates R_1 and R_2 (s^{-1}) as a function of $[Fe]$ (mM) for IO-APTS NPs in acidified water (pH 3.5) at 37°C and 1.41 T. (B) Comparison of the evolution of relaxation times T_1 and T_2 of IO-APTS NPs at 1 mM Fe between water at pH= 3.5 and 5.2 after three successive measurements

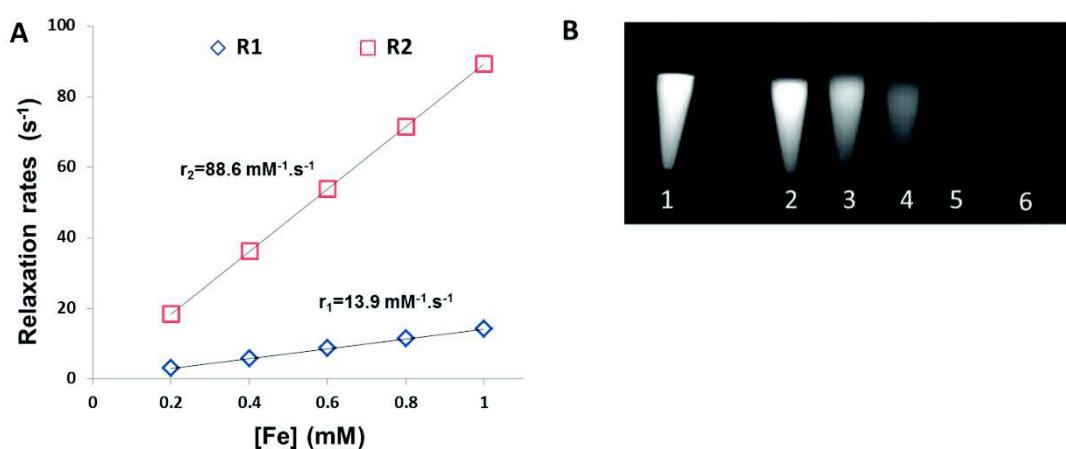


Figure 3-7: A. Relaxation rates R_1 and R_2 (s^{-1}) as a function of $[Fe]$ (mM) for IO-TPEDTA NPs in water at pH 7.5 at 37°C and 1.41 T. T_2w -MRI images in water at ambient T and 1.5 T of IO-TPEDTA NPs suspensions diluted in water. Position tubes from left to right are given by increasing Fe concentration: (1) control no NPs in water, (2) 0.219 mM, (3) 0.438 mM, (4) 0.875 mM, (5) 1.75 mM (6) 3.5 mM

Table 3-2: Summary of r_1 , r_2 relaxivities and r_2/r_1 values for mono-disperse IONPs on the market compared with the TPEDTA-silanzed IONPs

Type of IO NPs	Coating	$D_{H(\text{vol})}$ (nm)	r_1 ($\text{mM} \cdot \text{s}^{-1}$)	r_2 ($\text{mM} \cdot \text{s}^{-1}$)	r_2/r_1
Supravist	Carboxydextran	21	10.7	38	3.6
Sinerem	Dextran	15-30	9.9	65	6.7
Ferumoxyl	Carboxydextran	30	15	89	5.9
Resovist	Carboxydextran	60	9.7	189	19.5
NS11	TPEDTA	22	13.9	88.6	6.4

1.4.6 Cell viability study

As preliminary biological studies, the biocompatibility of IO-TPEDTA NPs was tested by MTT assay on A549luc cells. Cells were incubated with various IO-TPEDTA NPs concentrations from 0.31 to 322 $\mu\text{g}/\text{mL}$ $[Fe]$ for 24h. As shown in Figure 7, IO-TPEDTA NPs did not present any toxicity for a concentration up to 40 $\mu\text{g} \cdot \text{mL}^{-1}$ $[Fe]$. Above this NPs concentration, the cell viability

showed a slight continuous decrease with NPs concentration reaching ca. 60% viable cells at 322 $\mu\text{g}\cdot\text{mL}^{-1}$. These values are in the same range that was found in various cytotoxicity studies made with IONPs synthesized by hydrothermal or reductive routes and coated with positively or negatively charged silane coatings (220, 221), or with IONP synthesized by thermal decomposition methods and coated with neutral molecule/polymer (222, 223). Furthermore, the cytotoxicity experiments above cited, have been done on different cell lines (respectively for the cited examples (220–223): astrocytes, KB, RAW 264.7 B16F10, etc...) hence the variability in cell viability may arise from the nature of the different cell lines.

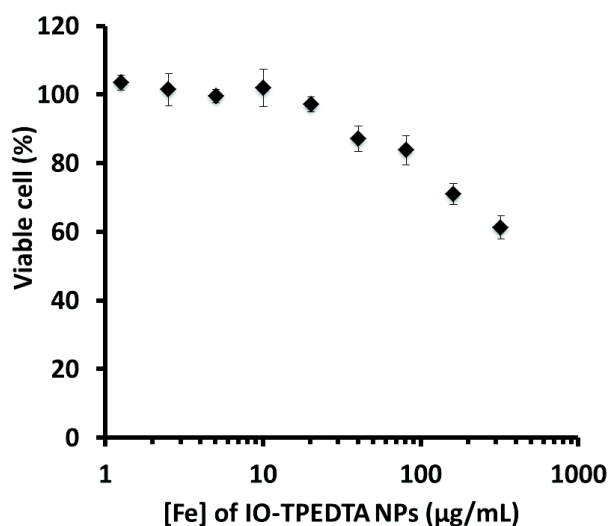


Figure 3-8: MTT cell viability study of A549Luc cells incubated with variable amounts of IO NPs

1.5 Conclusions

In this work, a novel and facile silanization method has been developed to efficiently stabilise highly monodisperse magnetic IONPs (ca. 11 nm diameter) synthesized by thermal decomposition in aqueous media. This new and improved process compared with the current methods was performed by exchanging oleic acid bound at the surface IO NPs by silane molecules in miscible EtOH : CHCl_3 (ca. 3:1) co-solvents in the presence of acetic acid as catalyst. This approach provides an excellent colloidal stability and core monodispersity with hydrodynamic diameter being ca. 20 nm in aqueous solutions. The silanized IONPs were thoroughly characterised to confirm the grafting of silane at the surface of IONPs. We have shown that the nature and charge of the end-group of the silanes determines the water-dispersibility of the NPs especially regarding the pH domains. Indeed, NH_2 endgroup could stabilise IONPs in ethanol or in acidified water ($\text{pH} \leq 5$), while COOH endgroups stabilise the IONPs in neutral and basic media ($\text{pH} \geq 5$) by ensuring a mean hydrodynamic size suitable for in vivo applications. Finally, these results combined with the MRI imaging properties of the TPEDTA modified IONPs demonstrate their potential of application as contrast agents for different biomedical applications. Future works will also be dedicated to translate this method to the silanisation of IONPs displaying therapeutic properties by hyperthermia and to study in details the interactions of these optimized silanized magnetic NPs with cells.

1.6 Supporting information

1.6.1 S1: FTIR follow-up of the purification of oleic acid-coated IONPs

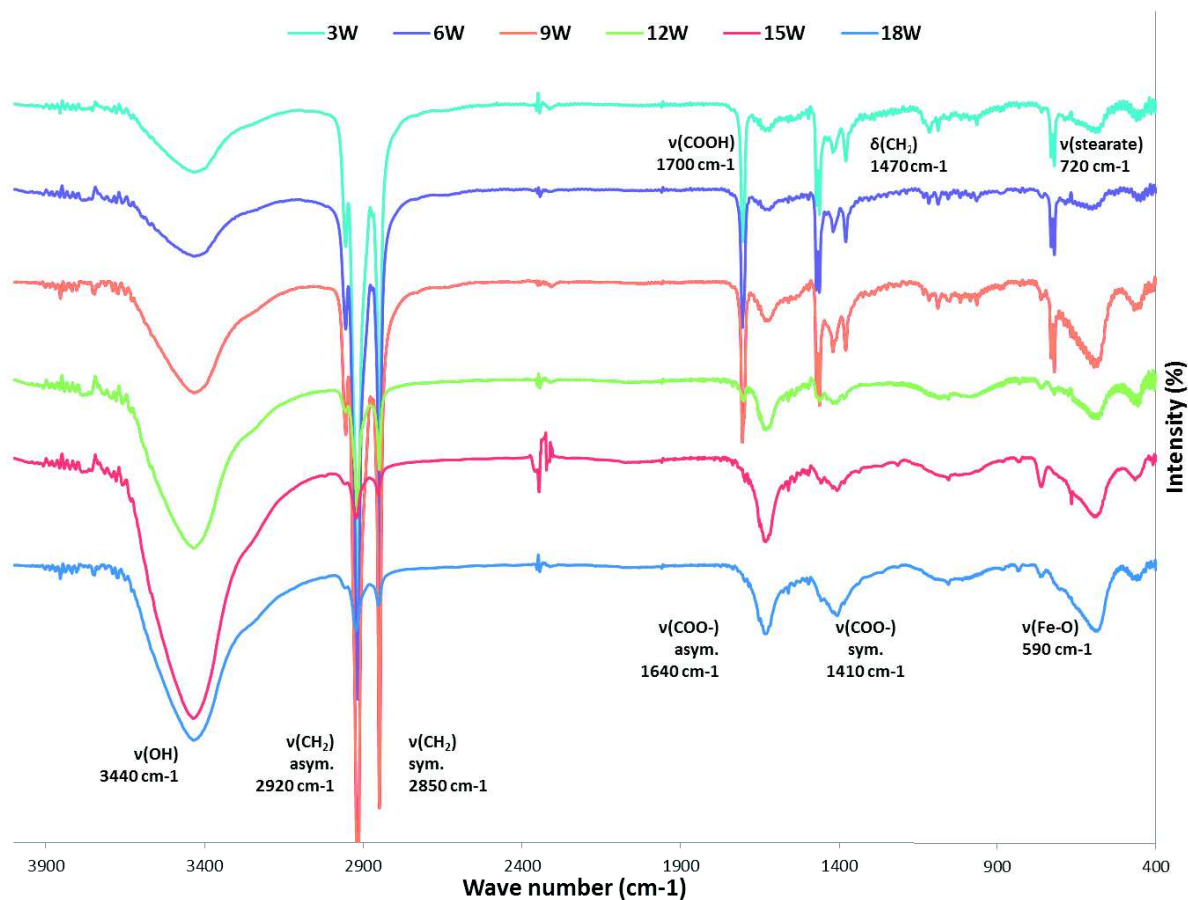


Figure S 3-1: FTIR follow-up of the purification of oleic acid -coated IONPs with the number of washing steps

IR spectra of the IO NPs were acquired after various washing steps to follow the purification of the IO NPs. The two peaks at 2920 and 2850 cm^{-1} are the characteristic bands of the asymmetric and symmetric stretching of CH_2 from the oleic acid and stearate chains. The band at 1700 cm^{-1} correspond to the $\text{C}=\text{O}$ bond (COOH) of the free oleic acid in suspension while the bands at 1640 and 1410 cm^{-1} correspond to asymmetric and symmetric bands (COO^-) of the oleic acid grafted at the surface of the IO NPs. The peak at 590 cm^{-1} corresponds to the Fe-O bond of the iron oxide. The iron stearate residue was revealed by the peak at 720 cm^{-1} . The efficacy of the purification of IONPs by washing was followed by the evolution of the ratio of the intensities of bands at 2920 cm^{-1} and 590 cm^{-1} . When the ratio is around 1.0, the NPs are empirically considered as cleaned (*i.e.*) assuming they are surrounded by one monolayer of oleic acid. Some studies have proved that when the ratio is too low, the oleic acid desorbs from the surface of IO and the IONPs may aggregate.

1.6.2 S2: Dosage of Fe in IONPs by relaxometry

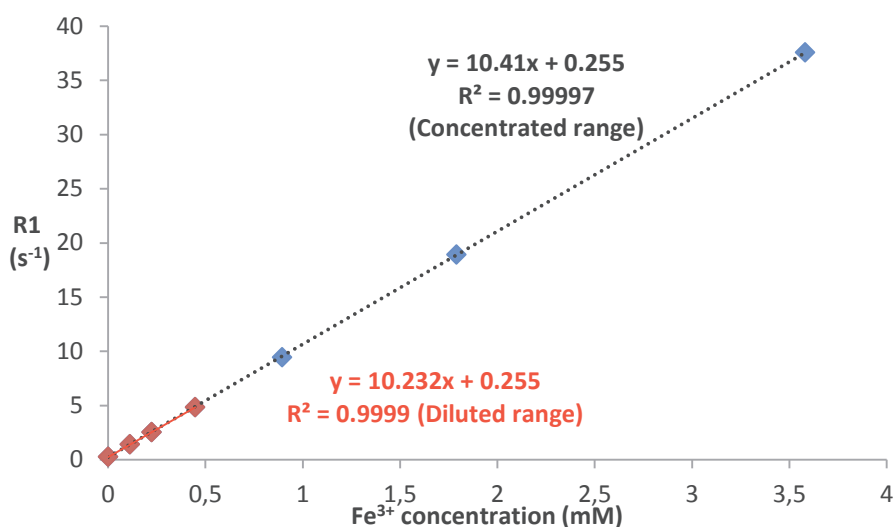


Figure S 3-2: Etalon-curve of the longitudinal relaxation rate (R1) as a function of [Fe³⁺] concentration for the dosage of Fe by relaxometry at 37°C 1,41T in aqueous HNO₃ 2%

1.6.3 S3: FTIR study of IO-APTS NPs

The spectrum of APTS was acquired as a reference. Compared with the FTIR spectrum of oleic acid stabilised IONPs shown in S1, several new bands were observed. First, the bands at 1040 and 1128 cm⁻¹ characteristic of the Si-O bonds indicate the efficient silane ligand exchange onto the IONPs surface. The complete disappearance of the CH₂ band vibrations at 2920 and 2850 and of the symmetric COO⁻ of bound oleic acid at 1410 cm⁻¹ indicates that oleic acid was removed from the IONPs surface. Furthermore, the FTIR spectrum shows N-H bendings at 1633 cm⁻¹, characteristic of the presence of NH₂ groups from APTS.

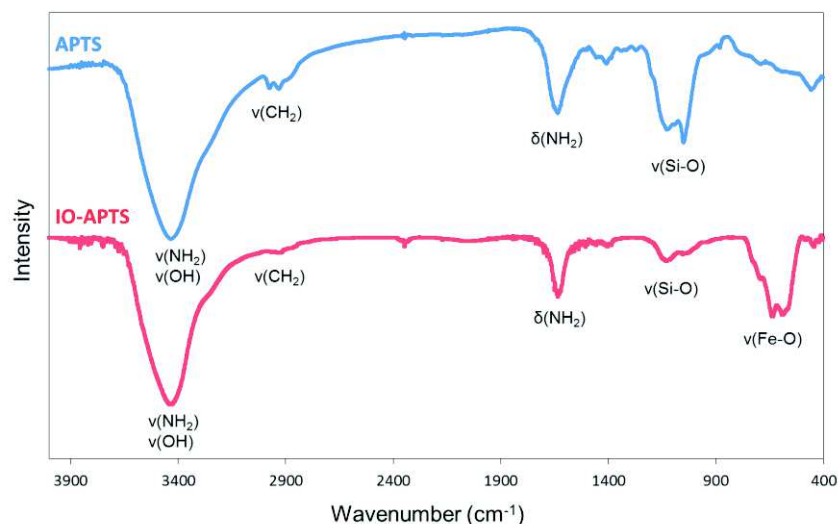


Figure S 3-3: FTIR spectra of APTS and IO-APTS NPs

1.6.4 S4: Energy dispersive X rays (EDX) analysis of IO-APTS NPs

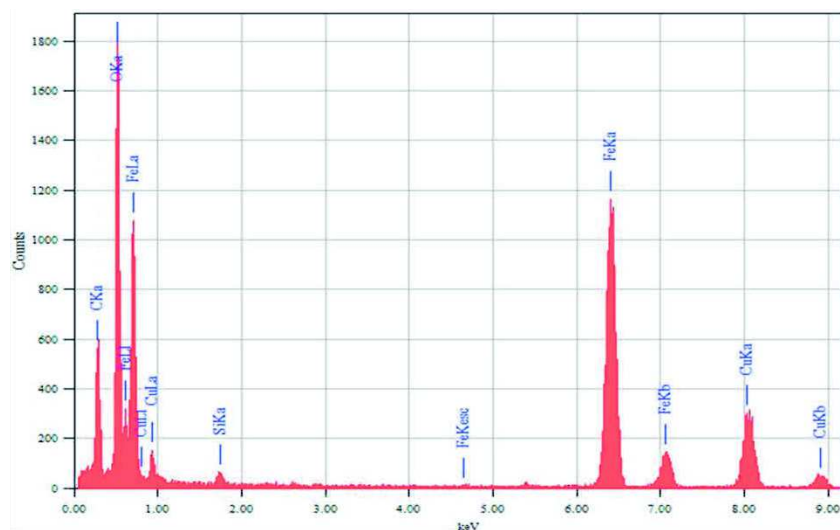


Figure S 3-4: EDX spectra performed on a zone containing thousands of IO -APTS NPs (magnitude 50000) confirming the simultaneous presence of Si and Fe elements

1.6.5 S5: DLS size distribution of IO-TPED and IO-TPDT NPs in acidified water (pH=3.5)

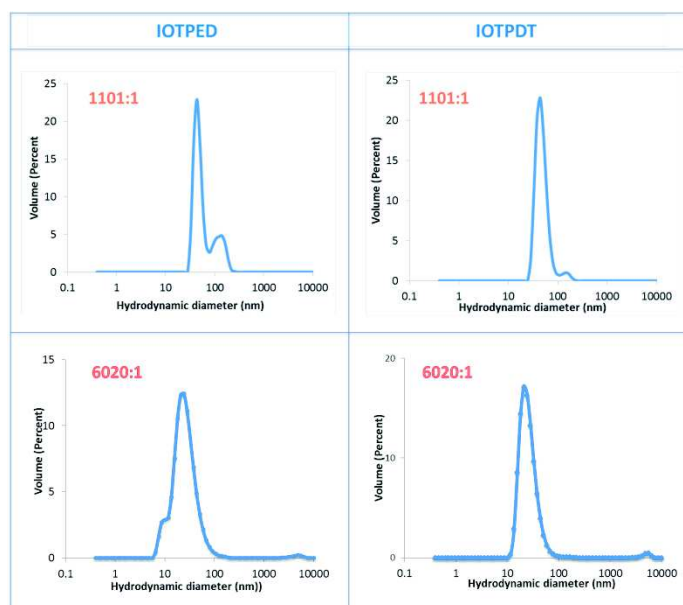


Figure S 3-5: DLS size distribution of IO-TPED NPs (at the left) and IO-TPDT NPs (at the right) in acidified water (pH=3.5) obtained at 24h reaction, at stoichiometries of 1101 and 6020 silanes/nm² IO NPs

1.6.6 S6: FTIR spectra of TPED and TPDT grafted IO-NPs

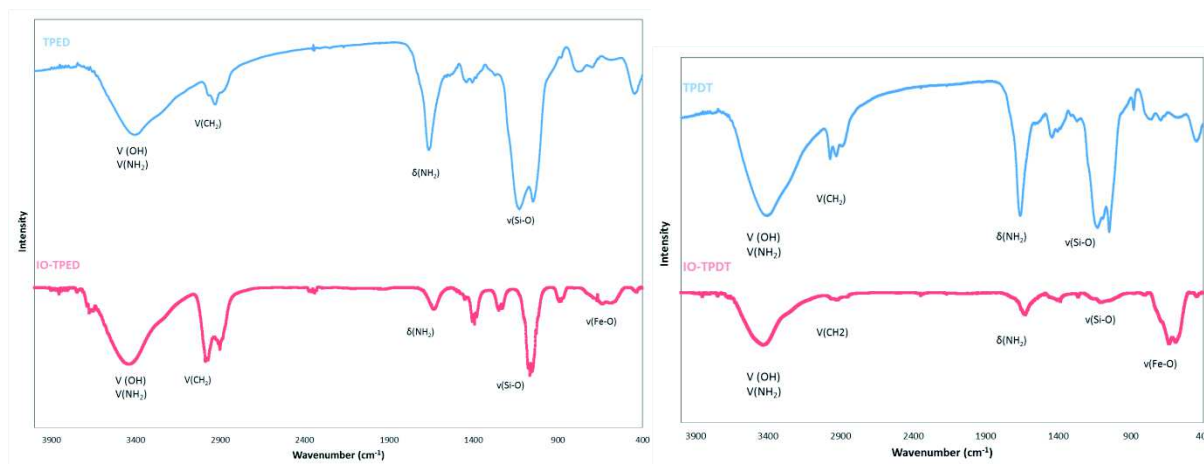


Figure S 3-6: IR spectra of TPED silane, IO-TPED NPs, and TPDT silane, IO-TPDT NPs

1.6.7 S7: Energy dispersive X rays (EDX) analysis of IO -TPEDTA NPs

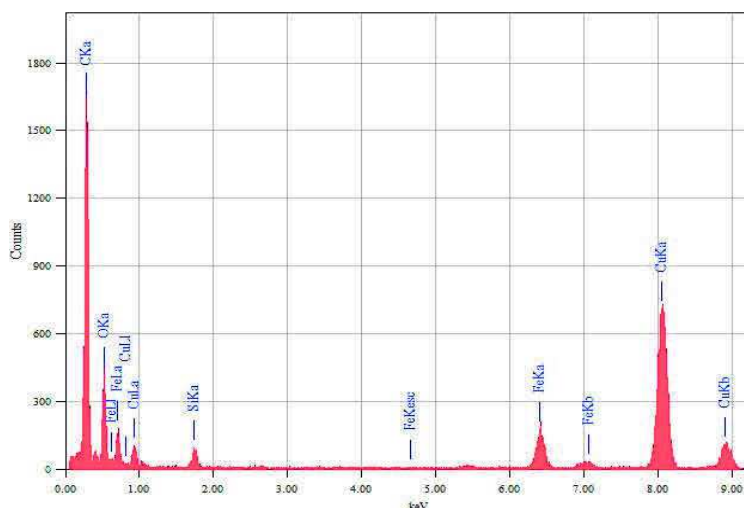


Figure S 3-7: EDX spectra performed on a zone containing thousands of IO -TPEDTA NPs (magnitude 50000) confirming the simultaneous presence of Si and Fe elements

1.6.8 S8: Tables

Table S 3-1: Summary table of the reaction parameters of IO NPs silanization used for the *starting conditions*: 2 mL IO NPs, incubated with 5.6 mL EtOH and 240 μ L acetic acid (25 % in water) at a stoichiometry 1101 silanes/ nm^2

Features	APTS	TPED	TPDT	TPEDTA
Stoichiometry/ nm^2	1101:1	1101:1	1101:1	1101:1
Volume (μ L)	183	172	197	628 (45% wt in water)
Reaction time (h)	4 and 24	24	24	4 and 24
Dispersant medium after washing steps	Acidified water pH=3.5	Acidified water pH=3.5	Acidified water pH=3.5	Water pH=7.5

Table S 3-2: Summary table of the silane volume used for the study of IO NPs silanization by varying the stoichiometry from 6020 to 100 silanes/nm²

Stoichiometry/nm ²	V(APTS) μL	V(TPED) μL	V(TPDT) μL	V(TPEDTA 45% water) μL
6020:1	1000	940	1080	n/a
1101:1	183	172	197	628
350:1	58	n/a	n/a	200
100:1	17	n/a	n/a	57

Table S 3-3: Summary table of the conditions used for the silanization of IONPs with APTS by varying the reaction time. * corresponds to the results obtained by following the silanization procedure of the reference method ²⁸

Amino-silane	Reaction time (h)	Reaction solvents	Stoichiometry silane/nm ²	Dispersant medium	Hydrodynamic DLS size (nm)/ (PDI)	Zeta potential (mV)
APTS	72 *	Hexane	1204:1	Water pH=3.5	24 (94%) (0.52)	n/a
	72 *	Hexane	1204:1	Water pH=7.5	≥ 1000	n/a
	24	EtOH/CHCl ₃ 3:1	1101:1	Water pH=3.5	26 (0.27)	+ 24
	24	EtOH/CHCl ₃ 3:1	1101:1	Water pH=7.5	≥ 1000	n/a
	24	EtOH/CHCl ₃ 3:1	1101:1	EtOH	19 (0.36)	n/a
	4	EtOH/CHCl ₃ 3:1	1101:1	Water pH=3.5	22(0.40)	+ 18
	4	EtOH/CHCl ₃ 3:1	1101:1	Water pH=7.5	≥ 1000	n/a
	4	EtOH/CHCl ₃ 3:1	1101:1	EtOH	25 (0.39)	n/a

Table S 3-4: Summary of the conditions used for the silanization of IONPs with APTS by varying the stoichiometry APTS/nm²

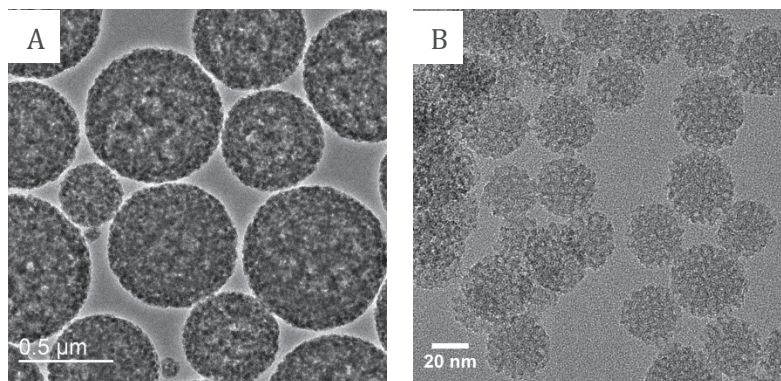
Amino-silane	Reaction time (h)	Reaction solvents	Stoichiometry silane/nm ²	Dispersant medium	Hydrodynamic DLS size (nm)	Zeta potential (mV)
APTS	24	EtOH/CHCl ₃ 3:1	6020:1	Water pH=3.5	24 (0.45)	+ 22
	24	EtOH/CHCl ₃ 3:1	1101:1	Water pH=3.5	26 (0.27)	+ 24
	24	EtOH/CHCl ₃ 3:1	350:1	Water pH=3.5	48 (70%) (0.20)	+ 36
	24	EtOH/CHCl ₃ 3:1	100:1	Water pH=3.5	78 (72%) (0.24)	+ 38

Table S 3-5: Summary of the conditions used for the silanization of IONPs with TPED and TPDT. * corresponds to results obtained following the silanization procedure of the reference method ²⁸

Amino-silane	Reaction time (h)	Reaction solvents	Stoichiometry silane/nm ²	Dispersant medium	Hydrodynamic DLS size (nm) (PDI)	Zeta potential (mV)
TPED	24	EtOH/CHCl ₃ 3:1	6020:1	Water pH=3.5	28 (0.34)	+ 18.5
	24	EtOH/CHCl ₃ 3:1	6020:1	Water pH =7.5	≥ 1000	+ 11
	24	EtOH/CHCl ₃ 3:1	1101:1	Water pH=3.5	47 (75%) (0.20)	+30
	24	EtOH/CHCl ₃ 3:1	1101:1	Water pH =7.5	≥ 1000	-4
	72 *	Hexane	1281:1	Water pH=3.5	125 (57%) (0.24)	n/a
	72 *	Hexane	1281:1	Water pH =7.5	≥ 1000	n/a
TPDT	24	EtOH/CHCl ₃ 3:1	6020:1	Water pH=3.5	27 (0.4)	+ 24
	24	EtOH/CHCl ₃ 3:1	6020:1	Water pH =7.5	≥ 1000	+ 3.5
	24	EtOH/CHCl ₃ 3:1	1101:1	Water pH=3.5	42 (0.26)	+26
	24	EtOH/CHCl ₃ 3:1	1101:1	Water pH =7.5	≥ 1000	-2
	72 *	Hexane	1115:1	Water pH=3.5	59 (0.24)	n/a
	72 *	Hexane	1115:1	Water pH =7.5	≥ 1000	n/a

Chapter 4:

MS NPs as sacrificial templates for the formation of Dox-loaded HSA NPs



MESOPOROUS SILICA NANOPARTICLES WITH TWO DIFFERENT POROSITY MORPHOLOGIES: (A) BIMODAL AND (B) RASBPERRY

1 Introduction

Design of nanoparticles as controlled drug delivery systems for cancer therapy have attracted great attention to overcome the problems of huge chemotherapeutics side effects such as the well-known cardiotoxicity of anthracyclines (224–228). That resulted in the development of “smart” nanoparticles that may release drugs locally in response to specific stimulus (161, 229–235). Among proposed strategies, enzyme-triggered drug release emerged as an attractive approach since the last years (153, 154, 236–239). Indeed, cellular enzymes called proteases can catalyze proteolysis, *i.e.* protein degradation, and thus proteins can be candidates for designing nano-objects for enzyme-sensitive controlled drug delivery.

As human serum albumin (HSA), the most abundant plasma protein (35–50 g/L human serum), presents non-toxic, non-immunogenic and biocompatible properties, and, as HSA nanoparticles are known to be degradable under enzymatic action (240), this protein represents promising material as carrier for controlled drug delivery (163, 164). Furthermore, HSA is the most versatile transport protein in the blood circulation with a molecular weight of 66.5 kDa and an high average half-life of 19 days which enhanced protein tumor uptake (241). HSA nanoparticles can be prepared through a multitude of techniques, the main one being desolvation (242–244), in which water soluble drugs are loaded either by incubation in the formed nanoparticles or by incorporation in the albumin solution before particle formation and crosslinkage (245). For example Dreis *et al.* prepared HSA nanoparticles and investigated an anti-cancer drug, doxorubicin (Dox), loading by incubation (adsorption on particle surface) compared to incorporation. For both loading strategies, high loading efficiencies (70–95 wt%) were obtained and Dox loaded HSA nanoparticles showed improved anti-cancer effects on *in-vitro* cell cultures compared to free Dox molecules (246).

In most HSA nanoparticles synthesis techniques, the use of covalent cross-linkers such as glutaraldehyde is often required. However potential release of such cross-linkers can induce some toxicity as glutaraldehyde is known to be genotoxic, mutagenic and carcinogenic (247–249). As an alternative Mertz *et al.* recently developed a new approach to form tight and robust HSA nanoparticles assembled non-covalently via *isobutyramide* (IBAM) grafts, hypothetically through hydrogen-bonding interactions, without the need of further cross-linkage or addition of adjuvants (165, 166, 187). In a typical procedure a sacrificial template is used to immobilize IBAM moieties and to give the final shape of the HSA nanoparticles. Silica nanoparticles, which were extensively studied in the past two decades, were chosen as sacrificial template. Indeed, they own outstanding intrinsic features like simple and well referred synthesis processes leading to nanoparticles with controlled size and shape, tunable morphologies, tunable pore structure and easy surface modification. Thus, the surface of silica could be modified with amine groups on which *isobutyrylchloride* can be grafted to form IBAM-functionalized surface. Furthermore tuning the silica nanoparticle morphology influences the design of the final HSA nanoparticles obtained after complete dissolution of silica template with hydrofluoric acid (HF): full silica particles lead to the formation of HSA hollow capsules (166) whereas mesoporous silica nanoparticles with large porosities, allowing the diffusion of HSA into the pores, will form replicate HSA nanoparticles (187). Finally, mesoporous silica nanoparticles exhibit large surface area and pore volume which provide great potential for drug adsorption and loading within the pore channels. In addition, the feature of tunable porosities enables better control of the drug loading and the type of drug loaded. Indeed, mesoporous silica nanoparticles with large porosities (> 3 nm) can load large drug molecules, SiRNA, plasmid, proteins, quantum dots, nanoparticles (34) whereas mesoporous silica nanoparticles with small porosities (~3 nm) are

well known for the loading of small drug molecules such as anthracyclines, ibuprofen, cisplatin, aspirin ... (47, 250, 251)

Based on these previous researches we developed two synthesis strategies for drug encapsulation into HSA NPs using silica as sacrificial template. Thus, we used two types of silica: with large porosities (> 3 nm) and with small porosities (~ 3 nm).

To synthesize large pores mesoporous silica, we chose to reproduce a synthesis strategy reported by Wang *et al.* (40) which led to the formation of bimodal mesoporous silica nanoparticles (BMS NPs) with primary mesopores of 3 nm and secondary nanopores of 20-50 nm. Thus, using this material as sacrificial template, we investigated the formation of self-supported Dox-HSA NPs after having covalently grafted the Dox to HSA beforehand.

In the second strategy, we synthesized silica NPs with porosities of about 3 nm inspired by Zhang *et al.* synthesis process (41). These NPs exhibited raspberry pore morphology and were thus called RB NPs. As these porosities were too small for HSA diffusion, they were used for Dox loading before the HSA shell formation on the silica surface via IBAM grafting strategy. Thus, after silica dissolution, Dox loaded HSA nanocapsules should be obtained.

These two strategies for Dox-HSA nanocarriers formation were investigated. In this chapter, part 2 is dedicated to the strategy involving BMS NPs whereas part 3 is dedicated to the use of RB NPs as sacrificial template.

2 Large pores mesoporous silica: Bimodal Mesoporous Silica Nanoparticles (BMS NPs)

2.1 Introduction

The project's goal developed in this chapter was to master the synthesis of silica particles which will serve as sacrificial templates to encapsulate cancer therapeutics into an IBAM-HSA shell. In this part, we investigated the use of mesoporous silica with large porosities for the formation of self-supported HSA_{Dox} NPs.

First, the synthesis parameters for the formation of BMS NPs according to Wang *et al.* protocol (40) and their impact on BMS NPs morphology and porosity were studied. As the porosities are large enough for HSA diffusion and formation of self-supported HSA NPs after silica dissolution, in parallel Dox molecules were covalently grafted to HSA before the HSA adsorption on BMS NPs. To be used for cancer therapy, this covalent bonding between HSA and Dox should be cleavable under specific stimuli. Thus, we choose to introduce a pH (<5) cleavable hydrazone bond between Dox and HSA, as after internalization of NPs in cells the endolysosomes are known to become acidic. After this covalent grafting between Dox and HSA, the so formed HSA_{Dox} was adsorbed on IBAM-modified BMS NPs followed by silica sacrificial template dissolution to form finally self-supported HSA_{Dox} NPs.

2.2 Synthesis

2.2.1 Synthesis strategy

To synthesize large pores silica nanoparticles the chosen synthesis strategy, reported by Wang *et al.* (40), produced nanoparticles of 400 nm diameter containing primary pores with a size of 3 nm and secondary pores of 20-50 nm. This synthesis strategy, illustrated in Figure 4-1, is based on the formation of an ordered and spherical mesomorphous complex between an anionic polymer, the poly(acrylic acid) (PAA) and a cationic surfactant, the cetyltrimethylammonium bromide (CTAB) in an ammonia solution. This solid-like surfactant-polymer complex is called PAA-C₁₆TA. When the tetraorthosilicate (TEOS) was added to the suspension, it hydrolyzed at pH 10-11 forming negatively charged silica oligomers. These silica oligomers penetrated into the ordered complexes and precipitated around the cationic micelles to form mesostructured silica. Consequently, this addition of TEOS disturbed the electrostatic interaction between PAA⁻ and CTA⁺ and some PAA⁻ chains were dissociated from the complexes. This phase separation of the polymer created large PAA⁻ chain areas which during the calcination step formed the large secondary nanopores (20-50 nm). The small primary nanopores (3 nm) resulted from the calcination of the CTA⁺ micelles.

The general procedure for BMS synthesis was detailed in Chapter 2 page 56.

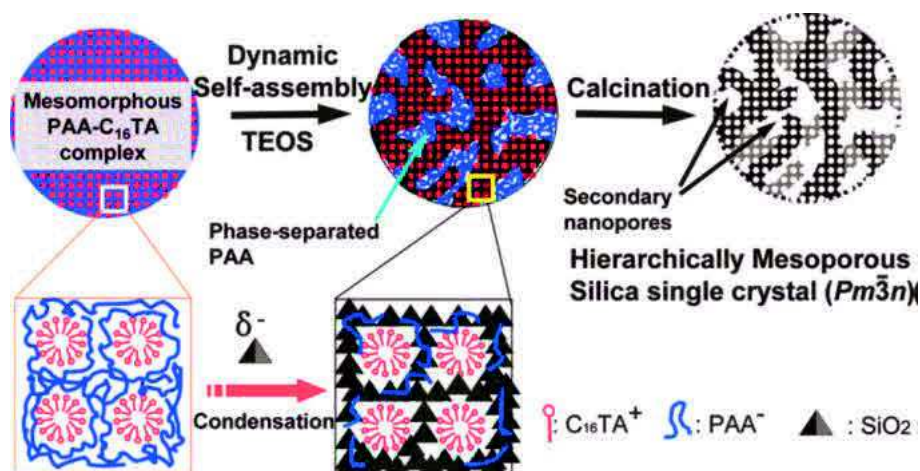


Figure 4-1 : Mechanism of formation of bimodal structure for silica nanoparticles from Wang *et al.* (40)

2.2.2 Control of size and porosity

According to Wang *et al.* (40) two synthesis parameters can influence the particles size and/or porosity: the temperature and the PAA quantity.

Indeed, after the addition of TEOS in the mixture, the reaction temperature played an important role to tune the pore size: higher the reaction temperature, larger the secondary nanopores and smaller are the primary mesopores. They explained that increasing reaction temperature would facilitate the interaction between silica precursors and CTAB and thus silica oligomers would replace more PAA chains from the complex micelles which would have as first consequence to reduce the primary pore size. As a second consequence this larger amount of PAA dissociated chains would regroup in larger domains and thus would create larger secondary nanopores after calcination.

It was also found that the PAA amount influences the size and the porosity of the BMS NPs. Indeed, a larger PAA amount will increase the size of the PAA-C₁₆TA organic complex particles and thus the size of the resulting BMS NPs. Furthermore, a larger PAA amount will increase the size of the secondary nanopores.

2.2.2.1 Influence of the PAA dissolution

First, we tried to produce our own PAA solution at 25 %wt by dissolving PAA powder at 450000 Da in water. This dissolution was not efficient: the mixture was very viscous and some PAA stayed undissolved. To overcome this problem the water content was increased to prepare a solution of PAA at 10 %wt. For this reaction, to reach a pH between 10 and 11 before TEOS addition, 2 g of supplementary NH₃ were needed. The SEM and TEM images of the resulting BMS NPs, Figure 4-2, showed that spherical nanoparticles were well obtained, and the contrast on the pictures indicated the presence of large pores as expected. But, unfortunately, a high polydispersity in size was also noticeable.

To determine the pore sizes as well as the BET surface area of the BMS NPs, nitrogen adsorption and desorption isotherms were performed. Figure 4-3 showed the sorption properties of the prepared BMS NPs. The graph a) represents the adsorption-desorption isotherms and the graph b) the PSD curve. The silica particles exhibited a shape characteristic of a type-IV curve which is significant for mesoporous materials. The total pore volume, obtained at P/P₀ of 0.98, was about 0.75 cm³/g. Furthermore, the PSD calculated from the adsorption branch using BJH method showed a narrow peak at about 2.5 nm and a second broad peak at

~20 nm corresponding to the secondary nanopores. According to the BET method, the surface area measured was around $609 \text{ m}^2 \cdot \text{g}^{-1}$.

To conclude, the synthesized BMS NPs presented as expected a global spherical structure, a high surface area as well as a bimodal porosity. However, the process needed to be optimized to improve the monodispersity of the BMS NPs.

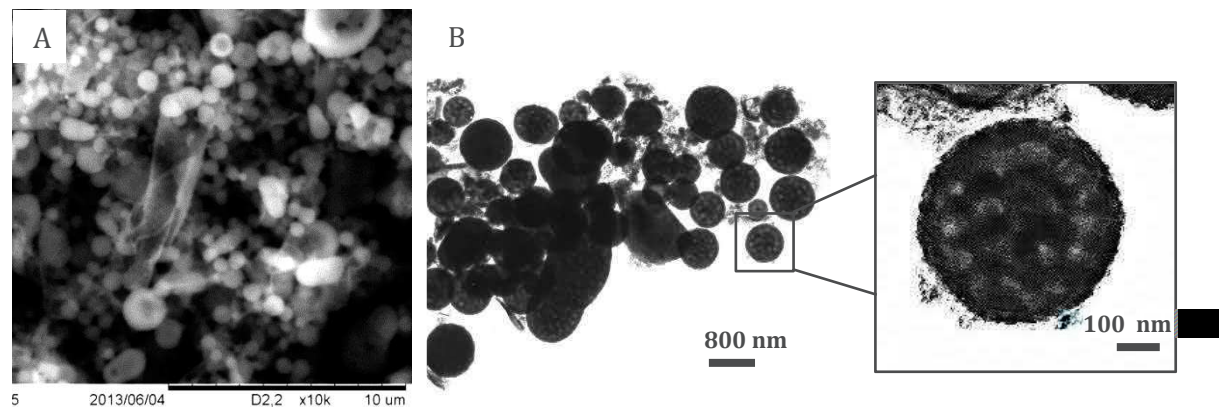


Figure 4-2: A) SEM and B) TEM images of BMS NPs synthesized at RT with “homemade” PAA solution

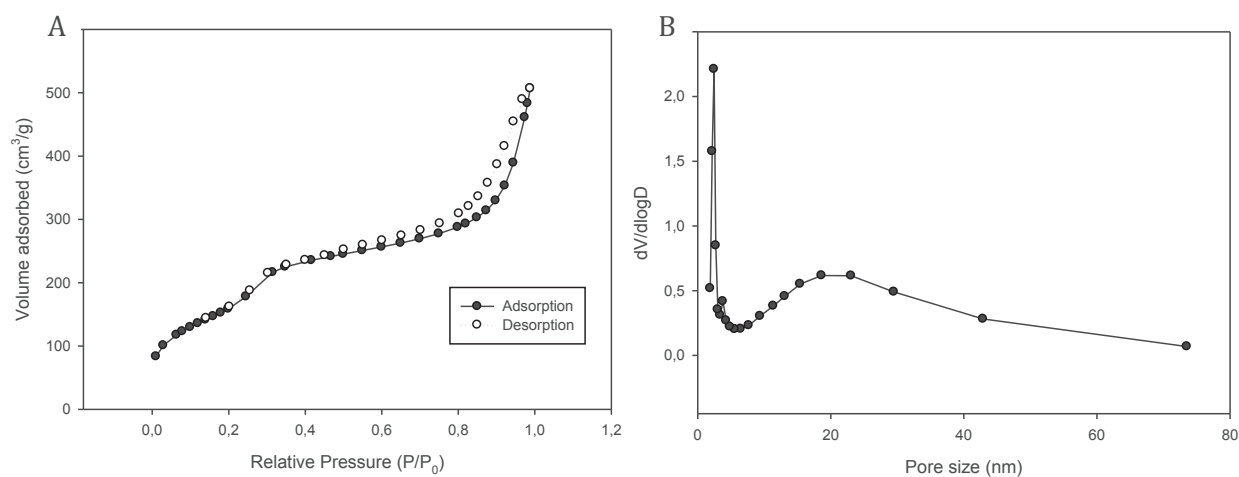


Figure 4-3: BMS NPs synthesized at RT with “homemade” PAA, A) N_2 adsorption-desorption isotherms; B) PSD curve

2.2.2.2 Influence of the temperature

Because a non-controlled dissolution of PAA and non-negligible variation of the room temperature over 48 h led to polydispersed BMS NPs, we bought PAA solution at 25 %wt from Alpha Aesar and we decided to control the reaction temperatures with oil bath. Two reaction temperatures were tested: 50 and 120 °C. These two reactions were carried out in round flask and a reflux was added for the 120 °C reaction. Furthermore the synthesis at 50 °C was repeated a second time with the use of an autoclave.

SEM images of the BMS NPs in Figure 4-4, showed that both samples synthesized at 50 °C without and with the help of an autoclave led to highly monodisperse porous NPs, whereas for the last sample synthesized at 120 °C, even if a porous morphology was also observed, it showed a highly polydispersity in size by contrast with reported published results. The size of the BMS NPs synthesized at 50 °C were measured from TEM images (Figure 4-5) and were of 534 ± 102 nm and 505 ± 94 nm for the BMS NPs synthesized without and with an autoclave respectively. Furthermore, the TEM images confirmed the presence of the bimodal porosity for BMS NPs as well as the alignment of the ordered mesopores. From these observations we may conclude that the presence or absence of autoclave did not induce any morphological modifications. Furthermore, the morphologies and porosities of the samples corresponded to what we expected from the literature, excepted for the 120°C sample that exhibited in our case high polydispersity.

To investigate more precisely the impact of the temperature on the porosities, N₂ adsorption and desorption isotherms were performed. The resulting isotherms and PSD graphs are presented in Figure 4-6, whereas the resulting BET surface area, the pore volume and the pore size obtained through BJH calculations were summarized in Table 4-1 and compared to the values from the literature. The N₂ adsorption and desorption isotherms were, as described in the literature, very different between the samples synthesized at 50 and 120 °C. These different behaviors led to different BET surface area: the BET surface area for the sample synthesized at 50 °C was of 772 m².g⁻¹ whereas the sample synthesized at 120 °C exhibited a lower value of 302 m².g⁻¹. Furthermore, the PSD curves showed that increasing the reaction temperature decreased the mesoporous contribution and in the same time increased the secondary nanoporous peak which was also shifted from ~25 to ~35 nm. This decrease in mesopores induced by higher temperatures was explained by Wang *et al.* as a consequence of an increase in the reaction rate leading to a higher silica cross-link degree that would increase the mesopore wall thickness. Thus, according to them, this increase in wall thickness implied a reduction of the mesoporosity. Furthermore, we also notice the presence of two mesoporous contributions, one at 27 and another at 37 Å, for the sample synthesized at 50 °C. This is due to the two types of globular cage-like mesopores exhibited by SBA-1 samples.

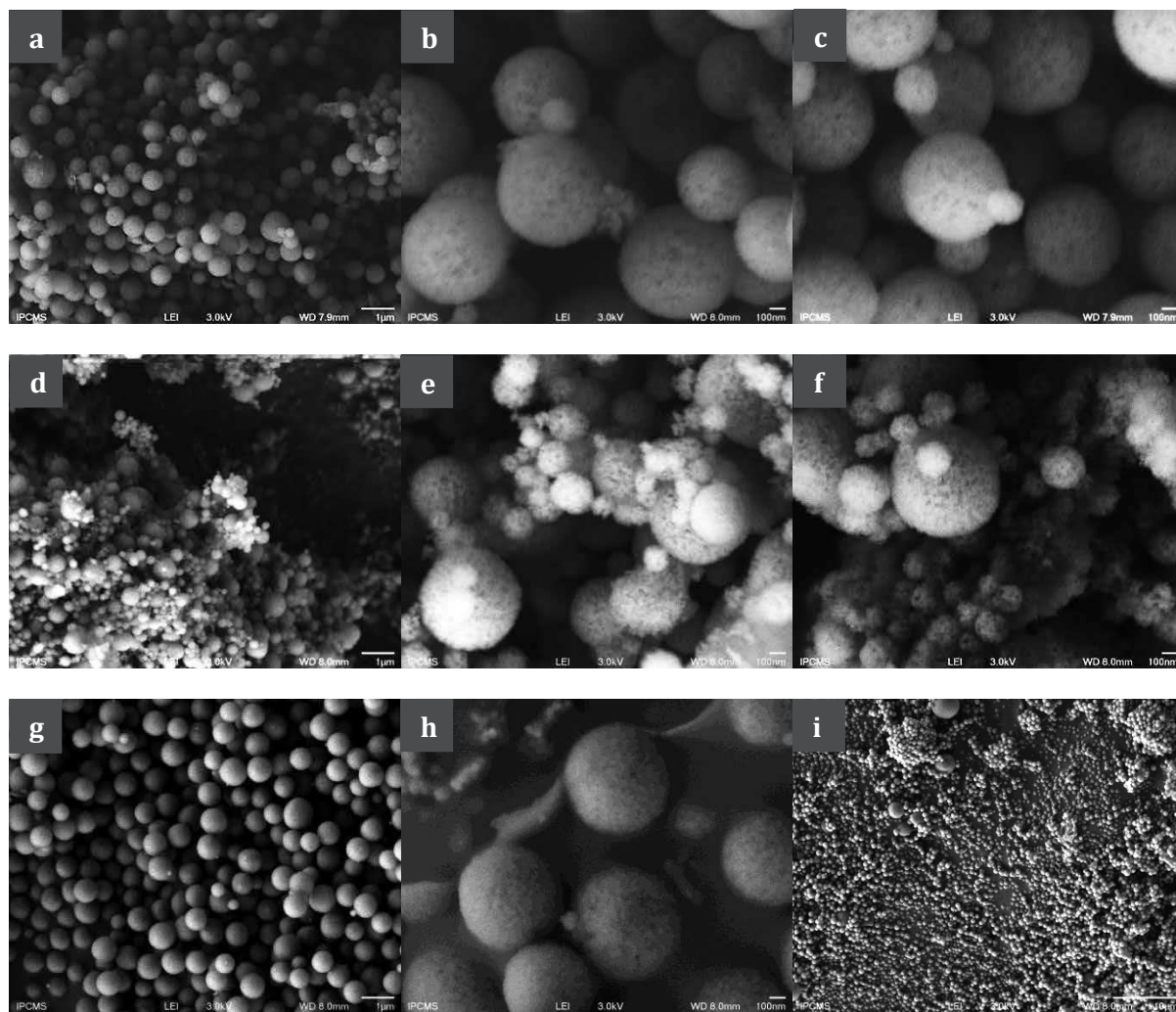


Figure 4-4: SEM images of BMS NPs synthesized without autoclave at 50°C (a,b,c); without autoclave at 120°C (d,e,f) and with an autoclave at 50°C (g,h,i)

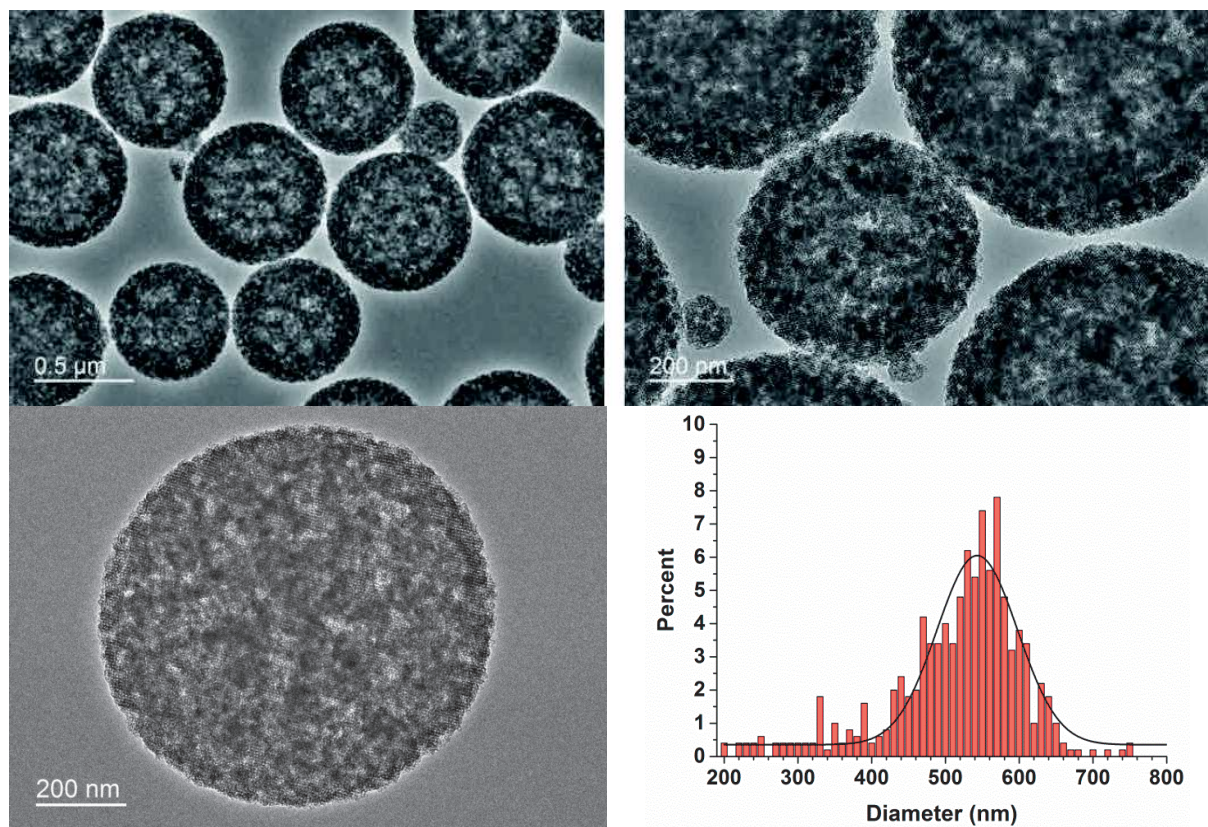


Figure 4-5: TEM images of BMS NPs synthesized at 50°C in an autoclave

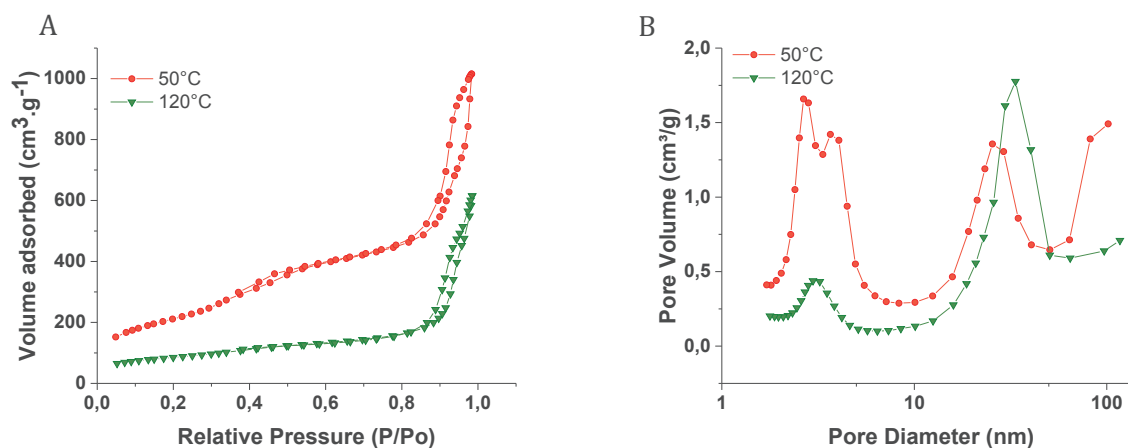


Figure 4-6: BMS NPs synthesized at 50 and 120°C in round flasks , A) N₂ adsorption-desorption isotherms; B) PSD curve

Table 4-1: Summary of porosity properties obtained through N₂ adsorption-desorption analyses for BMS NPs synthesized at 50 and 120 °C in comparison with literature values

Sample	S_{BET} (m ² /g)	V_{meso} (cm ³ /g)	V_{total} (cm ³ /g)	D_{mesopore} (nm)	$D_{\text{secondary pores}}$ (nm)
50°C Autoclave (40)	689	0.70	-	3.1	20
120°C Autoclave (40)	171	0.32	-	2.6	50
50°C Flask	772	-	1.57	2.7-3.7	25
120°C Flask reflux	302	-	0.95	3	35

2.2.2.3 PAA quantities variation

Inspired by a protocol developed by Cui (187), the amount of PAA in the synthesis was decreased by half in order to obtain smaller nanoparticles around 200-250 nm in size. Furthermore, the synthesis was carried out at 100 °C in autoclave.

Unfortunately, as shown in SEM images in Figure 4-7, a decrease in PAA amount led to polydisperse BMS NPs. This synthesis was carried out 4 times and for each sample the same high polydispersity was observed.

To keep only the particles of 200-250 nm in size a size separation process was needed. We choose to separate the sizes through sedimentation overnight of the samples dispersed in water. The idea was based on the principle that larger NPs as well as large silica sheets would sediment faster than smaller silica NPs. Figure 4-8 showed SEM images of the supernatants after 5 and 6 sedimentations (Figure 4-8 A and B respectively) and also SEM image of the sediment after 6 sedimentations (Figure 4-8 C). From these images we conclude that it was difficult to estimate the efficiency of the size separation by sedimentation; even if the SEM images from the sediments all showed, as on Figure 4-8 C, the efficient removal of large silica aggregates.

So, to investigate more precisely the efficiency of size separation by successive sedimentations, the evolutions of the particles sizes removed from the sample by sedimentation, called sediments, and of the sizes of the resulting supernatants were followed by DLS. These results were presented in Figure 4-9 and Figure 4-10 respectively. According to the DLS analyses of the sediments, by increasing the number of sedimentations the sizes of the sediments decreased. That validated the principle that larger particles will sediment faster than smaller ones. Comparing these results to the DLS analyses of the supernatants, we observed that the difference in sizes between the sediments and the supernatants slowly decreased with increasing the number of sedimentations, even if the size of the sediments were always higher than the size of supernatants. Furthermore, we also noticed that the size of the supernatant slowly decreased with sedimentations and at the same time that size distribution became narrower and centered on 250 nm in intensity. Thus, all these observations validated the size separation by sedimentation. Unfortunately, besides being time consuming, the fact to remove large particles by sedimentation led to a poor final yield.

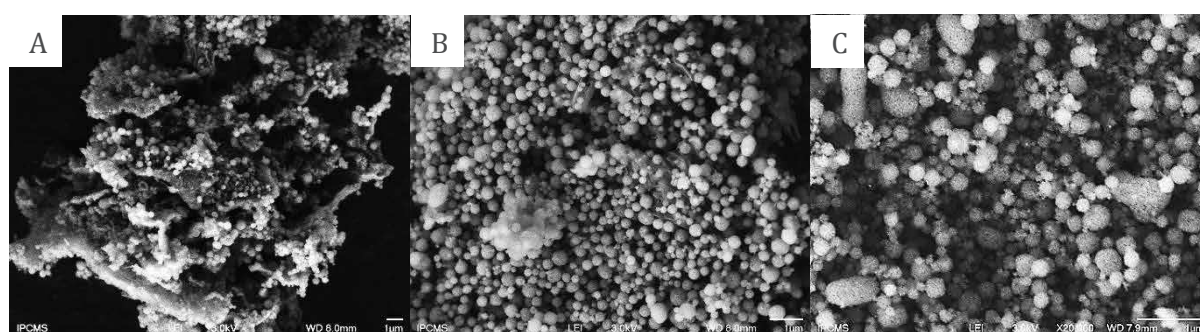


Figure 4-7: SEM images of BMS NPs synthesized with PAA/2

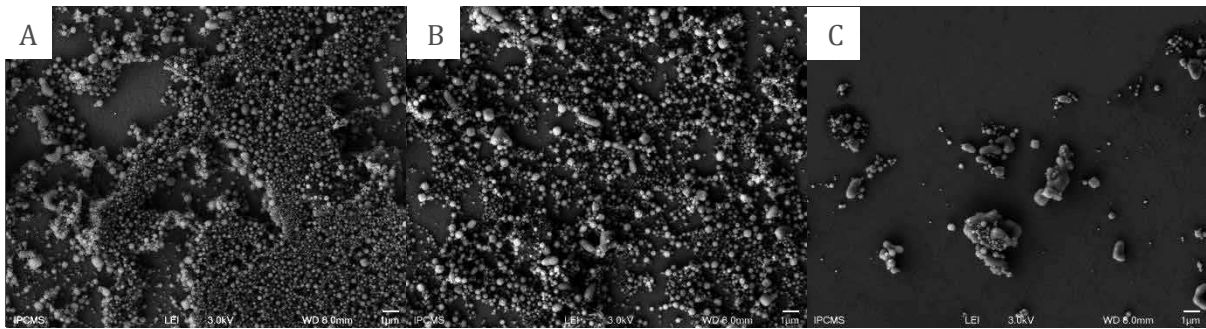


Figure 4-8: SEM images of A) supernatant after 5 sedimentations, B) supernatant after 6 sedimentations, C) sediment after 6 sedimentations

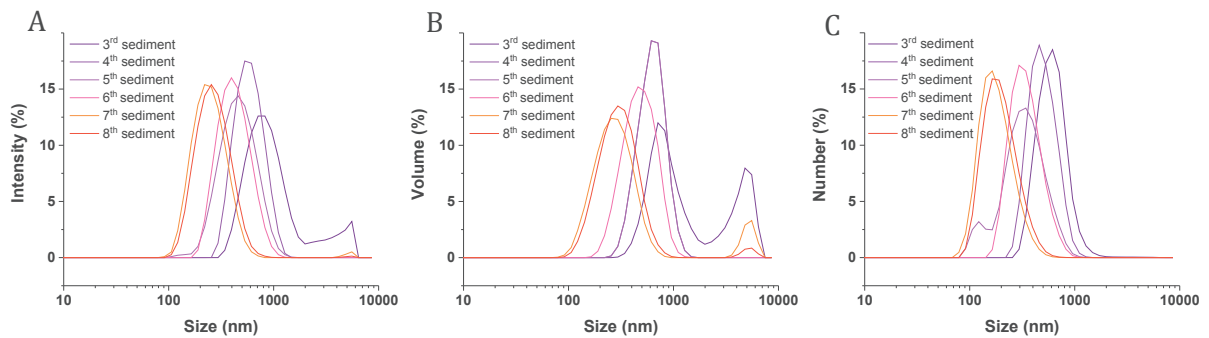


Figure 4-9: DLS analyses of the sediments from 3 to 8 sedimentations A) in intensity, B) in volume, C) in number

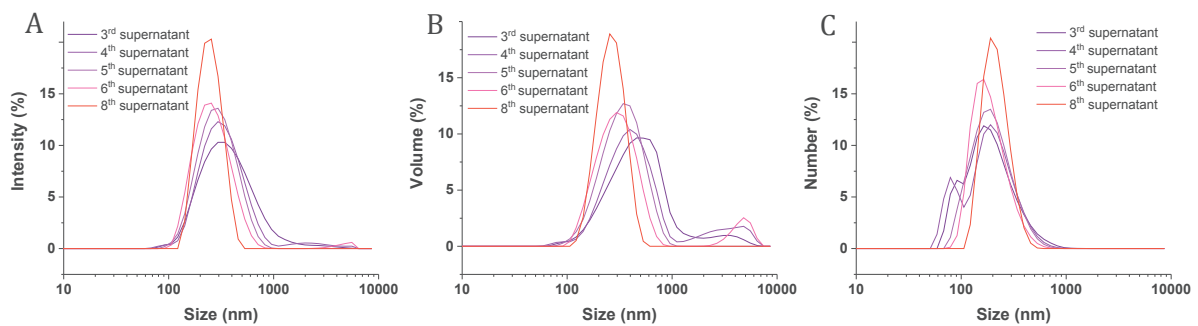


Figure 4-10: DLS analyses of the supernatants from 3 to 8 sedimentations A) in intensity, B) in volume, C) in number

2.3 Self-supported vesicles for drug delivery

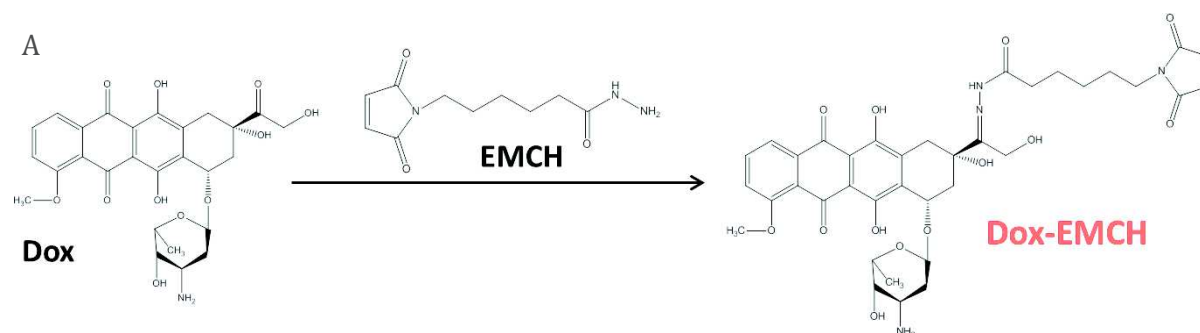
2.3.1 Dox covalent grafting to HSA

2.3.1.1 Grafting strategy

In this strategy, the idea was to covalently graft Dox molecules to HSA through a pH cleavable hydrazone bond. This HSA_{Dox} conjugate was synthesized by coupling a maleimide-hydrazone-doxorubicin derivative to thiolated albumin through a maleimide-thiol reaction. The hydrazone bond is known to be cleavable at pH<5 which corresponds to the pH of the endolysosomes. Thus, this strategy should allow controlled drug delivery under intracellular chemical conditions.

This concept was deeply developed by Kratz's group who synthesized initially two maleimide-hydrazone Dox derivatives: m-maleimidobenzoic acid hydrazide and p-maleimidophenylacetic acid hydrazide (252). One of these derivatives was successfully conjugated to the thiol group of the cysteine-34 position of albumin after intravenous injection (253). Based on the synthesis method developed earlier, this team synthesized four (maleinimidoalkanoyl)hydrazone derivatives of Dox with aliphatic spacers of different length. The highest rate constant to bind these Dox derivatives to cysteine-34 SH group presents on exogenous HSA, was found for the Dox-EMCH compound where EMCH is N-ε-maleimidocaproic acid hydrazide-TFA (254). This Dox-EMCH compound, first synthesized by Willner *et al.* (255) and then renamed INNO-206, was the first albumin-binding prodrug of doxorubicin to enter clinical trial (256). Indeed, it passed successfully the phase 1 of a clinical study (257) and showed promising antitumor effects against an orthotopic model of pancreatic cancer (258). Currently, CytRx, a biopharmaceutical research and development company specializing in oncology, focused its research on the clinical development of INNO-206, recalled Aldoxorubicin. The product has now been tested in approximately 600 patients with cancer, and is currently being studied in ongoing clinical trials across multiple cancer indications including soft tissue sarcoma (STS) and small cell lung cancer (SCLC). Concerning the results on STS the phase 3 clinical trial was successful and the company should meet soon the FDA to submit a New Drug Application for Aldoxorubicin in late 2017.

The strategy developed by our group was to graft the DOX-EMCH compound to the amine groups of the HSA with an optimized amount of Dox per HSA chain. HSA possess 81 amine groups coming from 58 Lysines sites and 23 Arginines sites. To allow this grafting, the HSA amine groups were functionalized with a disulfide crosslinker called SPDP (succinimidyl3-(2-pyridyldithio)propionate). The HSA-SPDP was then reduced with DTT in order to break the SPDP disulfide bonds and create thiol sites. These thiol sites reacted then with the maleimide sites of the DOX-EMCH with the aim to form HSA_{Dox} compound. The three steps of the synthesis strategy of HSA_{Dox} are summarized in Figure 4-11.



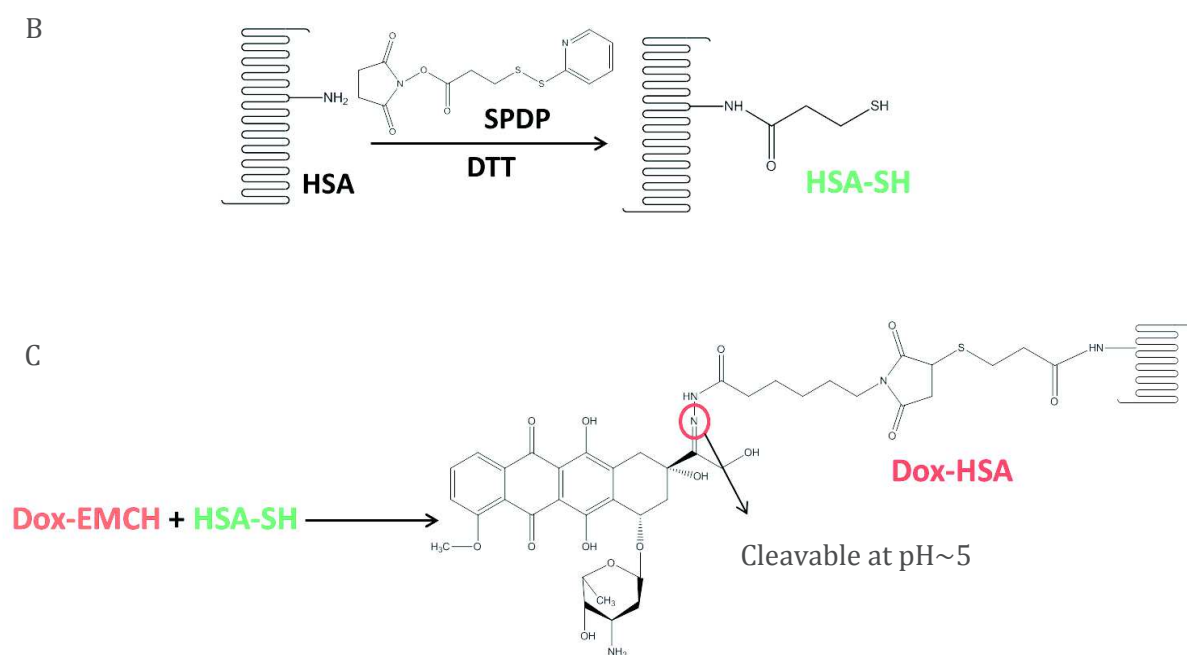


Figure 4-11: A) Synthesis of DOX-EMCH; B) Conversion of the amine groups of HSA into SH groups; C) Formation of the Dox-HSA through a thiol-maleimide reaction

2.3.1.2 Results and discussions

Our main goal was to optimize the amount of drug molecules per HSA while maintaining its physicochemical properties such as its solubility in aqueous conditions. First, we tried to graft 25 Dox equivalents per HSA applying the process described in Chapter 2 page 59. However, during the purification step of the final product HSA_{Dox} by dialysis, a precipitation occurred, as pictured on Figure 4-12. The supernatant containing some solubilized HSA_{Dox} in water was nevertheless used to form later the HSA_{Dox} self-supported macromolecular particles, part 2.3.3 page 96. After analysis of the supernatant by spectrofluorimetry, a grafting degree of *ca.* 1-2 Dox per HSA chain was estimated.

To solve this precipitation problem, we highlighted some ideas. The first one was to study the influence of the pH on the product solubility. This idea was inspired by Cheperegin *et al.* (259) who observed that the HSA precipitated at pH below 5 from yeast culture liquid. This precipitation is reversible and maybe in our case, because of Dox grafted to HSA, this phenomenon occurred at the pH value used for the study (pH 6). Furthermore, another solution could be also to introduce hydrophilic moieties to HSA to increase the solubility. For instance, Dosio *et al.* prepared HSA-Taxol conjugates by attaching covalently the drug to the lysyl groups of HSA through a succinyl spacer group and observed a drastic decrease of the protein solubility with the increase of the grafting degree (260). Later, they improved the stability and the solubility of the HSA-Taxol conjugates by grafting covalently poly(ethylene glycol) (PEG) chains to the HSA (261). Finally, the precipitation could be also due to massive disulfide bridge formation between different HSA chains, so another idea would be to use a faster method of purification to limit this parasite reaction for instance by using a size exclusion chromatography to purify the DTT reduced HSA / Dox-EMCH mixture instead of using a dialysis method which lasted several days.



Figure 4-12: Photograph of HSA_{Dox} compound with 25 Dox equivalents per HSA molecule

2.3.2 HSA coating on BMS NPs

The mesoporous silica particles previously synthesized were modified with IBAM grafts at their internal surface and then HSA modified with a fluorescent tracer, the fluorescein isothiocyanate (FITC), was adsorbed on the particles as pictured in Figure 4-13. The HSA^{FITC} solutions prepared contained 4 equivalents of FITC per protein of HSA. The adsorption of HSA^{FITC} on silica nanoparticles was done for different HSA^{FITC} concentrations ranging from 6.25 $\mu\text{g}/\text{mL}$ to 500 $\mu\text{g}/\text{mL}$ and for two kind of silica nanoparticles: the one that we synthesized in the laboratory (~ 500 nm diameter) and with a set produced by Dr Jiwei Cui (~ 900 nm diameter). By measuring the fluorescence intensity with a spectrophotometer ($\lambda_{\text{exc}} = 488$ nm; $\lambda_{\text{emi}} = 520$ nm) of FITC contained in the supernatant, the concentration of HSA^{FITC} in solution at the equilibrium was calculated using a standard curve. Then the mass of HSA^{FITC} adsorbed per unit of mass of silica was deducted. The graph represented in Figure 4-14, shows the mass of HSA^{FITC} adsorbed per unit of mass of silica nanoparticles as a function of the concentration of HSA^{FITC} at the equilibrium. The maximum loading observed was around 600 μg HSA/mg of silica for both BMS NPs.



Figure 4-13: Strategy of the formation of a HSA-FITC coating on mesoporous silica particles

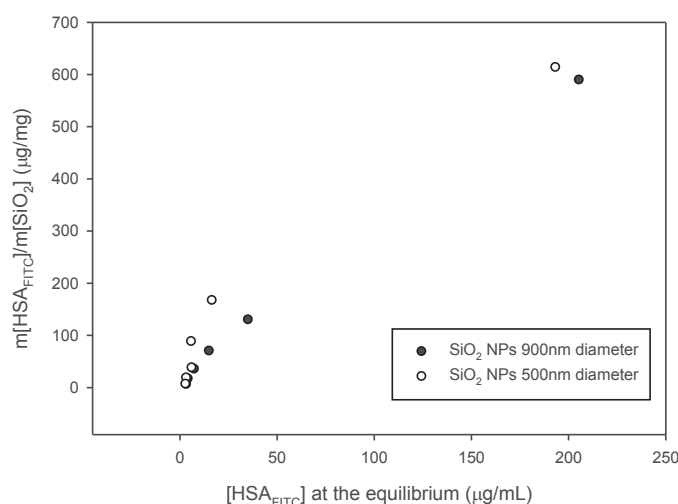


Figure 4-14: Adsorption isotherm of HSA^{FITC} on mesoporous silica nanoparticles

2.3.3 HSA_{DOX} nanoparticles

As seen previously, the HSA^{FITC} coated the IBAM-modified BMS NPs with a high degree of coverage (600 μg/mg of BMS). So, in a similar way, we adsorbed HSA_{DOX} (only the supernatant of the sample presented in Figure 4-12 was used) to the BMS-IBAM NPs of 900 nm and 500 nm in diameter (see detailed protocol in Chapter 2, page 59). The silica, used as sacrificial template, was then dissolved in HF/NH₄F buffer (buffered at pH 5) to form replicated particles made of HSA_{DOX}, as illustrated in Figure 4-15. The HSA_{DOX} NPs obtained were observed by optical (bright field) microscopy and also fluorescence microscopy given by the natural fluorescence of Dox (λ_{em}=470 nm, λ_{exc}=570 nm). Figure 4-16 shows that the replicated particles are relatively well dispersed, especially for the replicated particles made from the 900 nm diameter silica. The fluorescence microscopy images are similar to the microscopy images which proved that the Dox is well contained in all HSA nanoparticles. Furthermore, AFM imaging of the replicated particles was performed. AFM images presented in Figure 4-17, shows spherical NPs of approximately 600 nm in diameter and 160 nm high (see z-profile) due to flattening upon drying which correlates well with such soft macromolecular particles.

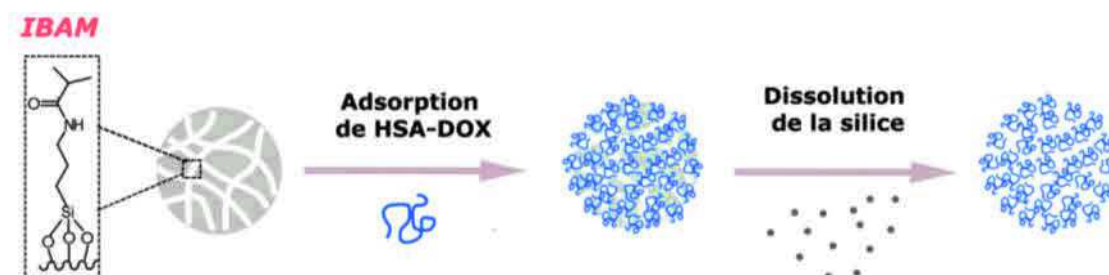


Figure 4-15: Strategy of the synthesis of HSA_{DOX} nanoparticles

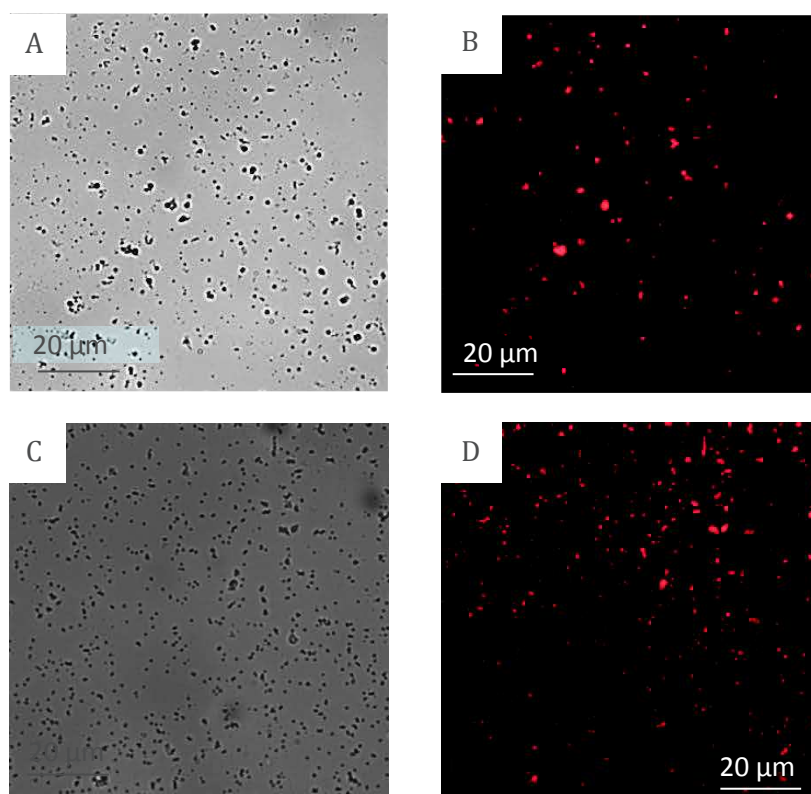


Figure 4-16 : Microscopy (A and C) and fluorescence microscopy (B and D) images of (IBAM-HSA) particles functionalized with doxorubicin replicated from silica nanoparticles with 500 nm in diameter (A, B) and 900 nm in diameter (C, D)

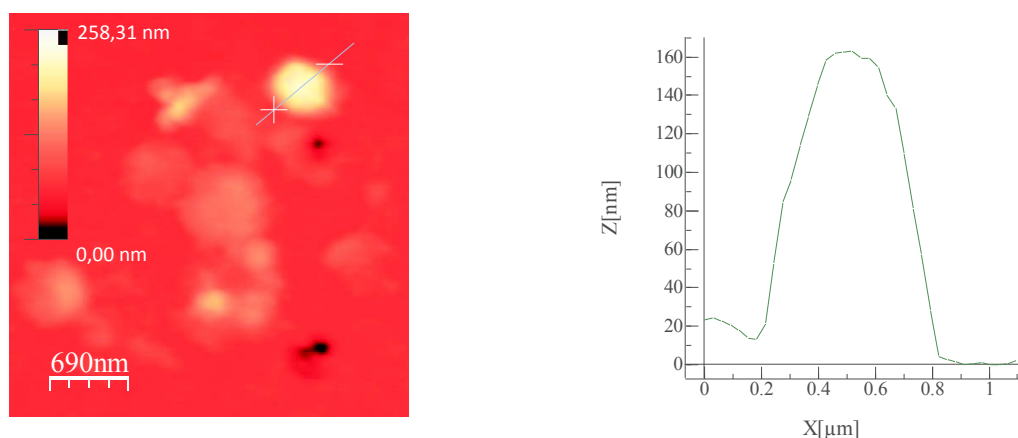


Figure 4-17: AFM picture of HSA-Dox nanoparticles and the corresponding Z profile

2.4 Conclusion and outlooks

After the investigation of some synthesis parameters, monodispersed BMS NPs of 500 nm were successfully synthesized inspired by Wang *et al.* protocol (40). In parallel, Dox was covalently grafted to HSA through a pH sensitive hydrazone bond. Unfortunately, this grafting led to precipitation of the product and thus could be improved. Finally, the HSA_{Dox} was adsorbed on the BMS NPs of 500 nm as well as on larger BMS NPs of 900 nm both previously modified with IBAM. After dissolution of silica template, HSA_{Dox} nanoparticles were obtained.

To improve this process an idea would be to graft the Dox to HSA after its adsorption on the silica template. If this would not be successful, an idea to increase the solubility of the final product would be to graft PEG to the surface of the HSA_{Dox} NPs.

3 Mesoporous silica with small porosity: Raspberry morphology (RB)

3.1 Introduction

Based on these previous researches, we developed the synthesis of self-supported HSA nanocapsules with a high doxorubicin loading using mesoporous silica nanoparticles as nanocontainers for drug loading and sacrificial template for HSA nanocapsules assembled via IBAM grafting strategy. The mesoporous silica nanoparticles used for this study exhibited a raspberry (RB) morphology with a narrow size distribution about 30 nm and small porosities of 3 nm. They are thus called RB NPs. This porosity has the benefits on one hand to be large enough to load chemotherapeutics into it by impregnation but, on another hand, to be too small to allow HSA diffusion in the pores leading thus in hollow-capsules formation after silica removal. As illustrated in Figure 4-18, the mesoporous silica nanoparticles were first synthesized and their surface was functionalized with amine groups previous doxorubicin (Dox) loading. After the drug loading, the amino-functionalized nanoparticle surface was modified with *isobutrylchloride* to form IBAM moieties. Then, HSA was absorbed on the IBAM-functionalized surface forming a tight protein shell onto the mesoporous silica nanoparticle through non-covalent H-bonding with IBAM. Finally, the mesoporous silica sacrificial template was dissolved in HF in order to form the self-supported HSA nanocapsules loaded with Dox molecules. As HSA nanoparticles are known to be degradable under enzymatic action (240), the Dox release should be controllable by proteases addition.

This study was divided in five parts following the five steps of the synthesis as described in the schematic representation of the process in Figure 4-18:

- 1) RB and RB-NH₂ NPs synthesis and characterization
- 2) Investigation of Dox loading capacity of RB-NH₂ NPs
- 3) Evaluation of protein coating of RB NPs via IBAM grafting
- 4) Study of the formation of HSA nanocapsules by silica dissolution
- 5) Evaluation of Dox-HSA NPs *in-vitro* anticancer efficacy

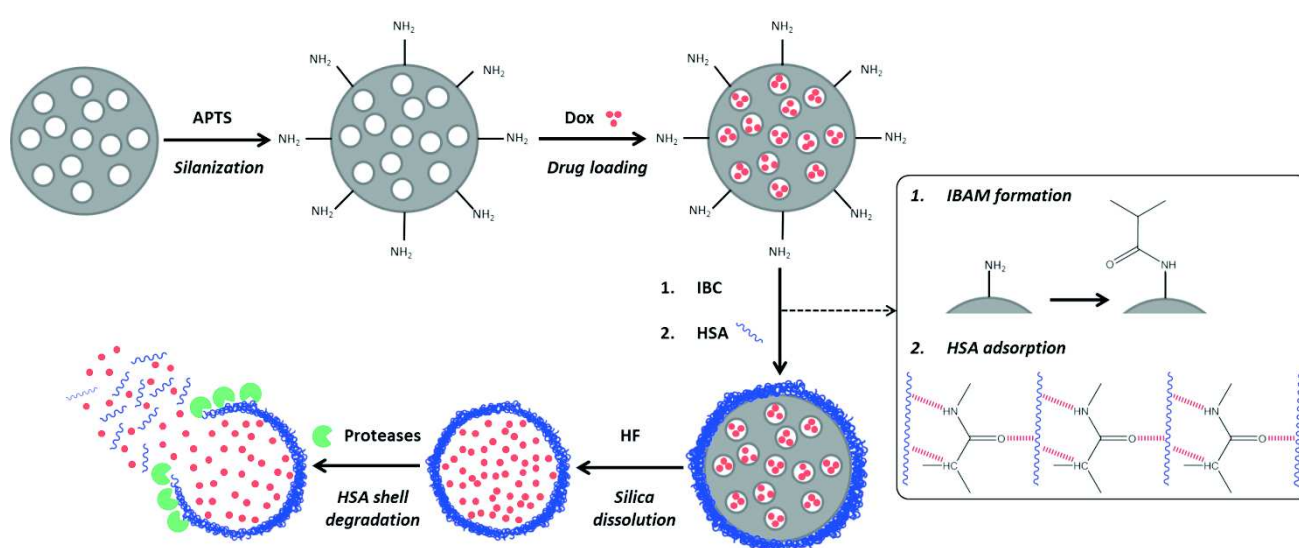


Figure 4-18: Schematic representation of the Dox loaded HSA nanocapsules synthesis strategy for drug delivery under HSA capsules enzymatic degradation

3.2 Synthesis and characterization of RB and RB-NH₂ NPs

3.2.1 Synthesis protocol

Mesoporous silica nanoparticles with a raspberry morphology (RB) were synthesized according to a modified literature method (41). In this process, small organic amines, such as triethylenamine, triethanolamine (TEAH₃) and 2-amino-2-(hydroxymethyl)propane-1,3-diol (AHMPD) are used as growth inhibitor additives to improve the particle size control. To see which small organic amine will lead to the best shaped RB NPs with the highest surface area and pore volume as well as the best reproducibility, syntheses with, on one hand, AHMPD and, on another hand, TEAH₃ were achieved. Thus, samples obtained using AHMPD were called RB1 whereas samples obtained using TEAH₃ were called RB2. The synthesis protocol is detailed in Chapter 2 page 57.

To functionalize the RB NPs with a layer of primary amine groups, the calcined RB NPs were redispersed in 40 mL of EtOH at a concentration of 1.5 mg.mL⁻¹ with 960 μL of NH₃ and 4 mL of APTES and the mixture was stirred for 2 hours at room temperature. The amino-functionalized mesoporous silica nanoparticles (RB-NH₂ NPs) were then washed three times with EtOH by centrifugation.

3.2.2 Characterization of the RB and RB-NH₂ NPs

Four batches were synthesized: two with each small organic amine type. The samples were named RB1-1 and RB1-2 for the two samples synthesized with AHMPD and RB2-1 and RB2-2 for those synthesized with TEAH₃.

The morphology and structure of as-synthesized RB NPs (before any functionalization) were characterized by TEM and SEM. TEM images showed that the four batches were very similar. As depicted on Figure 4-19 A and B showing the TEM images for the sample RB2-2, the synthesized RB NPs had a spherical morphology with a mean size of about 30 nm in size and porosities were visible throughout the entire particle. For the four batches, RB NPs statistical average diameters were determined by measuring more than 100 RB NPs from TEM images and are summarized in Table 4-2. The resulting size distribution histograms are all similar to that of RB2-2 presented in Figure 4-19 C, which is representative for the narrow size distribution of the RB NPs. The rough RB NPs surface observed in SEM images, Figure 4-20, demonstrated that the pore network was open to the outside. From these images we can also estimate that the pore mouths were lower than 4 nm.

To investigate more precisely the porosity of these nano-objects, N₂ adsorption-desorption isotherms were performed. The mesopore pore size distributions (PSD) were calculated on all samples through BJH method and the micropore PSD were investigated only on RB1-1 and RB2-1 samples by HK method. The N₂ adsorption-desorption isotherm of RB2-1, given in Figure 4-21 A, exhibited, according to IUPAC classification, a type IV isotherm which is characteristic for mesoporous channel. The BET surface area and the total pore volume of this sample were 708 m².g⁻¹ and 1.62 cm³.g⁻¹ respectively. Furthermore, this N₂ adsorption-desorption isotherm showed a H₁ steep narrow type of hysteresis loop characteristic for uniform mesopores. The corresponding pore size distribution (PSD), Figure 4-21 B, calculated by BJH method suitable for pore sizes above 2 nm, exhibited a single peak centered on 2.8 nm. However, the N₂ adsorption-desorption isotherm showed a high uptake already at very low p/p₀ associated with the filling of micropores. To investigate the contribution of microporosities, the Horvath-Kawazoe (HK) method was used. As pictured in Figure 4-21 B, this calculation gave a PSD curve with a single peak centered at 0.7 nm. To conclude, through these two PSD calculation methods, we found out

that these RB2-1 NPs showed a bimodal porosity of 7 and 28 Å. The N₂ adsorption-desorption isotherms and PSD curves of the other samples exhibited all a similar behavior than the RB2-1 sample. The resulting BET surface areas, pore volumes and PSD data obtained for the four samples were summarized in Table 4-2 and compared to those reported in literature for similar RB NPs (41). For all samples, the BET surface areas were slightly higher, between 700-820 m².g⁻¹, than that reported in the literature, 675 m².g⁻¹. This was probably related to the smaller size of our samples that were in average 7 nm smaller in size. All of our samples also exhibited pore volume of approximately 1.5 cm³.g⁻¹ which is very close to the literature value of 1.3 cm³.g⁻¹. The mesopore sizes calculated by BJH were around 2.8 nm for all samples, which is also higher than the literature value of 2.3 nm, and for the microporosities the size obtained by HK method was of 0.7 nm for both samples.

To conclude, the choice of AHMPD or TEAH₃ as small organic amines for the synthesis did not modify the morphology, the size and the porosities of the resulting RB NPs.

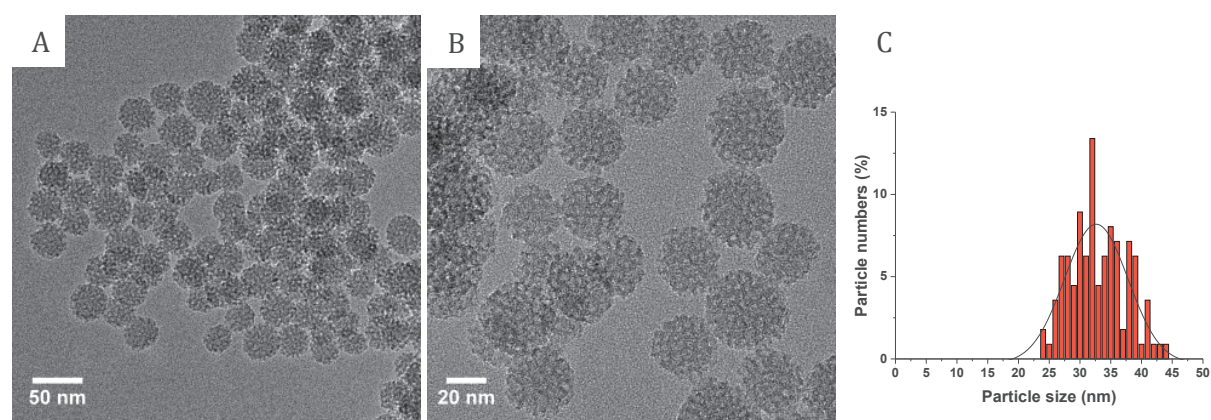


Figure 4-19: A) B) TEM images of RB NPs C) Particle size distribution of RB NPs from TEM pictures (>100 particles)

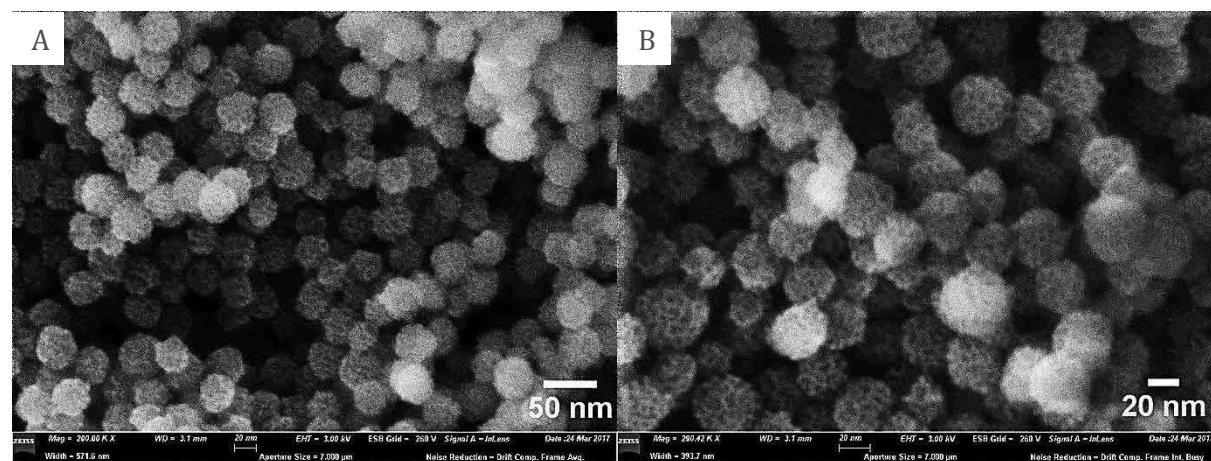


Figure 4-20: A) B) SEM images of RB NPs

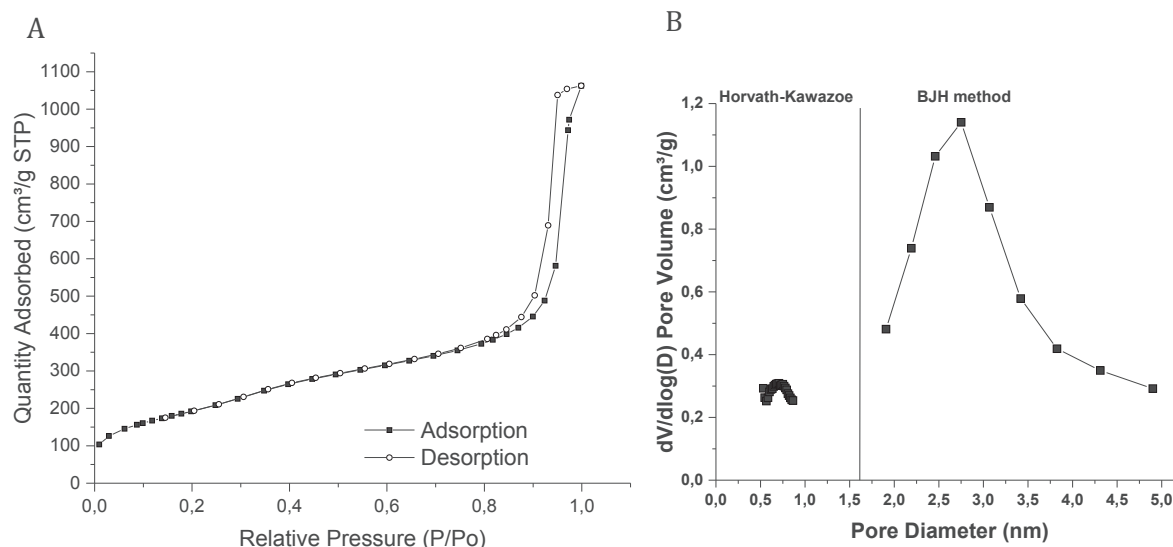


Figure 4-21: A) N_2 adsorption-desorption isotherms of RB NPs and B) the corresponding pore size distribution calculated by the BJH method for pore sizes above 2 nm and the Horvath-Kawazoe method for pore sizes <1 nm

Table 4-2: Summary of morphological properties of RB NPs (S: surface area, V: porous volume, D: pore size)

Sample	S_{BET} (m ² /g)	V (cm ³ /g)	D_{BJH} (nm)	D_{HK} (nm)	Size (nm)
Literature (41)	675	1.27	2.3	-	40 ± 3
RB2-1	708	1.46	2.8	0.7	33 ± 4
RB2-2	812	1.49	3	-	33 ± 4
RB1-1	680	1.33	2.7	0.7	30 ± 4
RB1-2	818	1.45	2.7	-	35 ± 4

ATR-IR analyses were achieved to confirm the RB surface modification by APTES. Figure 4-22 compares the IR spectra of RB NPs with RB-NH₂ NPs. The intense and broad absorption peak centered at 1065 cm⁻¹ is assigned to Si-O-Si asymmetric stretching vibration, whereas the peak around 800 cm⁻¹ is assigned to Si-O-Si symmetric stretching vibrations. The peak at 970 cm⁻¹ is attributed to Si-OH bond. Finally the IR band at 450 cm⁻¹ is due to O-Si-O bending vibrations. The appearance of new peaks for the RB-NH₂ sample at 1356 and 1408 cm⁻¹, specific for the stretching bands of C-N groups, and at 1573 and 1618 cm⁻¹, assigned to the bending vibration of N-H groups, proved the effective amino-functionalization of the RB surface.

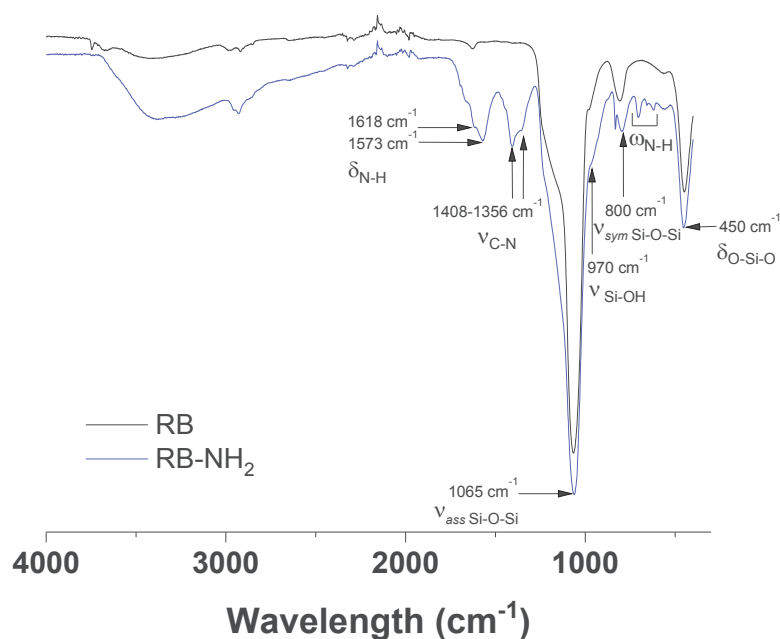


Figure 4-22: IR in ATR mode of RB and RB-NH₂ NPs

3.3 Dox loading studies on RB-NH₂ in water

3.3.1 Protocol

Doxorubicin loading was performed in Milli-Q water at different feed weight ratios (fwr).

In a typical procedure, solutions of Dox in Milli-Q water at various concentrations were prepared. 100 μ L of each Dox solutions were mixed with 100 μ L RB-NH₂ NPs dispersed in Milli-Q water at 2 mg/mL to obtain different fwr. Each fwr was carried out in triplicate. The mixtures were then stirred at room temperature in the dark for 24 h. Then the supernatant was collected by centrifugation (10000 G, 10 min) and analyzed by fluorescence spectroscopy for the low fwr and by absorbance ($\lambda = 480$ nm) for the high fwr using a spectrophotometer. Quantification of the amount of loaded Dox was calculated from calibration curves obtained with the Dox solutions at different concentration used for the experiment. As frequently described in the literature the Drug Loading Content (DLC) and the Drug Loading Efficiency (DLE) were used to evaluate the loading capacity of the RB-NH₂ NPs. Their formulas were presented in Chapter 1 page 30.

To cap Dox into porosities by forming a thick HSA shell on the silica surface Dox loaded RB-NH₂ NPs were transferred into DMF (see detailed protocol in Chapter 2 page 58). A solvent exchange from water, a polar protic solvent, to DMF, a polar aprotic solvent, can possibly induce some Dox desorption from the porosity. To investigate the possible Dox release during the solvent exchange, the previous samples at different fwr were washed by centrifugation twice in Milli-Q water after Dox impregnation and redispersed in 200 μ L of DMF. The samples were then centrifuged and the supernatants analyzed by fluorescent and absorption spectroscopies to quantify the amount of Dox release during solvent exchange. From these measurements the percentage of Dox released during solvent exchange and the subsequent final DLC (DLC_f), Equation 4-1, were evaluated.

$$DLC_f\% = \frac{\text{weight of Dox loaded} - \text{weight of Dox released}}{\text{weight of NPs}} \times 100$$

Equation 4-1: Formula of final Drug Loading Content (DLC)

3.3.2 Results and discussion

3.3.2.1 Dox loading study

In the present study, the loading characteristics of Dox into the porosities of amino-functionalized RB NPs in water media were investigated. To determine the best feed weight ratio (fwr) to reach the highest Drug Loading Content (DLC) with a high Drug Loading Efficiency (DLE), different fwr from 0.05 to 200 % were tested. As depicted in Figure 4-27 A showing photographs of the centrifuged RB-NH₂ NPs after Dox loading, the color of the NPs changed from white to red with increasing fwr. This demonstrated that Dox was successfully loaded into the NPs porosities and that the loading content increased with fwr. By looking at the supernatants of centrifuged Dox loaded RB-NH₂ NPs presented in Figure 4-23, we observed that the supernatant colors were very light until a fwr of 10% and started to be red colored over this threshold. That suggested that until Dox fwr of 10 % almost all the drug in the initial solution was impregnated in the NPs, *i.e.* that the DLE should be high.

To confirm these experimental observations the supernatants were collected and analyzed to obtain the corresponding DLC and DLE versus fwr curves (Figure 4-24). At low Dox fwr (from 0.02 to 20 %) DLC increased linearly up to ~10 %. Above this range, the DLC reached a plateau. The DLE remained between 70-90 % for Dox fwr from 0,1 to 10 % whereas for Dox fwr values higher than 10 % the DLE slowly decreased, as we previously predicted from the observations of supernatants.

These results suggested that the best Dox fwr used in this study was 20% because it led to the highest DLC value of 13%. However the DLE dropped from 85 to 64% for Dox fwr 10 and 20% respectively, leading to conclude that the best Dox fwr for RB-NH₂ loading is between 10 and 20%.

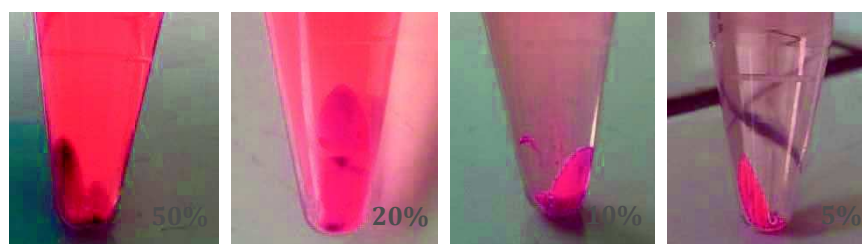


Figure 4-23: Photographs after centrifugation of Dox loaded RB-NH₂ NPs for 24h at different fwr: 50, 20, 10 and 5 %

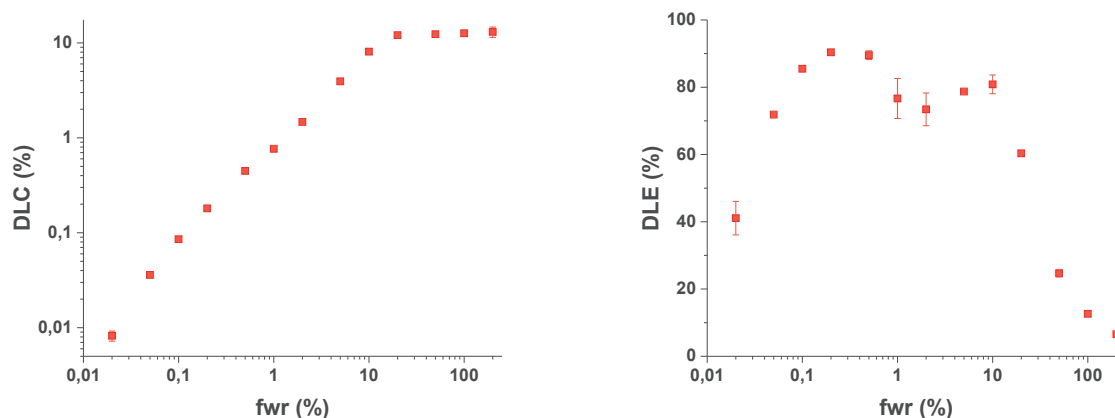


Figure 4-24: Drug Loading Content (DLC) and Drug Loading Efficiency (DLE) in RB-NH₂ NPs dispersed in Milli-Q water as a function of Dox feed weight ratio (fwr)

3.3.2.2 Estimation of Dox release from Dox loaded RB-NH₂ NPs after solvent exchange from water to DMF (necessary for IBAM coupling)

Several reaction steps for post-functionalization of the Dox loaded RB NPs are necessary to obtain the final HSA capsules but they can induce drug leakage. For example, the formation of IBAM grafts on the silica surface should occur in DMF, which commits the transfer of NPs from water to DMF. To evaluate the potential Dox release during solvent exchange, the previous particles loaded with Dox at different fwr were transferred into DMF after two washing steps in water. These two washing steps were necessary because, during the supernatant removal, few supernatant droplets containing free Dox are remaining in the sample which can falsify the upcoming Dox release measurement. As shown in Figure 4-25, the supernatants after washing did not show any red color which indicated that no significant drug leakage occurred during water washing steps so the Dox remained inside RB-NH₂ porosities (Figure 4-27 B). After being washed, the samples were redispersed in DMF (Figure 4-26 A). After centrifugation, the subsequent supernatants showed an orange color indicating that some drug release occurred (Figure 4-26 B). However, the RB NPs still contain a large amount of Dox loaded as depicted in Figure 4-27 C. To quantify this drug release, the supernatants were analyzed by spectroscopy. The resulted Drug Release Content (DRC) as well as the final Drug Loading Content (DLC_f) are represented in Figure 4-28. At very low fwr (0.1 and 0.2 %) the DRC was about 22 % and increased up to values in the narrow range of 29-34 % for fwr from 0.5 to 20 % before decreasing down to 19, 13 and 12 % for fwr 50, 100 and 200 % respectively. These results indicated that less than 35 % of Dox loaded in the RB-NH₂ were released during solvent exchange. Because most of DRC values were included in a narrow value range the resulting DLC_f curve obtained by removal of the Dox release for each fwr showed similar behavior than the previous DLC curve. Nevertheless the DLC_f displayed lower values and the drug loading plateau decreased from 13 % to 11 %.

In conclusion, even if some drug release was observed during phase transfer, it remains negligible regarding the Dox amount loaded in RB-NH₂ NPs.

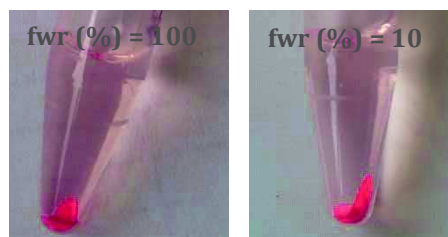


Figure 4-25: Photographs of centrifuged supernatant colors after water washing of Dox loaded RB-NH₂ NPs at fwr 100 and 10 %

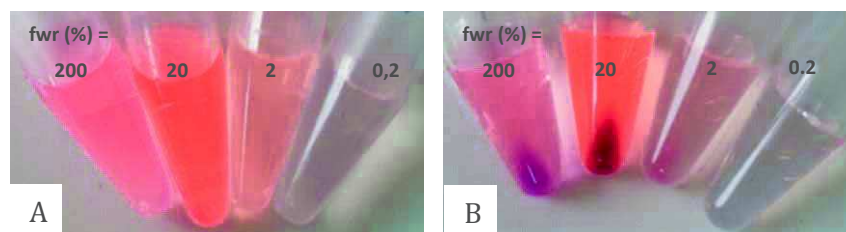


Figure 4-26: Photographs of A) Dox-loaded RB-NH₂ NPs redispersed in DMF B) centrifuged Dox-loaded RB-NH₂ NPs after redispersion in DMF at fwr 200, 20, 2 and 0.2 %

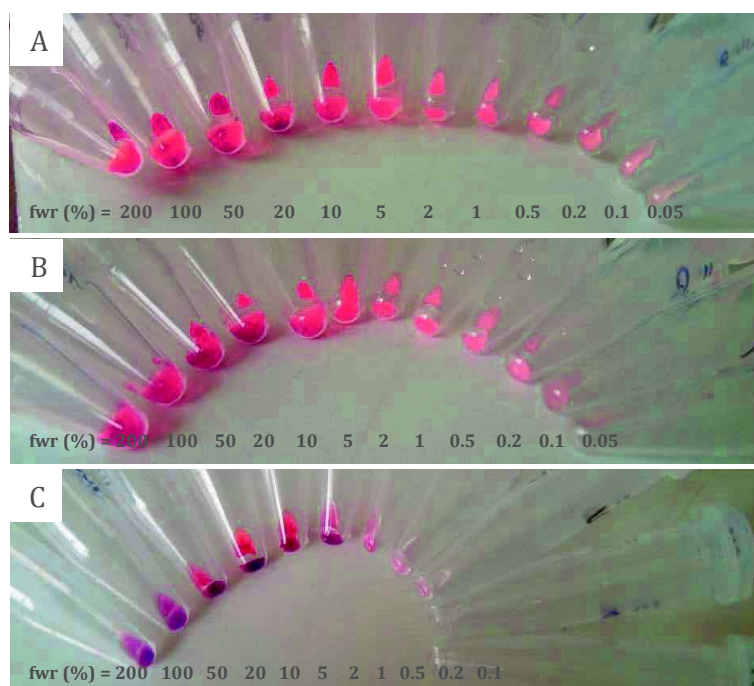


Figure 4-27: Photographs of centrifuged Dox loaded RB-NH₂ at various fwr after removal of supernatant A) directly after loading, B) after two washing steps in Milli-Q water, C) after solvent transfer in DMF

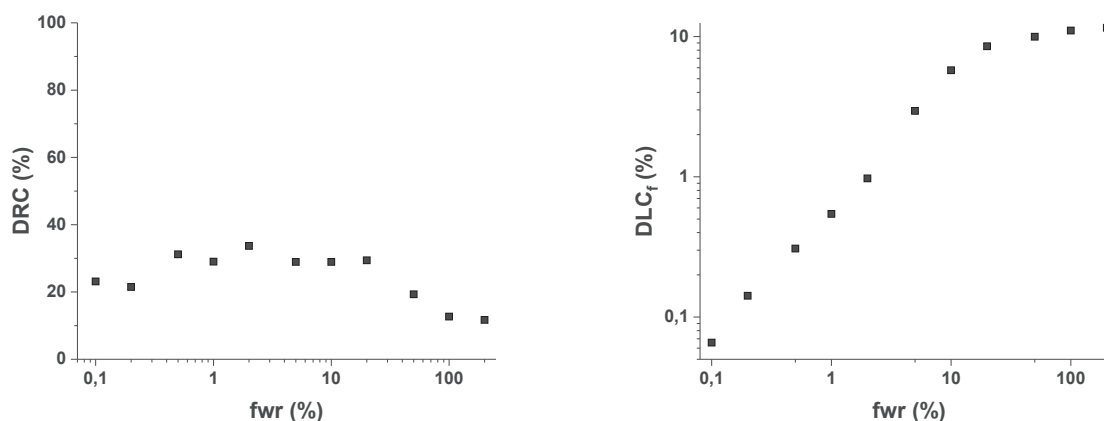


Figure 4-28: Dox released (%) and final Drug Loading Content (DLC_f) after redispersion of Dox loaded RB NPs in DMF as a function of Dox feed weight ratio (fwr) used for the loading

3.3.2.3 Influence of RB-NH₂ aging on Dox loading

According to the previous results, the maximal DLC value was reached at fwr about 20 %. But at this fwr, the DLE started to decrease suggesting that the best fwr to obtain maximal DLC and DLE is between 10 and 20 %. In order to investigate more precisely Dox loading in this fwr range, the previous Dox loading study on RB-NH₂ NPs was repeated but with fwr values ranking from 5 to 40 % with a step of 2 % for fwr values between 10 and 30 %. This study was carried out on the same RB-NH₂ batch than previously but 7 weeks later. As the first study was not achieved directly after RB silanization but already three weeks after, the second study was run 10 weeks after the NPs silanization.

Figure 4-29 shows the DLC and DLE curves obtained for this second Dox loading test in comparison with the first one. Similarly to the previous study, the maximal DLC value was obtained at fwr 20 % and stayed at this value for higher fwr. Consequently, the DLE values also started to decrease for fwr higher than 20 %. But compared to the study carried out on RB-NH₂ NPs silanized 3 weeks before the experiment, the DLC plateau decreased from 12 to 7 % for the study carried out 10 weeks after silanization. Furthermore, the DLE values were between 35 and 40 % before starting to decrease at fwr > 20 % whereas they were twice higher for the first study.

So the RB-NH₂ NPs showed an unexpected effect of aging that led to a consistent decrease in drug loading efficiency and subsequently to a decrease in the maximal drug loading content. Thus, a loss of amino-surface functionality, which is favorable to Dox loading, probably occurred with time affecting the drug loading efficiency and content. Therefore, to prevent this effect and reach the highest DLC and DLE, the drug loading should be carried out on RB-NH₂ NPs directly after the silanization of their surface.

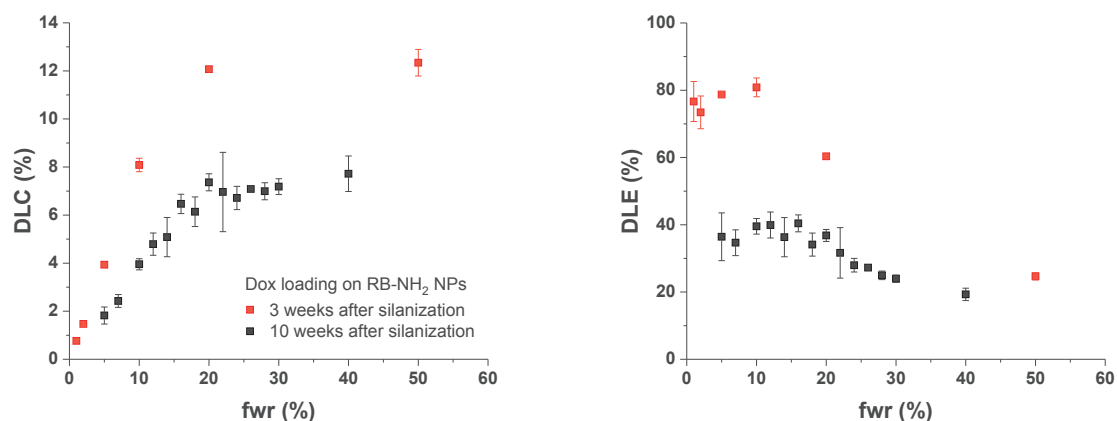


Figure 4-29: Drug Loading Content (DLC) and Drug Loading Efficiency (DLE) in RB-NH₂ NPs, 3 (in red) and 10 (in black) weeks after silanization, dispersed in Milli-Q water as a function of Dox feed weight ratio (fwr)

3.4 Protein coating studies on RB-IBAM

3.4.1 Protocol

RB-NH₂ NPs were functionalized with IBAM groups, according to the protocol described in Chapter page 58 adapted with these quantities: 160 μL Et₃N were mixed with 800 μL of RB-NH₂ at 10 $\text{mg}\cdot\text{mL}^{-1}$ in DMF before the quick addition of a IBC:DMF (216 μL : 1600 μL). Then HSA adsorption at the surface of the resulting RB-IBAM was investigated. For a better follow of HSA adsorption, HSA has been previously labelled with FITC (Chapter 2 page 58).

To study the HSA^{FITC} adsorption on RB-IBAM NPs 100 μL of RB-IBAM NPs at 2 $\text{mg}\cdot\text{mL}^{-1}$ in Milli-Q water were mixed with 100 μL of HSA^{FITC} at different concentrations leading to different fwr. After stirring for 1h30, the supernatants were collected by centrifugation (10000 G, 10 min) and analyzed by fluorescent spectroscopy to determine the amount of HSA adsorbed on the RB NPs surface. From these measurements the curves of the Coating Content (CC), Equation 4-2, and the Coating Efficiency (CE), Equation 4-3, versus fwr were plotted.

$$CC\% = \frac{\text{weight of HSA adsorbed}}{\text{weight of NPs}} \times 100$$

Equation 4-2: Formula of Coating Content (CC)

$$CE\% = \frac{\text{weight of HSA adsorbed}}{\text{weight of HSA fed}} \times 100$$

Equation 4-3: Formula of Coating Efficiency (CE)

3.4.2 Results and discussion

The resulting Coating Content (CC) and the Coating Efficiency (CE) versus fwr are represented in Figure 4-30. The CE curve, Figure 4-30 B, exhibited values around 85 % for all the fwr which indicates that almost all the HSA initially incubated is fully adsorbed on the silica surface. The corresponding CC curve, Figure 4-30 A, followed a stunning linearity with a so small standard deviation between the triplicates that it can not be observed in the graph. The highest CC obtained in this study was $128 \pm 0.22\%$ for fwr of 150 % with a CE of 85.5 %.

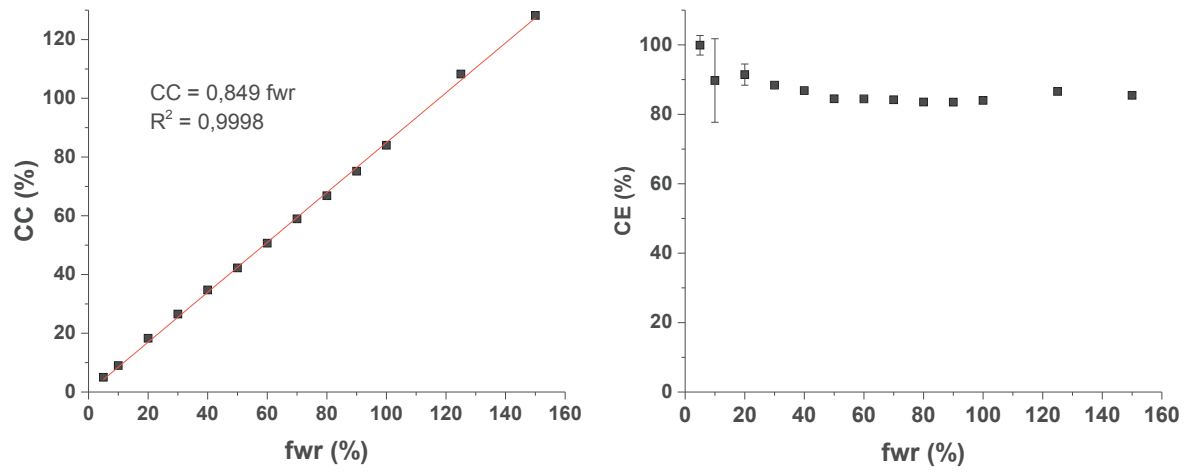


Figure 4-30: Coating Content (CC) and Coating Efficiency (CE) versus fwr for HSA adsorption onto RB-IBAM NPs

3.5 HSA capsules formation by silica dissolution

As pictured in Figure 4-31, the sacrificial silica template of RB-Dox-HSA NPs has to be dissolved to form self-supported HSA nanocapsules loaded with Dox

In our work, we also designed RB NPs but containing iron oxide (IO) cores, see Chapter 5 and 6. So we wanted to set up a silica dissolution procedure that can work also for these objects. Thus, the use of HF, as described in Mertz *et al.* papers (165–167, 187), was avoided because of its ability to easily dissolve IO. For this reason we first tried, as described in part 3.5.1, to set up a new procedure using NaOH as dissolving agent. However, as the use of NaOH for silica dissolution affected the Dox integrity, we then investigated the use of classical HF/NH₄F buffer on our systems, part 3.5.2.

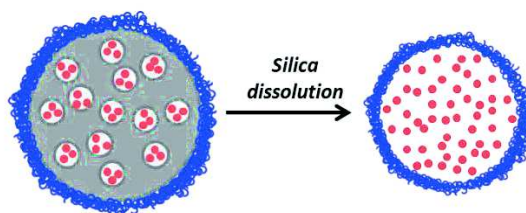


Figure 4-31: Schematic representation of silica template removal for the formation of free-standing Dox loaded HSA nanocapsules

3.5.1 Silica dissolution trials with NaOH

The RB-Dox-HSA NPs dispersed at 12.8 mg RB.mL⁻¹ in water was mixed with the same volume of NaOH solutions, leading to a final concentration of 6.4 mg RB.mL⁻¹.

In a first trial, we mixed RB-Dox-HSA NPs with NaOH at 2, 1 and 0.5 M. As shown in Figure 4-32, immediately after the addition of NaOH solution, the solutions became blue and after 24h transparent suggesting that the Dox was totally degraded.

In a second trial, to limit the Dox degradation under basic conditions, the NaOH concentrations were decreased to 50, 25 and 5 mM and the dissolution time to 1h. As pictured in Figure 4-33, the solutions turned from red to violet color with NaOH addition. The violet color was stronger at higher NaOH concentrations. After only 10 min, the violet color of the samples decreased and totally disappeared after 1h for the samples at NaOH concentrations of 50 and 20 mM suggesting strong Dox degradation. Thus, these two concentrations were too high and not suitable for the formation of Dox-loaded HSA nanocapsules. The solution of RB-Dox-HSA NPs mixed with NaOH at 5 mM was the only one showing a reddish color after 1h and was ultrafiltrated. After ultrafiltration, the NPs were collected from the filter and redispersed in water to be imaged by TEM. As presented in Figure 4-34, the silica template is still present in the sample, so the use of this NaOH concentration for 1 h was not efficient enough for silica removal.

In a third trial, the RB-Dox-HSA NPs were mixed with NaOH at 1000, 100, 10 and 1 mM and the dissolution reactions were stopped only after 10 min. But, as shown on Figure 4-35, the solutions started to lose their coloration even after only 10 min of reaction, so the Dox started already to degrade.

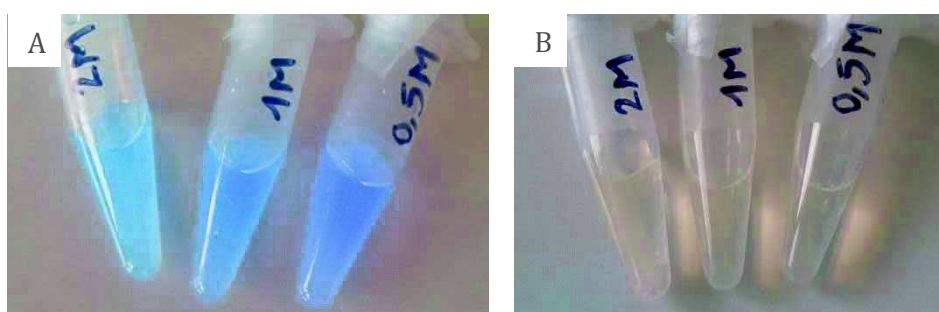


Figure 4-32: Photographs of the first trial of silica dissolution by NaOH at various concentrations: 2, 1 and 0.5 M; photographs were taken A) directly after NaOH addition, B) after 24 h



Figure 4-33: Photographs of second trial of silica dissolution by NaOH at various concentrations: 50, 20 and 5 mM; photographs were taken A) directly after NaOH addition, B) after 10 min, C) after 1 h

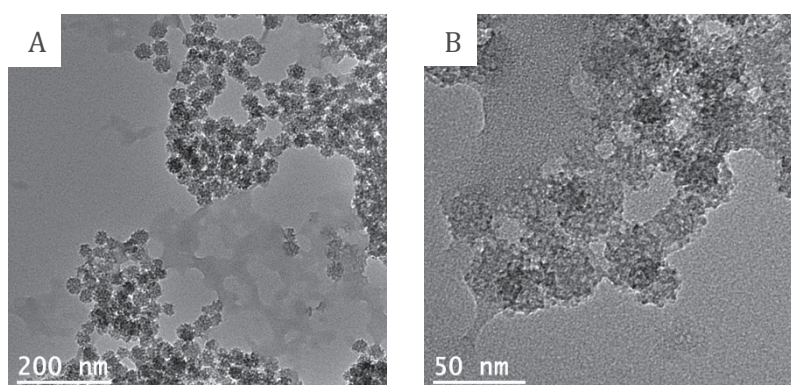


Figure 4-34: TEM images of silica dissolution trial with 5 mM of NaOH for 1h

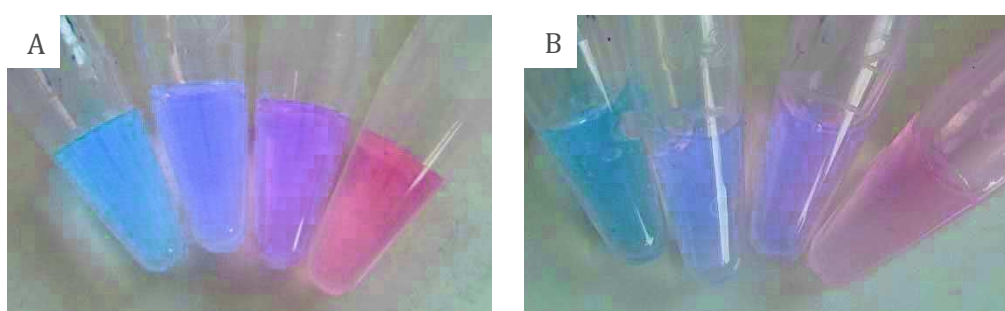


Figure 4-35: Photographs of third trial of silica dissolution by NaOH at various concentrations from left to right: 1000, 100, 10 and 1 mM; photographs were taken A) directly after NaOH addition, B) after 10 min

3.5.2 Silica dissolution trials with HF

As the silica dissolution trials with NaOH were not successful, we decided to dissolve the silica sacrificial template with the use of ammonium fluoride buffered HF, as described in Mertz *et al.* papers (165–167, 187). Basically, 150 μL of RB-HSA NPs were mixed with 150 μL of ammonium fluoride buffered HF (pH 5) for 1 h before being dialyzed for 3 days against 3 mL of Milli-Q water (changed every day). The dialysis was preferred to ultrafiltration because the total recovery of the NPs from the ultrafiltration membrane was difficult leading to a high product loss. Two HF concentrations were tested: 1 and 10 mM. As pictured in TEM images in Figure 4-36, a concentration of 1 mM of HF was not high enough to induce total silica dissolution. However, as shown on Figure 4-37, 10 mM of HF led to the successful dissolution of the silica template. HSA nanocapsules of ~ 40 nm were observed. Furthermore, the Dox was not degraded as in the case with using NaOH for dissolution as shown in Figure 4-43.

To conclude, the silica dissolution through HF is the best method to obtain Dox-HSA NPs from dissolution of RB template.

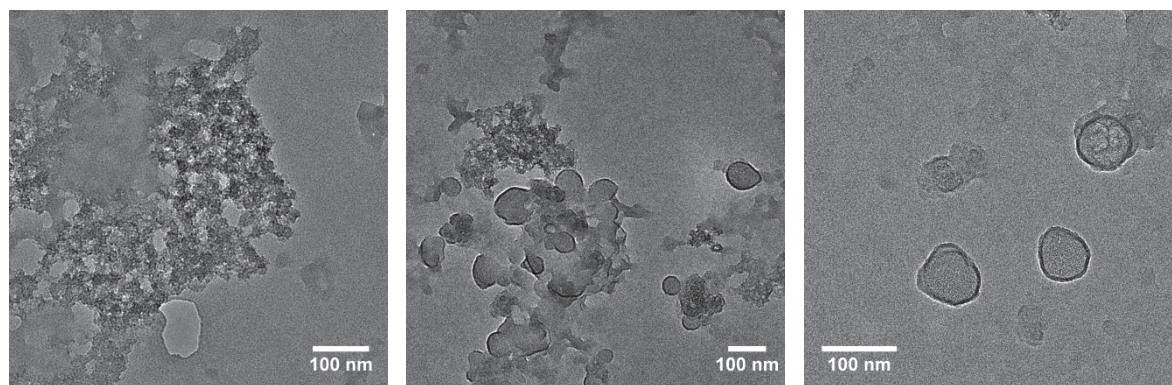


Figure 4-36: TEM images of RB-Dox-HSA sample after silica dissolution with 1 mM of HF

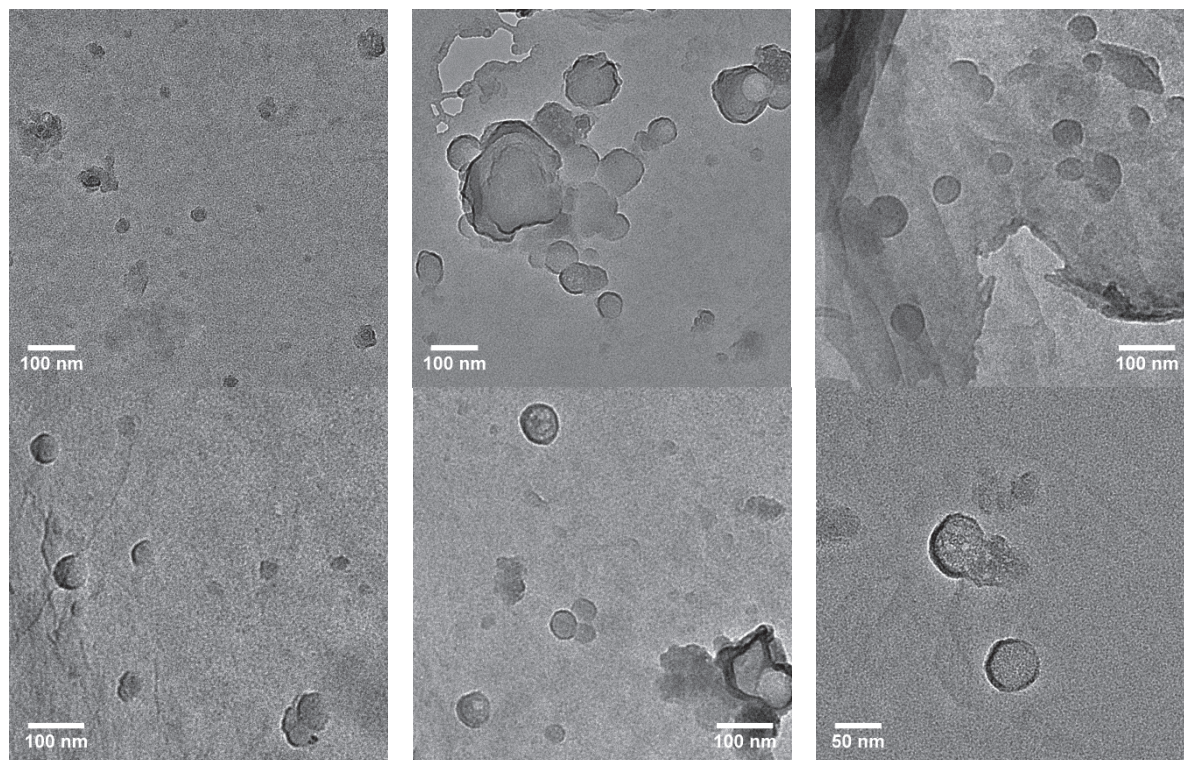


Figure 4-37: TEM images of RB-Dox-HSA sample after silica dissolution with 10 mM of HF

3.6 Dox-HSA nanocapsules: cargo for drug delivery

3.6.1 Synthesis

RB-Dox-HSA and the corresponding RB-HSA NPs were synthesized according to the best synthesis parameters issued from the previous investigations. As pictured in Figure 4-38 A the Dox loading into RB-NH₂ NPs was successful. Despite the visible drug release occurred during IBAM-HSA coating the final RB-Dox-HSA NPs were still charged in Dox (Figure 4-38).

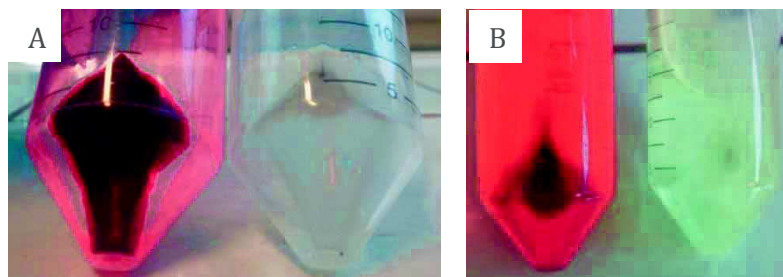


Figure 4-38: Photographs comparing A) Dox loaded RB-NH₂ NPs (left) to free RB-NH₂ NPs (right), B) centrifuged RB-Dox-HSA (left) to RB-HSA NPs (right) after the last synthesis step

3.6.2 Characterization of RB-Dox-HSA NPs

SEM and TEM analyses, Figure 4-39 and Figure 4-40 respectively, both showed RB NPs tangled in a dense HSA network. Thus, the RB NPs seemed to form large aggregates that were trapped into HSA. Furthermore on some TEM images we may also observe the presence of some organic capsules before the RB dissolution. IR spectra of the RB-HSA and RB-Dox-HSA samples presented in Figure 4-41, exhibited, for both, multiple peaks in the ranges of 1300-1800 cm⁻¹ and 2800-3000 cm⁻¹ highlighting the presence of organic compounds.

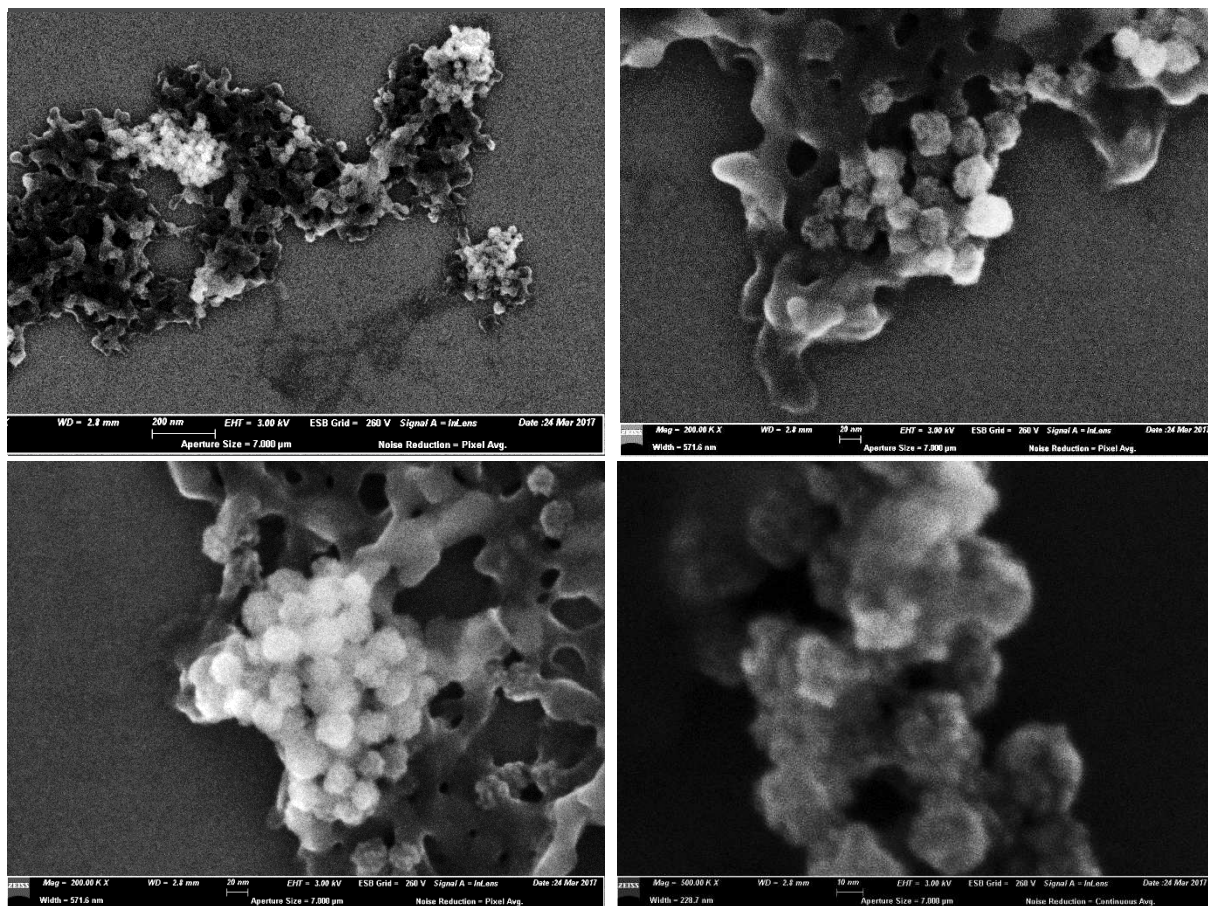


Figure 4-39: SEM images of RB-Dox-HSA-NPs

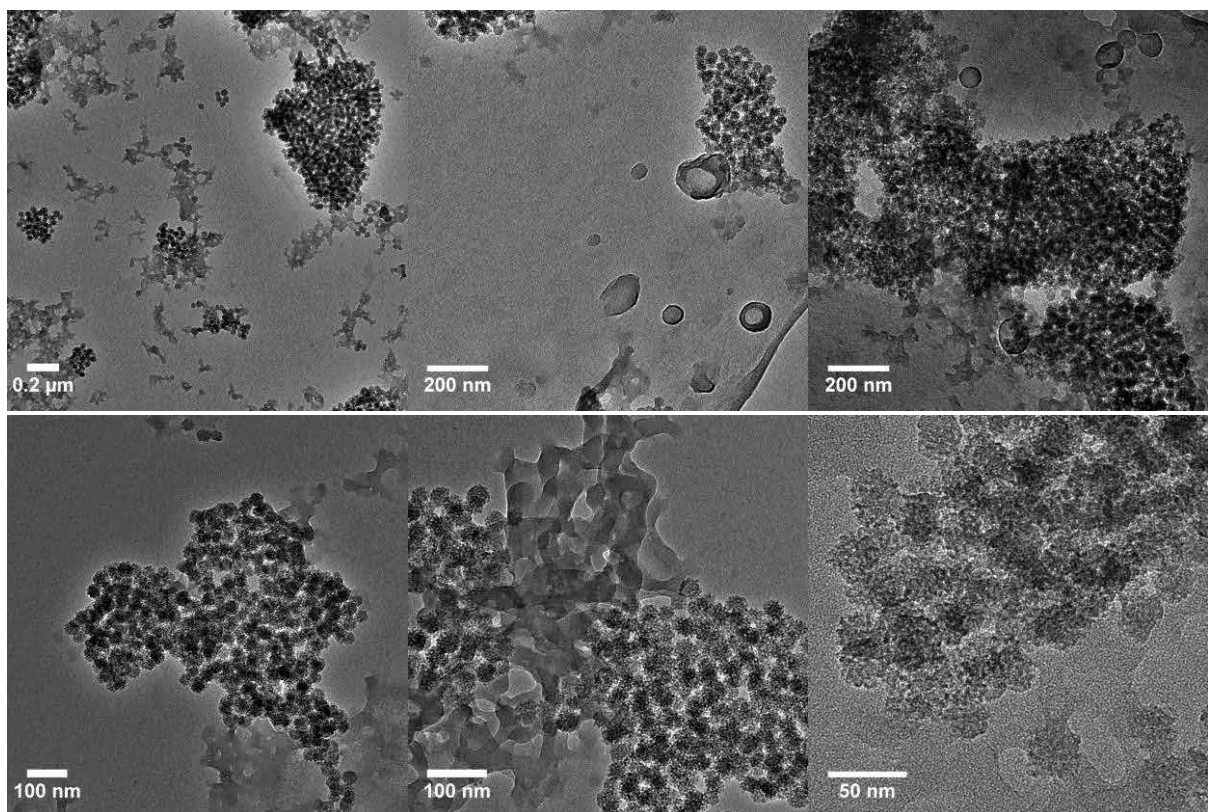


Figure 4-40: TEM images of RB-Dox-HSA-NPs

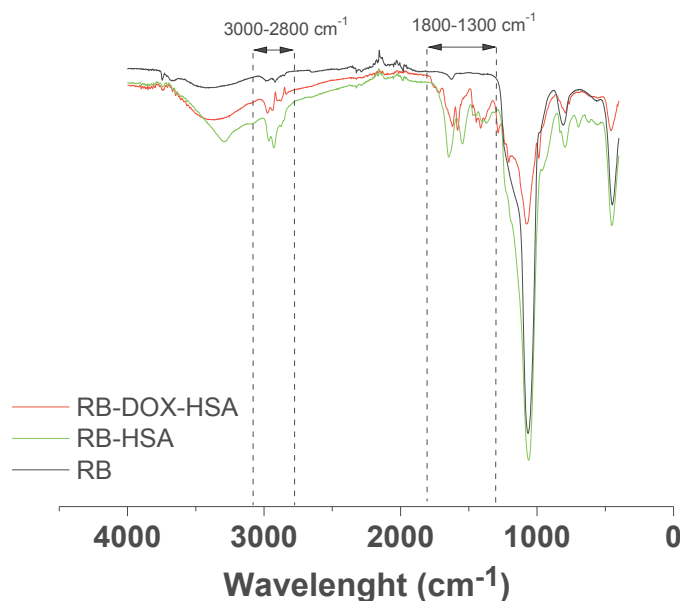


Figure 4-41: IR spectra of RB-DOX-HSA and RB-HSA samples (ATR mode)

3.6.3 Estimation of Dox loading

As some Dox was released during the further synthesis steps (Figure 4-38 B), the main difficulty in such drug loading studies is to determine the final DLC and DLE in the RB-Dox-HSA NPs. Indeed, the analysis of supernatants by fluorescence spectroscopy may induce some errors taking into account the different synthesis steps. Therefore, TGA analyses were run on RB-Dox-HSA and RB-HSA samples to evaluate the dox loading by comparing the weight loss of both samples. Figure 4-42 shows the resulting TGA curves. The difference in weight loss of 15.5 % between both samples suggested an efficient Dox loading. The first TGA curve on RB-HSA NPs indicated 53.3 w% of RB and 46.7 w% of HSA which would correspond to a CC of 87.6 %. The second TGA curve obtained on RB-Dox-HSA NPs indicated 37.8 w% of RB and 62.2 w% of Dox-HSA. Considering the hypothesis that protein coating occurred in a similar way for both samples (with and without Dox) a CC of 87.6 % would give a weight-percentage of 33.1 w% of HSA. Thus, the sample would contain 29.1 w% of Dox.

Considering the DLC to be the percentage of the ratio between the mass of Dox and the mass of HSA capsules after complete dissolution of silica template, a DLC value of 88 % was obtained.

Table 4-3 compares DLC and DLE values of Dox loaded in HSA NPs reported in the literature and the values obtained for our sample. Thus, compared to the various reported Dox encapsulation methods into HSA NPs, such as adsorption of Dox to preformed HSA NPs, incorporation of Dox to HSA matrix before desolvation or Dox conjugation to HSA molecules, our method of Dox soaking into sacrificial silica template led to quite high DLC.

Furthermore, even if the Dox amount is perhaps overestimated during its extrapolation in HSA capsule, the amount of 29.1 wt% determined before removal of the silica template is quite high and suitable for biological studies.

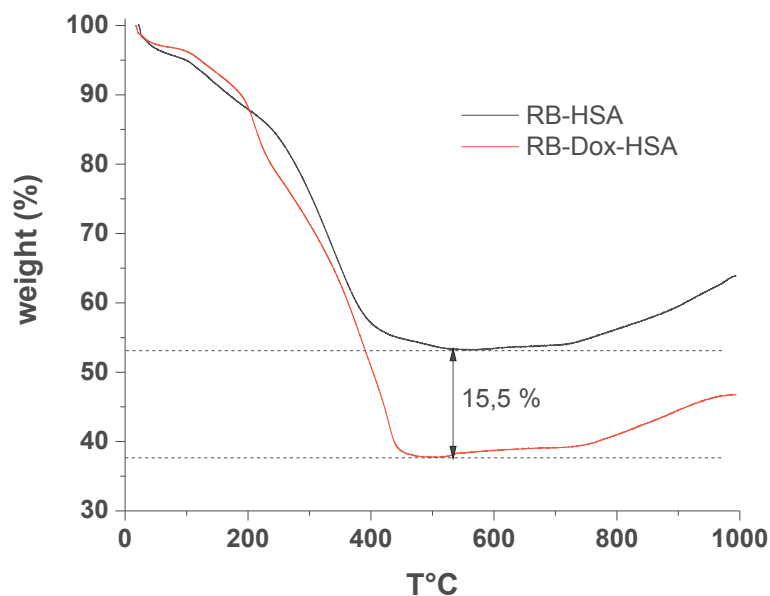


Figure 4-42: TGA curves of RB-HSA and RB-Dox-HSA NPs

Table 4-3: DLC and DLE value of Dox loading into HSA NPs from our sample compared to literature values

Ref.	Type of Dox loading	Size (nm)	DLC (%)	DLE (%)
Our sample	Soaking into sacrificial silica template	30	88	-
(262)	Adsorption to preformed HSA NPs	200	4.8	94.5
(263)	Conjugation via disulfide bonds (via RPA)+ physical adsorption	30	56.2	-
	Conjugation via disulfide bonds (via MPA) + physical adsorption		62.3	-
(264)	Incubation to HSA before desolvation	400	5.7	-
(246)	Adsorption to HSA in solution	-	14	75
	Adsorption to preformed HSA NPs	158	13.8	69
	Incorporation to HSA matrix before desolvation	404	4.82	96.3
(265)	Incorporation to HSA matrix before desolvation	183	5	-
(266)	Adsorption to preformed BSA NPs	100	27.8	74

3.6.4 Dox-HSA nanocapsules formation

After RB dissolution with HF, and washing by dialysis, the resulting sample, composed of Dox and HSA complexes dispersed in water, formed a stable red solution as pictured in Figure 4-43.

TEM analyses of the sample showed three different kinds of morphologies described in details below.

The first morphology, shown in Figure 4-44, was the major morphology observed for the Dox-HSA sample. This morphology was composed of a HSA network forming some kind of sticky like filaments that connected denser spherical HSA NPs together. These denser spherical HSA NPs, that can be distinguished behind the HSA filamentous network, exhibited sizes between 20 and 30 nm and thus, may correspond to HSA NPs formed from RB template dissolution as the RB NPs had sizes of 30 nm. As the HSA filamentous network was already present in the TEM images of RB-Dox-HSA sample (Figure 4-40) it did not result from the RB dissolution. Three hypotheses may explain the formation of this network. The first one is an effect of sample drying on TEM grid before imaging in which the HSA NPs tend to aggregate together during drying, forming this kind of network between them. A second hypothesis could be that this network formed already in solution: when the HSA adsorption around single RB NPs was completed further HSA addition started to deposit between the NPs. This phenomenon could be promoted by the fact that the redispersion of RB NPs after calcination was difficult. Thus the NPs tend to form large aggregates around which HSA could deposit forming this kind of network and bridges between the NPs that were too close from each other. This hypothesis was correlated to the observations made from SEM and TEM images of the RB-Dox-HSA compound before RB dissolution, Figure 4-39 and Figure 4-40 respectively, in which RB NPs seemed to form grapes stuck into a HSA matrix. Finally, the last hypothesis could be that the HSA coating through IBAM grafts was not tight enough and that HSA tend to desorb a little from the RB surface creating this kind of network.

The second morphology, showed in TEM images in Figure 4-45, exhibited spherical HSA NPs of 58 ± 21 nm. As this size was higher than the size of the original RB template, this could result for example from very thick HSA coatings on the RB NPs.

Finally the third morphology, showed in TEM images in Figure 4-46, was typical for organic capsules. These capsules exhibited a size of 43 ± 10 nm, that corresponded to the RB sacrificial template size. Thus, this morphology could result from dried HSA NPs on the TEM grid. However, in the literature, this type of morphology was also observed for Dox aqueous solution as Dox can form self-aggregates (267).

Similar observations were made on SEM images. It validated the prevalence of the first morphology, Figure 4-47 C and D. Furthermore, NPs of ~ 30 nm in size were also identified, Figure 4-47 A and B, that could correspond to the second or the third morphology observed in TEM. This could also be some RB NPs that did not dissolve well during the HF treatment.

To conclude, the real morphology of the sample was very difficult to determine through TEM and SEM analyses mostly because they involved drying of this organic sample before imaging. Imaging the sample in the humid state, through AFM or environmental SEM, or by freezing the humid state by cryoTEM could give more precise information on the morphology. If the HSA network (first morphology) would be still observed through these methods it would involve that it was not a result of the drying. Thus, some ideas to avoid this morphology could be for example to replace the calcination by the use of a nitrate ammonium solution to remove CTAB from the sample which will improve colloidal stability of the sample and avoid the formation of large aggregates (see Chapter 5, part 2.2). Another idea, to avoid the possible disassembling of the HSA coating, would be to reinitialize the IBAM-HSA coating a second time over the first coating.

Indeed, Mertz *et al.* showed a better HSA capsules assembly by the formation of minimum two IBAM-HSA coatings (166).



Figure 4-43: Photograph of the Dox-HSA sample after RB dissolution with HF

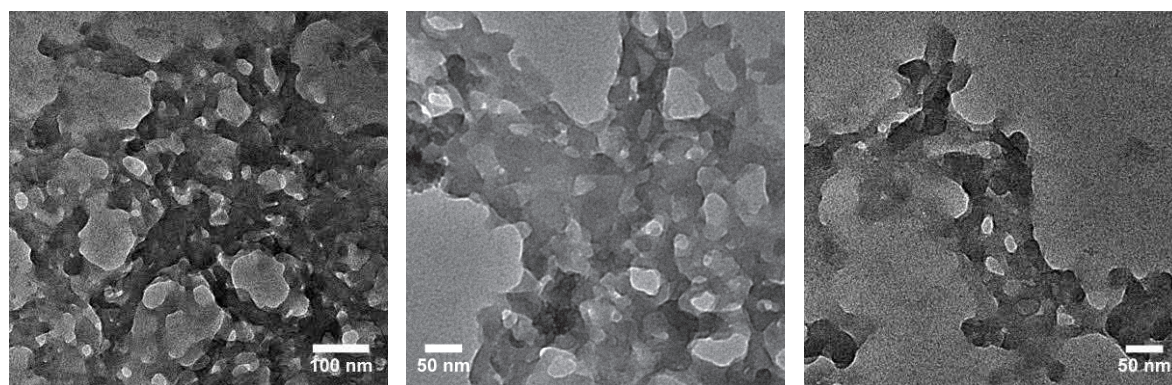


Figure 4-44: First morphology of Dox-HSA after RB dissolution observed by TEM

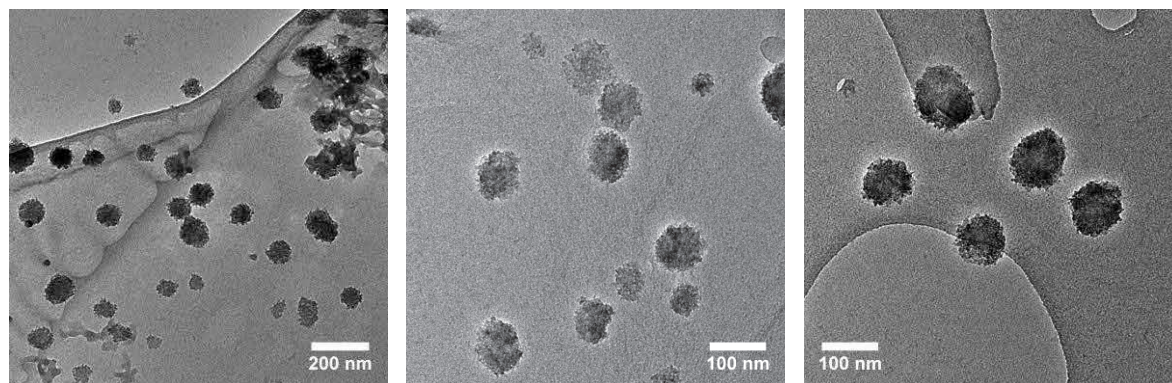


Figure 4-45: Second morphology of Dox-HSA after RB dissolution observed by TEM

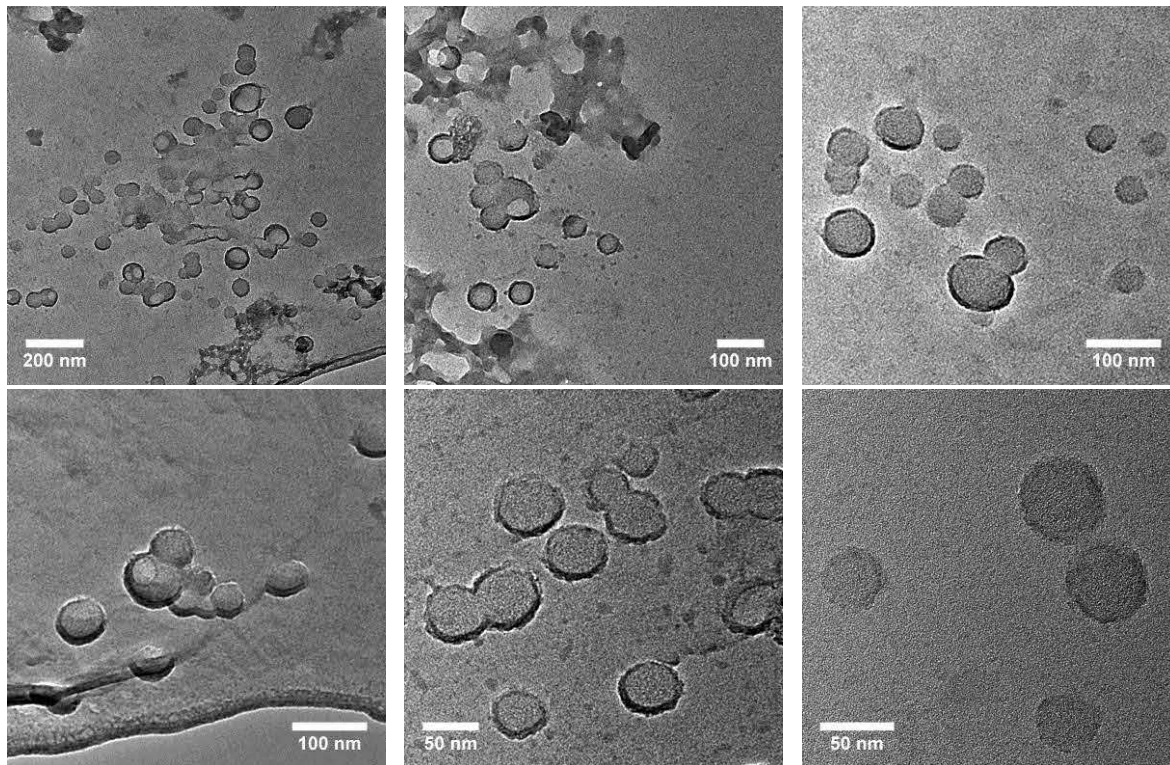


Figure 4-46: Third morphology of Dox-HSA after RB dissolution observed by TEM

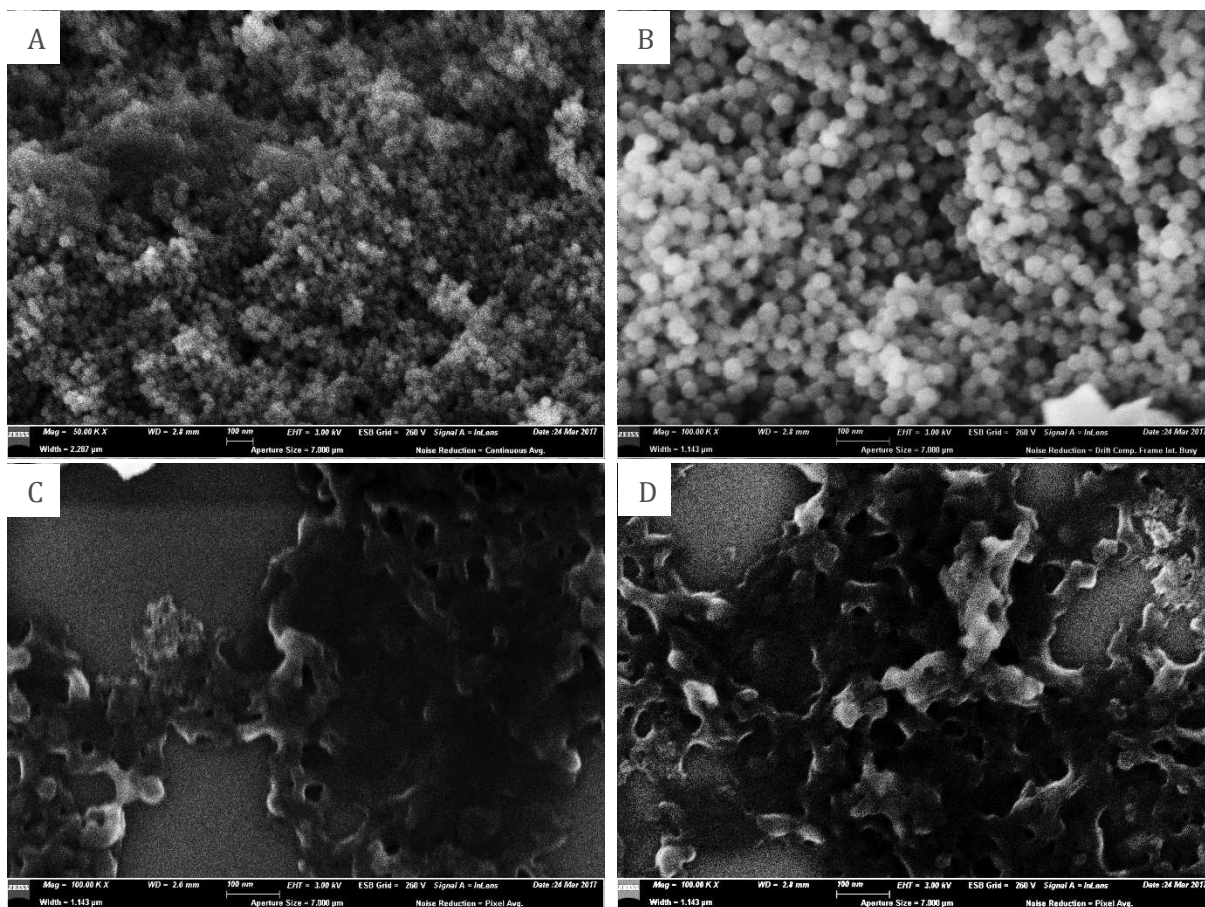


Figure 4-47: SEM images of Dox-HSA NPs

3.6.5 Drug release from capsules degradation by proteases

As illustrated in Figure 4-48, the aim of the formation of these Dox-loaded HSA capsules was to be degradable under enzymatic action in order to control the Dox delivery.

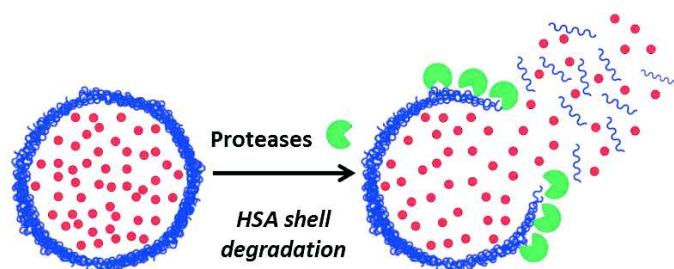


Figure 4-48: Schematic representation of HSA shell degradation by proteases and subsequent drug release

Unfortunately, the experiments conducted in presence of proteases (pH 5 and pH 7) were unsuccessful to induce a clear release of Dox loaded in capsules (data not shown but similar to the results discussed later in page 166). This may result from the fact that the large Dox loading into small porosities the silica template led to the encapsulation of a large amount of Dox molecules in a small volume. Thus, Dox molecules may tend to precipitate, to form aggregates by π stacking, or to covalently bond to itself forming Dox-Dox compounds (267–271). These aggregation states would so inhibit their abilities to diffuse through the dialysis membrane. Furthermore, no difference between the samples incubated with proteases and the controls was observed. Thus, the small drug release measured was not due to proteases action but to simple drug leakage

3.6.6 Multicellular spheroids growth inhibition study

Cytotoxicity assays were performed on a Huh7 Multicellular tumor spheroid model (Huh7 MCTS). Such model reproduces more closely the *in vivo* behavior of tumor cells than 2D culture system. We evaluate the toxicity of Dox-HSA and corresponding HSA NPs, by measuring the growth of the MCTS with time (2, 4 and 7 days). Huh7 MCTS were incubated with Dox-HSA and HSA NPs diluted in complete medium with concentrations of $35.4 \mu\text{g}\cdot\text{mL}^{-1}$ and $17.7 \mu\text{g}\cdot\text{mL}^{-1}$ of HSA which corresponded to Dox concentrations of $31 \mu\text{g}\cdot\text{mL}^{-1}$ and $15.5 \mu\text{g}\cdot\text{mL}^{-1}$ for the Dox-HSA sample. Figure 4-49, shows representative pictures of Huh7 MCTS at different days and with both NPs at the highest concentration tested. It shows that the HSA NPs did not modify the growth compared to non-treated MCTS but, that for DOX-HSA NPs MCTS exhibited a different morphology that could be related to massive cell death. Such images are characteristics of doxorubicin effect on MCTS (272, 273). Measurements of MCTS surface area were done and growth percentage calculated compared to the control experiment (Mock). As shown on the results presented in Figure 4-50, Huh7 MCTS growth in presence of Dox-HSA NPs is readily inhibited. At the two concentrations tested, we can observe a decrease of 80 % compared to the control. As the growth is not modified when the Huh7 MCTS are incubated with HSA NPs, we can hypothesize that the effect is related to Dox release. Our particles are made of human serum albumin and can be taken up by cells at least those of the outer layer of the cell aggregate by non-specific endocytosis and or pinocytosis. Dox could therefore be release after HSA degradation by lysosomal proteases. Furthermore, we know from other experiments (presented in Chapter 5 page 177) that Dox can diffuse through the entire Huh7 MCTS even if the NPs

internalization occurred only at the spheroid borders. So the effect recorded here is a proof that Dox can be released from the nanocapsules.

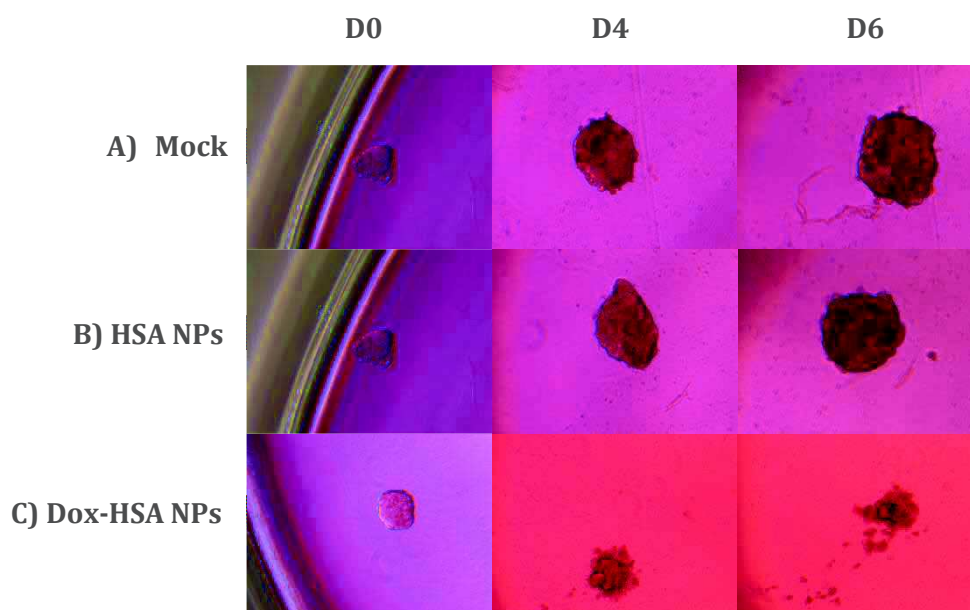


Figure 4-49: Photographs, taken by optical microscope (10X magnification), of A) non treated spheroids, B) spheroids treated with HSA NPs at $35.4 \mu\text{g.mL}^{-1}$ of HSA and C) spheroids treated with Dox-HSA NPs at $35.4 \mu\text{g.mL}^{-1}$ of HSA and $31 \mu\text{g.mL}^{-1}$ of Doxorubicin at 0, 4 and 6 days of incubation.

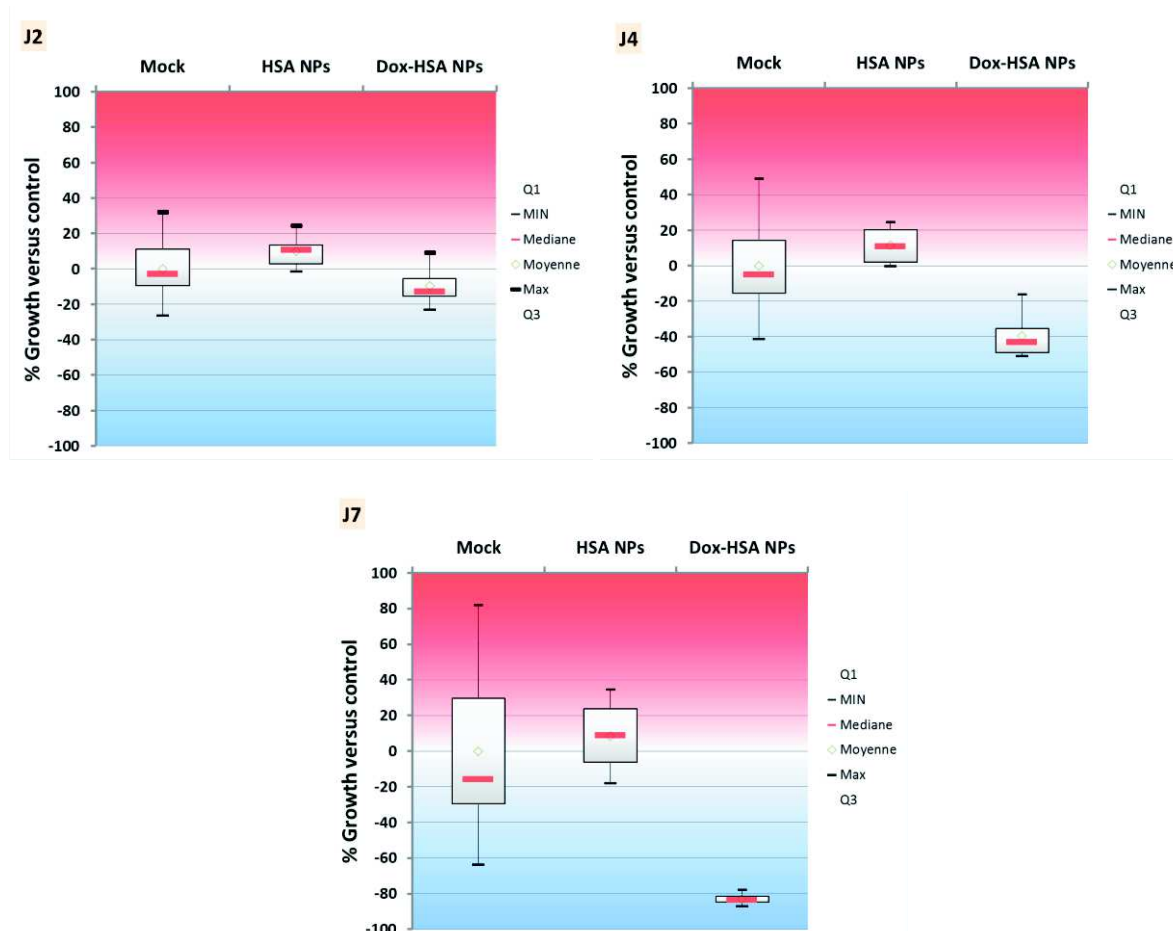


Figure 4-50: Box plot representing percentage of growth of Huh7 MCTS either treated with HSA NPs or Dox-HSA NPs in comparison with non-treated ones (Mock) after 2, 4 and 7 days of incubation at concentrations of $17,7 \mu\text{g}\cdot\text{mL}^{-1}$ of HSA and $15,5 \mu\text{g}\cdot\text{mL}^{-1}$ Dox

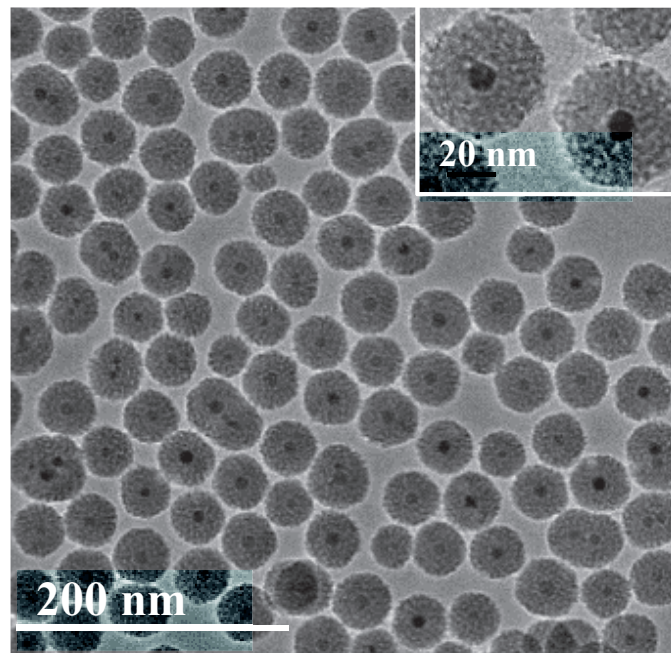
3.7 Conclusion and outlooks

To conclude we synthesized successfully Dox-HSA compound with a quite high Dox loading through drug soaking into RB sacrificial template. As already noticed, the determination of the amount of dox loaded is very difficult considering the different synthesis steps. However, by combining fluorescence spectroscopy and TGA analyses, loading amounts have been thus evaluated. Furthermore, even if the drug release has not been assessed *in vitro* by dialysis, this system showed an efficient cytotoxic activity on 3D tumor models. These encouraging results promote our Dox-HSA system as promising carrier for drug delivery.

However, there are always some further investigations to perform in order to elucidate the different observed morphologies after the silica removal and to understand why the drug release was difficult under *in vitro* dialysing conditions.

Chapter 5:

IO@RB core-shell NPs as theranostic agents



1 Introduction

In the previous chapters we introduced two nanoobjects for biomedical applications: on one hand iron oxide NPs, which showed efficient T_2 contrast for MRI, and on another hand mesoporous silica NPs, which exhibited high drug loading capacities. Thus in this chapter we aim to introduce a core-shell type magnetic mesoporous silica nanocomposite structure for simultaneous bioimaging and drug delivery.

Thus, based on the previous results and processes, we developed a synthesis strategy for these theranostic agents, illustrated in Figure 5-1. This strategy consists in building a thin silica shell with small pores (~ 3 nm) around superparamagnetic iron oxide nanoparticles, obtained by thermal decomposition. These NPs type was called IO@RB NPs. Doxorubicin (Dox), an antitumoral agent, is loaded by impregnation into the porosities of the silica shell. Then HSA is deposited on the silica shell surface which was previously modified with isobutyramide (IBAM) binders. Finally, incubation of the particles in proteases media should allow efficient HSA degradation and subsequent Dox release.

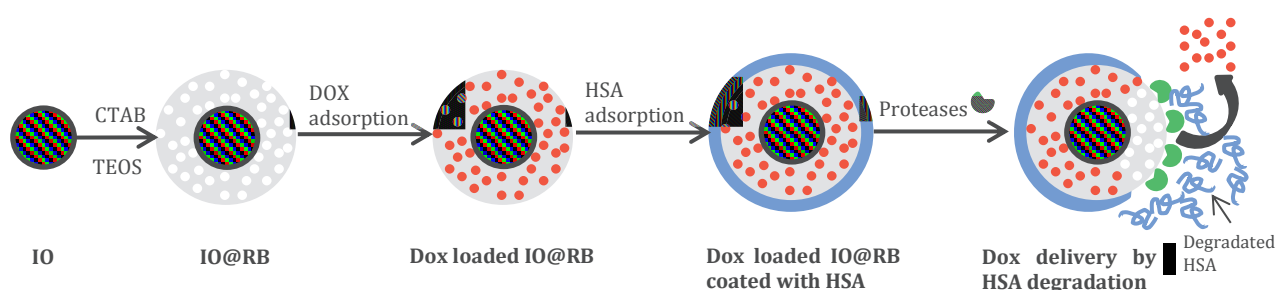


Figure 5-1: Schematic illustration of the synthetic procedure for IO-MS NPs loaded with Dox and coated with HSA and the Dox release by HSA degradation via proteases action

This chapter will be divided in five parts:

- The investigation of synthesis process
- The evaluation of T_2 contrast efficiency for MRI
- The investigation of the best Dox loading procedure
- The determination of the best protein coating strategy
- Biological studies

2 Synthesis

2.1 Parameter influences

2.1.1 Establishment of the best protocol inspired from literature

The first goal was to establish the best protocol, inspired from the literature, to produce spherical, monodispersed in size, core-shell NPs with open porosities in the silica shell. Hyeon's group was the first to report a protocol for the synthesis of homogenous spherical 53 nm IO@RB NPs (141):

0.5 mL of 15 nm IO NPs dispersed at 6.7 mg Fe/mL in chloroform was mixed to 5 mL of 0.55M aqueous CTAB solution. The resulting solution was vigorously stirred for 30 min resulting in the formation of a turbid brown oil-in-water microemulsion. Then, the mixture was heated up to 60°C and aged at that temperature for 10 min under stirring to evaporate the chloroform, resulting in a transparent black solution. Then this solution was added to a mixture of 45 mL of water and 0.3 mL of 2M NaOH solution and heated up to 70°C under stirring. Then, 0.5 mL of

TEOS, 50 μL of APTES solution, and 3 mL of EtOAc was added to the reaction solution in sequence. After 10 min, 50 μL of APTES was added and the solution was stirred for 3 h. The as-synthesized IO@RB NPs were washed 3 times with ethanol to remove the unreacted species and dispersed in 20 mL of ethanol.

In this part, to establish a protocol for the synthesis of IO@RB NPs, we worked with the same initial IO NPs batch in order to fix the parameters. The batch, presented in Figure 5-2, is composed of monodisperse spherical IO NPs of 9 ± 1 nm dispersed in chloroform at a concentration of 5 mg/mL (concentration measured after chloroform evaporation of a precise volume of the IO NPs solution).

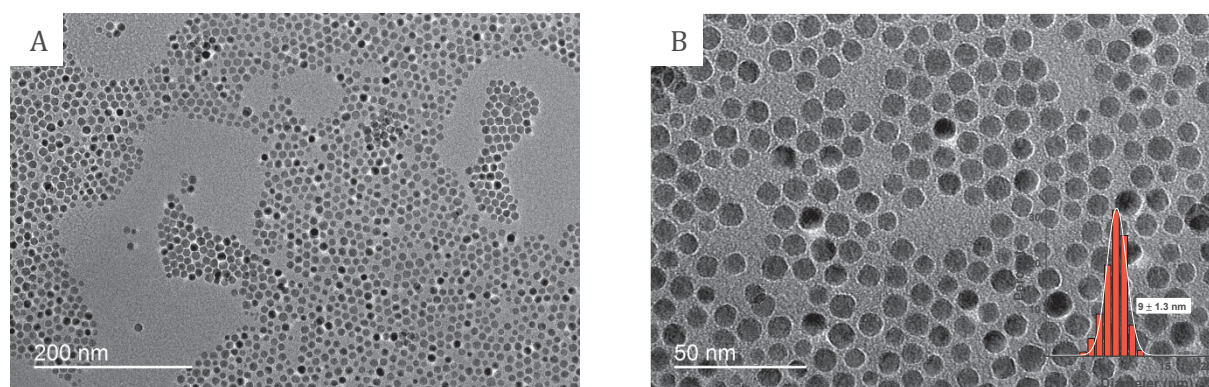


Figure 5-2: TEM images of the IO NPs used for the establishment of a general core-shell synthesis protocol with the histogram of the TEM size distribution measured on more than 500 particles in inset of B)

2.1.1.1 Highlighting of the phase transfer importance

In a first synthesis we reproduced exactly the protocol described by Hyeon's group, but unfortunately we never succeeded in achieving a complete dissolution of 1 g of CTAB in 5 mL of water to reach the final concentration of 0.55 M. If we tried to add the 0.5 mL of IO NPs solution to the CTAB solution, which was not completely dissolved, the mixture gained in mass after a few minutes forming a gel. We then tried a lower CTAB concentration of 55 mM: after at least 1 hour stirring at 60 °C, the CTAB was completely dissolved and Hyeon's protocol was further followed. The resulting particles are presented in TEM images in Figure 5-3 A and B. They exhibited a quite spherical shape but, at higher magnification, their shapes were not well-defined. We also noticed the presence of RB NPs without IO core. So this protocol had to be improved to reach a higher monodispersity in shape and size and with a single core for each NP.

In the second test, to avoid the formation of RB NPs without IO core, we decreased again the CTAB content from 55 mM to 27 mM and we kept the same amount of IO NPs and the same volume ratio between the CTAB and the IO solutions (5 and 0.5 mL). For the rest of the procedure we decided only to suppress the APTES, which is not necessary to form the IO@RB NPs, and to decrease the EtOAc volume to 1 mL. As shown in TEM images from Figure 5-4 A and B the resulting particles displayed a more spherical shape than the first trial, the monodispersity in size was also improved: we measured an average size of 88 ± 8 nm for 100 particles in TEM images. Unfortunately, most of NPs exhibited a double IO core which may be due to a poor phase transfer of the IO NPs from the chloroform to water, leading to a small aggregation of IO NPs. The IO@RB NPs also showed well-defined porosities in the silica shell. These porosities were investigated more precisely through nitrogen adsorption-desorption measurement after calcination of the resulting NPs at 550°C for 6h. The corresponding N_2 adsorption-desorption isotherms and the resulting PSD curve are depicted in Figure 5-4 C. The adsorption-desorption isotherms display a typical IV behavior characteristic of mesoporous materials with a steep capillary condensation step for relative pressures P/P_0 between 0.2 and 0.4. The resulting BET surface area was about 751 m^2/g , the pore volume calculated from BJH desorption was 0.84 cm^3/g and the PSD curve, Figure 5-4 C inset, obtained through BJH calculations showed a sharp

peak centered at 2.6 nm. Comparing these values to the values reported in the literature for similar systems, as summarized in Table 5-1, such a PSD of 2.6 nm is in total agreement with the values reported in literature, 2.4-2.8 nm, using CTAB micelles as pore template for silica shell. Furthermore, the obtained BET surface area is in the upper range of the literature values while the pore volume of 0.84 is in the middle range. So from these results we can conclude that the porosity obtained for this system is consistent with the porosity values, obtained from CTAB micelles, reported in the literature. Therefore, well-defined spherical monodispersed IO@RB NPs of 88 nm with open porosities of 2.6 nm but a lot of double IO cores were obtained probably due to the poor IO NPs phase transfer. So this synthesis key step has to be optimized.

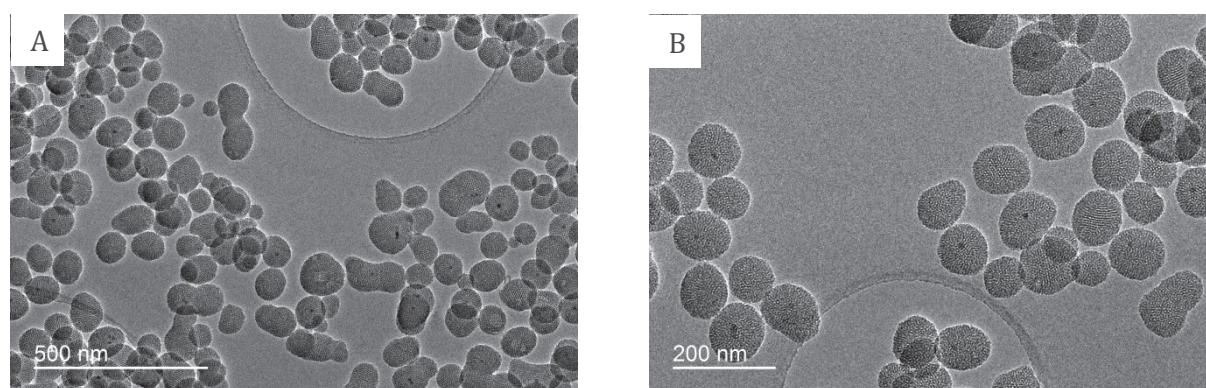


Figure 5-3: TEM images of IO@RB NPs obtained by following Hyeon's protocol

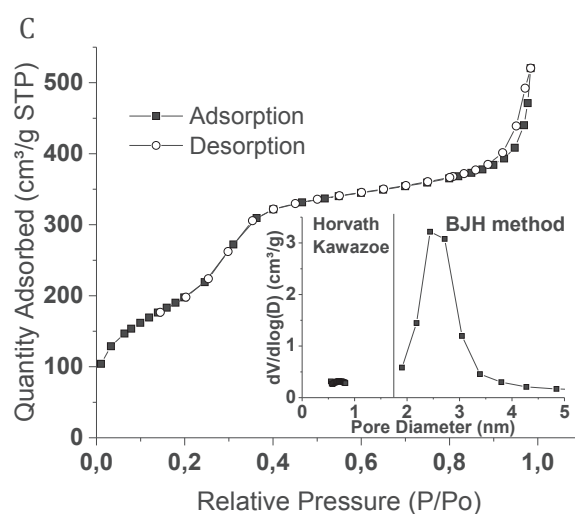
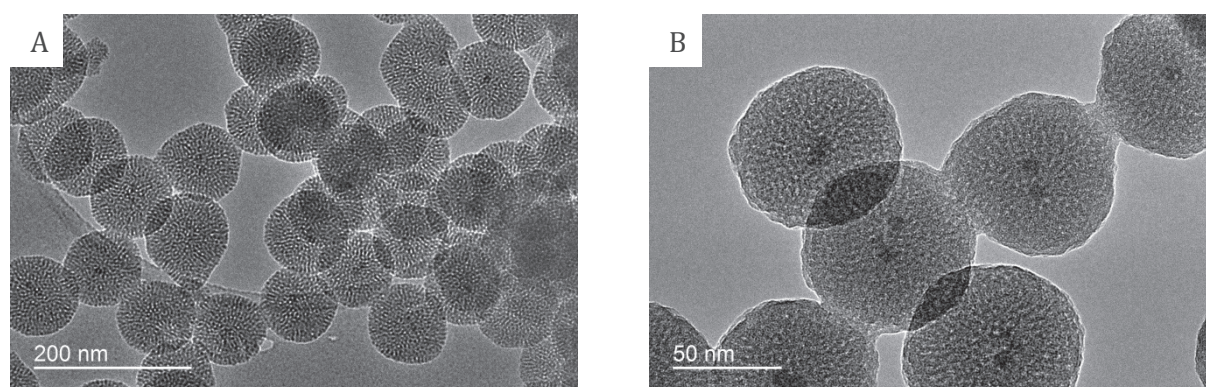


Figure 5-4: TEM images of IO@RB NPs obtained by following Hyeon's protocol but with an adapted CTAB concentration of 27 mM

Table 5-1: Comparison of pore parameters obtained from N₂ adsorption-desorption analyses for core-shell NPs with a RB shell

References	Core diameter (nm)	Particle diameter (nm)	BET surface area (m ² /g)	Pore volume (cm ³ /g)	Pore size (nm)
(141)	15	53	481	1.07	2.6
(140)		~100	893	-	2.7
(115)	12	75	202	0.29	1.4 and 2.7
(274)	15	67	452	1.11	2.5
(275)	11	67	1045	1.84	2.5
(139)	-	~100	967.8	1.05	2.8
(154)	20	60	326	0.285	2.4
Our experiment	9	88	751	0.84	2.6

2.1.1.2 Base type for base-catalyzed sol-gel process

In another protocol described by Hyeon's group (140), ammonium hydroxide was used as a base instead of 2M NaOH. The synthesis conditions were the same as previously excepted that 0.3 mL of ammonium hydroxide (25 wt%) were used instead of 0.3 mL of 2M NaOH. However, as shown on Figure 5-5 A and B, this change did not lead to the formation of homogeneous spherical core-shell NPs. Therefore, for the next syntheses, NaOH was kept as a base.

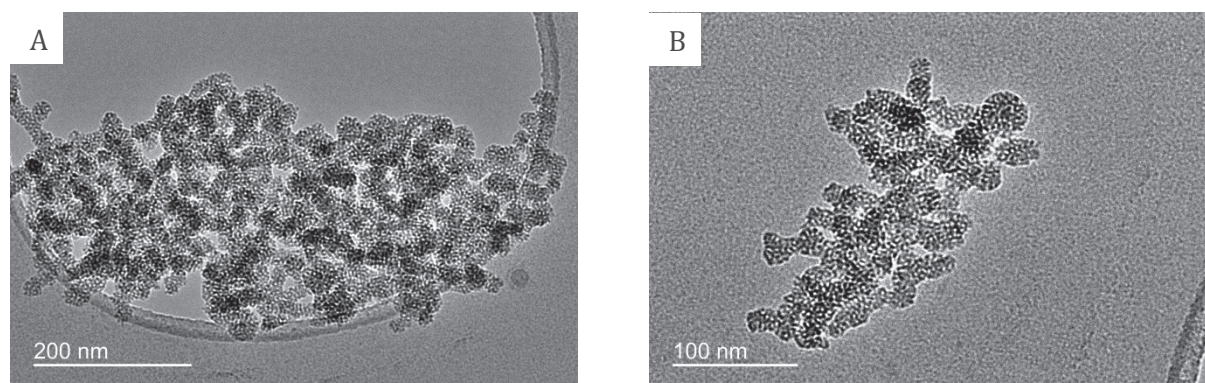


Figure 5-5: TEM images of IO@RB NPs obtained by following Hyeon's protocol with NH₃ instead of NaOH as base

2.1.1.3 Reactant molar ratio for controlling IO@RB sizes

Ye et al. (115) adapted Hyeon's protocol by controlling precisely synthesis parameters such as reactant concentrations in order to achieve uniform IO@RB NPs with tunable shell thickness. According to their experiments, for a [CTAB]/[Fe₃O₄] ratio of 12, they obtained IO@RB NPs with average diameters of 25 and 35 nm by applying [CTAB]:[TEOS]:[NaOH]:[H₂O] molar compositions of 1:4.9:1.1:5983 and 1:9.7:2.2:11966 respectively. Applying these molar ratios to our mixture of 0.5 mL of IO NPs with 5 mL of a CTAB solution at 28 mM after chloroform evaporation we obtained, as pictured in Figure 5-6, well-defined monodisperse spherical IO@RB NPs of 43 ± 4 nm and of 37 ± 3 nm for [CTAB]:[TEOS]:[NaOH]:[H₂O] molar compositions of 1:9.7:2.2:11966 and 1:4.9:1.1:5983 respectively.

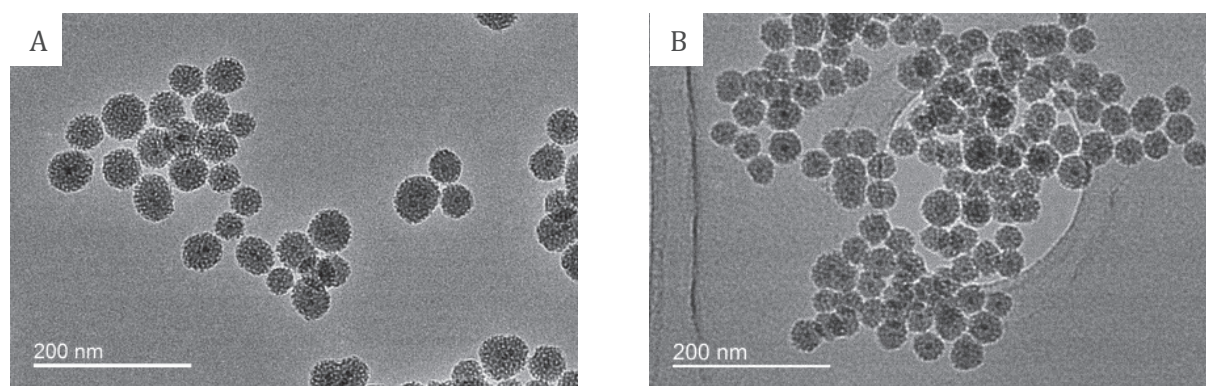


Figure 5-6: TEM images of IO@RB NPs obtained with [CTAB]:[TEOS]:[NaOH]:[H₂O] molar composition of A) 1:9.7:2.2:11966 and B) 1:4.9:1.1:5983

2.1.1.4 *In-situ silanization trials*

In Hyeon's protocol, the resulting IO@RB NPs are already silanized due to the addition of APTES during the synthesis after TEOS addition. In order to form also *in-situ* silanized IO@RB NPs we have added 0.03 and 0.06 mL of APTES in the reaction media with both previous [CTAB]:[TEOS]:[NaOH]:[H₂O] molar compositions. The resulting IO@RB NPs, as shown in Figure 5-7, are less defined than the previous IO@RB NPs obtained in the same conditions and the NPs borders seemed to merge together.

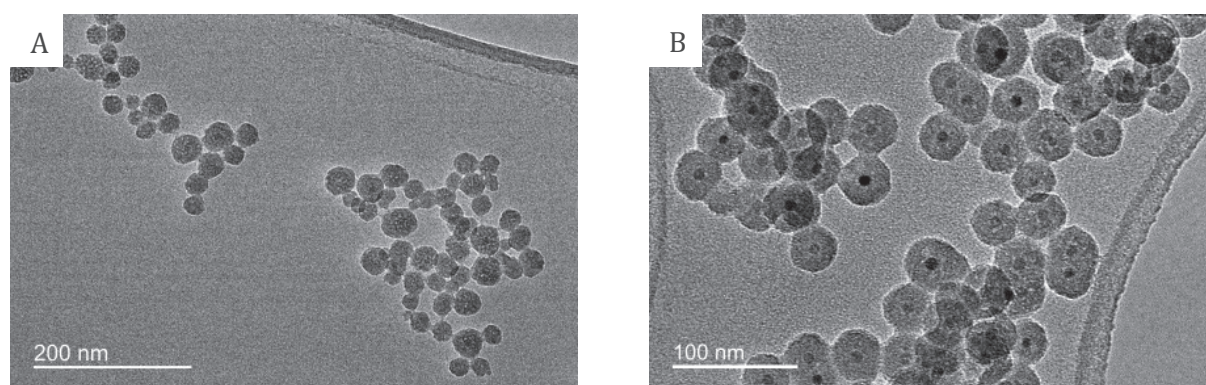


Figure 5-7: TEM images of IO@RB NPs obtained like previously with [CTAB]:[TEOS]:[NaOH]:[H₂O] molar composition of A) 1:9.7:2.2:11966 and B) 1:4.9:1.1:5983 but with addition of APTES

2.1.1.5 *Conclusion*

Regarding these preliminary experiments we can conclude the following points:

1. The IO NPs phase transfer from chloroform to water thanks to CTAB ligand addition and the chloroform evaporation are key steps for forming core-shell NPs with a single IO core
2. The addition of base is necessary for sol-gel process as the silica condensation occurs by slow pH decrease. NaOH and NH₃ bases can both be used for IO@RB NPs synthesis, but in our experiments only NaOH led to the desired IO@RB NPs morphology.
3. Silanization of the silica shell by adding APTES during the NPs synthesis led to less defined and merged IO@RB NPs
4. [CTAB]:[TEOS]:[NaOH]:[H₂O] molar composition of 1:4.9:1.1:5983 led to spherical well-defined monodispersed IO@RB NPs of 37 ± 3 nm with a unique IO core per NPs.

From these observations a general procedure for IO@RB synthesis was set up:

1. An aqueous solution of CTAB at 28 mM was prepared (50 mg in 5 mL of Milli-Q water)
2. 0.5 mL of IO NPs dispersed at ~5 mg/mL in chloroform were added to the CTAB solution under vigorous magnetic stirring for 30min. We obtained a brown turbid solution (Figure 5-8 A)
3. The mixture was elevated to 65°C and then maintained at this temperature for 10min under stirring to evaporate the chloroform. The solution obtained was black and transparent (Figure 5-8 B)
4. A solution of 15 mL of Milli-Q water and 6 μ L of a 2M NaOH solution were added to the solution. The mixture was heated up to 70°C under vigorous stirring
5. 0.15 mL of TEOS and 0.25 mL of EtOAc were added and the mixture was stirred for 3h at 70°C (Figure 5-8 C)
6. The particles were then washed 3 times in ethanol



Figure 5-8: Photos of the IO@RB synthesis A) the brown turbid solution during the water/oil emulsion at the 2nd step B) the black transparent solution after chloroform evaporation at the 3rd step C) the solution after the addition of all reactants at the 5th step

2.1.2 Scale-up

Unfortunately, following the previous established procedure, only a few amount of IO@RB NPs (less than 10 mg) were obtained. Thus, in order to increase the quantity of the final product to lead different analyses (physical and biological characterizations) on the same batch, we needed to drive a small scale up by multiplying by 10 the quantities of reactants.

For this study IO NPs with a size of 11 ± 1.8 nm, presented in Figure 5-9, and dispersed at 2 mg Fe/mL in chloroform (concentration measured by ICP-AES), have been used. First, we reproduced the previous protocol with the same quantities to check the reproducibility of IO@RB synthesis. Mixing 50 mg of CTAB with 0.5 mL of IO NPs at 2 mg Fe/mL gave a [CTAB]/[Fe] molar ratio of 7.7 and by applying a [CTAB]:[TEOS]:[NaOH]:[H₂O] molar composition of 1:4.9:1.1:5983, IO@RB NPs with an average size of 39 ± 5 nm and the perfect expected core-shell structure, were obtained, Figure 5-10.

For the scale-up the same molar compositions were used, but the quantities of the reactants were multiplied by 10. As pictured in TEM images in Figure 5-11, the two first trials failed: the pictures did not show any core-shell structure, only IO NPs clusters. This result may be due to an incomplete CTAB dissolution and/or from a poor phase transfer (incomplete chloroform evaporation, non-efficient stirring). Both can lead to poor CTAB alkyl chain coupling to oleic acid at the IO NPs surface by insufficient quantity of dissolved CTAB or non-efficient Van der Waals interactions. Without the CTAB layer at the IO NPs surface, no organic template was present for the efficient growth of the silica layer on the IO NPs. To overcome these problems, we modified two synthesis parameters without modifying the reactants content. First we improved the CTAB dissolution step by applying the following procedure:

1. 500 mg of CTAB were mixed with 50 mL of Milli-Q water and put under stirring at 60°C for at least 1h followed by ultra-sonication for 30 min to 1h. The solution should become transparent.
2. The mixture was then placed on the rotating wheel overnight to maintain homogenous stirring.
3. Just before the reaction the mixture was placed 30 min under sonication and stirred at least 1h at 60°C. Check before initiating the rest of the process, that the CTAB solution is totally transparent without cloudy gel resulting from partially dissolved CTAB which can be present on the bottom of the flask.

The second modification was in the glassware: in order to achieve a better stirring for the oil/water emulsion and a higher liquid/air interface to facilitate chloroform evaporation, we replaced the round-bottom flask used previously with an erlenmeyer. As depicted in TEM images in Figure 5-12 A) and B), the resulting IO@RB NPs were homogeneous spherical core-shell NPs of 50 ± 5 nm with apparent porosities. SEM images (Figure 5-12 C) and D)) confirmed the spherical shape and the high size monodispersity. DLS analysis of the IO@RB NPs dispersed in EtOH, Figure 5-12 E), exhibited a mean hydrodynamic diameter of about 50 nm with a secondary distribution at 200 nm. This small amount of larger NPs may result from NP aggregation or wider particles resulting from silica shell formed around multiple IO cores, as observed in one image presented in Figure 5-13. The FTIR spectra, Figure 5-12 F), also proved the SiO₂ framework presence with the identification of $\nu_{as}(\text{Si-O-Si})$ and $\nu_s(\text{Si-O-Si})$ characteristic peaks around 1098 and 804 cm⁻¹.

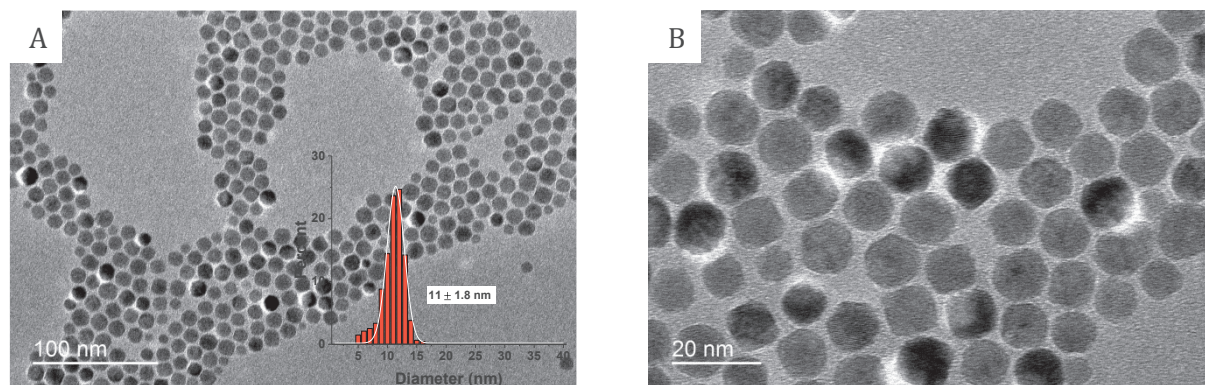


Figure 5-9: A) and B) TEM images of the IO NPs used for the scale-up of the IO@RB synthesis protocol with the histogram of the TEM size distribution measured on more than 500 particles in inset of A)

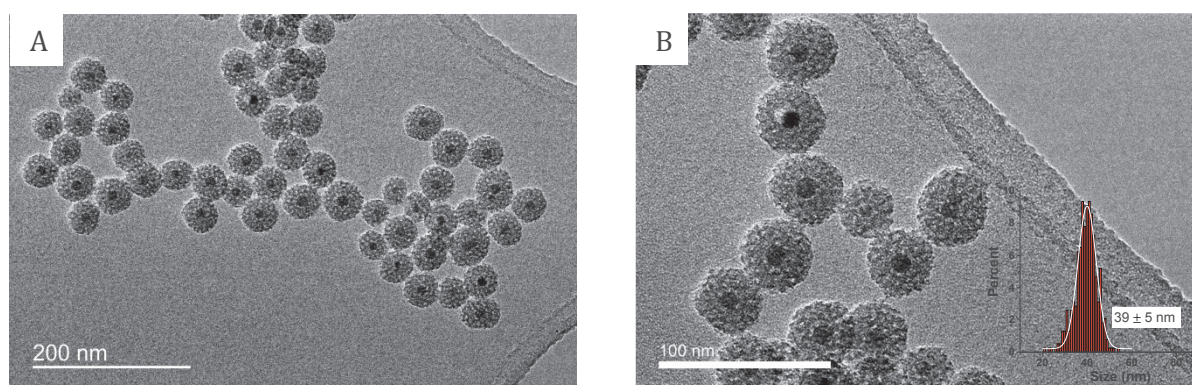


Figure 5-10: A) and B) TEM images of IO@RB NPs obtained with [CTAB]/[Fe] molar composition of 7.7 and [CTAB]:[TEOS]:[NaOH]:[H₂O] molar composition of 1:4.9:1.1:5983, the histogram of the TEM size distribution measured on 385 particles is in inset of B)

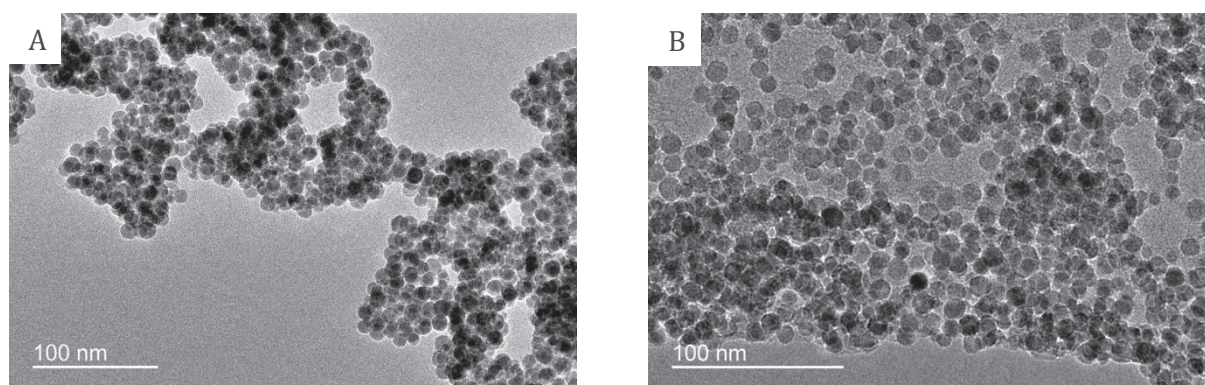


Figure 5-11: TEM images of IO@RB NPs after scale-up A) first trial B) second trial

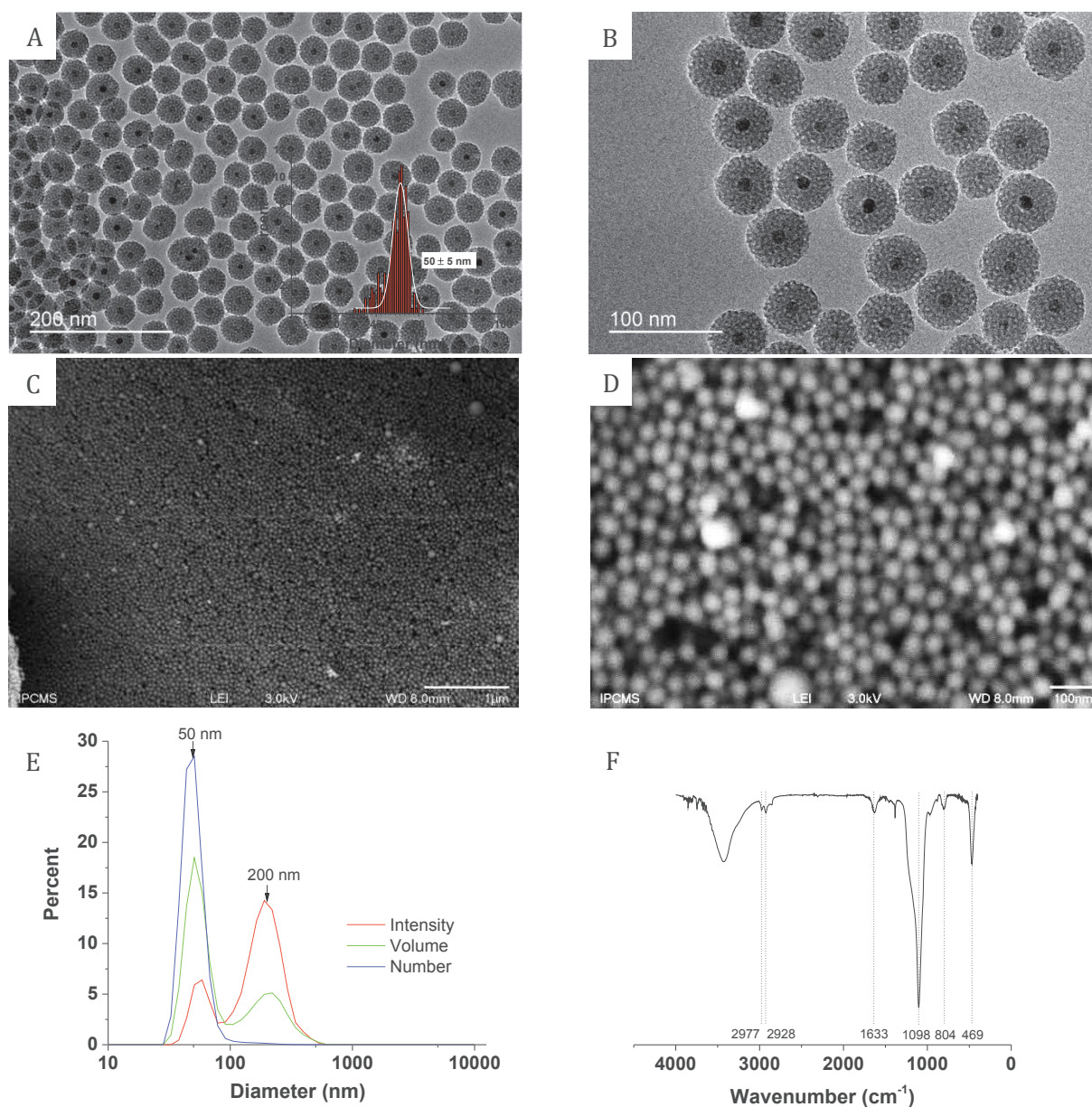


Figure 5-12: A) B) TEM images, C) D) SEM images E) DLS curves in EtOH and F) FTIR spectra of IO@RB NPs obtained with [CTAB]/[Fe] molar composition of 7.7 and [CTAB]:[TEOS]:[NaOH]:[H₂O] molar composition of 1:4.9:1.1:5983 after scale-up, the histogram of the TEM size distribution measured on 385 particles is in inset of A)

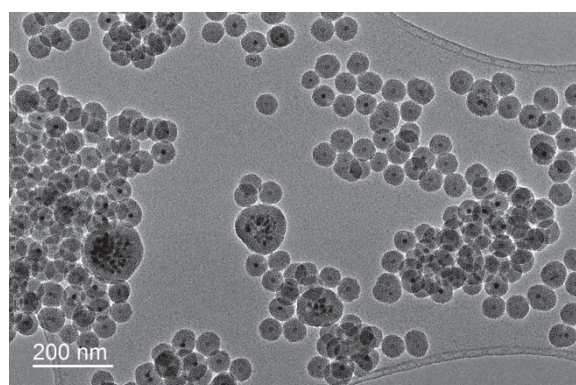


Figure 5-13: TEM image of the IO@RB sample obtained after scale-up in where multicore IO@RB NPs may be observed

2.1.3 Influence of [CTAB]/[Fe] ratio on shell thickness

According to Ye *et al.* (115) the molar ratio between the surfactant and the iron oxide during the first step of the synthesis process (phase transfer) can strongly influence the thickness of the subsequent mesoporous silica coating, and thus the size of the resulting IO@RB NPs. Indeed they reported that for a fixed amount of IO cores, an excess of CTAB will produce RB NPs without IO cores as by-products and on the contrary a deficit of CTAB will limit the shell thickness increase despite an excess of TEOS.

To modulate the shell thickness of IO@RB NPs, we decided to fix the CTAB concentration during the phase transfer at 28 mM, as well as the [CTAB]:[TEOS]:[NaOH]:[H₂O] molar composition at 1:4,9:1,1:5983, and to vary only the amount of IO NPs added in the reaction media. For these experiments, the same IO NPs batch was used. This batch, presented in Figure 5-14, exhibited spherical IO NPs with an average size of $9 \pm 1,2$ nm (*i.e.* $\pm 14\%$, average size obtained from the measurement of 300 particles on TEM images) and after sufficient washing (see Chapter 3) was dispersed in chloroform at a concentration of 1,835 g Fe/mL (concentration measured by ICP-AES). In order to vary the [CTAB]/[Fe] ratio, we added to the 50 mL of CTAB solution at 28 mM, 3, 2 and 1 mL of IO10 NPs, leading to [CTAB]/[Fe] ratios of 14, 21 and 43 respectively. For each molar ratio four batches were realized to study the reproducibility of the process.

Figure 5-15 shows the TEM images, with their respective size distributions in inset, of the quadruplets obtained for each [CTAB]/[Fe] molar ratio of 14, 21 and 43. Table 5-2 summarizes the mean sizes of the IO10@RB NPs obtained during these experiments. As expected, the IO10@RB NPs size increased with the [CTAB]/[Fe] molar ratio: the average diameter of IO10@RB NPs was 32 ± 3 , 42 ± 11 and 59 ± 7 nm for [CTAB]/[Fe] molar ratios of 14, 21 and 43 respectively. Furthermore, a good size reproducibility was only observed for the smallest [CTAB]/[Fe] molar ratio of 14, while for higher molar ratios the presence of few double-core NPs was sometimes observed. For the highest molar ratio of 43, some RB NPs without IO cores were also obtained for some batches as by-products. This last observation agrees with the results reported by Ye *et al.* (115).

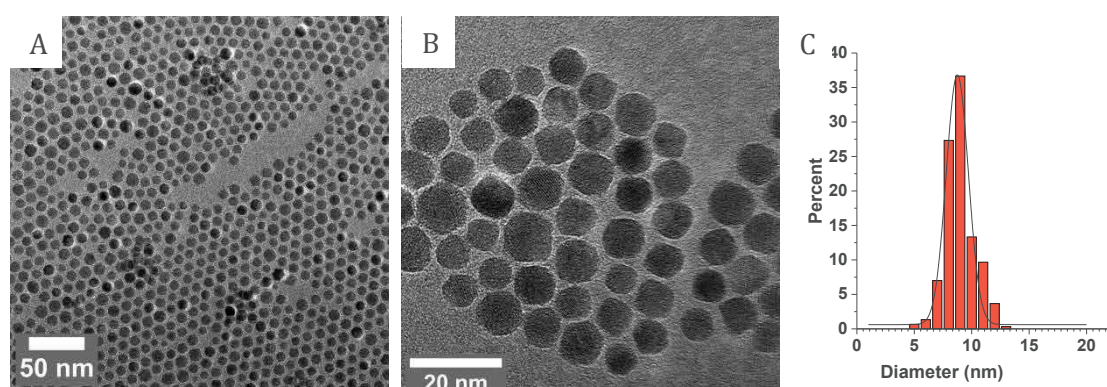


Figure 5-14: A) B) TEM images of IO NPs C) Particle size distribution of IO NPs from TEM pictures (300 particles)

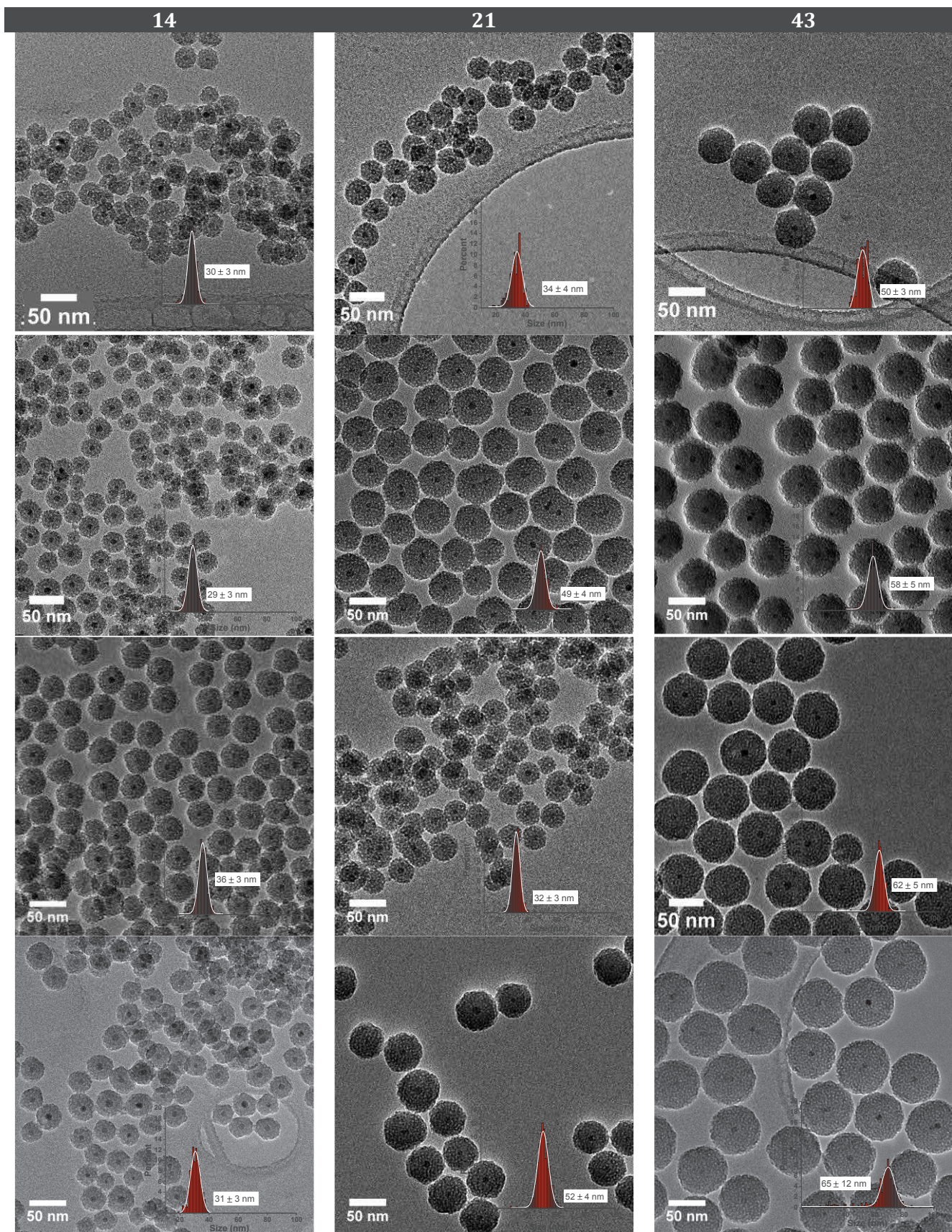


Figure 5-15: TEM images of the quadruplets IO@RB NPs syntheses obtained at different [CTAB]/[Fe] ratio 60, 90, 180) with their TEM size distribution in inset.

Table 5-2: Summary of the mean diameters of IO@RB NPs obtained by varying [CTAB]/[Fe] ratio

Ratio [CTAB]/[Fe]	d TEM (nm)	σ	d _{average} TEM (nm)
14	30 ± 3	10 %	32 ± 3
	29 ± 3	10 %	
	36 ± 3	8 %	
	31 ± 3	10 %	
21	34 ± 4	12 %	42 ± 11
	49 ± 4	8 %	
	32 ± 3	9 %	
	52 ± 4	8 %	
43	50 ± 3	6 %	59 ± 7
	58 ± 5	9 %	
	62 ± 5	8 %	
	65 ± 12	18 %	

2.2 Washing steps versus calcination

As explained previously, the mesoporous silica shell formation around IO core involved the use of a high amount of CTAB for phase transfer and pore templating. As pictured in Figure 5-16, CTAB like other cationic surfactants, is typically composed of two major domains: a positive charged headgroup and a hydrophobic tail.

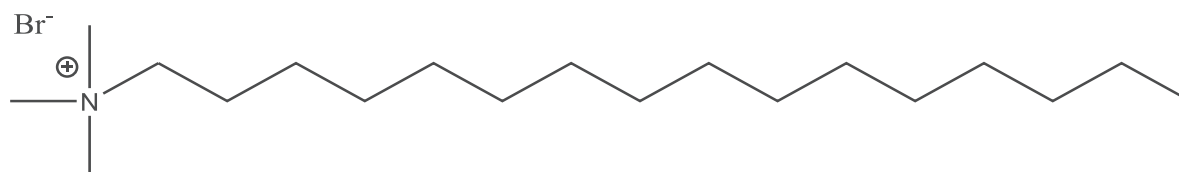


Figure 5-16: Chemical structure of CTAB

Both hydrophilic headgroup and hydrophobic tail may induce toxicity (276). First the contribution of hydrophobic tail on toxicity has not been fully understood yet, however the trend that single-tailed cationic surfactants are more toxic than their double-tailed counterparts seemed to be verified in several cases. Indeed Pinnaduwa *et al.* (277) reported that CTAB was more toxic than DOTMA and showed a very high *in-vitro* cytotoxicity at a concentration of 20 $\mu\text{g/mL}$ after 3 h incubation on L929 cells (mouse fibroblast cells). Besides the toxic effect of the hydrophobic tail, the cytotoxicity is mainly determined by the structure of the hydrophilic headgroup: the quaternary amine headgroup, presents in CTAB, is more toxic than tertiary amine (276).

Thus we investigated the cytotoxicity of free CTAB on the human cells commonly used in our studies: Kelly, Huh7-luc and A549-luc cells. MTT assays were performed on these three cell lines at 24h and 48h on triplicates of various CTAB concentrations. The measurements were carried out twice on Huh7-luc and Kelly cells but only once on A549-luc cells. The 100 % of cell viability was calculated from non-treated cells and the 0 % was calculated from cells treated with Triton, so we subtracted the absorbance values obtained at 595 nm with these cells to the other results. Figure 5-17 showed the resulting cell viabilities versus CTAB concentrations for the three cell lines. No major difference between cytotoxicity at 24 and 48 h was noticeable for the three cell lines suggesting that the toxicity of CTAB occurs in a short time period. Furthermore, Kelly cells

appeared to be the most sensitive to CTAB with a CTAB concentration at 50% of cell viability around 0.5 $\mu\text{g}/\text{mL}$ and very high toxicity for CTAB concentrations over 3 $\mu\text{g}/\text{mL}$. Huh7-luc and A549-luc showed higher toxicity resistance with CTAB concentration at 50 % of cell viability around 5 $\mu\text{g}/\text{mL}$ and 2 $\mu\text{g}/\text{mL}$ respectively and very high toxicity for CTAB concentrations over 10 $\mu\text{g}/\text{mL}$ for both. These cytotoxicity values are similar to those reported in the literature: CTAB IC_{50} on HeLa cells after 24h was found to be about 9.1 μM (*i.e.* 3 $\mu\text{g}/\text{mL}$) (278), on K562 cells (human leukemic cells) Connor *et al.* reported a CTAB IC_{50} around 0.01 μM (*i.e.* 0.003 $\mu\text{g}/\text{mL}$) after 3 days of incubation (279) and on the same cells Cortesi *et al.* found a IC_{50} of 0.62 μM (*i.e.* 0.21 $\mu\text{g}/\text{mL}$) after 5 days (280).

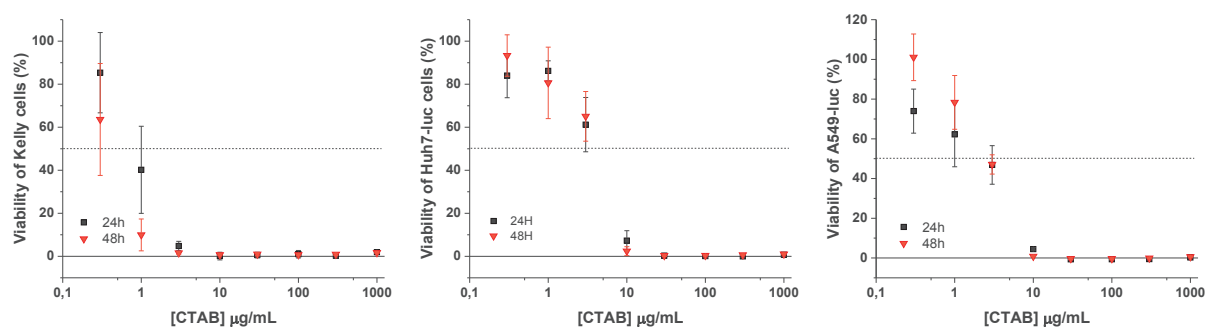


Figure 5-17: Viabilities of A) Kelly, B) Huh7-luc and C) A549-luc cells after 24 and 48h incubation

To overcome this toxicity effect, washing steps after IO@RB NPs synthesis are highly needed to remove efficiently CTAB. One direct and efficient procedure to remove entirely the CTAB molecules is to perform a calcination of IO@RB NPs after synthesis in the same way that we did for silica NPs with no IO core (see Chapter 4). In this previous calcination procedure, the silica NPs were heated up to 550 $^{\circ}\text{C}$ with a heating rate of 5 $^{\circ}\text{C}/\text{min}$ and kept at this temperature for 6 h. The calcination must be run under air atmosphere to burn the CTAB carbon chains into CO_2 . The problem of applying this calcination process for CTAB elimination to our IO@RB NPs is that the IO core, majority made of oxidized magnetite, may oxidize completely in maghemite around 160 $^{\circ}\text{C}$ (61) and perhaps may transform in hematite reaching temperatures around 500 $^{\circ}\text{C}$ (281). To decrease the calcination temperature in order to limit IO phase transformation, we investigated CTAB calcination by TGA. The TGA curve of pure CTAB, Figure 5-18, showed that the calcination of CTAB started at 200 $^{\circ}\text{C}$ and was completed around 300 $^{\circ}\text{C}$. According to this observation we decided to calcine our samples at 260 $^{\circ}\text{C}$ for 2h. Unfortunately, even if the CTAB surfactant molecules were well calcined, the IO@RB NPs were very difficult to redisperse in solvent after calcination due to their aggregation.

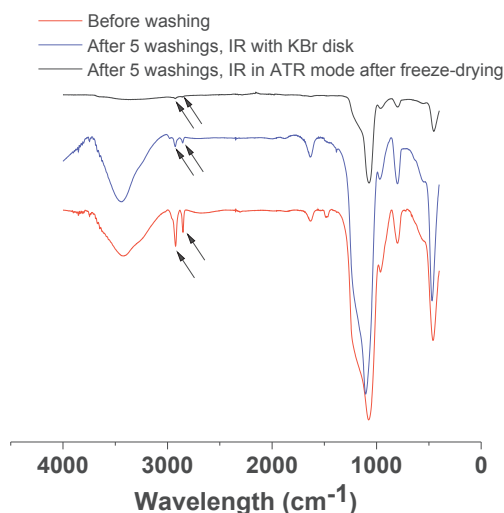


Figure 5-20: IR spectra of IO@RB NPs before CTAB washing, after 5 nitrate ammonium washings in KBr disks and after 5 nitrate ammonium washings and freeze-drying in ATR mode

2.3 Characterization of IO@RB NPs

Through the previous described protocol, we were able to successfully synthesize porous monodisperse IO@RB NPs with tunable silica shell thickness. For example, the three samples choose for illustration showed an increase in shell thickness: Sample 1 (Figure 5-21 A,D) < Sample 2 (Figure 5-21 B,E) < Sample 3 (Figure 5-21C,F). By measuring the sizes of these NPs from TEM images on more than 200 particles, the average diameters obtained were about 31 ± 3 nm, 58 ± 5 nm and 84 ± 7 nm for sample 1, 2 and 3 respectively. The resulting size distribution histograms, Figure 5-22, showed sharp peaks for each IO@RB NPs batch, representative for monodispersed NPs, with Gaussians centered on 31, 59 and 86 nm. By simplification, regarding these size measurements, we called these samples IO@RB 30 nm, IO@RB 60 nm and IO@RB 85 nm (IO@RB 30 and 85 nm will be used later for biological studies in section 6 page 167).

DLS measurements of these IO@RB NPs highlight their colloidal stability in water with mean hydrodynamic sizes centered at 60, 80 and 105 nm for IO@RB NPs of 30, 60 and 85 nm respectively. Thus, the hydrodynamic sizes were between 20 and 30 nm higher than the sizes measured from TEM images. After HSA coating of IO@RB NPs via IBAM grafting (see detailed protocol in Chapter 2 page 58) the resulting IO@RB-HSA NPs showed little aggregation by an increase of the secondary hydrodynamic size but were still stable in water with mean hydrodynamic diameters similar to those measured on IO@RB before HSA coating.

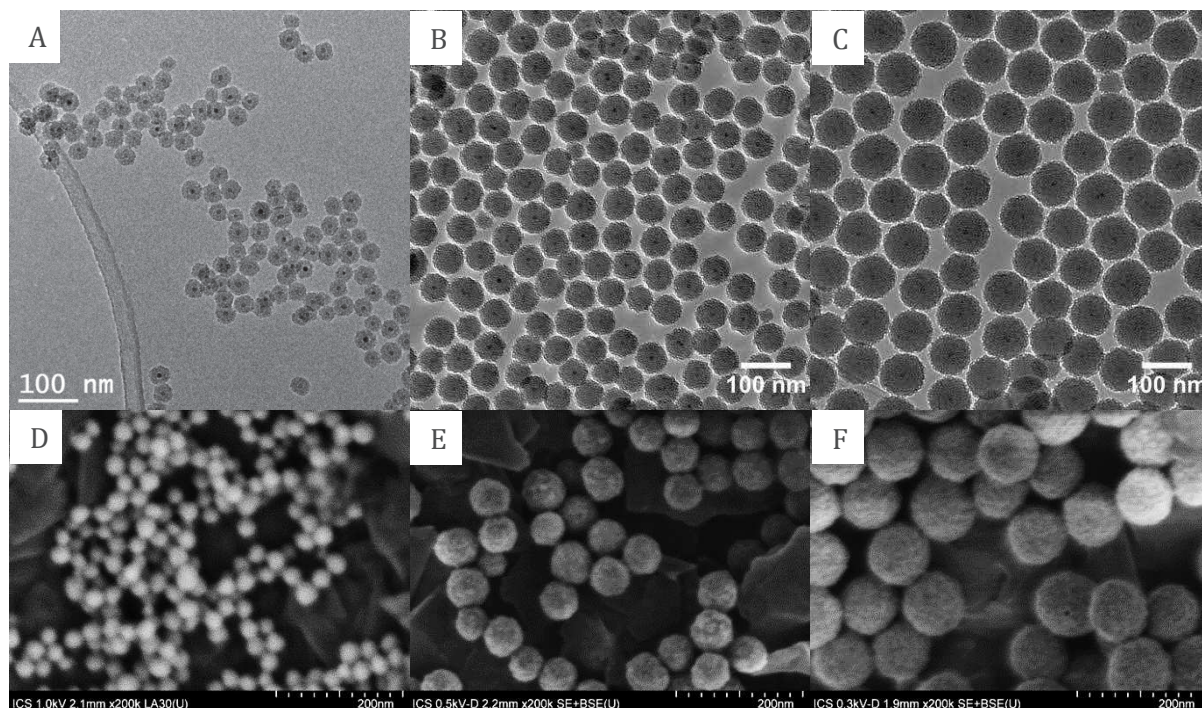


Figure 5-21: TEM (A, B, C) and SEM (D, E, F) images of IO@RB of 31 ± 3 nm (A, D), 58 ± 5 nm (B, E), 84 ± 7 nm (C, F)

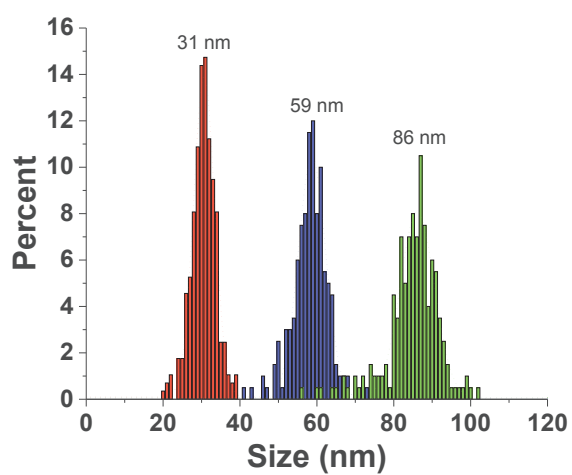


Figure 5-22: Histograms and Gaussians of the size distribution measured from TEM images for IO@RB NPs of 30, 60 and 85 nm

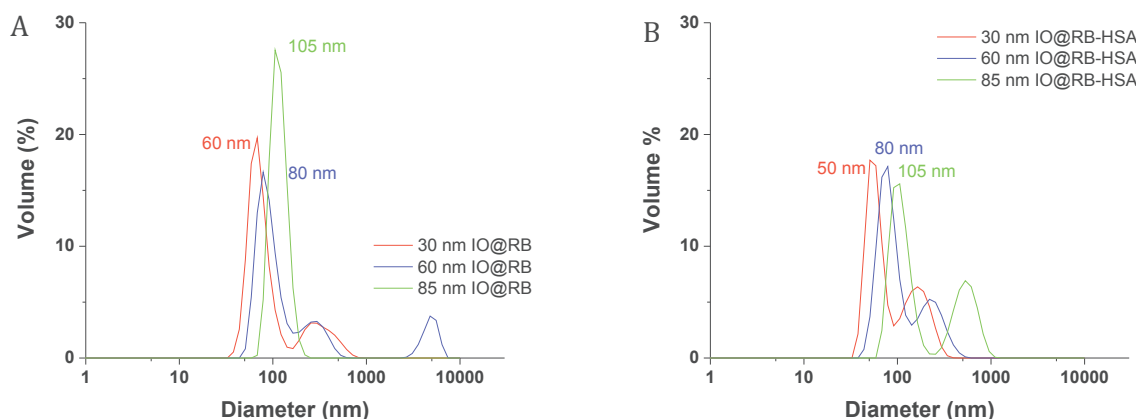


Figure 5-23: DLS measurements in volume (%) of A) IO@RB and B) IO@RB-HSA of various sizes (30, 60 and 85 nm) dispersed in Milli-Q water

As depicted in Figure 5-24 A, the IO@RB NPs exhibited the expected type IV isotherm typical for mesoporous materials. The corresponding PSD curve, obtained through BJH calculations, shows pore sizes about 2.3 nm. Table 5-3 summarizes the pore parameters of three of our samples obtained by BET analyses. All of the analyzed IO@RB samples showed porosities around 2.3 nm. However, excepted for the sample of 65 nm, the specific surface areas of ~ 120 m²/g were lower than the reported values or the value of the previous IO@RB sample obtained with non-optimized protocol (see Table 5-1 page 128). This difference was not due to some residual CTAB that obstructed the porosities because IR spectra in ATR mode, obtained from these freeze-dried samples before BET analyses, assessed of efficient CTAB removal by nitrate ammonium treatment. Nevertheless, specific surface areas of 100 m²/g are suitable for the loading and release of drug molecules. We also noticed, that the BET analyses of IO@RB NPs were tricky to execute as only 3 batches on 6 tested gave interpretable results. Furthermore, as these NPs are very small in size, large signal was obtained for porosities higher than 10 nm resulting from the interparticle voids. Thus, to get a more precise pore volume values we measured the pore volumes obtained for sizes below 4 nm.

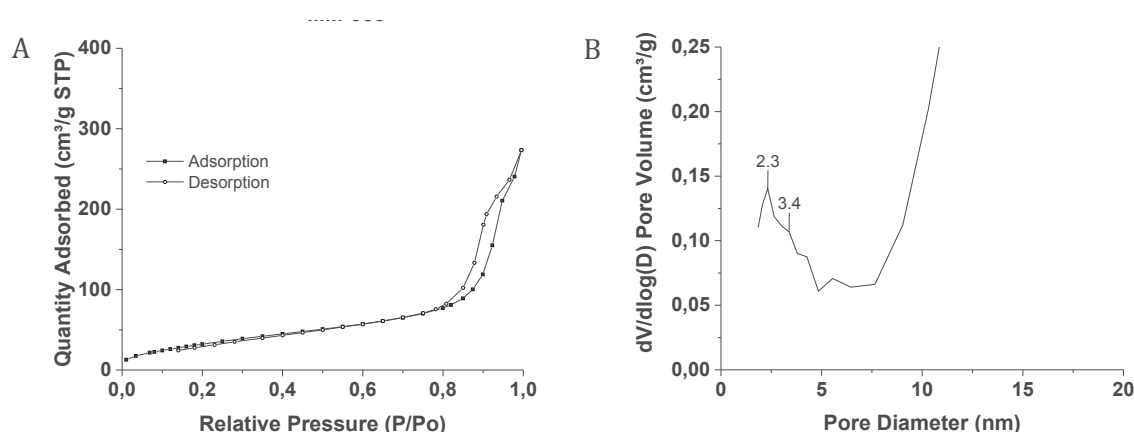


Figure 5-24: A) N₂ adsorption-desorption isotherms and B) corresponding PSD curve for IO@RB NPs

Table 5-3: Summary of pore parameters obtained from N₂ adsorption-desorption analyses for three of our IO@RB samples

Size (nm)	S _{BET} (m ² /g)	V _{total} (cm ³ /g)	V _{<4nm} (cm ³ /g)	D _{BJH} (nm)
65 ± 12	436	0.56	0.29	2.3
51 ± 4	117	0.34	0.04	2.4
52 ± 4	129	0.37	0.04	2.3

3 Evaluation of MRI contrast properties of IO@RB and IO@RB-HSA

In this part, the MRI diagnosis capacities of our theranostic nanosystems were investigated. Indeed, thanks to the superparamagnetic properties of the magnetite core of 9 ± 0.8 nm, the IO@RB and their corresponding HSA coated NPs, synthesized according to the procedure detailed in Chapter 2 page 58, could be used as T₂ contrast agent.

This property was assessed by proton NMR relaxometry at 37 °C and 1.41 T (60 MHz) on silanized, IO@RB-NH₂, and protein-coated, IO@RB-HSA, NPs with a global size of 41 ± 3 nm and IO core of 9 ± 0.8 nm. These NPs were dispersed in PBS buffer in order to avoid pH variation between measurements. Longitudinal (T₁) and transverse (T₂) relaxation times of protons were measured at various Fe concentrations, [Fe]. The highest [Fe] was measured initially by ICP-AES, and lower [Fe] were obtained by cascade dilution. The resulting relaxivity curves 1/T₁ and 1/T₂ in function of [Fe], presented in Figure 5-25, showed, as expected, a very linear behavior. The slopes of the linear fit of these curves gave the r₁ and r₂ values for the IO@RB-NH₂ and IO@RB-HSA NPs.

For the IO@RB-NH₂ the r₁ and r₂, 0.13 mM⁻¹s⁻¹ and 26.4 mM⁻¹s⁻¹ respectively giving a r₂/r₁ ratio of about 201, were very low compared to published values, see Table 1-7 page 29. Indeed, Ye *et al.* obtained such range of values for raw 95 nm IO@RB NPs with 11 nm IO core, whereas for raw 50 nm IO@RB NPs they found higher r₁ and r₂ of 1.31 mM⁻¹s⁻¹ and 92.13 mM⁻¹s⁻¹ giving a lower r₂/r₁ ratio of 70.3 (115). However, the silanized IO@RB-NH₂ NPs are particularly unstable at pH 7.4 in PBS. As it was already the case for the IO-APTS NPs, see page 71, the IO@RB-NH₂ NPs tended to aggregate under the magnetic field during the measurements. Even if mechanical redispersion of the suspensions by gently shaking between the measurements led to reproducible T₁ and T₂ values and very linear 1/T₁ and 1/T₂ curves, these values could be distorted by this strong aggregation and were maybe representative for clusters instead of single NPs.

The corresponding IO@RB-HSA NPs were more stable at pH 7. The specific relaxivity values obtained for those HSA coated NPs were of r₂ 116 mM⁻¹s⁻¹ and r₁ 0.083 mM⁻¹s⁻¹ giving a r₂/r₁ ratio of 1397. So compared to the same NPs but with amino-modified surface, IO@RB-NH₂ NPs, the addition of HSA coating increased the T₂ contrast agent properties of the system by decreasing the r₁ and increasing the r₂ leading to an impressively high r₂/r₁ ratio. This r₁ decrease can be explained by limited water accessibility to the magnetic core due to the tight HSA coating.

To confirm this result, the relaxometry measurements were reproduced on another IO@RB-HSA batch with IO core of 9 ± 1 nm. The new batch was a bit lower in size than the previous one with a diameter of 30 nm. As depicted in Figure 5-26, the r₁ value of 0.15 mM⁻¹s⁻¹ was not as low

as the previous one. But, this result is not surprising as the NPs were smaller in size, which means that the silica shell was smaller, so the water accessibility to the magnetic core was less limited. Furthermore the r_2 was still high with a value of $70 \text{ mM}^{-1}\text{s}^{-1}$ leading to a r_2/r_1 ratio of 467 which is still very high compared to the literature.

Furthermore, in our previous study on the same sizes of IO NPs but coated with APTES and TPEDTA, we obtained respectively a r_1 of $15.2 \text{ mM}^{-1}\text{s}^{-1}$ and a r_2 of $102.6 \text{ mM}^{-1}\text{s}^{-1}$ at pH 3.5, Figure 3-6, and a r_1 of $13.9 \text{ mM}^{-1}\text{s}^{-1}$ and a r_2 of $88.6 \text{ mM}^{-1}\text{s}^{-1}$ at pH 7.5, Figure 3-7. So our studies on IO@RB-HSA NPs showed that the RB-HSA coating on the IO NPs did not modify the r_2 value but strongly decrease the r_1 explaining the obtaining higher r_2/r_1 ratio.

Finally, in both cases the r_2 values of IO@RB-HSA were in the same range than r_2 of commercial IO, $120 \text{ mM}^{-1}\text{s}^{-1}$ for Feridex, $186 \text{ mM}^{-1}\text{s}^{-1}$ for Resovist and $65 \text{ mM}^{-1}\text{s}^{-1}$ for Combidex (cf Table 1-5 page 21), but they exhibited higher r_2/r_1 ratio due to the low r_1 induced by the silica coating. Thus these results place our system as potential candidate as T_2 contrast agents.

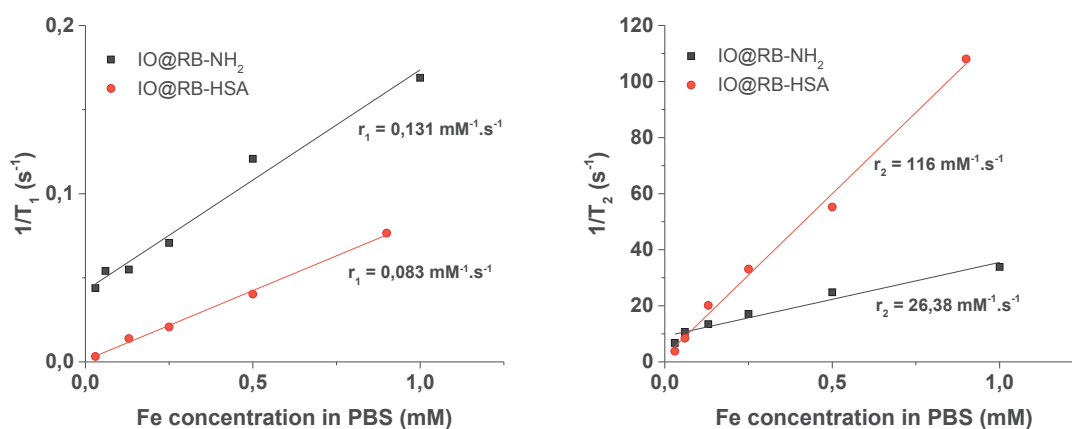


Figure 5-25: T_1 and T_2 relaxometry curves of IO@RB and IO@RB-HSA NPs of 41 nm in diameter

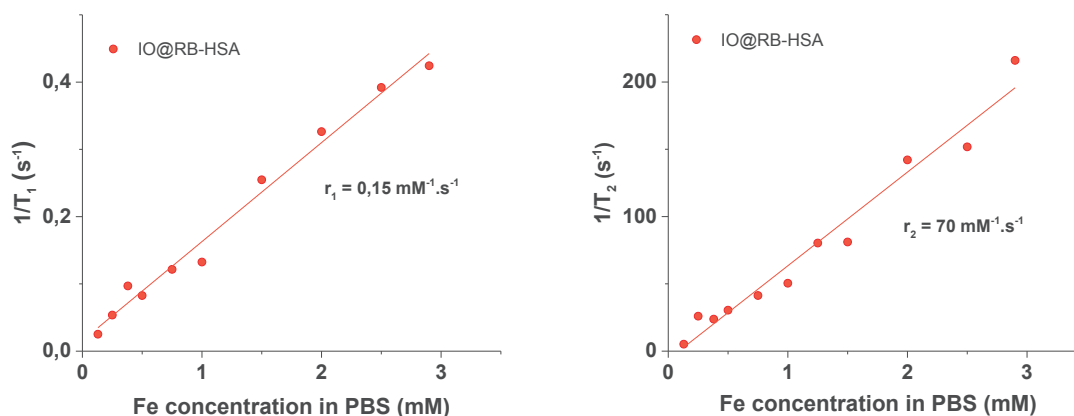


Figure 5-26: T_1 and T_2 relaxometry curves of IO@RB-HSA NPs of 30 nm in diameter

4 Dox impregnation and release studies

4.1 Introduction

In the previous part we demonstrated through relaxometry measurements that our IO@RB-HSA NPs may be used as T₂ contrast agent. But in order to make them good candidates as theranostics agents, their cargo capacities for drug delivery have to be tested.

4.2 Dox impregnation in the porosities

As shown in Table 1-8 page 33, the silica shell surface modification and the choice of solvent influence the Dox loading.

The goal of this part was to study the Dox amount loaded into the porosities of the silica shell of IO@RB NPs. First the influence of the silica shell surface modification on Dox loading was investigated. Regarding our synthesis protocol we have the possibility to load the Dox in IO@RB NPs either after the modification of the silica shell surface with IBAM moieties, *i.e.* in IO@RB-IBAM NPs, or before when the silica shell surface was modified with APTES, *i.e.* in IO@RB-NH₂ NPs. The loading was first investigated in DMF for IO@RB NPs modified with either NH₂ or IBAM moieties (IO@RB-NH₂ and IO@RB-IBAM respectively). Then the influence of the solvent, water EtOH 70 % and DMF, on Dox impregnation into the porosities of IO@RB-NH₂ was investigated and the previous trend observed for the influence of surface modification was once more confirmed.

4.2.1 Influence of the surface modification

The study of Dox loading into IO@RB-NH₂ NPs compared to IO@RB-IBAM NPs in DMF was investigated on 41 ± 3 nm IO@RB NPs. In the procedure 12 mL of raw IO@RB NPs dispersed at 20 µg Fe/mL in absolute EtOH (concentration measured by ICP-OES) were mixed for 2 hours with 1.280 mL of NH₃ and 6 mL of APTES. Then, the particles were washed once with EtOH and twice with DMF by centrifugation and finally dispersed in 9.6 mL of DMF. Half of these silanized particles were kept for the Dox impregnation in IO@RB-NH₂ NPs study, and the remaining 4.8 mL were mixed 2 hours with 960 µL Et₃N and a mixture of IBC:DMF of 1.296 :9.6 mL. After 2 hours of reaction, 1.5 mL of water were added to dissolve the precipitate formed, and the resulting IO@RB-IBAM NPs were washed three times in DMF by centrifugation and finally dispersed in 4.8 mL of DMF. The final concentrations of the resulting NPs were measured by ICP-OES and gave the following similar values of: 44 ± 2 µg Fe/mL and 462 ± 20 µg Si/mL for the IO@RB-NH₂ NPs and 46 ± 4 µg Fe/mL and 449 ± 21 µg Si/mL for the IO@RB-IBAM NPs.

Dox solutions with concentrations varying from 10 µg/mL to 3 mg/mL, which is the maximum Dox solubility in DMF, were prepared. 100 µL of NPs, IO@RB-NH₂ and IO@RB-IBAM respectively, were incubated for 24 h with 100 µL of different Dox solutions. For IO@RB-NH₂ and IO@RB-IBAM solutions at each Dox concentration duplicates were carried out. After 24 h of incubation the NPs were centrifuged, the supernatant concentration was measured by spectrofluorimetry, and a calibration curve allowed deducing the Dox concentration loaded into the particles. After the measurement of [Dox] loaded into the silica porosities of particles for each [Dox] initially fed, and because the concentration in Si atoms was measured by ICP-OES for IO@RB-NH₂ and IO@RB-IBAM NPs, the curves representing the amount of Dox loaded per mg of Si in function of the Dox concentration initially fed were plotted, Figure 5-27 B. These curves clearly showed that the Dox impregnation was more efficient in IO@RB-NH₂ than in IO@RB-

IBAM, suggesting that the amino functionalized silica surface is more suitable for Dox loading into silica porosities.

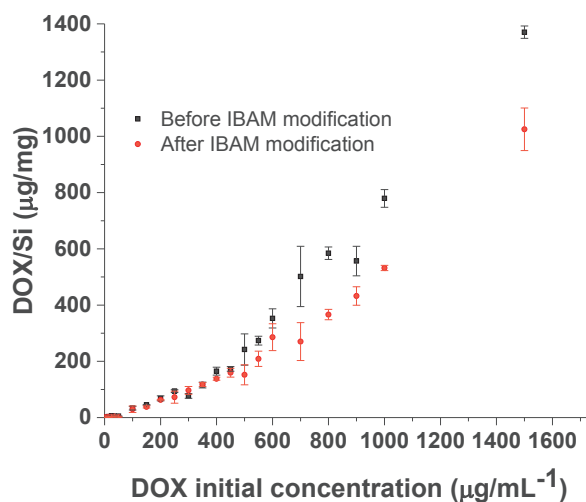


Figure 5-27: Curve of Dox loaded amount per mg of Si in function of the initial Dox incubated for IO@RB-NH₂ and IO@RB-IBAM NPs

4.2.2 Influence of the solvent

4.2.2.1 Experimental procedure

The previous study showed that the silica surface modification influences the Dox loading, and that amino functionalized silica induced higher Dox loading in DMF than the silica modified with IBAM. In the following part we investigated the influence of the solvent on Dox loading. The IO@RB-IBAM NPs can only be soluble in DMF but the in IO@RB-NH₂ NPs can be dispersed in many solvent such as: DMF, water and EtOH. Dox.HCl is soluble in DMF (until 3 mg/mL), water and also in EtOH 70 % (not soluble in absolute EtOH). So the Dox loading was investigated in IO@RB- NH₂ NPs in water in EtOH 70 % and in DMF, and to check the reproducibility of the previous study, Dox impregnation on IO@RB-IBAM NPs in DMF was also carried out.

For this study IO@RB NPs of 50 ± 3 nm were calcined at 260 °C for 2 h in order to first eliminate CTAB, as described in page 136, but mainly to obtain a powder of NPs that we could physically weight before the study to work with precise fwr and calculate the resulting DLC and DLE, as we did for silica NPs without core in Chapter 4. After calcination, the IO@RB NPs were dispersed into absolute EtOH to be silanized following a similar procedure than the one used for RB NPs described in Chapter 4 page 99. After silanization, the IO@RB-NH₂ were separated in 4 batches: the first one was further modified with IBAM and redispersed at 2 mg/mL in DMF, the three others were redispersed at 2 mg/mL in three different solvents, water, EtOH 70 % and DMF. Dox solutions at different concentrations were prepared in these three different solvents, 100 µL of each Dox solution were mixed at room temperature under dark conditions for 24 h with 100 µL of the previous NPs dispersed at 2 mg/mL in the same solvent, in order to obtain NPs dispersed at 1 mg/mL with various Dox fwr. Each fwr was carried out in triplicate.

After 24 h of Dox impregnation, the supernatants were collected by centrifugation and analyzed by fluorescence spectroscopy for the low fwr, and by absorbance ($\lambda = 495$ nm) for the high fwr using a SAFAS spectrophotometer (Monaco). Quantification of the amount of loaded

Dox was calculated from calibration curves made with the Dox solutions at different concentrations used for the experiments. From these measurements, the resulting DLC and DLE curves were plotted, Figure 5-28, Figure 5-29, Figure 5-30 and Figure 5-31.

4.2.2.2 Results and discussions

DLC and DLE curves obtained in water for silanized core-shell particles, IO@RB-NH₂ NPs are shown in Figure 5-28. The DLC curve, Figure 5-28 A, increased almost linearly before reaching a plateau at a maximum of 14 % for fwr values from 12 % to 100 %. The DLE values, shown in Figure 5-28 B, were always very high (over 80 % and mostly over 90 %) before starting to decrease drastically from fwr value of 25 %. These observations suggest that the drug loading is very efficient on IO@RB-NH₂ NPs in water in such a way that almost all the Dox fed initially was loaded into the silica shell porosities until reaching a maximum DLC value of 14 %. So, for fwr values over 15 %, not all the Dox fed can be loaded in the porosities, leading to a DLE decrease.

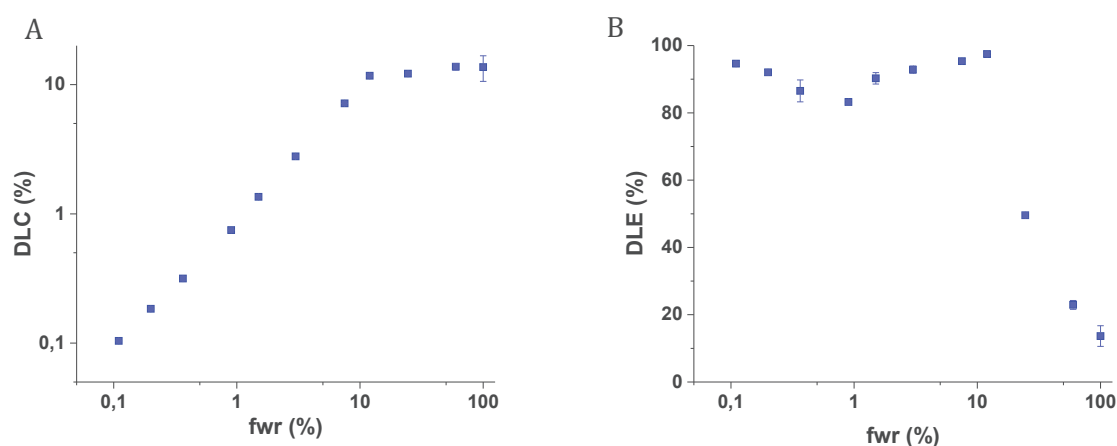


Figure 5-28: Dox impregnation study in porosities of IO@RB-NH₂ in water A) DLC curve B) DLE curve

The DLC curve resulting from Dox loading study in IO@RB-NH₂ NPs in EtOH 70 %, presented in Figure 5-29 A, increased almost linearly until slowing down its increase for fwr values over 5 %. The maximal DLC value observed in this study was 1.6 % for the maximal fwr of 50 %. This maximal DLC value is very low compared to the previous study of Dox loading in the same NPs but in water, in which this DLC value of 1.6 % was obtained for fwr of approximately 2 %. The DLE values associated to this study, Figure 5-29 B, were very low, mostly under 20 %, which proved that EtOH 70 % is not a proper solvent for Dox loading into IO@RB-NH₂ NPs.

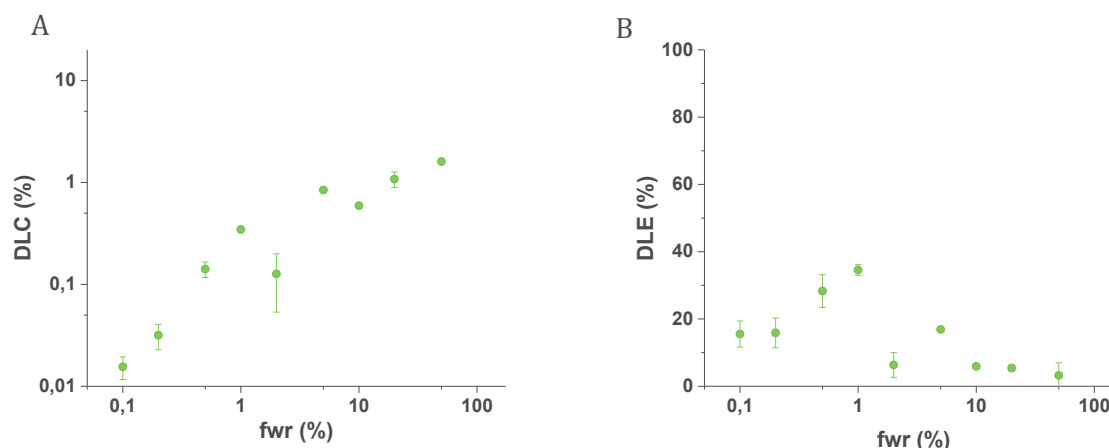


Figure 5-29: Dox impregnation study in porosities of IO@RB-NH₂ in EtOH 70 % A) DLC curve B) DLE curve

The DLC curve corresponding to the Dox loading in IO@RB-NH₂ NPs in DMF, Figure 5-30 A, increased almost linearly without reaching a plateau. So the maximal DLC value of 10 % was reached for the maximal fwr used in the study of 150 %. The DLE values, represented in Figure 5-30 B, were very low, mostly under 40 %, and decreased when fwr increased, to reach the 6 % value for the highest fwr values. From this study we can conclude that the maximum DLC value of 10 % is very close to the maximum value of 14 % obtained for Dox loading in the same NPs in water. But in the DMF this DLC value was reached at fwr 150 % which is the maximal fwr value, whereas in water the maximal value was already reached at fwr 12 %. So the Dox loading in water is 10 times more efficient than the impregnation in DMF.

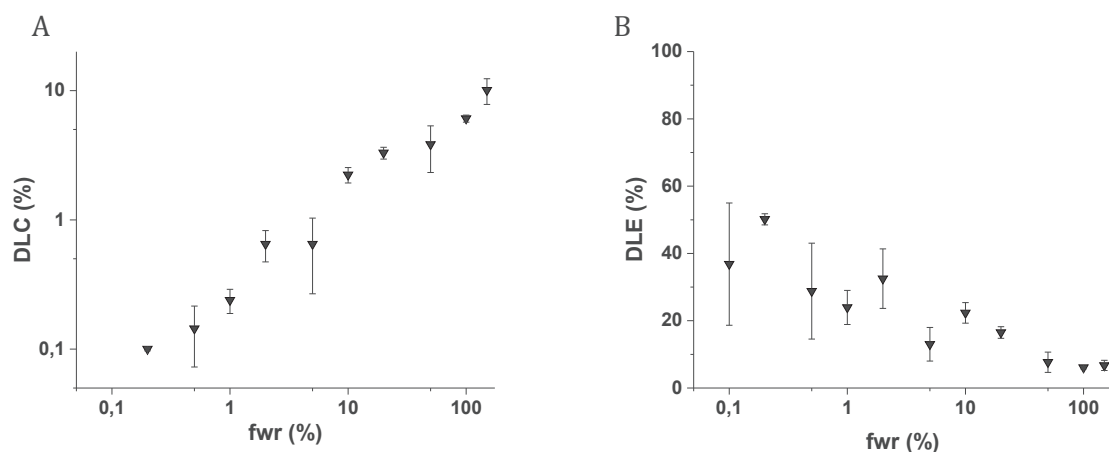


Figure 5-30: Dox impregnation study in porosities of IO@RB-NH₂ in DMF A) DLC curve B) DLE curve

Figure 5-31 shows the DLC (A) and DLE (B) curves for Dox impregnation into IBAM modified IO@RB in DMF. The DLC curve increased until reaching a plateau around 3 % from fwr 20 % to the highest fwr value of 150 %. This loading behavior is very similar to the one observed for IO@RB-NH₂ in water but the DLC plateau is much lower: 3 % compared to 14 % in the previous study. Furthermore, the DLC plateau at 3 % was reached for IO@RB-IBAM NPs in DMF, but for the IO@RB-NH₂ NPs dispersed in the same solvent no plateau was observed and the maximum DLC value of 10 % was reached for fwr 150 %. This result suggested that the silica surface modified with IBAM is less favorable for Dox loading than the amino modified surface. It confirmed the results obtained in the previous study described in section 4.2.1 page 144.

Probably the IBAM moieties, which are bigger than the NH_2 , obstructed more the porosities of the silica shell leading to a lower drug loading capacity. Concerning the DLE results for the Dox loading study on IO@RB-IBAM NPs in DMF, Figure 5-31 B, the values are mostly very low and stayed under 20 % for fwr values over 1 %, and were around 2 % for fwr 100 and 150 %. So the Dox impregnation in IO@RB-IBAM NPs in DMF was not very efficient.

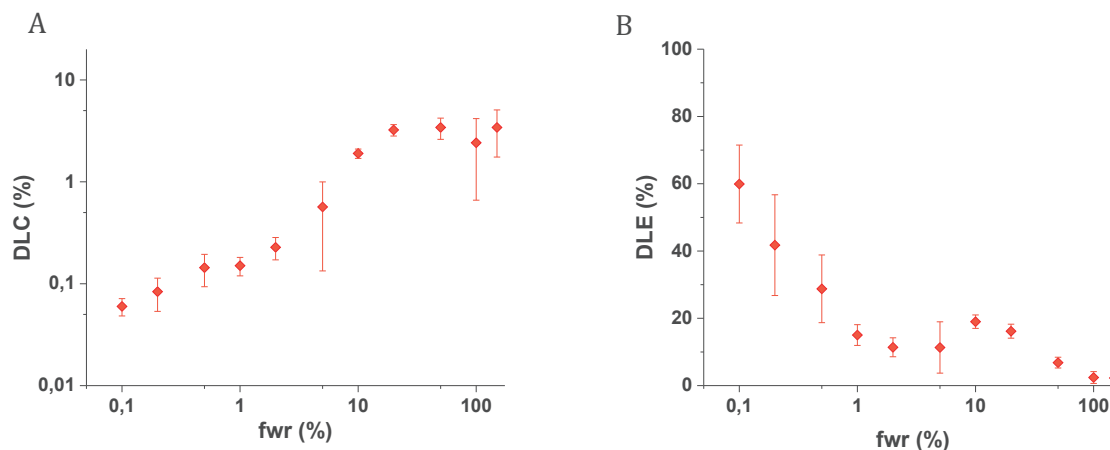


Figure 5-31: Dox impregnation study in porosities of IO@RB-IBAM in DMF A) DLC curve B) DLE curve

4.2.3 Conclusions on Dox impregnation studies

To conclude, these studies showed that the Dox loading content was higher in IO@RB modified with NH_2 than with IBAM. Comparing the Dox loading on IO@RB- NH_2 in different solvents, it appeared that for loading both in DMF and water, high DLC of 10 and 14 % were reached respectively. But very high DLE was only observed for the impregnation in water, which implied that the maximal DLC was reached around fwr 15 % in water, whereas it was reached at fwr 150 % in DMF. Thus the use of water solvent led to high DLC value at low fwr, thanks to high DLE, and so avoided the waste of Dox during the synthesis process compared to the impregnation in DMF.

Finally, to highlight the trend according to which the impregnation of Dox works better in water on IO@RB NPs modified with NH_2 , Figure 5-32 shows the comparison of DLC values obtained at fwr 50 % during the previous studies. It clearly shows that at this fwr the DLC reached high values only for IO@RB- NH_2 NPs in water. Furthermore, we can notice that the maximum DLC value around 14 %, reached for fwr value around 15 %, is very similar to the result obtained on the same systems without IO core, i.e. on RB- NH_2 NPs. Indeed, in the Dox loading study on RB- NH_2 NPs of 33 ± 4 nm in size, the highest DLC value was around 13 % and was already reached for fwr value between 10 and 20 %. So the presence of IO core in the nanosystems does not modify the drug loading behavior.

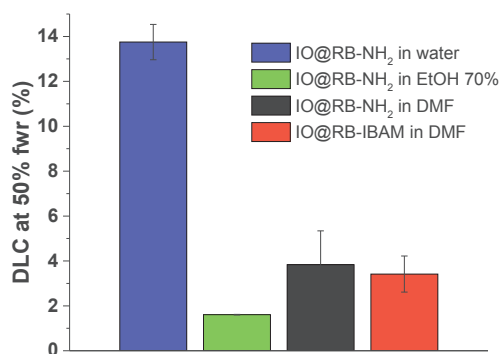


Figure 5-32: Comparison of DLC values at fwr 50% obtained for Dox impregnation in IO@RB NPs with surface modified with APTES in water, EtOH 70% and DMF and with surface modified with IBAM in DMF

4.3 Dox release studies

4.3.1 Concept validation: degradation of the protein shell

Applying the synthesis process detailed in Chapter 2 page 58, IO@RB NPs were coated with HSA^{FITC} through IBAM grafting. To assess the presence of HSA on IO@RB-HSA^{FITC} NPs confocal microscopy imaging was performed in dried conditions. As shown in Figure 5-33, the NPs exhibited a green fluorescence issued from the labelling of HSA with FITC. Thus, HSA coating on IO@RB NPs was efficient.

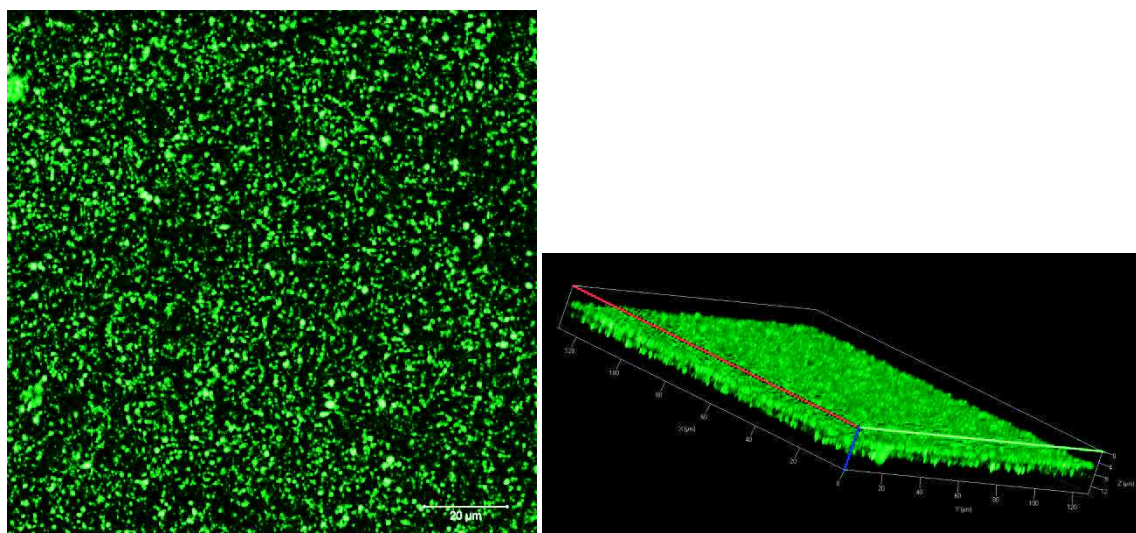


Figure 5-33: CLSM imaging of IO@RB-HSA^{FITC} NPs with the green channel displaying the FITC fluorescence

To demonstrate the bio-responsiveness of the protein nanocoating for controlled drug delivery IO@RB-HSA^{FITC} NPs were incubated with protease solutions at various concentrations. Releases of FITC-labelled-HSA were followed by spectrofluorimetry at 520 nm fluorescence emissions. Figure 5-34 shows the different kinetic releases of HSA^{FITC} at 37 °C obtained with various concentrations of proteases in PBS buffer (25, 50 and 100 μg.mL⁻¹) over 42 hours. Two controls without proteases were also studied, a first one at 37 °C and a second one at 50 °C. For control experiments, no significant fluorescence increase with time was observed, whereas in the presence of proteases HSA^{FITC} was observed to be progressively degraded. These results

confirmed that the shell is stable in time and that the proteases are necessary for the shell degradation. Furthermore, the higher the proteases concentration, the faster the HSA^{FITC} degradation. Indeed, a fluorescence intensity plateau was reached at the highest proteases concentration, 100 $\mu\text{g}\cdot\text{mL}^{-1}$, after 22 h, whereas for the protease concentration of 50 $\mu\text{g}\cdot\text{mL}^{-1}$, the same plateau was reached after 42 h.

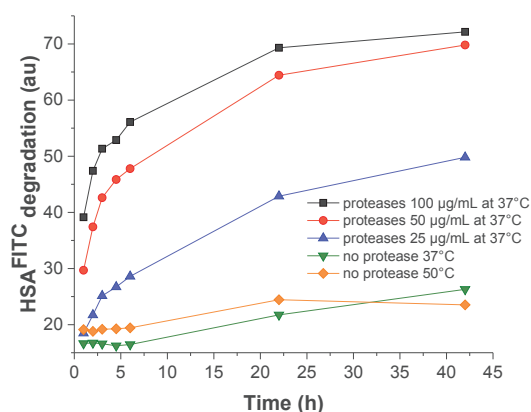


Figure 5-34: Kinetic profiles of HSA^{FITC} degradation under various proteases concentration at 37 °C (25, 50 and 100 $\mu\text{g}/\text{mL}$) and control experiments without proteases at 37 °C and 50 °C

4.3.2 Dox release trials

IO@RB NPs of 49 ± 4 nm in size were used to investigate the Dox release after HSA shell enzymatic degradation. For these experiments Dox was loaded either into IO@RB-NH₂ NPs in water or into IO@RB-IBAM NPs in DMF. A sample without Dox but with FITC-labelled HSA was also prepared. For each sample the typical procedure for HSA coating was followed as explained in Chapter 2 page 58. The sample without Dox but containing HSA^{FITC} was called IO@RB-IBAM-HSA^{FITC}, the sample containing the Dox loaded into IO@RB-NH₂ was called IO@RB-Dox-IBAM-HSA and the sample containing the Dox loaded into IO@RB-IBAM was called IO@RB-IBAM-Dox-HSA. After the synthesis, the samples were dispersed in the same water volume to reach the same concentrations. Then, the NPs were incubated at 37 °C in PBS at pH 7.4 with various proteases concentrations: 1000, 500 and 100 $\mu\text{g}/\text{mL}$. At predetermined time intervals, the mixtures were centrifuged and the supernatants were analyzed by fluorescence spectroscopy with $\lambda_{\text{exc}}=488$ nm and $\lambda_{\text{em}}=520$ nm for IO@RB-IBAM-HSA^{FITC} and with $\lambda_{\text{exc}}=488$ nm and $\lambda_{\text{em}}=595$ nm for the Dox-loaded samples. Figure 5-35 shows the HSA degradation and Dox release profiles of the samples. The HSA degradation profile under enzymatic degradation was similar to the previous one described in Figure 5-34, which proved the efficient HSA degradation under proteases action at this sample concentration. For the Dox release curves, the NPs incubated with proteases showed a slightly higher, but not significant, Dox release than the controls. But, we observed that the proteases alone exhibited also small fluorescence which can explain the small differences in Dox release measurements between the NPs incubated with a high proteases amount, with a low proteases amount and the controls. So to conclude, no significant Dox release was observed for IO@RB-Dox-IBAM-HSA and IO@RB-IBAM-Dox-HSA samples despite the HSA shell degradation certified by the study on IO@RB-IBAM-HSA^{FITC} sample.

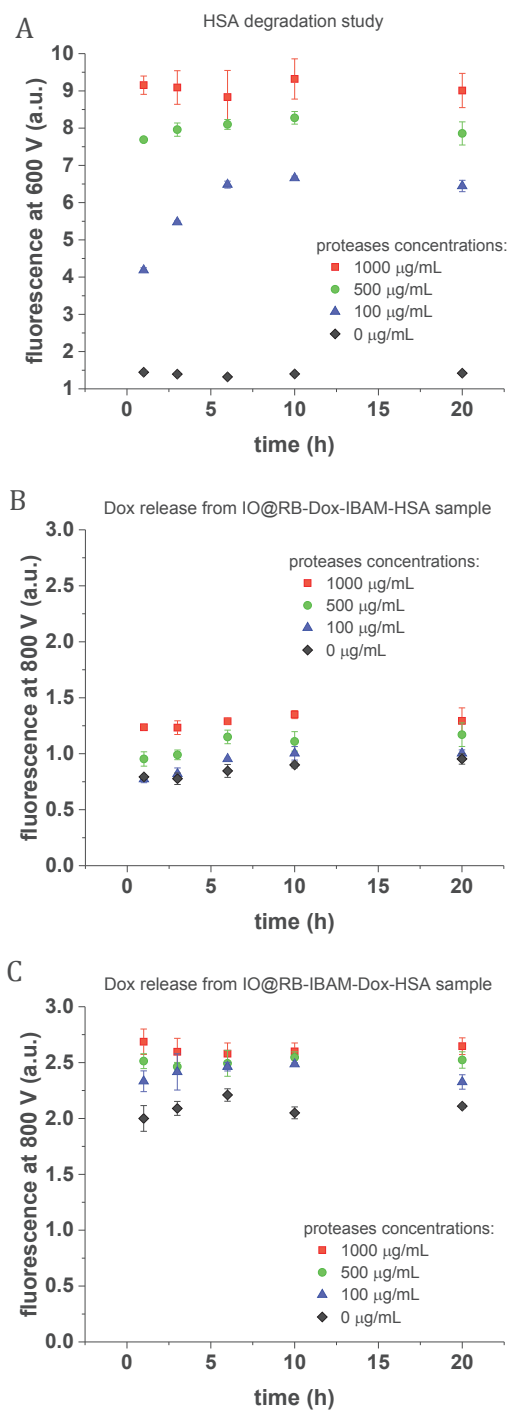


Figure 5-35: Kinetic profiles under various proteases concentration at 37 °C in PBS at pH 7.4 of A) HSA^{FITC} degradation, B) Dox release from IO@RB-Dox-IBAM-HSA sample, C) Dox release from IO@RB-IBAM-Dox-HSA sample

5 Dox encapsulation in IO@RB NPs by IBAM-HSA versus HSA-IBAM-HSA coatings

5.1 Introduction

Regarding the results of the previous Dox loading and release studies we were facing two major interrogations:

- The final amount of Dox encapsulated in NPs was very hard to measure, which led to this crucial question: is there still enough Dox into silica porosities after the all synthesis steps to run the release studies?
- In the case where significant amounts of Dox were present in the silica porosities, how can we explain that no Dox release can be observed after HSA degradation with proteases?

The first question is about finding a right procedure to measure precisely the Dox encapsulated content. Indeed, the measurement of the Dox loaded into the porosities by supernatant analysis is a very good estimation for the Dox loaded directly after the impregnation but did not inform about the potential Dox releases during the further synthesis steps (IBAM surface modification and HSA coating). So we do have no real measurement of the final Dox encapsulated into the NPs. To overcome this issue we decided to synthesize for each final Dox loaded NPs batch the exact equivalent sample produced following the exact same protocol but without the step of Dox loading. The idea was to run TGA analyses on both samples and to measure the difference in weight loss between them which should correspond to the weight of the Dox molecules loaded into the NPs. Furthermore, experimental observations showed that the washing steps in the typical procedure to form the IBAM-HSA coating after the Dox loading, led to massive Dox leakage. Herein, we developed a new procedure to decrease the amount of washing steps.

For the second point we were wondering if the IBAM moieties created on silica surface were not closing the porosities prohibiting the Dox to diffuse outside after the HSA shell degradation by proteases. To verify this hypothesis we decided to try a new coating strategy: HSA was first adsorbed on silica surface immediately after Dox loading. Then IBAM and HSA synthesis steps were further conducted. This should create a HSA-IBAM-HSA coating with the IBAM moieties bonding on HSA instead of directly on silica surface. With this strategy, after enzyme HSA degradation the silica surface should be free of molecules able to obstruct the porosities.

5.2 Protocols and observations

5.2.1 Synthesis of IO@RB NPs of 30 nm

The protocol, previously described in part 2 page 134, with a [CTAB]:[TEOS]:[NaOH]:[H₂O] molar composition of 1:4,9:1,1:5983 and [CTAB]/[Fe] ratio of 14 was used to synthesize IO@RB NPs of approximately 30 nm in diameter. Two batches of IO@RB NPs were synthesized.

5.2.2 Silanization of the batches

After CTAB elimination via ammonium nitrate ion exchange, the two batches of IO@RB NPs were both dispersed in 30 mL of EtOH and mixed overnight with 960 μ L NH₃ and 4.5 mL of

APTES. Then the particles were washed by centrifugation 3 times in EtOH and 3 times in water. The IO@RB-NH₂ NPs were finally dispersed in 25 mL in Milli-Q water.

5.2.3 Synthesis of IO@RB-Dox-HSA-IBAM-HSA and IO@RB-Dox-IBAM-HSA NPs

5.2.3.1 Dox loading

5 mL of each previous IO@RB-NH₂ NPs in Milli-Q water were mixed 24 h with 5 mL of Dox at 1 mg/mL in Milli-Q water. After 24 h of mixing, the solution was still red and homogeneous, Figure 5-36 A, and the resulting Dox loaded IO@RB-NH₂ NPs were collected by centrifugation. As pictured in Figure 5-36 B, the Dox loaded particles were well centrifuged for both samples and the supernatant had still a red color suggesting that the DLE was not close to 100%. So according to the high DLE values observed for Dox loading in IO@RB-NH₂ in water before reaching the highest DLC value, the fact that the supernatant in this experiment was red colored, which means that the DLE was not high, implies that the highest DLC value for these sample was reached. Furthermore the picture of the centrifuged Dox loaded IO@RB-NH₂ NPs obtained after supernatant removal presented in Figure 5-36 C showed clearly that the particles had a strong red color resulting from efficient Dox loading. The supernatants were collected and measured by spectrofluorimetry and absorbance to calculate the amount of Dox loaded into the NPs. Furthermore 500 μ L of each batch of IO@RB-NH₂ NPs dispersed in Milli-Q water were lyophilized and then weighted to determine the initial concentration of IO@RB-NH₂ NPs. From these measurements the DLC and DLE values were deduced.

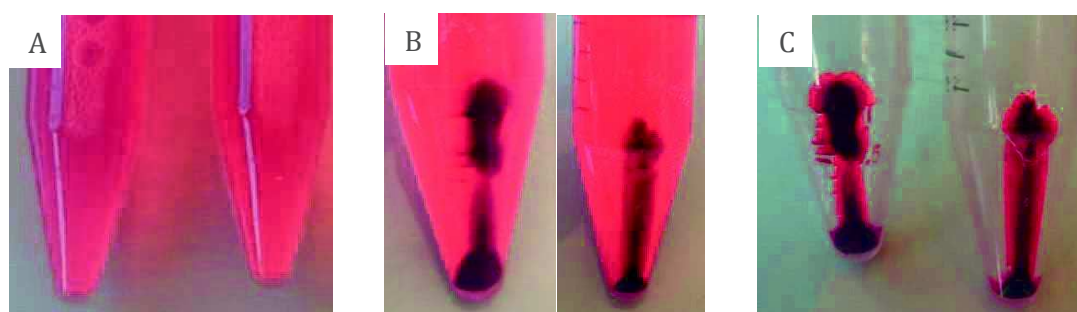


Figure 5-36: Photographs of the two IO@RB-NH₂ batches during Dox loading steps: A) mixture of Dox with IO@RB-NH₂ NPs during Dox loading before centrifugation B) centrifuged Dox loaded IO@RB-NH₂ NPs before supernatant removal C) Dox loaded IO@RB-NH₂ NPs obtained after centrifugation and removal of the supernatant

5.2.3.2 Protocol of HSA-IBAM-HSA and IBAM-HSA coatings

After the Dox loading one of the batches was used for the HSA-IBAM-HSA coating strategy and the other one for the IBAM-HSA. Strategy.

The sample selected for the HSA-IBAM-HSA coating strategy was redispersed manually in 1 mL of HSA solution at 5 mg/mL in Milli-Q water. The photograph in Figure 5-37 A showed the resulting solution. This mixture was then centrifuged at 14 000 G for 15 min in order to adsorb the HSA to the NPs surface and also to wash the excess of HSA. As pictured in the photograph in Figure 5-37 B, the resulting NPs had still a strong red color and the supernatant was very little colored suggesting that only a few or maybe no Dox was released from the NPs during the process if we consider that this few amount came from the small drop resulting from the last centrifugation after the Dox loading and containing still free Dox.

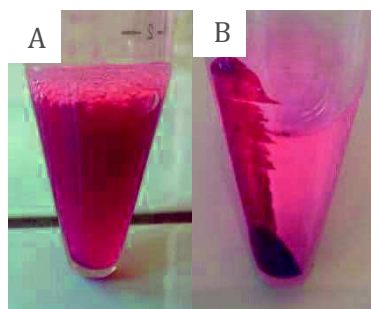


Figure 5-37: Photographs of the Dox loaded IO@RB-NH₂ NPs A) redispersed 1 mL of HSA solution at 5 mg/mL in Milli-Q water B) Dox loaded IO@RB-NH₂ NPs after HSA adsorption and centrifugation

After this HSA adsorption step for one sample, the rest of the protocol was identical for both batches. To modify the NPs with IBAM moieties, both samples were manually dispersed in 500 μL of DMF and 200 μL of Et_3N . The dispersion was harder to execute for the sample with HSA adsorption than for the other one and we observed that the NPs had the tendency to aggregate as it can be seen by looking closely to the photograph of the left tube in Figure 5-38 A. Then a mixture of 270 μL of IBC in 2,5 mL of DMF was quickly added to each sample. An orange precipitate, as pictured on Figure 5-38 B, was formed immediately for both samples. These mixtures were stirred for 1 h and then 10 mL of HSA at 2 mg/mL in Milli-Q water was added for each. After the addition of the HSA solution the precipitates were immediately dissolved as pictured in Figure 5-38 C. The solutions were stirred for additional 1h30 before being washed twice by centrifugation in water. As pictured in Figure 5-39 A, the supernatants were slightly orange for both samples after the first centrifugation suggesting a Dox release during this last synthesis step. However, the NPs contained still a large amount of Dox as they are still strong red colored as shown in Figure 5-39 B. Furthermore we noticed major centrifugation differences between the two samples. Indeed, the NPs centrifuged at the bottom of the tube took larger space for the IO@RB-Dox-HSA-IBAM-HSA (left) and IO@RB-Dox-IBAM-HSA (right) NPs. This observation can have two explanations: the IO@RB-Dox-IBAM-HSA sample centrifuged in a denser manner or the sample was too stable in solution leading to a poor centrifugation and lost NPs were still dispersed in the supernatant. After the redispersion of both samples in water, Figure 5-39 C, and the second centrifugation the supernatant was colorless for the IO@RB-Dox-HSA-IBAM-HSA which suggested that no Dox was released. But for the IO@RB-Dox-IBAM-HSA the supernatant was slightly colored and the amount of centrifuged NPs seemed to be lower than the previous centrifugation. This last observation was in favor of the second hypothesis: IO@RB-Dox-IBAM-HSA is more stable in water than the IO@RB-Dox-HSA-IBAM-HSA sample leading to centrifugation difficulties.

Finally the resulting IO@RB-Dox-HSA-IBAM-HSA and IO@RB-Dox-IBAM-HSA NPs were dispersed in 3 mL of Milli-Q water. Figure 5-40 shows the final and stable IO@RB-Dox-IBAM-HSA NPs dispersed in water and exhibiting a red color indicating the presence of Dox.

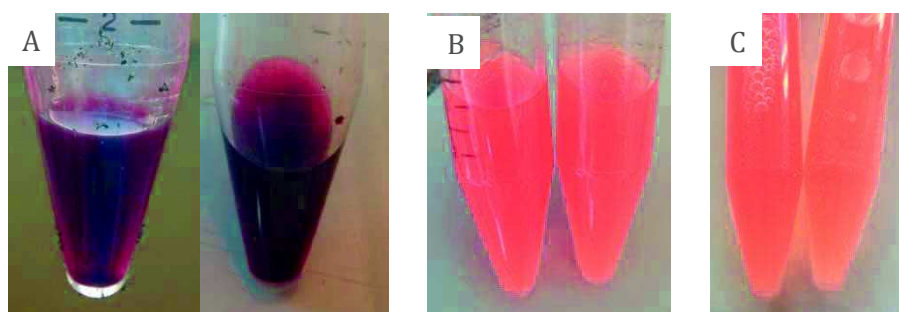


Figure 5-38: Photographs of the IBAM grafting synthesis step, at the left of each picture is the batch dedicated to the HSA-IBAM-HSA coating strategy and at the right is the batch dedicated to the IBAM-HSA coating strategy. A) pictures the batches after redispersion in DMF, B) shows the precipitates formation after IBC addition and C) represents the precipitate dissolution after the addition of HSA at 2 mg/mL in Milli-Q water

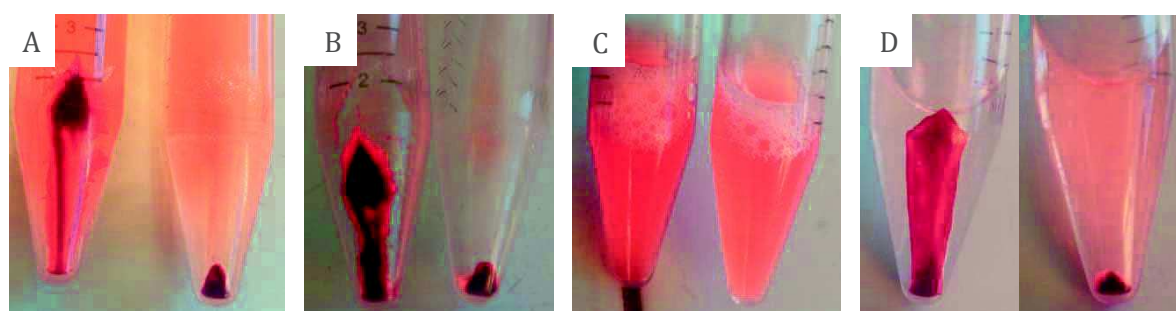


Figure 5-39: Photographs of the final washing steps, at the left of each picture is the batch dedicated to the HSA-IBAM-HSA coating strategy and at the right is the batch dedicated to the IBAM-HSA coating strategy. A) and B) represent the centrifuged NPs after the first centrifugation with A) and without B) supernatants, C) pictures the NPs after redispersion in water and D) shows the NPs after the second centrifugation with the supernatants



Figure 5-40: Picture of the final IO@RB-Dox-IBAM-HSA NPs dispersed in Milli-Q water

5.2.4 Synthesis of the IO@RB-HSA-IBAM-HSA and IO@RB-IBAM-HSA NPs

The exact same protocols were carried out again on the previous silanized IO@RB NPs to produce the corresponding final NPs with the same HSA-IBAM-HSA and IBAM-HSA coatings but without the loaded Dox. Two samples of each coating were executed: once using natural HSA and a second with FITC-labelled HSA. Compared to the previous Dox-loaded batches the initial reactant quantities were divided by two so the final samples were redispersed in 1.5 mL of Milli-Q water.

As pictured on the photographs in Figure 5-41, the NPs at the different synthesis steps did not show any red color like the precedent samples, which confirms that the previous red color is well due to Dox encapsulation into IO@RB NPs. Concerning the centrifugation behavior, the IO@RB NPs dedicated for HSA-IBAM-HSA coating and the IO@RB NPs dedicated for IBAM-HSA coating had first after the silanization step a similar centrifugation behavior, Figure 5-41 A and B. However, after the differentiation of the batches through the formation of the two different protein coatings a difference in centrifugation was visible between the samples. Indeed, the

previous behavior was reobserved for these samples: the two samples coated with HSA-IBAM-HSA centrifuged very well on a large area, Figure 5-41 E, whereas the two other samples coated with IBAM-HSA centrifuged in a denser manner. So this experimental visual difference in term of centrifugation between the samples coated with HSA-IBAM-HSA and with IBAM-HSA was observed three times: for the Dox loaded the natural and the FITC -labelled samples. So there is reproducibility for this observation.

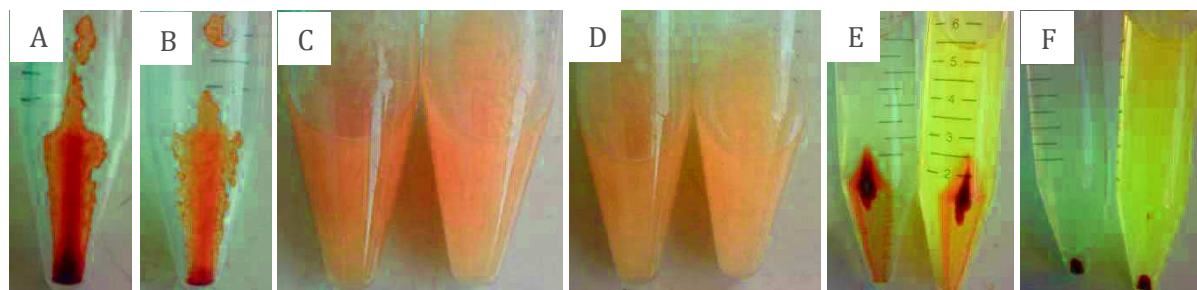


Figure 5-41: Photographs of the synthesis steps of IO@RB-HSA-IBAM-HSA and IO@RB-IBAM-HSA with natural HSA and HSA labelled with FITC. A) centrifuged IO@RB-NH₂ NPs dedicated for the HSA-IBAM-HSA coating strategy, B) centrifuged IO@RB-NH₂ NPs dedicated for the IBAM-HSA coating strategy, C) and D) are the precipitates after IBC addition in DMF for IBAM formation on the IO@RB NPs C) are the samples dedicated for the HSA-IBAM-HSA coating strategy (left HSA adsorption, right HSA^{FITC} adsorption) D) are the samples dedicated for the IBAM-HSA coating strategy (left HSA adsorption, right HSA^{FITC} adsorption), E) shows the centrifuged IO@RB-HSA-IBAM-HSA (left) and of IO@RB-HSA^{FITC}-IBAM-HSA^{FITC} (right) NPs and F) shows the centrifuged IO@RB-IBAM-HSA (left) and of IO@RB-IBAM-HSA^{FITC} (right)

5.3 Results and discussion

5.3.1 Characterization of raw IO@RB, IO@RB-NH₂, IO@RB-Dox-IBAM-HSA and IO@RB-Dox-HSA-IBAM-HSA NPs

The raw IO@RB of 36 ± 3 nm and the subsequent IO@RB-Dox-HSA-IBAM-HSA NPs are presented on TEM images in Figure 5-42 A, B, C and D, E, F respectively whereas the raw IO@RB of 31 ± 3 nm and the subsequent IO@RB-Dox-IBAM-HSA NPs are presented in TEM images in Figure 5-43 A, B, C and D, E, F. As shown in TEM images both samples were similar, spherical and highly monodispersed and had obviously the right IO@RB morphology with a 9 nm IO core surrounded by a porous silica shell of about 12 nm. The TEM pictures of the protein coated NPs show that the IO@RB structure was not affected by the further synthesis steps. Furthermore, both coating strategies were carried out successfully as we can distinguish that the porosities and the borders of the NPs appeared blurry on the pictures which can be ascribed to the HSA coatings. In addition the protein coatings are also clearly visible between the NPs. However, as expected the HSA content of the IO@RB-HSA-IBAM-HSA sample appeared to be higher than for the IO@RB-IBAM-HSA sample and this HSA-IBAM-HSA coating also seemed to lead to NPs aggregation.

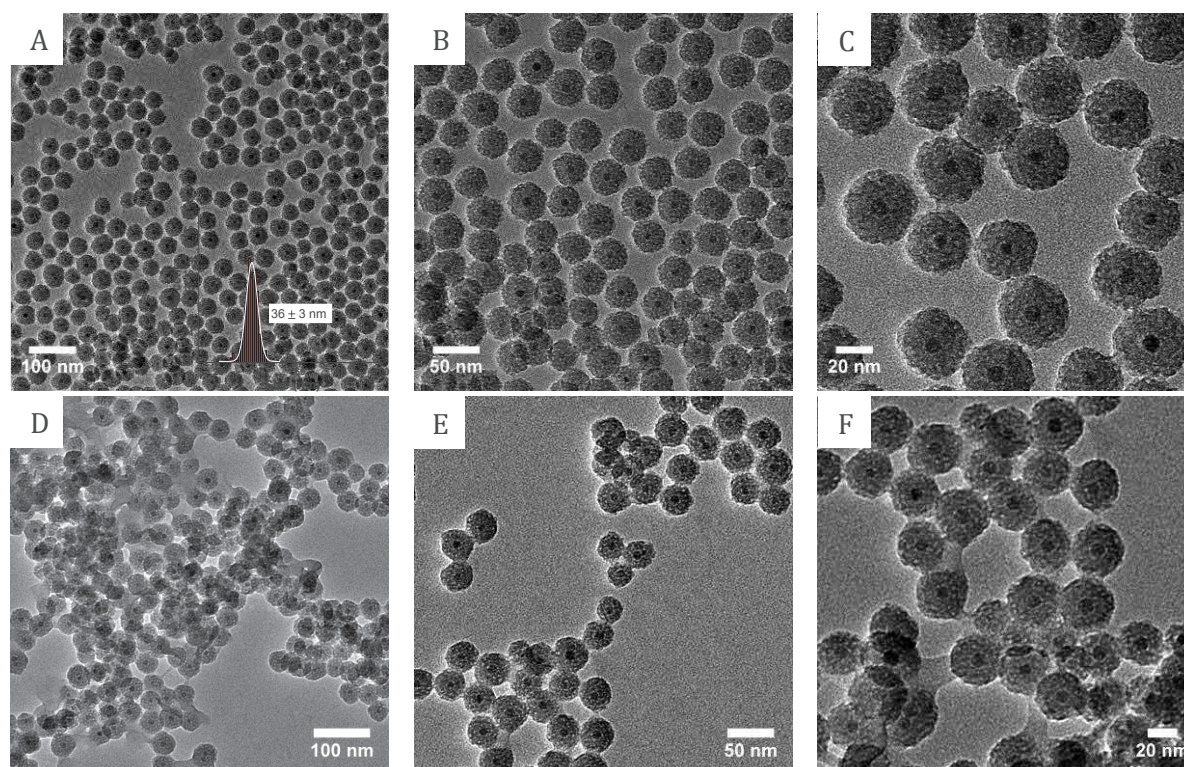


Figure 5-42: TEM images of (A, B, C) IO@RB NPs of 36 ± 3 nm with size distribution histogram in inset of (A) and (D, E, F) of the same NPs coated with HSA-IBAM-HSA

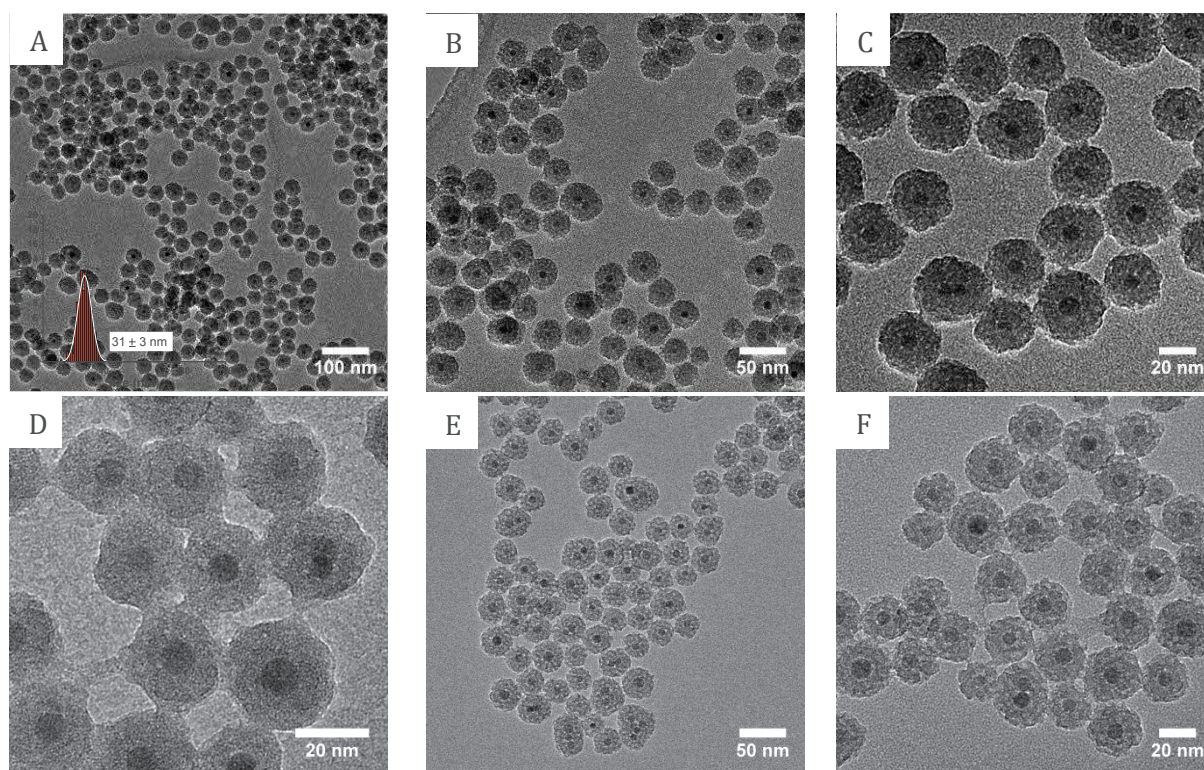


Figure 5-43: TEM images of (A, B, C) IO@RB NPs of 31 ± 3 nm with size distribution histogram in inset of (A) and (D, E, F) of the same NPs coated with IBAM-HSA

To investigate if the potential aggregation observed in TEM images for the IO@RB-HSA-IBAM-HSA sample depicted a real aggregation in solution after the protein coating or if it was only due to the drying of the sample on TEM grids, DLS analyses were performed on the NPs before any surface modification and after all synthesis steps. Thus, the hydrodynamic sizes of the raw IO@RB NPs dispersed in EtOH and the corresponding IO@RB-Dox-HSA-IBAM-HSA and IO@RB-Dox-IBAM-HSA NPs dispersed in Milli-Q water were measured.

Figure 5-44 presents the DLS curves of IO@RB in EtOH versus IO@RB-Dox-IBAM-HSA in water. These results showed exactly the same behavior than previous IO@RB NPs described in Figure 5-12, with in intensity and in volume, Figure 5-44 A and B respectively, a bimodal size distribution centered at 58 and 200 nm and in number a unique distribution centered at 50 nm. As it was explained previously, this second contribution at 200 nm certainly came from some larger multicore NPs created during the synthesis process as by products. However, what is more important to notice from these DLS measurements is that they were almost identical for IO@RB NPs in EtOH than for IO@RB-Dox-IBAM-HSA NPs. This means that the modification of the IO@RB with Dox loading and IBAM-HSA coating did not change the colloidal stability of the system, *i.e.* did not aggregate the NPs.

Nevertheless, it was not the same behavior for the IO@RB NPs coated with HSA-IBAM-HSA. Indeed, the DLS measurement presented in Figure 5-45, showed similar hydrodynamic sizes for raw IO@RB NPs in EtOH than the previous same type of NPs, Figure 5-12 and Figure 5-44, but also showed that after Dox loading and HSA-IBAM-HSA coating, these NPs aggregated a mean hydrodynamic diameter of 4000 nm was noticed. This would confirm the aggregation observed in the TEM images as well as the behavior of the sample during the centrifugation steps. Indeed it was observed, as depicted on the photographs in Figure 5-39 and Figure 5-41, that the IO@RB-HSA-IBAM-HSA NPs were easier to centrifuge than the IO@RB-IBAM-HSA NPs. Thus, these results gave the confirmation of the hypothesis developed through the experimental

observations according to which the IO@RB sample covered with IBAM-HSA was too stable to be well collected by centrifugation leading to some sample loss. As summarized in Table 5-4 the NPs weighting after sample freeze drying also indicated a weight loss for the sample prepared via IBAM-HSA coating strategy. Indeed, from the measurement of the initial concentration of the IO@RB-NH₂ NPs used in the syntheses, we deduced the minimal weight of NPs expected at the end of the synthesis procedure (minimal weight because it is the weight of the inorganic NPs without any organic compounds). From the difference between the minimal expected weight and the real weight obtained at the end of the synthesis (also measured by freeze-drying), the percentage of minimal loss was calculated. This calculation indicated that the IO@RB-Dox-IBAM-HSA sample lost more than 62 % of its weight during the synthesis whereas the IO@RB-Dox-HSA-IBAM-HSA only got a minimal sample loss of 8 %. The centrifugation seemed to had better worked on the IO@RB-IBAM-HSA than on IO@RB-Dox-IBAM-HSA sample, since the minimal weight loss decreased to 27 %.

The Zeta potential measurements, Figure 5-46, show that both IO@RB-NH₂ had an IEP around 7.7. Therefore, they were both, before the Dox loading, positively charged, with a Zeta potential over 20 mV, in the pH range of Milli-Q water, pH 6-7. As the Doxorubicin hydrochloride salt is as well positively charged in Milli-Q water we can conclude through this Zeta potential measurements that the interactions between the amino-modified silica surface and the Dox should not be electrostatic.

After Dox loading and IBAM-HSA coating the IEP of these particles dropped to 6. That meant that the IO@RB-Dox-IBAM-HSA were slightly negatively charged, with a Zeta potential between 0 and -20 mV, in Milli-Q water pH range. This should have led to poor colloidal stability by electrostatic interactions, but according to the DLS results for this compound, Figure 5-44, the suspension was stable suggesting thus a steric stabilization induced by the coating.

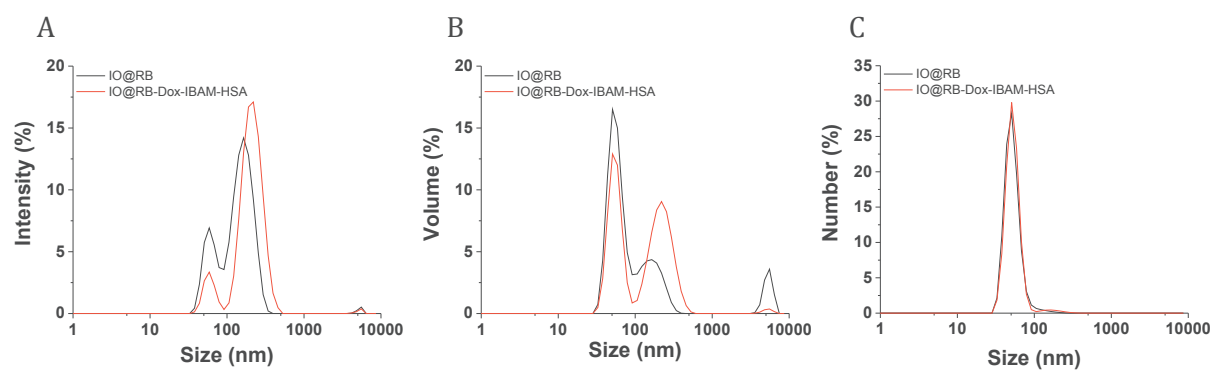


Figure 5-44: DLS measurement on IO@RB in EtOH versus IO@RB-Dox-IBAM-HSA in water A) in intensity, B) in volume and C) in number

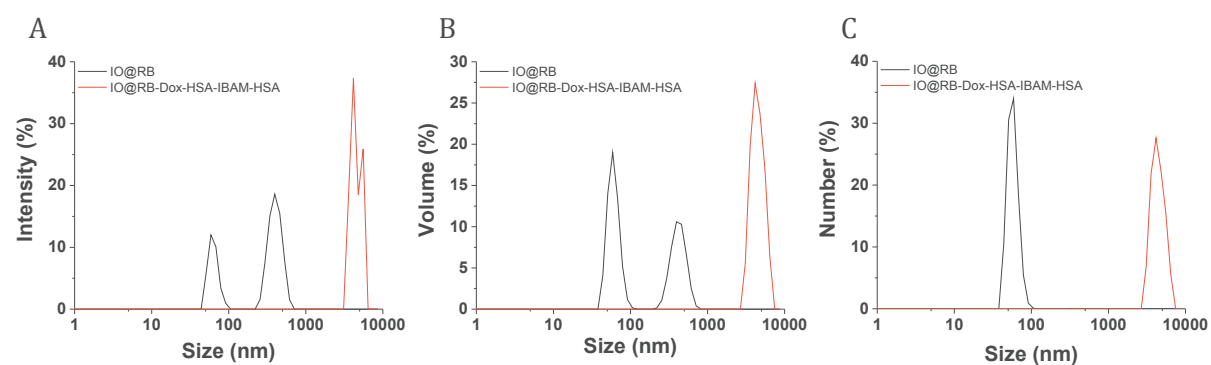


Figure 5-45: DLS measurement on IO@RB in EtOH versus IO@RB-Dox-HSA-IBAM-HSA in water A) in intensity, B) in volume and C) in number

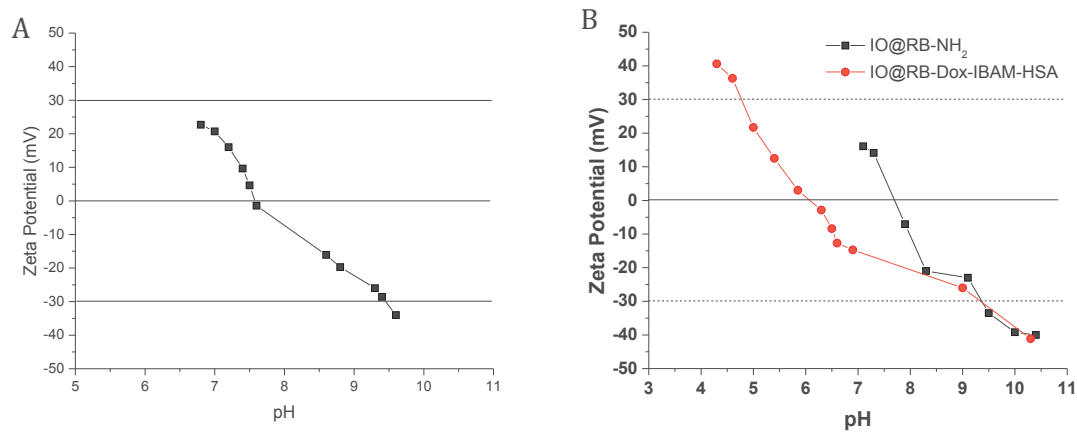


Figure 5-46: Zeta potentials of IO@RB-NH₂ NPs A) and B) and of the IO@RB-Dox-IBAM-HSA B)

Table 5-4: Estimation of the weight loss during IO@RB-HSA-IBAM-HSA and IO@RB-IBAM-HSA synthesis steps through weight measurements after freeze-drying

	Sample	V _{freeze-dried} (mL)	m _{weighted} (mg)	[NPs] in solution (mg/mL)	V _{total of the solution} (mL)	m _{total of NPs in solution} (mg)	m _{minimal of NPs expected} (mg)	loss (%)
HSA-IBAM-HSA coating strategy	IO@RB-NH ₂	0.5	0.5	1	-	-	-	-
	IO@RB-Dox-HSA-IBAM-HSA	0.5	0.77	1.54	3	4.62	5	8
	IO@RB-HSA-IBAM-HSA	1.5	2.14	1.43	1.5	2.14	2.5	14
IBAM-HSA coating strategy	IO@RB-NH ₂	0.5	0.3	0.6	-	-	-	-
	IO@RB-Dox-IBAM-HSA	0.5	0.19	0.38	3	1.14	3	62
	IO@RB-IBAM-HSA	1.5	1.1	0.74	1.5	1.1	1.5	27

5.3.2 Dox loading analyses

The concentrations of the Dox loaded in the IO@RB-NH₂ were calculated from the absorbance measurements of the supernatant concentrations by UV-vis spectroscopy. Thanks to the mass weighted after the freeze-drying of 500 μ L of both IO@RB-NH₂ NPs, the concentration of NPs of these solutions were deduced. From these values, the fwr, DLC and DLE for each batch were obtained and summarized in Table 5-5. For Dox loading the same amount of Dox was fed for both samples, but as the IO@RB-NH₂ batch for HSA-IBAM-HSA was more concentrated than the other, 1 mg/mL and 0.6 mg/mL respectively, the fwr were different: 100 and 167 %. Furthermore the DLC values obtained during this experiment are very high, around 30 %, compared to the values obtained in the previous studies. Indeed, for Dox loading on IO@RB-NH₂ NPs in Milli-Q water, the DLC was 28 % for the HSA-IBAM-HSA strategy and 34 % for the IBAM-HSA strategy. Nevertheless, the DLE were low, 27 and 20 % for HSA-IBAM-HSA and IBAM-HSA strategies respectively which explained the strong red color of the supernatants, Figure 5-36 B.

Table 5-5: Summary of DLC and DLE determined from the difference in Dox concentration between the initial solution and the residual supernatant measured by UV-vis spectroscopy at the characteristic absorbance peak of Dox (480 nm)

Batches for the	fwr (%)	DLC (%)	DLE (%)
HSA-IBAM-HSA strategy	100 %	28 %	27 %
IBAM-HSA strategy	167 %	34 %	20 %

After this drug loading step, various other synthesis steps were necessary to form the HSA-IBAM-HSA and IBAM-HSA protein coatings. During these steps, there was a probability for Dox loaded molecules to leak-out from the NPs. In order to measure the Dox loaded in the final protein coated NPs after a possible leakage, TGA analyses were run on Dox-loaded and non-loaded IO@RB NPs with the two protein coatings. The difference in weight loss between the samples should be due to the weight of Dox loaded into the NPs.

Figure 5-47 B shows the TGA curves obtained for the IO@RB-IBAM-HSA and the IO@RB-Dox-IBAM-HSA NPs. A weight loss difference of 20 % was observed between both samples suggesting that the final DLC was about 20 % for the IO@RB-Dox-IBAM-HSA NPs. However, this DLC came from the calculation of the percentage of the ratio between the weight of the Dox loaded and the weight of the final IO@RB-IBAM-HSA NPs. According to the TGA 58 % of this sample corresponded to the inorganic IO@RB NPs whereas 22 % came from the IBAM-HSA coating and 20 % from the Dox loading. Thus this corresponds to a DLC of 34 % of Dox loaded into raw RB@IO NPs. This result is perfectly matching the result obtained with the supernatant analysis after Dox impregnation suggesting that no Dox was released from the NPs during the synthesis steps for the protein coating.

For the NPs coated with the HSA-IBAM-HSA strategy, the analyses of the TGA curves, Figure 5-47 A, did not lead to the same conclusion. Indeed, the organic weight losses were almost identical for the IO@RB-Dox-HSA-IBAM-HSA and the IO@RB-HSA-IBAM-HSA samples. Nevertheless, the red color of the IO@RB-Dox-HSA-IBAM-HSA NPs, Figure 5-39 D, certified that Dox was indeed loaded in the NPs. This implies that for the non-loaded IO@RB-NH₂ NPs more HSA was deposited on the silica surface during the first HSA coating step than for the Dox loaded NPs. In order to try to determine the Dox loaded amount in the IO@RB-Dox-HSA-IBAM-HSA NPs, TGA analyses were done on free HSA and Dox, Figure 5-48. Unfortunately the curves are interwoven excepting at low temperatures, before 200 °C, where the Dox seemed not to be degraded. Thus, for the IO@RB-Dox-HSA-IBAM-HSA, no estimation of the final Dox loaded amount could be determined. According to the previous Dox loading estimation before the protein coating synthesis steps of 28 % in DLC and according to the TGA curve showing an inorganic IO@RB weight of 60 % of the final product, we estimated the Dox loading contribution to be of 16.8 %w if no drug leakage occurred during the protein coating.

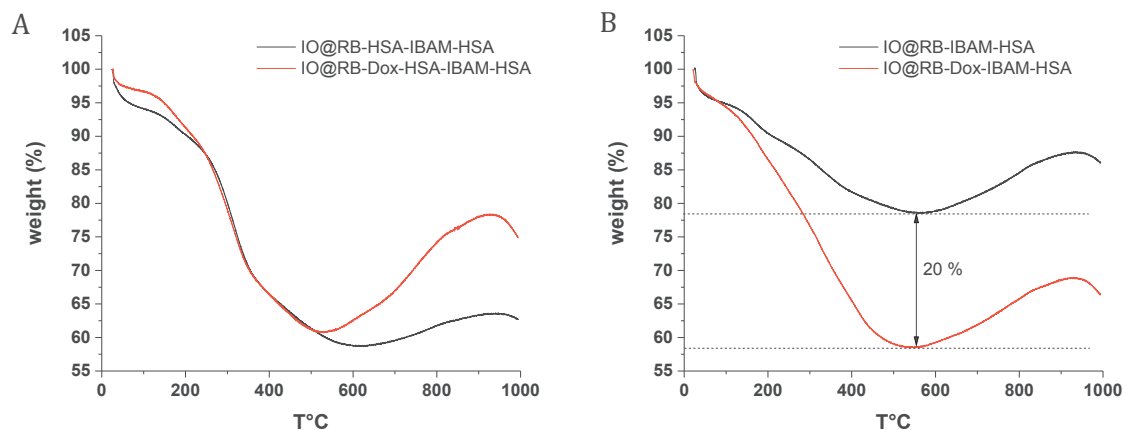


Figure 5-47: TGA curves of the Dox-loaded and non-loaded protein coated IO@RB NPs with A) HSA-IBAM-HSA strategy B) IBAM-HSA strategy

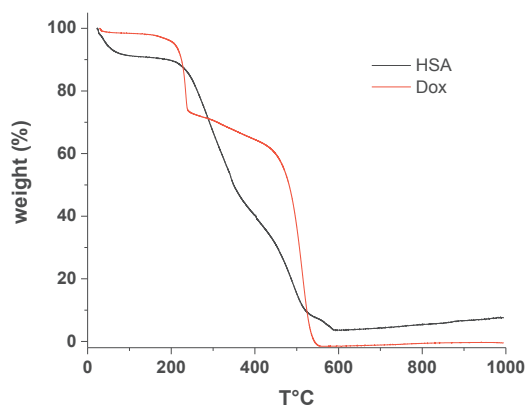


Figure 5-48: TGA of free Dox and free HSA

To estimate the maximal drug loading amount that can be loaded in these IO@RB-NH₂ systems, DLC and DLE curves at different Dox fwr for both IO@RB-NH₂ samples in water were determined. Figure 5-49 shows the photographs of the centrifuged IO@RB-NH₂ NPs after the Dox loading. We observed that the supernatants were highly colored for Dox impregnation into IO@RB-NH₂ NPs in water.

As pictured in Figure 5-50 A, the DLC curve reached a plateau of 27 % for the sample used for the HSA-IBAM-HSA strategy and a plateau of 23 % for the other sample. These values are still very high for Dox loading into IO@RB-NH₂ in water compared to the values obtained in the previous studies. However, these Dox loaded studies were investigated on non-calcined NPs, so this parameter had probably an impact on the loading. Furthermore, for the sample used for the IBAM-HSA strategy, the maximal DLC is lower than the DLC of 34 % obtained previously at a fwr of 167 %. This can be explained by the fact that these DLC and DLE experiments were done one week after the previous study, so the IO@RB-NH₂ NPs dispersed in water started probably to hydrolyze. This hypothesis is confirmed by the fact that the DLE values for this study were very low (under 40 %) for Dox impregnation in water on silanized particles, even at low fwr. This behavior was already observed in chapter 4 on RB NPs: in the time the DLE decreased and the resulting DLC also.

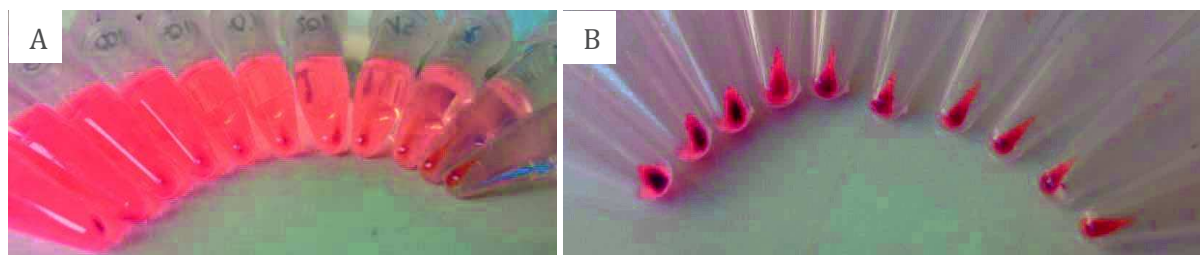


Figure 5-49: Photographs of the centrifuged IO@RB-NH₂ NPs after the Dox loading A) with supernatants B) without supernatants

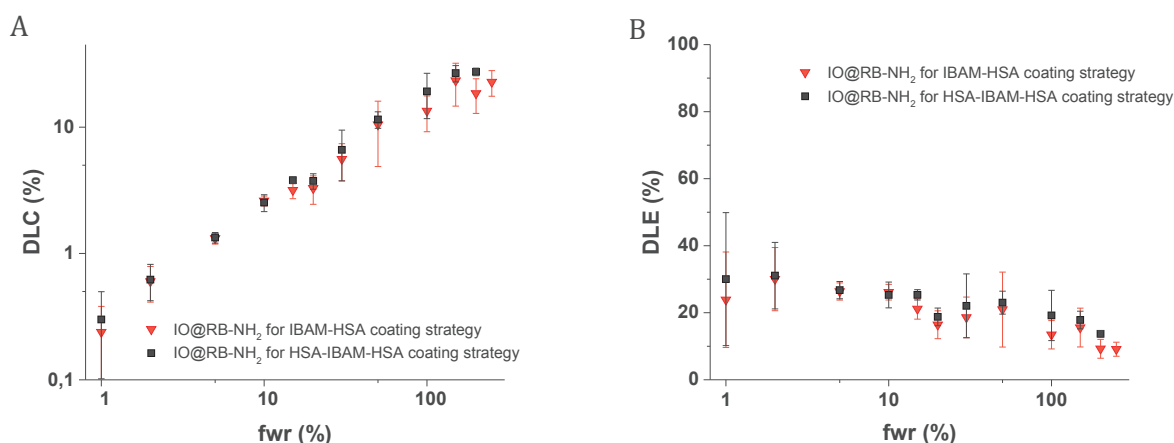


Figure 5-50: A) DLC and B) DLE graphs for Dox loading on IO@RB-NH₂ NPs dedicated for IBAM-HSA and HSA-IBAM-HSA protein coatings

5.3.3 Dox release trials from IO@RB-Dox-HSA-IBAM-HSA NPs

In this part we assessed the release of Dox from IO@RB-DOX-HSA-IBAM-HSA NPs. First the protein coating degradation was investigated in the IO@RB-HSA^{FITC}-IBAM-HSA^{FITC} sample. Briefly, 200 μ L of NPs dispersed at 0.8 mg/mL in water were mixed with various concentration of proteases dispersed either in PBS buffer at pH 7.4 or in acetate buffer at pH 5 and placed at 37 $^{\circ}$ C for several hours. At pH 5, the weight ratios of 2.5, 1.25, 0.25 and 0 between proteases and NPs were tested whereas at pH 7, as the proteases are known to be more active at this pH, the weight ratios 1.25, 0.25, 0.125 and 0 were tested. Each experiment was carried out in triplicate. At specific reaction times, the mixtures were centrifuged and the supernatant analyzed by fluorescence spectroscopy, λ_{exc} = 488 nm and λ_{em} = 520 nm, to measure the FITC fluorescence.

Figure 5-51 shows HSA^{FITC} degradation curves at pH 7 and pH 5 under various proteases concentrations over 50 h. The curves obtained were very similar to the previous one shown in Figure 5-34: in the presence of proteases, a progressive release of FITC in the supernatant marking the degradation of HSA was observed, whereas the control experiments did not show significant release. As expected from enzyme activity at different pH, the HSA degradation was faster at pH 7 than for pH 5, even at low proteases/IO@RB-HSA-IBAM-HSA ratio. At pH 5 the HSA degradation rate increases with enzyme concentration. For both pH, at the highest proteases content, the HSA seemed to reach a plateau after 20 h. HSA coating is thus effectively degraded by action of non-specific proteases. So for, we can expect Dox release after cell internalization that would be due to the presence of proteases in endolysosomes (see Figure 1-5 page 11).

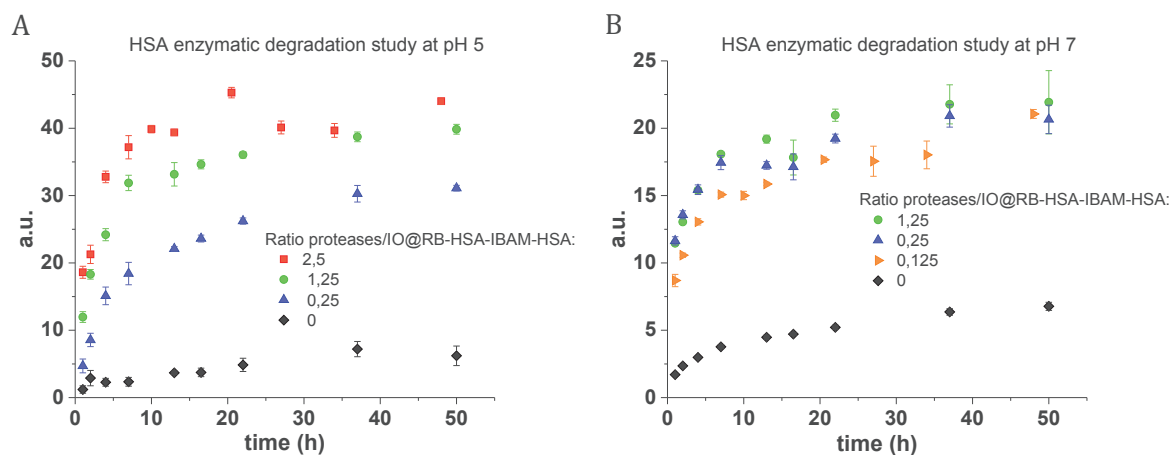


Figure 5-51: HSA degradation studies on IO@RB-HSA^{FITC}-IBAM-HSA^{FITC} at A) pH 5 and B) pH 7.4 under various proteases/IO@RB-HSA^{FITC}-IBAM-HSA^{FITC} ratios

To evaluate the Dox release from the IO@RB-Dox-HSA-IBAM-HSA NPs, these particles were incubated at pH 5 and 7.4 with proteases/IO@RB-Dox-HSA-IBAM-HSA ratios that showed previously fast protein coating degradation. In a similar procedure than for HSA degradation study, at various reaction times, the mixtures were centrifuged and the supernatants analyzed by fluorescence spectroscopy at $\lambda_{exc} = 488$ nm and $\lambda_{em} = 595$ nm characteristics for Dox fluorescence. From these measurements and thanks to Dox calibration curves made at pH 5 and 7.4, the concentration of Dox released in the media was calculated. The resulting Dox release curves in function of reaction time under various proteases/IO@RB-Dox-HSA-IBAM-HSA ratios and at pH 5 and 7.4 are presented in Figure 5-52. According to these curves the Dox release was more efficient at pH 7.4 than at pH 5.

As explained previously, if we consider that no drug leakage occurred during the protein coating synthesis steps, a DLC of 16.8 %w of the final NPs was obtained. Using this DLC estimation, we calculated from the maximal concentration of Dox released in the media through enzymatic action, the percentage of the ratio between the amount of Dox released and the amount of Dox encapsulated. We also calculated the DRC, drug release content, which correspond to the weight of Dox release in function of the weight of the NPs incubated. These results, summarized in Table 5-6, showed that even under the best release conditions in our studies, *i.e.* at pH 7 with a proteases/IO@RB-Dox-HSA-IBAM-HSA ratio of 1.25, less than 4 % of the Dox loaded was released, which corresponds to a DRC of 0.62 %. These results are very poor in comparison with the literature, Table 1-8.

Furthermore, as shown in Figure 5-53, the proteases had a small fluorescence contribution at these excitation and emission wavelengths. Because the differences in term of Dox released concentrations between NPs incubated with proteases and the controls without proteases were very low, the higher Dox released amount observed for the NPs incubated with proteases compared to the NPs incubated without proteases, could come from the auto-fluorescence of the proteases. We also observed during the experiments that the procedure of centrifugation was not always the same between the batches and in the time, because of the difference in colloidal stability. Indeed, the difference in pH as well as in protease concentrations could influence the colloidal stability of the systems and change their centrifugation. Thus, some measured fluorescence could come from too stable NPs containing Dox that did not centrifuge well. Through these two experimental problems, the auto-fluorescence of proteases and the poor reproducibility of centrifugation, a small variation of fluorescence as we measured from the

previous samples are not fully trustable. To overcome this problem, we decided, for the future experiments, to work by dialysis. Using mini-dialyzer, 200 μL of the mixture of NPs with enzymes could be dialyzed against 2 mL of fresh media. With a membrane of 12000-14000 MWCO, the NPs and the enzymes are trapped into it and only the small Dox molecules can cross the membrane and be released in the media. Thus, analyzing the release media by fluorescence spectroscopy will lead to the determination of Dox release curves without the measurement of fluorescence parasites from the proteases or residual Dox-loaded NPs.

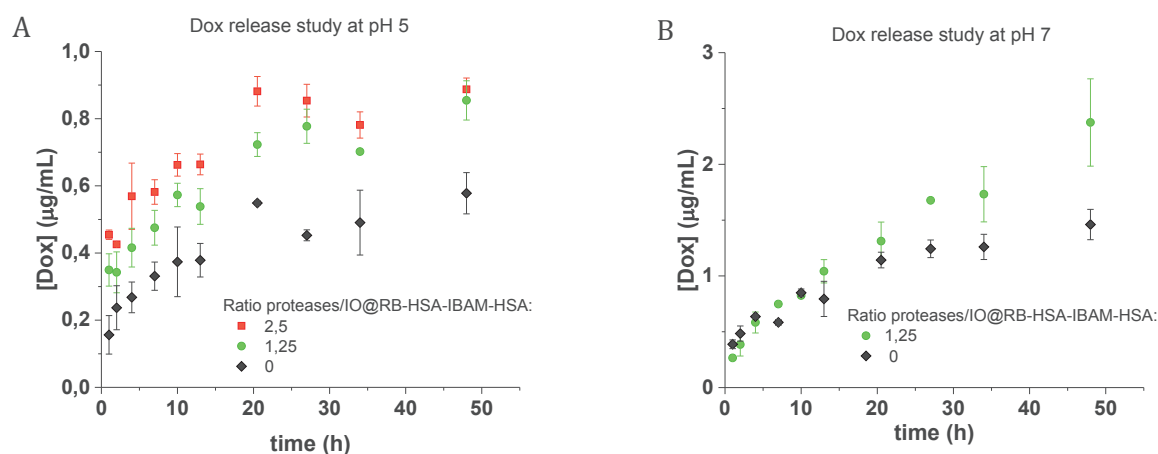


Figure 5-52: Dox release studies on IO@RB-HSA^{FITC}-IBAM-HSA^{FITC} at A) pH 5 and B) pH 7.4 under various proteases/IO@RB-HSA^{FITC}-IBAM-HSA^{FITC} ratios

Table 5-6: Estimation of percentage of drug released and DRC from the hypothesis of a final DLC of 16.8 %w

	Proteases/NPs ratio	[Dox] at 50h incubation ($\mu\text{g/mL}$)	Maximal Dox release (%)	DRC (%)
pH 5	1.25	0.85	1.37	0.23
	0	0.58	0.89	0.15
pH 7	1.25	2.4	3.7	0.62
	0	1.46	2.2	0.36

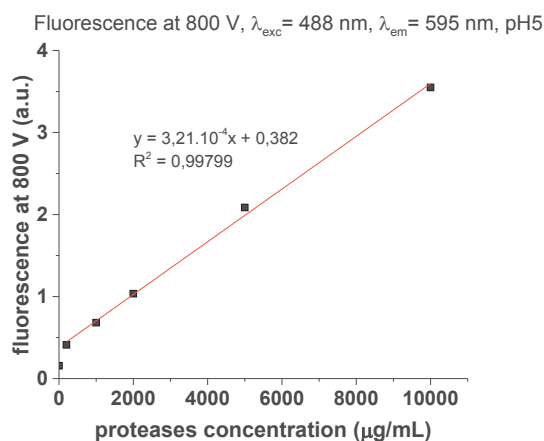


Figure 5-53: Curve of auto-fluorescence in a.u. of proteases at various concentrations in acetate buffer at pH 5 with λ_{exc} = 488 nm and λ_{em} = 595 nm and at 800 V

5.3.4 Conclusion

To conclude the HSA-IBAM-HSA coating strategy did not lead to improve the previous IBAM-HSA coating strategy. Indeed, the colloidal stability of the resulting IO@RB-Dox-HSA-IBAM-HSA NPs was poor, the particles tend to aggregate and resulting sedimentation was observed. Furthermore, in the contrary to the IBAM-HSA coating strategy, the DLC estimation by TGA analysis failed for the HSA-IBAM-HSA strategy. Finally, Dox release experiments showed that this coating did not lead to high drug release despite HSA enzymatic degradation.

6 Influence of the mesoporous silica shell thickness on biological activities

6.1 Introduction

The goal of this section was to investigate the influence of mesoporous silica shell thickness of IO@RB-HSA NPs on the biological activities such as cytotoxicity, cellular uptake on 2D and 3D cell cultures. For this purpose, two IO@RB samples, made from the same IO NPs of $9 \pm 1,2$ nm, but with different silica shell thickness were studied. The first one exhibited a mean size of 31 ± 3 nm (Figure 5-21 A and D page 140) and the second one had a mean size 84 ± 7 nm (Figure 5-21 C and F page 140). These samples were called IO@RB 30 nm and IO@RB 85 nm for the rest of this study.

IO@RB NPs were coated with IBAM-HSA^{FITC} following the standard protocol described in Chapter 2 page 58, and for each IO@RB NPs size a batch with Dox loaded was also prepared. Unfortunately, when these experiments were executed the Dox encapsulation was not well set up. Thus, during the further synthesis steps after the Dox loading to form the IBAM-HSA coating, a lot of Dox was released. As TGA is a destructive method and requests a lot of product, the final Dox encapsulated content could not be determined.

6.2 Comparative biological studies on IO@RB-HSA NPs of 30 and 85 nm

In a concern of preserving homogeneity in the measurements, the biological analyses, presented in the following, were achieved for specific Fe concentrations in the NPs (measured by ICP-AES). Thus, as the cores of the studied IO@RB-HSA NPs came from the same IO NPs batch, it can be considered, assuming that each NP had a single IO core, that working at the same Fe concentration for the IO@RB-HSA batches of 30 and 85 nm was equivalent to work with the same number of NPs for each batch. Therefore it's important to keep in mind in the following studies that our scientific reasoning is based on a fixed number of NPs and not on NPs weights.

6.2.1 Cytotoxicity studies

6.2.1.1 Impact of the silica shell thickness on cytotoxicity

To compare the impact of silica shell thickness on the toxicity of IO@RB-HSA NPs, MTT assays were performed on three human cancer cell lines, Kelly, Huh7-luc and A549-luc, at 24 and 48 h and for various Fe concentrations. Analyses were performed on well triplicates and reproduced 3 times. The resulting graphs are presented in Table 5-8, and the Fe concentrations at 50 % of cell viability for each experiment were summarized in Table 5-10.

This study showed that the Kelly cells are the most sensitives to the IO@RB-HSA NPs. For this cell line the cytotoxicity at 24 h was identical for 30 and 85 nm IO@RB-HSA NPs with a minimum cell viability reached for 3 $\mu\text{g Fe/mL}$. However, at 48 h of incubation, the cytotoxicity of IO@RB-HSA 85 nm seemed higher, with Fe concentrations at 50 % of cell viability and at minimal cell viability of 0.16 $\mu\text{g Fe/mL}$ and 1 $\mu\text{g Fe/mL}$ respectively compared to Fe concentrations of 0.4 $\mu\text{g Fe/mL}$ and 3 $\mu\text{g Fe/mL}$ for 30 nm IO@RB-HSA NPs.

The two others cancer cell lines showed a similar toxicity response to the NPs and no major cytotoxicity difference between both silica shell sizes were noticed. Only after 48 h of incubation the IO@RB-HSA 85 nm NPs showed slightly more toxic behavior than the IO@RB-HSA 30 nm NPs with slightly lower Fe concentrations at 50% of cell viability. However, this small gap disappeared at high Fe concentrations leading to similar toxicities at 10 $\mu\text{g Fe/mL}$ for both shell sizes.

To conclude the silica shell thickness does not exhibit a major impact of IO@RB-HSA NPs toxicity on these three cancer cell lines. This is consistent with the results obtained by Ye *et al.* (115) who observed no severe time- or dose-dependent toxicity for various sized IO@RB NPs. So in our case the addition of a HSA shell did not modify this trend.

In the following, MTT measurements were also performed on the same IO@RB-HSA NPs but loaded with Dox.

6.2.1.2 Effect of the Dox loaded into IO@RB NPs on cytotoxicity

6.2.1.2.1 Cytotoxicity of free Dox on three human cancer cell lines

Beforehand the cytotoxicity of free Dox was investigated on the three cancer cell lines through MTT assays at 24 and 48 h and at different Dox. The resulting cytotoxicity curves are presented in Figure 5-54 and Table 5-7 summarized the free Dox concentration values at 50 % of cell viability during the MTT assays. Once again, Kelly cells were the most sensitive to the drug. 50 % of Kelly cell viability was already reached at Dox concentrations of 0.56 and 0.016 $\mu\text{g/mL}$ for 24 and 48 h respectively. In contrary A549-luc cells seemed to be the most resistant

to the Dox especially at 24 h incubation with a high Dox concentration of 77 $\mu\text{g}/\text{mL}$ at 50 % cell viability, which dropped to 0.25 after 48 h incubation. Finally Huh7-luc cells showed similar results than A549-luc cells after 48 h incubation whereas the toxicity of Dox on these cells is much higher for 24 h of incubation with a Dox concentration of 2.5 $\mu\text{g}/\text{mL}$ at 50 % of cell viability.

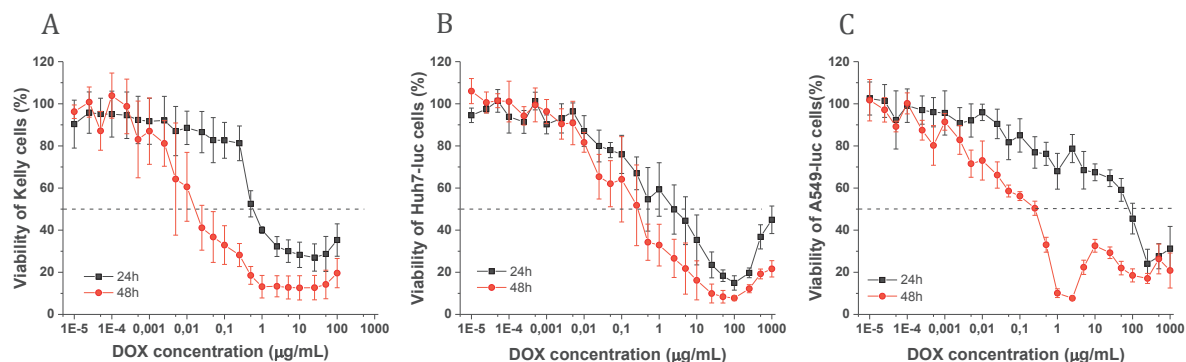


Figure 5-54: Cytotoxicity of free Dox at 24 and 48h measured via MTT assays on A) Kelly cells, B) Huh7-luc cells, C) A549-luc cells

Table 5-7: Free Dox concentration values from MTT assays at 50% of cell viability

	Time (h)	Dox concentration at 50% of cell viability ($\mu\text{g}/\text{mL}$)
Kelly	24h	0.56
	48h	0.016
Huh7-luc	24h	2.5
	48h	0.26
A549-luc	24h	77
	48h	0.25

6.2.1.2.2 Preliminary study of cytotoxicity of IO@RB-Dox-HSA NPs

Table 5-9 showed the MTT cytotoxicity curves obtained with the NPs containing Dox compared to the same NPs without Dox on the three cancer cell lines in function of Fe concentration, i.e. in function of the NPs number. The Table 5-10 summarized the Fe concentrations values at 50 % of cell viability for the NPs without Dox and the NPs with Dox.

For all three cell lines the MTT curves at 24 and 48 h of Dox loaded IO@RB-HSA 85 nm NPs are almost identical to the MTT curves of the corresponding non-loaded NPs. For Huh7-luc and A549-luc cell lines the difference in cytotoxicity between NPs with and without Dox was barely noticeable excepted at the highest Fe concentration of 10 $\mu\text{g}/\text{mL}$ at which the Dox loaded IO@RB-HSA 85 nm NPs showed a higher toxicity than the non-loaded IO@RB-HSA 85 nm NPs. Indeed, for the Huh7-luc cell line the cell viability dropped to 37 % for Dox-loaded NPs compared to 55 % for non-loaded NPs at 24 h. At 48 h of incubation the cell viability reached the very low value of 10 % for the Dox-loaded NPs whereas it only decreased to 32 % for the non-loaded NPs.

On a similar way, the A549-luc cell line showed lower cell viability values at 10 $\mu\text{g Fe/mL}$ for Dox-loaded than for non-loaded NPs of 37 % versus 55 % at 24 h and 10 % versus 32 % at 48 h.

For the Kelly cells no significant difference on the MTT curves was observed between Dox loaded and non-loaded IO@RB-HSA 85 nm NPs.

These MTT results on Huh7-luc and A549-luc cell lines incubated with IO@RB-Dox-HSA versus IO@RB-HSA 85 nm NPs, suggested that the amount of Dox released from IO@RB-Dox-HSA 85 nm NPs started to be enough at 10 $\mu\text{g Fe/mL}$ to induce cell death. This imply that with improving the Dox loading, the amount of Dox released will increase at lower Fe concentrations inducing higher cell death than empty NPs.

For the IO@RB-HSA 30 nm, the Dox loaded NPs seemed to be slightly more toxic than the non-loaded NPs as for all cell lines the MTT curves for Dox-loaded NPs was always under the MTT curves for non-loaded NPs.

The difference in cytotoxicity between Dox-loaded and not NPs was more significant on the Kelly cells. A decrease of approximately a factor 2 in the Fe concentration at 50% of cell viability was observed for the Kelly cells incubated 24 h with Dox loaded NPs compared to non-loaded NPs. For the cells incubated 48 h, the Fe concentration at 50 % of cell viability was divided by 4 for the NPs containing Dox comparing with the non-loaded NPs. Furthermore at this incubation time we can notice that the maximal cell death was obtained already at a Fe concentration of 1 $\mu\text{g Fe/mL}$ for Dox loaded NPs at both shell thickness whereas it was reached around 3 $\mu\text{g Fe/mL}$ for non Dox loaded NPs.

For the Huh7-luc cell line the difference in cytotoxicity between NPs with and without Dox was barely noticeable. Indeed, the Fe concentration at 50 % of cell viability were really near to each other for NPs with and without Dox with values of 4.9 and 3.7 $\mu\text{g Fe/mL}$ at 24 h and of 3 and 2.1 $\mu\text{g Fe/mL}$ at 48 h for Dox loaded and non-loaded NPs respectively. After 48 h incubation at Fe concentration of 10 $\mu\text{g Fe/mL}$ for the 30 nm NPs the cell viability dropped from 27 % for non-drug-loaded NPs to 14 % for Dox loaded NPs whereas at 24 h of incubation the cell viability at 10 $\mu\text{g Fe/mL}$ was closed for Dox-loaded NPs and non-loaded NPs with values of 36 % and 42 % respectively.

The MTT curves of Dox-loaded versus non-loaded IO@RB-HSA 30 nm NPs for A549-luc cells at 24 and 48 h exhibited similar behavior than the MTT curves for Huh7-luc cells: the Dox-loaded NPs were slightly more toxic than the non-loaded NPs. At the highest Fe concentration of 10 $\mu\text{g Fe/mL}$ the cell viability dropped from 38 % to 24 % at 24 h and from 19 % to 10 % at 48 h with addition of Dox into the 30 nm IO@RB-HSA NPs.

To conclude no significant difference in term of cytotoxicity was measured between Dox-loaded and non-loaded IO@RB-HSA NPs for both shell sizes. Only a small trend of higher toxicity for Dox-loaded NPs was noticeable, especially at high Fe concentration. These experiments need to be done again on IO@RB-HSA NPs loaded with a larger amount of Dox to confirm the trend of this preliminary study.

Table 5-8: Cytotoxicity at 24 and 48h, based on MTT assays, of IO@RB-HSA 30 and 85 nm at various Fe concentrations on Kelly, Huh7-luc and A549-luc cells

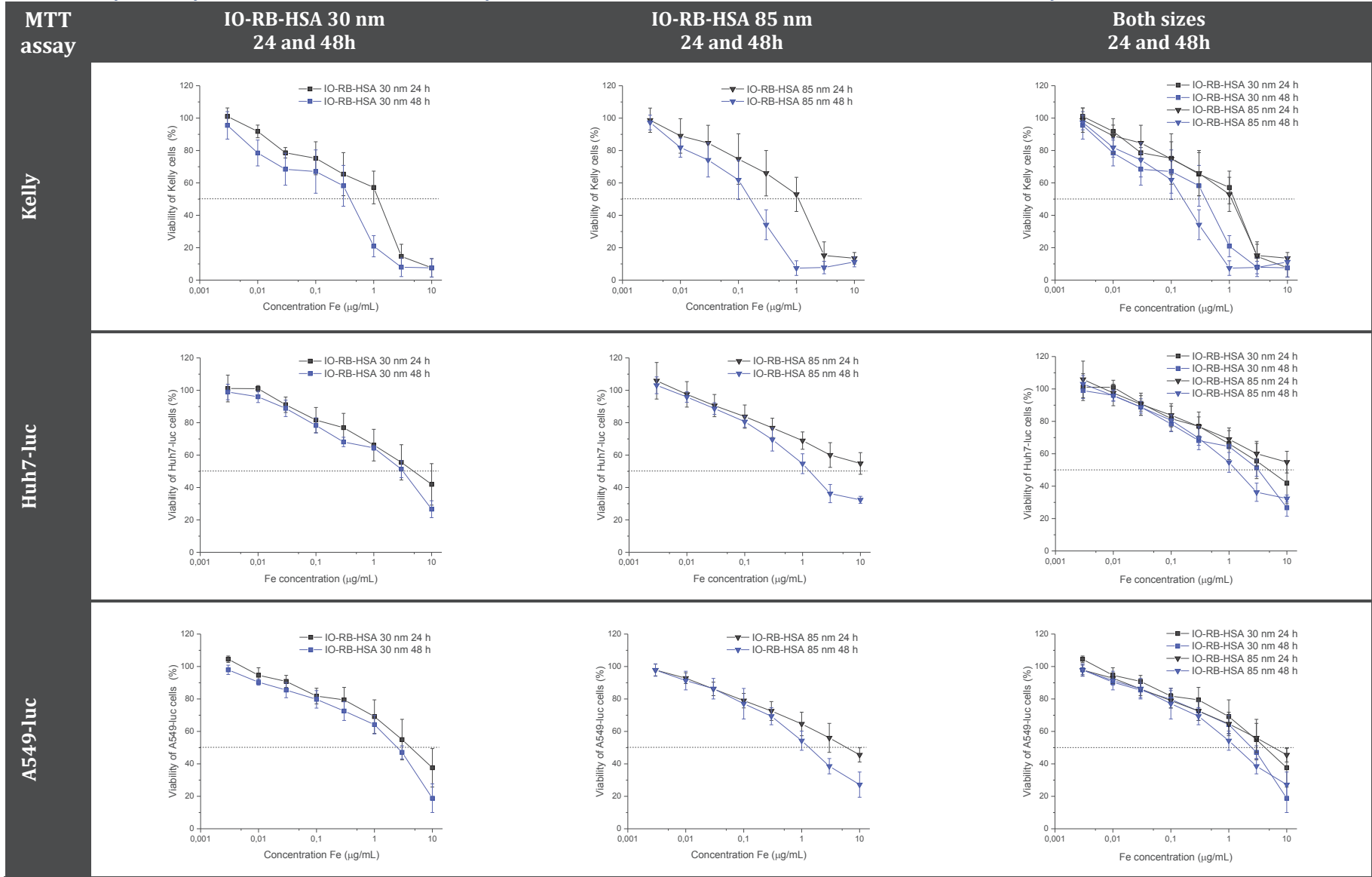


Table 5-9: Cytotoxicity assay of IO@RB-HSA NPs and their corresponding IO@RB-Dox-HSA NPs on three different cell lines related to size and incubation time

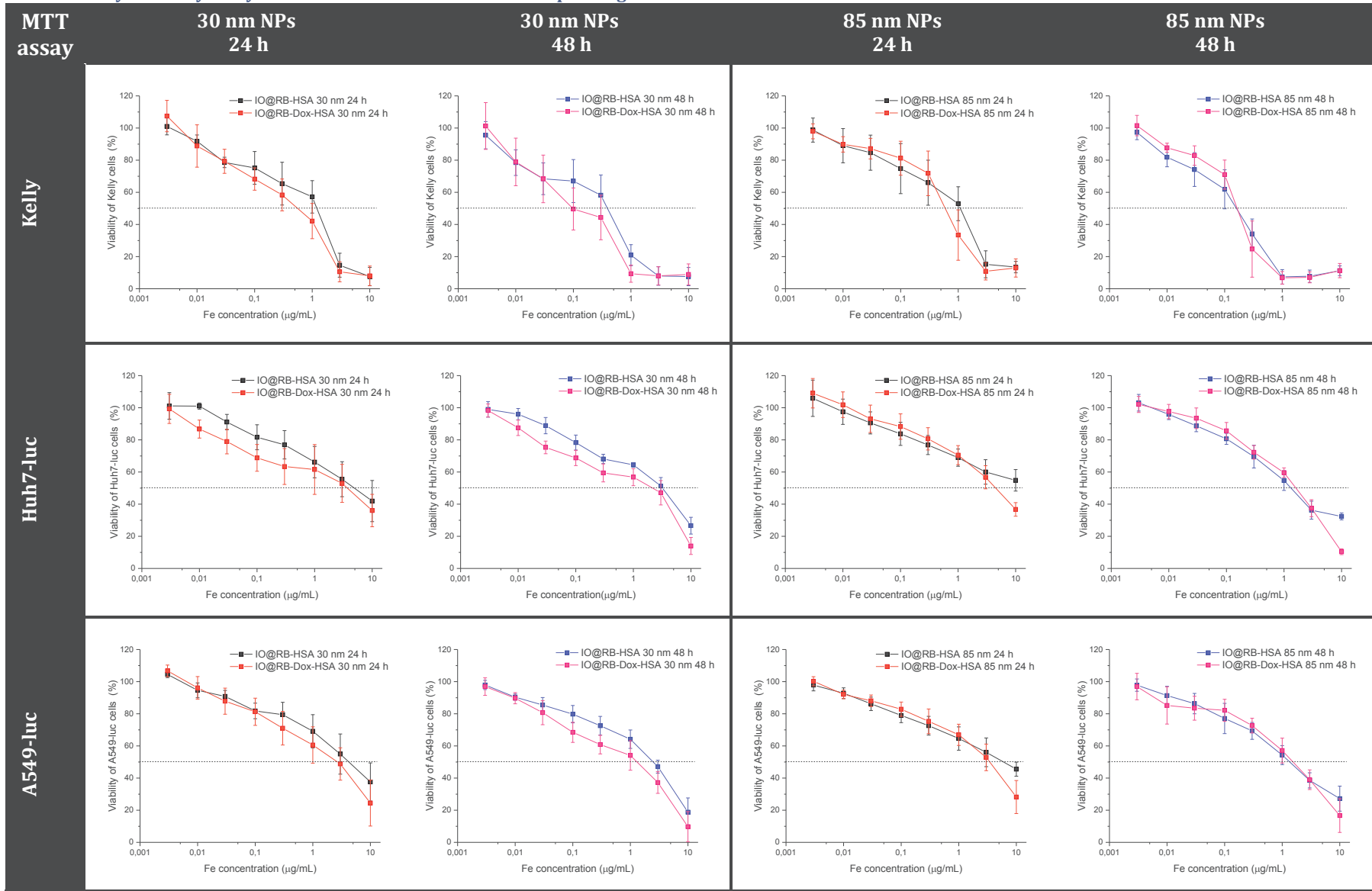


Table 5-10: IO@RB-HSA and IO@RB-Dox-HSA concentration values from MTT assays at 50% of cell viability for Kelly, Huh7-luc and A549-luc cells after 24h and 48h incubations

	IO@RB size (nm)	Time (h)	IO@RB-HSA NPs		IO@RB-Dox-HSA NPs	
			[Fe] at 50% of cell viability ($\mu\text{g}/\text{mL}$)	Cell viability at 10 μg Fe/mL (%)	[Fe] at 50% of cell viability ($\mu\text{g}/\text{mL}$)	Cell viability at 10 μg Fe/mL (%)
Kelly	30 nm	24 h	1.2	8	0.55	8
		48 h	0.4	8	0.1	9
	85 nm	24 h	1.1	14	0.6	13
		48 h	0.16	11	0.16	11
Huh7-luc	30 nm	24 h	4.9	42	3.7	36
		48 h	3	27	2.1	14
	85 nm	24 h	>10	55	4.5	37
		48 h	1.3	32	1.6	10
A549-luc	30 nm	24 h	4.2	38	2.7	24
		48 h	2.4	19	1.3	10
	85 nm	24 h	6	46	3.5	28
		48 h	1.3	27	1.5	16

6.2.2 Cellular uptake studies

6.2.2.1 NPs internalization study in 2D culture system

To investigate the cellular uptake of our IO@RB-HSA nanosystems, flow cytometry measurements combined to fluorescent microscopy analyses were performed using fluorescent-labelled IO@RB-HSA^{FITC} NPs.

Thus, internalization of IO@RB-HSA^{FITC} NPs of 30 and 85 nm in size was assessed after 24 h incubation at various Fe concentrations by flow cytometry measurement. Results are presented in Figure 5-55 as percentage of fluorescent cells and mean fluorescence intensity according to NPs' size and concentration.

From these results two main observations were made: the NPs internalization was dependent first of the NPs size and second of Fe concentration. Indeed, for all cancer cell lines and IO@RB-HSA sizes tested, percentage of fluorescent cell increased with Fe concentration. That is the sign of non-specific internalization process. Such kind of process relies on pinocytosis and therefore is directly related to the concentration of the particle in solution, or relies on endocytosis after non-specific adsorption of NPs on the plasma membrane.

Furthermore, for all cancer cell lines, the IO@RB-HSA NPs of 85 nm had a higher internalization rate than the smaller NPs. This can have two explanations. The first one, the most evident, is that the internalization is size-dependent and that bigger NPs internalized culture cells better than smaller NPs. Thus, a higher surface would enhance the interaction with the plasma cell membrane. Another explanation to be considered is that potentially more HSA^{FITC} is adsorbed on 85 nm size NPs due to the increase in surface area compare to 30 nm size NPs. Thus, as we work with a fix number of particle per cell, it could explain that higher internalization rates were obtained for the widest sample.

Furthermore, a difference in cell behavior was also observed. The Kelly cells internalized better the IO@RB-HSA NPs than the other cells, with high internalization rates. At [Fe] 0.8 µg/mL, after 24 h incubation, internalization rates of 84 % and 39 % were recorded for 85 and 30 nm NPs respectively. At this Fe concentration of 0.8 µg/mL the other cells showed similar internalization rates of 63 % on A549-luc cells and 65% on Huh7-luc cells for 85 nm NPs and 36 % for both cell lines for the 30 nm NPs. In addition, the internalization for A549-luc cell line was less affected than the other by the Fe concentration decrease. Indeed, even at the lowest Fe concentration of 0.2 µg/mL, the internalization rates for this cell line were about 34 % and 14 % for 85 and 30 nm NPs respectively, whereas they were about 21 % and 9 % for the Kelly cells and about 12 % and 7 % for the Huh7-luc cells.

As flow cytometry measurement do not inform on NPs cellular localization (intra vs extracellular), images of cells after 1, 2 and 24 h of incubation with the NPs were taken by epifluorescence microscopy. For this purpose, the nuclei, the cell membranes and the IO@RB-HSA were labelled with three different fluorescent probes (DAPI, PKH 26 and FITC respectively). The resulting images are presented in Table 5-11. They showed that already after 1 h and 4 h of incubation, IO@RB-HSA NPs started to be internalized in the cells.

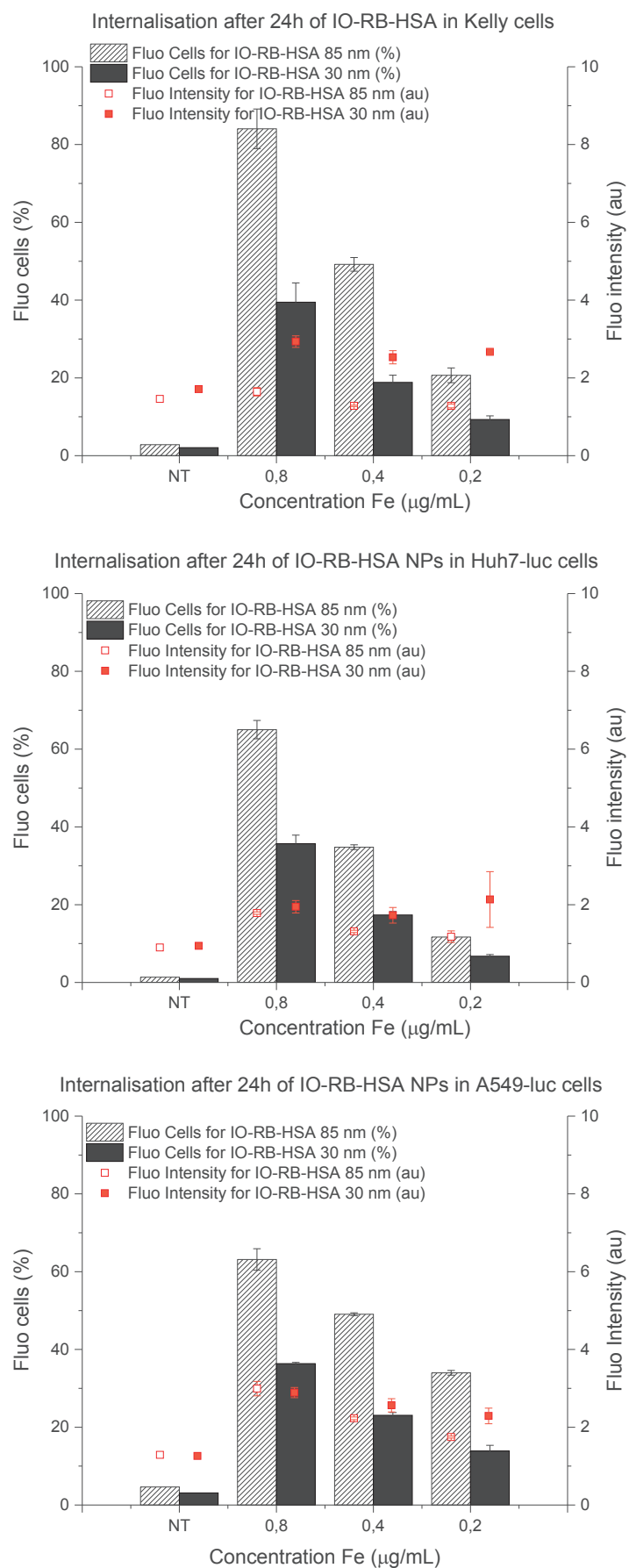
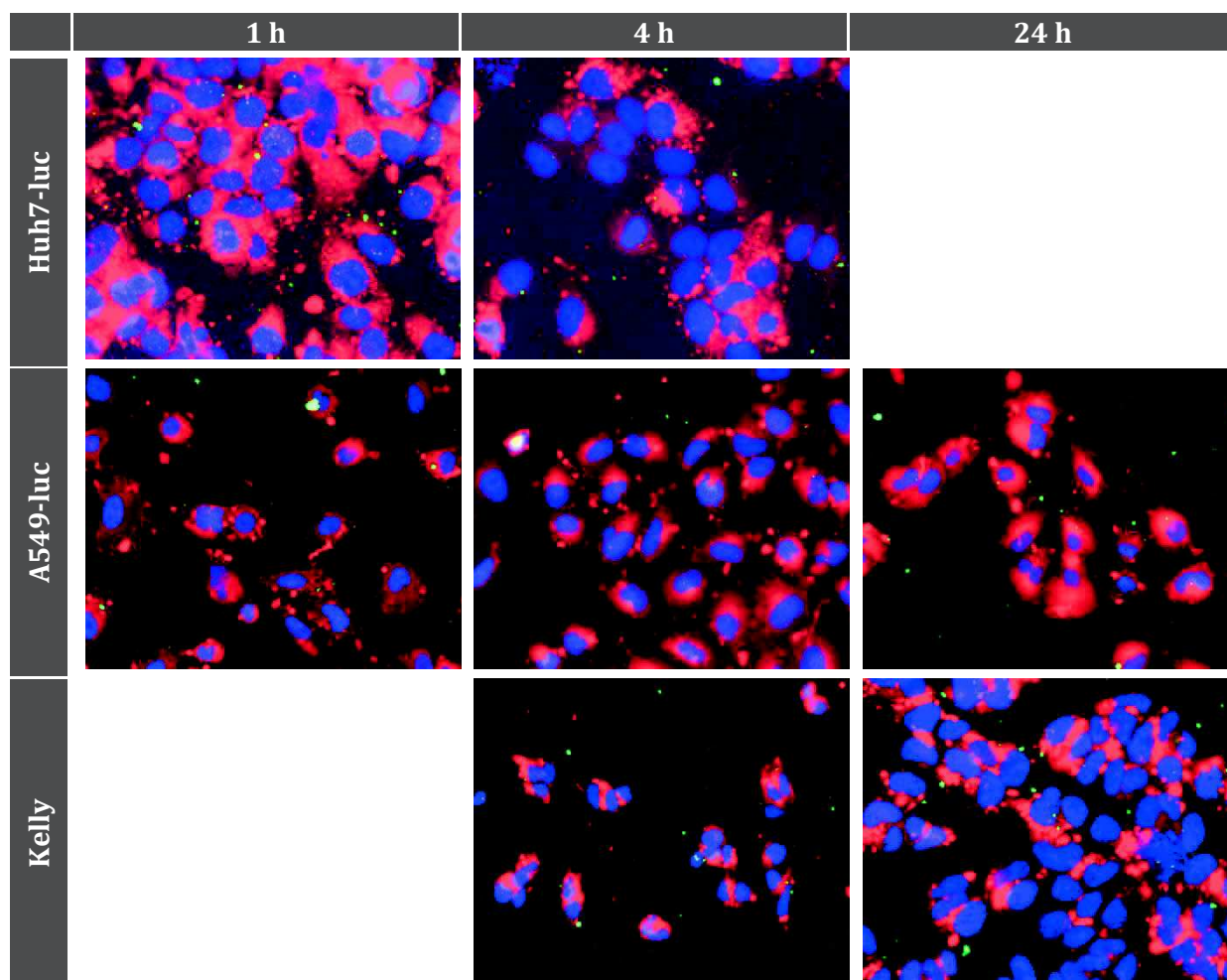


Figure 5-55: Cellular uptake studies by flow cytometry

Table 5-11: Epifluorescence images of IO@RB-HSA^{FITC} internalization into Huh7-luc, A549-luc and Kelly cells after 1, 4 and 24 h of incubation

6.2.2.2 Confocal study on 3D IO@RB internalization into spheroids

This part is dedicated to the study of NPs internalization and subsequent Dox diffusion into Huh7-luc MCTS after 24 h incubation performed on the previous IO@RB-HSA^{FITC} and IO@RB-Dox-HSA samples with 30 and 85 nm sizes.

6.2.2.2.1 Particle internalization into spheroids

First, the IO@RB-HSA^{FITC} internalization into spheroids was imaged for both particles sizes (30 and 85 nm) at two Fe concentrations (0.4 and 0.8 $\mu\text{g Fe/mL}$). Z-stack analyses performed on the entire spheroids indicated that the IO@RB-HSA^{FITC} NPs seemed for both sizes to be internalized after 24 h at the border of the spheroid. Furthermore, without any surprise, the fluorescence intensity, corresponding to the content of NPs internalized, was more important for both samples at the highest concentration of 0.8 $\mu\text{g Fe/mL}$ than at 0.4 $\mu\text{g Fe/mL}$. They seemed to be located either on the surface of the cells and into the cytoplasm but restricted to the first layer of cells forming the spheroids.

To investigate more precisely this internalization behavior, confocal images at higher image resolution were performed for each condition. The resulting images are presented in Table 5-12. The first and last lines showed images taken at the top and the bottom of the spheroids, *i.e.* the periphery region, whereas the two middle table lines showed the pictures obtained in the core region of the spheroids. At low concentration, 0.4 $\mu\text{g Fe/mL}$, the internalization occurred in a short depth, thus the green fluorescence resulting from IO@RB-HSA^{FITC} NPs was clearly visible only in the top and bottom images where the penetration depth was not high. At 0.8 $\mu\text{g Fe/mL}$, as the concentration was higher than previously, the internalization depth and the amount of internalized particles were higher resulting in a better visualization by fluorescence. Thus, images of the core region of the spheroids showed clearly for both IO@RB-HSA^{FITC} sizes, the internalization of NPs occurred at the spheroid border with a penetration depth of about 10 to 20 μm . Furthermore we could also notice that the smallest NPs seemed to penetrate a little deeper than the largest ones. Such result is in accordance with previous work showing size-dependent localization and penetration of gold nanoparticles in multicellular spheroids. Indeed, it was proved that smaller NPs penetrate more deeply into tumor models whereas larger NPs were primarily localized in the periphery (283, 284).

Table 5-12: High resolution CLSM imaging of Huh-7 MCTS after 24h incubation with IO@RB-HSA^{FITC} NPs of 30 and 85 nm at 0.4 and 0.8 µg Fe/mL

	IO@RB-Dox-HSA 30 nm		IO@RB-Dox-HSA 85 nm	
	0.4 µg Fe/mL	0.8 µg Fe/mL	0.4 µg Fe/mL	0.8 µg Fe/mL
Top				
Middle				
Bottom				

6.2.2.2.2 Dox diffusion into Huh7-luc MCTS

Previous study showed that the IO@RB-HSA NPs were internalized at the border of the spheroids with a depth of 10 to 20 μm . However, we aimed to investigate if this depth internalization was enough to allow Dox release and its diffusion into the entire spheroid.

First, to have a positive control to our experiment, the diffusion behavior of free Dox on Huh7-luc MCTS was investigated. Thus, the spheroids were incubated for 24 h with various concentrations of Dox. As pictured on the images summarized in Table 5-13, Dox accumulated after 24 h of incubation into the nuclei of the cells, even at the very low concentration of 0.01 $\mu\text{g}/\text{mL}$.

To investigate the Dox penetration into MCTS after release from IO@RB-Dox-HSA NPs, Z-stack analyses were performed on each spheroid. Like previously, both IO@RB-Dox-HSA sizes were studied at Fe concentrations of 0.8 and 0.4 $\mu\text{g}/\text{mL}$. To compare the fluorescence behaviors Z-stack images were also performed with the same instrument parameters (laser intensity, image resolution, zoom, pinhole...) on spheroids incubated 24 h with free Dox.

Compared to previous confocal study on IO@RB-HSA^{FITC}, Dox released from IO@RB-Dox-HSA NPs was not accumulated at the border but diffused through the entire spheroid no matter the particle diameter. It is the sign that Dox released after the NPs internalization. Furthermore, it showed a fluorescence intensity close to the one observed for free Dox at 0.3 $\mu\text{g}/\text{mL}$. To highlight this effect images performed at higher resolution, presented in Table 5-14, were performed. For the smallest sample of 30 nm, the Dox fluorescence intensity in the spheroids increased with the NPs concentration whereas for the widest sample of 85 nm we can observe a change in the fluorescence localization depending on particle concentration. Indeed, for IO@RB-Dox-HSA 85 at 0.4 $\mu\text{g Fe}/\text{mL}$ and the 30 nm sample at both concentrations, the fluorescence was shallow thus Dox seemed to be homogeneously dispersed in the cell membrane whereas at for the sample of 85 nm at 0.8 $\mu\text{g Fe}/\text{mL}$ the Dox fluorescence intensity started to concentrate in the nuclei. To observe even more precisely the Dox presence in the nuclei for the spheroids incubated with IO@RB-Dox-HSA at 0.8 $\mu\text{g Fe}/\text{mL}$, images with higher resolution and zoom were performed (Table 5-15).

Table 5-13: CLSM imaging of free Dox penetration into spheroids after 24 h of incubation at various concentrations: 0, 0.01 and 3 $\mu\text{g}/\text{mL}$

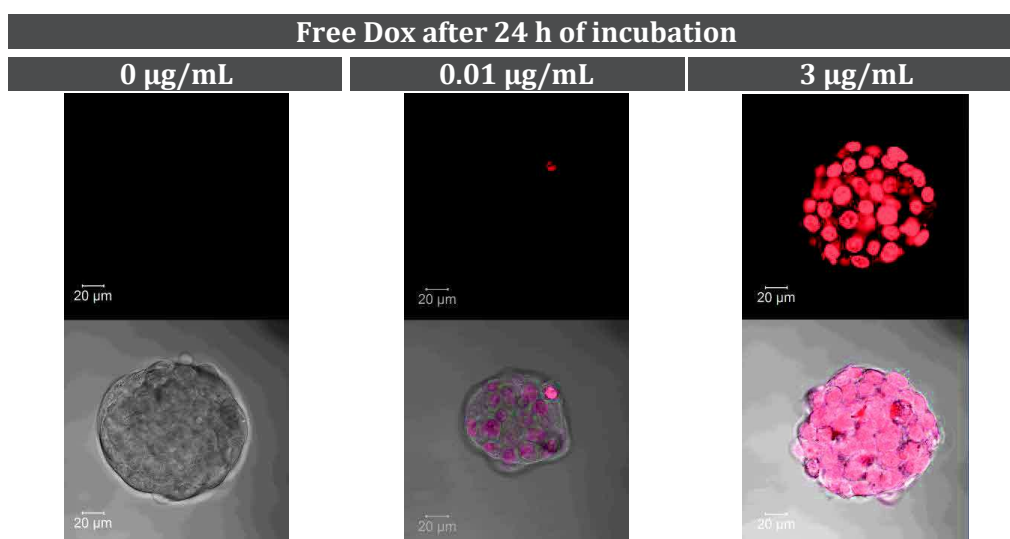


Table 5-14: : High resolution CLSM imaging of Huh-7 MCTS after 24h incubation with IO@RB-Dox-HSA NPs of 30 and 85 nm at 0.4 and 0.8 µg Fe/mL

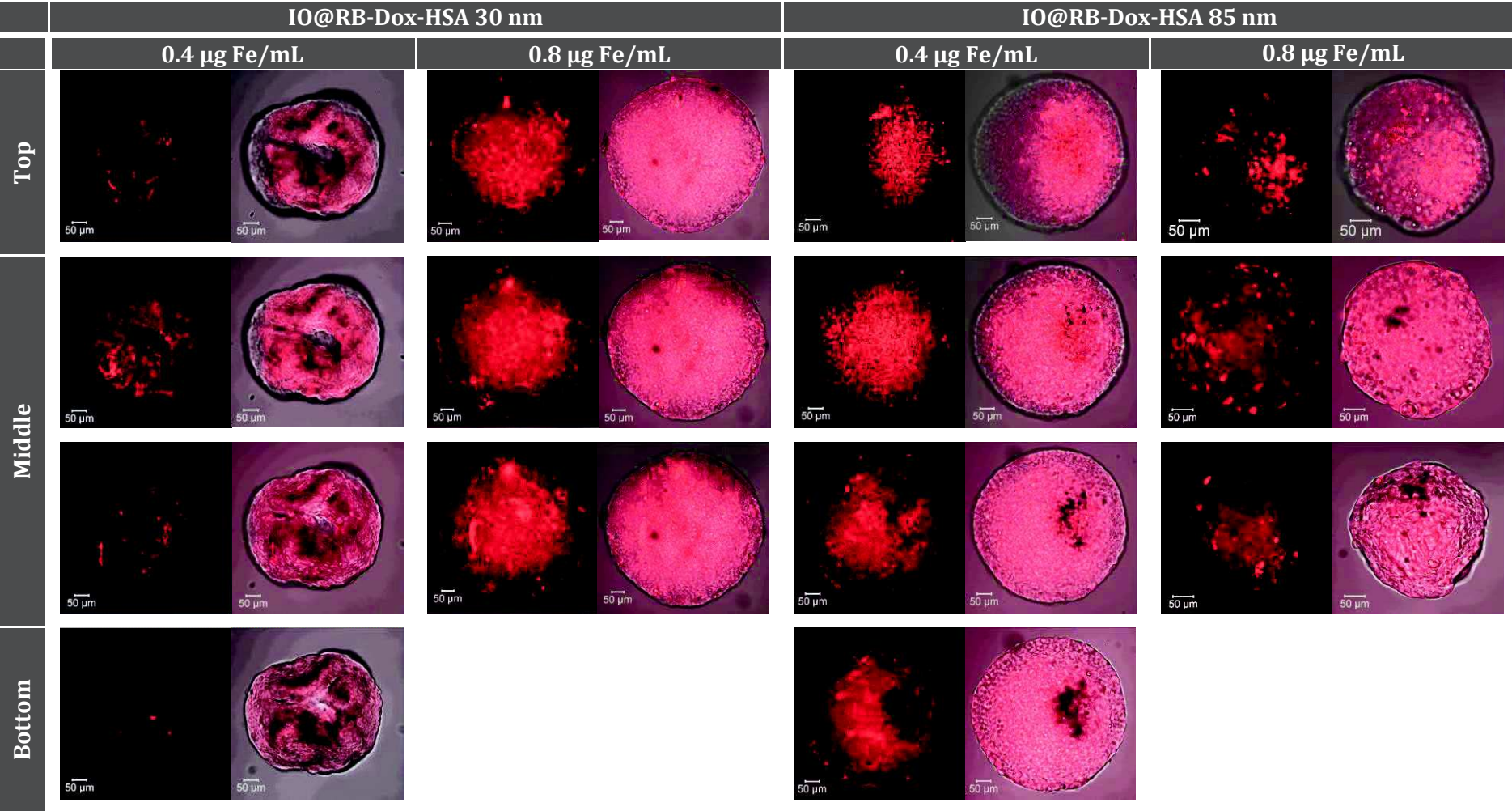
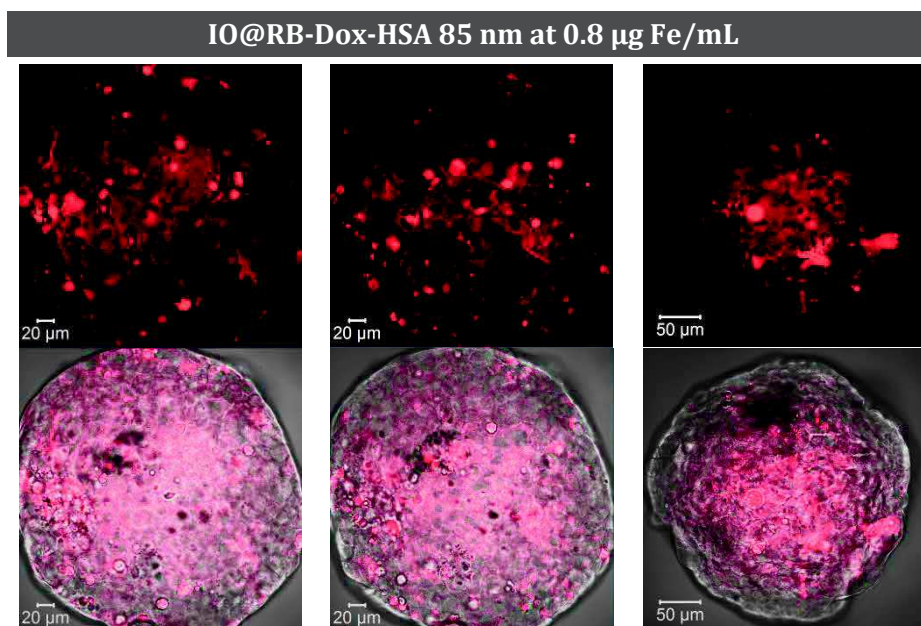


Table 5-15: High resolution CLSM imaging of Huh-7 MCTS after 24h incubation with IO@RB-HSA^{FITC} NPs of 85 nm at 0.8 $\mu\text{g Fe/mL}$ (x 40 objective)



6.2.2.2.3 Conclusion

To conclude, even if the NPs internalized only at the periphery of the spheroids it allowed the local release of Dox that can in a second step diffuse into the entire 3D model. This is illustrated in the 3D reconstitution of Z-stacks from the 30 nm sample incubated at 0.8 $\mu\text{g Fe/mL}$ (Figure 5-56) in which we can clearly see the NPs stuck at the edges of the spheroid and the Dox homogeneously dispersed. Such behavior could sign the lag between the particle internalization and Dox release as it is triggered by HSA digestion by endocytic proteases.

Such 3D culture system is a model of early tumorigenesis process. So for these results helps to envision how such particle could works on *in vivo* models

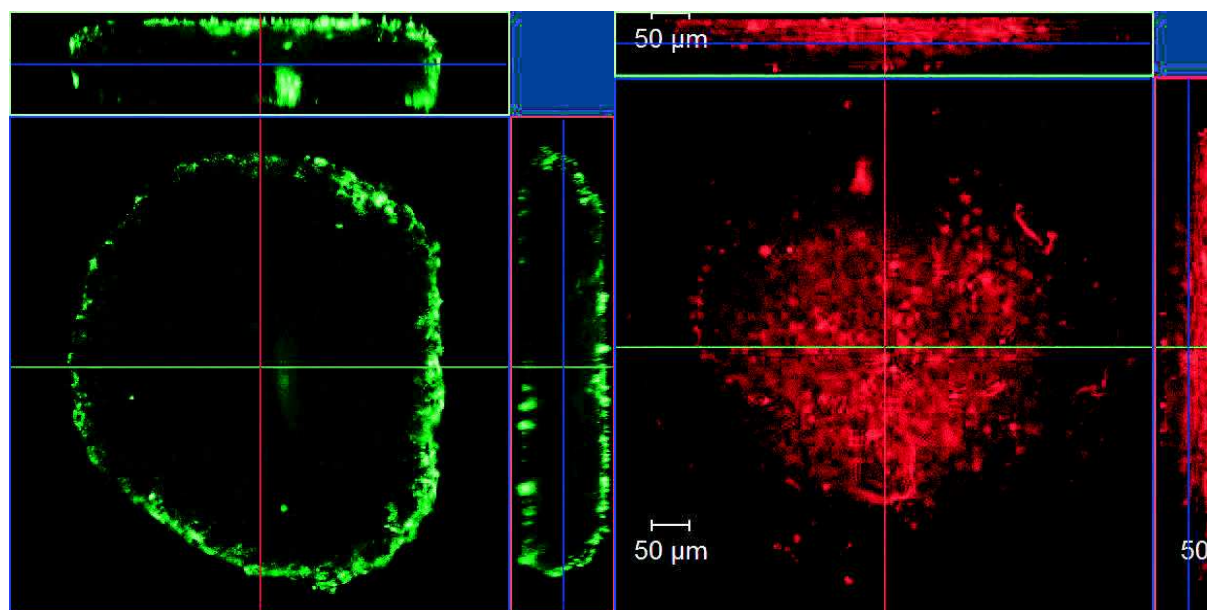


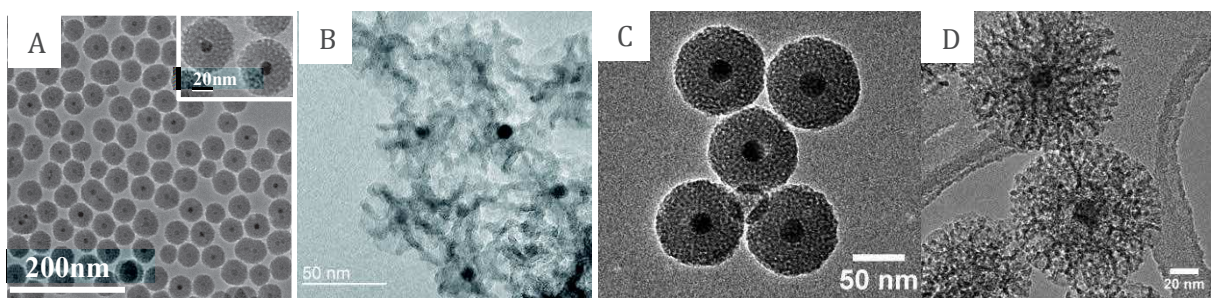
Figure 5-56: 3D reconstitution of Z-stack images from IO@RB-HSA^{FITC} (left) and IO@RB-Dox-HSA (right) of 30 nm at 0.8 $\mu\text{g Fe/mL}$

7 Conclusion

To conclude we set up firstly the best protocol parameters for reproducible synthesis of spherical monodispersed IO@RB NPs. These NPs were analyzed by proton relaxometry and showed promising T_2 contrast for MRI diagnosis especially thanks to a high r_2/r_1 ratio due to an important decrease in r_1 value compared to silanized IO NPs. Furthermore the addition of HSA coating on the IO@RB NPs enhanced significantly their T_2 contrast properties. Then Dox loading studies have established that the best soaking conditions to reach high DLC and DLE values were to work on IO@RB NPs with amino-modified surface in water. Furthermore, we found out that, after Dox loading and capping by tight HSA shell, an efficient HSA degradation with proteases was not sufficient to allow Dox release from the IO@RB NPs. We then improved the IBAM-HSA coating process to avoid any leakage of loaded-Dox during this synthesis steps and we also improved the final DLC estimation by TGA analyses. Furthermore, we studied if the change of IBAM-HSA into HSA-IBAM-HSA coating would enhance drug release. Unfortunately, the same results than with IBAM-HSA was observed than for HSA-IBAM-HSA: efficient protein shell degradation was observed under enzymatic action, however no significant drug release was obtained. Finally, biological activities of our systems were investigated. Thus, IO@RB-HSA NPs showed a size-dependent cytotoxicity and internalized well in all cancer cell lines studied in 2 D and in 3D models. Furthermore, the Dox-loaded NPs, prepared under non-optimized conditions, showed a slightly more cytotoxic effect and diffused into entire MCTS even if the NPs were internalized only at the spheroid's periphery, stating of their efficient release and diffusion properties.

Chapter 6:

Core-shell morphology tuning for enhancement of theranostic properties



1 Introduction

In the previous chapter we demonstrated the potential of IO@RB-Dox-HSA NPs for theranostic applications. Indeed, these nano-objects were able to encapsulate a large amount of Dox into the silica shell porosities for therapy and also showed promising T_2 contrast properties for MRI diagnosis. However, we thought that the design of our system could be optimized for enhancing theranostic effects.

Indeed, it is well known that the pore morphology of mesoporous silica could influence the loading of molecules (34, 47, 52, 156, 285). Furthermore, saturation magnetization M_s varies with the size of IO NPs and influences thus their T_2 contrast efficiency. Indeed, larger the IO NPs M_s value and thus higher the T_2 contrast efficiency (286). Studies showed that the optimized mean size to reach high SAR value was around 20 nm (4–6). Thereby, our core-shell system was tuned with various IO core sizes (10 or 20 nm) and various silica shell porosity morphologies (raspberry and stellar) leading to four types of core shell NPs as presented in Figure 6-1. Then the potential enhancement of their theranostic abilities was investigated.

Thus this chapter, dedicated to the tuning of core-shell structures for enhancement of theranostic efficiency, is divided in three parts:

1. The synthesis and characterization of the NPs
2. The impact of pore morphology on Dox loading
3. The advantages of an IO core of about 20 nm on theranostic effects

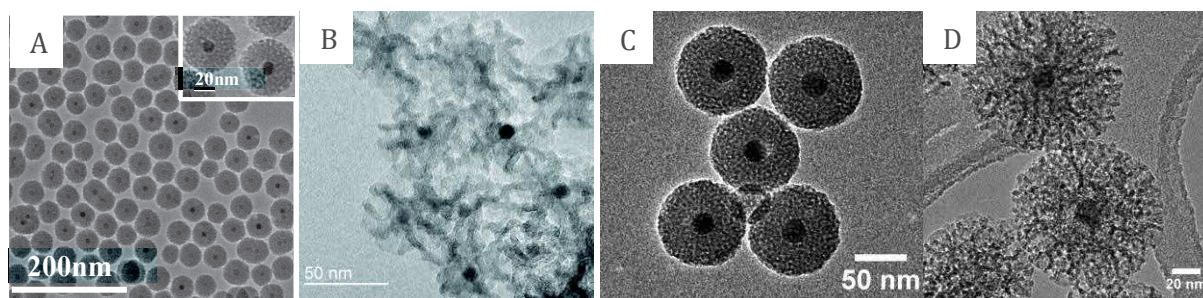


Figure 6-1: The four types of core-shell structures: A) IO core of 10 nm surrounded by a RB shell, B) IO core of 10 nm surrounded by a ST shell, C) IO core of 20 nm surrounded by a RB shell and D) IO core of 20 nm surrounded by a ST shell

2 Syntheses

2.1 IO@RB with 20 nm core size

The synthesis of IO@RB NPs starting with an IO core of about 10 nm was deeply investigated in chapter 2 part 2 page 125 to 136. Based on this study we applied the resulting protocol for the synthesis of IO@RB NPs using larger IO NPs of about 20 nm as seeds. As pictured in TEM images in Figure 6-2, the resulting IO@RB NPs showed the expected core-shell morphology. Furthermore, as it was the case for 10 nm IO NPs used as seeds (see page 134), the sizes of IO@RB NPs obtained from IO 20 nm NPs were tuned by changing the [CTAB]/[Fe] ratio. As summarized in Table 6-1, N_2 adsorption-desorption analyses obtained on three of our samples resulted in the calculation of similar pore size (around 2.5 nm) than the data reported in literature on the same kind of NPs. However, the surface areas and pore volumes resulting from these analyses were for our samples lower than reported data.

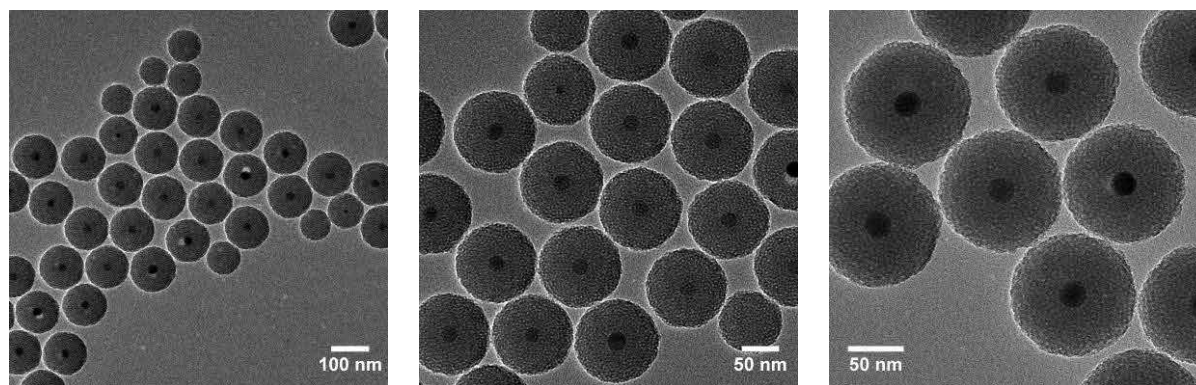


Figure 6-2: TEM images of various IO@RB NPs samples obtained with a core of ~20 nm

Table 6-1: Pore parameters obtained from N₂ adsorption-desorption analyses for IO@RB NPs

References	Core diameter (nm)	Particle diameter (nm)	BET surface area (m ² /g)	Pore volume (cm ³ /g)	Pore size (nm)
(141)	15	53	481	1.07	2.6
(274)	15	67	452	1.11	2.5
(154)	20	60	326	0.285	2.4
Sample 1	18	66 ± 9	132	0.35	2.6
Sample 2	18	66 ± 4	116	0.42	2.4
Sample 3	18	54 ± 3	308	0.63	2.3

2.2 IO@ST with various core size

2.2.1 Synthesis strategies

Our first idea to produce a silica shell with larger pores was to add IO NPs, transferred from chloroform into aqueous media thanks to CTAB, during the BMS NPs synthesis, detailed in Chapter 2 page 56. We wished that the IO NPs would act as seeds, like in the IO@RB synthesis, leading to IO@BMS core-shell structure. Unfortunately, these experiments were unsuccessful. Thus after many trials, we decided to abort this strategy.

Recently Zhang *et al.* (41) reported the synthesis of small monodispersed mesoporous silica nanoparticles (sizes < 200 nm) with three different kinds of porosity morphologies: stellate, raspberry-like and worm-like. We previously deeply investigated the formation of RB NPs with small porosities (~3 nm) in Chapter 4 part 3 page 98 to 121 and their IO@RB derivatives in Chapter 5. In this part, we focused on the stellate morphology (ST) that, according to Zhang *et al.*, exhibited sizes under 100 nm and pore sizes around 15 nm which seemed perfect to replace our previous strategy.

2.2.2 Synthesis of ST NPs

To investigate the feasibility of this idea we first reproduced the ST NPs synthesis from Zhang *et al.* procedure. Their ST NPs synthesis process is based on the same strategy than the one they developed for RB NPs synthesis: surfactant micelles are used as soft templates for the formation of porosity. The difference between both syntheses is in the choice of surfactant. Indeed, for RB synthesis, CTAB is used leading, according to Zhang *et al.*, to strong templating

conditions whereas, for ST synthesis, CTATOs, that induces weaker templating conditions, is used (for more details see Chapter 1 page 10).

The synthesis procedure, described in Chapter 2 page 57, led, as shown on TEM images in Figure 6-3 A and B, to monodisperse spherical NPs of 101 ± 10 nm with stellar pore channel morphology. Intensity DLS measurement of ST NPs dispersed in EtOH exhibited a hydrodynamic diameter of 138 nm (Figure 6-3 C). SEM images, shown in Figure 6-4, confirmed the monodispersity in size of ST NPs and attested that the stellar pore mouths were open to the outside. Furthermore, N_2 adsorption-desorption isotherms and PSD analyses, Figure 6-5 A and B respectively, showed similar behavior than that reported by Zhang *et al.*. Indeed, N_2 adsorption-desorption isotherms displayed a type IV hysteresis and PSD curve obtained by BJH calculations, showed porosities of 9.4 and 15.5 nm (porosities observed around 40 nm were due to the interparticle voids). Table 6-2 summarized the resulting surface specific area, pore volume and PSD values of the sample compared to the literature values. Thus our sample showed very similar physical characteristics with literature values: for our sample surface specific area was of $528 \text{ m}^2/\text{g}$, pore volume was of $1.15 \text{ cm}^3/\text{g}$ and pore sizes were of 9.4 and 15.5 nm compared to the respective values of $590 \text{ m}^2/\text{g}$, $1.38 \text{ cm}^3/\text{g}$ and 17 nm reported in the literature.

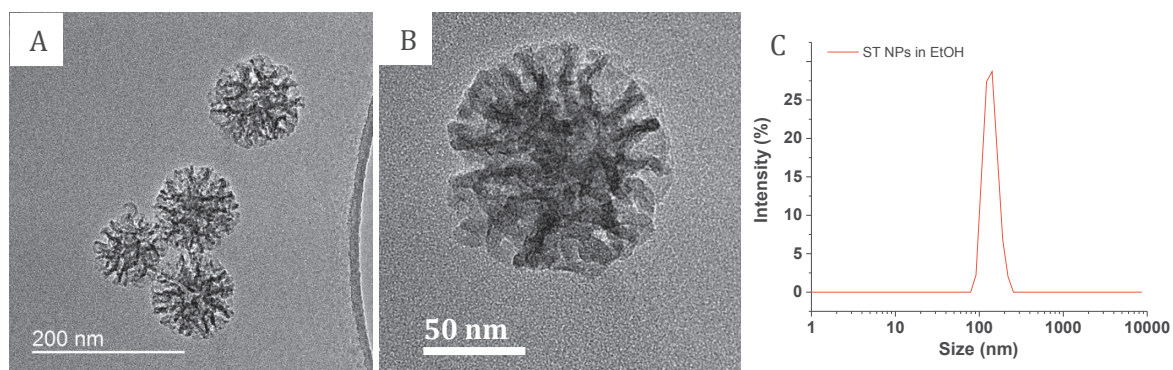


Figure 6-3: A) and B) TEM images of ST NPs and C) DLS measurement of ST NPs dispersed in EtOH

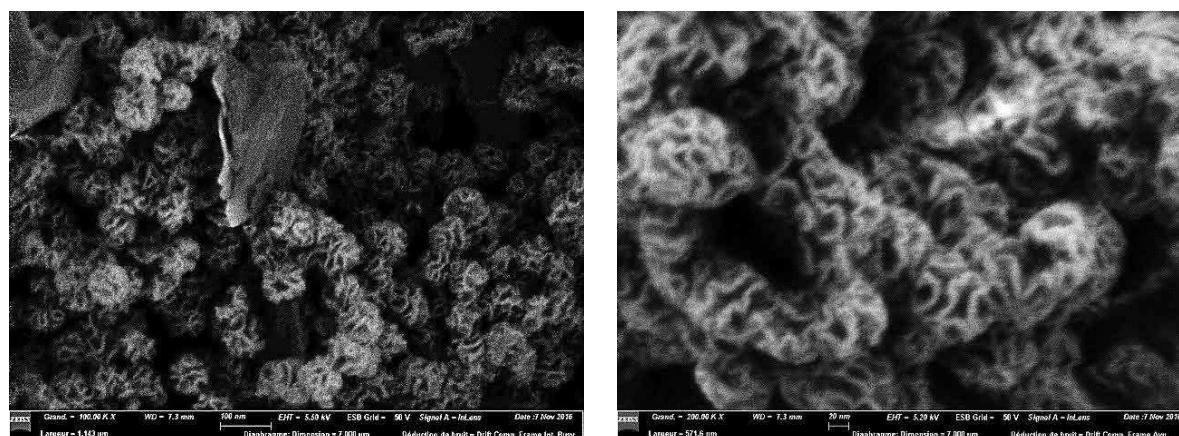


Figure 6-4: SEM images of ST NPs

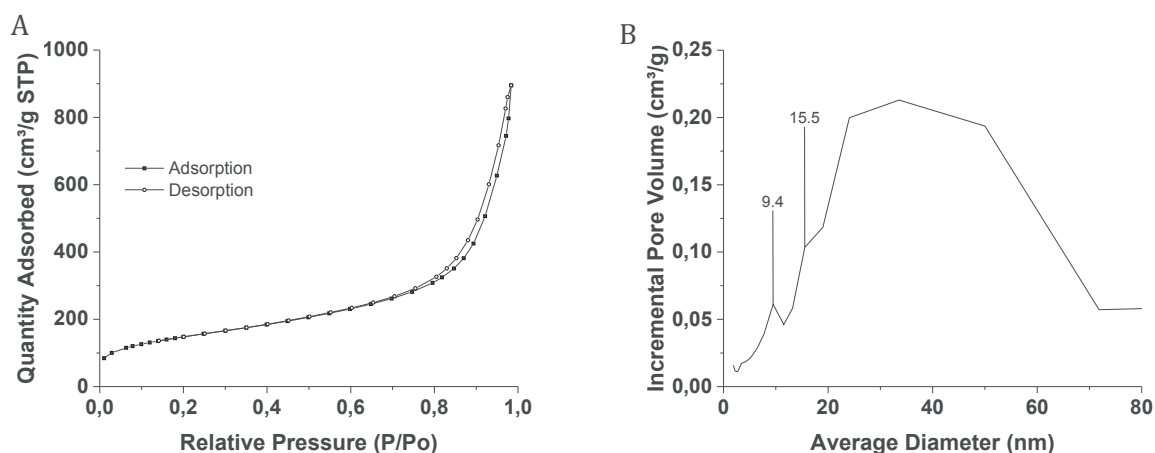


Figure 6-5: A) N₂ adsorption-desorption isotherms and B) corresponding PSD curves for ST NPs

2.2.3 Synthesis of IO@ST NPs

The addition of IO NPs of 10 nm to the previous ST NPs synthesis process (see detailed protocol in page 57), led to IO@ST NPs. As shown in SEM images in Figure 6-6, the same surface morphology than ST NPs was obtained for IO@ST NPs. TEM images and size distribution histograms of three IO@ST samples, presented in Figure 6-7, showed spherical monodisperse NPs with sharp sizes around 60 nm.

However, as shown in STEM and TEM images Figure 6-8, Figure 6-7 and Figure 6-9, the IO cores were difficult to distinguish. For example, the IO cores of three NPs annotated in TEM images from Figure 6-9, were barely visible in Figure 6-9 A. They started to appear on the images B and C at higher magnifications but only for NPs n°1 and 2. Changing the focus of the instrument finally showed the IO core of NP n°3 whereas the core of NP n°1 disappeared in the image D. This TEM images analysis showed the difficulty we had to estimate if all of our IO@ST NPs had an IO core.

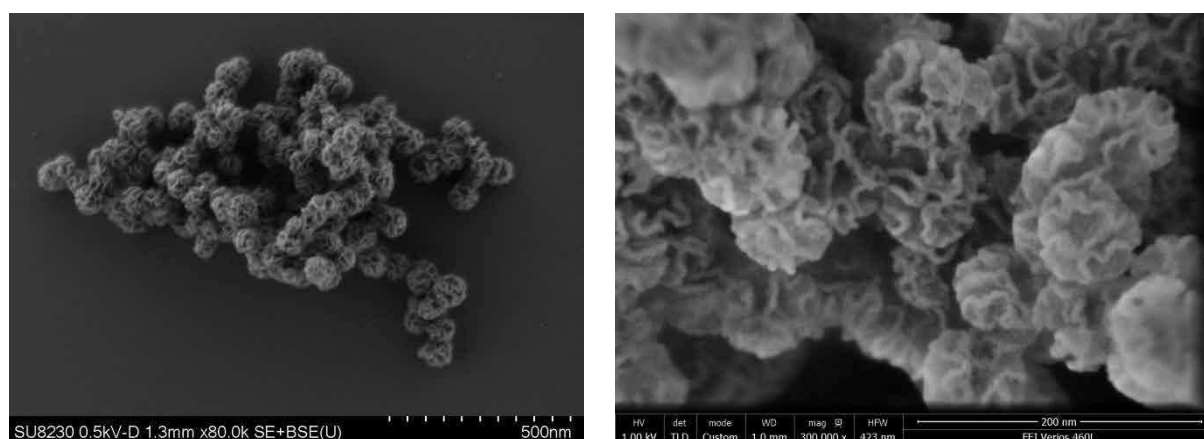


Figure 6-6: SEM images of IO@ST NPs with IO cores of 10 nm

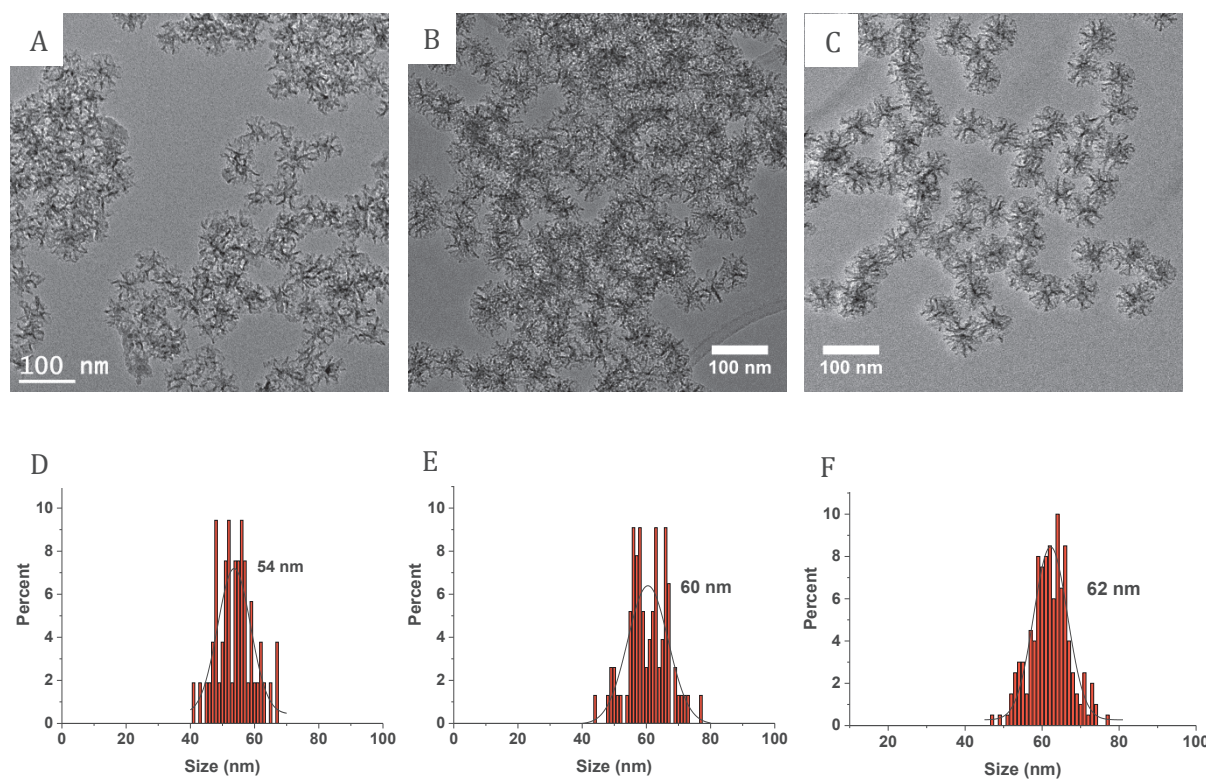


Figure 6-7: TEM images (A, B, C) and size distribution histograms (D, E, F) of three IO@ST samples obtained with IO core of 9 ± 1 nm: sample 1 with average size of 54 ± 6 nm (A, D), sample 2 with average size of 60 ± 6 nm (B, E) and sample 3 with average size of 62 ± 5 nm (C, F)

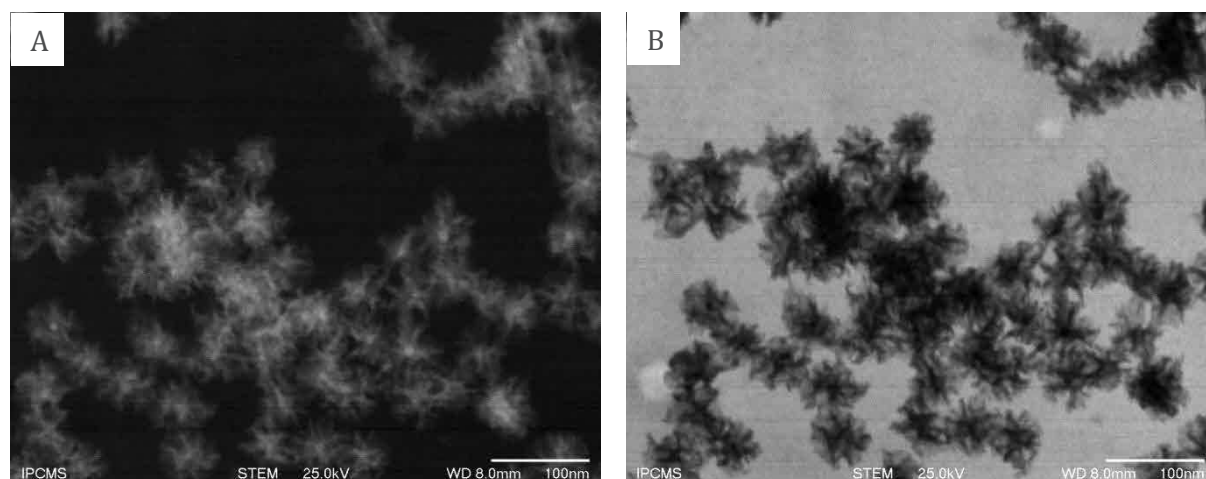


Figure 6-8: STEM images of IO@ST NPs with IO cores of 10 nm

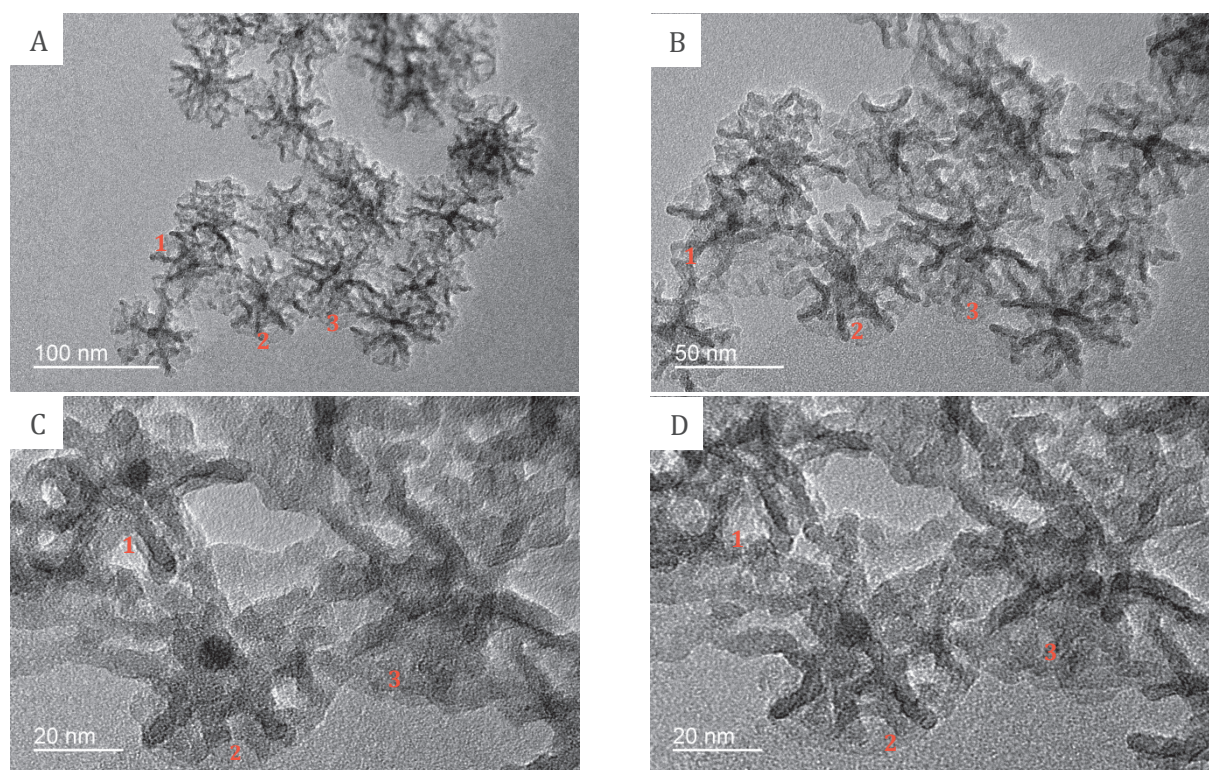


Figure 6-9: TEM images of IO@ST NPs with IO cores of 10 nm

Changing IO cores of 10 nm by IO cores of 20 nm in the synthesis process also led to spherical IO@ST NPs, Figure 6-10. As the IO core was wider it was easier to distinguish in TEM images of these samples than for the previous ones. However, these samples seemed to have two populations of NPs: larger ones around 120 nm with a clearly visible IO core and smaller NPs of 80 nm which not seemed to have IO core. The size distribution determined from TEM images is similar and bimodal for the three samples, Figure 6-10. One peak is quite small and the main peak centered at 117, 118 and 84 nm for samples 1, 2 and 3 respectively. The only difference between these samples was the [CTATos]/[Fe] molar ratios. Indeed, we tried to tune the IO@ST NPs sizes by modifying [CTATos]/[Fe] ratios as we did for IO@RB NPs, page 134. Thus, molar ratios of 3, 4 and 6 were used for samples 1, 2 and 3 respectively. We observed that these modifications in [CTATos]/[Fe] molar ratios did not induce a tuning of IO@ST sizes as expected, but changed the proportions between both NPs populations. Thus, the increase in [CTATos]/[Fe] ratio tend to increase the number of smaller core-less NPs around 80 nm. To conclude, these preliminary studies showed that an excess of surfactant in the contrary to IO@RB NPs synthesis did not lead to an increase in IO@ST NPs size but to an increase in ST NPs number. Unfortunately, we did not achieve yet enough syntheses to give a statistical study as we did for IO@RB NPs page 134. Thus, the influence of [CTATos]/[Fe] ratio on IO@ST morphology need to be further investigate to give a more precise conclusion based on reproducibility.

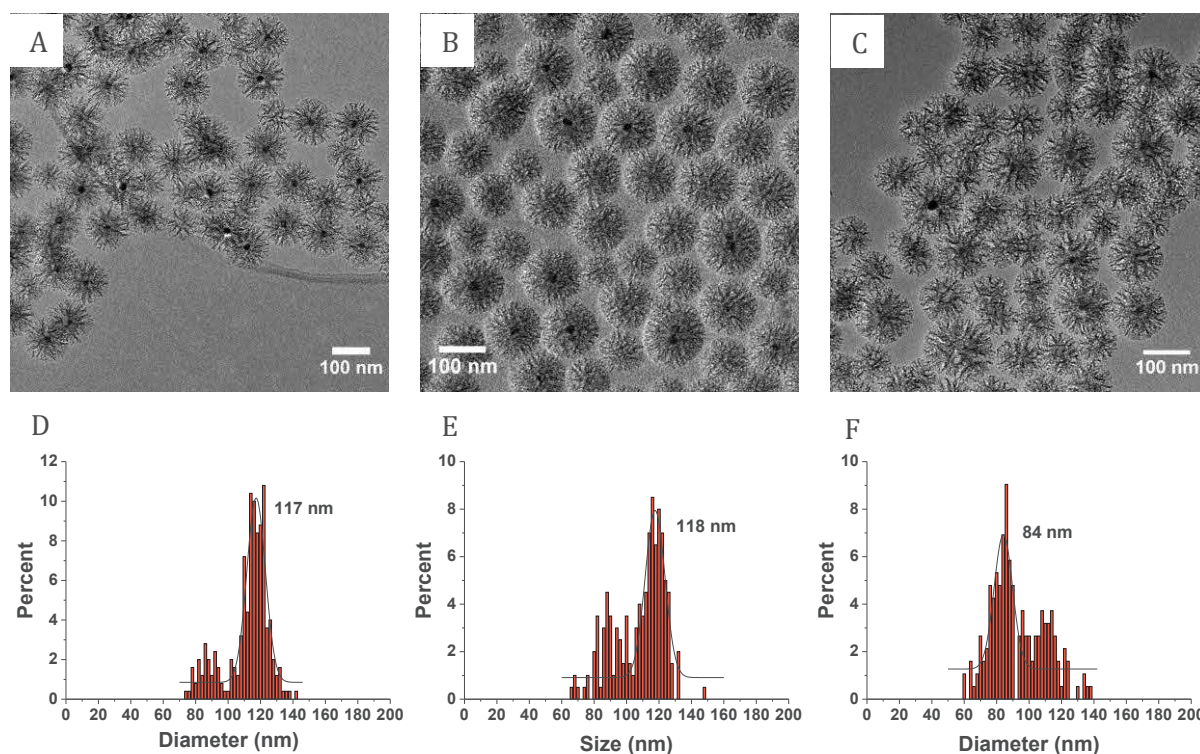


Figure 6-10: TEM images (A, B, C) and size distribution histograms (D, E, F) of three IO@ST samples obtained with IO core of 18 ± 1 nm: sample 1 with average size of 111 ± 14 nm and gaussian centered at 117 nm (A, D), sample 2 with average size of 107 ± 16 nm and gaussian centered at 118 nm (B, E) and sample 3 with average size 97 ± 17 nm of and gaussian centered at 84 nm (C, F)

To investigate if IO NPs were well present as core in each NP or if, as the TEM results suggested, the sample presented smaller particles without core, STEM EDX experiments were achieved on sample 2. As illustrated in Figure 6-11, EDX analyses were performed locally on single NPs. For example, NPs n°5, 7, 9, 17 and 20 clearly exhibited an IO core whereas no core was visible for NPs n°6, 8, 10, 18 and 19.

For sample 2, 67 NPs were analyzed. 42 % of the analyzed NPs did not exhibit clearly an IO core on the STEM images. EDX analyses showed that from these 28 % of analyzed NPs did not have Fe signal. From these 28 %, 25 % were part of the 42 % of NPs that did not exhibit clearly an IO core on the STEM images. Thus the analyses gave 3 % of false negative results and 16 % of analyzed NPs for which no IO cores were visible finally owned IO core. Furthermore, 68 % of the core-less NPs had sizes below 100 nm.

To conclude, these analyses confirmed that the IO cores were not always visible by imaging and that core-less NPs were also present in the samples. Furthermore, most of these core-less NPs exhibited sizes below 100 nm.

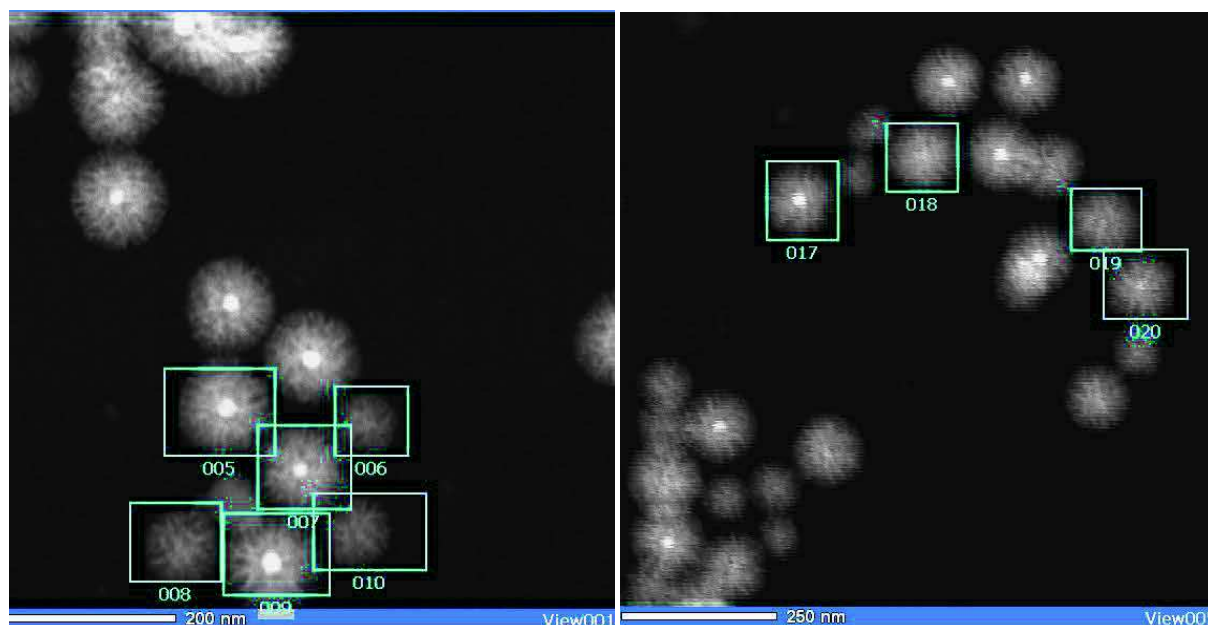


Figure 6-11: Illustration of STEM EDX experiments achieved on IO@ST NPs

As depicted in Figure 6-12, N₂ adsorption-desorption isotherms analyses of IO@ST NPs gave information on the surface area, pore volume and pore size distribution. The resulting values are summarized in Table 6-2. All samples, without distinction in the core size, exhibited large specific surface area higher than 500 m²/g, pore volume around 1.3 cm³/g and large porosities around 10 nm.

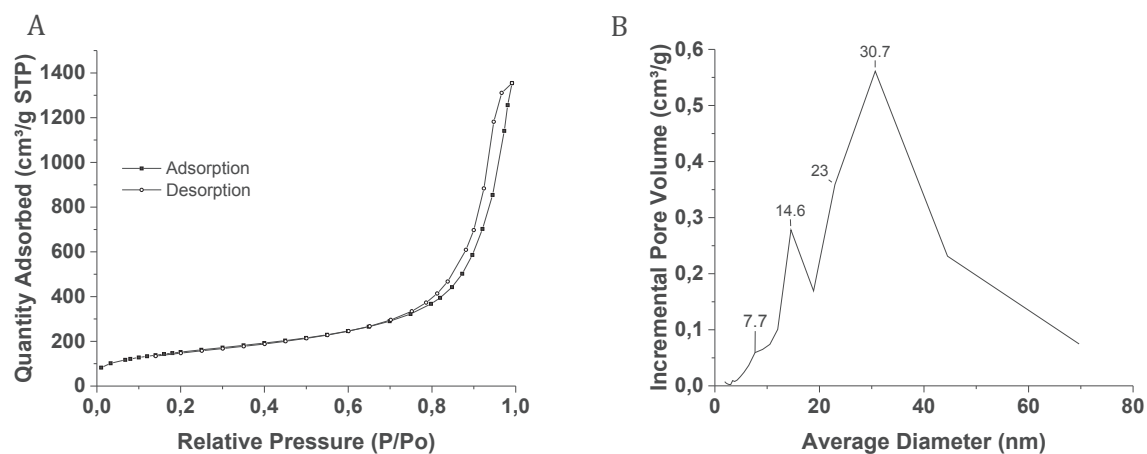


Figure 6-12: A) N₂ adsorption-desorption isotherms and B) corresponding PSD curves for IO-ST NPs with IO core of 9 ± 1 nm (sample 1)

Table 6-2: Summary of pore parameters obtained from N₂ adsorption-desorption analyses for ST and IO@ST NPs

	Ref.	Size core (nm)	Size total (nm)	S _{BET} (m ² /g)	V _{total} (cm ³ /g)	V _{<20nm} (cm ³ /g)	D _{BJH} (nm)
ST	(41)	-	130	590	1.38	-	17
	us	-	101 ± 10	528	1.15	0.62	15.5-9.4
IO@ST			~150	596	-	0.86	12.5-3.2
	(152)		~150	508	-	0.62	7.9-3.4
			~150	464	-	0.62	10.7-3.4
	(162)		~150	372	1.44	-	3
	Sample 1	9 ± 1	54 ± 6	549	1.76	0.87	14.6-7.7
	Sample 2	9 ± 1	60 ± 6	541	1.38	0.67	13.3-9.4
	Sample 3	9 ± 1	62 ± 5	536	1.34	0.70	9.4
	Sample 4	18 ± 1	103 ± 14	600	1.26	0.78	11.3-3.4

3 Improvement of Dox soaking into IO@ST compared to IO@RB

To investigate the impact of the porosity morphology on Dox loading, the same experiment as described in Chapter 5 part 4.2 page 145 was repeated but on IO@ST instead of IO@RB NPs. Thus, the Dox loading efficiencies (DLE) and Dox loading capacities (DLC) of IO@ST NPs in various solvents and with the silica surface modified with APTES or IBAM were first measured and then compared to the previous results obtained on IO@RB NPs.

DLC and DLE curves obtained for Dox loading in water for silanized core-shell particles, IO@ST-NH₂ NPs, are shown in Figure 6-13. The same behavior than the one observed for IO@RB-NH₂ was obtained. Indeed, the DLC curve increased almost linearly before reaching a plateau with a maximal DLC of 25 % for fwr values above 25 % and the DLE were very high, mostly over 90 % until fwr 25 %, before starting to decrease drastically from fwr value of 50 %. This suggested, as it was the case for IO@RB-NH₂ NPs, that almost all the Dox initially fed was loaded into the ST shell porosities until a maximal DLC of 25 % obtained for fwr above 25 %. Thus, for fwr values above 25 % not all the Dox fed can be loaded in the porosities anymore, leading to DLE decrease. But the DLC plateau for Dox soaking into IO@ST-NH₂ NPs was higher, 25 compared to 14 %, for IO@RB-NH₂ NPs in water

To conclude, the Dox loading into IO@ST-NH₂ NPs in water was as efficient as for IO@RB-NH₂ NPs but leading to a higher DLC maximal value of 25 % compared to 14 %.

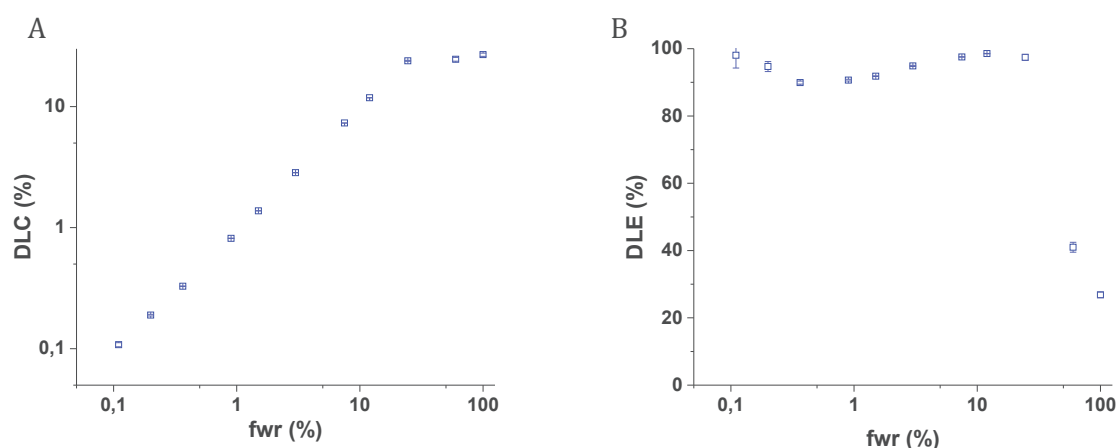


Figure 6-13: Dox impregnation study in porosities of IO@ST-NH₂ in water A) DLC curve B) DLE curve

The same experiment was repeated on IO@ST-NH₂ for Dox soaking in EtOH at 70%. The resulting DLC and DLE curves are presented in Figure 6-14. As for IO@RB-NH₂ NPs, the DLC curve obtained for IO@ST-NH₂ NPs dispersed in EtOH 70 %, increased almost linearly but without reaching a plateau. Thus, the maximal DLC value of 16 % was obtained for the maximal studied fwr of 50 % with a DLE value of only 32 %. However, this maximal value of 16 % was 10 times higher than the value obtained for IO@RB-NH₂ NPs at the same fwr. Furthermore, the DLE values associated to this study were mostly around 30 %, which proved that EtOH 70 % was less efficient as solvent for Dox loading into IO@ST-NH₂ than water.

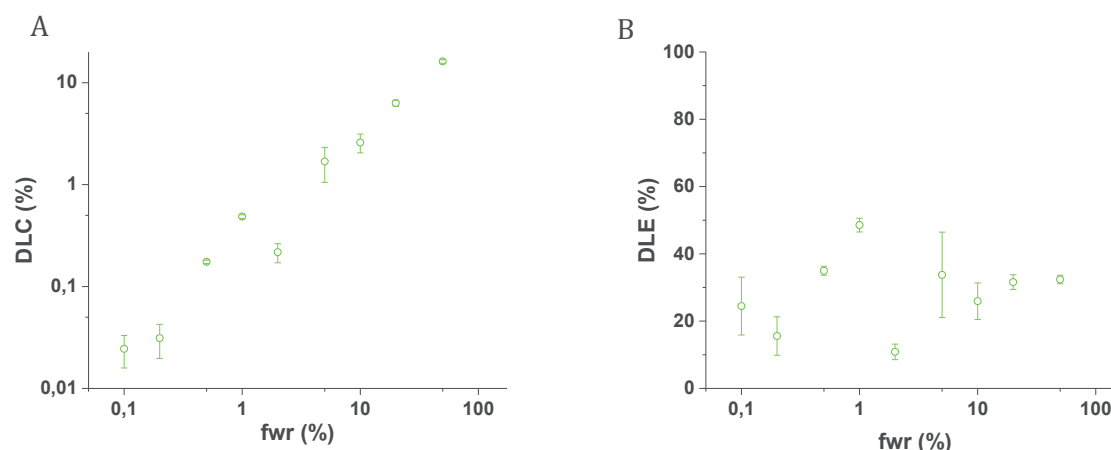


Figure 6-14: Dox impregnation study in porosities of IO@ST-NH₂ in EtOH 70% A) DLC curve B) DLE curve

Finally, the Dox loading into IO@ST-NH₂ was performed in DMF. The corresponding DLC curve, shown in Figure 6-15 A, increased almost linearly until staying constant around 11 % at highest fwr of 100 and 150 %. The DLE curve, presented in Figure 6-15 B, showed values mostly under 30 % that decreased to values under 12 % for fwr above 50 %. Thus the Dox loading into IO@ST-NH₂ was also less efficient and led to a lowest maximal DLC value that the loading in water.

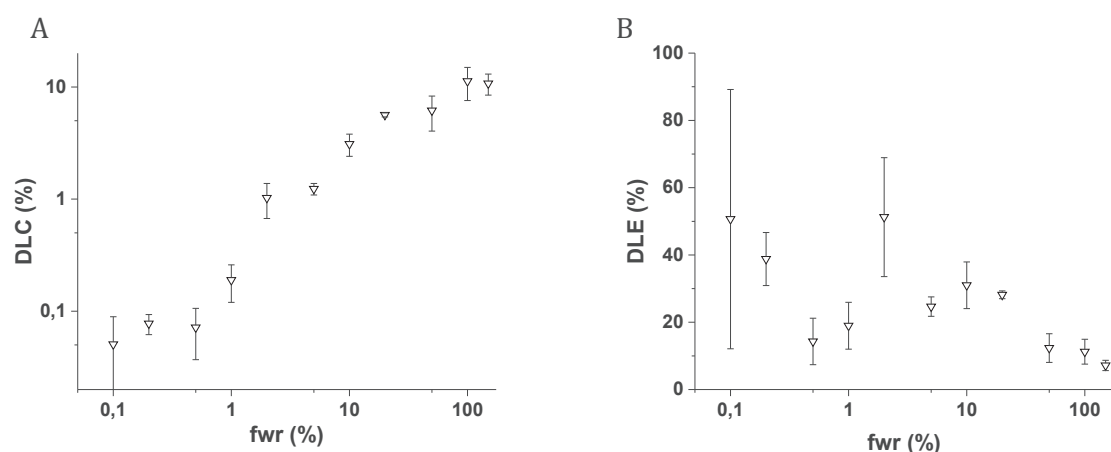


Figure 6-15: Dox impregnation study in porosities of IO@ST-NH₂ in DMF A) DLC curve B) DLE curve

To investigate the influence of the silica surface modification on the Dox loading, IBAM grafting was achieved on the particles leading to IO@ST-IBAM NPs. As these NPs modified with IBAM are stable in DMF the Dox loading was performed in this solvent and compared to the results obtained on the IO@ST-NH₂ and IO@RB-IBAM NPs in DMF. The DLC and DLE curves resulting from the Dox loading of IO@ST-IBAM NPs in DMF are presented in Figure 6-16. Compared to the Dox loading in the same solvent but on amino-modified silica surface, the loading on IBAM-modified silica led to lower DLC values. Indeed, as pictured in Figure 6-16 A, the DLC values reached a plateau of about 3 % for fwr above 20 % which was very low compared to the previous DLC values observed for Dox loading with the same solvent but for amino-modified silica surface (plateau around 11 % for fwr > 100 %). Furthermore, the corresponding DLE values, Figure 6-16 B, were also very low with values mostly below 20 % and were below 3 % for fwr 100 and 150 %. However, these results were very similar to that

observed for Dox loading into IO@RB-IBAM NPs in DMF, see Figure 5-31 page 148. Thus, as it was already the case for IO@RB-IBAM NPs, the Dox loading into IO@ST-IBAM NPs in DMF led to the poorest and the less efficient Dox loading observed for these NPs. That confirmed that the silica surface modification with IBAM moieties is less suitable for Dox loading than amino modified surface.

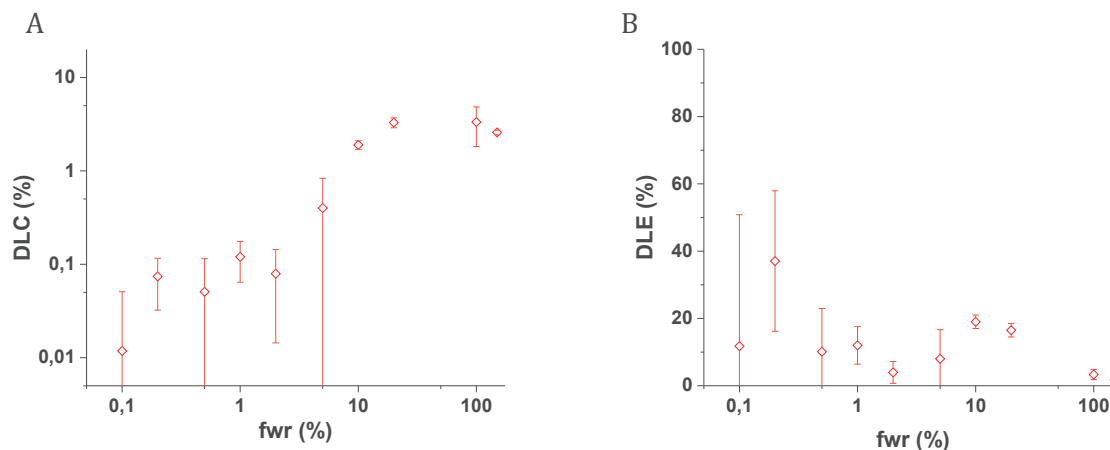


Figure 6-16: Dox impregnation study in porosities of IO@ST-IBAM in DMF A) DLC curve B) DLE curve

To summarize, a similar trend than the trend observed for Dox loading into IO@RB NPs was obtained for IO@ST NPs. To highlight this trend, Figure 6-17 shows the DLC values obtained at fwr 50 % during the previous Dox loading studies described above on IO@ST NPs. For more clarity, these results were compared to the results obtained under the same conditions for Dox loading into IO@RB NPs. Thus, this graph clearly shows that the use of water as soaking solvent for Dox loading into amino-modified IO@ST-NH₂ NPs led to the highest DLC value of 25 %. Furthermore, the results also showed that high DLE values (over 90 %) were obtained for these choices of surface functionalization and soaking solvent, see Figure 6-13 B. As it was the case for IO@RB NPs, other solvents and surface modifications led to poor DLC results for IO@ST NPs excepted for Dox loading into IO@ST-NH₂ in EtOH 70 %. Indeed, these conditions led to DLC value around 16 % that was high compared to the low DLC value of 1.6 % observed for IO@RB NPs with the same Dox impregnation conditions. This graph also points out the influence of the porosity morphology on Dox loading. Indeed, the Dox loading into stellar porosity led to higher DLC values than for small porosity with raspberry morphology, excepted when the silica surface was modified with IBAM. In this last case the same DLC values were observed for both porosity morphologies.

To conclude, these experiments highlighted the impact of three major parameters on the Dox loading into mesoporous silica shell: the silica surface modification, the solvent used for drug soaking and the porosity morphology. The conclusion of these studies was that the three best conditions to reach the highest DLC and DLE values were to load the drug into NPS *stellar porosities*, with an *amino-modified silica surface* and using *water* as soaking solvent (in this order of priority).

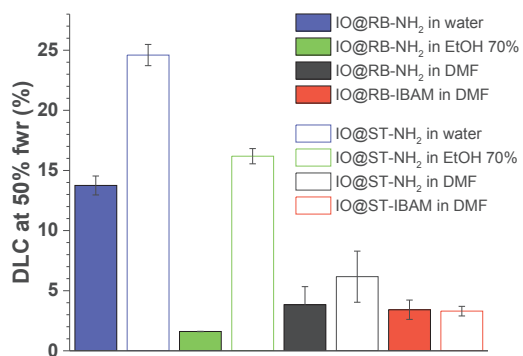


Figure 6-17: Comparison of DLC values at fwr 50 % obtained for Dox impregnation into IO@RB (plain bars) and IO@ST (empty bars) with silica surface modified with APTES in water (blue), EtOH 70 % (green) and DMF (black), and with IBAM-modified silica surface in DMF (red)

4 IO@ST versus IO@RB with IO core of 20 nm as theranostic agents

4.1 Introduction

Previously in the thesis we investigated the theranostic abilities of IO@RB and IO@ST NPs containing an IO core of about 10 nm in terms of drug loading capacities and efficiencies for therapy and in terms of proton relaxivity properties for diagnosis by MRI. However, to enhance these parameters we only modify the shell properties such as the porosity size and shape of the silica shell, the size of the silica shell, the coating of NPs with tight HSA... But until now we did not investigate the impact of the core size on the theranostic abilities of our systems. Nevertheless, increasing the IO core size to 20 nm should have an impact on T₂ contrast but also should introduce an additional therapy, as this size is suitable for magnetic hyperthermia (4–6).

Thus, five batches were used to investigate the impact of larger IO core on theranostic properties. These batches are divided in two groups depending on the silica shell porosity morphology they exhibited. Thus, three samples exhibiting IO@RB morphology, presented in Table 6-3, with various sizes 55, 75 and 81 nm and two samples exhibiting IO@ST morphology, presented in Table 6-4, with sizes of 97 and 107 nm were studied.

Table 6-3: TEM images of the IO@RB NPs with 20 nm IO core

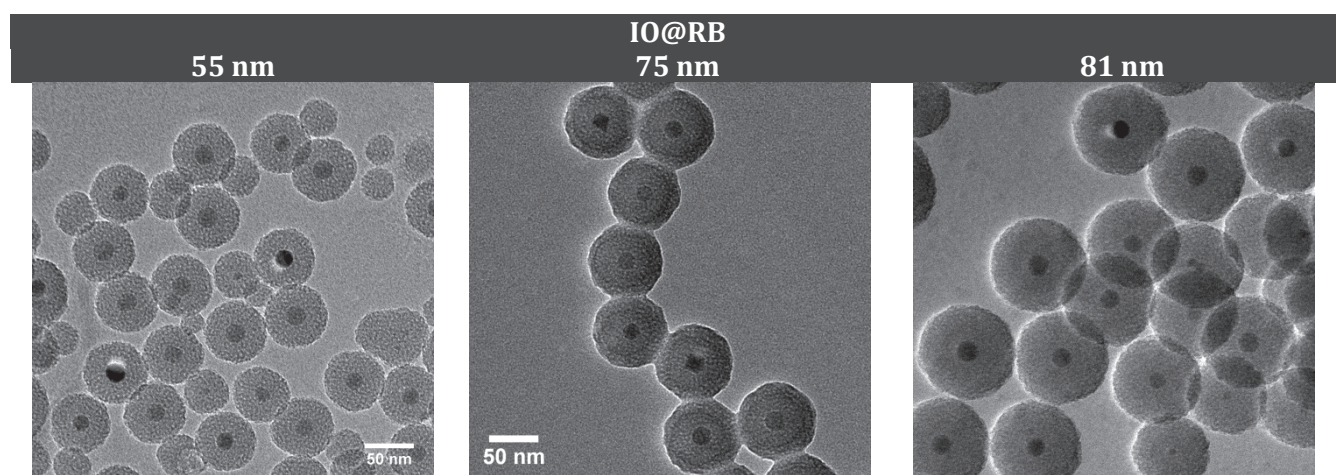
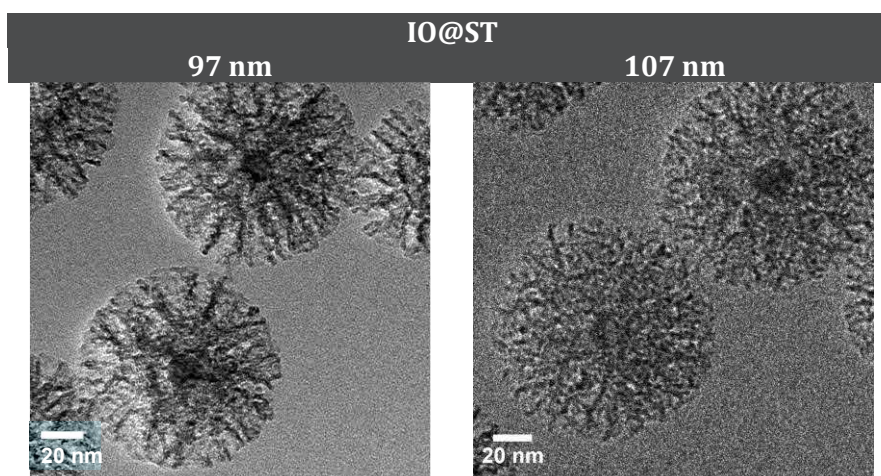


Table 6-4: TEM images of the IO@ST NPs with 20 nm IO core



4.2 IO@ST and IO@RB as MRI contrast agents

4.2.1 Relaxivity measurements and MRI images of raw IO@ST and IO@RB NPs

In this part the abilities of IO@ST and IO@RB NPs and their HSA-coated derivatives to be T_2 contrast agents for MRI imaging were investigated.

First the MRI contrast properties of raw IO@ST and IO@RB NPs dispersed in water were assessed by proton NMR relaxometry studies performed at 37 °C and 1.41 T (60 MHz). Longitudinal (T_1) and transverse (T_2) relaxation times of protons were measured at various Fe concentrations (the highest [Fe] was determined by ICP-AES and lower [Fe] were obtained by dilution). Figure 6-18 shows the resulting $1/T_1$ and $1/T_2$ relaxivity curves in function of [Fe] that exhibited as expected very linear behaviors. The slopes from the linear fits of these curves gave respectively the r_1 and r_2 values for the samples. These r_1 and r_2 values of the samples as well as the resulting r_2/r_1 ratios are summarized in Table 6-5. To be used as T_2 contrast agents, the NPs have to display both a high r_2 and a high r_2/r_1 ratio.

For IO@ST NPs, the results obtained for the two studied samples of respectively 107 and 97 nm in size were in a similar range of values. Indeed, the IO@ST NPs of 107 nm exhibited r_1 and r_2 values of 0.80 and 125 $\text{mM}^{-1}\cdot\text{s}^{-1}$ respectively giving a r_2/r_1 ratio of 156 whereas the IO@ST NPs of 97 nm exhibited a slightly lower r_1 value of 0.63 $\text{mM}^{-1}\cdot\text{s}^{-1}$ and a slightly higher r_2 value of 177 $\text{mM}^{-1}\cdot\text{s}^{-1}$ giving thus a higher r_2/r_1 ratio of 281. Thus, even if the range of values were similar for both samples, the smaller one, at 97 nm, seemed to have a better T_2 contrast potential.

For the IO@RB NPs of 81 nm, the r_2 value of 105 $\text{mM}^{-1}\cdot\text{s}^{-1}$ was still in the same range than the r_2 values of the previous IO@ST samples. However, the r_1 was 10 times lower with the value of 0.04 $\text{mM}^{-1}\cdot\text{s}^{-1}$. This led to an outstanding high r_2/r_1 ratio of 2400. The same range of values were obtained for IO@RB of 75 nm (Table 6-5): r_2 value of 218 $\text{mM}^{-1}\cdot\text{s}^{-1}$ and low r_1 of 0.05 $\text{mM}^{-1}\cdot\text{s}^{-1}$. This strong r_1 decrease for IO@RB NPs compared to IO@ST NPs could be explained by the difference of silica shell porosity. Indeed, small porosities limited water accessibility to the magnetic core and thus its diffusion around it whereas large porosities let probably the water circulate closer to the magnetic core through the stellar pore channels and with an enhanced diffusion speed impacting thus more water molecules.

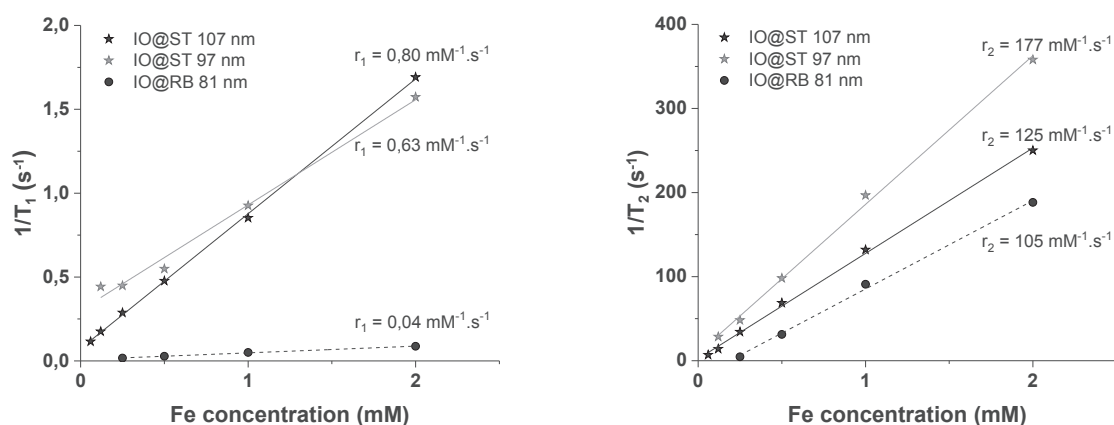


Figure 6-18: A) $1/T_1$ and B) $1/T_2$ relaxometry curves of IO@ST and IO@RB NPs in function of [Fe] obtained at 37 °C on a Bruker Minispec working at 60 MHz (1.41 T)

Magnetic resonance images of these samples were performed on a mouse sized instrument, called Optimouse, running at 1.5 T. This instrument gave images in T_1 and T_2 ponderation and

calculated from these images the corresponding T_1 and T_2 values for each sample concentration. From these values the longitudinal relaxation rate ($1/T_1$) and the transversal relaxation rate ($1/T_2$) in function of Fe concentration were plotted, Figure 6-19.

As pictured on Figure 6-19 A, unlike the previous results obtained from Bruker Minispec, the longitudinal relaxation rates ($1/T_1$) of the raw IO@ST and IO@RB samples obtained with Optimouse did not exhibit a linear behavior over [Fe] ranking from 0.003 to 2 mM. To get linear fits we had to zoom on low [Fe] (< 0.5 mM), but even this way, as pictured on Figure 6-19 B, the linear fits obtained were less precised than those from Bruker Minispec. This is explained by the different method used to calculate the T_2 enhancement based on pixels analysis (see Chapter 2 page 47). Thus, as summarized in Table 6-5, excepted for IO@ST 107 nm, the resulting r_1 values were very different, mostly higher, than the values obtained with Bruker Minispec. For example, for IO@RB 81 nm the difference between both measurement was huge: the r_2 obtained with Optimouse was 50 higher than the value from Bruker Minispec.

For the transversal relaxation rates ($1/T_2$) even if a saturation was observed at 100 s^{-1} for almost all samples at high [Fe] (Figure 6-19 C), linear fits, more precise than in $1/T_1$ curves, were obtained for [Fe] < 0.5 mM (Figure 6-19 D). The resulting r_2 values, summarized in Table 6-5, got the same magnitude than those measured with Bruker Minispec. The results obtained for both IO@ST NPs were relatively similar and were also similar to the r_2 value obtained for IO@RB 81 nm. But, for the 2 other IO@RB samples with lower silica shell, the r_2 values were significantly lower. Thus, according to this measurement method the two samples (one for each type of NP) which had the highest r_2 were IO@ST 97 nm and IO@RB 81 nm.

As the r_1 values measured with Optimouse were mostly higher than those from Bruker Minispec this led to huge differences in r_2/r_1 values between both methods. But considering the difficulty to obtain linear fits on the $1/T_1$ curves, we thought that the results obtained with Optimouse instrument were less trustable than the results obtained on the Bruker Minispec. However it may help to compare different samples.

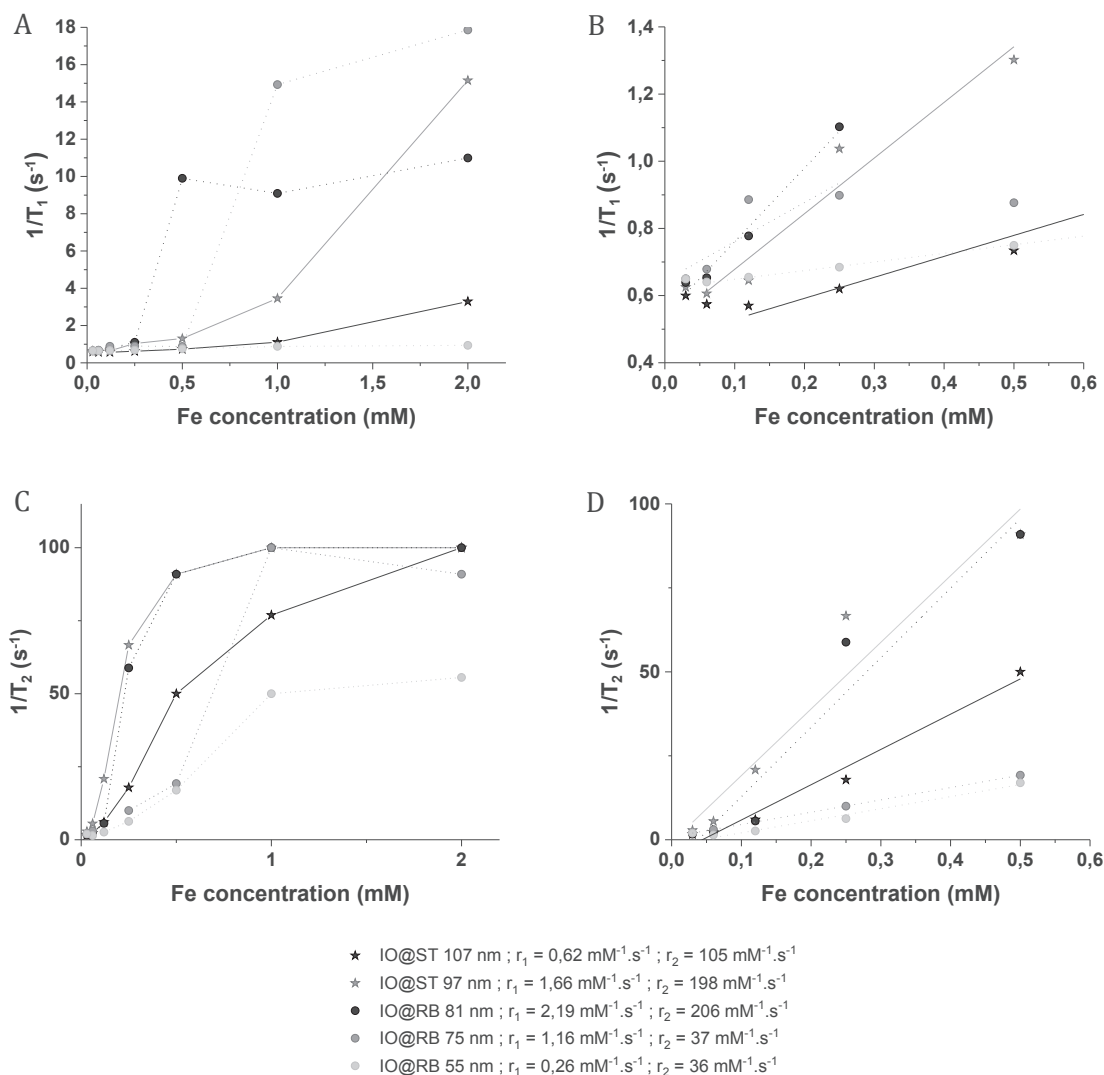


Figure 6-19: $1/T_1$ (A) all values, B) zoom on lower values) and $1/T_2$ (C) all values, D) zoom on lower values) relaxometry curves and their corresponding linear fits of IO@ST and IO@RB NPs in function of [Fe] obtained on Optimouse 1.5 T

Table 6-5: Summary of longitudinal relaxivity r_1 , transversal relaxivity r_2 and r_2/r_1 ratio for raw IO@ST and IO@RB NPs obtained at 37 °C on a Bruker Minispec working at 60 MHz (1.41 T) and on Optimouse at 1.5 T

	Bruker Minispec 1.41 T			Optimouse 1.5 T		
	r_1 ($\text{mM}^{-1} \cdot \text{s}^{-1}$)	r_2 ($\text{mM}^{-1} \cdot \text{s}^{-1}$)	r_2/r_1	r_1 ($\text{mM}^{-1} \cdot \text{s}^{-1}$)	r_2 ($\text{mM}^{-1} \cdot \text{s}^{-1}$)	r_2/r_1
IO@ST 107 nm	0.80	125	156	0.62	105	169
IO@ST 97 nm	0.63	177	281	1.66	198	119
IO@RB 81 nm	0.04	105	2625	2.19	206	94
IO@RB 75 nm	0.05	218	4360	1.16	37	32
IO@RB 55 nm	-	-	-	0.26	36	138
IO-dendron 20nm	3.83	129	34	-	-	-





















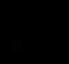






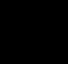






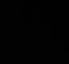





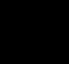
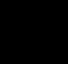












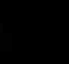
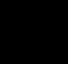













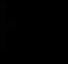
The contrast enhancement properties of IO@ST and IO@RB NPs were finally evaluated with a clinical instrument, the GE Signa HDxt, running at 3 T. Table 6-6 presented the resulting MRI-phantoms for raw IO@ST and IO@RB NPs.

First, on the T_{2w} images obtained for the IO@ST NPs, small brightening is observed at low Fe concentrations followed by pronounced darkening, starting at [Fe] 0.25 mM for IO@ST 97 nm NPs and 0.5 mM for IO@ST 107 nm, which led to complete signal extinction for [Fe] > 1 mM and [Fe] > 2 mM for IO@ST 97 nm and 107 nm respectively. Thus, T_2 contrast effect was slightly higher for the 97 nm sample. This confirmed the observation made from previous relaxivity results according to which the IO@ST 97 nm sample seemed to have a better T_2 contrast potential than the 107 nm one. Thus, this sample was selected for the further investigation of the HSA coating impact on contrast properties.

For raw IO@RB NPs we observed a strong influence of silica shell on T_2 contrast: thicker the silica shell, higher the T_2 contrast. Indeed, for 55 nm sample a slight darkening was observed only at the highest [Fe] of 2 mM, whereas for 75 nm sample the darkening effect started at 1 Fe mM and reached complete extinction for 2 Fe mM and finally for 81 nm sample the darkening was more pronounced: starting at 0.5 Fe mM and reaching complete extinction already for 1 Fe mM. Thus, as the IO@RB NPs of 81 nm showed the best T_2 contrast effect, this sample was selected for the later study of HSA coating effect on contrast properties.

For all NPs a hyposignal in T_{1w} images was observed. This darkening effect only occurred at high Fe concentrations and was correlated to complete T_2 signal extinction observed on T_{2w} images.

Table 6-6: T₁ and T₂ weighted MR images of IO@RB and IO@ST NPs of various sizes

[Fe] (mM)	T ₁							T ₂						
	0.03	0.06	0.125	0.25	0.5	1	2	0.03	0.06	0.125	0.25	0.5	1	2
IO@RB 55 nm														
IO@RB 75 nm														
IO@RB 81 nm														
IO@ST 97 nm														
IO@ST 107 nm														

4.2.2 Effect of HSA coating on MRI contrast

To investigate the impact of the HSA coating of IO@RB and IO@ST NPs on MRI contrast properties, the raw NPs showing the best T_2 contrast on the previous study were selected: the sample with a size of 81 nm for IO@RB NPs and the sample of 97 nm for the IO@ST NPs. Thus, the HSA coating on IO@RB 81 nm and IO@ST 97 nm samples was achieved, following the protocol described page 58, leading to IO@RB-HSA and IO@ST-HSA NPs. These samples were then analyzed by the Optimouse instrument (1.5 T) and the GE Signa HDxt (3 T).

Figure 6-20 shows the $1/T_1$ and $1/T_2$ relaxometry curves obtained on Optimouse 1.5 T and their corresponding linear fits for IO@ST 97 nm and IO@RB 81 nm with and without HSA coating NPs. Table 6-7 summarized the r_1 , r_2 and r_2/r_1 values deduced from the linear fits of the previous curves. First, we noticed that r_2 values were not modified by HSA coating. For the r_1 values, a difference between both silica shell morphologies was observed. Indeed, the addition of HSA coating on IO@RB NPs did not affect the r_1 , whereas protein coating on IO@ST NPs increased drastically r_1 value. This had for consequence to reduce by a factor two the r_2/r_1 ratio. However, we observed previously a major difference between relaxivities obtained on Bruker Minispec and Optimouse instruments creating doubts on results reliability. Unfortunately, the totality of samples were sent for measurements by Optimouse (1.5 T) and GE Signa HDxt (3 T), thus analyses by Bruker Minispec were not achieved.

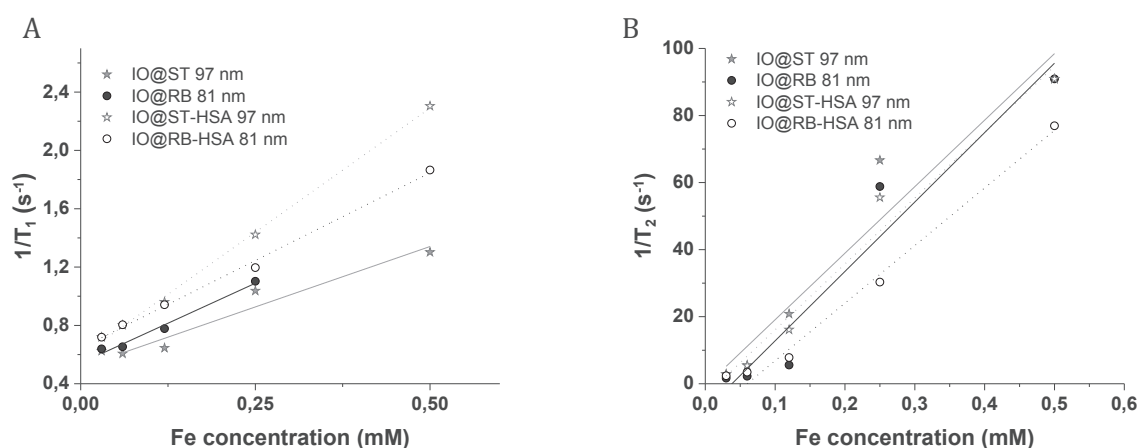


Figure 6-20: (A) $1/T_1$ and (B) $1/T_2$ relaxometry curves obtained on Optimouse 1.5 T and their corresponding linear fits of IO@ST 97 nm and IO@RB 81 nm with and without HSA coating NPs in function of $[Fe]$

Table 6-7: Summary of longitudinal and transversal relaxivities (r_1 and r_2) and their corresponding r_2/r_1 values obtained for IO@ST 97 nm and IO@RB 81 nm with and without HSA coating NPs on Bruker Minispec 1.41 T and Optimouse 1.5 T

	Bruker Minispec 1.41 T			Optimouse 1.5 T		
	r_1 (mM^{-1},s^{-1})	r_2 (mM^{-1},s^{-1})	r_2/r_1	r_1 (mM^{-1},s^{-1})	r_2 (mM^{-1},s^{-1})	r_2/r_1
IO@ST	0.63	177	281	1.66	198	119
IO@RB	0.04	96	2400	2.19	206	94
IO@ST-HSA	-	-	-	3.40	196	57
IO@RB-HSA	-	-	-	2.40	172	72

The contrast properties of HSA-coated NPs were then evaluated with a clinical instrument, the GE Signa HDxt, running at 3 T. Table 6-8 presented the resulting MRI-phantoms of IO@ST-HSA and IO@RB-HSA NPs compared to their corresponding raw IO@ST and IO@RB NPs.

First, an enhancement of dark contrast was observed in T_{2w} images of HSA-coated samples compared to the corresponding raw NPs. Indeed, complete signal extinction previously observed from 1 Fe mM was through HSA coating already observed for 0.5 Fe mM. Furthermore, on raw NPs a slightly higher T_2 contrast effect was observed for IO@ST sample compared to IO@RB, as the darkening was a bit stronger at 0.25 and 0.5 Fe mM, whereas for their corresponding HSA-coated samples this trend seemed attenuated.

For T_{1w} images the raw samples started to show hyposignal at [Fe] where complete T_{2w} extinction was observed. For the HSA-coated samples this effect seemed to be attenuated as no hyposignal was observed on T_{1w} images for 0.5 Fe mM whereas at this concentration complete signal extinctions were observed on T_{2w} images.

To conclude, even if the relaxivities measurements were difficult to interpret, IO@RB-HSA, IO@ST-HSA showed promising T_2 contrast and thus could be used as negative contrast agents for MRI diagnosis.

Table 6-8: T_1 and T_2 weighted MR images of IO@RB and IO@ST NPs without and with HSA coating

[Fe] (mM)	T_1						T_2					
	0.03	0.06	0.125	0.25	0.5	1	0.03	0.06	0.125	0.25	0.5	1
IO@RB												
IO@ST												
IO@RB-HSA												
IO@ST-HSA												

4.3 IO@ST and IO@RB for cancer therapy

4.3.1 Magnetic Hyperthermia

Nowadays it is well admitted that the design of IO NPs strongly influences their magnetic hyperthermia properties (122, 199, 287, 288). According to recent studies, superparamagnetic IO of about 20 nm in size are suitable for cancer therapy by magnetic hyperthermia (4–6). Based on these observations, students in our team working on dendronized IO NPs showed that the size and the morphology of the IO NPs have a huge impact of the heating capacities. On spherical IO NPs they found out that a size of 10 nm did not provide any heating whereas a size of 20 nm led to high SAR values at 571 kHz and 250 G: 0 versus 338 W/g respectively.

However, to the best of our knowledge, the impact of mesoporous silica shell on IO NPs heating power was poorly studied. Thus, in the following we presented our preliminary heating capacity study of IO@MS with IO core of about 20 nm. To investigate the abilities of our core-shell NPs for nanothermotherapy, SAR measurements were performed at various frequencies and magnetic fields on NPs dispersed at an average of 0.5 mg Fe₃O₄/mL in water (precise measurements of Fe concentration were performed on each batch by ICP AES).

First, the heating powers of NPs were evaluated at 796 Hz under various magnetic fields: 200, 150 and 100 G. Figure 6-21 shows the SAR values obtained with these measurement parameters for core-shell NPs, IO@ST 107 and 97 nm and IO@RB 75 nm, and for CTAB coated IO NPs of 18 nm. At the lowest magnetic field, 100 G, the samples exhibited all similar SAR values around 75 W/g excepted for IO@RB 75 nm NPs that showed the lower value of 42 W/g. Then with increasing the magnetic field, the resulting SAR of the sample increased almost linearly, as demonstrated by the values obtained after linear fits summarized in Table 6-9. This behavior is coherent with the linear response theory (LRT) developed by Rosensweig in 2002 (289). We found out that the slopes of the linear fits were higher for both IO@ST samples than for the IO@RB one and that the three of them were higher than the non-silica coated IO NPs. Thus, that behavior led, for the highest magnetic field of 200 G, to higher SAR values for core-shell samples than for IO-CTAB NPs. Indeed, SAR values of 334 W/g for IO@ST 107 nm, and of 277 W/g for IO@ST 97 nm and IO@RB 75 nm were obtained whereas the IO-CTAB sample exhibited a SAR value of 228 W/g.

As depicted on Figure 6-22, SAR study at 579 kHz gave similar results. For example at 200 G the same trend was observed: IO@ST 107 nm NPs showed the highest SAR value of 254 W/g, IO@ST 97 nm and IO@RB 75 nm showed the same SAR value of 190 W/g and IO-CTAB NPs exhibited the lowest SAR value of 170 W/g. Compared to the previous observations made at 579 Hz and 200 G, at higher magnetic field, 272 G, the gap between the SAR values observed for IO-CTAB NPs and IO@ST 97 nm / IO@RB 75 nm increased from 20 to 100 W/g.

As the SAR values tend to increase with magnetic field and because on the instrument the maximal magnetic field we could use at a specific frequency decrease with increasing the frequency, we decided to measure SAR values at three different frequencies using for each times the highest magnetic field allowed. Thus, as presented on Figure 6-23, measurements were performed at 796 kHz - 200 G, 579 kHz - 272 G and 395 kHz - 300 G. According to the results, the hyperthermia measurements parameters leading to the highest SAR values for our systems at a concentration about 0.5 mg Fe₃O₄/mL are a frequency of 579 kHz and a magnetic field of 272 G.

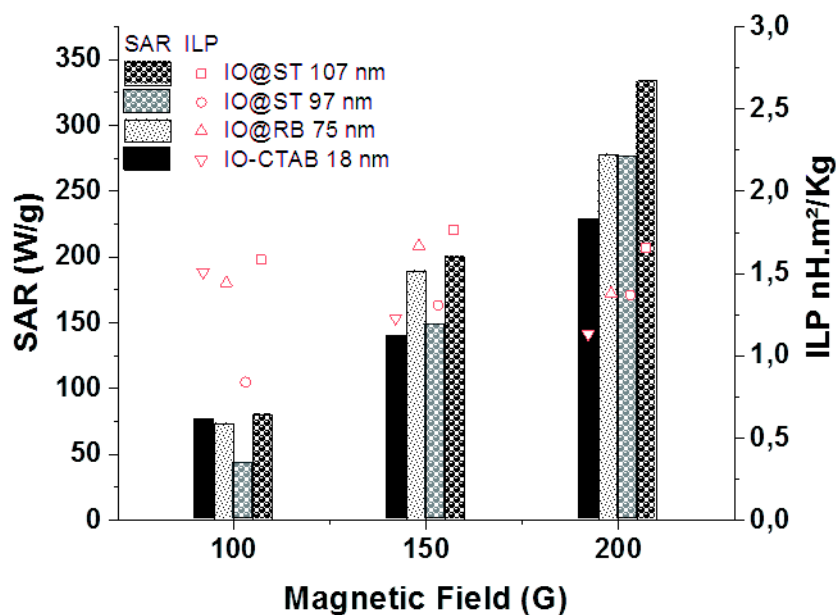


Figure 6-21: SAR and ILP values obtained on IO@ST NPs of 107 and 97, IO@RB NPs of 75 nm and IO-CTAB NPs of 18 nm at a frequency of 796 kHz under various magnetic field: 200, 150 and 100 G

Table 6-9: Slopes and R^2 values from linear fits of SAR values obtained at 796 kHz under various magnetic fields (200, 150 and 100 G)

	Slope	R^2
IO@ST 107 nm	2.54	0.99899
IO@ST 97 nm	2.34	0.99706
IO@RB 75 nm	2.05	0.99425
IO-CTAB 18 nm	1.52	0.99082

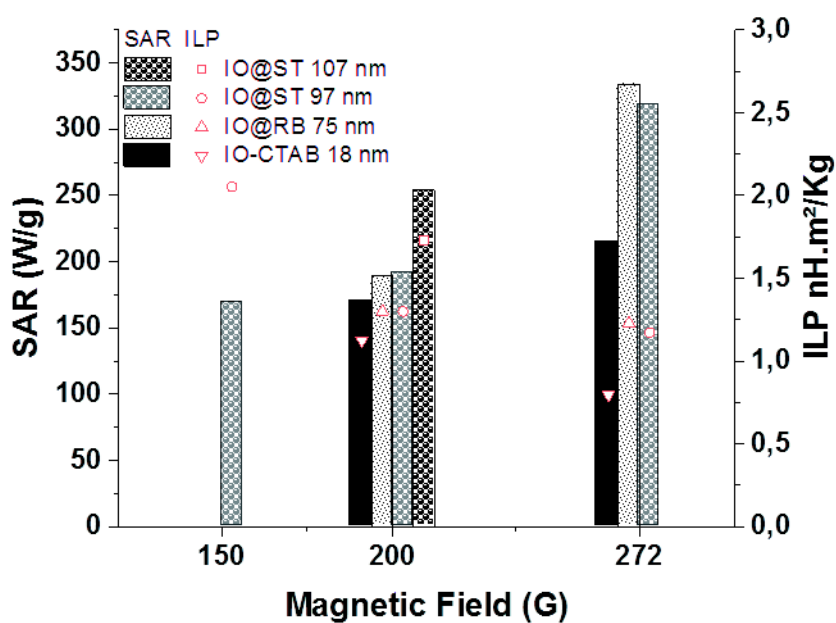


Figure 6-22: SAR and ILP values obtained on IO@ST NPs of 107 and 97 nm, IO@RB NPs of 75 nm and IO-CTAB NPs of 18 nm at a frequency of 579 kHz under various magnetic fields: 272, 200 and 150 G

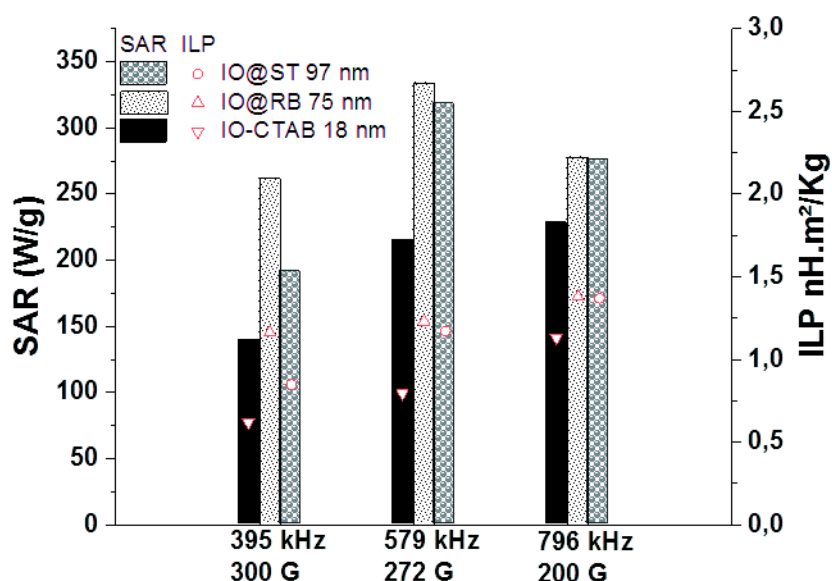


Figure 6-23: SAR and ILP values obtained on IO@ST NPs of 97 nm, IO@RB NPs of 75 nm and IO-CTAB NPs of 18 nm at various frequencies applying the highest magnetic field allowed at each frequency

As the choice of magnetic hyperthermia measurement parameters such as concentration of the sample, field amplitude or frequency lead to a multitude of combinations, SAR values are very difficult to compare to each other from one article to another. Furthermore, as we explained previously, for the best of our knowledge SAR values issued from iron oxide-silica core-shell structures are not well documented. The only values that we found in the literature were reported by Zhu and Tao on IO@ST NPs (152, 162). They found SAR values at 409 kHz and 180 G of 9 and 12 W/g for their IO@ST NPs with IO core sizes ranging from 15 to 20 nm. For comparison we found a higher value of 85 W/g with our IO@ST 97 nm NPs under similar conditions (395 kHz, 200 G). Furthermore, they noticed a decrease in SAR values from 40 to 12 W/g (409 kHz, 180 G) between their raw IO NPs and their corresponding IO@ST NPs (152) which is the contrary of the tendency we observed. However, as synthesis method for IO NPs formation are known to affect significantly the SAR values and as an increase of polydispersity also greatly decrease SAR (122, 287), we could not really compare the heating capacity our monodispersed IO NPs synthesized by thermal decomposition and their polydispersed IO NPs synthesized by coprecipitation. Furthermore, Majeed *et al.* reported that non porous silica coating of IO NPs enhances their heating efficacy. They explained this increase by the fact that the silica coating helped in preventing IO agglomeration and thus preserved the Brownian motion of NPs that helped in the heat generation (148).

Thus, according to these contradictory reports, further investigations on mesoporous silica coating on IO NPs have to be added to this preliminary study to validate our observations.

4.3.2 Dox loading and release

4.3.2.1 Dox loading and release from IO@ST and IO@RB samples

Dox loading of amino-modified IO@RB-NH₂ and IO@ST-NH₂ NPs of 81 and 97 nm dispersed at 15 and 30 µg Fe/mL respectively was performed by simple soaking in water. As pictured in the photographs presented in Figure 6-24 A, the Dox loading efficiency was higher for IO@ST

NPs than for IO@RB NPs as the supernatants were colorless in the first case and reddish in the second case. However, both samples showed a strong red color, statement of their effective Dox loading, after redispersion in water (Figure 6-24 B).

To quantify the DLC of these samples, TGA analyses were achieved. The resulting curves presented in Figure 6-25 A, clearly showed, as expected from the study developed in chapter 6 part 3 page 194, that the DLC was higher for IO@ST-Dox sample than for IO@RB-Dox. The measurement of weight losses indicated DLC values of 30 and 21% for IO@ST-Dox and IO@RB-Dox respectively. These DLC values directly given by TGA curves lecture were the ratios between the weight of Dox loaded and the total weight of the NPs loaded with Dox. However, DLC can also be expressed as the ratio between the weight of Dox loaded and the weight of raw NPs before loading. In this case, we obtained DLC values of 42.9 % and 26.6 % for IO@ST and IO@RB samples respectively. Both definitions are suitable and defined in literature, but in this manuscript until now we always used the second one. Zeta-potential was also measured at various pH for both samples, the resulting curves, presented in Figure 6-25 B, were very similar and showed IEP at pH 8.

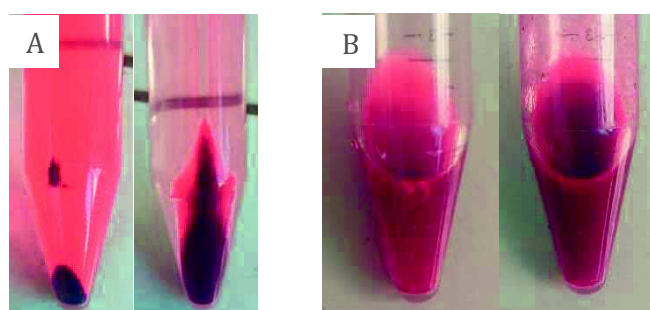


Figure 6-24: IO@RB-Dox (left) and IO@ST-Dox NPs (right), after Dox loading A) with the supernatants, B) redispersed in 1 mL of water

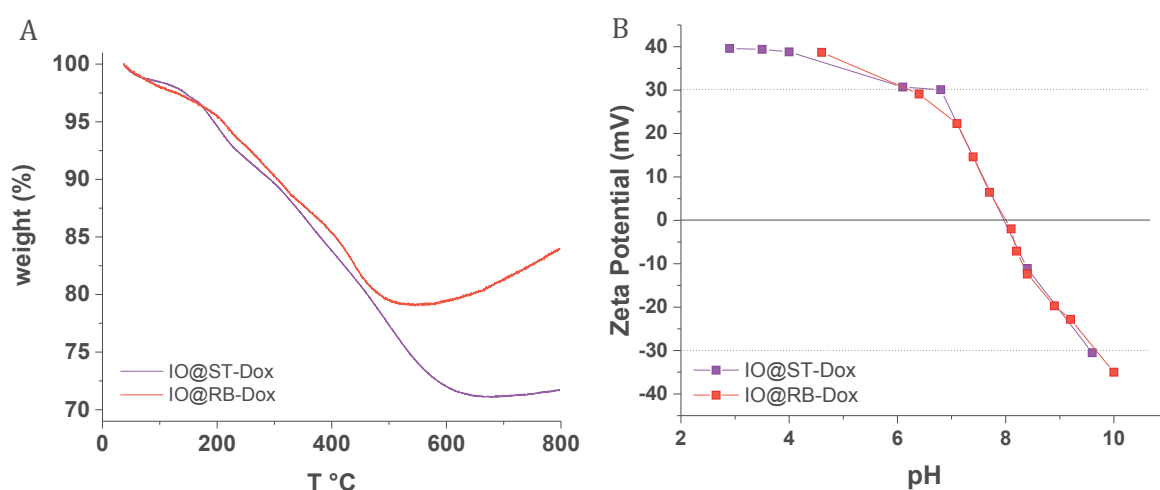


Figure 6-25: A) TGA and B) Zeta-potential curves of IO@ST-Dox and IO@RB-Dox

Dox release studies from IO@RB-Dox and IO@ST-Dox were performed. As the pH in endolysosomes is close to 5 and the NPs showed promising heating powers by magnetic hyperthermia, the Dox release from IO@RB-Dox and IO@ST-Dox was studied at pH 5 and 7.4 and under temperatures of 37 °C and 50 °C to investigate the effect of each of these factors on drug release. The curves showing the resulting percentages of Dox released with time under

various pH and temperature conditions are presented in Figure 6-26 A for IO@RB-Dox NPs and Figure 6-26 B for IO@ST-Dox NPs. For both sample, pH was the condition that influenced the most the drug release. Indeed, pH 5 enhanced Dox release from NPs compared to pH 7. This behavior could come from the fact that, as shown in Figure 6-25 B, the NPs were highly positively charged at pH 5 creating probably more electrostatic repulsion with positive charged Dox that promoted its release. Furthermore, an increase in temperature from 37 °C to 50 °C also enhanced Dox release. Thus as hoped, the combined effect of pH and temperature caused the release of more Dox than either mechanism alone which is promising to envisage our systems as cargo for dual pH and temperature triggered drug release. We also noticed that for both samples and for all conditions, a maximal Dox release was reached after 20 h. However, even if the DLC was higher for IO@ST than for IO@RB sample, it was interesting to see that the % of Dox released was much higher for IO@RB-Dox than for IO@ST-Dox with maximal values at pH 5 and 50 °C of approximately 55 and 20 % respectively.

Nevertheless, as we explained in Chapter 1 page 30, in a concern of reducing the amount of NPs that have to be injected to patients we thought that the most important is to know the amount of drug that can be released from a precise quantity of NPs. We introduced this value as Drug Release Content (DRC). As DLC, DRC can be expressed either by the ratio between weight of Dox released and weight of Dox loaded NPs or by the ratio between weight of Dox released and weight of raw NPs. Thus, the DRC values for our samples obtained after approximately 20 h of dialysis at pH 5 at 50 °C were of 11.6 % and 6 % in the first case and of 14.6 % and 8.6 % in the second calculation for IO@RB and IO@ST NPs respectively. These values are very high compared to the majority of those reported in literature (Table 1-8 page 33).

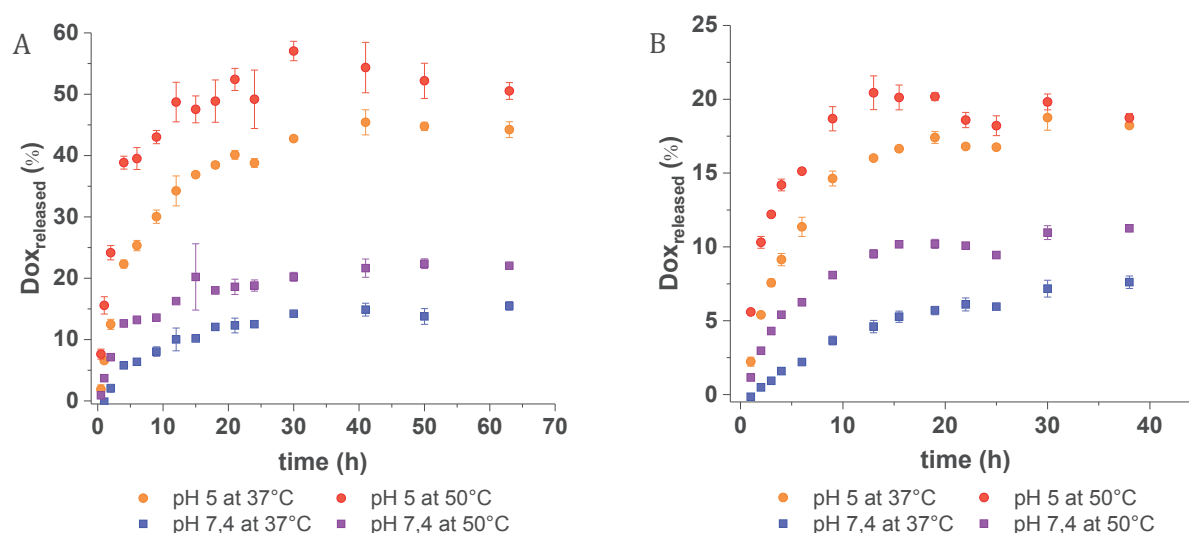


Figure 6-26: Dox release at pH 5 and 7.4 and at 37 and 50 °C from A) IO@RB-Dox NPs and B) IO@ST-Dox NPs

4.3.2.2 Dox release study from IO@RB-Dox-HSA sample

Dox release behavior from protein coated IO@RB-Dox-HSA sample was also investigated at 37 °C and pH 5 or 7.4, with and without proteases in the media. As the Dox released during the protein coating step was hard to quantify and as we did not have enough material for the synthesis of corresponding IO@RB-HSA sample for comparative TGA analysis, the amount of

Dox finally loaded in the NPs could not be measured. However, the weight of IO@RB-Dox-HSA NPs before Dox release experiments was estimated by freeze-drying, thus the Dox release graphs, presented in Figure 6-27, could be expressed as the evolution of DRC values with time. These DRC values were so expressed by the ratio between the weight of Dox release and the total weight of IO@RB-Dox-HSA NPs.

Firstly, we noticed that the presence or absence of proteases did not influence the Dox release. Thus, the proteases did not trigger Dox release as we expected. Furthermore, unlike the previous study, the Dox release seemed to be similar between pH 7.4 and pH 5. Indeed, the highest DRC values obtained at 37 °C at pH 7.4 and pH 5 were about 3 and 2 % respectively. Compared to the previous study on IO@RB-Dox NPs, DRC values obtained at pH 7.4 were similar whereas DRC obtained at pH 5 were highly different: 2 % against 9 % for IO@RB-Dox-HSA and IO@RB-Dox respectively. This may come from the variation of Zeta-potential after protein coating. Indeed, in the previous chapter in Figure 5-46 page 160, the IEP was estimated to be at pH 6 for IO@RB-Dox-IBAM-HSA NPs. Thus at pH 7.4 and 5 the NPs were not highly charged, around -20 and 20 mV respectively, which is less favorable for electrostatic repulsion than the Zeta-potential value of 40 mV observed at pH 5 for IO@RB-Dox NPs. Another explanation could be that the amount of Dox loaded by electrostatic interactions into the NPs already released during the protein coating synthesis step.

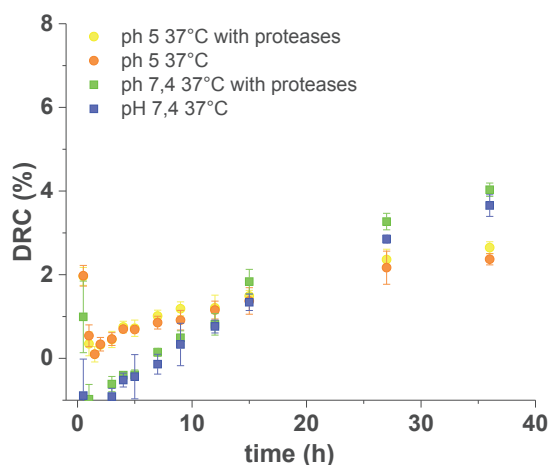


Figure 6-27: Dox release from IO@RB-Dox-HSA NPs at pH 5 and 7.4 at 37 °C with and without proteases

4.3.2.3 Conclusion

To conclude, IO@RB-Dox and IO@ST-Dox NPs showed both pH and temperature controlled drug delivery behaviors. Thus, the addition of HSA shell as gatekeeper was not necessary for controlled drug release. Furthermore, the results showed that finally, a high Dox loading content value was not the only parameter to take into account for cargo design. Indeed, IO@RB NPs that showed lower DLC values compared to IO@ST NPs, exhibited finally higher DRC values. Thus, DLC measurements alone are not enough to decide if a type of NPs could be good cargo for drug delivery. Moreover, the addition of HSA shell through IBAM strategy on IO@RB-Dox sample finally decreased the efficiency of the system for controlled drug delivery which was the total opposite of the effect we aimed.

However, previous studies done on Dox-HSA nanocapsules, chapter 4, showed that even if the drug release was not achieved by dialysis these NPs showed important cytotoxic effect on

MCTS, which implies that Dox release occurred in MCTS. Furthermore, studies on IO@RB-Dox-HSA NPs, chapter 5, showed similar results: Dox release was not observed by dialysis studies whereas confocal images of MCTS incubated with the NPs showed Dox diffusion through the entire MCTS, even though if the Dox loading was not optimized. Thus, studies of cytotoxic effect on MCTS of these four types of NPs (IO@RB-Dox, IO@ST-Dox, IO@RB-Dox-HSA and IO@ST-Dox-HSA NPs) would be interesting to achieve in order to determine which one of these systems would be the most promising cargo for drug delivery. Furthermore, hyperthermia treatment of MCTS could be added to these studies in order to investigate the impact of combined therapy.

4.4 Conclusion

The tuning of core-shell morphology showed firstly an enhancement in the theranostic properties of NPs. Indeed, the increase in the pore size from RB to ST pore channels led to an enhancement of DLC and the replacement of IO cores of 10 nm by larger cores about 20 nm in size gave the possibility to use the systems for treatment by hyperthermia additionally to their use as T₂ contrast agents. However, drug release studies showed that IO@RB-Dox NPs got higher controlled Dox release abilities than IO@ST-Dox or IO@RB-Dox-HSA NPs and in addition, as the silica shell on IO@RB NPs is less permeable to water than stellar pore morphology, these NPs exhibited lower r_1 values that led to enhancement of r_2/r_1 ratio. Thus, after all, the NP design that showed the best theranostic properties seemed to be IO@RB-Dox NPs.

To investigate more in details the abilities of IO@RB-Dox NPs as theranostic agents these NPs should be still tested *in vitro* on cancer cell lines.

Chapter 7: General Conclusion and Outlooks

The aim of this PhD work was to produce and test new composite nano-objects for the diagnosis and treatment of cancer. Specifications were to design nanoparticles that can, in the same time, be used for hyperthermia and chemotherapy and would have as well imaging properties. For this purpose, we developed hybrid nanoparticles made of an inorganic core surrounded by a HSA organic coating. The inorganic core is also a composite by itself as it is made of an iron oxide core (IO) and a mesoporous silica shell (MS). These nano-objects were thus named IO@MS NPs.

We thus succeed in the synthesis of two main kinds of IO@MS NPs: IO@RB and IO@ST. These IO@MS NPs share the same core made of IO NPs of 10 or 20 nm but differ from the morphology of their outer MS shell. Furthermore, these NPs exhibited a nanometric size suitable for biological applications with diameters between 30 and 120 nm depending on the synthesis procedures.

Inspired by the literature, the best parameters for reproducible synthesis of monodisperse and well-define IO@RB NPs with an IO core of about 10 nm were first established. This synthesis process was then successfully translated to larger IO core of about 20 nm.

Besides the wide described and reported IO@RB NPs type, the design of MS shell around IO NPs with large porosities above 10 nm remains scarcely explored. We thus unsuccessfully tried to combine, in a first time, the synthesis of BMS NPs with IO NPs. Fortunately, the recent paper of Zhang *et al.* (41) describing the synthesis of ST NPs, gave the opportunity to investigate a new synthesis strategy. Hence, the translation of this method to IO cores was investigated. This led to well defined IO@ST NPs exhibiting high surface area and pore volume and pore sizes of ~ 10 nm. The synthesis parameters have still to be perfected in order to avoid the formation of core less ST NPs and to achieve the tuning of IO@ST sizes. For the best of our knowledge, beside us, only Tao and Zhu (152, 162) synthesized IO@ST NPs based on Zhang *et al.* process but they used polydispersed IO NPs formed by coprecipitation as core. Thus, there is no report describing the synthesis and characterization of IO@ST NPs.

As imaging is of paramount importance in cancer therapy to detect tumors and follow their response to treatment, we analyzed the potential abilities of our IO@MS NPs as T_2 MRI contrast agents.

First, the properties of silanized water-dispersible IO NPs of 10 nm for MRI diagnosis were investigated. The results obtained with the best water-dispersible silane coating, TPEDTA, showed that IO-TPEDTA NPs had similar relaxivities than commercial IO NPs demonstrating their potential as contrast agents (r_1 and r_2 values around 10 and 100 $\text{mM}^{-1}\cdot\text{s}^{-1}$ respectively).

The relaxivities studies at pH 7.4 on IO@RB-NH₂ with same size of IO, showed that both r_1 and r_2 strongly decreased which is in accordance with the pH dependence observed on IO-APTES NPs probably due to a strong aggregation state. However, for IO@RB-HSA NPs the r_2 value increased to a value suitable for T_2 contrast ($\sim 100 \text{ mM}^{-1}\cdot\text{s}^{-1}$) whereas the r_1 stayed low ($< 1 \text{ mM}^{-1}\cdot\text{s}^{-1}$) which is related to the fact that MS shell decreases the water accessibility to the magnetic core. The same results (low $r_1 < 1 \text{ mM}^{-1}\cdot\text{s}^{-1}$ and r_2 values around 100 $\text{mM}^{-1}\cdot\text{s}^{-1}$) were obtained on raw IO@RB NPs with a larger IO core of 18 nm whereas for IO@ST with the same IO core the r_2 value stayed high (over 100 $\text{mM}^{-1}\cdot\text{s}^{-1}$) but the r_1 increased, even if its value stayed under 1 $\text{mM}^{-1}\cdot\text{s}^{-1}$, which indicated that the water accessibility to the core increased with ST shell. This result pointed out that the morphology of MS shell strongly influences the longitudinal relaxivity as it modifies the water access to the magnetic core. Aside r_2 values were kept high enough for all our systems to insure that they can be used as T_2 contrast agents.

IO NPs of 20 nm are also known to be suitable for magnetic hyperthermia. That is the reason why we also produce IO@RB and IO@ST NPs with an IO core of 20 nm. To the best of our knowledge, there is no report so far on the impact of the addition of MS shell on IO hyperthermia abilities. Thus, our preliminary studies performed on IO@RB and IO@ST NPs showed, that the addition of MS shell did not affect the hyperthermia abilities of the IO core and may even improve it to some extent. But this preliminary study has to be reproduced further times before drawing final conclusions.

The MS pore morphology did reveal to be crucial for drug loading as well. We first investigated the best Dox loading strategy depending on silica pore morphology: either by Dox-HSA, with Dox covalently binds to HSA with hydrazone linkage, diffusion into large pore BMS NPs or by simple impregnation into small RB porosities followed by pore capping with an HSA shell. The subsequent silica dissolution gave in the first case self-supported HSA_{Dox} NPs and in the second case Dox loaded HSA nanocapsules. On one hand, the covalent grafting of Dox to HSA was not fruitful as it led to strong aggregation. Thus the ratio Dox/HSA has to be kept low to avoid precipitation. On another hand, the soaking of Dox into RB porosities led to high DLC values and after silica dissolution the Dox HSA nanocapsules reached a much higher DLC. Thus the strategy of Dox soaking is preferable.

Dox soaking into IO@MS NPs with different pore morphologies (ST versus RB), in different solvents and with different silica surface modification showed that for both morphologies the highest DLC and DLE values were obtained in water on amino-modified silica surface. Moreover, between both morphologies IO@ST allowed higher Dox loading.

Dox release from HSA coated NPs remains still challenging. Indeed, for all studied HSA coated formulations, efficient controlled release of Dox by HSA degradation with proteases was never achieved, even at high Dox loadings and under various proteases concentrations and pH.

The coating with HSA implies a specific surface treatment with IBAM. First we envisaged that this IBAM surface functionalization may close the pore mouths inhibiting thus the Dox release. However, further studies showed that, even by replacing these IBAM groups grafted on the silica by the deposition of a first HSA layer on the NPs prior the classical IBAM-HSA coating, Dox did not release after proteolytic treatment. Furthermore, we also noticed that without HSA coating, IO@RB-Dox showed a pH and temperature dependent partial Dox release with a maximal Dox release of about 55 % at pH 5 and 50 °C. This implies that still 45 % of the Dox stayed in silica porosities. This result suggests the presence of different types of interactions or aggregation states of Dox that are more or less strong. Furthermore, after HSA coating on these systems the Dox release was very poor. Thus, the Dox released during the HSA coating synthesis steps may be the Dox that had the weakest interactions or aggregation states in the silica. The final Dox remaining in the HSA-coated NPs is thus the hardest to release. We concluded so that Dox molecules may get some strong interactions with amino-modified silica surface or aggregate with themselves or have difficulties to diffuse from the porosities.

In parallel, the fail in Dox release experiments from Dox-HSA nanocapsules obtained after silica dissolution proved that this Dox release problem is not related to the porosity of silica template. Furthermore, experiments on MCTS showed that Dox-HSA nanocapsules had a strong cytotoxic effect which was in accordance to the CLSM images obtained on IO@RB-Dox-HSA NPs that showed Dox diffusion into MCTS. Those results finally attest of an efficient Dox release from these systems into 3D *in vitro* models that we were not able to mimic through our Dox release experiments by dialysis.

We thus hypothesized that an interaction between APTES from amino-modified silica surface and Dox may happen. To understand this potential interaction and its behavior, we started to analyze by electrospray and ^1H NMR mixture of Dox and APTES obtained at different pH. The results are currently being interpreted and other experiments on the “Dox complex” obtained after silica dissolution before and after IBAM-HSA coating are envisaged.

Finally, the abilities of MS for diagnosis was not studied in this thesis but was investigated in a parallel master project. In this work, small CdSe quantum dots were grafted into IO@ST porosities through a carbo-diimidation reaction and the final NPs were covered by an HSA shell (adsorbed by IBAM strategy) in order to afford a biocompatible and also protective layer towards QDs or Cd ion release. Then, regarding applications for bimodal imaging, longitudinal and transversal relaxivities were measured and *in vitro* cellular fluorescence studies were performed. A paper about this work is currently under writing.

To conclude we succeed in the synthesis of IO@MS NPs that have a real theranostic potential. Indeed they exhibited abilities for proper magnetic hyperthermia and Dox delivery as well as for T_2 MRI imaging. To show all their potential, we still need to do an extensive *in vitro* study on 2 D cancer cell culture and 3D tumor models followed by *in vivo* experiments. We plan to perform antitumoral activity testing on an ectopic xenograft tumor in mouse model by direct injection of the particles. We will also be able to assess first separately and then combined, the effect of both drug delivery and hyperthermia of our systems.

Chapter 8

Résumé en français

**SYNTHESE DE NANOPARTICULES HYBRIDES DE TYPE
CŒUR-COQUILLE A VISEES THERANOSTIQUES**

Dans le cadre de la recherche contre le cancer, les nano-systèmes appelés théranostiques, combinant à la fois des capacités de thérapie et de diagnostic (Figure 8-1 (290)), ont été largement développés au cours des dernières années. Le diagnostic de cancer peut être réalisé par plusieurs techniques d'imagerie telles que l'imagerie optique, la fluorescence proche infrarouge (NIR), la tomographie par émission de positons (PET), la résonance magnétique (MR), la tomodensitométrie d'émission de photons (SPECT), la tomodensitométrie (CT) et/ou l'imagerie par ultrasons (US). La thérapie cancéreuse, quant à elle, peut être effectuée par hyperthermie magnétique, par délivrance d'agents chimiothérapeutiques, de SiRNA ou de gènes, ainsi que par radiothérapie ou photothérapie. Comme représenté en Figure 8-2, l'avantage majeur de combiner la thérapie et le diagnostic dans un même objet est de pouvoir suivre par imagerie l'endroit spécifique où le médicament est délivré dans le corps, la façon dont il est relargué dans les tumeurs ainsi que l'efficacité du traitement (1).

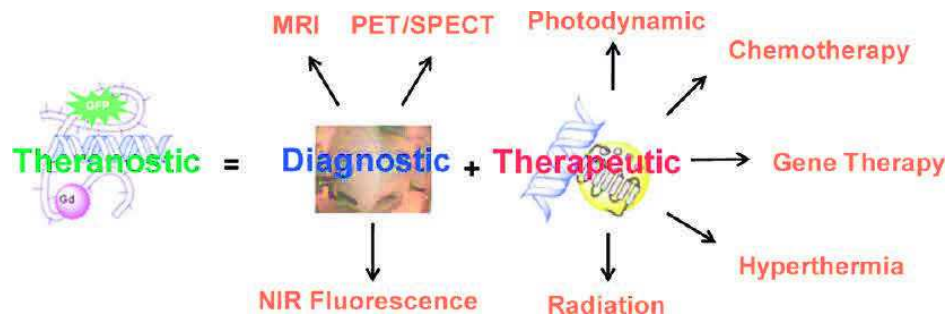


Figure 8-1 : Définition du concept d'objet théranostique (290)

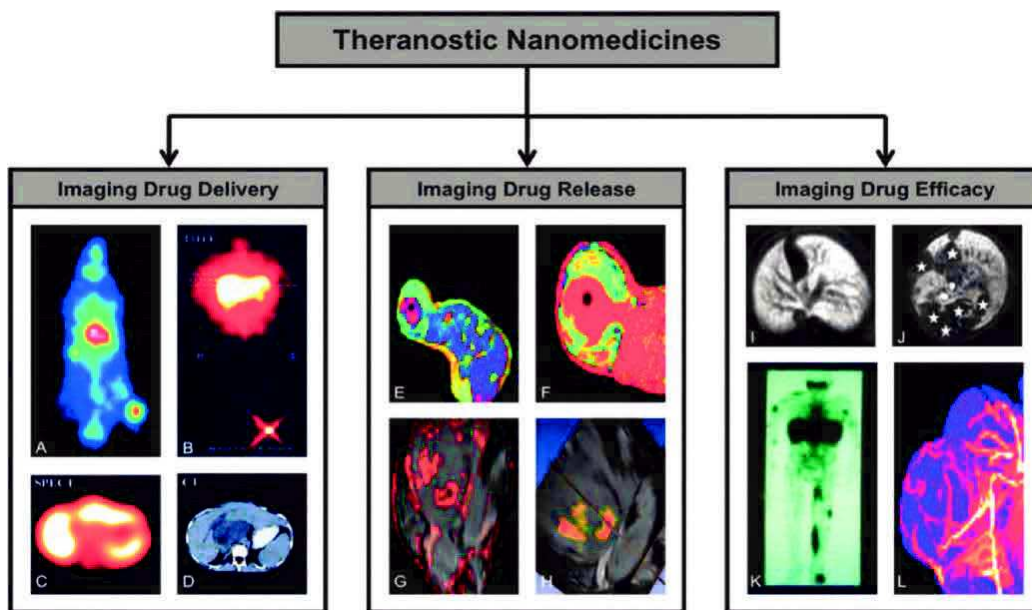


Figure 8-2: L'intérêt de l'imagerie par un objet théranostique (1)

Parmi les agents théranostiques actuellement développés, un grand intérêt est porté aux nanoparticules d'oxyde de fer (IO NPs) puisqu'elles ont l'avantage d'être, d'une part biocompatibles ainsi que biodégradables et montrent d'autre part des capacités à la fois en diagnostique et en thérapie. En effet, les IO NPs sont déjà approuvées par la FDA, sont commercialisées et utilisées comme agents de contraste négatifs pour l'IRM. Plus récemment elles ont également démontré des propriétés thérapeutiques par hyperthermie magnétique.

Par ailleurs, il est aujourd'hui largement admis que l'association de plusieurs thérapies augmente considérablement l'efficacité du traitement anticancéreux. Ainsi, la conception de nano-objets combinant l'hyperthermie magnétique à la délivrance de médicaments semble être une approche très prometteuse. Le principal défi de cette stratégie est donc de réussir à charger une grande quantité de médicaments sur les nano-objets à base d'oxyde de fer présentant des propriétés d'hyperthermie. En 2001, l'équipe de Vallet-Régi fut la première à utiliser les porosités de silices mésoporeuse (MS) pour encapsuler des médicaments (45). De plus, le revêtement de nanoparticules d'oxyde de fer par une coquille de silice mésoporeuse a déjà été démontré et est largement référencé. Ainsi, comme illustré en Figure 8-3, le projet de recherche développé lors de cette thèse, porte sur la synthèse d'un agent théranostique de type cœur-coquille possédant un cœur d'oxyde de fer revêtu d'une coquille de silice mésoporeuse. Le cœur d'oxyde de fer assure, de par ses propriétés magnétiques, le diagnostic par IRM ainsi que la thérapie par hyperthermie magnétique, tandis que la coquille de silice poreuse permet l'encapsulation d'agents fluorescents pour le diagnostic par imagerie optique et/ou de médicaments anticancéreux pour la chimiothérapie.

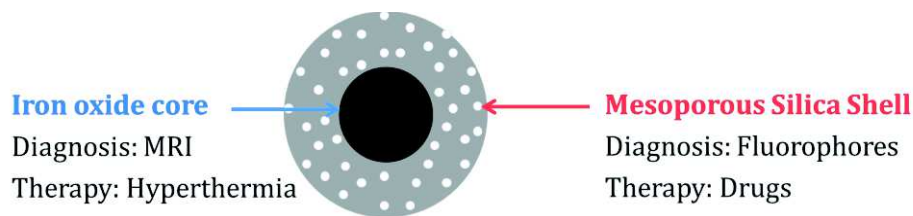


Figure 8-3: Schéma descriptif du système cœur-coquille « oxyde de fer »-« silice mésoporeuse » pour la théranostique

Pour la coquille de silice mésoporeuse, les principaux défis demeurent l'efficacité du chargement et le contrôle de la libération des médicaments. En effet, si la libération du médicament n'est pas contrôlée, le médicament imprégné dans les porosités de la silice pourrait lentement diffuser en dehors du système dans le milieu au fur et mesure du temps. Une des possibilités pour garder le médicament à l'intérieur de la porosité est de lier le médicament de manière covalente à la silice par une liaison chimique qui peut se rompre avec des stimuli spécifiques. Une autre façon de contrôler la délivrance du médicament consiste à utiliser des gatekeepers pour bloquer les porosités, dans lesquelles les médicaments sont emprisonnés et par la suite les libérer par des stimuli spécifiques. Ainsi, dans ce projet de doctorat, nous envisageons d'encapsuler le médicament en recouvrant la coquille de silice avec des protéines et en testant la libération en utilisant soit une dégradation enzymatique, soit par chauffage par hyperthermie magnétique. A partir de cet objectif global le projet s'est alors divisé en 3 grandes sous-parties (Figure 8-4) :

1. **L'étude de la résistance et la capacité à contenir des médicaments de la coquille d'HSA.** Pour se faire, des nanocapsules d'HSA contenant de la Doxorubicine (Dox, agent anticancéreux) ont été formées après dissolution de la silice mésoporeuse ayant servie au préalable au chargement en médicament et à la formation de la coquille d'HSA. Dans cette stratégie la silice est donc un template sacrificiel et seulement l'aspect chimio-thérapeutique du système final est étudié.
2. **La création de nanoparticules cœur-coquille pour le diagnostic par IRM et la délivrance de médicament.** Dans cette partie l'ajout au système d'un cœur

d'oxyde de fer permet de créer l'aspect diagnostique des nanoparticules. Ces objets cœur-coquille chargés en médicaments sont donc à présent théranostiques.

3. **Optimisation de la morphologie des nanoparticules afin d'obtenir les meilleures propriétés théranostiques.** Ainsi la taille du cœur d'oxyde de fer est modifiée pour voir son impact à la fois pour l'imagerie IRM et pour l'hyperthermie magnétique. Différents types de porosités de la silice sont également étudiés afin de déterminer lequel se prête le mieux l'encapsulation et au relargage de médicaments.

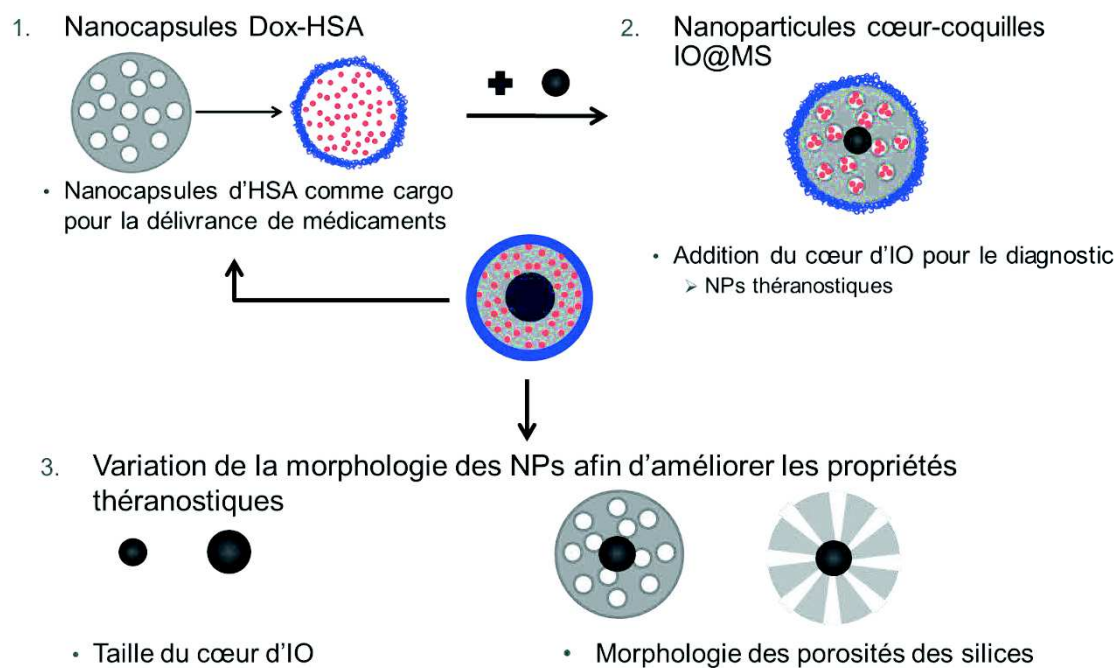


Figure 8-4: Schéma synthétisant les principaux travaux présentés dans cette thèse

1 Formation de nanocapsules d'HSA chargée en Dox pour la délivrance de médicament en utilisant la silice mésoporeuse comme modèle sacrificiel

1.1 Introduction

Le design de nanoparticules comme systèmes de délivrance contrôlée de médicaments est un domaine phare qui permettrait de réduire les importants effets secondaires de ces médicaments comme la cardiotoxicité des anthracyclines (291–295). Ainsi de nouvelles nanoparticules dites « intelligentes » ayant la capacité de délivrer les médicaments localement en réponse à des stimuli spécifiques ont vu le jour (296–303). Parmi l'ensemble des stratégies développées, la délivrance de médicaments contrôlée par action enzymatique est une approche qui a séduit plus d'un chercheur ces dernières années (153, 154, 236–239). En effet, les protéases (enzymes cellulaires) ont la capacité de catalyser la protéolyse, c'est-à-dire la dégradation protéique. Ainsi les protéines devraient être de bons candidats pour la création de nano-objets pour la délivrance de médicaments contrôlée par action enzymatique.

Comme l'albumine de sérum humaine (HSA) (protéine la plus abondante dans le plasma) est non toxique, non immunogénique et biocompatible et que les nanoparticules fabriquées à partir d'HSA sont connues pour être dégradées par action enzymatique (304), cette protéine semble être un matériau prometteur en tant que cargo pour la délivrance contrôlée en médicaments (163, 164). Dans les méthodes classiques de formation de nanoparticules d'HSA l'utilisation d'agents réticulants comme le glutaraldéhyde est souvent requise. Cependant, comme le glutaraldéhyde est connu pour être génotoxique, mutagène et cancérigène, son relargage potentiel peut induire de la toxicité (247–249). Comme alternative à ce problème une nouvelle approche a récemment développé consistant à former de solides particules d'HSA assemblées de façon non-covalentes par des liaisons, vraisemblablement de type hydrogène, avec l'*isobutyramide* (IBAM) et ne nécessitant pas de réticulation supplémentaire ni addition d'adjuvants (165, 166, 187). Lors d'une procédure type, des nanoparticules de silices sont utilisées comme modèle sacrificiel afin d'immobiliser les molécules d'IBAM et induire la forme finale des nanoparticules d'HSA. Ainsi, la morphologie originelle des nanoparticules de silice a un impact majeur sur celle des nanoparticules d'HSA obtenues après la dissolution complète de la silice par l'acide fluorhydrique (HF): les NPs de silices pleines conduisent à la formation de capsules d'HSA (166) alors que les NPs de silices mésoporeuses (MS) contenant de larges porosités permettant la diffusion d'HSA au sein des pores, conduisent à la formation de NPs d'HSA répliquées (187).

Ainsi, basé sur ces précédentes recherches, nous avons développé des nanocapsules auto-supportées d'HSA contenant de la Dox en utilisant des NPs de silices comme modèle sacrificiel. La Dox chargée pourrait ensuite être relarguée après destruction des capsules d'HSA par action enzymatique. La stratégie de synthèse est donc basée sur l'utilisation de NPs de silices possédant des pores de 3 nm et présentant une morphologie de type « framboise » (raspberry, RB NPs) (305). Ces porosités étant trop petites pour permettre la diffusion d'HSA au sein de la nanoparticule, les molécules de Dox ont donc été chargées dans ces porosités avant qu'une coquille d'HSA soit formée en surface de la nanoparticule. Ainsi, après dissolution de la silice cette stratégie devrait permettre d'obtenir des capsules d'HSA contenant de la Dox.

Comme illustré en Figure 8-5, dans un premier temps des RB NPs ont été synthétisées puis leur surface a été silanisée avant de réaliser l'imprégnation de Dox dans les porosités. Après le chargement de Dox la surface des nanoparticules fonctionnalisée avec des groupements amines a été modifiée par de l'*isobutrylchloride* (IBC) afin de former des groupements IBAM en surface. Par la suite, la HSA a été adsorbée par liaisons H non covalentes sur les groupements IBAM formant ainsi une solide coquille de protéine en surface des nanoparticules de silices. Pour finir, le modèle sacrificiel de silice mésoporeuse fut dissous dans de l'acide fluorhydrique (HF) afin de former les nanocapsules auto-supportées d'HSA contenant de la Dox : Dox-HSA. Ces nanocapsules devraient ensuite pouvoir libérer la Dox de façon contrôlée après leur dégradation par l'action d'enzymes.

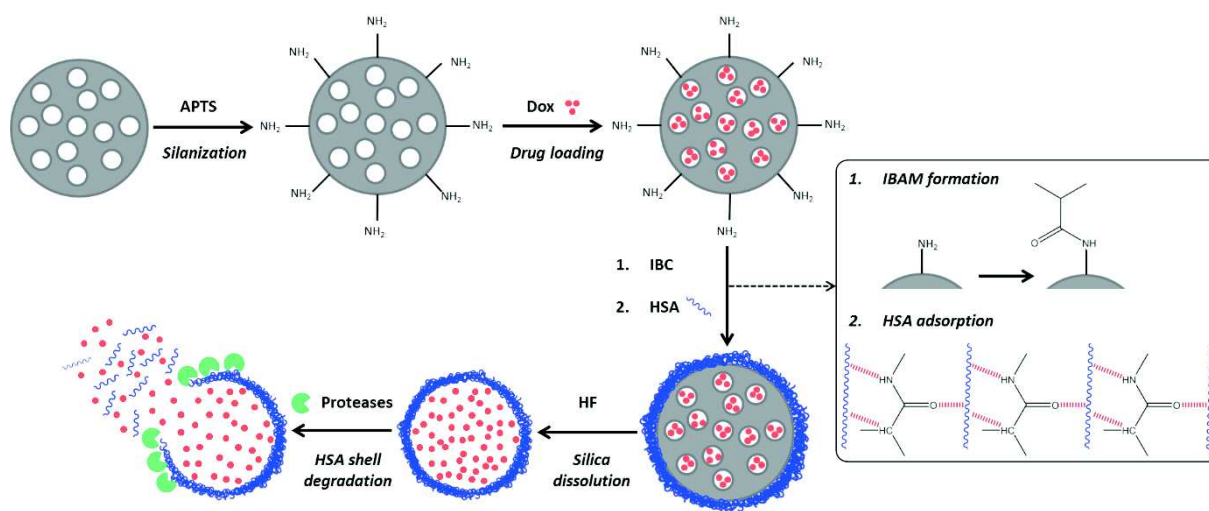


Figure 8-5: Représentation schématique de la stratégie de synthèse de nanocapsules d'HSA chargée en Dox pour la délivrance de médicament contrôlée par dégradation enzymatique de ces nanocapsules

1.2 Synthèse du modèle sacrificiel RB NPs

Les nanoparticules de silices mésoporeuses avec une morphologie de type « raspberry » (RB NPs) ont été synthétisées à partir d'une adaptation d'une méthode décrite dans la littérature (305). Comme illustré par l'image MET en Figure 8-6 A, les RB NPs obtenues sont des nanosphères poreuses. Leur taille, mesurée à partir des images MET, est de 33 ± 4 nm. Les isothermes d'adsorption et désorption d'azote obtenues sur ces systèmes ont permis de déterminer une surface spécifique et un volume total de pores de $708 \text{ m}^2 \cdot \text{g}^{-1}$ and $1.62 \text{ cm}^3 \cdot \text{g}^{-1}$ respectivement. Par ailleurs, la taille des pores pour ces RB NPs a été calculée comme étant de 2.8 et 0.7 nm.

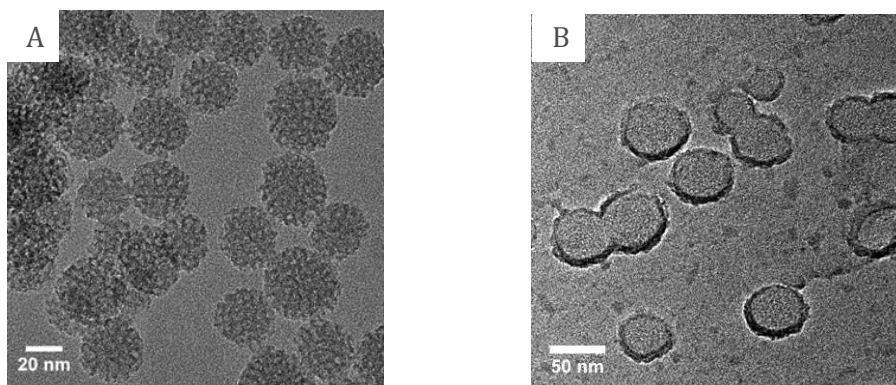


Figure 8-6: Images MET des A) RB NPs et B) Dox-HSA nanocapsules

1.3 Encapsulation de Doxorubicine

Après silanisation de la surface des NPs de silices, RB-NH₂ NPs, des études approfondies sur l'imprégnation en Doxorubicine (Dox) à l'intérieur des porosités des silices dans l'eau ainsi que le relargage observé en changeant le média pour du DMF ont été réalisées. Pour se faire trois valeurs importantes ont été introduites :

- Le fwr (feed weight ratio, le ratio massique d'imprégnation) qui correspond au pourcentage du rapport entre la masse de Dox utilisée lors de l'imprégnation et la masse de nanoparticules :

$$fwr\% = \frac{\text{masse de Dox ajoutée}}{\text{masse de NPs}} \times 100$$

- La DLC (Drug Loading Content, la teneur en médicament encapsulé) qui correspond au pourcentage du rapport entre la masse de Dox encapsulée et la masse de nanoparticules :

$$DLC\% = \frac{\text{masse Dox encapsulée}}{\text{masse NPs}} \times 100$$

- La DLE (Drug Loading Efficiency, l'efficacité de l'encapsulation du médicament) qui correspond au pourcentage du rapport entre la masse de Dox encapsulée et la masse de Dox ajoutée pour réaliser l'encapsulation :

$$DLE\% = \frac{\text{masse Dox encapsulée}}{\text{masse de Dox ajoutée}} \times 100$$

Ces études de chargement dans l'eau Milli-Q en Dox dans les porosités des RB-NH₂ NPs ont démontrées que la DLC atteignait un plateau autour de 13 % dans les conditions utilisées et que jusqu'à cette valeur maximale la DLE était toujours supérieure à 70%. Par ailleurs, le fait de changer le milieu de dispersion de l'eau Milli-Q pour le DMF induit très peu de modification sur le chargement en Dox du système. Cependant, nous avons remarqué que le « vieillissement » de la surface amino des particules avait un impact insoupçonné sur le taux maximal de chargement que l'on peut obtenir. En effet, comme illustré en Figure 8-7, pour les nanoparticules silanisées depuis 10 semaines le taux maximal de chargement descend à 7% alors qu'il était mesuré à 13% pour des nanoparticules silanisées depuis 3 semaines. En conséquence, la DLE mesurée est également plus faible pour les nanoparticules silanisées depuis plus longtemps. Ainsi, pour la

suite, le chargement en Dox a été réalisé directement après silanisation des RB NPs. Cependant, comme les étapes suivant le chargement de Dox sont nombreuses (changement de média, réaction avec l'IBC pour former la couche IBAM, revêtement par la HSA puis lavages), la DLC finale a été calculée en mesurant la différence de perte de masse obtenue en ATG entre des nanoparticules de silices revêtues d'HSA vides, RB-HSA, et des nanoparticules de silices revêtues d'HSA chargées en Dox, RB-Dox-HSA. Ces deux types de nanoparticules ont été obtenus dans les mêmes conditions de synthèse excepté, bien entendu, pour l'étape de chargement en Dox. Ainsi, d'après les courbes d'ATG obtenues (Figure 8-8) la DLC a été mesurée à 29 w% en Dox ce qui correspond, après dissolution du modèle sacrificiel de silice, à une valeur de DLC finale de 88 % en Dox contenue dans les capsules d'HSA (Figure 8-6B montre une image MET des nanocapsules de Dox-HSA obtenues après dissolution de la silice). Le

Tableau 8-1 compare les valeurs référencées dans la littérature de DLC et DLE obtenues pour des chargements en Dox dans des nanoparticules d'HSA aux valeurs obtenues pour notre système. Ainsi, par rapport aux diverses méthodes d'encapsulation de Dox référencées telles que, l'adsorption de Dox dans des NPs d'HSA préformées, l'incorporation de Dox à la HSA avant désolvatation ou la conjugaison chimique de Dox à la HSA, notre méthode d'imprégnation de Dox dans une matrice sacrificielle de silice a conduit à une DLC élevée qui convient parfaitement pour des études biologiques.

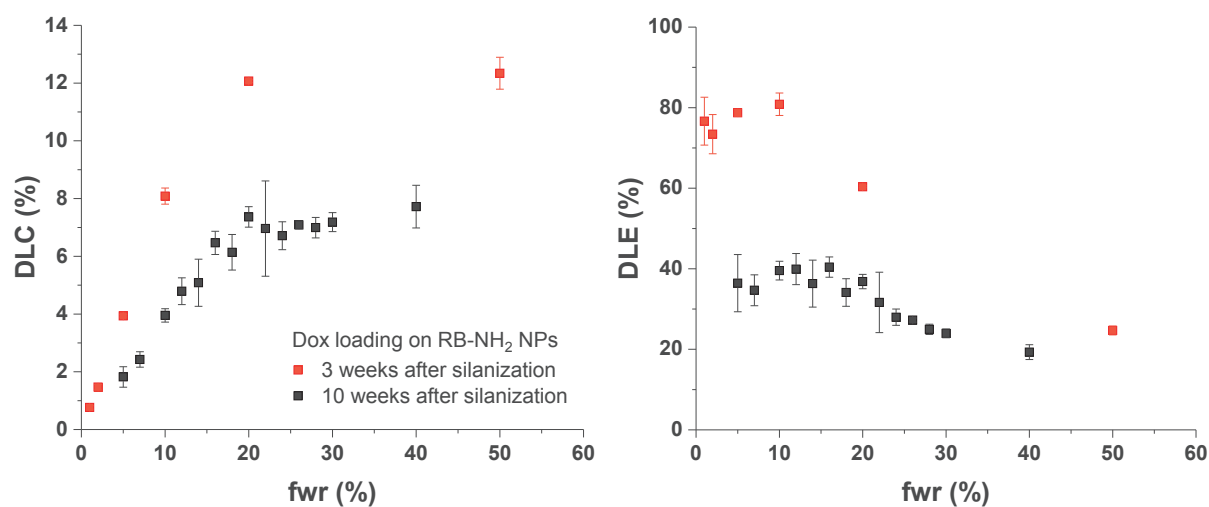


Figure 8-7: Graphiques des DLC et DLE pour le chargement en Dox dans l'eau Milli-Q des RB-NH₂ NPs en fonction du vieillissement de la surface amino: en rouge 3 semaines après silanisation et en noir 10 semaines après silanisation

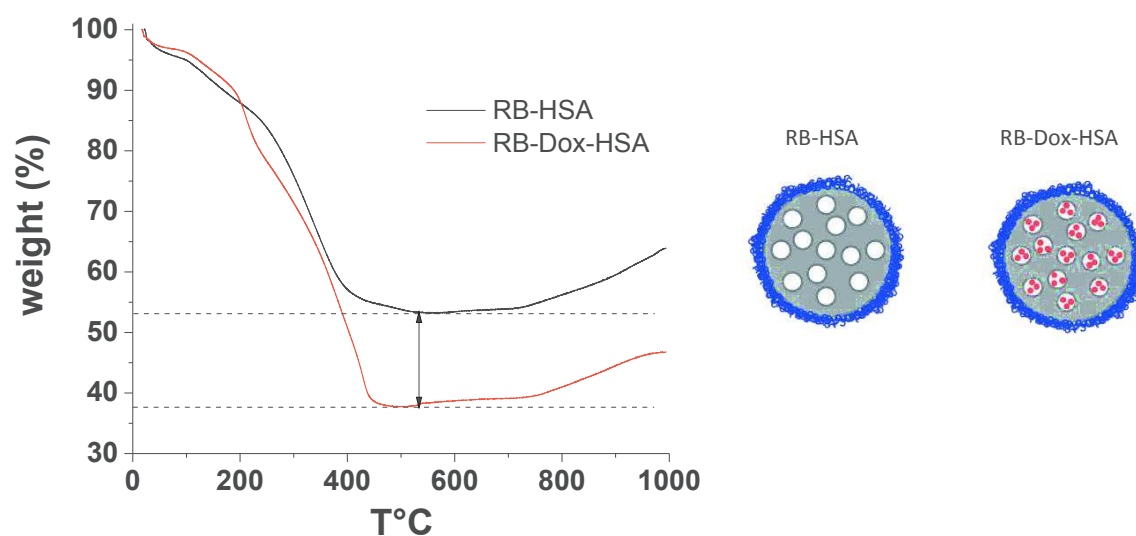


Figure 8-8: Courbes d'ATG des RB-HSA et RB-Dox-HSA NPs

Tableau 8-1: Valeurs de DLC et DLE de chargement en Dox dans des nanoparticules d'HSA

Ref.	Type d'encapsulation de Dox	Taille (nm)	DLC (%)	DLE (%)
Notre échantillon	Imprégnation dans un template de silice sacrificielle	30	88	-
(262)	Adsorption dans des NPs d'HSA déjà formées	200	4.8	94.5
(263)	Conjugation par des liaisons disulfide (via RPA)+ adsorption physique	30	56.2	-
	Conjugation par des liaisons disulfide (via MPA) + adsorption physique		62.3	-
(264)	Incubation avec la HSA avant désolvation	400	5.7	-
(246)	Adsorption dans une solution d'HSA	-	14	75
	Adsorption dans des NPs d'HSA déjà formées	158	13.8	69
	Incorporation dans la matrice d'HSA avant désolvation	404	4.82	96.3
(265)	Incorporation dans la matrice d'HSA avant désolvation	183	5	-
(266)	Adsorption dans des NPs de BSA déjà formées	100	27.8	74

1.4 Etude in-vitro des nanocapsules Dox-HSA sur des modèles cellulaires en 3D

Les études de cytotoxicité des nanocapsules ont été réalisées sur des modèles de sphéroïdes tumorales multicellulaires obtenus à partir de cellules d'hépatocarcinoma Huh7. Un tel modèle reproduit plus étroitement le comportement *in vivo* des cellules tumorales que les systèmes de culture en 2D. Ainsi la toxicité des nanocapsules de Dox-HSA et d'HSA vide a été évaluée en mesurant la croissance des sphéroïdes dans le temps (à 2, 4 et 7 jours). Les sphéroïdes ont donc été incubées avec les NPs de Dox-HSA et d'HSA diluées dans du milieu de culture à des concentrations de 35,4 $\mu\text{g.mL}^{-1}$ et 17,7 $\mu\text{g.mL}^{-1}$ en HSA ce qui correspond à des concentrations de Dox de 31 $\mu\text{g.mL}^{-1}$ et 15,5 $\mu\text{g.mL}^{-1}$ pour l'échantillon Dox-HSA. La Figure 8-9, montre des images de microscopie optique des sphéroïdes à différents jours après incubation et avec les deux types de NPs à la plus forte concentration testée. Ces images montrent que les NPs d'HSA n'ont pas impacté la croissance des sphéroïdes si l'on compare aux sphéroïdes non traitées alors que, pour les NPs de Dox-HSA, les sphéroïdes présentent une morphologie différente pouvant être liée à une mort cellulaire massive. De telles images sont caractéristiques de l'effet de la Dox sur les sphéroïdes (272, 273). Des mesures de la surface des sphéroïdes ont également été effectuées et le pourcentage de croissance a été calculé par rapport à l'expérience contrôle (Mock). Comme le montrent les résultats présentés à la Figure 8-10, la croissance des sphéroïdes en présence de NPs de Dox-HSA est rapidement inhibée. En effet, on observe une diminution de la croissance de 80% par rapport au témoin. Ainsi, comme la croissance n'est pas modifiée lorsque les sphéroïdes sont incubées avec des NPs d'HSA non chargées, on peut supposer que cette inhibition de croissance est liée à la libération de Dox. En effet, ces particules sont constituées d'albumine et peuvent être absorbées par les cellules, du moins celles constituant la couche externe des sphéroïdes, par endocytose non spécifique et/ou pinocytose. De ce fait la Dox pourrait donc être libérée après la dégradation de HSA par les protéases lysosomales. En outre, nous savons par d'autres expériences que la Dox peut diffuser à travers l'ensemble du modèle 3D et cela même si l'internalisation des NPs se produit seulement aux frontières des sphéroïdes. Donc l'effet observé dans ces travaux prouve que la Dox peut être libérée des nanocapsules d'HSA après internalisation cellulaire.

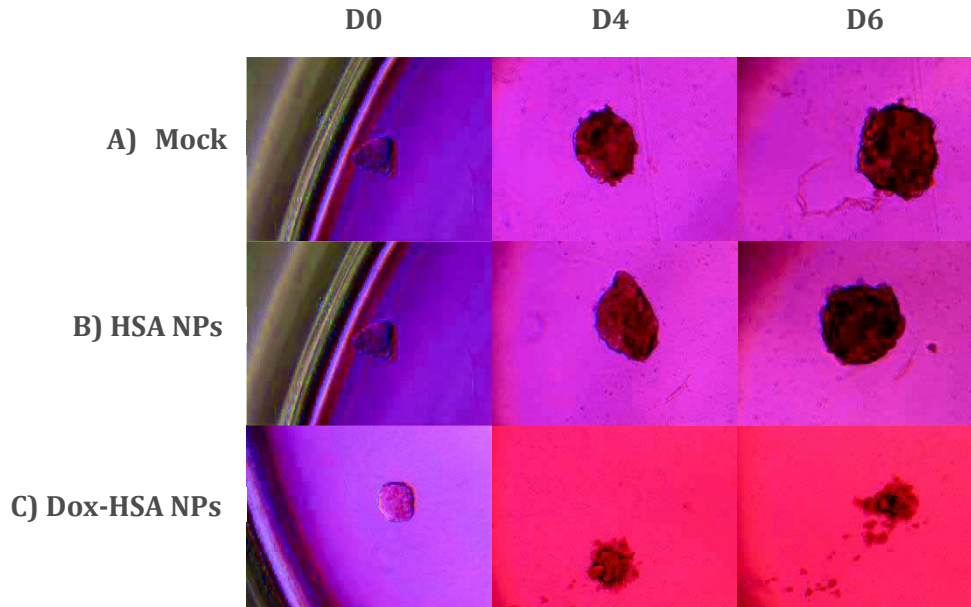


Figure 8-9: Images obtenues par un microscope optique (10x) des A) sphéroïdes non traitées, B) sphéroïdes traités avec des NPs d'HSA à 35.4 $\mu\text{g}\cdot\text{mL}^{-1}$ d'HSA, C) sphéroïdes traitées avec Dox-HSA NPs à 35.4 $\mu\text{g}\cdot\text{mL}^{-1}$ d'HSA et 31 $\mu\text{g}\cdot\text{mL}^{-1}$ de Doxorubicin le tout à différents jours d'incubation: jours 0, 4 et 6.

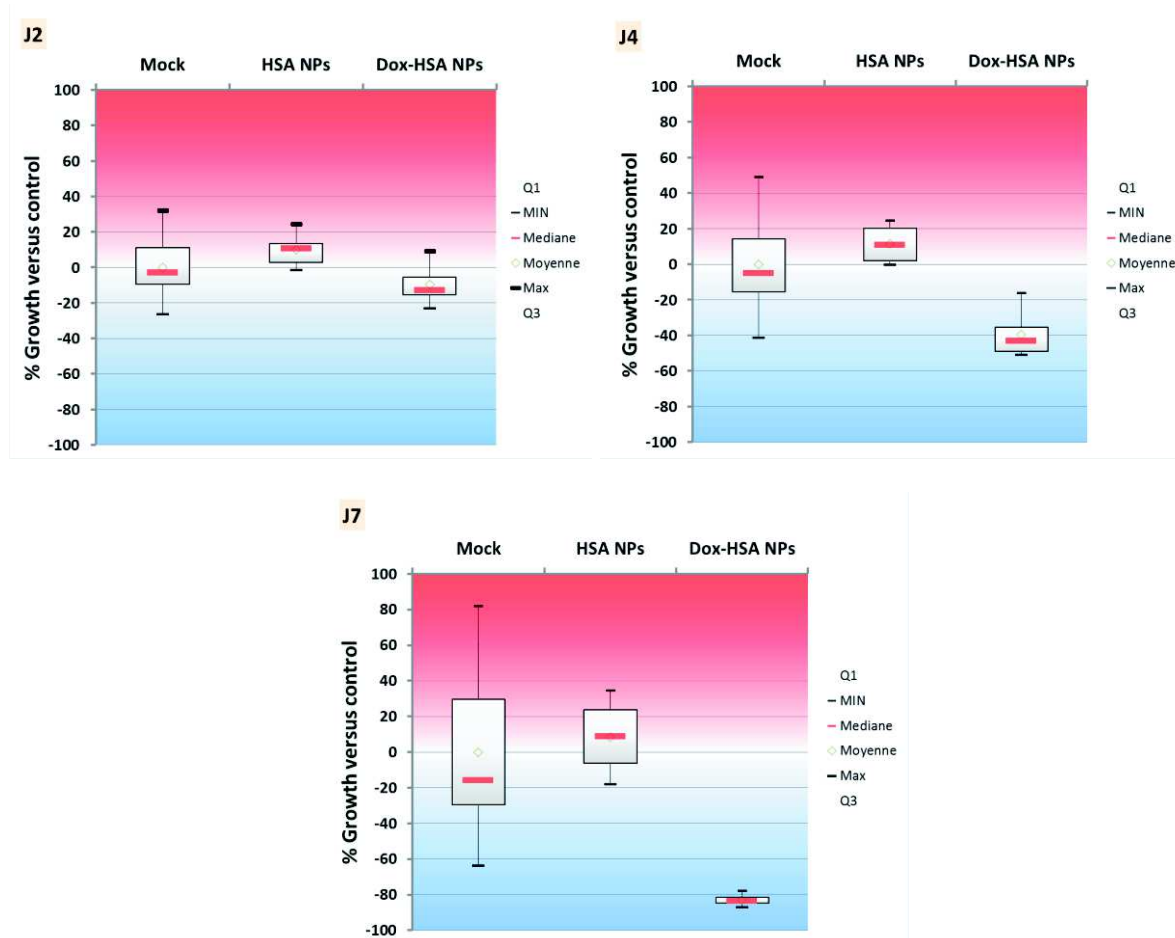


Figure 8-10: Boîtes à moustache représentant le pourcentage de croissance des sphéroïdes Huh7 traitées avec des NPs d'HSA ou Dox-HSA en comparaison des sphéroïdes non traitées (Mock) après 2, 4 et 7 jours d'incubation à des concentrations de 17,7 $\mu\text{g}\cdot\text{mL}^{-1}$ en HSA et 15,5 $\mu\text{g}\cdot\text{mL}^{-1}$ en Dox

2 Création de nanoparticules cœur-coquille pour le diagnostic par IRM et la délivrance de médicament

Cette partie porte sur la création de nanoparticules de type cœur-coquille pour le diagnostic par IRM et la délivrance de médicament anti-cancéreux. Comparativement à précédemment la silice mésoporeuse n'est pas dissoute et on y ajoute en son sein un cœur d'oxyde de fer permettant de créer l'aspect diagnostique des nanoparticules. Ces objets cœur-coquille chargés en médicaments sont donc à présent théranostiques.

Ainsi, comme illustré en Figure 8-11, la stratégie de synthèse consiste à faire croître une coquille de silice mésoporeuse autour de nanoparticules d'oxyde de fer superparamagnétiques obtenues par décomposition thermique. Ce type de NPs est appelé IO@RB. Ensuite la Doxorubicine, Dox, est imprégnée dans les porosités de la coquille de silice puis la HSA est déposée sur la surface de la silice préalablement modifiée avec des groupements IBAM. Pour finir ces nanoparticules devrait libérer la Dox après dégradation par les protéases présentes dans les cellules de la coquille d'HSA servant de gatekeeper au système.

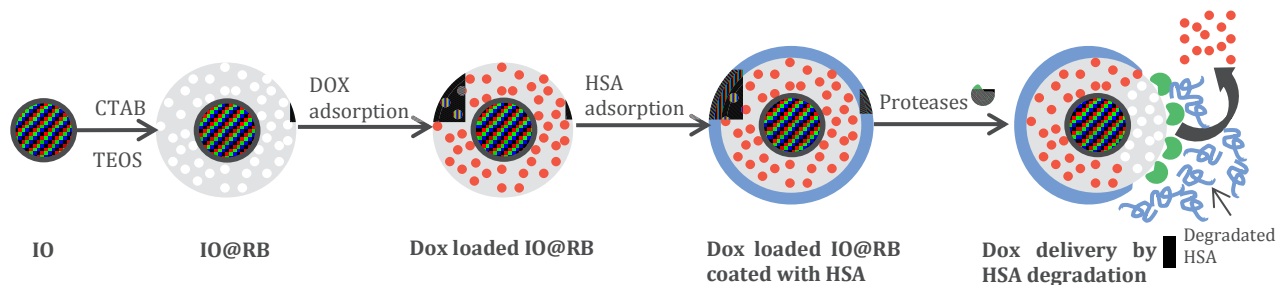


Figure 8-11: Schéma du procédé de synthèse de nanoparticules cœur-coquille oxyde de fer-silice chargées en Dox et recouvertes d'une couche d'HSA pour la délivrance en médicament contrôlée par la dégradation d'HSA par action enzymatique

2.1 IO@RB NPs synthèse et caractérisation

De nombreux paramètres peuvent influencer sur la synthèse des IO@RB NPs tels que la température, le temps de réaction, la qualité du transfert de phase des IO, le ratio CTAB/Fe... Ainsi, après avoir trouvé le meilleur protocole pour obtenir des NPs cœur-coquille monodisperses et possédant un cœur d'IO unique pour toute nanoparticule, la taille de la coquille a été modulée. Ainsi, comme présenté en Figure 8-12, partant d'un cœur d'IO de 9 nm on a pu obtenir des objets cœur-coquille de taille variable : échantillon 1 (Figure 8-12 A, D) < échantillon 2 (Figure 8-12 B, E) < échantillon 3 (Figure 8-12 C, F). En mesurant les tailles de ces NPs à partir d'images TEM sur plus de 200 particules, les diamètres moyens obtenus étaient d'environ 31 ± 3 nm, 58 ± 5 nm et 84 ± 7 nm pour les échantillons 1, 2 et 3 respectivement. Les histogrammes de distribution de taille résultants de ces mesures, Figure 8-12 G, montrent des pics nets pour chaque lot d'IO@RB NPs, ce qui est représentatif de NPs monodisperses. Par ailleurs les gaussiennes calculées à partir de ces histogrammes sont centrées sur 31, 59 et 86 nm. Les mesures DLS de ces IO@RB NPs, Figure 8-12 H, mettent en évidence leur stabilité colloïdale dans l'eau avec des tailles hydrodynamiques moyennes centrées à 60, 80 et 105 nm pour les échantillons 1, 2 et 3 respectivement.

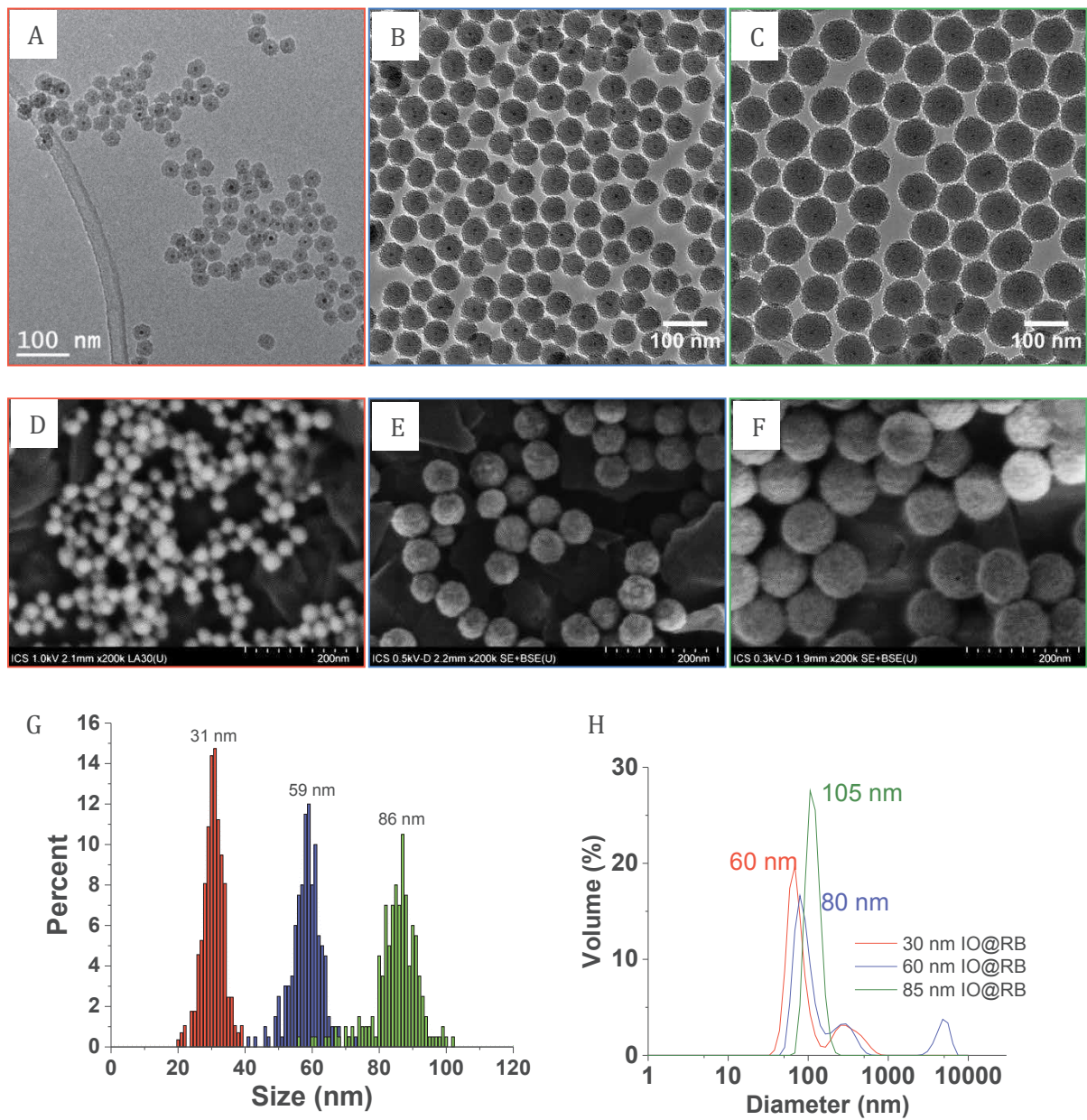


Figure 8-12: Images MET (A, B, C) et MEB (D, E, F) des IO@RB NPs de 31 ± 3 nm (A, D), 58 ± 5 nm (B, E), 84 ± 7 nm (C, F)

2.2 IO@RB NPs pour l'imprégnation de Doxorubicine

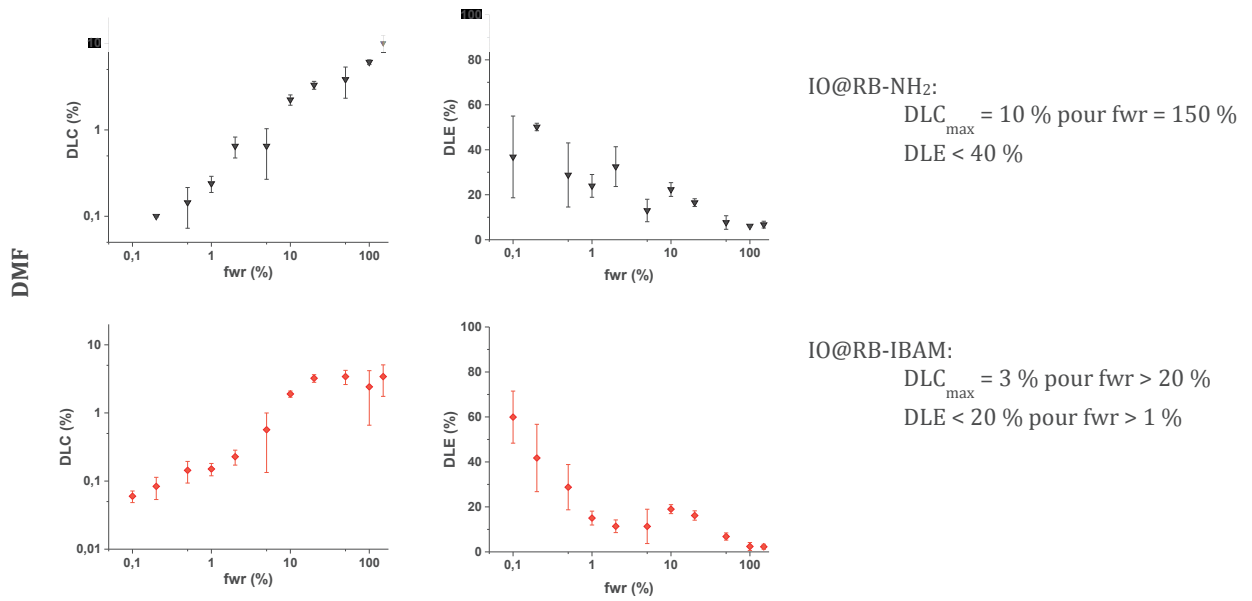
La modification de la surface de la coquille de silice et le choix du solvant peuvent grandement influencer l'imprégnation en doxorubicine (Dox). Ainsi le taux de chargement en Dox ainsi que l'efficacité en chargement ont été mesurés pour différentes conditions d'imprégnation.

Tout d'abord, l'influence de la modification de la surface de la coquille de silice sur le taux d'imprégnation en Dox a été étudiée. En accord avec notre protocole de synthèse, nous avons la possibilité de charger le Dox dans les NPs IO@RB soit après modification de la surface de silice par les groupements IBAM, IO@RB-IBAM NPs, soit sur les NPs silanisées IO@RB-NH₂. L'imprégnation en Dox pour ces deux types de modifications de surface a été réalisée dans le DMF et les courbes resultants sont présentées en Figure 8-13 A.

Nous pouvons alors remarquer qu'un plateau à une DLC de 3% est atteint pour l'imprégnation de Dox dans les NPs IO@RB-IBAM dans le DMF, alors que pour les NP IO@RB-NH₂ dispersés dans le même solvant, aucun plateau n'a été observé et la valeur DLC maximale de 10% a été atteinte pour un fwr de 150%. Ce résultat suggère que la surface de silice modifiée avec IBAM est moins favorable à l'imprégnation en Dox que la surface modifiée des amines.

Ensuite l'influence du solvant: eau, EtOH 70% et DMF, sur l'imprégnation de Dox dans les porosités des NPs IO@RB-NH₂ a été étudiée, Figure 8-13 B. En comparant les résultats il est apparu que pour l'imprégnation dans le DMF et dans l'eau, des DLC élevées respectivement de 10 et 14% sont atteintes alors qu'une DLC maximale de 1.6% a été mesurée dans l'EtOH 70%. Ainsi l'EtOH 70% est un très mauvais solvant pour l'imprégnation en Dox. Par ailleurs, une DLE très élevée n'a été observée que pour l'imprégnation dans l'eau : la DLC maximale est atteinte autour d'un fwr de 15% dans l'eau, alors qu'elle est atteinte pour un fwr de 150% dans le DMF. Ainsi, l'utilisation d'eau comme solvant d'imprégnation conduit à une valeur DLC élevée à faible fwr, évitant ainsi le gaspillage de Dox pendant le processus de synthèse par rapport à l'imprégnation dans DMF.

A. Influence de la modification de surface



B. Influence du solvant d'imprégnation

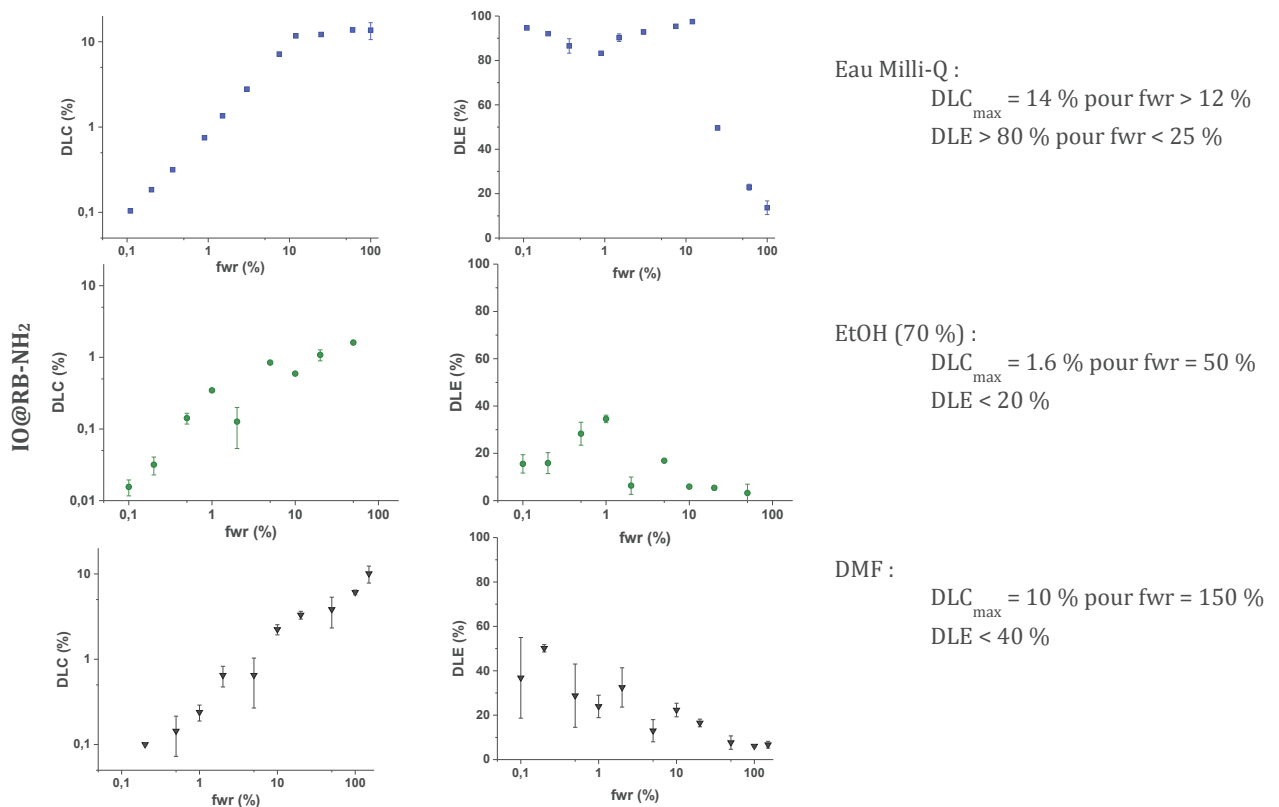


Figure 8-13: Etude de l'imprégnation en Dox dans les porosités des IO@RB NPs en fonction A) de la modification de surface IO@RB-NH₂ et IO@RB-IBAM dans le DMF B) du solvant d'imprégnation (eau, EtOH 70% et DMF) sur IO@RB-NH₂

2.3 Revêtement d'HSA, son rôle en tant que gatekeeper: dégradation par les enzymes et libération de Dox

Après imprégnation en Dox dans les IO@RB la HSA est déposée en surface des NPs afin de jouer un rôle de gatekeeper. La Figure 8-14 A et B montre les images MET des NPs avant et après dépôt d'HSA. En effet sur la seconde image on peut deviner le revêtement de protéine en surface des particules. Des mesures de DLS ont également été réalisées sur les IO@RB et IO@RB-Dox-HSA, Figure 8-14 C. Il est important de noter que les courbes de DLS obtenues sont presque identiques pour les NPs IO@RB que pour les NPs IO@RB-Dox-IBAM-HSA. Cela signifie que la modification des IO@RB par le chargement de Dox et le revêtement IBAM-HSA n'a pas modifié la stabilité colloïdale du système, c'est-à-dire n'a pas agrégé les NPs. Les mesures du potentiel Zêta, Figure 8-14 D, montrent que IO@RB-NH₂ ont un PIE autour de 7,7. Après le chargement en Dox et le revêtement IBAM-HSA, le PIE des particules chute à 6. Cela signifie que les IO@RB-Dox-IBAM-HSA sont légèrement chargées négativement, avec un potentiel Zêta entre 0 et -20 mV, à un pH proche du physiologique.

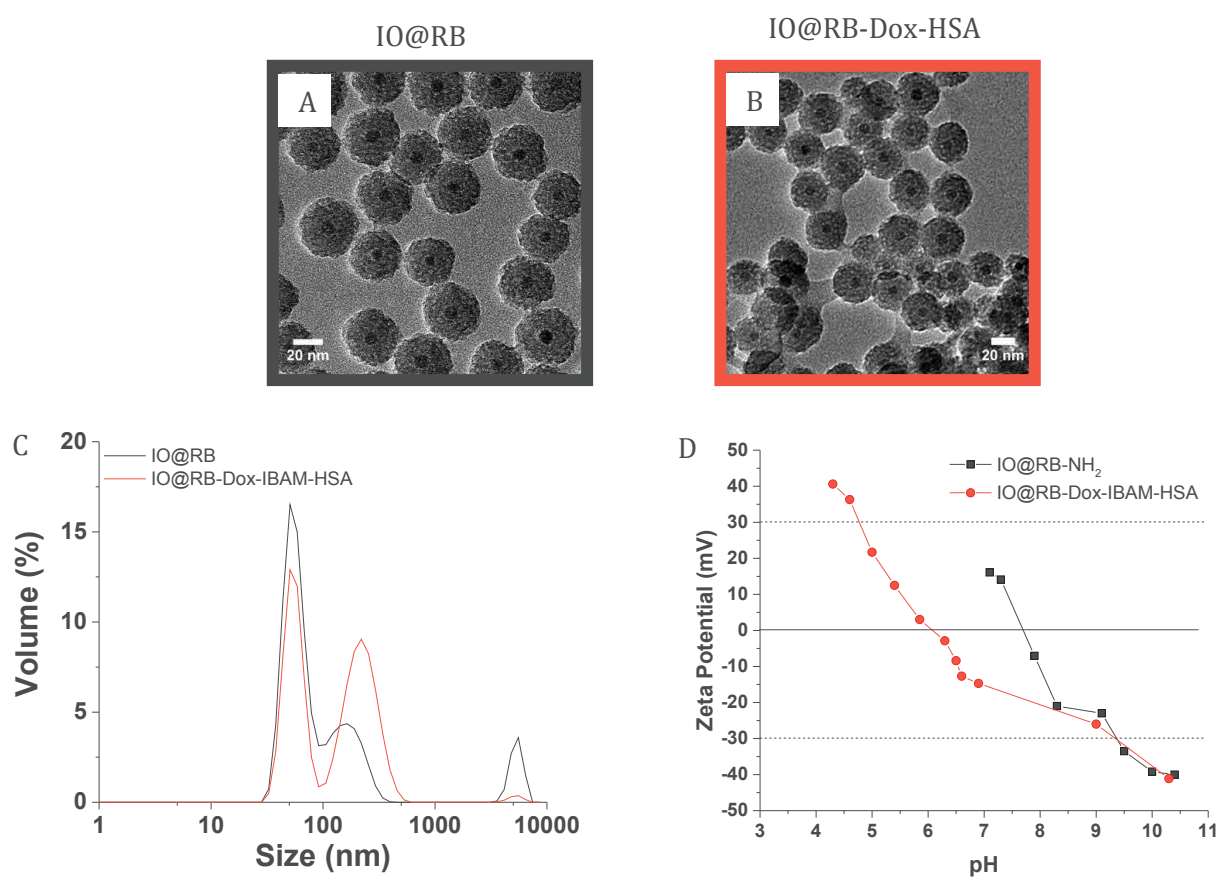


Figure 8-14: A) Image MET des IO@RB NPs, B) Image MET des IO@RB-Dox-HSA NPs, C) étude DLS et D) étude du potentiel Zêta des IO@RB et des IO@RB-Dox-HSA NPs

Des études de libération de Dox après dégradation enzymatique de la coquille d'HSA ont été réalisées. Pour ces expériences la Dox a été imprégnée dans des NPs IO@RB-NH₂ dans de l'eau. La Figure 8-15 montre les profils de dégradation de HSA et de libération de Dox des échantillons. Le profil de dégradation HSA sous dégradation enzymatique ne montre aucune dégradation de la HSA au cours du temps pour les contrôles alors qu'en présence de protéases, il a été observé que le HSA se dégradait progressivement. Ces résultats confirment que la coquille d'HSA est stable

dans le temps et que les protéases sont nécessaires à sa dégradation. En outre, plus la concentration de protéases est élevée, plus la dégradation d'HSA est rapide. Pour les courbes de libération de Dox, les NPs incubées avec des protéases ont présenté une libération de Dox légèrement plus élevée que le témoin, mais non significative. De plus, nous avons observé que les protéases seules présentaient également une faible fluorescence qui peut expliquer les petites différences dans les mesures de libération de Dox entre les NPs incubées avec une quantité élevée de protéases, avec une faible quantité de protéases et les témoins. Donc, pour conclure, aucune libération significative de Dox n'a été observée malgré la dégradation effective de la coquille d'HSA.

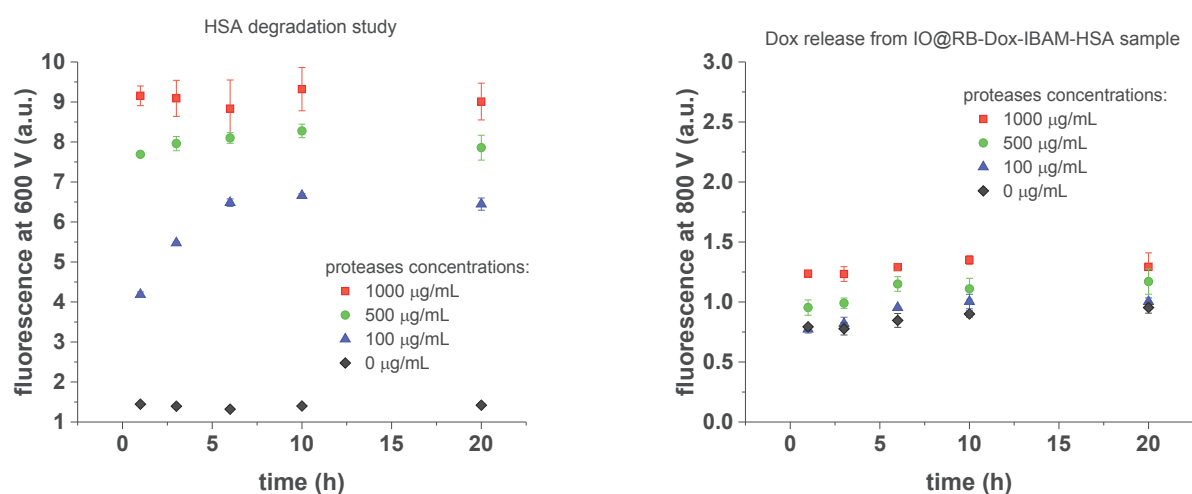


Figure 8-15: Profils cinétiques à différentes concentrations des protéases à 37°C dans le PBS à pH 7.4 de A) dégradation d'HSA B) libération en Dox pour les IO@RB-HSA NPs

2.4 IO@RB NPs comme agents de contrastes pour l'imagerie IRM

Dans cette partie, les capacités de diagnostic IRM de nos nanosystèmes théranostiques ont été étudiées. En effet, grâce aux propriétés superparamagnétiques du noyau de magnétite de $9 \pm 0,8$ nm, les IO@RB et leurs équivalents revêtus de HSA pourraient être utilisés comme agent de contraste T_2 . Ainsi cette propriété a été évaluée par relaxométrie RMN du proton à 37°C et $1,41$ T (60 MHz) sur des nanoparticules silanisées, IO@RB-NH₂ et enrobées de protéines, IO@RB-HSA, possédant une taille globale de 41 ± 3 nm et un cœur d'IO de $9 \pm 0,8$ nm.

Les courbes de relaxivité résultantes $1/T_1$ et $1/T_2$ en fonction de [Fe], présentées en , ont montré, comme attendu, un comportement très linéaire. Les pentes de l'ajustement linéaire de ces courbes ont donné les valeurs r_1 et r_2 pour les NP IO@RB-NH₂ et IO@RB-HSA.

Pour IO@RB-NH₂, les valeurs de r_1 et r_2 de $0,13 \text{ mM}^{-1}\text{s}^{-1}$ et $26,4 \text{ mM}^{-1}\text{s}^{-1}$, donnant un rapport r_2/r_1 d'environ 201, sont très faibles par rapport aux valeurs trouvées dans la littérature. En effet, Ye *et al.* ont obtenu une telle fourchette de valeurs pour des NPs IO@RB de 95 nm avec un cœur d'IO de 11 nm, tandis que pour des IO@RB de 50 nm, ils ont trouvé des valeurs r_1 et r_2 plus élevées de $1,31 \text{ mM}^{-1}\text{s}^{-1}$ et $92,13 \text{ mM}^{-1}\text{s}^{-1}$, soit un rapport r_2/r_1 de seulement 70,3.

Les valeurs de relaxivité obtenues pour les NPs correspondantes revêtues de HSA IO@RB-HSA sont de $116 \text{ mM}^{-1}\text{s}^{-1}$ pour r_2 et de $0,083 \text{ mM}^{-1}\text{s}^{-1}$ pour r_1 donnant un rapport r_2/r_1 de 1397. Ainsi si l'on compare aux mêmes NPs modifiées en surface par des groupements amines, IO@RB-NH₂, l'ajout d'HSA a eu pour effet d'augmenter les propriétés d'agent de contraste T_2 du système en diminuant le r_1 et en augmentant le r_2 conduisant ainsi à un ratio r_2/r_1 particulièrement élevé. Cette diminution de r_1 peut être expliquée par l'accessibilité limitée de l'eau au cœur magnétique en raison de l'ajout du revêtement d'HSA.

Ainsi, ces résultats montre que notre système est un candidat potentiel comme agent de contraste T_2 .

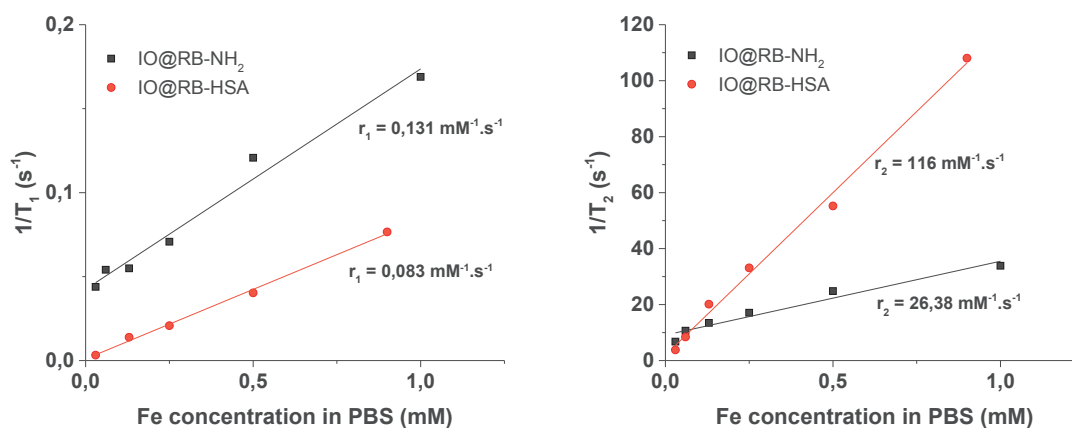


Figure 8-16: courbes de relaxivité en T_1 et T_2 pour les NPs IO@RB et IO@RB-HSA NPs de 41 nm de diameter

2.5 Etudes *in-vitro*

Pour finir nos systèmes ont été étudiés en *in-vitro*. Les études ont montré que les NPs IO@RB-HSA avaient une cytotoxicité dépendante de leur taille et présentaient une bonne internalisation dans plusieurs lignées cellulaires cancéreuses. De plus, les NPs chargées en Dox, préparées dans des conditions non optimisées, ont montré un effet légèrement plus cytotoxique que les NPs vides. Enfin des études d'internalisation des NPs sur des modèles cellulaires en 3D ont montré que même si les NPs ne s'internalisent qu'en périphérie des sphéroïdes cela permet une libération locale de la Dox qui peut dans un second temps diffuser dans l'ensemble du modèle 3D. Cet effet est illustré en Figure 8-17 dans laquelle on peut voir clairement les NPs internalisées aux bords du sphéroïde et la Dox dispersée de manière homogène dans tout le sphéroïde.

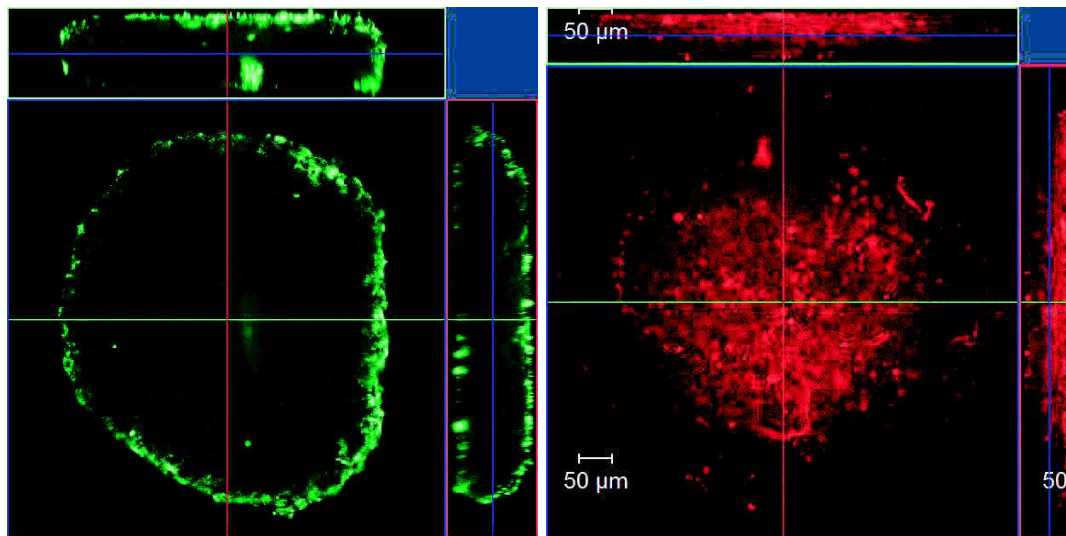


Figure 8-17: Reconstitution 3D des images confocales Z-stack pour IO@RB-HSA^{FITC} (gauche) et IO@RB-Dox-HSA (droite) de 30 nm à 0.8 μg Fe /mL

3 Optimisation de la morphologie des nanoparticules afin d'obtenir les meilleures propriétés théranostiques

Précédemment, nous avons démontré le potentiel des IO@RB-Dox-HSA NPs contenant un noyau d'IO d'environ 10 nm pour les applications théranostiques. En effet, ces nano-objets sont capables d'encapsuler une grande quantité de Dox dans les porosités de la coquille de silice (thérapie) et présentent également des propriétés de contraste T_2 prometteuses pour le diagnostic IRM. Cependant, des optimisations pourraient être apportées pour améliorer les propriétés théranostiques du système.

En effet, il est bien connu que la morphologie des pores de la silice mésoporeuse pourrait influencer le chargement des molécules (34, 47, 52, 156, 285). De plus, l'aimantation de saturation varie avec la taille des IO NPs et influence ainsi leur efficacité de contraste T_2 . En effet, plus la valeur d'aimantation à saturation est élevée et plus l'efficacité du contraste T_2 sera importante (286). Par ailleurs, des études ont montré que la taille moyenne optimale des IO NPs pour atteindre une valeur de pouvoir chauffant (SAR) élevée était d'environ 20 nm (4–6). Ainsi, l'augmentation de la taille du noyau d'IO à 20 nm devrait avoir un impact sur le contraste T_2 mais devrait également introduire une thérapie supplémentaire: l'hyperthermie magnétique.

De ce fait notre système cœur-coquille a été ajusté avec une taille de cœur d'IO de 20 nm et diverses morphologies de porosité de la coquille de silice (framboise RB et stellaire ST) conduisant à deux nouveaux types de NPs comme présenté dans la Figure 8-18. Enfin leurs capacités en tant qu'agents théranostiques ont été étudiées et comparées.

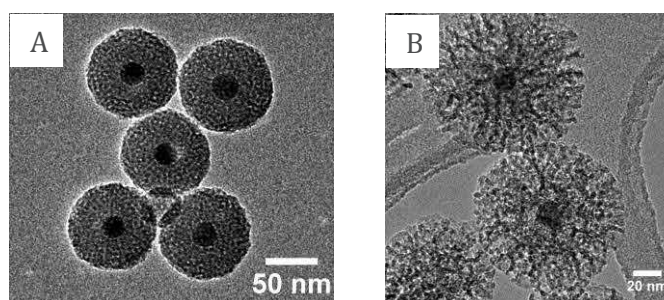


Figure 8-18: Deux types de structures cœur-coquille contenant un cœur IO de 20 nm et A) une coquille de silice type framboise RB et B) une coquille de silice type stellaire ST

3.1 IO@ST et IO@RB NPs comme agents de contrastes pour l'imagerie IRM

La Figure 8-19 montre les courbes de relaxation $1/T_1$ et $1/T_2$ en fonction de la concentration en fer [Fe] obtenues pour les nanoparticules IO@ST et IO@RB. On observe alors que IO@ST NPs présentent une valeur r_1 de $0.63 \text{ mM}^{-1}\cdot\text{s}^{-1}$ et une valeur r_2 de $177 \text{ mM}^{-1}\cdot\text{s}^{-1}$ donnant ainsi un rapport r_2/r_1 plus élevé de 281. Pour les NPs IO@RB, la valeur r_2 de $105 \text{ mM}^{-1}\cdot\text{s}^{-1}$ est du même ordre de grandeur que le r_2 mesuré pour IO@ST. Cependant, le r_1 est 10 fois plus faible avec une valeur de $0,04 \text{ mM}^{-1}\cdot\text{s}^{-1}$. Ceci a conduit à un rapport r_2/r_1 élevé de 2400. Cette forte diminution de r_1 pour les IO@RB NPs par rapport aux IO@ST NPs pourrait s'expliquer par la différence de porosité de la coquille de silice. En effet, les petites porosités limitent l'accessibilité de l'eau au noyau magnétique tandis que les grandes porosités laissent probablement circuler l'eau plus près du noyau magnétique à travers les canaux poreux stellaires.

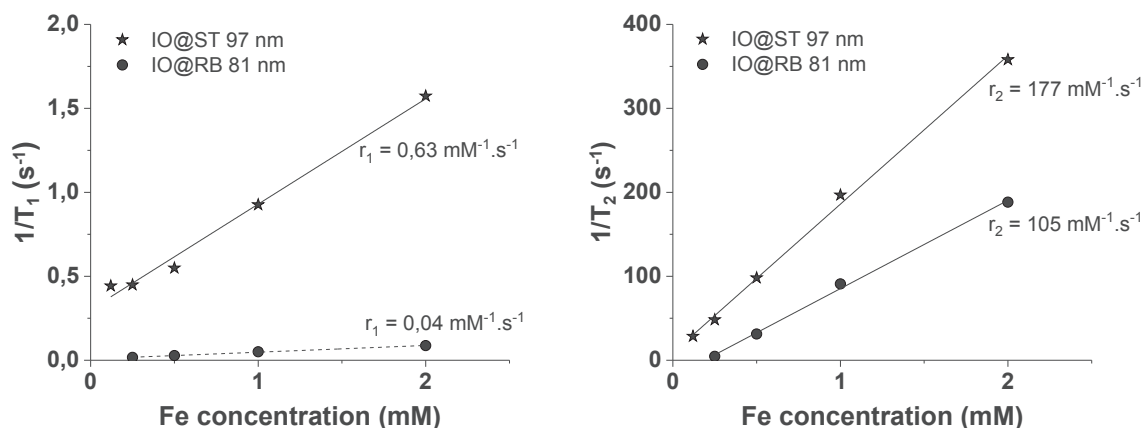


Figure 8-19: Courbes de relaxation A) $1/T_1$ and B) $1/T_2$ obtenues à 37 °C avec un Bruker Minispec réglé à 60 MHz (1.41 T) des IO@ST and IO@RB NPs en fonction de [Fe]

Des images de contraste T_2 sur les IO@RB et IO@ST NPs avant et après recouvrement avec la HSA, Figure 8-20, ont montré une amélioration du contraste sombre pour d'échantillons revêtus de HSA par rapport aux NPs nues correspondants. En effet, l'extinction complète du signal observée à partir de 1 Fe mM pour les NPs nues est déjà observé à 0,5 [Fe] mM pour les NPs revêtues d'HSA. En outre, pour les NPs brutes, un effet de contraste T_2 légèrement supérieur a été observé pour l'échantillon IO@ST par rapport à IO@RB (l'assombrissement étant un peu plus fort à 0,25 et 0,5 [Fe] mM) alors que pour les échantillons avec HSA correspondants cette tendance semble atténuée. Pour conclure, IO@RB et IO@ST revêtus ou non d'HSA présentent un contraste T_2 prometteur (meilleur pour les NPs avec HSA) et pourrait donc être utilisés comme agent de contraste négatif pour le diagnostic IRM.

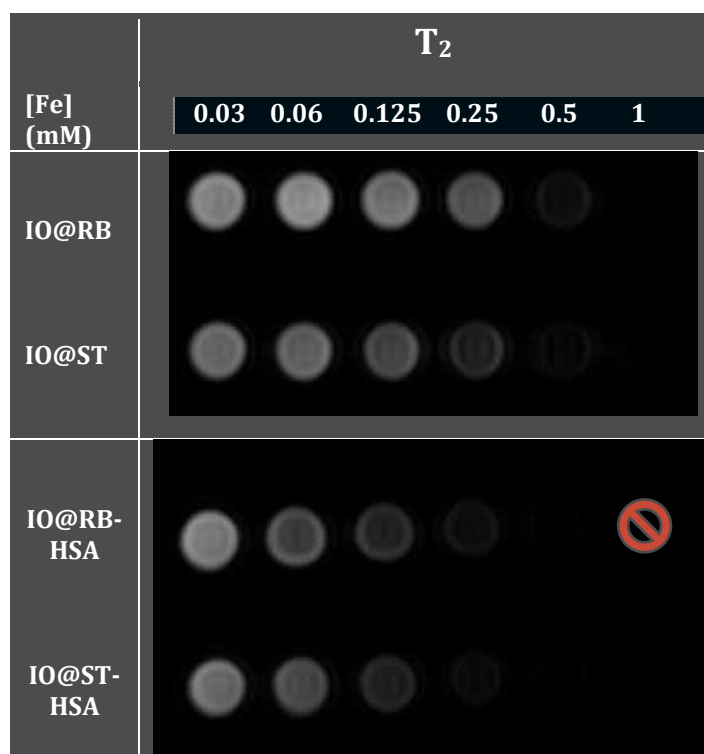


Figure 8-20: Images de résonance magnétique en T_2 (T_{2w} MR) des nanoparticules IO@RB et IO@ST NPs avec et sans revêtement HSA

3.2 IO@ST et IO@RB pour la thérapie cancéreuse

3.2.1 Par hyperthermie magnétique

Le design des IO NPs influence fortement leurs propriétés d'hyperthermie magnétique (122, 199, 287, 288). Selon des études récentes, des IO NPs superparamagnétiques d'environ 20 nm conviennent à la thérapie anticancéreuse par hyperthermie magnétique (4–6). Sur la base de ces observations, des travaux précédents au sein de l'équipe ont montré qu'une taille de 10 nm ne fournissait aucun chauffage, soit 0 W/g, alors qu'une taille de 20 nm conduisait à des valeurs SAR élevées d'environ 338 W/g à 571 kHz et 250 G.

Cependant, à notre connaissance, l'impact d'une coquille de silice mésoporeuse sur la puissance de chauffage des IO NPs a été peu étudié jusqu'à présent. Ainsi, nous avons réalisé une étude préliminaire de la capacité de chauffage d'IO@MS possédant un cœur d'IO d'environ 20 nm. La Figure 8-21 montre les valeurs de SAR obtenues à 796 Hz à des champs magnétiques de 100, 150 et 200 G pour des IO@ST 107 et 97 nm et IO@RB 75 nm, et pour les IO NPs seulement revêtues de CTAB de 18 nm. Au champ magnétique le plus bas, 100 G, les échantillons présentent toutes les valeurs SAR similaires autour de 75 W/g à l'exception des IO @ RB 75 nm NPs qui ont montré la valeur inférieure de 42 W/g. Puis, avec l'augmentation du champ magnétique, les valeurs de SAR des échantillons ont augmentés presque linéairement, comme le montrent les valeurs obtenues après les régressions linéaires résumées dans le Tableau 8-2. Nous avons pu noter que les pentes des régressions linéaires étaient plus élevées pour les deux échantillons IO@ST que pour les échantillons IO@RB et que les trois étaient plus élevés que les IO non revêtus de silice. Ainsi, ce comportement a conduit, pour le champ magnétique le plus élevé de 200 G, à des valeurs SAR plus élevées pour les échantillons de type cœur-coquille que pour les IO-CTAB NPs. En effet, des valeurs SAR de 334 W/g pour IO@ST 107 nm et de 277 W/g pour IO@ST 97 nm et IO@RB 75 nm ont été obtenues alors que l'échantillon IO-CTAB présentait une valeur SAR de 228 W/g. Cette augmentation du pouvoir chauffant des IO NPs après recouvrement par une coquille de silice a été également observé par Majeed *et al.*. Ils ont expliqué cette augmentation par le fait que le revêtement de silice aidait à empêcher l'agglomération IO NPs et préservait ainsi leur mouvement brownien qui contribue à la génération de chaleur (148).

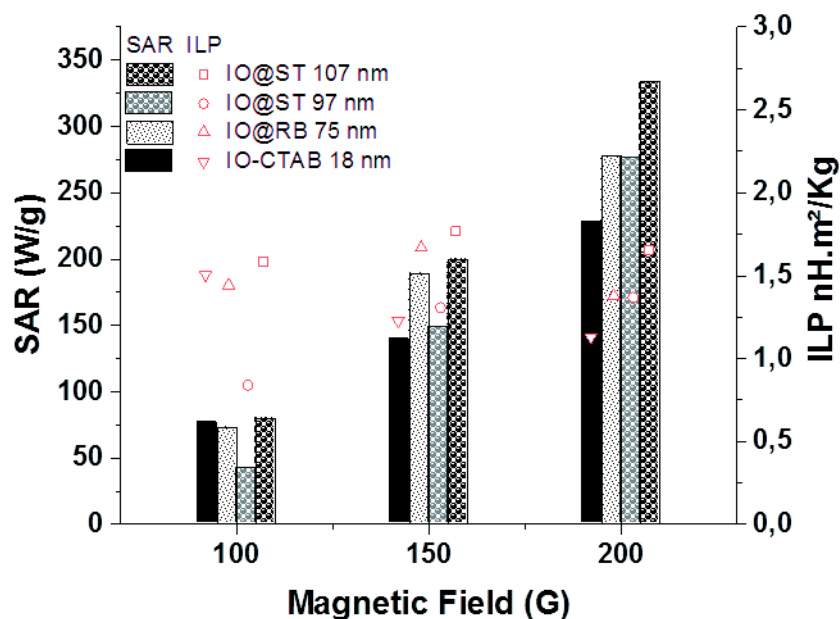


Figure 8-21: Valeurs des SAR et ILP obtenues pour des NPs IO@ST de 107 et 97 nm, IO@RB de 75 nm et IO-CTAB de 18 nm à une fréquence de 796 kHz et un champ magnétique variable: 200, 150 et 100 G

Tableau 8-2: Pentes et R^2 déduits des régressions linéaires pour les valeurs de SAR obtenues à une fréquence de 796 kHz et un champ magnétique variable (200, 150 et 100 G)

	Slope	R^2
IO@ST 107 nm	2.54	0.99899
IO@ST 97 nm	2.34	0.99706
IO@RB 75 nm	2.05	0.99425
IO-CTAB 18 nm	1.52	0.99082

3.2.2 Par chimio-thérapie

L'imprégnation en Dox a été réalisée sur les NPs silanisées: IO@RB-NH₂ et IO@ST-NH₂ 81 et 97 nm respectivement. Comme le montre les photographies en Figure 8-22, après imprégnation en Dox et redispersion des particules dans l'eau, les deux échantillons présentent une forte couleur rouge, ce qui prouve que le chargement en Dox a été efficace. Afin de quantifier la DLC de ces échantillons, des analyses TGA ont été réalisées. Les courbes résultantes, présentées en Figure 8-22, montrent clairement que la DLC est plus élevée pour l'échantillon IO@ST-Dox que pour IO@RB-Dox. L'analyse de ces courbes a donné des valeurs de DLC de 42,9% et 26,6% pour les échantillons IO@ST et IO@RB respectivement. Le potentiel zêta a également été mesuré à divers pH pour les deux échantillons. Les courbes résultantes, présentées en Figure 8-22, sont très similaires et présentent un point isoélectrique (PIE) à pH 8 après l'imprégnation en Dox.

Des études de libération de Dox à partir des nanoparticules IO@RB-Dox et IO@ST-Dox ont été réalisées. Comme le pH des endolysosomes est proche de 5 et que les NPs présentent des pouvoirs chauffants prometteurs par hyperthermie magnétique, la libération de Dox des IO@RB-Dox et IO@ST-Dox a été étudiée à pH 5 et 7,4 et à des températures de 37°C et 50°C pour étudier l'effet de chacun de ces facteurs sur la libération du médicament. La Figure 8-23 montre les courbes du pourcentage de Dox libérée dans le temps à différentes conditions de pH et de température pour les NPs IO@RB-Dox (A) et IO@ST-Dox (B). D'après les graphique le pH est la

condition ayant le plus d'influence sur la libération de Dox et ce pour les deux échantillons. En effet, à pH 5 la libération de Dox des de types de NPs est beaucoup plus effective qu'à pH 7. Ce comportement pourrait provenir du fait que, comme le montre les courbes de potentiel Zeta, les NPs étaient fortement chargées positivement à pH 5 créant probablement plus de répulsion électrostatique avec la Dox chargée également positivement ce qui améliore sa libération. Par ailleurs, l'augmentation de température 37°C à 50°C a également eu pour effet d'améliorer la libération de Dox. Ainsi, comme souhaité, l'effet combiné du pH et de la température a provoqué une plus grande libération de Dox que l'une ou l'autre des conditions seules, ce qui rend nos systèmes prometteurs en tant que cargo pour la délivrance contrôlée de médicaments par l'action combinée du pH et de la température.

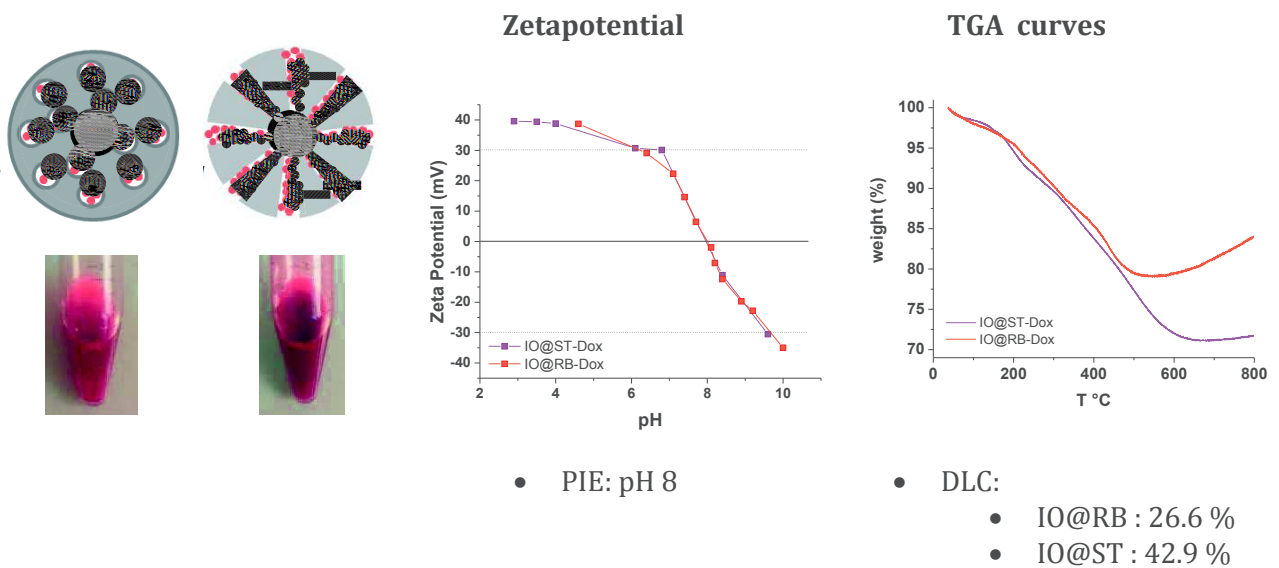


Figure 8-22: Photographies de Dox imprégnée dans IO@RB et IO@ST ainsi que les courbes de potentiel Zeta et ATG et les DLC résultantes des échantillons IO@RB-Dox et IO@ST-Dox

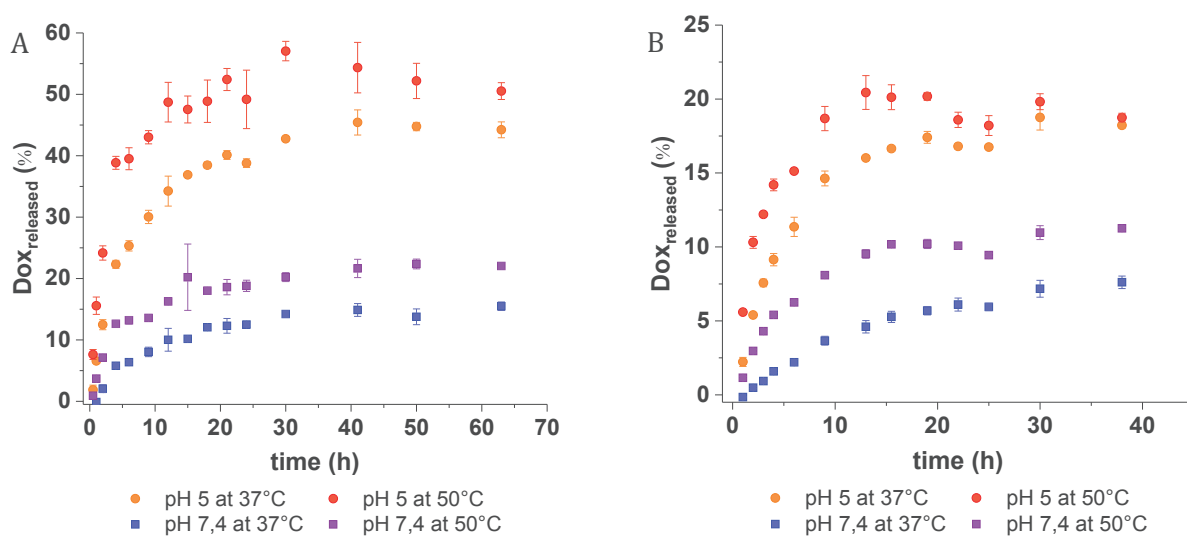


Figure 8-23: Dox release at pH 5 and 7.4 and at 37 and 50 °C from A) IO@RB-Dox NPs and B) IO@ST-Dox NPs

References

1. T. Lammers, S. Aime, W. E. Hennink, G. Storm, F. Kiessling, Theranostic Nanomedicine, *Acc. Chem. Res.* **44**, 1029–1038 (2011).
2. D.-E. Lee, H. Koo, I.-C. Sun, J. H. Ryu, K. Kim, I. C. Kwon, Multifunctional nanoparticles for multimodal imaging and theragnosis, *Chem Soc Rev* **41**, 2656–2672 (2012).
3. J. E. Lee, N. Lee, H. Kim, J. Kim, S. H. Choi, J. H. Kim, T. Kim, I. C. Song, S. P. Park, W. K. Moon, others, Uniform mesoporous dye-doped silica nanoparticles decorated with multiple magnetite nanocrystals for simultaneous enhanced magnetic resonance imaging, fluorescence imaging, and drug delivery, *J. Am. Chem. Soc.* **132**, 552–557 (2009).
4. J.-P. Fortin, C. Wilhelm, J. Servais, C. Ménager, J.-C. Bacri, F. Gazeau, Size-Sorted Anionic Iron Oxide Nanomagnets as Colloidal Mediators for Magnetic Hyperthermia, *J. Am. Chem. Soc.* **129**, 2628–2635 (2007).
5. M. Lévy, C. Wilhelm, J.-M. Siaugue, O. Horner, J.-C. Bacri, F. Gazeau, Magnetically induced hyperthermia: size-dependent heating power of γ -Fe₂O₃ nanoparticles, *J. Phys. Condens. Matter* **20**, 204133 (2008).
6. E. C. Vreeland, J. Watt, G. B. Schober, B. G. Hance, M. J. Austin, A. D. Price, B. D. Fellows, T. C. Monson, N. S. Hudak, L. Maldonado-Camargo, A. C. Bohorquez, C. Rinaldi, D. L. Huber, Enhanced Nanoparticle Size Control by Extending LaMer's Mechanism, *Chem. Mater.* **27**, 6059–6066 (2015).
7. C. T. Kresge, M. E. Leonowicz, W. J. Roth, J. C. Vartuli, J. S. Beck, Ordered mesoporous molecular sieves synthesized by a liquid-crystal template mechanism, *Nature* **359**, 710–712 (1992).
8. J. S. Beck, J. C. Vartuli, W. J. Roth, M. E. Leonowicz, C. T. Kresge, K. D. Schmitt, C. T. W. Chu, D. H. Olson, E. W. Sheppard, S. B. McCullen, others, A new family of mesoporous molecular sieves prepared with liquid crystal templates, *J. Am. Chem. Soc.* **114**, 10834–10843 (1992).
9. Composition of synthetic porous crystalline material, its synthesis (available at <http://www.google.com/patents/US5102643>).
10. Synthetic mesoporous crystalline material (available at <http://www.google.com/patents/US5098684>).
11. G. J. T. Tiddy, Surfactant-water liquid crystal phases, *Phys. Rep.* **57**, 1–46 (1980).
12. C. T. Kresge, W. J. Roth, The discovery of mesoporous molecular sieves from the twenty year perspective, *Chem. Soc. Rev.* **42**, 3663 (2013).
13. P. Selvam, S. K. Bhatia, C. G. Sonwane, Recent Advances in Processing and Characterization of Periodic Mesoporous MCM-41 Silicate Molecular Sieves, *Ind. Eng. Chem. Res.* **40**, 3237–3261 (2001).
14. S. Inagaki, Y. Fukushima, K. Kuroda, K. Kuroda, Adsorption Isotherm of Water Vapor and Its Large Hysteresis on Highly Ordered Mesoporous Silica, *J. Colloid Interface Sci.* **180**, 623–624 (1996).
15. Q. Huo, D. I. Margolese, U. Ciesla, P. Feng, T. E. Gier, P. Sieger, R. Leon, P. M. Petroff, F. Schüth, G. D. Stucky, Generalized synthesis of periodic surfactant/inorganic composite materials, *Nature* **368**, 317–321 (1994).

16. Q. Huo, R. Leon, P. M. Petroff, G. D. Stucky, Mesostructure Design with Gemini Surfactants: Supercage Formation in a Three-Dimensional Hexagonal Array, *Science* **268**, 1324–1327 (1995).
17. D. Zhao, Q. Huo, J. Feng, J. Kim, Y. Han, G. D. Stucky, Novel Mesoporous Silicates with Two-Dimensional Mesostructure Direction Using Rigid Bolaform Surfactants, *Chem. Mater.* **11**, 2668–2672 (1999).
18. D. Zhao, Q. Huo, J. Feng, B. F. Chmelka, G. D. Stucky, Nonionic Triblock and Star Diblock Copolymer and Oligomeric Surfactant Syntheses of Highly Ordered, Hydrothermally Stable, Mesoporous Silica Structures, *J. Am. Chem. Soc.* **120**, 6024–6036 (1998).
19. Lukens Wayne W., P. Schmidt-Winkel, D. Zhao, J. Feng, G. D. Stucky, Evaluating Pore Sizes in Mesoporous Materials: A Simplified Standard Adsorption Method and a Simplified Broekhoff–de Boer Method, *Langmuir* **15**, 5403–5409 (1999).
20. S. Inagaki, S. Guan, Y. Fukushima, T. Ohsuna, O. Terasaki, Novel Mesoporous Materials with a Uniform Distribution of Organic Groups and Inorganic Oxide in Their Frameworks, *J. Am. Chem. Soc.* **121**, 9611–9614 (1999).
21. S. A. Bagshaw, E. Prouzet, T. J. Pinnavaia, Templating of Mesoporous Molecular Sieves by Nonionic Polyethylene Oxide Surfactants, *Science* **269**, 1242–1244 (1995).
22. E. Prouzet, F. Cot, G. Nabias, A. Larbot, P. Kooyman, T. J. Pinnavaia, Assembly of Mesoporous Silica Molecular Sieves Based on Nonionic Ethoxylated Sorbitan Esters as Structure Directors, *Chem. Mater.* **11**, 1498–1503 (1999).
23. P. T. Tanev, Y. Liang, T. J. Pinnavaia, Assembly of Mesoporous Lamellar Silicas with Hierarchical Particle Architectures, *J. Am. Chem. Soc.* **119**, 8616–8624 (1997).
24. S. S. Kim, W. Zhang, T. J. Pinnavaia, Ultrastable Mesostructured Silica Vesicles, *Science* **282**, 1302–1305 (1998).
25. W. Zhang, T. R. Pauly, T. J. Pinnavaia, Tailoring the Framework and Textural Mesopores of HMS Molecular Sieves through an Electrically Neutral (S⁰I⁰) Assembly Pathway, *Chem. Mater.* **9**, 2491–2498 (1997).
26. R. Ryoo, J. M. Kim, C. H. Ko, C. H. Shin, Disordered Molecular Sieve with Branched Mesoporous Channel Network, *J. Phys. Chem.* **100**, 17718–17721 (1996).
27. R. Ryoo, C. H. Ko, I.-S. Park, Synthesis of highly ordered MCM-41 by micelle-packing control with mixed surfactants, *Chem. Commun.* , 1413–1414 (1999).
28. T. Kimura, Y. Sugahara, K. Kuroda, K. Kuroda, Synthesis of mesoporous aluminophosphates using surfactants with long alkyl chain lengths and triisopropylbenzene as a solubilizing agent, *Chem. Commun.* , 559–560 (1998).
29. W. Stöber, A. Fink, E. Bohn, Controlled growth of monodisperse silica spheres in the micron size range, *J. Colloid Interface Sci.* **26**, 62–69 (1968).
30. M. Grün, I. Lauer, K. K. Unger, The synthesis of micrometer- and submicrometer-size spheres of ordered mesoporous oxide MCM-41, *Adv. Mater.* **9**, 254–257 (1997).
31. Q. Cai, Z.-S. Luo, W.-Q. Pang, Y.-W. Fan, X.-H. Chen, F.-Z. Cui, Dilute Solution Routes to Various Controllable Morphologies of MCM-41 Silica with a Basic Medium, *Chem. Mater.* **13**, 258–263 (2001).

32. C. E. Fowler, D. Khushalani, B. Lebeau, S. Mann, Nanoscale Materials with Mesostructured Interiors, *Adv. Mater.* **13**, 649–652 (2001).
33. R. I. Nooney, D. Thirunavukkarasu, Y. Chen, R. Josephs, A. E. Ostafin, Synthesis of Nanoscale Mesoporous Silica Spheres with Controlled Particle Size, *Chem. Mater.* **14**, 4721–4728 (2002).
34. N. Ž. Knežević, J.-O. Durand, Large pore mesoporous silica nanomaterials for application in delivery of biomolecules, *Nanoscale* **7**, 2199–2209 (2015).
35. H. Zhang, Z. Li, P. Xu, R. Wu, Z. Jiao, A facile two step synthesis of novel chrysanthemum-like mesoporous silica nanoparticles for controlled pyrene release, *Chem. Commun.* **46**, 6783–6785 (2010).
36. X. Du, J. He, Fine-Tuning of Silica Nanosphere Structure by Simple Regulation of the Volume Ratio of Cosolvents, *Langmuir* **26**, 10057–10062 (2010).
37. L. Wu, Z. Jiao, M. Wu, T. Song, H. Zhang, Formation of mesoporous silica nanoparticles with tunable pore structure as promising nanoreactor and drug delivery vehicle, *RSC Adv.* **6**, 13303–13311 (2016).
38. A. B. D. Nandiyanto, S.-G. Kim, F. Iskandar, K. Okuyama, Synthesis of spherical mesoporous silica nanoparticles with nanometer-size controllable pores and outer diameters, *Microporous Mesoporous Mater.* **120**, 447–453 (2009).
39. J.-Y. Liu, J.-G. Wang, N. Li, H. Zhao, H.-J. Zhou, P.-C. Sun, T.-H. Chen, Polyelectrolyte–Surfactant Complex as a Template for the Synthesis of Zeolites with Intracrystalline Mesopores, *Langmuir* **28**, 8600–8607 (2012).
40. J.-G. Wang, H.-J. Zhou, P.-C. Sun, D.-T. Ding, T.-H. Chen, Hollow Carved Single-Crystal Mesoporous Silica Templated by Mesomorphous Polyelectrolyte–Surfactant Complexes, *Chem. Mater.* **22**, 3829–3831 (2010).
41. K. Zhang, L.-L. Xu, J.-G. Jiang, N. Calin, K.-F. Lam, S.-J. Zhang, H.-H. Wu, G.-D. Wu, B. Albela, L. Bonneviot, P. Wu, Facile Large-Scale Synthesis of Monodisperse Mesoporous Silica Nanospheres with Tunable Pore Structure, *J. Am. Chem. Soc.* **135**, 2427–2430 (2013).
42. X. Lv, L. Zhang, F. Xing, H. Lin, Controlled synthesis of monodispersed mesoporous silica nanoparticles: Particle size tuning and formation mechanism investigation, *Microporous Mesoporous Mater.* **225**, 238–244 (2016).
43. Y.-J. Yu, J.-L. Xing, J.-L. Pang, S.-H. Jiang, K.-F. Lam, T.-Q. Yang, Q.-S. Xue, K. Zhang, P. Wu, Facile Synthesis of Size Controllable Dendritic Mesoporous Silica Nanoparticles, *ACS Appl. Mater. Interfaces* **6**, 22655–22665 (2014).
44. Y. Wang, Y. A. Nor, H. Song, Y. Yang, C. Xu, M. Yu, C. Yu, Small-sized and large-pore dendritic mesoporous silica nanoparticles enhance antimicrobial enzyme delivery, *J. Mater. Chem. B* **4**, 2646–2653 (2016).
45. M. Vallet-Regi, A. Rámila, R. P. del Real, J. Pérez-Pariente, A New Property of MCM-41: Drug Delivery System, *Chem. Mater.* **13**, 308–311 (2001).
46. Y. Wang, Q. Zhao, N. Han, L. Bai, J. Li, J. Liu, E. Che, L. Hu, Q. Zhang, T. Jiang, S. Wang, Mesoporous silica nanoparticles in drug delivery and biomedical applications, *Nanomedicine Nanotechnol. Biol. Med.* **11**, 313–327 (2015).

47. M. Vallet-Regí, F. Balas, D. Arcos, Mesoporous Materials for Drug Delivery, *Angew. Chem. Int. Ed.* **46**, 7548–7558 (2007).
48. I. I. Slowing, B. G. Trewyn, S. Giri, V. S.-Y. Lin, Mesoporous Silica Nanoparticles for Drug Delivery and Biosensing Applications, *Adv. Funct. Mater.* **17**, 1225–1236 (2007).
49. Z. Li, J. C. Barnes, A. Bosoy, J. F. Stoddart, J. I. Zink, Mesoporous silica nanoparticles in biomedical applications, *Chem. Soc. Rev.* **41**, 2590 (2012).
50. S. Angelos, Y.-W. Yang, N. M. Khashab, J. F. Stoddart, J. I. Zink, Dual-Controlled Nanoparticles Exhibiting AND Logic, *J. Am. Chem. Soc.* **131**, 11344–11346 (2009).
51. D. Tarn, C. E. Ashley, M. Xue, E. C. Carnes, J. I. Zink, C. J. Brinker, Mesoporous Silica Nanoparticle Nanocarriers: Biofunctionality and Biocompatibility, *Acc. Chem. Res.* **46**, 792–801 (2013).
52. P. Horcajada, A. Rámila, J. Pérez-Pariente, M. Vallet-Regí, Influence of pore size of MCM-41 matrices on drug delivery rate, *Microporous Mesoporous Mater.* **68**, 105–109 (2004).
53. S. Kapoor, R. Hegde, A. J. Bhattacharyya, Influence of surface chemistry of mesoporous alumina with wide pore distribution on controlled drug release, *J. Controlled Release* **140**, 34–39 (2009).
54. T. Ukmar, U. Maver, O. Planinšek, V. Kaučič, M. Gaberšček, A. Godec, Understanding controlled drug release from mesoporous silicates: Theory and experiment, *J. Controlled Release* **155**, 409–417 (2011).
55. G. Sahay, D. Y. Alakhova, A. V. Kabanov, Endocytosis of nanomedicines, *J. Controlled Release* **145**, 182–195 (2010).
56. I. Canton, G. Battaglia, Endocytosis at the nanoscale, *Chem. Soc. Rev.* **41**, 2718 (2012).
57. S. Bonacchi, D. Genovese, R. Juris, M. Montalti, L. Prodi, E. Rampazzo, N. Zaccheroni, Luminescent Silica Nanoparticles: Extending the Frontiers of Brightness, *Angew. Chem. Int. Ed.* **50**, 4056–4066 (2011).
58. C.-P. Tsai, Y. Hung, Y.-H. Chou, D.-M. Huang, J.-K. Hsiao, C. Chang, Y.-C. Chen, C.-Y. Mou, High-Contrast Paramagnetic Fluorescent Mesoporous Silica Nanorods as a Multifunctional Cell-Imaging Probe, *Small* **4**, 186–191 (2008).
59. H. Chen, Z. Zhen, W. Tang, T. Todd, Y.-J. Chuang, L. Wang, Z. Pan, J. Xie, Label-Free Luminescent Mesoporous Silica Nanoparticles for Imaging and Drug Delivery, *Theranostics* **3**, 650–657 (2013).
60. M. W. Ambrogio, C. R. Thomas, Y.-L. Zhao, J. I. Zink, J. F. Stoddart, Mechanized Silica Nanoparticles: A New Frontier in Theranostic Nanomedicine, *Acc. Chem. Res.* **44**, 903–913 (2011).
61. R. M. Cornell, U. Schwertmann, *The iron oxides: structure, properties, reactions, occurrence, and uses* (Weinheim ; New York : VCH, 1996; <http://trove.nla.gov.au/version/46513978>).
62. W. Wu, Z. Wu, T. Yu, C. Jiang, W.-S. Kim, Recent progress on magnetic iron oxide nanoparticles: synthesis, surface functional strategies and biomedical applications, *Sci. Technol. Adv. Mater.* **16**, 023501 (2015).

63. M. Mahmoudi, S. Sant, B. Wang, S. Laurent, T. Sen, Superparamagnetic iron oxide nanoparticles (SPIONs): Development, surface modification and applications in chemotherapy, *Adv. Drug Deliv. Rev.* **63**, 24–46 (2011).
64. R. Massart, Preparation of aqueous magnetic liquids in alkaline and acidic media, *IEEE Trans. Magn.* **17**, 1247–1248 (1981).
65. T. Sugimoto, E. Matijević, Formation of uniform spherical magnetite particles by crystallization from ferrous hydroxide gels, *J. Colloid Interface Sci.* **74**, 227–243 (1980).
66. T. Sen, S. Magdassi, G. Nizri, I. J. Bruce, Dispersion of magnetic nanoparticles in suspension, *IET Micro Nano Lett.* **1**, 39–42 (2006).
67. O. Karaagac, H. Kockar, T. Tanrisever, Properties of Iron Oxide Nanoparticles Synthesized at Different Temperatures, *J. Supercond. Nov. Magn.* **24**, 675–678 (2010).
68. O. Karaagac, H. Kockar, Effect of Synthesis Parameters on the Properties of Superparamagnetic Iron Oxide Nanoparticles, *J. Supercond. Nov. Magn.* **25**, 2777–2781 (2011).
69. L. Babes, B. Denizot, G. Tanguy, J. J. Le Jeune, P. Jallet, Synthesis of Iron Oxide Nanoparticles Used as MRI Contrast Agents: A Parametric Study, *J. Colloid Interface Sci.* **212**, 474–482 (1999).
70. C. Pereira, A. M. Pereira, C. Fernandes, M. Rocha, R. Mendes, M. P. Fernández-García, A. Guedes, P. B. Tavares, J.-M. Grenèche, J. P. Araújo, C. Freire, Superparamagnetic MFe₂O₄ (M = Fe, Co, Mn) Nanoparticles: Tuning the Particle Size and Magnetic Properties through a Novel One-Step Coprecipitation Route, *Chem. Mater.* **24**, 1496–1504 (2012).
71. J.-P. Jolivet, C. Froidefond, A. Pottier, C. Chanéac, S. Cassaignon, E. Tronc, P. Euzen, Size tailoring of oxide nanoparticles by precipitation in aqueous medium. A semi-quantitative modelling, *J. Mater. Chem.* **14**, 3281–3288 (2004).
72. N. M. Griбанov, E. E. Bibik, O. V. Buzunov, V. N. Naumov, Physico-chemical regularities of obtaining highly dispersed magnetite by the method of chemical condensation, *J. Magn. Mater.* **85**, 7–10 (1990).
73. S. Ge, X. Shi, K. Sun, C. Li, C. Uher, J. R. Baker, M. M. Banaszak Holl, B. G. Orr, Facile Hydrothermal Synthesis of Iron Oxide Nanoparticles with Tunable Magnetic Properties, *J. Phys. Chem. C* **113**, 13593–13599 (2009).
74. J. Wang, J. Sun, Q. Sun, Q. Chen, One-step hydrothermal process to prepare highly crystalline Fe₃O₄ nanoparticles with improved magnetic properties, *Mater. Res. Bull.* **38**, 1113–1118 (2003).
75. M.-T. Liang, S.-H. Wang, Y.-L. Chang, H.-I. Hsiang, H.-J. Huang, M.-H. Tsai, W.-C. Juan, S.-F. Lu, Iron oxide synthesis using a continuous hydrothermal and solvothermal system, *Ceram. Int.* **36**, 1131–1135 (2010).
76. Z. Jing, S. Wu, Synthesis and characterization of monodisperse hematite nanoparticles modified by surfactants via hydrothermal approach, *Mater. Lett.* **58**, 3637–3640 (2004).
77. Z. Jing, S. Wu, S. Zhang, W. Huang, Hydrothermal fabrication of various morphological α -Fe₂O₃ nanoparticles modified by surfactants, *Mater. Res. Bull.* **39**, 2057–2064 (2004).

78. S. Giri, S. Samanta, S. Maji, S. Ganguli, A. Bhaumik, Magnetic properties of α -Fe₂O₃ nanoparticle synthesized by a new hydrothermal method, *J. Magn. Magn. Mater.* **285**, 296–302 (2005).
79. Y. Zheng, Y. Cheng, F. Bao, Y. Wang, Synthesis and magnetic properties of Fe₃O₄ nanoparticles, *Mater. Res. Bull.* **41**, 525–529 (2006).
80. S. Takami, T. Sato, T. Mousavand, S. Ohara, M. Umetsu, T. Adschiri, Hydrothermal synthesis of surface-modified iron oxide nanoparticles, *Mater. Lett.* **61**, 4769–4772 (2007).
81. X. Liu, G. Qiu, A. Yan, Z. Wang, X. Li, Hydrothermal synthesis and characterization of α -FeOOH and α -Fe₂O₃ uniform nanocrystallines, *J. Alloys Compd.* **433**, 216–220 (2007).
82. C. Xu, A. S. Teja, Continuous hydrothermal synthesis of iron oxide and PVA-protected iron oxide nanoparticles, *J. Supercrit. Fluids* **44**, 85–91 (2008).
83. Y. B. Kholam, S. R. Dhage, H. S. Potdar, S. B. Deshpande, P. P. Bakare, S. D. Kulkarni, S. K. Date, Microwave hydrothermal preparation of submicron-sized spherical magnetite (Fe₃O₄) powders, *Mater. Lett.* **56**, 571–577 (2002).
84. T. J. Daou, G. Pourroy, S. Bégin-Colin, J. M. Grenèche, C. Ulhaq-Bouillet, P. Legaré, P. Bernhardt, C. Leuvrey, G. Rogez, Hydrothermal Synthesis of Monodisperse Magnetite Nanoparticles, *Chem. Mater.* **18**, 4399–4404 (2006).
85. C. Okoli, M. Sanchez-Dominguez, M. Boutonnet, S. Järås, C. Civera, C. Solans, G. R. Kuttuva, Comparison and Functionalization Study of Microemulsion-Prepared Magnetic Iron Oxide Nanoparticles, *Langmuir* **28**, 8479–8485 (2012).
86. D. Langevin, Micelles and Microemulsions, *Annu. Rev. Phys. Chem.* **43**, 341–369 (1992).
87. C. Solans, P. Izquierdo, J. Nolla, N. Azemar, M. J. Garcia-Celma, Nano-emulsions, *Curr. Opin. Colloid Interface Sci.* **10**, 102–110 (2005).
88. M. A. Malik, M. Y. Wani, M. A. Hashim, Microemulsion method: A novel route to synthesize organic and inorganic nanomaterials: 1st Nano Update, *Arab. J. Chem.* **5**, 397–417 (2012).
89. S. Santra, R. Tapeç, N. Theodoropoulou, J. Dobson, A. Hebard, W. Tan, Synthesis and Characterization of Silica-Coated Iron Oxide Nanoparticles in Microemulsion: The Effect of Nonionic Surfactants, *Langmuir* **17**, 2900–2906 (2001).
90. L.-H. Han, H. Liu, Y. Wei, In situ synthesis of hematite nanoparticles using a low-temperature microemulsion method, *Powder Technol.* **207**, 42–46 (2011).
91. C. Okoli, M. Boutonnet, L. Mariey, S. Järås, G. Rajarao, Application of magnetic iron oxide nanoparticles prepared from microemulsions for protein purification, *J. Chem. Technol. Biotechnol.* **86**, 1386–1393 (2011).
92. M. Darbandi, F. Stromberg, J. Landers, N. Reckers, B. Sanyal, W. Keune, Heiko Wende, Nanoscale size effect on surface spin canting in iron oxide nanoparticles synthesized by the microemulsion method, *J. Phys. Appl. Phys.* **45**, 195001 (2012).
93. C. B. Murray, D. J. Norris, M. G. Bawendi, Synthesis and characterization of nearly monodisperse CdE (E = sulfur, selenium, tellurium) semiconductor nanocrystallites, *J. Am. Chem. Soc.* **115**, 8706–8715 (1993).

94. X. Peng, J. Wickham, A. P. Alivisatos, Kinetics of II-VI and III-V Colloidal Semiconductor Nanocrystal Growth: "Focusing" of Size Distributions, *J. Am. Chem. Soc.* **120**, 5343–5344 (1998).
95. S. Sun, C. B. Murray, Synthesis of monodisperse cobalt nanocrystals and their assembly into magnetic superlattices (invited), *J. Appl. Phys.* **85**, 4325–4330 (1999).
96. S. O'Brien, L. Brus, C. B. Murray, Synthesis of Monodisperse Nanoparticles of Barium Titanate: Toward a Generalized Strategy of Oxide Nanoparticle Synthesis, *J. Am. Chem. Soc.* **123**, 12085–12086 (2001).
97. V. Biju, T. Itoh, A. Anas, A. Sujith, M. Ishikawa, Semiconductor quantum dots and metal nanoparticles: syntheses, optical properties, and biological applications, *Anal. Bioanal. Chem.* **391**, 2469–2495 (2008).
98. J. Rockenberger, E. C. Scher, A. P. Alivisatos, A New Nonhydrolytic Single-Precursor Approach to Surfactant-Capped Nanocrystals of Transition Metal Oxides, *J. Am. Chem. Soc.* **121**, 11595–11596 (1999).
99. A.-H. Lu, E. L. Salabas, F. Schüth, Magnetic Nanoparticles: Synthesis, Protection, Functionalization, and Application, *Angew. Chem. Int. Ed.* **46**, 1222–1244 (2007).
100. L. Zhang, R. He, H.-C. Gu, Oleic acid coating on the monodisperse magnetite nanoparticles, *Appl. Surf. Sci.* **253**, 2611–2617 (2006).
101. T. K. Jain, S. P. Foy, B. Erokwu, S. Dimitrijevic, C. A. Flask, V. Labhasetwar, Magnetic resonance imaging of multifunctional pluronic stabilized iron-oxide nanoparticles in tumor-bearing mice, *Biomaterials* **30**, 6748–6756 (2009).
102. L. Shen, P. E. Laibinis, T. A. Hatton, Bilayer Surfactant Stabilized Magnetic Fluids: Synthesis and Interactions at Interfaces, *Langmuir* **15**, 447–453 (1999).
103. R. De Palma, S. Peeters, M. J. Van Bael, H. Van den Rul, K. Bonroy, W. Laureyn, J. Mullens, G. Borghs, G. Maes, Silane Ligand Exchange to Make Hydrophobic Superparamagnetic Nanoparticles Water-Dispersible, *Chem. Mater.* **19**, 1821–1831 (2007).
104. H. B. Na, I. C. Song, T. Hyeon, Inorganic Nanoparticles for MRI Contrast Agents, *Adv. Mater.* **21**, 2133–2148 (2009).
105. C. Rügenapp, B. Gleich, A. Haase, Magnetic Nanoparticles in Magnetic Resonance Imaging and Diagnostics, *Pharm. Res.* **29**, 1165–1179 (2012).
106. P. Sharma, S. Brown, G. Walter, S. Santra, B. Moudgil, Nanoparticles for bioimaging, *Adv. Colloid Interface Sci.* **123–126**, 471–485 (2006).
107. Y. Jun, J. Choi, J. Cheon, Heterostructured magnetic nanoparticles: their versatility and high performance capabilities, *Chem. Commun.* , 1203–1214 (2007).
108. M. Hofmann-Antenbrink, H. Hofmann, X. Montet, Superparamagnetic nanoparticles - a tool for early diagnostics, *Swiss Med. Wkly.* (2010), doi:10.4414/smw.2010.13081.
109. R. A. Heesakkers, G. J. Jager, A. M. Hövels, B. de Hoop, H. C. van den Bosch, F. Raat, J. A. Witjes, P. F. Mulders, C. H. van der Kaa, J. O. Barentsz, Prostate Cancer: Detection of Lymph Node Metastases Outside the Routine Surgical Area with Ferumoxtran-10-enhanced MR Imaging 1, *Radiology* **251**, 408–414 (2009).

110. European Medicines Agency - - Sinerem (available at http://www.ema.europa.eu/ema/index.jsp?curl=pages/medicines/human/medicines/000801/wapp/Initial_authorisation/human_wapp_000064.jsp).
111. K. M. Hasebroock, N. J. Serkova, Toxicity of MRI and CT contrast agents, *Expert Opin. Drug Metab. Toxicol.* **5**, 403–416 (2009).
112. M. Rogosnitzky, S. Branch, Gadolinium-based contrast agent toxicity: a review of known and proposed mechanisms, *BioMetals* **29**, 365–376 (2016).
113. J. Ramalho, R. C. Semelka, M. Ramalho, R. H. Nunes, M. AlObaidy, M. Castillo, Gadolinium-Based Contrast Agent Accumulation and Toxicity: An Update, *Am. J. Neuroradiol.* **37**, 1192–1198 (2016).
114. C. W. Jung, P. Jacobs, Physical and chemical properties of superparamagnetic iron oxide MR contrast agents: Ferumoxides, ferumoxtran, ferumoxsil, *Magn. Reson. Imaging* **13**, 661–674 (1995).
115. F. Ye, S. Laurent, A. Fornara, L. Astolfi, J. Qin, A. Roch, A. Martini, M. S. Toprak, R. N. Muller, M. Muhammed, Uniform mesoporous silica coated iron oxide nanoparticles as a highly efficient, nontoxic MRI T2 contrast agent with tunable proton relaxivities: Fe₃O₄@mSiO₂ WITH TUNABLE RELAXIVITIES, *Contrast Media Mol. Imaging* **7**, 460–468 (2012).
116. Y.-X. J. Wang, Superparamagnetic iron oxide based MRI contrast agents: Current status of clinical application, *Quant. Imaging Med. Surg.* **1**, 35–40 (2011).
117. S. Laurent, D. Forge, M. Port, A. Roch, C. Robic, L. Vander Elst, R. N. Muller, Magnetic Iron Oxide Nanoparticles: Synthesis, Stabilization, Vectorization, Physicochemical Characterizations, and Biological Applications, *Chem. Rev.* **108**, 2064–2110 (2008).
118. M. De, S. S. Chou, H. M. Joshi, V. P. Dravid, Hybrid magnetic nanostructures (MNS) for magnetic resonance imaging applications, *Adv. Drug Deliv. Rev.* **63**, 1282–1299 (2011).
119. P. Reimer, T. Balzer, Ferucarbotran (Resovist): a new clinically approved RES-specific contrast agent for contrast-enhanced MRI of the liver: properties, clinical development, and applications, *Eur. Radiol.* **13**, 1266–1276.
120. Y.-X. J. Wang, S. M. Hussain, G. P. Krestin, Superparamagnetic iron oxide contrast agents: physicochemical characteristics and applications in MR imaging, *Eur. Radiol.* **11**, 2319–2331 (2001).
121. H. M. Joshi, Multifunctional metal ferrite nanoparticles for MR imaging applications, *J. Nanoparticle Res.* **15**, 1235 (2012).
122. C. Blanco-Andujar, A. Walter, G. Cotin, C. Bordeianu, D. Mertz, D. Felder-Flesch, S. Begin-Colin, Design of iron oxide-based nanoparticles for MRI and magnetic hyperthermia, *Nanomed.* **11**, 1889–1910 (2016).
123. Y. Jun, Y.-M. Huh, J. Choi, J.-H. Lee, H.-T. Song, KimKim, S. Yoon, K.-S. Kim, J.-S. Shin, J.-S. Suh, J. Cheon, Nanoscale Size Effect of Magnetic Nanocrystals and Their Utilization for Cancer Diagnosis via Magnetic Resonance Imaging, *J. Am. Chem. Soc.* **127**, 5732–5733 (2005).
124. L. E. W. LaConte, N. Nitin, O. Zurkiya, D. Caruntu, C. J. O'Connor, X. Hu, G. Bao, Coating thickness of magnetic iron oxide nanoparticles affects R2 relaxivity, *J. Magn. Reson. Imaging* **26**, 1634–1641 (2007).

125. F. Hajesmaeelzadeh, S. Shanehsazzadeh, C. Grüttner, F. J. Daha, M. A. Oghabian, Effect of coating thickness of iron oxide nanoparticles on their relaxivity in the MRI, *Iran. J. Basic Med. Sci.* **19**, 166–171 (2016).
126. H. Duan, M. Kuang, X. Wang, Y. A. Wang, H. Mao, S. Nie, Reexamining the Effects of Particle Size and Surface Chemistry on the Magnetic Properties of Iron Oxide Nanocrystals: New Insights into Spin Disorder and Proton Relaxivity, *J. Phys. Chem. C* **112**, 8127–8131 (2008).
127. F. Hu, K. W. MacRenaris, E. A. Waters, T. Liang, E. A. Schultz-Sikma, A. L. Eckermann, T. J. Meade, Ultrasmall, Water-Soluble Magnetite Nanoparticles with High Relaxivity for Magnetic Resonance Imaging, *J. Phys. Chem. C* **113**, 20855–20860 (2009).
128. P.-E. L. Renard, F. Buchegger, A. Petri-Fink, F. Bosman, D. Rüfenacht, H. Hofmann, E. Doelker, O. Jordan, Local moderate magnetically induced hyperthermia using an implant formed in situ in a mouse tumor model, *Int. J. Hyperthermia* **25**, 229–239 (2009).
129. K. Maier-Hauff, R. Rothe, R. Scholz, U. Gneveckow, P. Wust, B. Thiesen, A. Feussner, A. von Deimling, N. Waldoefner, R. Felix, A. Jordan, Intracranial Thermotherapy using Magnetic Nanoparticles Combined with External Beam Radiotherapy: Results of a Feasibility Study on Patients with Glioblastoma Multiforme, *J. Neurooncol.* **81**, 53–60 (2007).
130. K. Maier-Hauff, F. Ulrich, D. Nestler, H. Niehoff, P. Wust, B. Thiesen, H. Orawa, V. Budach, A. Jordan, Efficacy and safety of intratumoral thermotherapy using magnetic iron-oxide nanoparticles combined with external beam radiotherapy on patients with recurrent glioblastoma multiforme, *J. Neurooncol.* **103**, 317–324 (2011).
131. MagForce AG – Home (available at <http://www.magforce.de/en/home.html>).
132. K. Maier-Hauff, R. Rothe, R. Scholz, U. Gneveckow, P. Wust, B. Thiesen, A. Feussner, A. von Deimling, N. Waldoefner, R. Felix, A. Jordan, Intracranial Thermotherapy using Magnetic Nanoparticles Combined with External Beam Radiotherapy: Results of a Feasibility Study on Patients with Glioblastoma Multiforme, *J. Neurooncol.* **81**, 53–60 (2007).
133. G. Szakács, J. K. Paterson, J. A. Ludwig, C. Booth-Genthe, M. M. Gottesman, Targeting multidrug resistance in cancer, *Nat. Rev. Drug Discov.* **5**, 219–234 (2006).
134. H. Fan, K. Yang, D. M. Boye, T. Sigmon, K. J. Malloy, H. Xu, G. P. López, C. J. Brinker, Self-Assembly of Ordered, Robust, Three-Dimensional Gold Nanocrystal/Silica Arrays, *Science* **304**, 567–571 (2004).
135. H. Fan, E. W. Leve, C. Scullin, J. Gabaldon, D. Tallant, S. Bunge, T. Boyle, M. C. Wilson, C. J. Brinker, Surfactant-Assisted Synthesis of Water-Soluble and Biocompatible Semiconductor Quantum Dot Micelles, *Nano Lett.* **5**, 645–648 (2005).
136. H. Fan, E. Leve, J. Gabaldon, A. Wright, R. E. Haddad, C. J. Brinker, Ordered Two- and Three-Dimensional Arrays Self-Assembled from Water-Soluble Nanocrystal-Micelles, *Adv. Mater.* **17**, 2587–2590 (2005).
137. Fan, Z. Chen, C. J. Brinker, J. Clawson, T. Alam, Synthesis of Organo-Silane Functionalized Nanocrystal Micelles and Their Self-Assembly, *J. Am. Chem. Soc.* **127**, 13746–13747 (2005).
138. H. Fan, A. Wright, J. Gabaldon, A. Rodriguez, C. J. Brinker, Y.-B. Jiang, Three-Dimensionally Ordered Gold Nanocrystal/Silica Superlattice Thin Films Synthesized via Sol–Gel Self-Assembly, *Adv. Funct. Mater.* **16**, 891–895 (2006).

139. L. Zhang, S. Qiao, Y. Jin, H. Yang, S. Budihartono, F. Stahr, Z. Yan, X. Wang, Z. Hao, G. Q. Lu, Fabrication and Size-Selective Bioseparation of Magnetic Silica Nanospheres with Highly Ordered Periodic Mesostructure, *Adv. Funct. Mater.* **18**, 3203–3212 (2008).
140. T. Suteewong, H. Sai, J. Lee, M. Bradbury, T. Hyeon, S. M. Gruner, U. Wiesner, Ordered mesoporous silica nanoparticles with and without embedded iron oxide nanoparticles: structure evolution during synthesis, *J. Mater. Chem.* **20**, 7807 (2010).
141. J. Kim, H. S. Kim, N. Lee, T. Kim, H. Kim, T. Yu, I. C. Song, W. K. Moon, T. Hyeon, Multifunctional Uniform Nanoparticles Composed of a Magnetite Nanocrystal Core and a Mesoporous Silica Shell for Magnetic Resonance and Fluorescence Imaging and for Drug Delivery, *Angew. Chem. Int. Ed.* **47**, 8438–8441 (2008).
142. S. L. C. Pinho, G. A. Pereira, P. Voisin, J. Kassem, V. Bouchaud, L. Etienne, J. A. Peters, L. Carlos, S. Mornet, C. F. G. C. Geraldès, J. Rocha, M.-H. Delville, Fine Tuning of the Relaxometry of γ -Fe₂O₃@SiO₂ Nanoparticles by Tweaking the Silica Coating Thickness, *ACS Nano* **4**, 5339–5349 (2010).
143. S. L. C. Pinho, S. Laurent, J. Rocha, A. Roch, M.-H. Delville, S. Mornet, L. D. Carlos, L. Vander Elst, R. N. Muller, C. F. G. C. Geraldès, Relaxometric Studies of γ -Fe₂O₃@SiO₂ Core Shell Nanoparticles: When the Coating Matters, *J. Phys. Chem. C* **116**, 2285–2291 (2012).
144. T. Ahmad, H. Bae, I. Rhee, Y. Chang, J. Lee, S. Hong, Particle size dependence of relaxivity for silica-coated iron oxide nanoparticles, *Curr. Appl. Phys.* **12**, 969–974 (2012).
145. C. Zhang, B. Wängler, B. Morgenstern, H. Zentgraf, M. Eisenhut, H. Untenecker, R. Krüger, R. Huss, C. Seliger, W. Semmler, F. Kiessling, Silica- and Alkoxysilane-Coated Ultrasmall Superparamagnetic Iron Oxide Particles: A Promising Tool To Label Cells for Magnetic Resonance Imaging, *Langmuir* **23**, 1427–1434 (2007).
146. K. C. Souza, N. D. S. Mohallem, E. M. B. Sousa, Mesoporous silica-magnetite nanocomposite: facile synthesis route for application in hyperthermia, *J. Sol-Gel Sci. Technol.* **53**, 418–427 (2010).
147. F. M. Martín-Saavedra, E. Ruíz-Hernández, A. Boré, D. Arcos, M. Vallet-Regí, N. Vilaboa, Magnetic mesoporous silica spheres for hyperthermia therapy, *Acta Biomater.* **6**, 4522–4531 (2010).
148. J. Majeed, L. Pradhan, R. S. Ningthoujam, R. K. Vatsa, D. Bahadur, A. K. Tyagi, Enhanced specific absorption rate in silanol functionalized Fe₃O₄ core-shell nanoparticles: Study of Fe leaching in Fe₃O₄ and hyperthermia in L929 and HeLa cells, *Colloids Surf. B Biointerfaces* **122**, 396–403 (2014).
149. W. Guo, C. Yang, H. Lin, F. Qu, P(EO-co-LLA) functionalized Fe₃O₄@mSiO₂ nanocomposites for thermo/pH responsive drug controlled release and hyperthermia, *Dalton Trans.* **43**, 18056–18065 (2014).
150. Y. Xu, Y. Zhu, S. Kaskel, A smart magnetic nanosystem with controllable drug release and hyperthermia for potential cancer therapy, *RSC Adv.* **5**, 99875–99883 (2015).
151. X. Yu, Y. Zhu, Preparation of magnetic mesoporous silica nanoparticles as a multifunctional platform for potential drug delivery and hyperthermia, *Sci. Technol. Adv. Mater.* **17**, 229–238 (2016).
152. C. Tao, Y. Zhu, Magnetic mesoporous silica nanoparticles for potential delivery of chemotherapeutic drugs and hyperthermia, *Dalton Trans.* **43**, 15482–15490 (2014).

153. C. Yang, W. Guo, L. Cui, N. An, T. Zhang, G. Guo, H. Lin, F. Qu, Fe₃O₄@mSiO₂ core-shell nanocomposite capped with disulfide gatekeepers for enzyme-sensitive controlled release of anti-cancer drugs, *J. Mater. Chem. B* **3**, 1010–1019 (2015).
154. C. Yang, W. Guo, N. An, L. Cui, T. Zhang, R. Tong, Y. Chen, H. Lin, F. Qu, Enzyme-sensitive magnetic core-shell nanocomposites for triggered drug release, *RSC Adv.* **5**, 80728–80738 (2015).
155. F. Balas, M. Manzano, P. Horcajada, M. Vallet-Regí, Confinement and Controlled Release of Bisphosphonates on Ordered Mesoporous Silica-Based Materials, *J. Am. Chem. Soc.* **128**, 8116–8117 (2006).
156. M. Manzano, V. Aina, C. O. Areán, F. Balas, V. Cauda, M. Colilla, M. R. Delgado, M. Vallet-Regí, Studies on MCM-41 mesoporous silica for drug delivery: Effect of particle morphology and amine functionalization, *Chem. Eng. J.* **137**, 30–37 (2008).
157. B. Chang, X. Sha, J. Guo, Y. Jiao, C. Wang, W. Yang, Thermo and pH dual responsive, polymer shell coated, magnetic mesoporous silica nanoparticles for controlled drug release, *J. Mater. Chem.* **21**, 9239 (2011).
158. L.-B. Chen, F. Zhang, C.-C. Wang, Rational Synthesis of Magnetic Thermosensitive Microcontainers as Targeting Drug Carriers, *Small* **5**, 621–628 (2009).
159. S. Li, Y. Ma, X. Yue, Z. Cao, Z. Dai, One-pot construction of doxorubicin conjugated magnetic silica nanoparticles, *New J. Chem.* **33**, 2414 (2009).
160. J. E. Lee, D. J. Lee, N. Lee, B. H. Kim, S. H. Choi, T. Hyeon, Multifunctional mesoporous silica nanocomposite nanoparticles for pH controlled drug release and dual modal imaging, *J. Mater. Chem.* **21**, 16869 (2011).
161. J. Liu, C. Detrembleur, M.-C. De Pauw-Gillet, S. Mornet, L. V. Elst, S. Laurent, C. Jérôme, E. Duguet, Heat-triggered drug release systems based on mesoporous silica nanoparticles filled with a maghemite core and phase-change molecules as gatekeepers, *J Mater Chem B* **2**, 59–70 (2014).
162. Y. Zhu, C. Tao, DNA-capped Fe₃O₄/SiO₂ magnetic mesoporous silica nanoparticles for potential controlled drug release and hyperthermia, *RSC Adv.* **5**, 22365–22372 (2015).
163. F. Kratz, Albumin as a drug carrier: Design of prodrugs, drug conjugates and nanoparticles, *J. Controlled Release* **132**, 171–183 (2008).
164. B. Elsadek, F. Kratz, Impact of albumin on drug delivery — New applications on the horizon, *J. Controlled Release* **157**, 4–28 (2012).
165. D. Mertz, P. Tan, Y. Wang, T. K. Goh, A. Blencowe, F. Caruso, Bromoisobutyramide as an Intermolecular Surface Binder for the Preparation of Free-standing Biopolymer Assemblies, *Adv. Mater.* **23**, 5668–5673 (2011).
166. D. Mertz, J. Cui, Y. Yan, G. Devlin, C. Chaubaroux, A. Dochter, R. Alles, P. Lavalle, J. C. Voegel, A. Blencowe, P. Auffinger, F. Caruso, Protein Capsules Assembled *via* Isobutyramide Grafts: Sequential Growth, Biofunctionalization, and Cellular Uptake, *ACS Nano* **6**, 7584–7594 (2012).
167. D. Mertz, H. Wu, J. S. Wong, J. Cui, P. Tan, R. Alles, F. Caruso, Ultrathin, bioresponsive and drug-functionalized protein capsules, *J. Mater. Chem.* **22**, 21434 (2012).

168. K. S. W. Sing, Reporting physisorption data for gas/solid systems with special reference to the determination of surface area and porosity (Recommendations 1984), *Pure Appl. Chem.* **57**, 603–619 (1985).
169. M. Thommes, K. Kaneko, A. V. Neimark, J. P. Olivier, F. Rodriguez-Reinoso, J. Rouquerol, K. S. W. Sing, Physisorption of gases, with special reference to the evaluation of surface area and pore size distribution (IUPAC Technical Report), *Pure Appl. Chem.* **87** (2015), doi:10.1515/pac-2014-1117.
170. E. P. Barrett, L. G. Joyner, P. P. Halenda, others, The determination of pore volume and area distributions in porous substances. I. Computations from nitrogen isotherms, *J Am Chem Soc* **73**, 373–380 (1951).
171. C. Henoumont, S. Laurent, L. Vander Elst, How to perform accurate and reliable measurements of longitudinal and transverse relaxation times of MRI contrast media in aqueous solutions, *Contrast Media Mol. Imaging* **4**, 312–321 (2009).
172. S. Boutry, D. Forge, C. Burtea, I. Mahieu, O. Murariu, S. Laurent, L. Vander Elst, R. N. Muller, How to quantify iron in an aqueous or biological matrix: a technical note, *Contrast Media Mol. Imaging* **4**, 299–304 (2009).
173. D. J. Giard, S. A. Aaronson, G. J. Todaro, P. Arnstein, J. H. Kersey, H. Dosik, W. P. Parks, In Vitro Cultivation of Human Tumors: Establishment of Cell Lines Derived From a Series of Solid Tumors, *J. Natl. Cancer Inst.* **51**, 1417–1423 (1973).
174. M. Lieber, G. Todaro, B. Smith, A. Szakal, W. Nelson-Rees, A continuous tumor-cell line from a human lung carcinoma with properties of type II alveolar epithelial cells, *Int. J. Cancer* **17**, 62–70 (1976).
175. R. Brown, U. Boger-Brown, *Methods in Molecular Medicine. Vol 28: Cytotoxic Drug Resistance Mechanism* (Totowa, NJ: Humana Press, 1999).
176. G. Hamilton, Multicellular spheroids as an in vitro tumor model, *Cancer Lett.* **131**, 29–34 (1998).
177. L. A. Kunz-Schughart, Multicellular tumor spheroids: intermediates between monolayer culture and in vivo tumor, *Cell Biol. Int.* **23**, 157–161 (1999).
178. R.-Z. Lin, H.-Y. Chang, Recent advances in three-dimensional multicellular spheroid culture for biomedical research, *Biotechnol. J.* **3**, 1172–1184 (2008).
179. F. Hirschhaeuser, H. Menne, C. Dittfeld, J. West, W. Mueller-Klieser, L. A. Kunz-Schughart, Multicellular tumor spheroids: An underestimated tool is catching up again, *J. Biotechnol.* **148**, 3–15 (2010).
180. D. W. Hutmacher, Biomaterials offer cancer research the third dimension, *Nat. Mater.* **9**, 90–93 (2010).
181. G. Mehta, A. Y. Hsiao, M. Ingram, G. D. Luker, S. Takayama, Opportunities and challenges for use of tumor spheroids as models to test drug delivery and efficacy, *J. Controlled Release* **164**, 192–204 (2012).
182. K. A. Fitzgerald, M. Malhotra, C. M. Curtin, F. J. O' Brien, C. M. O' Driscoll, Life in 3D is never flat: 3D models to optimise drug delivery, *J. Controlled Release* **215**, 39–54 (2015).

183. W. Asghar, R. El Assal, H. Shafiee, S. Pitteri, R. Paulmurugan, U. Demirci, Engineering cancer microenvironments for in vitro 3-D tumor models, *Mater. Today* **18**, 539–553 (2015).
184. T. Jacks, R. A. Weinberg, Taking the Study of Cancer Cell Survival to a New Dimension, *Cell* **111**, 923–925 (2002).
185. N. E. Timmins, L. K. Nielsen, Generation of multicellular tumor spheroids by the hanging-drop method, *Tissue Eng.*, 141–151 (2007).
186. W. Baaziz, B. P. Pichon, S. Fleutot, Y. Liu, C. Lefevre, J.-M. Greneche, M. Toumi, T. Mhiri, S. Bégin-Colin, Magnetic Iron Oxide Nanoparticles: Reproducible Tuning of the Size and Nanosized-Dependent Composition, Defects, and Spin Canting, *J. Phys. Chem. C* **118**, 3795–3810 (2014).
187. D. Mertz, C. Affolter-Zbaraszczuk, J. Barthès, J. Cui, F. Caruso, T. F. Baumert, J.-C. Voegel, J. Ogier, F. Meyer, Templated assembly of albumin-based nanoparticles for simultaneous gene silencing and magnetic resonance imaging, *Nanoscale* **6**, 11676–11680 (2014).
188. X.-Y. Wang, D. Mertz, C. Blanco-Andujar, A. Bora, M. Ménard, F. Meyer, C. Giraudeau, S. Bégin-Colin, Optimizing the silanization of thermally-decomposed iron oxide nanoparticles for efficient aqueous phase transfer and MRI applications, *RSC Adv.* **6**, 93784–93793 (2016).
189. N. Lee, T. Hyeon, Designed synthesis of uniformly sized iron oxide nanoparticles for efficient magnetic resonance imaging contrast agents, *Chem Soc Rev* **41**, 2575–2589 (2012).
190. I. Hilger, W. A. Kaiser, Iron oxide-based nanostructures for MRI and magnetic hyperthermia, *Nanomed.* **7**, 1443–1459 (2012).
191. J. Lodhia, G. Mandarano, N. Ferris, P. Eu, S. Cowell, Development and use of iron oxide nanoparticles (Part 1): Synthesis of iron oxide nanoparticles for MRI, *Biomed. Imaging Interv. J.* **6** (2010), doi:10.2349/bijj.6.2.e12.
192. A. Hervault, N. T. Kim Thanh, Magnetic nanoparticle-based therapeutic agents for thermo-chemotherapy treatment of cancer, *Nanoscale* **6**, 11553–11573 (2014).
193. C. S. S. R. Kumar, F. Mohammad, Magnetic nanomaterials for hyperthermia-based therapy and controlled drug delivery, *Adv. Drug Deliv. Rev.* **63**, 789–808 (2011).
194. S. Laurent, S. Dutz, U. O. Häfeli, M. Mahmoudi, Magnetic fluid hyperthermia: Focus on superparamagnetic iron oxide nanoparticles, *Adv. Colloid Interface Sci.* **166**, 8–23 (2011).
195. F. M. Kievit, M. Zhang, Surface engineering of iron oxide nanoparticles for targeted cancer therapy, *Acc. Chem. Res.* **44**, 853–862 (2011).
196. P. Guardia, R. Di Corato, L. Lartigue, C. Wilhelm, A. Espinosa, M. Garcia-Hernandez, F. Gazeau, L. Manna, T. Pellegrino, Water-Soluble Iron Oxide Nanocubes with High Values of Specific Absorption Rate for Cancer Cell Hyperthermia Treatment, *ACS Nano* **6**, 3080–3091 (2012).
197. R. Hachani, M. Lowdell, M. Birchall, A. Hervault, D. Mertz, S. Bégin-Colin, N. T. K. Thanh, Polyol synthesis, functionalisation, and biocompatibility studies of superparamagnetic iron oxide nanoparticles as potential MRI contrast agents, *Nanoscale* **8**, 3278–3287 (2016).
198. S. Sun, H. Zeng, Size-Controlled Synthesis of Magnetite Nanoparticles, *J. Am. Chem. Soc.* **124**, 8204–8205 (2002).

199. A. Walter, C. Billotey, A. Garofalo, C. Ulhaq-Bouillet, C. Lefèvre, J. Taleb, S. Laurent, L. Vander Elst, R. N. Muller, L. Lartigue, F. Gazeau, D. Felder-Flesch, S. Begin-Colin, Mastering the Shape and Composition of Dendronized Iron Oxide Nanoparticles To Tailor Magnetic Resonance Imaging and Hyperthermia, *Chem. Mater.* **26**, 5252–5264 (2014).
200. A. Ruiz, P. C. Morais, R. B. de Azevedo, Z. G. M. Lacava, A. Villanueva, M. del P. Morales, Magnetic nanoparticles coated with dimercaptosuccinic acid: development, characterization, and application in biomedicine, *J. Nanoparticle Res.* **16**, 2589 (2014).
201. G. Salas, C. Casado, F. J. Teran, R. Miranda, C. J. Serna, M. P. Morales, Controlled synthesis of uniform magnetite nanocrystals with high-quality properties for biomedical applications, *J. Mater. Chem.* **22**, 21065–21075 (2012).
202. C. Boyer, V. Bulmus, P. Priyanto, W. Y. Teoh, R. Amal, T. P. Davis, The stabilization and bio-functionalization of iron oxide nanoparticles using heterotelechelic polymers, *J. Mater. Chem.* **19**, 111–123 (2008).
203. T. J. Daou, J. M. Grenèche, G. Pourroy, S. Buathong, A. Derory, C. Ulhaq-Bouillet, B. Donnio, D. Guillon, S. Begin-Colin, Coupling Agent Effect on Magnetic Properties of Functionalized Magnetite-Based Nanoparticles, *Chem. Mater.* **20**, 5869–5875 (2008).
204. T. J. Daou, G. Pourroy, J. M. Greneche, A. Bertin, D. Felder-Flesch, S. Begin-Colin, Water soluble dendronized iron oxide nanoparticles, *Dalton Trans.* , 4442–4449 (2009).
205. V. Torrisi, A. Graillot, L. Vitorazi, Q. Crouzet, G. Marletta, C. Loubat, J.-F. Berret, Preventing Corona Effects: Multiphosponic Acid Poly(ethylene glycol) Copolymers for Stable Stealth Iron Oxide Nanoparticles, *Biomacromolecules* **15**, 3171–3179 (2014).
206. I. J. Bruce, T. Sen, Surface Modification of Magnetic Nanoparticles with Alkoxysilanes and Their Application in Magnetic Bioseparations, *Langmuir* **21**, 7029–7035 (2005).
207. Y. Liu, Y. Li, X.-M. Li, T. He, Kinetics of (3-Aminopropyl)triethoxysilane (APTES) Silanization of Superparamagnetic Iron Oxide Nanoparticles, *Langmuir* **29**, 15275–15282 (2013).
208. M. Yamaura, R. L. Camilo, L. C. Sampaio, M. A. Macêdo, M. Nakamura, H. E. Toma, Preparation and characterization of (3-aminopropyl)triethoxysilane-coated magnetite nanoparticles, *J. Magn. Magn. Mater.* **279**, 210–217 (2004).
209. M. Zhu, M. Z. Lerum, W. Chen, How To Prepare Reproducible, Homogeneous, and Hydrolytically Stable Aminosilane-Derived Layers on Silica, *Langmuir* **28**, 416–423 (2012).
210. R. G. Acres, A. V. Ellis, J. Alvino, C. E. Lenahan, D. A. Khodakov, G. F. Metha, G. G. Andersson, Molecular Structure of 3-Aminopropyltriethoxysilane Layers Formed on Silanol-Terminated Silicon Surfaces, *J. Phys. Chem. C* **116**, 6289–6297 (2012).
211. S. Guha Thakurta, A. Subramanian, Fabrication of dense, uniform aminosilane monolayers: A platform for protein or ligand immobilization, *Colloids Surf. Physicochem. Eng. Asp.* **414**, 384–392 (2012).
212. M. Bloemen, W. Brullot, T. T. Luong, N. Geukens, A. Gils, T. Verbiest, Improved functionalization of oleic acid-coated iron oxide nanoparticles for biomedical applications, *J. Nanoparticle Res.* **14**, 1100 (2012).
213. A. Walter, A. Parat, A. Garofalo, S. Laurent, L. V. Elst, R. N. Muller, T. Wu, E. Heuillard, E. Robinet, F. Meyer, D. Felder-Flesch, S. Begin-Colin, Modulation of Relaxivity, Suspension Stability,

and Biodistribution of Dendronized Iron Oxide Nanoparticles as a Function of the Organic Shell Design, *Part. Part. Syst. Charact.* **32**, 552–560 (2015).

214. A. Walter, A. Garofalo, A. Parat, J. Jouhannaud, G. Pourroy, E. Voirin, S. Laurent, P. Bonazza, J. Taleb, C. Billotey, L. V. Elst, R. N. Muller, S. Begin-Colin, D. Felder-Flesch, Validation of a dendron concept to tune colloidal stability, MRI relaxivity and bioelimination of functional nanoparticles, *J. Mater. Chem. B* **3**, 1484–1494 (2015).

215. N. Rathor, S. Panda, Aminosilane densities on nanotextured silicon, *Mater. Sci. Eng. C* **29**, 2340–2345 (2009).

216. J. Zhao, Y. Li, H. Guo, L. Gao, Relative Surface Density and Stability of the Amines on the Biochip, *Chin. J. Anal. Chem.* **34**, 1235–1238 (2006).

217. J.-L. Bridot, D. Stanicki, S. Laurent, S. Boutry, Y. Gossuin, P. Leclère, R. Lazzaroni, L. Vander Elst, R. N. Muller, New carboxysilane-coated iron oxide nanoparticles for nonspecific cell labelling, *Contrast Media Mol. Imaging* **8**, 466–474 (2013).

218. D. Stanicki, S. Boutry, S. Laurent, L. Wacheul, E. Nicolas, D. Crombez, L. V. Elst, D. L. J. Lafontaine, R. N. Muller, Carboxy-silane coated iron oxide nanoparticles: a convenient platform for cellular and small animal imaging, *J. Mater. Chem. B* **2**, 387–397 (2013).

219. N. Reinhardt, L. Adumeau, O. Lambert, S. Ravaine, S. Mornet, Quaternary Ammonium Groups Exposed at the Surface of Silica Nanoparticles Suitable for DNA Complexation in the Presence of Cationic Lipids, *J. Phys. Chem. B* **119**, 6401–6411 (2015).

220. Z. Sun, V. Yathindranath, M. Worden, J. Thliveris, S. Chu, F. Parkinson, T. Hegmann, D. Miller, Characterization of Cellular Uptake and Toxicity of Aminosilane-Coated Iron Oxide Nanoparticles with Different Charges in Central Nervous System-Relevant Cell Culture Models, *Int. J. Nanomedicine*, 961–970 (2013).

221. M. Shen, H. Cai, X. Wang, X. Cao, K. Li, S. H. Wang, R. Guo, L. Zheng, Guixiang Zhang, X. Shi, Facile one-pot preparation, surface functionalization, and toxicity assay of APTS-coated iron oxide nanoparticles, *Nanotechnology* **23**, 105601 (2012).

222. M. Gonzales, L. M. Mitsumori, J. V. Kushleika, M. E. Rosenfeld, K. M. Krishnan, Cytotoxicity of iron oxide nanoparticles made from the thermal decomposition of organometallics and aqueous phase transfer with Pluronic F127, *Contrast Media Mol. Imaging* **5**, 286–293 (2010).

223. D. Maity, S. N. Kale, R. Kaul-Ghanekar, J.-M. Xue, J. Ding, Studies of magnetite nanoparticles synthesized by thermal decomposition of iron (III) acetylacetonate in tri(ethylene glycol), *J. Magn. Magn. Mater.* **321**, 3093–3098 (2009).

224. L. Rochette, C. Guenancia, A. Gudjoncik, O. Hachet, M. Zeller, Y. Cottin, C. Vergely, Anthracyclines/trastuzumab: new aspects of cardiotoxicity and molecular mechanisms, *Trends Pharmacol. Sci.* **36**, 326–348 (2015).

225. K. Ylänen, T. Poutanen, P. Savikurki-Heikkilä, I. Rinta-Kiikka, A. Eerola, K. Vettenranta, Cardiac Magnetic Resonance Imaging in the Evaluation of the Late Effects of Anthracyclines Among Long-Term Survivors of Childhood Cancer, *J. Am. Coll. Cardiol.* **61**, 1539–1547 (2013).

226. C. Elalouani, M. A. Benhmidoun, H. Rida, M. AitRaiss, N. Derhem, A. Elomrani, M. Khouchani, A. Tahri, A. Errehmouni, R. Faouzi, A. Elguenzri, M. Elhattaoui, I. Tazi, L. Mahmal, Cardiotoxicité à court et à moyen terme des anthracyclines : étude prospective, *Ann. Cardiol. Angéiologie* **61**, 257–266 (2012).

227. M. Cruz, J. Duarte-Rodrigues, M. Campelo, Cardiotoxicity in anthracycline therapy: Prevention strategies, *Rev. Port. Cardiol. Engl. Ed.* **35**, 359–371 (2016).
228. Á. Ancochea, A. Salar, F. García-Pallarols, E. Gimeno, C. Fernández-Rodriguez, B. Sánchez-González, Prognostic impact of anthracyclines in the treatment of aggressive lymphoma in patients over 70 years, *Med. Clínica Engl. Ed.* **144**, 544–547 (2015).
229. E. Cabane, X. Zhang, K. Langowska, C. G. Palivan, W. Meier, Stimuli-Responsive Polymers and Their Applications in Nanomedicine, *Biointerphases* **7**, 9 (2012).
230. C. I. C. Crucho, Stimuli-Responsive Polymeric Nanoparticles for Nanomedicine, *ChemMedChem* **10**, 24–38 (2015).
231. J. Liu, Z. Luo, J. Zhang, T. Luo, J. Zhou, X. Zhao, K. Cai, Hollow mesoporous silica nanoparticles facilitated drug delivery via cascade pH stimuli in tumor microenvironment for tumor therapy, *Biomaterials* **83**, 51–65 (2016).
232. L. Chen, Z. Zhang, X. Yao, X. Chen, X. Chen, Intracellular pH-operated mechanized mesoporous silica nanoparticles as potential drug carries, *Microporous Mesoporous Mater.* **201**, 169–175 (2015).
233. Z. Luo, Y. Hu, K. Cai, X. Ding, Q. Zhang, M. Li, X. Ma, B. Zhang, Y. Zeng, P. Li, J. Li, J. Liu, Y. Zhao, Intracellular redox-activated anticancer drug delivery by functionalized hollow mesoporous silica nanoreservoirs with tumor specificity, *Biomaterials* **35**, 7951–7962 (2014).
234. S. Mornet, S. Vasseur, F. Grasset, E. Duguet, Magnetic nanoparticle design for medical diagnosis and therapy, *J. Mater. Chem.* **14**, 2161–2175 (2004).
235. G. Kong, G. Anyarambhatla, W. P. Petros, R. D. Braun, O. M. Colvin, D. Needham, M. W. Dewhirst, Efficacy of Liposomes and Hyperthermia in a Human Tumor Xenograft Model: Importance of Triggered Drug Release, *Cancer Res.* **60**, 6950–6957 (2000).
236. J. Vandooren, G. Opdenakker, P. M. Loadman, D. R. Edwards, Proteases in cancer drug delivery, *Adv. Drug Deliv. Rev.* **97**, 144–155 (2016).
237. K. Patel, S. Angelos, W. R. Dichtel, A. Coskun, Y.-W. Yang, J. I. Zink, J. F. Stoddart, Enzyme-Responsive Snap-Top Covered Silica Nanocontainers, *J. Am. Chem. Soc.* **130**, 2382–2383 (2008).
238. H. He, L. Sun, J. Ye, E. Liu, S. Chen, Q. Liang, M. C. Shin, V. C. Yang, Enzyme-triggered, cell penetrating peptide-mediated delivery of anti-tumor agents, *J. Controlled Release* **240**, 67–76 (2016).
239. L. Palanikumar, E. S. Choi, J. Y. Cheon, S. H. Joo, J.-H. Ryu, Noncovalent Polymer-Gatekeeper in Mesoporous Silica Nanoparticles as a Targeted Drug Delivery Platform, *Adv. Funct. Mater.* **25**, 957–965 (2015).
240. K. Langer, M. G. Anhorn, I. Steinhauser, S. Dreis, D. Celebi, N. Schrickel, S. Faust, V. Vogel, Human serum albumin (HSA) nanoparticles: Reproducibility of preparation process and kinetics of enzymatic degradation, *Int. J. Pharm.* **347**, 109–117 (2008).
241. Y. Matsumura, H. Maeda, A New Concept for Macromolecular Therapeutics in Cancer Chemotherapy: Mechanism of Tumor-tropic Accumulation of Proteins and the Antitumor Agent Smancs, *Cancer Res.* **46**, 6387–6392 (1986).

242. C. Weber, C. Coester, J. Kreuter, K. Langer, Desolvation process and surface characterisation of protein nanoparticles, *Int. J. Pharm.* **194**, 91–102 (2000).
243. K. Langer, S. Balthasar, V. Vogel, N. Dinauer, H. von Briesen, D. Schubert, Optimization of the preparation process for human serum albumin (HSA) nanoparticles, *Int. J. Pharm.* **257**, 169–180 (2003).
244. H. Wartlick, B. Spänkuch-Schmitt, K. Strebhardt, J. Kreuter, K. Langer, Tumour cell delivery of antisense oligonucleotides by human serum albumin nanoparticles, *J. Controlled Release* **96**, 483–495 (2004).
245. A. O. Elzoghby, W. M. Samy, N. A. Elgindy, Albumin-based nanoparticles as potential controlled release drug delivery systems, *J. Controlled Release* **157**, 168–182 (2012).
246. S. Dreis, F. Rothweiler, M. Michaelis, J. Cinatl Jr., J. Kreuter, K. Langer, Preparation, characterisation and maintenance of drug efficacy of doxorubicin-loaded human serum albumin (HSA) nanoparticles, *Int. J. Pharm.* **341**, 207–214 (2007).
247. E. Zeiger, B. Gollapudi, P. Spencer, Genetic toxicity and carcinogenicity studies of glutaraldehyde—a review, *Mutat. Res. Mutat. Res.* **589**, 136–151 (2005).
248. W. Fürst, A. Banerjee, Release of Glutaraldehyde From an Albumin-Glutaraldehyde Tissue Adhesive Causes Significant In Vitro and In Vivo Toxicity, *Ann. Thorac. Surg.* **79**, 1522–1528 (2005).
249. G. Speit, S. Neuss, P. Schütz, M. Fröhler-Keller, O. Schmid, The genotoxic potential of glutaraldehyde in mammalian cells in vitro in comparison with formaldehyde, *Mutat. Res. Toxicol. Environ. Mutagen.* **649**, 146–154 (2008).
250. S. Wang, Ordered mesoporous materials for drug delivery, *Microporous Mesoporous Mater.* **117**, 1–9 (2009).
251. P. Yang, S. Gai, J. Lin, Functionalized mesoporous silica materials for controlled drug delivery, *Chem. Soc. Rev.* **41**, 3679 (2012).
252. M. Kruger, U. Beyer, P. Schumacher, C. Unger, H. Zahn, F. Kartz, Synthesis and Stability of Four Maleimide Derivatives of the Anticancer Drug Doxorubicin for the Preparation of Chemoimmunoconjugates, *Chem. Pharm. Bull. (Tokyo)* **45**, 399–401 (1997).
253. F. Kratz, R. Müller-Driver, I. Hofmann, J. Drevs, C. Unger, A Novel Macromolecular Prodrug Concept Exploiting Endogenous Serum Albumin as a Drug Carrier for Cancer Chemotherapy, *J. Med. Chem.* **43**, 1253–1256 (2000).
254. F. Kratz, A. Warnecke, K. Scheuermann, C. Stockmar, J. Schwab, P. Lazar, P. Drückes, N. Esser, J. Drevs, D. Rognan, C. Bissantz, C. Hinderling, G. Folkers, I. Fichtner, C. Unger, Probing the Cysteine-34 Position of Endogenous Serum Albumin with Thiol-Binding Doxorubicin Derivatives. Improved Efficacy of an Acid-Sensitive Doxorubicin Derivative with Specific Albumin-Binding Properties Compared to That of the Parent Compound, *J. Med. Chem.* **45**, 5523–5533 (2002).
255. D. Willner, P. A. Trail, S. J. Hofstead, H. D. King, S. J. Lasch, G. R. Braslawsky, R. S. Greenfield, T. Kaneko, R. A. Firestone, (6-Maleimidocaproyl) hydrazone of doxorubicin. A new derivative for the preparation of immunoconjugates of doxorubicin, *Bioconjug. Chem.* **4**, 521–527 (1993).

256. F. Kratz, DOXO-EMCH (INNO-206): the first albumin-binding prodrug of doxorubicin to enter clinical trials, *Expert Opin. Investig. Drugs* **16**, 855–866 (2007).
257. C. Unger, B. Häring, M. Medinger, J. Dreves, S. Steinbild, F. Kratz, K. Mross, Phase I and Pharmacokinetic Study of the (6-Maleimidocaproyl)Hydrazone Derivative of Doxorubicin, *Clin. Cancer Res.* **13**, 4858–4866 (2007).
258. R. Graeser, N. Esser, H. Unger, I. Fichtner, A. Zhu, C. Unger, F. Kratz, INNO-206, the (6-maleimidocaproyl hydrazone derivative of doxorubicin), shows superior antitumor efficacy compared to doxorubicin in different tumor xenograft models and in an orthotopic pancreas carcinoma model, *Invest. New Drugs* **28**, 14–19 (2010).
259. S. E. Cheperegin, B. D. Efremov, D. G. Kozlov, Precipitation of human serum albumin from yeast culture liquid at pH values below 5, *Protein Expr. Purif.* **72**, 205–208 (2010).
260. F. Dosio, P. Brusa, P. Crosasso, S. Arpicco, L. Cattel, Preparation, characterization and properties in vitro and in vivo of a paclitaxel–albumin conjugate, *J. Controlled Release* **47**, 293–304 (1997).
261. F. Dosio, S. Arpicco, P. Brusa, B. Stella, L. Cattel, Poly(ethylene glycol)–human serum albumin–paclitaxel conjugates: preparation, characterization and pharmacokinetics, *J. Controlled Release* **76**, 107–117 (2001).
262. S. Bae, K. Ma, T. H. Kim, E. S. Lee, K. T. Oh, E.-S. Park, K. C. Lee, Y. S. Youn, Doxorubicin-loaded human serum albumin nanoparticles surface-modified with TNF-related apoptosis-inducing ligand and transferrin for targeting multiple tumor types, *Biomaterials* **33**, 1536–1546 (2012).
263. R. Xu, M. Fisher, R. L. Juliano, Targeted Albumin-Based Nanoparticles for Delivery of Amphipathic Drugs, *Bioconjug. Chem.* **22**, 870–878 (2011).
264. S. Wagner, F. Rothweiler, M. G. Anhorn, D. Sauer, I. Riemann, E. C. Weiss, A. Katsen-Globa, M. Michaelis, J. Cinatl Jr., D. Schwartz, J. Kreuter, H. von Briesen, K. Langer, Enhanced drug targeting by attachment of an anti αv integrin antibody to doxorubicin loaded human serum albumin nanoparticles, *Biomaterials* **31**, 2388–2398 (2010).
265. H. Lee, S. Park, J. B. Kim, J. Kim, H. Kim, Entrapped doxorubicin nanoparticles for the treatment of metastatic anoikis-resistant cancer cells, *Cancer Lett.* **332**, 110–119 (2013).
266. F. Li, C. Zheng, J. Xin, F. Chen, H. Ling, L. Sun, T. J. Webster, X. Ming, J. Liu, Enhanced tumor delivery and antitumor response of doxorubicin loaded albumin nanoparticles formulated based on a Schiff base *Int. J. Nanomedicine* (2016) (available at <https://www.dovepress.com/enhanced-tumor-delivery-and-antitumor-response-of-doxorubicin-loaded-a-peer-reviewed-fulltext-article-IJN>).
267. Z. Fülöp, R. Gref, T. Loftsson, A permeation method for detection of self-aggregation of doxorubicin in aqueous environment, *Int. J. Pharm.* **454**, 559–561 (2013).
268. K. Kataoka, T. Matsumoto, M. Yokoyama, T. Okano, Y. Sakurai, S. Fukushima, K. Okamoto, G. S. Kwon, Doxorubicin-loaded poly (ethylene glycol)–poly (β -benzyl-l-aspartate) copolymer micelles: their pharmaceutical characteristics and biological significance, *J. Controlled Release* **64**, 143–153 (2000).
269. X. Li, D. J. Hirsh, D. Cabral-Lilly, A. Zirkel, S. M. Gruner, A. S. Janoff, W. R. Perkins, Doxorubicin physical state in solution and inside liposomes loaded via a pH gradient, *Biochim. Biophys. Acta BBA - Biomembr.* **1415**, 23–40 (1998).

270. A. Fritze, F. Hens, A. Kimpfler, R. Schubert, R. Peschka-Süss, Remote loading of doxorubicin into liposomes driven by a transmembrane phosphate gradient, *Biochim. Biophys. Acta BBA - Biomembr.* **1758**, 1633–1640 (2006).
271. A. Sosnik, Drug self-assembly: A phenomenon at the nanometer scale with major impact in the structure–biological properties relationship and the treatment of disease, *Prog. Mater. Sci.* **82**, 39–82 (2016).
272. X. Wang, X. Zhen, J. Wang, J. Zhang, W. Wu, X. Jiang, Doxorubicin delivery to 3D multicellular spheroids and tumors based on boronic acid-rich chitosan nanoparticles, *Biomaterials* **34**, 4667–4679 (2013).
273. S. Eetezadi, R. De Souza, M. Vythilingam, R. Lessa Cataldi, C. Allen, Effects of Doxorubicin Delivery Systems and Mild Hyperthermia on Tissue Penetration in 3D Cell Culture Models of Ovarian Cancer Residual Disease, *Mol. Pharm.* **12**, 3973–3985 (2015).
274. L. Han, H. Wei, B. Tu, D. Zhao, A facile one-pot synthesis of uniform core–shell silver nanoparticle@mesoporous silica nanospheres, *Chem. Commun.* **47**, 8536–8538 (2011).
275. Y.-S. Lin, C. L. Haynes, Synthesis and Characterization of Biocompatible and Size-Tunable Multifunctional Porous Silica Nanoparticles, *Chem. Mater.* **21**, 3979–3986 (2009).
276. H. Lv, S. Zhang, B. Wang, S. Cui, J. Yan, Toxicity of cationic lipids and cationic polymers in gene delivery, *J. Controlled Release* **114**, 100–109 (2006).
277. P. Pinnaduwege, L. Schmitt, L. Huang, Use of a quaternary ammonium detergent in liposome mediated DNA transfection of mouse L-cells, *Biochim. Biophys. Acta BBA-Biomembr.* **985**, 33–37 (1989).
278. H. Takahashi, Y. Niidome, T. Niidome, K. Kaneko, H. Kawasaki, S. Yamada, Modification of Gold Nanorods Using Phosphatidylcholine to Reduce Cytotoxicity, *Langmuir* **22**, 2–5 (2006).
279. E. E. Connor, J. Mwamuka, A. Gole, C. J. Murphy, M. D. Wyatt, Gold Nanoparticles Are Taken Up by Human Cells but Do Not Cause Acute Cytotoxicity, *Small* **1**, 325–327 (2005).
280. R. Cortesi, E. Esposito, E. Menegatti, R. Gambari, C. Nastruzzi, Effect of cationic liposome composition on in vitro cytotoxicity and protective effect on carried DNA, *Int. J. Pharm.* **139**, 69–78 (1996).
281. X. Ye, D. Lin, Z. Jiao, L. Zhang, The thermal stability of nanocrystalline maghemite ##IMG## [http://ej.iop.org/images/0022-3727/31/20/006/toc_img1.gif], *J. Phys. Appl. Phys.* **31**, 2739 (1998).
282. N. Lang, A. Tuel, A Fast and Efficient Ion-Exchange Procedure To Remove Surfactant Molecules from MCM-41 Materials, *Chem. Mater.* **16**, 1961–1966 (2004).
283. K. Huang, H. Ma, J. Liu, S. Huo, A. Kumar, T. Wei, X. Zhang, S. Jin, Y. Gan, P. C. Wang, S. He, X. Zhang, X.-J. Liang, Size-Dependent Localization and Penetration of Ultrasmall Gold Nanoparticles in Cancer Cells, Multicellular Spheroids, and Tumors in Vivo, *ACS Nano* **6**, 4483–4493 (2012).
284. S. Huo, H. Ma, K. Huang, J. Liu, T. Wei, S. Jin, J. Zhang, S. He, X.-J. Liang, Superior Penetration and Retention Behavior of 50 nm Gold Nanoparticles in Tumors, *Cancer Res.* **73**, 319–330 (2013).

285. M. Manzano, M. Colilla, M. Vallet-Regí, Drug delivery from ordered mesoporous matrices, *Expert Opin. Drug Deliv.* **6**, 1383–1400 (2009).
286. J.-H. Lee, Y.-M. Huh, Y. Jun, J. Seo, J. Jang, H.-T. Song, S. Kim, E.-J. Cho, H.-G. Yoon, J.-S. Suh, J. Cheon, Artificially engineered magnetic nanoparticles for ultra-sensitive molecular imaging, *Nat. Med.* **13**, 95–99 (2007).
287. F. Gazeau, M. Lévy, C. Wilhelm, Optimizing magnetic nanoparticle design for nanothermotherapy, *Nanomed.* **3**, 831–844 (2008).
288. E. C. Abenojar, S. Wickramasinghe, J. Bas-Concepcion, A. C. S. Samia, Structural effects on the magnetic hyperthermia properties of iron oxide nanoparticles, *Prog. Nat. Sci. Mater. Int.* **26**, 440–448 (2016).
289. R. E. Rosensweig, Heating magnetic fluid with alternating magnetic field, *J. Magn. Magn. Mater.* **252**, 370–374 (2002).
290. S. S. Kelkar, T. M. Reineke, Theranostics: Combining Imaging and Therapy, *Bioconjug. Chem.* **22**, 1879–1903 (2011).
291. L. Rochette, C. Guenancia, A. Gudjoncik, O. Hachet, M. Zeller, Y. Cottin, C. Vergely, Anthracyclines/trastuzumab: new aspects of cardiotoxicity and molecular mechanisms, *Trends Pharmacol. Sci.* **36**, 326–348 (2015).
292. K. Ylänen, T. Poutanen, P. Savikurki-Heikkilä, I. Rinta-Kiikka, A. Eerola, K. Vettenranta, Cardiac Magnetic Resonance Imaging in the Evaluation of the Late Effects of Anthracyclines Among Long-Term Survivors of Childhood Cancer, *J. Am. Coll. Cardiol.* **61**, 1539–1547 (2013).
293. C. Elalouani, M. A. Benhmidoun, H. Rida, M. AitRaiss, N. Derhem, A. Elomrani, M. Khouchani, A. Tahri, A. Errehmouni, R. Faouzi, A. Elguenzri, M. Elhattaoui, I. Tazi, L. Mahmal, Cardiotoxicité à court et à moyen terme des anthracyclines : étude prospective, *Ann. Cardiol. Angéiologie* **61**, 257–266 (2012).
294. M. Cruz, J. Duarte-Rodrigues, M. Campelo, Cardiotoxicity in anthracycline therapy: Prevention strategies, *Rev. Port. Cardiol. Engl. Ed.* **35**, 359–371 (2016).
295. Á. Ancochea, A. Salar, F. García-Pallarols, E. Gimeno, C. Fernández-Rodríguez, B. Sánchez-González, Prognostic impact of anthracyclines in the treatment of aggressive lymphoma in patients over 70 years, *Med. Clínica Engl. Ed.* **144**, 544–547 (2015).
296. E. Cabane, X. Zhang, K. Langowska, C. G. Palivan, W. Meier, Stimuli-Responsive Polymers and Their Applications in Nanomedicine, *Biointerphases* **7**, 9 (2012).
297. C. I. C. Crucho, Stimuli-Responsive Polymeric Nanoparticles for Nanomedicine, *ChemMedChem* **10**, 24–38 (2015).
298. J. Liu, C. Detrembleur, M.-C. De Pauw-Gillet, S. Mornet, L. V. Elst, S. Laurent, C. Jérôme, E. Duguet, Heat-triggered drug release systems based on mesoporous silica nanoparticles filled with a maghemite core and phase-change molecules as gatekeepers, *J Mater Chem B* **2**, 59–70 (2014).
299. J. Liu, Z. Luo, J. Zhang, T. Luo, J. Zhou, X. Zhao, K. Cai, Hollow mesoporous silica nanoparticles facilitated drug delivery via cascade pH stimuli in tumor microenvironment for tumor therapy, *Biomaterials* **83**, 51–65 (2016).

300. L. Chen, Z. Zhang, X. Yao, X. Chen, X. Chen, Intracellular pH-operated mechanized mesoporous silica nanoparticles as potential drug carries, *Microporous Mesoporous Mater.* **201**, 169–175 (2015).
301. Z. Luo, Y. Hu, K. Cai, X. Ding, Q. Zhang, M. Li, X. Ma, B. Zhang, Y. Zeng, P. Li, J. Li, J. Liu, Y. Zhao, Intracellular redox-activated anticancer drug delivery by functionalized hollow mesoporous silica nanoreservoirs with tumor specificity, *Biomaterials* **35**, 7951–7962 (2014).
302. S. Mornet, S. Vasseur, F. Grasset, E. Duguet, Magnetic nanoparticle design for medical diagnosis and therapy, *J. Mater. Chem.* **14**, 2161–2175 (2004).
303. G. Kong, G. Anyarambhatla, W. P. Petros, R. D. Braun, O. M. Colvin, D. Needham, M. W. Dewhirst, Efficacy of Liposomes and Hyperthermia in a Human Tumor Xenograft Model: Importance of Triggered Drug Release, *Cancer Res.* **60**, 6950–6957 (2000).
304. K. Langer, M. G. Anhorn, I. Steinhauser, S. Dreis, D. Celebi, N. Schrickel, S. Faust, V. Vogel, Human serum albumin (HSA) nanoparticles: Reproducibility of preparation process and kinetics of enzymatic degradation, *Int. J. Pharm.* **347**, 109–117 (2008).
305. K. Zhang, L.-L. Xu, J.-G. Jiang, N. Calin, K.-F. Lam, S.-J. Zhang, H.-H. Wu, G.-D. Wu, B. Albela, L. Bonneviot, P. Wu, Facile Large-Scale Synthesis of Monodisperse Mesoporous Silica Nanospheres with Tunable Pore Structure, *J. Am. Chem. Soc.* **135**, 2427–2430 (2013).

Synthèse de nanoparticules hybrides de type cœur-coquille à visées théranostiques

Résumé

Le but de ce travail de thèse a été de synthétiser de nouveaux nano-objets pour le diagnostic et le traitement du cancer. Ainsi, nous avons développé des nanoparticules hybrides constituées d'un noyau inorganique recouvert d'une couche organique de sérum albumine humaine (HSA). Le noyau inorganique est un composite constitué d'un cœur d'oxyde de fer (IO) et d'une coquille de silice mésoporeuse (MS). L'IO permet, grâce à ses propriétés magnétiques, le diagnostic par imagerie par résonance magnétique (IRM) et la thérapie par hyperthermie magnétique (HM), tandis que les porosités de la MS permettent l'encapsulation de médicaments pour la chimiothérapie. La taille des pores de la coquille MS a été modulée afin d'augmenter le taux d'encapsulation en médicament et la taille du cœur d'IO a été ajustée pour améliorer les propriétés d'HM et d'IRM. L'utilisation d'un revêtement final d'HSA en tant que gatekeeper pour la délivrance de médicaments contrôlée par action enzymatique a également été étudiée. En parallèle, des nanocapsules d'HSA chargées en médicament ont été synthétisées. Enfin, les activités biologiques de ces nanoparticules ont été testées sur différentes lignées cellulaires cancéreuses.

Mots clés : nanoparticules, théranostique, cœur-coquille, oxyde de fer, silice mésoporeuse, nanocapsule d'HSA, albumine, IRM, hyperthermie magnétique, délivrance contrôlée de médicaments

Summary

The aim of this PhD work was to synthesize and test new nano-objects for the diagnosis and treatment of cancer. For this purpose, we developed hybrid nanoparticles made of an inorganic core surrounded by a human serum albumin (HSA) organic coating. The inorganic core is a composite by itself as it is made of an iron oxide core (IO) surrounded by a mesoporous silica (MS) shell. The IO core ensures, through its magnetic properties, diagnosis by magnetic resonance imaging (MRI) and therapy by magnetic hyperthermia, whereas the MS shell allows the loading of anticancer drugs for chemotherapy within its porosities. The pore sizes of the silica shell were modulated to enhance the drug loading content and the IO core size was also tuned to improve magnetic hyperthermia as well as T_2 MRI imaging properties of the final core-shell system. The use of a thick shell of HSA as gatekeeper for controlled drug delivery triggered by its degradation with proteases was also studied. In parallel the synthesis of drug loaded HSA nanocapsules using MS as sacrificial template was performed. Finally, the biological activities of these nanoparticles were tested on various cancer cell lines.

Keywords : Nanoparticles, theranostic, core-shell, iron oxide, mesoporous silica, HSA nanocapsule, albumin, MRI, magnetic hyperthermia, controlled drug release